High Temperature Corrosion and Heat Transfer Studies of Zirconium-Silicide Coatings for Light Water Reactor Cladding Applications

By

Hwasung Yeom

A dissertation submitted in partial fulfillment of
the requirements for the degree of

Doctor of Philosophy

(Engineering Physics)

at the

UNIVERSITY OF WISCONSIN-MADISON

2017

Date of final oral examination: 07/20/2017

The dissertation is approved by the following members of the Final Oral Committee:

Michael L. Corradini, Professor, Engineering Physics

Kumar Sridharan, Research Professor, Engineering Physics

James P. Blanchard, Professor, Engineering Physics

Douglass L. Henderson, Professor, Engineering Physics

Frank E. Pfefferkorn, Associate Professor, Mechanical Engineering

© Copyright by Hwasung Yeom 2017

All Rights Reserved

Abstract

Development of protective coatings for fuel claddings (i.e., zirconium-alloys) in light water reactors has been extensively investigated to enhance safety margins in accidents as well as fuel performance under normal operation conditions. Such surface modification could also beneficially affect fuel rod heat transfer characteristics. Zirconium-silicide, a candidate coating material, is particularly attractive because zirconium-silicide coating is expected to bond strongly to zirconium-alloy substrate. Intermetallic compound phases of zirconium-silicide have high melting points and oxidation of zirconium silicide produces highly corrosion resistant glassy zircon ($ZrSiO_4$) and silica (SiO_2) which possessing self-healing qualities.

Given the long-term goal of developing such coatings for use with nuclear reactor fuel cladding, this work describes results of oxidation and corrosion behavior of bulk zirconium-silicide and fabrication of zirconium-silicide coatings on zirconium-alloy test flats, tube configurations, and SiC test flats. In addition, boiling heat transfer of these modified surfaces (including $ZrSi_2$ coating) during clad quenching experiments is discussed in detail.

Oxidation of bulk $ZrSi_2$ was found to be negligible compared to Zircaloy-4 (a common Zr-alloy cladding material) and mechanical integrity of $ZrSi_2$ was superior to that of bulk Zr_2Si at high temperatures in ambient air. Very interesting and unique multi-nanolayered composite of ZrO_2 and SiO_2 were observed, which is unlike other commonly observed in oxidation of transition metal silicides such as $MoSi_2$. A physical model for the oxidation has been proposed wherein Zr–Si–O mixture undergoes a spinodal phase decomposition into ZrO_2 and SiO_2, which is manifested as a nanoscale assembly of alternating layer of the two oxides.

Steam corrosion at high pressure (10.3 MPa) led to weight loss of $ZrSi_2$ and produced oxide scale with depletion of silicon, possibly attributed to volatile silicon hydroxide, gaseous silicon monoxide, and a solubility of silicon dioxide in water. Only Zircon phase ($ZrSiO_4$) formed during oxidation of $ZrSi_2$ at 1400 °C in air, and allowed for immobilization silicon species in oxide scale in the aqueous environments.

Zirconium-silicide coatings (on zirconium-alloy substrates) investigated in this study were deposited primarily using magnetron sputter deposition method, although powder spray deposition processes cold spray and thermal spray methods were also investigated. The optimized $ZrSi_2$ sputtered coating exhibited a highly protective nature at elevated temperatures (700 °C, 1000 °C, and 1200 °C) in ambient air by mitigating oxygen permeation to the underlying zirconium alloy substrate. The high oxidation resistance of the coating has been shown to be due to nanocrystalline SiO_2 and $ZrSiO_4$ phases in the amorphous oxide film matrix which develops at high temperatures. The coating prevented oxide formation in Zircaloy-4 substrate in high-pressure steam condition even if the top surface of the coating was degraded by formation of zirconium-rich oxide layer. Cold spray and thermal spray deposition of $ZrSi_2$ have been performed by systematically varying deposition parameters. While deposition of coating was achieved, further process optimization is required to improve coating quality deposited using these methods.

A quench test facility was designed and built to study boiling and quenching behavior of modified Zircaloy-4 surfaces (e.g., roughened surfaces, oxidized surfaces, zirconium-silicide coated surfaces) at various system conditions (e.g., elevated pressures and water subcooling). The efficacy of this test facility has been demonstrated using bare Zircaloy-4 rodlets. The experiments consisted of pressurized tests (pressure range of 0.1 MPa to 0.6 MPa in saturated water) and subcooling tests (atmospheric pressure in 0 K to 40 K subcooled water). The minimum film boiling temperature for bare Zircaloy-4 increased with increasing system pressure and water subcooling consistent with past literature data. Quenching behavior was notably affected by the type of surface modification from the reference condition (saturated water at atmospheric pressure), to pressurized conditions, and subcooled conditions. Boiling heat transfer was improved by the presence of a surface coating, surface oxidation, and surface roughening. For example, large surface heat flux was observed with vigorous bubble generation for the roughened surfaces even at high superheat, and the lower limit point of stable film boiling increased with a degree of surface oxidation. To explain the augmented boiling heat transfer by the surface modifications, a plausible hypothesis has been proposed, which is based on instantaneous and conductive heat transfer when intermittent liquid-solid contact occurs. The theoretical model successfully explains bubble dynamics of the modified surfaces

qualitatively and predicts minimum film boiling temperature of the oxidized surfaces, which is in good agreement with experimental data.

Acknowledgements

I would like to thank Professor Michael Corradini, Professor Kumar Sridharan, Professor James Blanchard, and Professor Douglass Henderson. Without their supports, the guidance, limitless trust, and encouragement, I would lose the right direction in my life and would not be here today. They are my academic advisors and my life mentors. I also would like to thank all of my committee members.

I would like to thank several individuals for their help on my research and the long journey in Madison. First, I am grateful to Dr. Hangjin Jo, my old friend, for his scientific advice. Second, Mr. Paul Brooks for his technical guidance to build experimental facility; I am indebted to him. Third, to the friends in our research group who gave me technical insights, helps, and discussions, namely Ben Maier, Greg Johnson, Dr. Alex Mairov, Cody Lockhart, Ben Hauch, Steven Fronek, Muhammet Arik, and Dhongik Yoon. In particular, I am thankful to Kathy Wegner and Dr. Scott Greenwood. They are my friends with warm heart.

I would like to say thank to friends at Wisconsin including Junho Lee, Hongseung Yeon, Yegu Kang, and Tammy Park. I never forget Professor Hyun Sun Park's hug and encouragement when I went through a difficult time.

Finally, I am grateful for the endless support and love from my family members: my father Gwonchul, my dearest mother Sunhee, and my two brothers Woosung and Insik.

I would like to address closing remarks with mentioning one sentence which I kept in mind every day during my PhD program.

"The greatest glory in living lies not in never falling but in rising every time we fall."

Table of Contents

Abstract ..... **i**
Acknowledgements ..... **iv**
Table of Contents ..... **v**
List of Figures ..... **viii**
List of Tables ..... **xxii**
Nomenclature ..... **xxiii**
1. Introduction **1**
1.1. Motivation 1
1.2. Research Goals and Scope 4
2. Literature Review **6**
2.1. High Temperature Corrosion of Zirconium Alloy 6
2.2. Pool Boiling 9
2.3. Zirconium silicide 11
2.4. Coating Methods 13
2.5. Oxidation of Transition Metal Silicides 17
2.6. Oxidation of Zr-silicide 26
2.7. Surface Modification for Heat Transfer in Quenching Process 27
2.8. Pressure Effect on Minimum Film Boiling Temperature (T_{min}) 31
2.9. Conclusion of Literature Review 36
3. Experimental Description **38**
3.1. Raw Materials 38
3.2. Coating Fabrication 39
3.3. Mechanical Test and Corrosion Test 42
3.4. Material Characterization 43
3.5. Quenching Test 44
3.5.1. Facility Description 44
3.5.2. Quench Experimental Procedures 51
3.5.3. Post-processing of Measured Data 52
4. Results and Discussions **63**
4.1. Oxidation/Corrosion behavior of bulk Zr-silicide material 63
4.1.1. High temperature air oxidation 63
4.1.2. High pressure steam corrosion 84
4.2. Optimization of magnetron sputter coating on Zr-alloy for oxidation resistance 96

4.2.1. Parametric investigation for coating quality 96
4.2.2. High temperature air oxidation 112
4.2.3. High pressure steam corrosion 125
4.3. Investigation of spray deposition coating 133
4.3.1. Cold spray 134
4.3.2. Thermal spray coating deposition process 138
4.4. Quenching experiment for bare Zircaloy-4 146
4.4.1. Reference condition (saturated water in atmospheric pressure) 146
4.4.2. Pressurized conditions 153
4.4.3. Subcooling conditions 163
4.5. Quenching experiments for the modified surfaces 172
4.5.1. Surface preparation and characterization 173
4.5.2. Reference condition 181
4.5.3. Pressurized condition (0.5 MPa) 192
4.5.4. Subcooling condition (ΔT_{sub} = 15K) 200
4.6. Hypothesis of minimum film boiling temperature for the modified surfaces 208
4.6.1. Hypothesis and Assumptions 209
4.6.2. Estimation of localized temperature drop 216
4.6.3. Prediction of minimum film boiling temperature for oxidized surfaces 225
5. Summary & Future Work 233
6. Publications 235
6.1. Journal Articles: 235
6.2. Conference Proceedings 236
6.3. Conference Presentations/Abstracts. 237
References Cited 238
Appendix 248
Appendix A: Matlab code for T_{min} calculation 248
Appendix B: Matlab code for vapor film thickness 250
Appendix C: Labview code for data acquisition in quenching experiment 252
Appendix D: CAD design for quenching facility 254
Appendix E: Quenching/Boiling curves of three repeated tests 263
Appendix F: Thickness of vapor layer on bare Zirc-4 samples with pressures and degrees of subcooling 272
Appendix G: Oscillations of vapor layer for $ZrSi_2$ coating surfaces and $ZrSi_2$ coating on rough surfaces 274

Appendix H: Summary of quenching time and minimum film boiling temperatures for all test conditions (environmental effect and surface effect)..... 276

List of Figures

Figure 1: Various stages of loss of coolant accident in LWR [4]. 2
Figure 2: Design objective of ATF system addressed in DOE report to U.S. Congress. 3
Figure 3: Cross-sectional light microscopy image of Zircaloy-4 after oxidation at 1400 °C steam for two minutes [23]. 7
Figure 4: Zirconium-oxygen binary phase diagram showing various crystallographic phases which have a profound effect on mechanical behavior of Zr-alloy cladding under LOCA conditions [30]. 8
Figure 5: Pool boiling curve showing heat flux vs. wall superheat [31]. 10
Figure 6: Zr-Si binary phase diagram [38]. 12
Figure 7: (a) Atomic arrangements on (001) atomic plane [34], and (b) a conventional unit cell of $ZrSi_2$ [35]. 13
Figure 8: Schematic illustration of magnetron plasma vapor deposition process. 15
Figure 9: Schematic representation of microstructure of coatings by magnetron sputtering using argon ions. T is substrate temperature and T_m is a melting point of the coating material. [49]. 16
Figure 10: Schematic illustration of cold spray system [52]. 16
Figure 11: Thickness of oxide layer of $MoSi_2$, $TaSi_2$, WSi_2, and $TiSi_2$ in wet oxygen or dry oxygen environments as a function of time [54]. 18
Figure 12: Proposed model for thermal growth SiO_2 layer on transition metal silicide [54]. 19
Figure 13: Possible oxidation pathway for oxidation of transition metal disilicides [56]. 21
Figure 14: Gibbs free energies of oxide formation for Zr, Ti, Si, Ta, W, and Mo per 1 mole O_2, calculated by HSC Chemistry thermodynamics software. 22
Figure 15: Isothermal weight gain curves for $MoSi_2$ at high temperature in ambient air [61]. 23
Figure 16: Backscatter secondary electron (BSE) cross sectional SEM images of $MoSi_2$ oxidized in air at (a) 1400 °C, (b) 1550 °C, and (c) 1700 °C for 100 hours [61]. 23
Figure 17: Cross-sectional images of $TiSi_2$ oxidized in air at 1100 °C for 100 hour at different region of the sample [63]. 25
Figure 18: Weight gain of $TiSi_2$ in air at elevated temperatures [63]. 25
Figure 19: Weight gain curve for $ZrSi_2$ with 4 at.% Al in air in the range of 600 °C to 1100 °C for 160 hours. 26
Figure 20: Differential thermal analysis (DTA), thermogravimetric mass analysis (TG), and differential thermogravimetric mass analysis (DTG) curves during $ZrSi_2$ oxidation in flowing air. Heating rate was 10 °C/min. 27
Figure 21: Boiling curve of aluminum cylinder as a function of repeated quenching tests. [71] 28

Figure 22: Quench phenomena (bubble dynamics) on SS rodlet at 20 K subcooling. (a) a quench test in pure water and (b) is the test of alumina nanoparticle coated surface in the nanofluid (4^{th} test in the nanofluid). The arrows indicate quench front propagation. 30
Figure 23: SEM images of (a) bare zirconium, (b) roughened surface, and (c) anodized surface. The upper inset is the water droplet on the surface showing contact angle. 30
Figure 24: (a) Temperature history during the quench test and (b) estimated boiling curve. BZS is bare zirconium surface, RZS is roughened zirconium surface and CWS is completely wettable surface. 31
Figure 25: T_{min} vs. system pressure in saturated water with different heater diameter. Berenson model is plotted as the dot line [82]. 34
Figure 26: T_{min} vs. pressure curve of saturated liquids. 35
Figure 27: T_{min} vs. Pressure for different materials [84]. 36
Figure 28: A photograph of PVD chamber, showing Zr-4 flat and tube samples for coating deposition in the present study. 40
Figure 29: Photograph of the cold spray system in University of Wisconsin-Madison. 41
Figure 30: Photographs of thermal spray system at Thermal Spray Technologies used for the current study. 41
Figure 31: A photograph of the high pressure/high temperature autoclave (NS4653, Parr Instrument Company) 43
Figure 32: Schematic illustration of the quenching test facility designed and built for this research. 45
Figure 33: A photograph of the quenching test facility. 45
Figure 34: Photograph of the air actuator and the aluminum connector. 46
Figure 35: (a) Schematic illustration of the Teflon seal assembly and (b) a picture of the assembly. 47
Figure 36: Photographs of the heating zone, consisting of (a) a heating tape, (b) kawool insulation, and (c) microtherm insulation molding. 48
Figure 37: (a) Schematic illustration and (b) a photo of the test section. 49
Figure 38: Photograph of the quenching chamber. 50
Figure 39: A schematic diagram of the electric circuit of the quenching facility. 51
Figure 40: Two-dimensional transient heat conduction problem for plane wall [88] 53
Figure 41: Problem definition for INTEMP model in the current study. 55
Figure 42: Boiling curves calculated with three different smoothing factors. 56
Figure 43: Boiling curves of bare Zirc-4 plotted by lumped capacitance method, one-dimensional INTEMP, and two-dimensional INTEMP analysis. 57
Figure 44: Boiling curves with different heat transfer coefficients on the top surface in INTEMP model. 58

Figure 45: Boiling curves of a bare Zirc-4 quenching experiment calculated with three different square mesh sizes in the two-dimensional INTEMP model. 59
Figure 46: (a) Surface heat flux and rate of the surface heat flux are plotted in quenching time. The red dots indicate dq"/dt equals to zero. (b) the minimum film boiling temperature and minimum heat flux are defined by the criterion shown in the boiling curve. 61
Figure 47: Binary images of (a) a reference image without vapor film and (b) an image with vapor film in Matlab code. The red arrows indicate boundary at the center of the test section to count the number of pixels. 62
Figure 48: Weight gain vs. exposure time for (a) Zirc-4 and (b) bulk $ZrSi_2$ samples constructed with least square fits at 700 °C, 1000 °C, and 1200 °C in ambient air 64
Figure 49: Cross-sectional SEM images of the dense $ZrSi_2$ at (a) 700 °C, (b) 1000 °C, (c) 1200 °C, and (d) 1400 °C for 5-hour exposure in air. The red arrows indicate the oxide layer between a mounting resin and unreacted $ZrSi_2$ 65
Figure 50: Gibbs free energies of oxide formation for Zr, Ti, Si, Ta, W, and Mo per 1 mole O_2, calculated by HSC Chemistry thermodynamics software. 66
Figure 51: XRD patterns of the $ZrSi_2$ oxidized at (a) 700 °C, (b) 1000 °C, and (c) 1200 °C for 5 hours showing monoclinic zirconia, silicon, and $ZrSi_2$ peaks. 67
Figure 52: XRD pattern of oxidized $ZrSi_2$ at 1200 °C for 50 hours in ambient air, revealing crystalline $ZrSiO_4$ (zircon) phase 68
Figure 53: Plan-view of SEM images of (a) as-received $ZrSi_2$, (b) $ZrSi_2$ oxidized at 700 °C for 5 hours, (c) high voltage SEM (12 kV) image of the oxidized sample, and (d) EDS compositions in regions indicated in (c). Points 1 and 2 indicate the regions of spherical phases shown in the image (b). 69
Figure 54: SEM plan-view images of oxidized $ZrSi_2$ at (a) 1000 °C for 5-hours, (b) 1200 °C for 5-hours, (c) 1200 °C for 50-hours and (d) 1400 °C for 5-hours in ambient air. 70
Figure 55: XPS spectrum (Si2p, Zr3d, O1s binding energy) of $ZrSi_2$ oxidized at 700 °C, 1000 °C, and 1200 °C after 5-hour oxidation. Position of the peak maximum (eV) is specified and the arrows indicate the trend in binding energy shift with increasing temperature (from 700 °C to 1000 °C/1200 °C). The red arrows and blue arrows are associated with silicon and zirconium, respectively. 72
Figure 56: (a) HAADF STEM cross sectional image of $ZrSi_2$ oxidized at 700 °C for 10 hours and (b) corresponding EDS line-scan showing composition fluctuation even in the thin (~630 nm) oxide layer. The red arrows indicate Si-rich oxide. (c) cross sectional SEM image with low voltage (3 kV) of the oxide layer on $ZrSi_2$ formed at 1000 °C for 5 hours at low magnification and (d) and at high magnification near the top layer. 74

Figure 57: SEM images of $ZrSi_2$ oxidized at 1200 °C for 5 hours, taken at (a) 12kV and (b) 3kV at low magnifications. High magnification 3kV SEM images (c) at interface between air and oxide layer and (d) in the middle of oxide scale showing different shapes of nanoscale structures. 75
Figure 58: EDS spectra mapping (a) of oxidized $ZrSi_2$ at 1200 °C for 5 hours showing Si depleted region, and point EDS analysis (b) at the interface between oxide layer and unreacted $ZrSi_2$. The carbon signal is an artifact from the mounting resin. 76
Figure 59: HAADF STEM cross sectional images of $ZrSi_2$ oxidized at 1200 °C for 5 hours. (a) nanoscale spherical phases at the interface with air (i.e., top surface) and (b) irregular structures uniformly dispersed in oxide scale. The inset shows SiO_2 diffraction pattern indicating an amorphous structure. The platinum layer was deposited on the top of the sample during sample preparation by FIB. Higher atomic number material exhibits brighter contrast in these images. (c) Bright field STEM image and STEM-EDS elemental mapping images of the irregular structures. These images clearly indicate the irregular structures consist of ZrO_2 and amorphous SiO_2 77
Figure 60: (a) SEM cross sectional images of oxidized $ZrSi_2$ at 1400 °C for 5 hours and (b) schematic diagram of a reaction model for the formation of $ZrSiO_4$ by a reaction of ZrO_2 and SiO_2 solid phases by Veytizou et al. [103]. 78
Figure 61: Schematic illustration of the microstructural evolution during isothermal oxidation of $ZrSi_2$ oxidation at (a) 700 °C, (b) 1000 °C, (c) 1200 °C, (d) 1400 °C. c=crystalline and a=amorphous. The features in the figures are disproportionately scaled for clarity. 81
Figure 62: Photograph showing the oxidized $ZrSi_2$ and Zr_2Si after oxidation at 1200 °C for 1 hour in air. 82
Figure 63: Cross-sectional SEM images of a Zr_2Si samples oxidized at 1200 °C for 1 hour. (a) Red dots in the high voltage (12kV) SEM image indicate the particle boundary, (b) cracks leading to structural disintegration were identified in ZrO_2 region, and (c) spinodal structures are seen locally near $ZrSi_2$ phase. 83
Figure 64: Full-theta X-ray diffraction (XRD) peaks of the Zr_2Si oxidized at 1200 °C for 1 hour in air... 84
Figure 65: Photographs of (a) as-polished bulk $ZrSi_2$ before corrosion test at 330 °C and 18.6 MPa in pure water for 72 hours and (b) the samples after the autoclave test. 85
Figure 66: SEM plan-view images of (a) as-polished $ZrSi_2$ and (b) $ZrSi_2$ after 330 °C, 18.6 MPa water corrosion test. 85
Figure 67: Cross-sectional SEM images of bulk $ZrSi_2$ after the water corrosion tests at 330 °C and 18.6 MPa for 72 hours: (a) low magnification, and (b-d) local areas with high magnifications. The red arrows indicate pores in $ZrSi_2$ matrix. 87

Figure 68: EDS analysis of cross-section of bulk $ZrSi_2$ after the water corrosion test at 330 C and 18.6 MPa for 72 hours: (a) elemental mapping and (b) elemental point scan. 87
Figure 69: Formation of thin oxide layers on bare silicon surface after high temperature oxidation at (a) 700 °C for 100 hours and (b) 1400 °C for 5 hours. The images are SEM cross-sectional fracture surface images. 88
Figure 70: Weight change for bare Zirc-4, $ZrSi_2$, Si, and pre-oxidized samples (700 °C for 100 hours and 1400 C for 5 hours) after the steam test at 400 °C and 10.3 MPa for 72 hours. 89
Figure 71: SEM plan view images for (a) bare $ZrSi_2$ and (b) pre-oxidized $ZrSi_2$ (700 °C for 100 hours in ambient air) after steam corrosion test at 400 C and 10.3 MPa for 72 hours. 90
Figure 72: (a) High magnification SEM plan-view image of pre-oxidized $ZrSi_2$ (700 °C for 100hrs) after the steam autoclave tests (400C, 10.3 MPa for 72 hrs) and (b) results of corresponding EDS average scan. 91
Figure 73: SEM plan-view images of (a) bare Si, (b) bare Si after steam test, (c) pre-oxidized Si at 700 °C for 100 hours, (d) pre-oxidized Si (700 °C) after the steam test, (e) pre-oxidized Si at 1400 °C for 5 hours, and (f) pre-oxidized Si (1400 °C) after the steam test. The steam test was performed at 400 °C and 10.3 MPa for 72 hours in pure water. The silicon and oxygen atomic percent on each surface are specified. 93
Figure 74: (a) SEM plan-view image of pre-oxidized $ZrSi_2$ (1400 °C for 5 hours in air) after the steam corrosion test at 400 °C at 400 °C and 10.3 MPa for 72 hours in pure water, and (b) results of EDS chemical analysis for the corresponding area. 96
Figure 75: (a) SEM image of $ZrSi_2$ coating without the plasma surface cleaning of Zirc-4 substrate and (b) photograph of Zirc-4 flats after plasma surface cleaning. 98
Figure 76: SEM plan-view images of coatings of (a) $ZrSi_2$ deposited at 1.33 Pa Ar gas pressure and (b) $ZrSi_2$ deposited at 0.53 Pa Ar gas pressure on Zirc-4 substrate. SEM cross-sectional fracture surface images of (c) $ZrSi_2$ deposited at 1.33 Pa Ar gas pressure and (d) $ZrSi_2$ deposited at 0.53 Pa Ar gas pressure on a silicon wafer. The dimensional difference for the microstructure in Figure 76a and Figure 76c is attributed to nature and roughness of the substrates. The image in Figure 76a was from the coating deposited on 600 grit surface finish Zirc-4 substrate while Figure 76c is the image of the coating deposited on atomically smooth Si wafers. 99
Figure 77: XRD patterns of thin coatings (Zr_2Si, ZrSi, and $ZrSi_2$) deposited at 1.33Pa Ar and 135 W at room temperature for 150 minutes with 2° incident x-ray beam. Only zirconium peaks from the underlying substrate were identified. 100
Figure 78: (a) Cross-sectional bright field TEM image and (b) diffraction pattern of $ZrSi_2$ (deposited at 0.53 Pa Ar pressure and room temperature). The coating thickness was 3 μm and was prepared by a four-step deposition for the diffraction pattern observation because an electron beam should illuminate the area of

interested through the SAD aperture (1 μm diameter). Coating growth direction is indicated by the black dot arrow. 101
Figure 79: Weight gain of the zirconium-silicide coatings with different compositions (Zr_2Si, ZrSi, and $ZrSi_2$) in 700 °C air oxidation test. The coatings were deposited at 0.53 Pa argon pressure. 103
Figure 80: SEM cross sectional images of (a, d) Zr_2Si, (b, e) ZrSi, and (c, f) $ZrSi_2$ coatings at low and high magnifications after 700 °C for 5-hours air oxidation test. The high magnification images were acquired in the areas indicated by the red frames in the low magnification images. Cu layer was deposited on the coating surface by electroplating to minimize coating damage and edge retention during the sample preparation. All the coatings were deposited at 0.53 Pa argon pressure. 103
Figure 81: SEM plan-view images of oxidized zirconium-silicide coatings (a) Zr_2Si, (b) ZrSi, and (c) $ZrSi_2$ after the scratch test (250g, applied load). The red arrows indicate scratch tracks. 105
Figure 82: XPS O1s spectra of zirconium-silicide coatings after 700 °C for 5-hours oxidation: (a) Zr_2Si, (b) ZrSi, and (c) $ZrSi_2$. The O1s spectra were resolved into possible oxide components (red curve: $ZrSiO_4$, green curve: SiO_2, and blue curve: ZrO_2). The measured spectrum is indicated by dark curve. The coatings were deposited on Zirc-4 substrate under 0.53 Pa Ar pressure and room temperature. 107
Figure 83: SEM cross-sectional images (5kV) of the multilayered coating on Si wafer at (a) low magnification and (b) high magnification. The red arrows indicate the interface between each compositional layer. (c) SEM image with high voltage (12kV) for EDS line scan and (d) corresponding the EDS line scan result for Si and Zr concentration. 108
Figure 84: SEM cross-sectional images of the multilayered coating on Zirc-4 substrate after exposure at 700 °C for 5 hours: (a) imaged at 3 kV and (b) imaged at 12 kV. The red arrows indicate tapered structures being initiated in the Zr_2Si layer. (c, d) results of EDS line scan in terms of Zr, Si, O, and Cu. 109
Figure 85: SEM cross-sectional images of (a) Zr_2Si, (b, c) ZrSi, and $ZrSi_2$ annealed at 700 °C for 5 hours in argon gas. Interface between the coating and the substrate and silicon diffused zone are indicated by the red dot line and red arrow, respectively. A ratio of zirconium-to-silicon at the dark cross is stated on each figure as measured by EDS point scan analysis. 112
Figure 86: SEM cross-sectional image of as-deposited $ZrSi_2$ coating on silicon water for the 700 °C, 1000 °C, and 1200 °C oxidation tests. 113
Figure 87: SEM cross-sectional image of (a) oxidized $ZrSi_2$ coating on Zirc-4 at 700 °C for 20 hours. Interface between the coating and the substrate is indicated by the red dots. (b) XRD pattern for the oxidized $ZrSi_2$ on Zirc-4 at 700 °C for 20 hours. The dark arrow in Figure 87b points to broad halo (or hump) associating with the thin oxide layer in Figure 87a. 115
Figure 88: SEM plan-view images of (a) $ZrSi_2$ oxidized at 1000 °C for 1 hour, (b) $ZrSi_2$ with pre-oxidation (700 °C for 5 hours) oxidized at 1000 °C for 1 hour, and (c) cross-sectional image of $ZrSi_2$ with pre-

oxidation (700 °C for 5 hours) oxidized at 1000 °C for 1 hour, showing cracks and Si rich area in the thick oxide scale. The samples were rapidly heated up to the high temperature air. After the exposure, the coating was air-cooled to room temperature..... 117
Figure 89: SEM cross-sectional images and EDS line scan of $ZrSi_2$ with the pre-oxidation (700 °C for 5 hours) after the 1000 °C for 1-hour air oxidation: (a) Low magnification and (b) EDS line scan result. The red dots and the solid red arrow in Figure 89a refer to interface between the coating and substrate and the EDS scan direction, respectively. High magnification cross-sectional SEM images of top surface of the pre-oxidized coatings after (c) the 1000 °C for 1 hour and (d) the 1200 °C for 10 minutes. The red solid arrows in Figure 89c-d refer to the thin protective layer consisting of nanoscale ZrO_2 phases in SiO_2 matrix.... 118
Figure 90: Photograph of (a) oxidized $ZrSi_2$ coatings on Zirc-4 flats and (b) oxidized $ZrSi_2$ coatings on SiC flats at 1400 C for 5 hours in ambient air. 120
Figure 91: SEM plan-view images of (a) bare SiC sample, (b) as-deposited $ZrSi_2$ coating on SiC and (c) and (d) as-deposited $ZrSi_2$ coating on SiC after oxidation at low magnification and high magnification, respectively. The insets show area-average EDS results on each surface. The oxidation test was performed at 1400 °C for 5 hours in ambient air..... 121
Figure 92: XRD pattern for oxidized $ZrSi_2$ coating on SiC after exposure at 1400 °C for 5 hours in ambient air. 122
Figure 93: SEM cross-sectional images of oxidized $ZrSi_2$ coating on SiC substrate at 1400 °C for 5 hours in ambient air with (a) low and (b) high magnification. 124
Figure 94: (a) Cross-sectional image of oxidized $ZrSi_2$ coating on SiC for EDS line scan analysis. The red arrow indicates a path of data collections and (b) the results for Si, Zr, O, and Cu are plotted. The Cu signal was detected from Cu plated layer prepared during a sample preparation. 125
Figure 95: (a) SEM cross-sectional image of the double-layered Zr-Si coating on Si wafer and (b) EDS line scan result corresponding to the red arrow. 128
Figure 96: SEM plan view images of zirconium-silicide coatings on Zirc-4 and results of EDS analysis after the steam autoclave test: (a, b) as-deposited $ZrSi_2$ coating (ZrSi#1) at low and high magnifications, (c, d) pre-oxidized $ZrSi_2$ coating (ZrSi#2) at low and high magnifications, and (e, f) pre-oxidized double-layered coating (ZrSi#4) with magnification..... 129
Figure 97: SEM cross-sectional images of (a) bare Zirc-4, (b) as-deposited $ZrSi_2$ (ZrSi#1), (c) pre-oxidized $ZrSi_2$ at 700 °C (ZrSi#2), and (d) pre-oxidized double-layered coating (ZrSi#4) after the steam corrosion test. Cu plating was performed on the corroded surfaces as a surface protection. The white arrows indicate the oxide scales. 131
Figure 98: EDS spectra mapping of the pre-oxidized $ZrSi_2$ at 700 °C (ZrSi#2) after the steam corrosion test, showing unreacted $ZrSi_2$ coating on Zirc-4 substrate. 131

Figure 99: Plan-view SEM images of (a-b) as-prepared zircon surface (ZrSi#5) on SiC with magnification, and (c-d) the zircon surface (ZrSi#5) after the steam corrosion test. 133
Figure 100: SEM plan-view images of (a) as-received $ZrSi_2$ powder and (b) a local area of $ZrSi_2$ cold-sprayed coating on Zirc-4 surface. 135
Figure 101: X-ray diffraction patterns for as-received $ZrSi_2$ powders and (b) $ZrSi_2$ coating deposited by cold spray process. 136
Figure 102: Cross-sectional SEM images of cold spray coatings of $ZrSi_2$ deposited at (a) 600 °C, (b) 700 °C, and (c) 800 °C gas preheat temperatures. Single-pass deposition was used in the spraying process. 136
Figure 103: SEM plan-view images of (a) $ZrSi_2$ cold sprayed surface using the as-received powder and (b) the sprayed surface using the ball-milled powder. Two-pass deposition was performed in the both cases. 137
Figure 104: SEM cross-sectional images of $ZrSi_2$ cold sprayed coating with the ball-milled power at (a) 600 °C, (b) 700 °C, and (c) 800 °C gas pre-heat temperatures. Single-pass deposition was used in the spraying process. 137
Figure 105: SEM cross-sectional images of $ZrSi_2$ cold spray coating on Zirc-4 substrate at (a) a single pass (b) four passes. The preheat gas temperature was 700 °C. 138
Figure 106: SEM plan-view image of a $ZrSi_2$ splat on thermal sprayed Zirc-4 substrate. 139
Figure 107: Surface morphologies of the $ZrSi_2$ coatings at different spray distance. (a) 7.6 cm, (b) 10.2 cm, and (c) 12.7 cm. 141
Figure 108: SEM image of cross-section of the $ZrSi_2$ coatings at different spraying distance. (a) 7.6 cm, (b) 10.2 cm, and (c) 12.7 cm. 142
Figure 109: XRD patterns of the $ZrSi_2$ thermal spray coatings prepared using various spraying distances. 143
Figure 110: SEM cross-sectional image of (a) local area of the thermal sprayed $ZrSi_2$ coating, (b) arc-melted bulk $ZrSi_2$, and (c) Zr-Si binary phase diagram [120] indicating cooling path and possible phase formation. 144
Figure 111: Cross-sectional image of thermal spray coating of $ZrSi_2$ without grit blast of Zirc-4 substrate. The red arrows indicate the local area showing coating damages during sample preparations. Only 320 grit SiC grinding was used. 145
Figure 112: Photograph of oxidized thermal spraying ($ZrSi_2$ coating) at 700 °C air for 10 hours. Coating delamination was clearly identified. 146
Figure 113: Quenching curves of (a) three consecutive tests for the same Zirc-4 sample and (b) three individual tests for different Zirc-4 samples. The tests were performed under saturated water in ambient pressure. 147

Figure 114: Measured temperature at the center of bare Zirc-4 sample and estimated surface temperatures by INTEMP with two assumptions (non-oxidized and 50 μm oxide on the surface). 149
Figure 115: Typical boiling curve of bare Zirc-4 specimen during quenching at saturated water in ambient pressure, estimated by using INTEMP. 150
Figure 116: High speed images (100 fps) of bare Zirc-4 specimen during quenching at saturated water in ambient pressure, showing transition of boiling regime over time. 151
Figure 117: Film thickness (green) with polynomial fit (thick dark line) and surface temperature (blue dash) during quenching test. 152
Figure 118: (a) Quenching curves (temperature-time history at the center of the sample) and corresponding boiling curves estimated by INTEMP software at elevated pressures. 155
Figure 119: High-speed images (100 fps) of bare Zirc-4 specimen during quenching in saturated water at 0.33 MPa. 156
Figure 120: Vapor layer thickness (green) with a quadratic polynomial fit (thick dark line) and estimated surface temperature (blue dash) during a quenching test at 0.55 MPa. 157
Figure 121: Averaged vapor film thickness using a quadratic polynomial fit using the high-speed images in stable film boiling regime at different pressures. 159
Figure 122: Prediction of vapor layer thickness based on Lubin's analytical derivation [136]. Vapor properties were determined by the film temperature, $(T_{wall}+T_{water})/2$. 159
Figure 123: Wavy motion of vapor film in the stable film boiling regime at 0.1 MPa (black solid line) and 0.63 MPa (red dots). The vapor film thickness was converted from high-speed images (100 fps). 160
Figure 124: Minimum film boiling wall temperatures for water at elevated system pressures. 163
Figure 125: Quenching curves (temperature-time history at the center of the sample) and corresponding boiling curves for bare Zirc-4 estimated by INTEMP software in subcooled water. 165
Figure 126: High-speed images (100fps) of bare Zirc-4 sample during quenching at ΔT_{sub} = 25 K water (75 °C water). 166
Figure 127: Vapor film thickness (thin green line) with a quadratic polynomial fit (thick black line) and estimated surface temperature (blue dash) during quenching test at 85 °C water. 167
Figure 128: Vapor film thickness using a quadratic polynomial fit of high-speed images in stable film boiling regime at different water subcooling. 168
Figure 129: Predicted vapor film thicknesses on a vertical surface based on Michiyoshi et al. [141]. Vapor properties were determined at the film temperature. 169
Figure 130: Oscillation of vapor film interface in the stable film boiling regime at the saturation condition (black solid line) and at 20 K subcooled water (red dots). The vapor film thickness was measured using high-speed images (100 fps). 170

Figure 131: Comparison of present results with predictions by experimental data and correlations for the minimum film boiling wall temperature for water. 171
Figure 132: Film boiling heat flux (experimental results and theoretical predictions) at saturation in ambient pressure and 0.5 MPa and 15 K subcooling for bare Zirc-4 samples. 172
Figure 133: (a) A photograph of the facility for a sand blaster at UW-Madison, and (b) SEM plan-view image for alumina media for the surface roughening process. 173
Figure 134: A schematic diagram of magnetron sputter deposition for the cylindrical test sections. Two-step deposition was performed to make coating deposition uniform. 174
Figure 135: Photograph of (a) a cylindrical Zirc-4 sample on the aluminum supports and (b) a $ZrSi_2$ thin coating on Zirc-4 samples (CS-surface). 175
Figure 136: Images of the modified surfaces on Zirc-4 flats and cylindrical Zirc-4 samples after three consecutive quenching tests (1: bare surface, 2: CS-surface, 3: pre-oxidized surface, 4: roughened surface, and 5: CR-surface). 176
Figure 137: Microscopic surface morphology characterized by SEM on (a) bare surface, (b) thin $ZrSi_2$ coating on smooth surface (CS-surface), (c) rough surface, and (d) thin $ZrSi_2$ coating on rough surface (CR-surface) flats. 177
Figure 138: Roughness profile of a bare surface and a CS-surface (acquisition area: 177 μm × 177 μm) flats after three quenching tests, measured by a white light interferometer at UW-Madison. 178
Figure 139: Cross-sectional SEM images of (a) rough surface and (b) CR-surface flats after three quenching tests. The R_a values were averaged from images on five different locations of the sample. 179
Figure 140: SEM cross-sectional images of (a) bare surface, (b) pre-oxidized surface, and (c) CS-surface after three repeated quenching tests. All the images were acquired at the same magnification. The oxide layer and coating on the surfaces were indicated by the red arrows. 180
Figure 141: Water static contact angle measurements of the quenched surfaces: (a) smooth surface, (b) thin coating on smooth surface (CS-surface), (c) pre-oxidized surface, (d) rough surface, and (e) thin coating on rough surface (CR-surface). 181
Figure 142: (a) Quenching curves and (b) boiling curves of modified surfaces in saturation water at atmospheric pressure. The experimental reliability of the tests was discussed in section 4.4.1. 183
Figure 143: High-speed images (100fps) of bubble evolution on the modified surfaces during quenching tests in saturated water at atmospheric pressure. 186
Figure 144: Vapor layer thickness (green) and estimated surface temperature (black dash) for the modified surfaces during a quenching test in saturated water at ambient pressure. 187
Figure 145: Averaged vapor film thickness for the modified surfaces using a quadratic polynomial fit suing the high-speed images at initial quenching process. 188

Figure 146: Fluctuation of vapor film at high wall superheat for the bare surface (black line) and the rough surface (red dots). The vapor film thickness was measured by high-speed images (100 fps). 189
Figure 147: Surface temperature of minimum film boiling point for bare surface, CS-surface, and pre-oxidized surface at saturated conditions. 190
Figure 148: Comparison of the boiling curves for modified surfaces in saturated water reported in literatures and the present study. (a) Silica nanoparticle coating on a 304 stainless steel sphere (diameter of 10 mm) and the bare sphere [77], (b) CuO microparticle coating on a brass sphere (diameter of 15 mm) and the bare sphere [145], and (c) the cylindrical Zirc-4 sample with the rough surface and the bare sample. The extended lines indicate possible boiling curves above the temperature range. 191
Figure 149: (a) Quenching curves and (b) boiling curves for the modified surfaces in saturation water at 0.5 MPa condition. 194
Figure 150: High-speed images (125 fps) of bubble dynamics on the modified surfaces during quenching experiments in the saturated water around 0.5 MPa. 196
Figure 151: Vapor film thickness (green) and estimated surface temperature (black dash) for the modified surfaces during quenching tests in saturated water at 0.5 MPa. 197
Figure 152: Average vapor film thickness for the modified surfaces at 0.5 MPa using a quadratic polynomial fitting of the high-speed images at initial quenching process. 198
Figure 153: Wavy motion of vapor film of the bare Zirc-4 (black line) and the roughened Zirc-4 (red dots) at the initial quenching under the pressurized condition (0.5 MPa). The vapor layer thickness was measured by the high-speed images (125 fps). 199
Figure 154: Average minimum film boiling temperature for bare surfaces, CS-surfaces, and pre-oxidized surfaces in saturation water at 0.5 MPa. 200
Figure 155: (a) Quenching curves and (b) boiling curves for the modified surfaces in subcooled water (ΔT_{sub}=15K) at atmospheric condition. 202
Figure 156: High-speed images (125 fps) of bubble dynamics on the modified surfaces during quenching experiments in the subcooled water (ΔT_{sub} = 15 K) at atmospheric pressure. 204
Figure 157: Vapor film thickness (green) and surface temperature (black dash) for the modified surfaces during quenching tests in subcooled water (ΔT_{sub} = 15 K) at atmospheric pressure. 205
Figure 158: Average vapor film thickness for the modified surfaces in subcooled water (ΔT_{sub} = 15 K) using a quadratic polynomial fit of the high-speed images at early quenching process. 206
Figure 159: Wavy motion of vapor film of bare Zirc-4 (black line) and the roughened Zirc-4 (red dots) at the early quenching under subcooled water (ΔT_{sub}= 15 K) measured by the high speed-images (125 fps). 207

Figure 160: Average minimum film boiling temperature for bare surfaces, CS-surfaces, and pre-oxidized surfaces in subcooled water (ΔT_{sub}= 15 K) at atmospheric pressure. 208
Figure 161: Schematic illustration of bubble dynamics during liquid-solid contact at high wall superheat depending on different surface properties: (a) bare surface, (b) surface with thick oxide layer, and (c) surface feature on roughened surface. 213
Figure 162: A linear fit and experimental results of average heat flux during droplet impingement experiments by Chen (1995) [155]. 215
Figure 163: Schematic illustration of half space with a thin surface layer with axisymmetric surface heat flux, simulating instantaneous liquid contact on heated surface. 219
Figure 164: Temperature change of bulk Zirc-4 and bulk ZrO_2 at the simulated liquid-solid contact under constant heat flux (Chen's data [155]) and constant contact area (D = 40 μm) using the one-dimensional model and the two-dimensional model. 220
Figure 165: Illustrations of the numerical simulation of the liquid-solid contact using COMSOL: (a) flat surface and (b) the surface with a triangular surface feature. The variation of surface color in the model represents the localized cooling due to the liquid contact. 221
Figure 166: Temperature transients for various surface conditions postulating the modified surfaces under period liquid-solid contact (t_w = 1 ms, t_v = 2 ms). 223
Figure 167: Minimum contact surface temperature for various surfaces during a liquid-solid contact as a function of the initial temperature of the model, calculated by the analytical model and COMSOL. Duration of the contact is 3 ms, and contact diameter is 40 μm. The black arrows indicate the initial temperature when the local temperature for the contact area equals to the homogenous nucleation temperature of water at atmospheric pressure. 225
Figure 168: Cross-sectional SEM images of oxidized Zirc-4 samples after three repeated quenching tests in saturated water at atmospheric pressure: (a) bare Zirc-4, (b) pre-oxidized at 700 °C for 30 minutes, (c) pre-oxidized at 700 °C for 120 minutes, and (d) pre-oxidized at 700 °C for 300 minutes. 226
Figure 169: Oxide layer thickness in Zirc-4 samples vs. pre-test oxidation time in 700 °C ambient air. 227
Figure 170: (a) Quenching curves and (b) boiling curves of oxidized surfaces with different thickness of oxide layer in saturated water at atmospheric pressure. 228
Figure 171: Predicted minimum film boiling temperature on various thickness of ZrO_2 layer on Zirc-4 solid and experimental data for saturated water in atmospheric pressure. 230
Figure 172: Effect of (a) liquid contact duration and (b) liquid contact area on prediction of minimum film boiling temperature depending on oxide layer thickness. 231
Figure 173: Labview code for data acquisition and data processing (sample temperature, water temperature, room temperature, and system pressure). 252

Figure 174: Labview code for data record (sample temperature, water temperature, room temperature, and system pressure). 252
Figure 175: Display of data acquisition in Labview system. 253
Figure 176: Full Drawing of quenching experiment facility. 254
Figure 177: Top and front view of the top flange for the air actuator (dimensional scale is inch). 255
Figure 178: Top and front view of the top flange welded with the heating pipe. 256
Figure 179: Top and front view of the aluminum connector. 257
Figure 180: Top, front, and bottom view of the Teflon seal assembly. 258
Figure 181: Top, front, and bottom view of the stainless steel connector for the heating pipe and the connecting pipe. 259
Figure 182: Front view of the heating pipe and the connecting pipe. 260
Figure 183: Front view of the tee pipe. 261
Figure 184: Top and front view of aluminum V-shaped block. 262
Figure 185: Boiling curves of bare Zirc-4 in saturated water at atmospheric pressure 263
Figure 186: Quenching and Boiling curves of $ZrSi_2$ coatings in saturated water at atmospheric pressure. 263
Figure 187: Quenching and Boiling curves of oxidized Zirc-4 (700 °C for 5 hours) in saturated water at atmospheric pressure. 264
Figure 188: Quenching and Boiling curves of oxidized Zirc-4 (700 °C for 30 minutes) in saturated water at atmospheric pressure. 264
Figure 189: Quenching and Boiling curves of oxidized Zirc-4 (700 °C for 120 minutes) in saturated water at atmospheric pressure. 265
Figure 190: Quenching and Boiling curves of roughened Zirc-4 in saturated water at atmospheric pressure. 265
Figure 191: Quenching and Boiling curves of $ZrSi_2$ coating on roughened Zirc-4 in saturated water at atmospheric pressure. 266
Figure 192: Quenching and Boiling curves of bare Zirc-4 in saturated water at 0.5 MPa 266
Figure 193: Quenching and Boiling curves of $ZrSi_2$ coating in saturated water at 0.5 MPa. 267
Figure 194: Quenching and Boiling curves of oxidized Zirc-4 (700 °C for 5 hours) in saturated water at 0.5 MPa. 267
Figure 195: Quenching and Boiling curves of roughened Zirc-4 in saturated water at 0.5 MPa 268
Figure 196: Quenching and Boiling curves of $ZrSi_2$ coating on roughened Zirc-4 in saturated water at 0.5 MPa. 268

Figure 197: Quenching and Boiling curves of bare Zirc-4 in 15 K subcooled water at atmospheric pressure. 269
Figure 198: Quenching and Boiling curves of $ZrSi_2$ coating in 15 K subcooled water at atmospheric pressure. 269
Figure 199: Quenching and Boiling curves of oxidized Zirc-4 (700 °C for 5 hours) in 15 K subcooled water at atmospheric pressure. 270
Figure 200: Quenching and Boiling curves of roughened Zirc-4 in 15 K subcooled water at atmospheric pressure. 270
Figure 201: Quenching and Boiling curves of $ZrSi_2$ coating on roughened Zirc-4 in 15 K subcooled water at atmospheric pressure. 271
Figure 202: Vapor film vs. quenching time of bare Zirc-4 in saturated water at elevated system pressures. 272
Figure 203: Vapor film vs. quenching time of bare Zirc-4 at different water subcooling at atmospheric pressure. 273
Figure 204: Fluctuation of vapor film at high wall superheat for $ZrSi_2$ coating (blue line) and $ZrSi_2$ coating on rough surface (black dots). The vapor film thickness was measured by high-speed images (100 fps). 274
Figure 205: Fluctuation of vapor film at high wall superheat for $ZrSi_2$ coating (blue line) and $ZrSi_2$ coating on rough surface (black dots). The vapor film thickness was measured by high-speed images (100 fps). 275
Figure 206: Fluctuation of vapor film at high wall superheat for $ZrSi_2$ coating (blue line) and $ZrSi_2$ coating on rough surface (black dots). The vapor film thickness was measured by high-speed images (125 fps). 275
Figure 207: Quenching time and minimum film boiling temperature for the bare surfaces, $ZrSi_2$ coating surfaces, the pre-oxidized surfaces (~55 μm oxide layer), and the rough surfaces in the three experimental conditions - atmospheric water, saturated water at 0.5 MPa, and atmospheric subcooled water (ΔT_{sub} = 15 K). 276

List of Tables

Table 1: Composition of the Zirconium alloy (weight percent, Zr balanced) [3] 1
Table 2: The lattice constants (Å) of orthorhombic $ZrSi_2$ 13
Table 3: Thermal conductivity, density, and heat capacity of Zircaloy-2 [89]. 54
Table 4: XPS near-surface chemical compositional analysis of as-received and $ZrSi_2$ oxidized at high temperatures. 71
Table 5: Deposition rate of $ZrSi_2$ coating at 10 mtorr Ar pressure as a function of sputter power. 97
Table 6: Deposition rate of $ZrSi_2$ coating at 135 W sputter power as a function of Ar pressure. 97
Table 7: Composition, phase content, microstructure, and thickness of the as-deposited coatings. 101
Table 8: XPS compositional analysis of the optimized coatings ($ZrSi_2$) after the oxidation tests. The numbers are in atomic percent of each element on the very near-surface. The last column shows the atomic percent ratio of zirconium and silicon. 114
Table 9: Composition, coating thickness, coating substrate, and heat treatment conditions of zirconium-silicide coatings for steam corrosion experiment (400 ℃ pure steam and 10.3 MPa for 72 hours). 127
Table 10: Summary of corrosion of the zirconium-silicide coatings under 400 °C and 10.3 MPa steam for 72 hours 132
Table 11: Thermal conductivity, density, and heat capacity of ZrO_2. 148
Table 12: Summary of minimum film boiling temperature and heat flux for cylindrical samples for saturated water in ambient pressure as reported in the literature. 153
Table 13: Viscosity of vapor, thermal conductivity of vapor, density of vapor and liquid, and enthalpy of vaporization at saturation condition with different pressures. Temperature of the hot surface is assumed to be 600 °C. 160

Nomenclature

Abbreviation	
ATF	Accident tolerant fuel
BWR	Boiling water reactor
CS	Cold spray
LOCA	Loss of coolant accident
PVD	Plasma vapor deposition
PWR	Pressurized water reactor
TS	Thermal spray
Zirc-2	Zircaloy-2
Zirc-4	Zircaloy-4
Zr-alloy	Zirconium alloy
Zr-silicide	Zirconium silicide

Nomenclature	
A	Surface area
Bi	Biot number
c	Specific heat
D	Diameter of liquid contact area
g	Acceleration of gravity
h_{fg}	Latent heat of vaporization
q”	Heat flux
k	Thermal conductivity
P	Pressure
Pr	Prandtl number
r	Radial coordinate
R_a	Arithmetic mean roughness
T	Temperature

t	Time
T_{min}	Minimum film boiling temperature
T_{hm}	Homogeneous nucleation temperature of water
ΔT_{sub}	Water subcooling ($T_{sat} - T_{water}$)
ΔT_{sup}	Surface superheat ($T_{surface} - T_{sat}$)
V	Volume
W	Weight
x	axial coordinate
α	Thermal diffusivity
δ_{ox}	Thickness of oxide scale
η	Dummy variable
θ	Static contact angle of water droplet
ρ	Density
σ	Surface tension
μ	Viscosity
τ	Duration

Subscripts

g	Gas
i	Interface
l	Liquid
local	Local area
min	Minimum
ox	Oxide
s	Surface
sat	Saturation
w	Water
z	Zirconium

1. Introduction

1.1. Motivation

Zirconium-alloy (Zr-alloy) fuel claddings have been widely used in light water nuclear reactors (LWR), for over four decades due to their excellent neutron transparency and combination of corrosion resistance and mechanical properties in normal operating conditions [1]. Boiling water reactors (BWR) currently use Zircaloy-2 (Zirc-2) but cladding of pressurized water reactors (PWR) has transitioned from Zircaloy-4 (Zric-4) to zirconium-niobium claddings (i.e., M5 and ZIRLO) due to its improved corrosion resistance behavior [2].

Table 1: Composition of the Zirconium alloy (weight percent, Zr balanced) [3]

Alloy	Nb	Sn	Fe	Cr	O
Zirc-2	-	1.4	0.1	0.1	0.12
Zirc-4	-	1.5	0.2	0.1	0.14
M5	1	-	0.05	0.02	0.14
Zirlo	1	1	0.1	<0.01	0.11

Since the Fukushima accident in 2011, the behavior of the UO_2-zirconium alloy fuel system under the severe accident conditions has been an issue. As a result, interest on advanced fuels for LWR has shifted from improving fuel performance under normal operating conditions to maximizing safety margins under design-basis and beyond-design-basis accident scenarios. One accident scenario is the degradation of the reactor core by the coolant-limited condition, where the primary cooling system does malfunctions as was the case in the Fukushima accident. Therefore, removing decay heat from fuel rods to a level of about 5 to 6% of full power immediate after scram [4], is a critical issue. Figure 1 illustrates the progress of postulated events during an accident when cooling capability is lost via pipe leakage or pump failure. During the lead-up phase, the fuel cladding temperature increases due to decay heat and the remaining coolant starts to boil. As the fuel reaches about 800 °C, chemical and physical degradation of zirconium alloy cladding becomes significant. If pressure inside the reactor vessel is low and the emergency core cooling system (ECCS) is active at this point, additional coolant is ejected into the core and the fuels could be quenched and cooled

down. Otherwise, a large amount of zirconium alloy claddings in the core would react with high temperature steam, leading to loss of intrinsic mechanical properties of the fuel cladding because of oxide layer formation and hydrogen embrittlement, also referred to as hydriding [5–7]. This fuel cladding degradation would induce fuel failure and a release of radioactive materials into the reactor vessel. Since the oxidation of Zr-alloy is highly exothermic, the core temperature continues to increase to about 1500 ºC when extensive fuel cladding failure occurs. In this phase, management and retention of radioactive material inside reactor containment is important while avoiding hydrogen combustion (hydrogen is a byproduct of the Zr-alloy oxidation in steam).

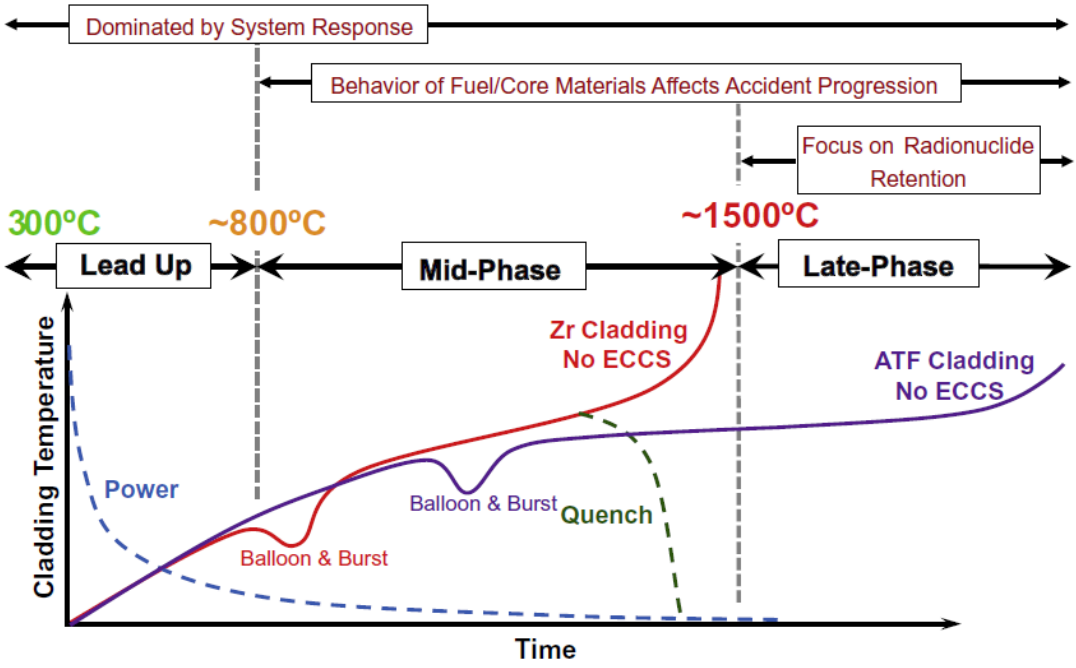

Figure 1: Various stages of loss of coolant accident in LWR [4].

In response to accident scenarios, the concept of innovative approaches in the development of advanced technology fuels (ATF) was introduced by the Department of Energy in the aftermath of the Fukushima accident. The ATF program is aimed at developing fuels that can tolerate higher temperatures that can a result of the loss of active cooling, for a longer time than conventional UO_2-zirconium alloy fuel system [2] to increase coping time in response the accident. The technical requirement for ATF is addressed in the

DOE report [8] as shown in Figure 2. First, ATF cladding is required to have slower reaction kinetics in high temperature steam, minimizing hydrogen generation compared to the current Zr alloy claddings. It is necessary to maintain the cladding's mechanical stability in excess of 1200 °C and thermal shock (due to activation of ECCS) in order to prevent a large release of fission products. Moreover, enhanced heat removal from the fuel would be beneficial to mitigating further core degradation. Second, it is recommended that the ATF fuel pellet has improved thermal/mechanical properties such as higher density, higher thermal conductivity, and higher melting point to make accident progress slower. It also minimizes both the fuel cladding chemical interactions (FCCI) and fuel cladding mechanical interactions (FCMI) and has structurally to improve retention of fission products. Last, ATF has to maintain its good performance under normal operation conditions and must be compliant with current core design, reactor operation, as well as the economic and safety requirements.

Figure 2: Design objective of ATF system addressed in DOE report to U.S. Congress.

There have been three major approaches to enhance the safety margin of LWR fuels: development of alternative fuel rod cladding materials as complete replacement for Zr-alloy, a fabrication of thin protective coatings on Zr alloy cladding surface, and investigation of alternative fuel forms. Some examples of replacements for Zr-alloy include FeCrAl alloys [9,10], SiC-SiC composites [7,11], and molybdenum cladding [12]. For oxidation resistant coatings, chromium [13,14], Ti_2AlC [15], and TiN [16] thin coatings deposited on the Zr-alloy cladding are being investigated to take advantage of their protective behavior. Uranium-silicide and uranium-nitride are being explored as alternative fuel forms [17].

The main goal of this study is to develop novel corrosion resistant thin coatings on the Zr-alloy surface, minimizing modification of the existing fuel system; e.g., using zirconium silicide (Zr-silicide) coating material. In this work, Zr-silicide surface coatings are prepared using various techniques; i.e., magnetron sputter deposition (PVD), cold spray (CS), and thermal spray (TS). Performance of the modified surfaces has been evaluated in terms of oxidation and heat transfer using high temperature air tests, high temperature water tests, and heat transfer quench tests followed by metallurgical characterization methods. Detailed extension of this work will be the focus of the proposed research program.

1.2. Research Goals and Scope

The primary goal of this research is the development of an optimized zirconium silicide coating on zirconium alloy surface showing improved oxidation resistance and transient boiling performance compared to untreated zirconium alloys. The main objectives are summarized as follows:

- Engineering Goals:
    - Fabricate zirconium-silicide coatings on zirconium alloy substrate using magnetron sputtering, cold spray, and thermal spray techniques.
    - Oxidation test of the zirconium-silicide coatings at high temperature air or pressurized steam conditions. Characterize oxidation resistance of the zirconium-silicide coatings.
    - Construct a pressurized quenching system and evaluate transient boiling heat transfer performance of modified surfaces including the zirconium-silicide coated surfaces under the quenching process.
- Scientific Goals:
    - Understand fundamental oxidation mechanism of bulk zirconium-silicides at high temperature air or pressurized steam conditions.
    - Understand fundamental oxidation mechanism of zirconium-silicide coatings on zirconium alloy at high temperature air or pressurized steam conditions.

- Investigate boiling heat transfer behaviors of modified surfaces (e.g., thin zirconium silicide coating, roughened surfaces, and oxidized surfaces) in various system conditions.

2. Literature Review

2.1. High Temperature Corrosion of Zirconium Alloy

High temperature corrosion refers to material deterioration in harsh and high temperature environments (e.g., air, steam, sulfur dioxide), resulting from chemical reactions with the environments. In general, at high temperature in dry air/gas conditions, a metal surface usually reacts with oxygen molecules via physisorption (Van der Waal force) and chemisorption (chemical bonding) readily. It leads to the formation of a thin oxide layer on the surface followed by a growth of a thick oxide layer by diffusion of metal ions and oxygen ions through the oxide layer. If the oxide layer does not have protective nature or poor adherence on the base material, the metal would be continually consumed and lose all its inherent mechanical properties due to thinning of the base metal and growing of the brittle oxide scale. Generation of the oxide debris would be a concern in many applications, particularly those involving flowing environments.

As mentioned earlier, zirconium-alloy fuel cladding undergoes corrosion in normal operation conditions (i.e., pressurized water) as well as by a mixture of water/steam or high temperature air in possible accident scenarios. For instance, Mardon et al. [18], reported that 100 μm oxide thickness and 600 ppm of hydrogen were generated in Zircaloy-4 cladding after a 60GWd/kg U burnup (end of life Zircaloy-4 cladding), potentially having a deleterious effect on rupture tolerance of the cladding at activation of the emergency core cooling system. It is generally known that the oxidation of zirconium (and its alloy) involves an anionic type of diffusion process, where the growth of the oxide layer is controlled by transport of oxygen to the metal/oxide interface [19]. Reaction of zirconium-alloys with steam or air environments has been widely investigated. The exothermic reactions are described as follows [20]:

$$Zr + 2H_2O \rightarrow ZrO_2 + 2H_2;\ \Delta H = -616\ kJ\ per\ mole\ at\ 298K \quad (1)$$

$$Zr + O_2 \rightarrow ZrO_2;\ \Delta H = -1100\ kJ\ per\ mole\ at\ 298K \quad (2)$$

At high temperatures, oxygen reacts with zirconium to form on its outer surface tetragonal ZrO_2 (1000-1600 ºC) or cubic ZrO_2 (>1600 ºC), followed by a layer of oxygen stabilized α-Zr, and then the unreacted substrate, as shown in the cross-sectional image of Zircaloy-4 after the steam oxidation (Figure 3). The oxygen-stabilized layer is formed due to a high oxygen dissolution (and solubility) in the zirconium matrix. The prior β phase in Figure 3 refers to regions where the β phase transformed into α-Zr containing the basket weave-like structures during cool down. The kinetics of zirconium oxidation depends on temperature, and oxidation kinetics in air and in steam are comparable at high temperatures [21]:

- Logarithmic kinetics (< 400 °C) [22]; $W = K_l \cdot \log(t) + \text{Constant}$ (3)
- Cubic kinetics (600 - 800 °C) [23]; $W = K_c \cdot t^{1/3}$ (4)
- Parabolic kinetics (> 1000 °C) [23]; $W = K_p \cdot t^{1/2}$ (5)

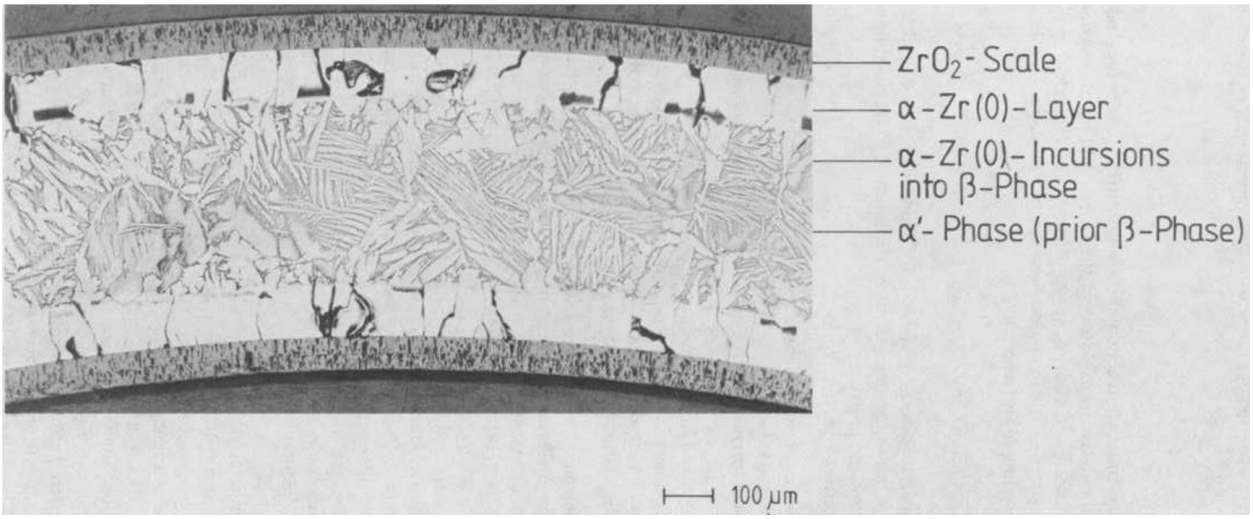

Figure 3: Cross-sectional light microscopy image of Zircaloy-4 after oxidation at 1400 °C steam for two minutes [23].

In particular, evaluation of the parabolic rate constant in high temperature steam and air has been rigorously studied to estimate ZrO_2 layer thickness under postulated accident conditions [24–27]. One important degradation mechanism of zirconium-alloy during high temperature corrosion is a breakaway oxidation, which is a sudden increase of oxidation rate from parabolic to linear growth followed by significant spallation of the oxide scale. In both steam and air conditions, a protective oxide layer grows in

the initial stages obeying the parabolic growth behavior. After a certain duration of the reactions, the growth behavior abruptly transitions to fast linear kinetics, associated with porous and non-protective oxides scales. It is postulated that the breakdown of zirconium-alloy oxide scale is attributable to phase transformation in ZrO_2 phase [28] (tetragonal to monoclinic crystallographic transformation at 1000 °C; Figure 4) and formation of zirconium nitride phases in nitrogen containing environments [6,20]. Additionally, as seen in equation 1, gaseous hydrogen is generated if zirconium reacts with steam. Some of the hydrogen species is absorbed in zirconium alloy cladding, leading to mechanical degradation of the fuel cladding due to hydriding. The hydrogen present in excess of solubility limit in Zr-alloy matrix precipitates out as extremely brittle zirconium hydride phases, which can lead to fracture, spallation of ZrO_2, and deterioration of elasticity and plasticity of zirconium-alloy [29].

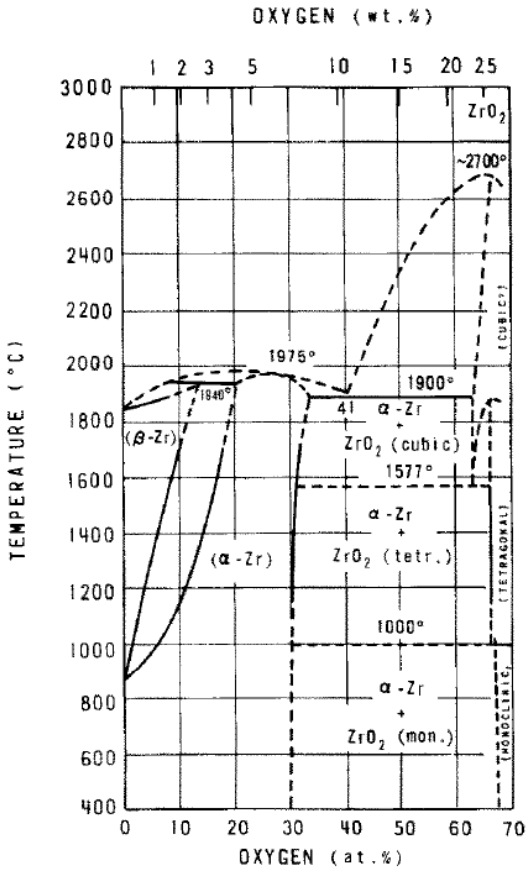

Figure 4: Zirconium-oxygen binary phase diagram showing various crystallographic phases which have a profound effect on mechanical behavior of Zr-alloy cladding under LOCA conditions [30].

In short, zirconium-alloy cladding undergoes corrosion with water, and forms oxide layer on the surface and loses ductility of the material due to hydrogen pickup in normal operating conditions. Under possible accident conditions, fuel temperature increases rapidly, resulting in severe corrosion by high temperature steam and water environment. The corrosion process would be associated effects of non-protective oxide formation, hydriding, and nitriding. When cold water is ejected to the core before core meltdown by activation of ECCS, temperature of the fuel bundles decreases. However, the fuel cladding would experience a significant thermal stress, resulting in cladding failure if the corroded cladding is unable to withstand the thermal shock. For example, Baker-Just correlation [27] has been used to determine an upper limit of oxide thickness on Zr-alloy claddings, called equivalent cladding reacted (ECR). Below the limit, fuel claddings would be able to survive during water quenching. For example, ECCS criteria were established for postulated LOCA of 17% ECR at 1200 °C [23].

$$ECR(\%) = 2.693\times10^{-3}\left(3.36\times10^{11}\exp\left(-\frac{22900}{T}\right)\times t\right)^{0.5} \quad (6)$$

where T is oxidation temperature in Kelvin and t is duration of the oxidation in seconds.

2.2. Pool Boiling

Boiling heat transfer is one of effective ways to remove a large amount of thermal energy from a hot surface by phase change. In a nuclear reactor, boiling phenomena are important to improve the efficiency of power generation and provide safety margins in BWR, and to determine operational margins and ECCS performance in PWR. Heterogeneous pool boiling is a simple way to encompass boiling phenomena in light water nuclear reactors, and distinctive boiling regimes are illustrated in Figure 5. At low superheat (temperature difference between the heated surface and saturated liquid), the heat transfer mode near the hot surface to the liquid is mainly convection (natural convection here but forced convection under flow conditions) and the heat transfer coefficient is relatively low. Once the heater temperature reaches a certain temperature (point A), nucleation of isolated bubbles on the surface initiates, being referred to onset of nucleate boiling (ONB). Further increase in the heat flux or wall temperature causes generation of many

small bubbles on nucleation sites, corresponding to curve A-B, which is referred to as the isolated bubble regime or partial nucleated boiling regime. Beyond point B, larger bubbles get closely spaced and merged to form vapor columns. This regime is called to as a regime of slugs and columns or fully developed nucleation boiling. The peak value of heat flux (point C) is called the critical heat flux (CHF). At higher superheat than this point, a sudden drop in heat transfer coefficient occurs due to formation of a coherent vapor film blanket on a heater surface, resulting in a sudden temperature surge on the heater (curve C-E). If the wall temperature is hot enough to sustain a stable vapor blanket, the vapor blanket covers the entire area of the heater (curve D-E and beyond E), and this regime is called film boiling regime. If wall superheat decreases while film boiling regime (e.g., a transient quenching test) is dominated, the vapor blanket becomes destabilized at a certain temperature and liquid starts to contact frequently a hot surface again (point D). This is referred to Leidenfrost point or the minimum heat flux (q''_{min}). The surface temperature at this point is defined as the minimum film boiling temperature (T_{min}). The regime where combination of nucleation and film boiling is called as the transition boiling regime (curve C-D).

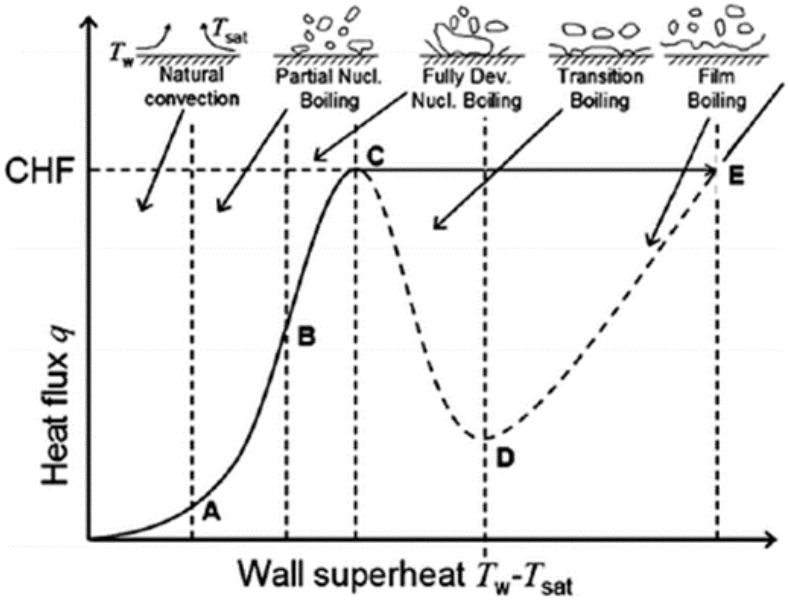

Figure 5: Pool boiling curve showing heat flux vs. wall superheat [31].

During possible accident conditions, transition from the post-CHF heat transfer in film boiling to a nucleate boiling regime is desired as cold water via ECCS actuation refloods overheated vessel, and interacts with the fuel cladding surface. The temperature of the fuel cladding surface would be very high as the fuel claddings immediately immerses in cold water so that the hot surface would be insulated by a continuous vapor blanket with a low heat transfer rate. If the boiling mode changes from the film boiling to nucleate boiling, continuous wetting of the surface begins and the stable vapor blanket starts collapsing followed by vigorous nucleation of bubbles. Since the nucleation boiling regime has a high heat transfer coefficient, the fuel claddings would be effectively cooled down to equilibrium conditions. Therefore, acceleration of transition of boiling regimes (increasing T_{min} point) would be beneficial to mitigate further degradation of fuel claddings and to improve cooling performance of ECCS. The modulation of surface characteristic via zirconium-silicide coatings on Zr-alloy cladding surfaces would be one of methods to induce the acceleration by changing surface properties such as wettability, roughness, and thermal properties is addressed in the later sections.

2.3. Zirconium silicide

Transition-metal silicides have been widely used in many fields (e.g., aerospace, microelectronics, and medical) due to its superior oxidation resistance, a low electrical resistance, a low density, and excellent mechanical properties at high temperatures [32–37]. Among silicides, zirconium-silicides are expected to be a promising material in nuclear industry as a neutron reflector [37] or accident tolerant coatings for fuel cladding in LWR. The materials have a good high temperature stability as seen in Zr-Si binary phase diagram (Figure *6*). Intermetallic of Zr-Si phases has a high melting point. For examples, Zr_2Si, ZrSi, and $ZrSi_2$ are stable up to 1927 ºC, 2203 ºC, and 1626 ºC, respectively.

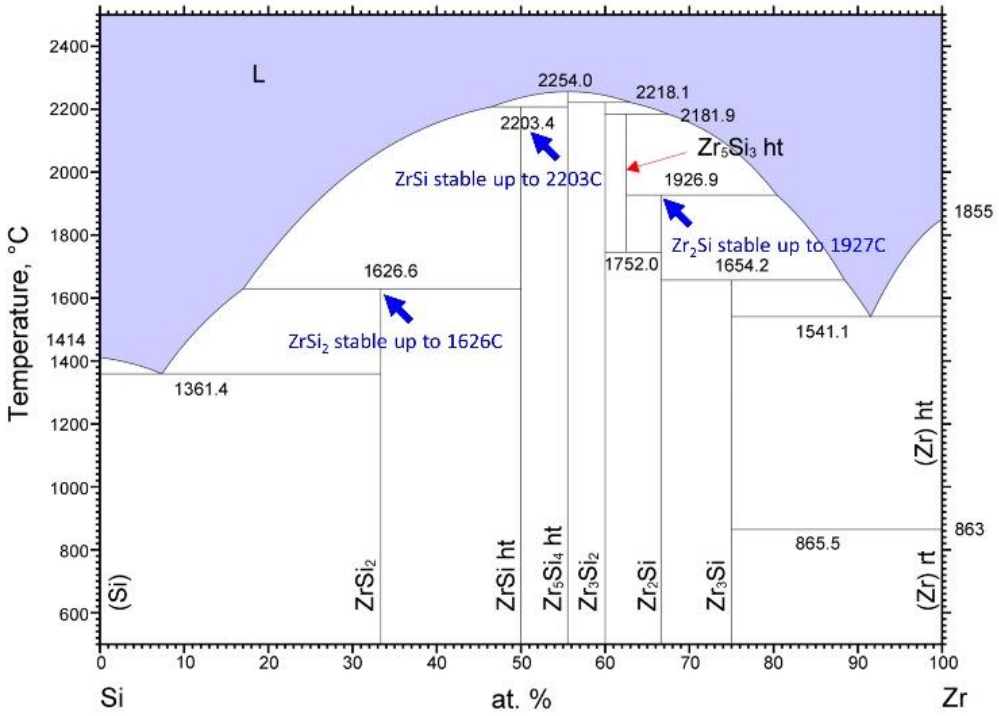

Figure 6: Zr-Si binary phase diagram [38].

Silicon-rich zirconium silicide stoichiometries, $ZrSi_2$, has an orthorhombic base-centered lattice structure (C49) and the conventional unit cell has a total of 12 atoms (see Figure *7*). Based on theoretical calculations and experiments, the lattice parameters and atomic arrangement are summarized in Table *2*. It is generally known that a ratio of distortion (b/a) is large compared to other metal silicides having similar structures (e.g., $NbSi_2$, $TiSi_2$, $MoSi_2$), leading to anisotropic mechanical and electrical properties. In addition, physical and mechanical properties of $ZrSi_2$ were reported as follows: a high hardness (> 850HV), a low density (4.89 g/cm^3), high creep deformation at high temperatures [33], high Young's modulus (230 GPa - 268 GPa at room temperature) [35], and a large yield stress at elevated temperatures (70 MPa - 175 MPa at 1000 ºC) [34]. A linear thermal expansion coefficient of $ZrSi_2$ is on the same order as zirconium alloy [33,39] so that significant shear stress evolution at the interface between $ZrSi_2$ coating and zirconium alloy cladding at elevated temperature would not be expected; a linear thermal expansion coefficient of $ZrSi_2$ at 200 °C was determined to be $8.5 \cdot 10^{-6}$ K^{-1} and that of zirconium alloy at 100 °C was in the range of

$5.5 \cdot 10^{-6}$ K^{-1} to $11 \cdot 10^{-6}$ K^{-1}. Finally, its resistance to oxidation via formation of a tenacious oxide layer (ZrO_2 and SiO_2) is highly probable.

Table 2: The lattice constants (Å) of orthorhombic $ZrSi_2$

	a_o	b_o	c_o
Rosenkranz et al. (1992) [33]	3.721	14.68	3.683
Nakano et al. (2003) [34]	3.72	14.68	3.72
Hao et al. (2015) [36]	3.706	14.735	3.672

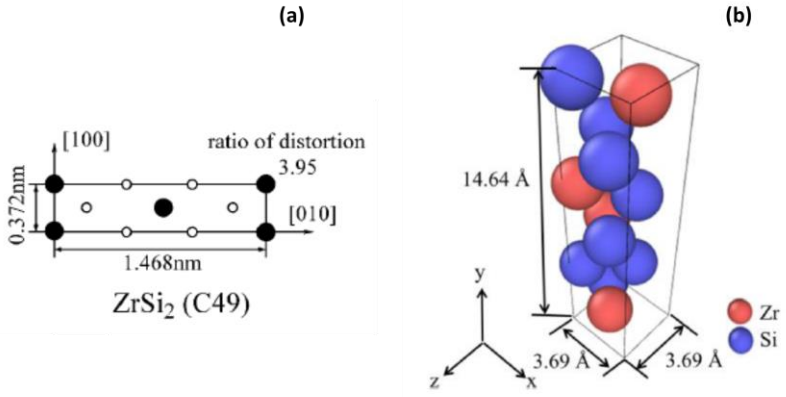

Figure 7: (a) Atomic arrangements on (001) atomic plane [34], and (b) a conventional unit cell of $ZrSi_2$ [35].

2.4. Coating Methods

Methods for deposition of coatings and surface modification of materials as attempts to improve corrosion/oxidation resistance of structural materials has been extensively investigated. In general, deposition processes is categorized into the four techniques as follows [40]:

- Gaseous state process: Chemical vapor deposition (CVD), physical vapor deposition (PVD), and ion beam assisted deposition (IBAD)
- Solution state process: Chemical solution deposition, electrochemical deposition, and sol-gel (e.g., slurry method) deposition
- Molten or semi-molten state process: Thermal spraying deposition (TS) and welding
- Solid state process: Cold spraying deposition (CS)

Since each deposition technique has distinct characteristics such as deposition rate, deposition temperature, and limitations of substrate and coating material, many studies have been performed to enhance oxidation resistance of materials by applying protective surface coatings. Examples are thin TiN film deposited on stainless steel bars by a pulsed laser deposition method [41], molybdenum-disilicide coating using high velocity oxyfuel process on carbon steel substrate [42], and chromium coating by reactive radio frequency magnetron sputtering on low carbon steel [43], and the coatings showed a certain level of success.

Relatively few studies have been performed using thin coatings as anti-oxidation layers for Zr-alloy substrates [44]. The presence of a native zirconia layer on the surface is one limitation. The other reason for this is that many of the surface treatments are performed at high temperatures or require high temperature post-deposition treatments, which could adversely affects the critically heat-treated microstructure of the Zr-alloy for LWR fuel claddings [45]. Due to microstructure-specific properties of Zr-alloys, the substrate temperature must be maintained at temperatures below 850 °C to prevent phase transformation [46]. Furthermore, from a practical stand-point in fuel cladding application, it is recommended that any post-heat treatments should not exceed 400 °C. Normal LWR operations use coolant temperatures around 300 °C and maximum cladding service temperatures near 400 °C [47]. In this regard, magnetron sputter deposition and cold spray, low temperature coating processes (i.e., room temperature), appear to be appropriate coating methods to deposit zirconium-silicide on Zr-alloy substrate in the present study. In addition, thermal spray deposition also was investigated to evaluate its feasibility.

Magnetron sputter deposition is one of the physical vapor deposition (PVD) methods. As seen in Figure 8, glow discharge plasma is formed in front of a cathode by high electric potential at very low pressure. Energetic ions generated (generally Ar^{+}) in the glow discharge plasma bombard a target and sputtered target atoms, then condense on a substrate and form a thin film. To improve the low deposition rate and substrate heating effects, magnetron sputtering has been developed and uses a magnetic field to constrain secondary electron motion near the target. Increasing probability of Ar ion generation, in turn, leads to higher

deposition rates of the thin film [48]. The main benefits for the PVD coating are summarized as follows [40]: Surface cleaning via plasma prior to deposition, a high purity of coating, uniform coating thickness, flexibility over a wide range of coating and substrate materials, and controllable coating structure varying deposition parameters. Thornton postulated that a coating morphology is a function of argon pressure and substrate temperature (see Figure 9) [49]. At higher substrate temperatures, sputtered atoms have high surface and bulk diffusivity so that the dense columnar or equiaxed grains would be formed (Zone 2 and Zone 3). At high argon gas pressure, increasing collision between argon atoms and sputtered atoms leads to a shifting boundary of Zone 1 to high temperatures.

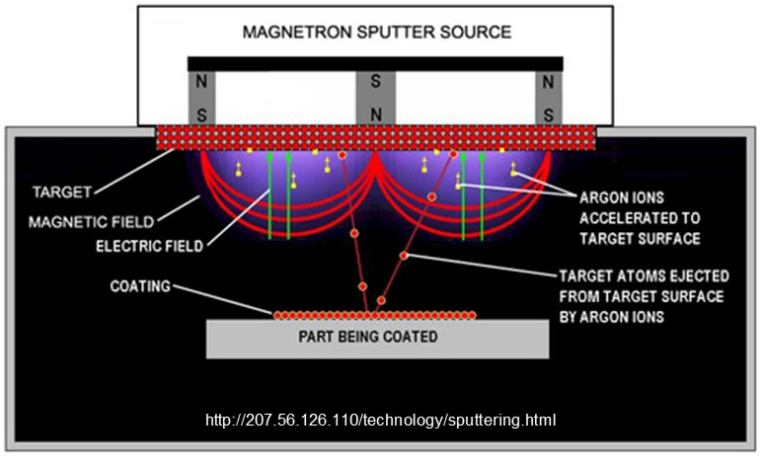

Figure 8: Schematic illustration of magnetron plasma vapor deposition process.

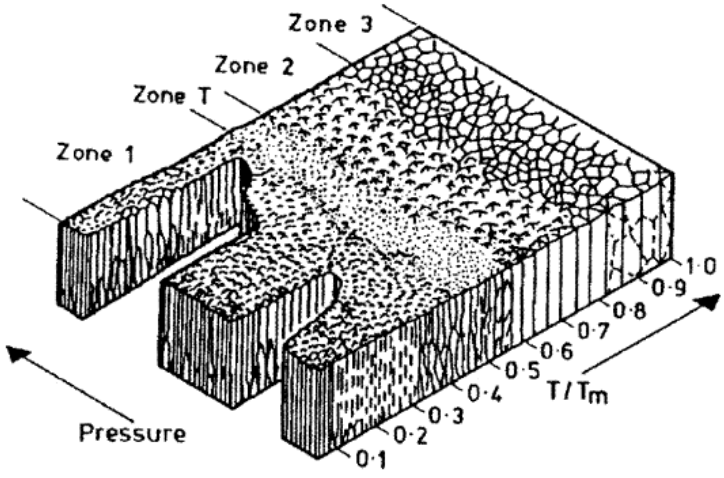

Figure 9: Schematic representation of microstructure of coatings by magnetron sputtering using argon ions. T is substrate temperature and T_m is a melting point of the coating material. [49]

Cold spray method is a solid-state deposition processes for fabricating a coating by propelling micron size particles with a supersonic velocity to a substrate. The conventional cold spray system is illustrated in Figure 10. The particles are accelerated by a high pressure gas and undergo adiabatic shear deformation during the impact on the substrate, resulting in adhesion to the surface and subsequently cohesion between particles [50]. Depending on gas pressure and cold spray nozzle system, velocity of the particle is in the range of 300 to 1400 m/s and the powder particle must exceed a certain critical impact velocity to achieve adhesion, but it should be below a certain velocity to minimize erosion [51]. The main advantage of cold spray deposition is as follows: a high efficiency of deposition, avoidance of undesirable phases or oxide formation, and a short deposition time.

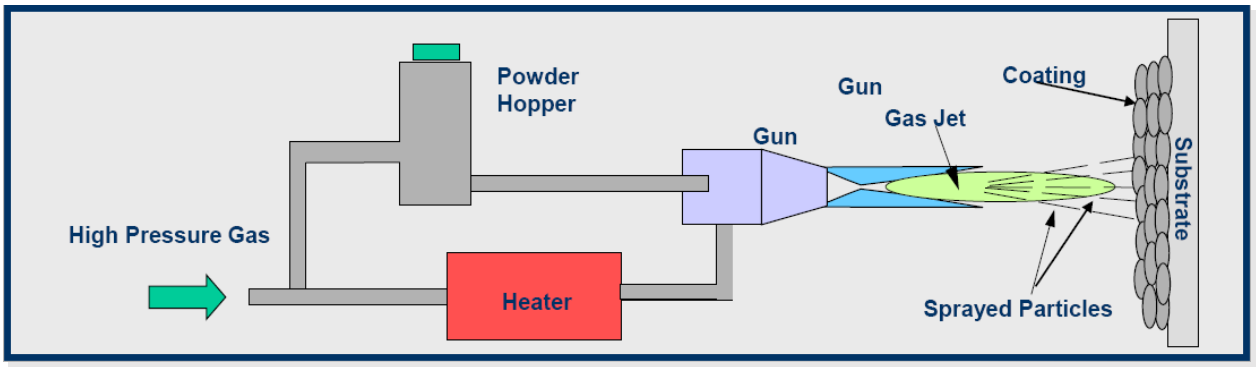

Figure 10: Schematic illustration of cold spray system [52].

Thermal spray process uses concentrated heat source to melt powder feed-stock and then propels the molten droplets on to the surface of a substrate or the part to be coated [53]. The molten particles form a ‘splat’ on the substrate surface, spread out, and cool rapidly to form a coating. Plasma spray process, one of thermal spray techniques, provides for high plume temperatures, higher particle kinetic energy, and higher coating density and phase purity. Since melting process of feedstock powders is important parameter in thermal spray technique, a distance between a spraying nozzle and a target substrate can be adjusted during the spraying. In addition, effect of surface preparation such as a grit blasting to evaluate its role on interface bonding strength.

2.5. Oxidation of Transition Metal Silicides

Transition-metal silicides generally have outstanding oxidation resistance due to formation of SiO_2 layer on the surface at high temperatures. Lie et al. [54] proposed a linear-parabolic kinetic model of oxidation for transition metal silicide films deposited on Si wafer in dry oxygen and wet oxygen environments. They found that $MoSi_2$, $TaSi_2$, WSi_2, and $TiSi_2$ thin film produced approximately a micron thick oxide film at 1000 °C for 10 hours (see Figure 11).

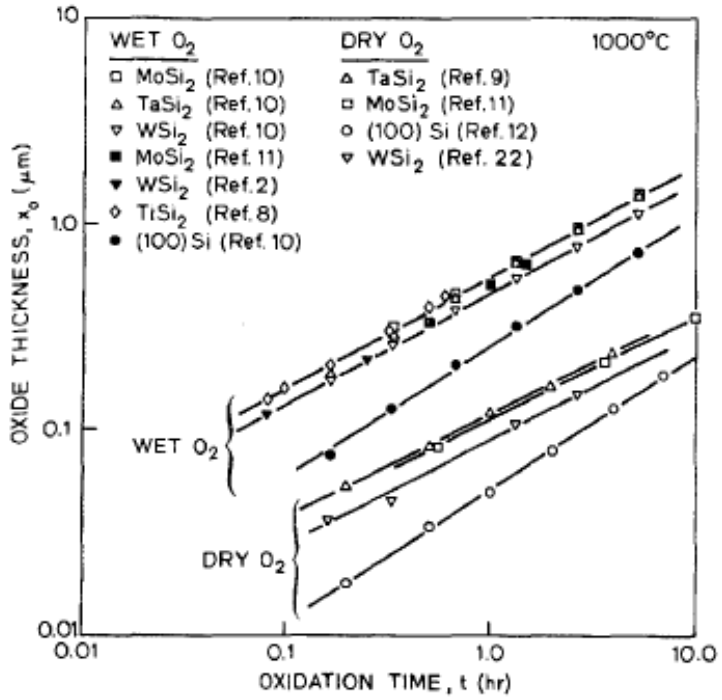

Figure 11: Thickness of oxide layer of $MoSi_2$, $TaSi_2$, WSi_2, and $TiSi_2$ in wet oxygen or dry oxygen environments as a function of time [54].

The authors utilized the Deal-Grove model [55] to predict thickness of oxide scale on transition metal silicides; SiO_2 layer growth on the surface is a reaction which is controlled by transport of Si diffusing from the Si substrate through the transition metal silicide as well as oxygen flux through native SiO_2 as shown in Figure 12.

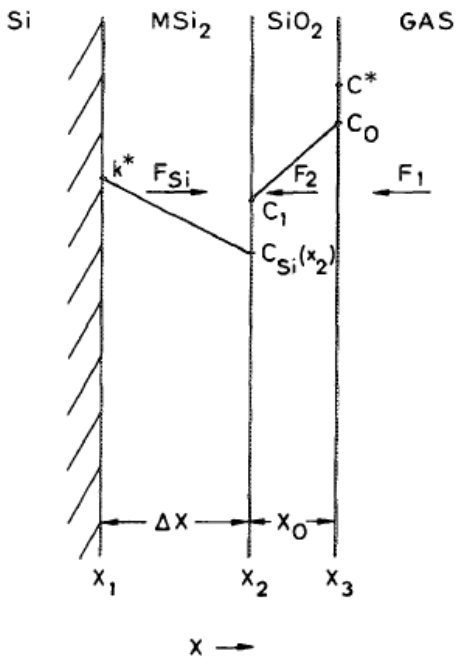

Figure 12: Proposed model for thermal growth SiO_2 layer on transition metal silicide [54].

Under steady state conditions, the linear-parabolic oxidation kinetic model was postulated, by solving an equilibrium equation for Si and oxygen flux denoted by the following equations:

$$\frac{x_o^2}{B} + \frac{x_o}{(\frac{B}{A})} = t + \tau \tag{7}$$

where

$$B = \frac{2C^* \cdot D_{eff,ox}}{N} \tag{8}$$

$$\frac{B}{A} = \frac{C^*}{N}\left(\frac{1}{\frac{1}{h} + C^* \cdot \frac{\Delta x}{k^* \cdot D_{eff,Si}} + \frac{1}{k_i \cdot k^*}}\right) \tag{9}$$

$$\tau = \frac{x_i^2}{B} + \frac{x_i}{(\frac{B}{A})} \tag{10}$$

where x_0 is the thickness of SiO_2, t is oxidation time, C^* is the equilibrium concentration of the oxidizing species in the oxide layer, $D_{eff,ox}$ is the effective diffusion coefficient of the oxidizing species, N is the number of oxidant species per unit volume of the oxide layer, k^* is the partition coefficient of Si, h is the

gas-phase mass transfer coefficient, k_i is an interface reaction constant, $D_{eff,Si}$ is the effective diffusion coefficient of Si, and x_i is the initial oxide layer thickness. As a result, linear kinetics and parabolic kinetics would be estimated for short- and long-oxidation:

At short term oxidation, $x_o^2 \sim \frac{B}{A}(t+\tau)$ (11)

At long term oxidation, $x_o^2 \sim B \cdot t$ (12)

The linear kinetic region is an interfacial reaction controlled process at short durations and the parabolic kinetic region is a diffusion-controlled process. In addition, the authors note that the linear rate constants for transition metal silicide films are larger than that for silicon oxidation but the parabolic rate constants were found to be similar to that of silicon. Therefore, the mechanism of oxidation resistance for transition metal silicide is the same as that for silicon for long term high temperature oxidation.

However, this model, assuming Si substrate supplies Si atoms to silicide matrix, cannot be directly applied to the oxidation behavior of bulk materials and thin films deposited on different materials. Also, this work only focused on silicon and oxidant diffusion but the transition metal plays an important role in the entire oxidation process depending on oxidation temperature.

Kurokawa and Yamuchi [56] proposed classification of oxidation behavior of transition metal disilicides based on thermodynamics and kinetics. As shown in Figure 13, the first step is an affinity for oxygen with transition metal and Si, and the second step is a comparison of diffusivity of Si in silicides and oxygen in the oxide scale. The last step is a comparison of vapor pressure of the transition metal oxide and system pressure. Based on the criteria, final products of oxidation would be a SiO_2 layer or a mixture of SiO_2 and a transition metal oxide or two-layered scale (SiO_2/transition metal oxide). The Gibbs free energy of oxide formation is plotted in Figure 14. If the thermodynamic driving force of SiO_2 is much larger than that of a transition metal oxide (e.g., WO_2, $MoSi_2$, $TaSi_2$), selective oxidation of Si is favored, leading to SiO_2 formation. Otherwise, it is speculated that mixed oxide scale would form due to concurrent Si and transition metal oxidation (e.g., $TiSi_2$ and $ZrSi_2$). In addition, SiO_2 scale tends to form if Si diffusivity is

larger than oxygen even if oxidation of metal is dominant compared to silicon oxidation (path A). Metal oxides with a high vapor pressure during the transition metal silicide oxidation would likely evaporate, resulting in only SiO_2 scale formation (path B). For example, vapor pressure of MoO_3 is relatively high [57] so that it appears to be beneficial to form uniform SiO_2 layer. It was concluded that transition metal silicides forming a continuous uniform film of SiO_2 at high temperatures provides excellent oxidation resistance.

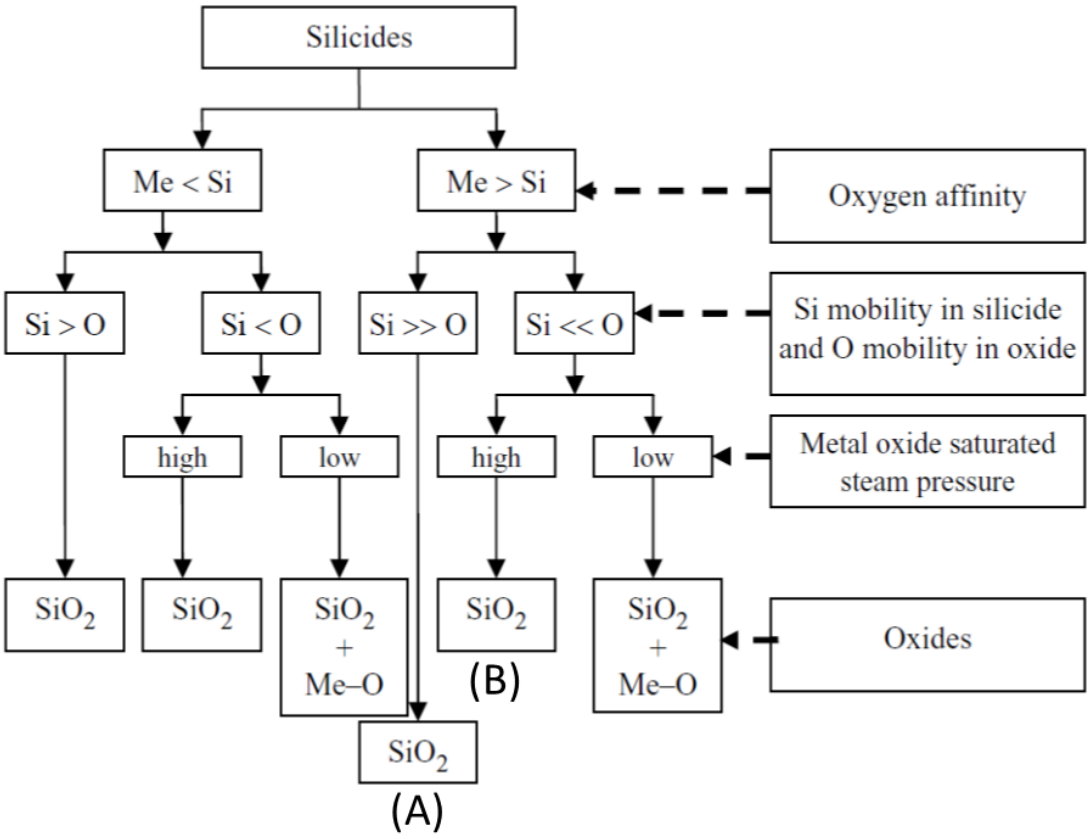

Figure 13: Possible oxidation pathway for oxidation of transition metal disilicides [56].

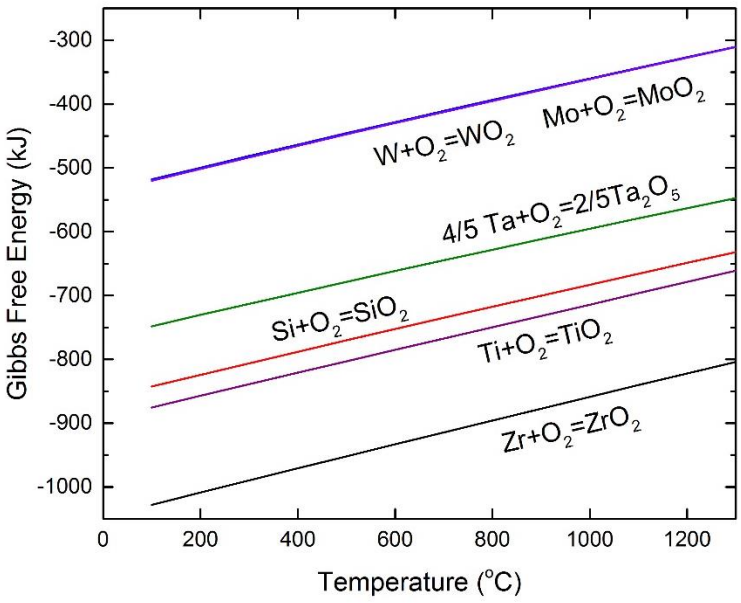

Figure 14: Gibbs free energies of oxide formation for Zr, Ti, Si, Ta, W, and Mo per 1 mole O_2, calculated by HSC Chemistry thermodynamics software.

Compared with other transition metal silicides, $MoSi_2$ has been widely investigated as a high temperature structural material. It has been shown that $MoSi_2$ exhibits formation of very thin protective oxide layer and a small weight gain over long periods of time at high temperatures (1000 °C - 1700 °C) but it shows accelerated oxidation with a loss of the protective nature of the oxide layer at intermediate temperatures (500 °C - 800 °C) [58]. Berztiss et al. [57] concluded that the degradation $MoSi_2$ around 500 °C, known to pest oxidation [59], occurred due to formation of voluminous MoO_3, leading to microcracks in the oxide scale. The experiment showed that formation of a continuous SiO_2 layer occurred above 1000 °C, resulting from MoO_3 vaporization (high vapor pressure) and Si diffusion to oxide layer. Therefore, oxidation kinetics was linear at low temperature and parabolic at high temperatures [60]. The parabolic weight gain of $MoSi_2$ oxidation at high temperature air is displayed in Figure 15, and the cross-sectional images of the same temperatures are shown in Figure 16. The two possible reactions of $MoSi_2$ are shown below [60]:

$$\frac{2}{7}MoSi_2 + O_2 \rightarrow \frac{2}{7}MoO_3 + \frac{4}{7}SiO_2 \quad (13)$$

$$\frac{5}{7}MoSi_2 + O_2 \rightarrow \frac{1}{7}Mo_5Si_3 + SiO_2 \quad (14)$$

Mo_5Si_3 formation in Figure 16c is explained by the equation 14. This is likely attributable to increased oxygen vapor pressure because of phase transformation from quartz SiO_2 to the cristobalite SiO_2 layer at 1700 °C [61]. The oxygen reacted with Si in $MoSi_2$ faster, leading to Mo-excess silicide would remain at the interface between SiO_2 scale and $MoSi_2$.

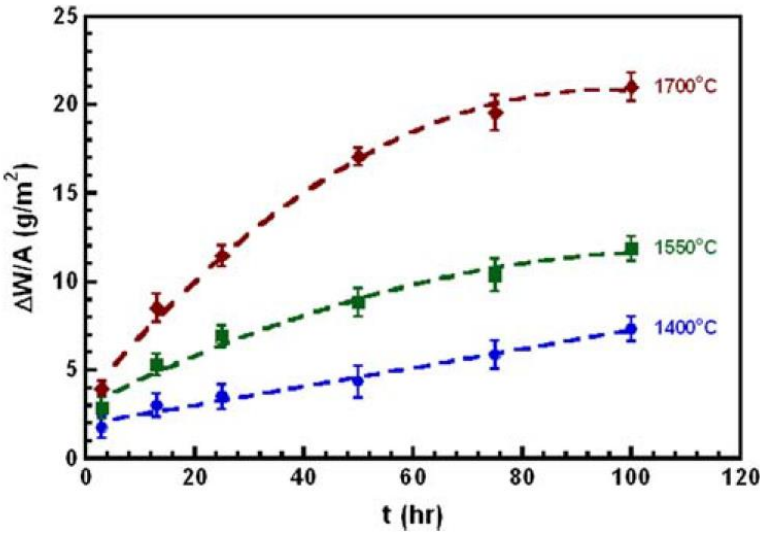

Figure 15: Isothermal weight gain curves for $MoSi_2$ at high temperature in ambient air [61].

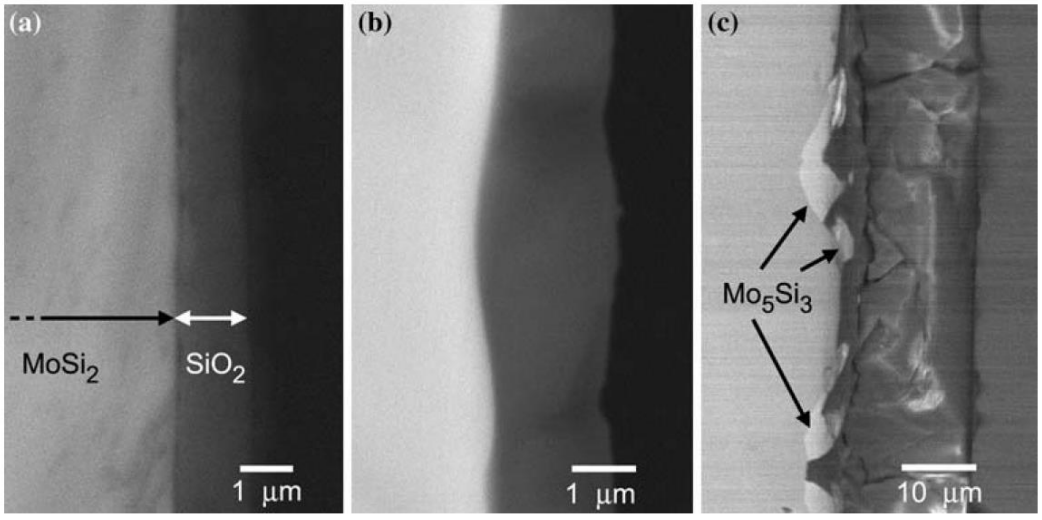

Figure 16: Backscatter secondary electron (BSE) cross sectional SEM images of $MoSi_2$ oxidized in air at (a) 1400 °C, (b) 1550 °C, and (c) 1700 °C for 100 hours [61].

Another high temperature structural material is titanium-disilicide. Understanding oxidation behavior of $TiSi_2$ may be beneficial to understand oxidation behavior of $ZrSi_2$ due to similarities between Ti and Zr (e.g., a proximity in the periodic table). Titanium and zirconium have a high oxygen affinity, neither metals form a volatile oxide, and oxygen diffusion in TiO_2 and ZrO_2 matrix is faster than in SiO_2 [58]. However, little research has been reported on the oxidation of $TiSi_2$ [62–64]. According to the experimental results performed by Schwettmann et al., [62] oxidation behavior of $TiSi_2$ depends strongly on oxidation temperature. Below 600 °C, a glassy Ti-Si-O protective layer forms on the surface. Above 600 °C, crystalline islands of TiO_2 were incorporated in a glassy SiO_2 scale. From 1000 °C to 1300 °C, parabolic kinetics were observed. The author hypothesized that oxygen diffused inward and Ti species diffused outward simultaneously through SiO_2 scale at high temperatures. As shown in Figure 17, $TiSi_2$ oxidation produced TiO_2 islands on top of a mixed SiO_2 and TiO_2 scale. Figure 18 shows parabolic kinetics of $TiSi_2$ at high temperatures. It was reported that the oxidation rate of $TiSi_2$ is roughly five times larger than that of $MoSi_2$ [65], which may be related to larger oxygen diffusion through the heterogeneous mixture of TiO_2 and SiO_2 rather pure SiO_2. In addition, Melsheimer et al. [63] suggested that lower valence Ti oxides (e.g., Ti_3O_5 and Ti_2O_3) particles were identified in the SiO_2 layer above 1200 °C, and the TiN phase was revealed in the interface between the oxide scale for long period oxidation in air (for 1000 hour at 1000 °C).

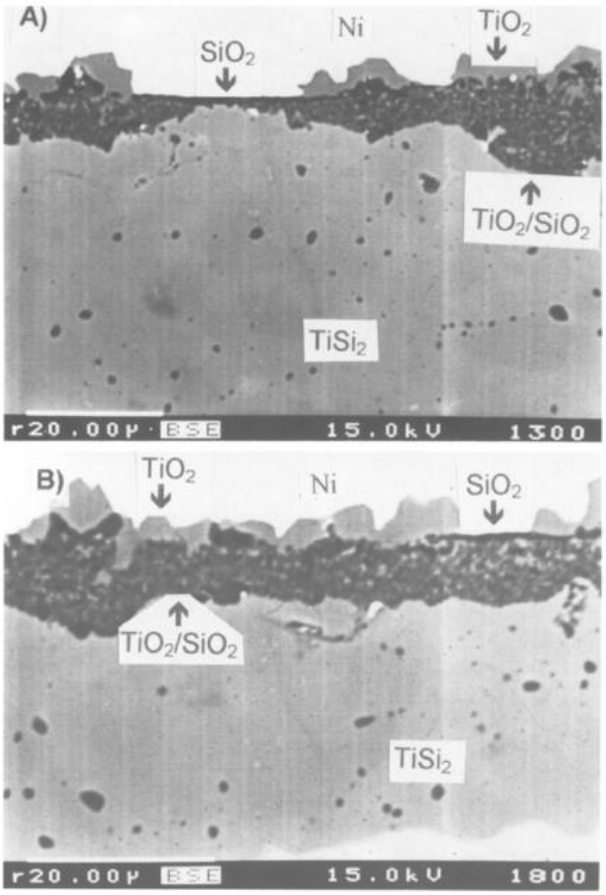

Figure 17: Cross-sectional images of $TiSi_2$ oxidized in air at 1100 °C for 100 hour at different region of the sample [63].

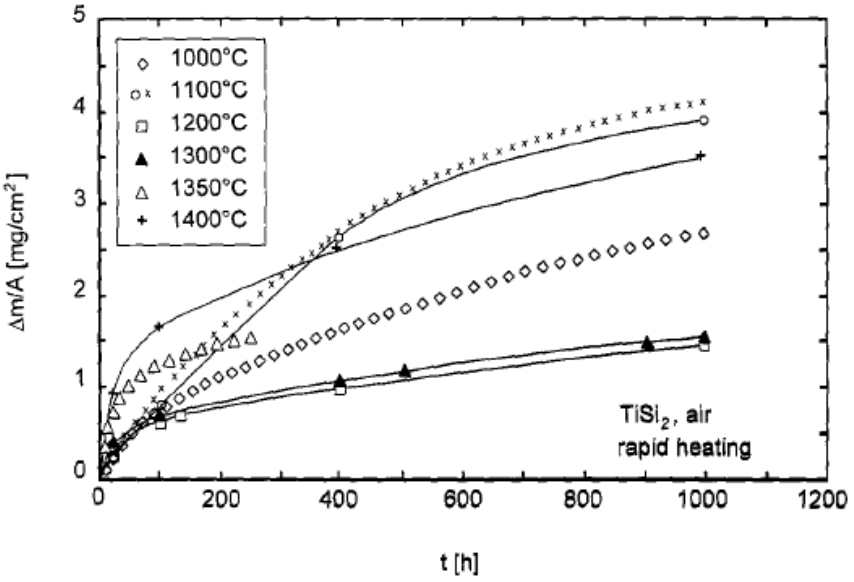

Figure 18: Weight gain of $TiSi_2$ in air at elevated temperatures [63].

2.6. Oxidation of Zr-silicide

Compared to other transition-metal silicides, there have been very limited studies on evaluation of oxidation behavior of zirconium-silicilides at high temperatures, which provides uniqueness to the present research. Strydom and Lombaard [66] oxidized thin film of transition metal silcides ($CoSi_2$, $CrSi_2$, $PtSi_2$, $TiSi_2$, and $ZrSi_2$) on Si wafers between 750 °C and 1100 °C in steam and dry oxygen environments. The authors reported that oxidation of $ZrSi_2$ in the environment did not result in a continuous SiO_2 layer, differing from other silicides. Silicon is very mobile in silicides which was observed by the radioactive silicon tracer measurement. Pérez [67] investigated air oxidation of $ZrSi_2$ with 4 at.% Aluminum in the range of 600 °C and 1100 °C for 160 hours. The small amount of aluminum was added to improve the oxidation resistance of $ZrSi_2$. The oxidation kinetics obeyed the parabolic law as seen in Figure 19, indicating high oxidation resistance at the elevated temperatures. Two oxidation stages above 700 °C were proposed: early stage (formation of ZrO_2 and $ZrSiO_4$) and steady-state stage (formation of Al_2O_3).

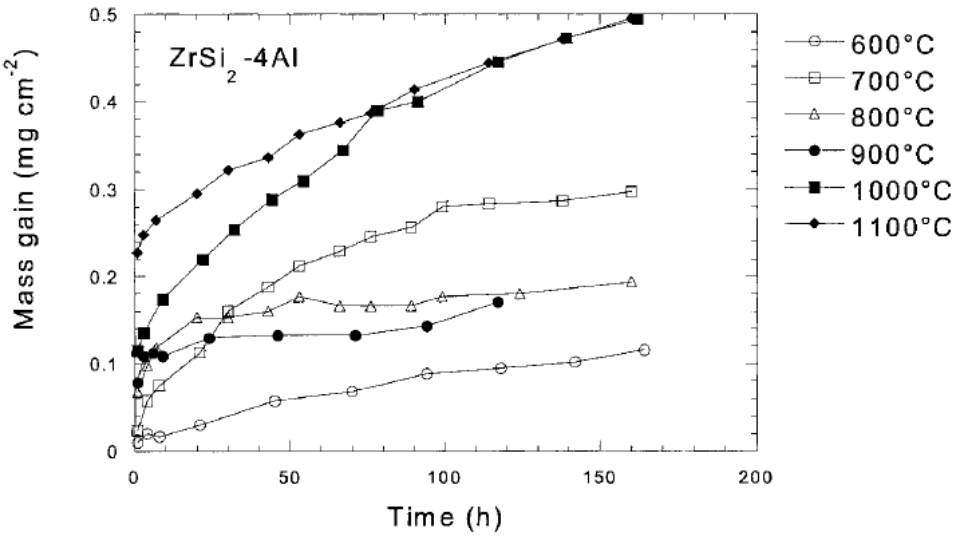

Figure 19: Weight gain curve for $ZrSi_2$ with 4 at.% Al in air in the range of 600 °C to 1100 °C for 160 hours.

Geβwein et al. [68] conducted thermogravimetry (TG) and differential thermal analysis (DTA) experiments for $ZrSi_2$ powders up to 1450 °C in ambient air. Based on the DTA-TG-DTG curves shown in Figure 20, the mass gain was negligible below 500 °C, increased continuously up to 900 °C with exothermic reactions

(ZrO_2 and SiO_2 formation), and gradually increased at higher temperatures. The weight gain at 1400 °C was explained by formation of crystalline $ZrSiO_4$. The authors postulated the complex step of reactions for $ZrSi_2$ particles in flowing air as follows:

$$ZrSi_2 \xrightarrow{O_2} ZrO_2 + (2-y)SiO_x + ySi \ (>500\,℃) \xrightarrow{O_2} ZrO_2 + 2SiO_2 (>800℃) \xrightarrow{O_2} ZrSiO_4 (>1400℃) \quad (15)$$

Nevertheless, oxidation data of bulk $ZrSi_2$ at high temperatures is still limited.

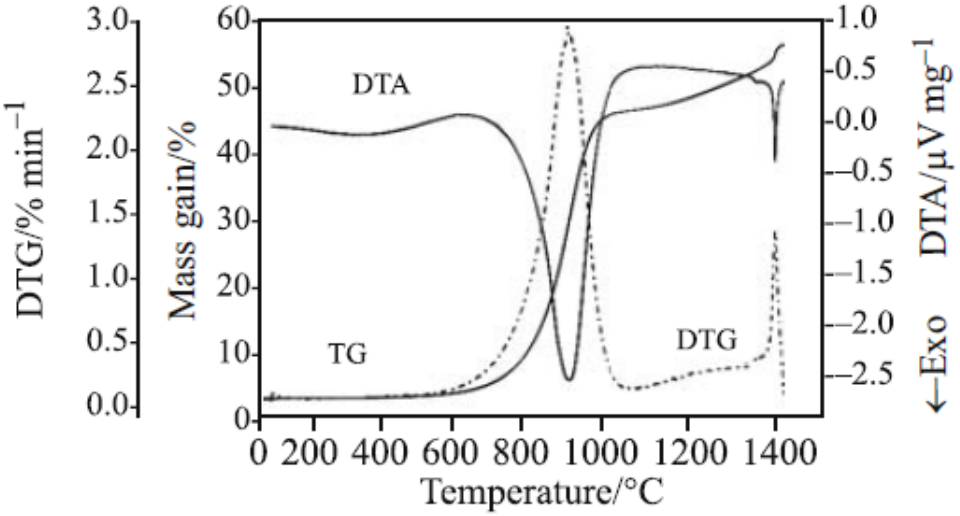

Figure 20: Differential thermal analysis (DTA), thermogravimetric mass analysis (TG), and differential thermogravimetric mass analysis (DTG) curves during $ZrSi_2$ oxidation in flowing air. Heating rate was 10 °C/min.

2.7. Surface Modification for Heat Transfer in Quenching Process

Under accident conditions, successful cooling of fuel rods via ECCS water injection is essential. However, a stable vapor film is initially present on hot cladding surfaces when cold water refloods the reactor core fuel assemblies. This is because the surface temperature of the fuel cladding is higher than the Leidenfrost temperature [69]. The boiling regime has a low cooling rate of the fuel pin, arising from a low heat transfer through the vapor layer. It has been reported that one of factors affecting the boiling heat transfer is properties of a heater surface (e.g., thermal properties, roughness, and wettability) [70]. For example, Chowdhury and Winterton [71] investigated the surface roughness and wettability effects on boiling heat transfer by performing quenching tests of cylindrical aluminum and copper specimens (18 mm

in diameter and 40 mm in length) in saturated water and methanol at atmospheric pressure. The roughness of the samples was modified by grinding with different grades of abrasive papers and the wettability was modulated by aging and anodizing process. They concluded that higher surface roughness improved heat transfer in nucleate boiling regime and more wettable surface increased minimum heat flux temperature (T_{min}). Figure 21 shows the wettability (contact angle) effects on the boiling curves.

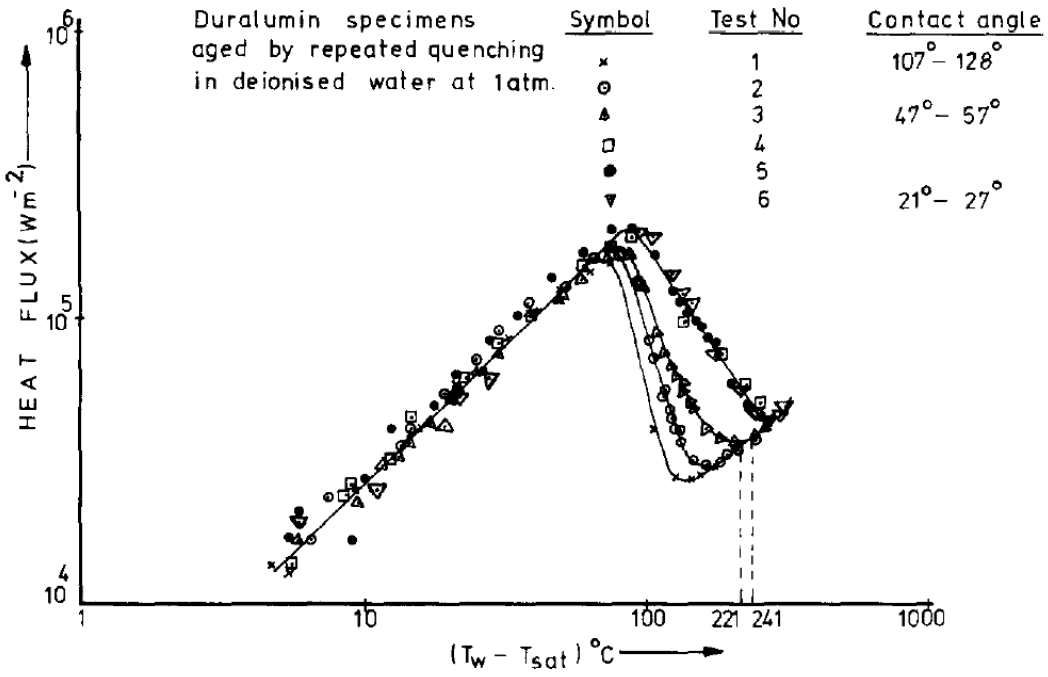

Figure 21: Boiling curve of aluminum cylinder as a function of repeated quenching tests. [71]

Shoji et al. [72] reported that the surface roughness effect was significant if the maximum height of the roughness is higher than vapor film thickness. Increased oxidation led to an increase in the minimum film boiling superheat by temperature observations of a hot copper sphere (12 mm diameter) cooled in Freon-113 at ambient pressure. It is interesting to note that the oxidation effect on the transition boiling was decreased with increasing subcooling of quenchant. Lee et al. [73] performed quenching experiments of copper and stainless steel 304 rodlet (10 mm in diameter and 60 mm in length) in water at ambient conditions. The samples had different surface conditions prepared by pre-oxidation in an air furnace. Only copper samples with 2-hours of oxidation showed shorter film boiling duration. They postulated that modulated surface morphology disrupted the vapor film, leading to the earlier transition of boiling regimes.

It was not correlated to wetting effects because the oxidized stainless steel and the oxidized copper surface revealed similar contact angle values.

Recently, modification of surface morphology with nano/micro structures has been extensively performed to improve the boiling heat transfer in quenching process [74–77]. Vakarelski et al. [74] studied effects of super-hydrophilicity (contact angle < 10 °) and super-hydrophobicity (contact angle > 160 °) on quenching heat transfer in pure water at atmospheric condition for stainless steel spheres (24 mm in diameter). The super-hydrophobic surface was prepared by a thin coating of a hydrophobic agent with nanoparticles. The super-hydrophilic surface was fabricated by plasma cleaning of the organic agent on the super-hydropholic surface. The authors noted that the Leidenfrost transition in the super-hydorphilic surfaces occurred at higher temperatures than bare surfaces (contact angle < 30 °) but the super-hydrophobic surface did not reveal the distinct boiling regime transition in the quench experiments. In addition, Kim et al. [76] noted that characteristics of film boiling heat transfer were affected by Al_2O_3 nanoparticles (~39 nm) deposited on the surface. The modified surfaces were fabricated by a repetitive quenching of stainless steel rodlet (7.9 mm in diameter and 50 mm in length) and stainless steel sphere (9.5 mm in diamter) in Al_2O_3 nanofluid pool. The authors reported that stable vapor film was destabilized at higher temperature and faster quench front speed (see Figure 22) was observed, which is attributed to hydrophilic nature of the nanoparticle layer on the surface. However, the nanoparticle deposited surface was not mechanically robust during the quench tests so the performance was not repeatable during multiple tests.

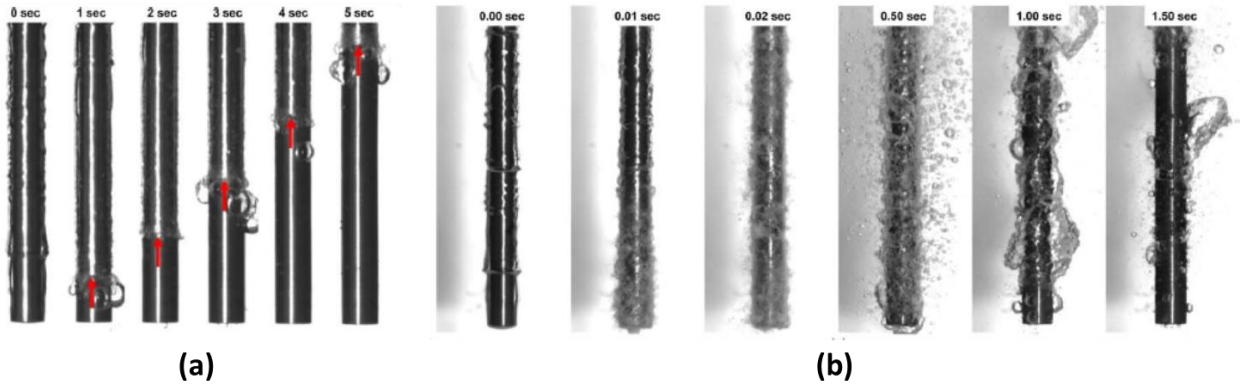

Figure 22: Quench phenomena (bubble dynamics) on SS rodlet at 20 K subcooling. (a) a quench test in pure water and (b) is the test of alumina nanoparticle coated surface in the nanofluid (4th test in the nanofluid). The arrows indicate quench front propagation.

Kang et al. [75] performed quenching tests of completely wettable surface in saturated water at atmospheric pressure. Two types of modified surfaces were prepared for the study. Roughened surfaces and nanostructured surfaces were fabricated by surface polishing and anodic oxidation in acidic solution, respectively. Super-hydrophilic surface (completely wettable surface) was obtained by the nanostructured surface morphology. Figure 23 shows the surface morphologies and water contact angles for the prepared samples. Results of the quenching tests (Figure 24) showed that film boiling heat transfer, minimum film b oiling heat flux, and minimum film boiling temperature for the nanostructured surface were increased compared to those of bare surface. It was speculated that improved water capillary wicking could supply liquid to heated surface during intermittent water-surface contact by the nanostructures, finally resulting in enhanced film boiling heat transfer.

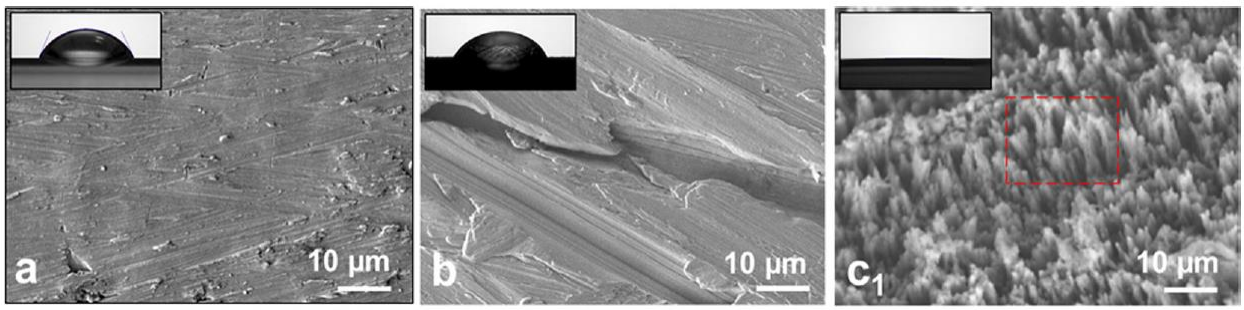

Figure 23: SEM images of (a) bare zirconium, (b) roughened surface, and (c) anodized surface. The upper inset is the water droplet on the surface showing contact angle.

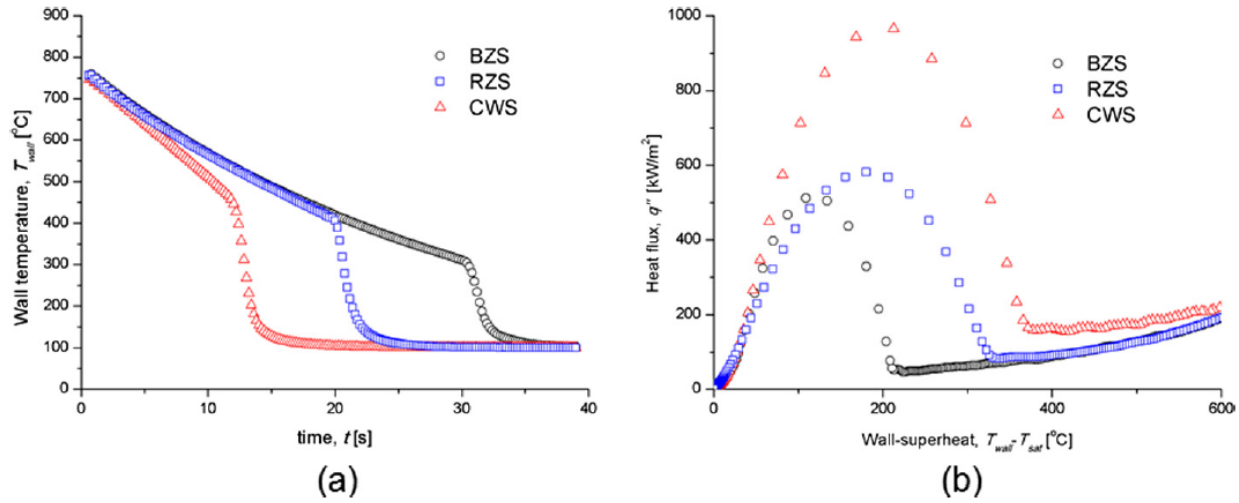

Figure 24: (a) Temperature history during the quench test and (b) estimated boiling curve. BZS is bare zirconium surface, RZS is roughened zirconium surface and CWS is completely wettable surface.

2.8. Pressure Effect on Minimum Film Boiling Temperature (T_{min})

One of goals on this study is to investigate pressure effects on heat transfer performance of modified surfaces during quenching process with an assumption that a certain level of pressure is sustained in a reactor vessel as ECCS is active under a loss-of-coolant accident. However, there are very limited data regarding minimum film boiling point above atmospheric pressure.

Zuber [78] first proposed that the minimum heat flux occurs if the vapor production on the hot surface was not enough to sustain the continuous vapor film and thereby collapse. Zuber considered the hydrodynamics aspects (i.e., Instability) of vapor film boiling (i.e., bubble size, number of bubble per unit area, bubble departure frequency) on upward facing horizontal surfaces to formulate the minimum heat flux. In other words, growth of disturbances due to the instability predominates when vapor production rate is small, leading to liquid contact on the heater surface and trigger for the transition boiling regime. Based on Zuber's analysis, Berenson [79] modeled the local heat transfer coefficient and predicted the minimum heat flux temperature on a horizontal surface to sustain the vapor film. It is given by:

$$T_{min}^{B} - T_{sat} = 0.127 \frac{\rho_v h_{lv}}{k_v} \left[\frac{g(\rho_l - \rho_v)}{\rho_l - \rho_v}\right]^{\frac{2}{3}} \cdot \left[\frac{\sigma}{g(\rho_l - \rho_v)}\right]^{\frac{1}{2}} \cdot \left[\frac{\mu_v}{g(\rho_l - \rho_v)}\right]^{\frac{1}{3}} \quad (16)$$

where T^B_{min} is Berenson's minimum film boiling temperature and T_{sat} is saturation temperature for water. ρ_v, h_{lv}, and k_v are a gas density, a latent heat, and a thermal conductivity of gas, respectively. g, ρ_l, σ are the acceleration of gravity, a liquid density, and a surface tension, respectively. μ_v is a viscosity of gas. The gas properties were evaluated at film temperature. The above equation was formulated by dividing the predicted minimum heat flux by Zuber by the derived expression for heat transfer coefficient. The predicted values were in a good agreement with film boiling data under n-pentane and carbon tetrachloride within 10 percent range of deviation. The equation shows that higher pressure increases T_{min}, which is mainly due to the increased density of the vapor. As discussed later, this prediction does not account for thermal properties of the surfaces and different geometries.

Henry [80] pointed out that the assumption of Berenson's model was an isothermal wall condition, resulting in underestimation of T_{min} values. This was because transient fluctuations of vapor-liquid interface were sufficient to make transient wetting spots on the surface near minimum heat flux point, which takes account of effects of thermal properties of surface and subcooling of the liquid. The author suggested that a vapor film collapse started if the cold spot once contacted with liquid and was unable to be recovered the next period. Thus, the vapor generation rate decreased below the minimum level. In addition, he postulated that an amount of surface cooling was dependent on a liquid microlayer remaining on the surface, a latent heat of vaporization, and a heat capacity of the surface. He assumed that the surface wettability was large enough to generate a liquid microlayer. With consideration of the transient contacting and the microlayer evaporation, the following correlation incorporating Berenson's equation was proposed:

$$T^H_{min} = T^B_{min} + 0.42\left(T^B_{min} - T_l\right) \cdot \left[\left[\frac{k_l \rho_l c_l}{k_s \rho_s c_s}\right] \cdot \frac{h_{lv}}{c_s (T^B_{min} - T_{sat})}\right]^{0.6} \quad (17)$$

where T^H_{min} and T^H_{min} are Henry's minimum film boiling temperature and Berenson's minimum film boiling temperature. T_l is bulk water temperature. k_s, ρ_s, c_s are thermal conductivity of heater surface, a density of heater surface, and a thermal capacity of heater surface. The liquid properties are determined at the bulk liquid temperature, surface properties are evaluated from the wall temperature and the vapor

properties are evaluated at film temperature: $0.5\cdot(T^{H}_{min} + T_{sat})$. In short, vapor film destabilization begins if local interface temperature is the same as Berenson's isothermal T_{min} although bulk surface temperature is higher than T^{B}_{min}.

Yao and Henry [81] measured a frequency and a magnitude of liquid-solid contacts on a flat stainless steel and a gold coated copper surfaces in saturated ethanol and water using electrical conductance probes. They concluded that minimum film boiling temperature was determined either by a Taylor instability vapor removal limitation or by spontaneous nucleation upon contact. If the system is controlled by Taylor instability (e.g., ambient pressure condition), significant liquid-solid contacts occurs even in stable film boiling regime. On the other hand, significant liquid-solid contacts do not occur if the heater temperature is above the minimum film boiling temperature when the system is controlled by spontaneous nucleation upon contacts (e.g., high pressure conditions).

Sakurai et al. [82] conducted film boiling heat transfer experiments on a horizontal platinum rod at a wide range of pressure conditions (20 kPa to 2 MPa). A part of experimental results is shown in Figure 25; T_{min} increases with increasing system pressure up to 1 MPa. After reaching the pressure, increase in T_{min} showed an asymptotic behavior. Additionally, it is worth noting that the experimental values do not agree with the prediction using Berenson's model. The authors postulated that hydrodynamic Taylor instability determines T_{min} below 1.1 MPa but spontaneous nucleation phenomena enable the vapor film to be stable even at a certain lower temperature. Finally, empirical correlation to predict T_{min} and q_{min}, taking into consideration of bubble dynamics at elevated pressure was proposed by the authors.

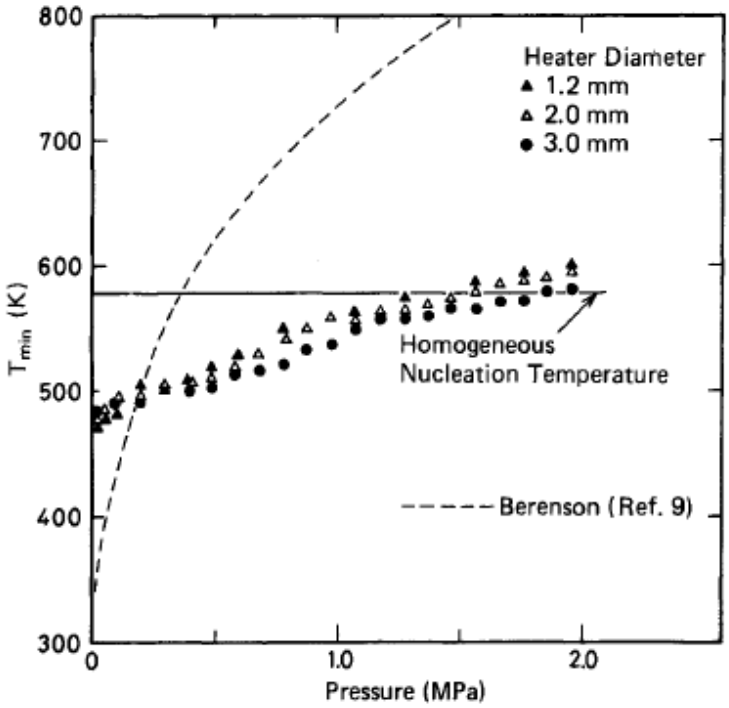

Figure 25: T_{min} vs. system pressure in saturated water with different heater diameter. Berenson model is plotted as the dot line [82].

Nishio [83] proposed that three pressure regions would be categorized by the slope of T_{min} vs. Pressure curve based on observation of extensive published experimental data: 1) a slope of the curve is negative at low pressures, 2) a slope is slightly positive or nearly zero at intermediate pressure, and 3) a slope is negative again in high pressures. As seen in Figure 26, an upper limit of the low pressure region and the intermediate pressure region for saturated water appears to be 0.04 MPa and 2 MPa, respectively. In addition, it was stated that T_{min} is not sensitive to heater configuration (e.g., cylinder diameter) and geometry (e.g., sphere, horizontal cylinder, flat plate).

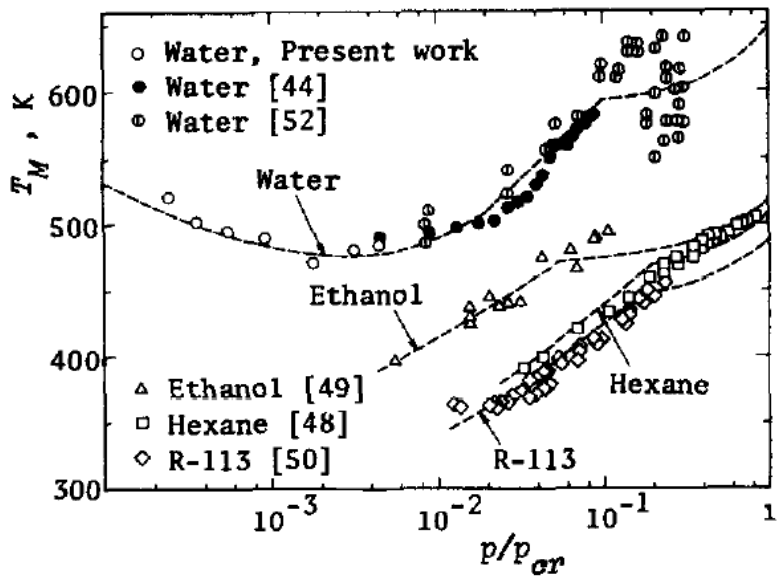

Figure 26: T_{min} vs. pressure curve of saturated liquids.

Peterson[84] performed quenching tests of vertical cylinders in water at high pressure up to 3 MPa with different materials and different surface preparation. He mentioned that the theoretical models and experimental correlations for a horizontal plane and a horizontal cylinder could not predict film boiling temperature on the vertical cylinders due to effects of a laminar or turbulent vapor flow on transient wetting on the surface. As Sakurai and Nishio noted, the effect of pressure on T_{min} was strong below 1 MPa but it was asymptotic at higher pressures as shown in Figure 27. It was also reported that minimum film boiling point for Zirc-4 was affected by surface oxidation and surface roughness.

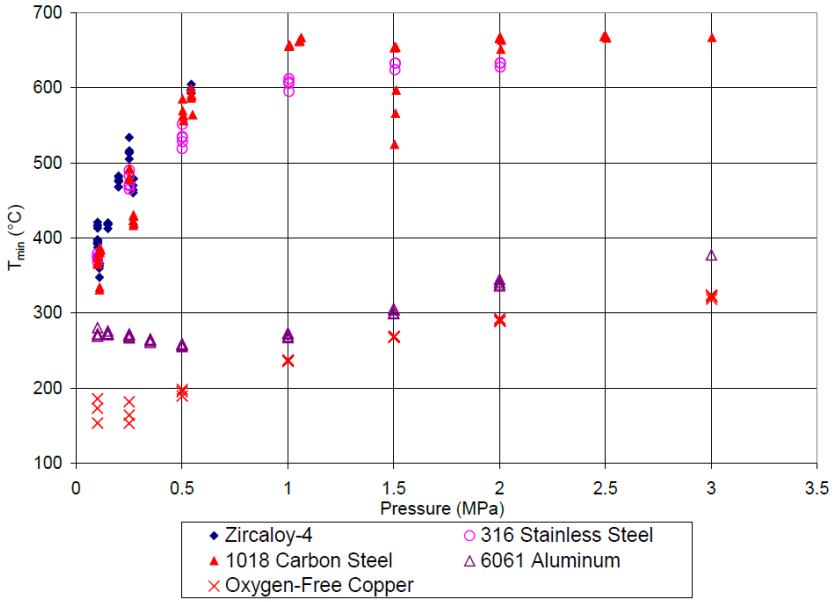

Figure 27: T_{min} vs. Pressure for different materials [84].

2.9. Conclusion of Literature Review

The preceding sections present background information and literature review in regards to the proposed research. In general, transition-metal silicides are known as structural materials for high temperature applications due to their excellent oxidation resistance. A transition-metal silicide material, zirconium-silicides have a potential to serve as a protective coating material for LWR zirconium alloy cladding based on their promising properties such as a small neutron cross-section and high melting points. A high oxygen affinity of zirconium would be protected by a passive oxide layer formed on zirconium-silicide coating possibly consisting of SiO_2 or $ZrSiO_4$. Nevertheless, experimental data of oxidation of zirconium-silicides at high temperature conditions (air or water vapor) is very limited. Furthermore, there are no previous studies on fabrication of zirconium-silicide coating on zirconium alloy surface to mitigate high temperature oxidation.

For a coolant-limited accident scenario, effective cooling of the fuel pins via ECCS injection is essential but formation of stable vapor layer on overheated fuel cladding surface would hinder heat removal from the hot surface due to a low heat transfer coefficient. Surface modifications (e.g., surface oxidation, surface roughening, and artificial surface texturing) have been investigated to improve heat transfer performance

during quenching process. Nevertheless, most modified surfaces were very weak to endure thermal shocks or mechanical disturbances. The surfaces were also vulnerable to excessive oxidation at elevated temperatures even if the modulated surfaces appeared to enhance the boiling heat transfer. To the best of the author's knowledge, little research data investigating the sensitivity of the modified surfaces on the quenching phenomena under pressures or subcooled quenchant has been published. In postulated accident conditions, a reactor vessel may maintain a certain level of pressure so it is worth investigating whether the boiling performance at atmospheric pressure sustains at higher prototypical pressure. In general, minimum film boiling temperature (T_{min}) increases with increasing system pressure up to approximately 1.0 MPa. Clear explanation of surface properties and system effects (pressure and subcooled liquid) has not been proposed. Moreover, a visualization study would be beneficial to elucidate the underlying mechanisms of the quenching behavior at the various conditions.

3. Experimental Description

3.1. Raw Materials

In order to investigate oxidation behavior of zirconium-silicides, two different stoichiometries of bulk zirconium silicide have been procured. Si-rich zirconium-silicide, $ZrSi_2$, was purchased from American Elements Inc. (Los Angeles, CA) having a reported purity of >99.5 % and Zr-rich zirconium-silicide, Zr_2Si, was shipped from SCI Engineered Material Inc. (Columbus, OH) having 99.9% reported purity. In addition, Zircaloy-4 plates (ATI Wah Chang, Albany, OR) were procured for this study. The densities of the bulk $ZrSi_2$ and the bulk Zr_2Si were about 95% and 70% of theoretical densities, respectively [85]. All materials were cut and ground into 12.7 x 12.7 mm^2, 3.2 mm thick square coupons for oxidation testing and characterizations. The phases in the as-received materials were confirmed by X-ray diffraction analysis (XRD), but few micron-sized Si particles were revealed in as-received $ZrSi_2$ matrix as an impurity.

For magnetron sputter deposition on Zirc-4 substrates, $ZrSi_2$, ZrSi, and Zr_2Si sputter targets were procured from American Elements Inc. and SCI Engineered Materials, Inc. All targets had dimensions of 76 mm in diameter and 3.2 mm in thickness. The targets were of 99.5% nominal purity and with 3.2 mm thick copper backing plates for enhancing thermal conductivity during the deposition process.

Two kilograms of $ZrSi_2$ powder (99.5% purity) with average diameter of 20 μm were procured from Kurt J. Lesker Inc. Additionally, two kilograms of $ZrSi_2$ powder of less than 25 μm in size has been procured from SCI Engineered Materials, Inc. The powders were used for cold spray method and thermal spray method.

For quench tests specimen, ten 300 mm-length Zr-alloy (Zircaloy-4 grade) rods were procured from Eagle alloys corporation (Talbott, TN). The rods were machined to short rodlets (50 mm in length and 10 mm in diameter).

3.2. Coating Fabrication

Prior to initiating the coating deposition process in the magnetron sputter system, the substrates were subjected to in-situ plasma cleaning (dc 500W for 5 minutes under 1.6 Pa argon pressure) to remove any residual surface contamination and a native oxide layer on the surface of the substrate. Zirconium-silicide coating deposition was performed under a base pressure of 2.6×10^{-4} Pa. Argon sputter gas pressures were 0.53 Pa and 1.33 Pa with a flow rate of 20 sccm - these parameters were selected based on previous studies of magnetron sputter deposited coatings for high-temperature oxidation resistance [86,87]. DC sputter power was 138 W. The distance between the sputter target and the sample stage was 150 mm and the sample stage was rotated at 10 rpm during the deposition to achieve improved uniformity of the coating. The deposition was performed at 19 °C, as monitored *in situ* by thermocouples, to avoid any phase transformations and thermal stresses in the coatings. In order to investigate the effect of argon pressure and composition of coating on oxidation resistance, the depositions were performed under 0.53 Pa and 1.33 Pa Ar environment. The coating deposition for a single step took 150 minutes, and six steps were performed to achieve thicker coatings that were also investigated in this study. For this multiple step deposition, a plasma cleaning step was employed between the steps to remove any contamination due to interruptions in the coating process. In addition to Zirc-4 substrates, the coatings were also deposited on plasma cleaned Si (100) wafers, which were used for measuring film thickness and observing coating cross-sectional microstructure. As shown in Figure *28*, batches of eight to ten substrates were placed on a stage in the vacuum chamber.

Figure 28: A photograph of PVD chamber, showing Zr-4 flat and tube samples for coating deposition in the present study.

A commercially available cold spray system (400-34 Kintetik) at University of Wisconsin-Madison has been used to spray $ZrSi_2$ powders on Zirc-4 flat substrates, as shown in Figure 29. A carrier gas in the deposition process was pressurized nitrogen gas (3.5 MPa) and nitrogen gas was pre-heated up to 800 °C to increase velocity of powder flow. Prior to the deposition, the flat substrates were ground using 320 grit abrasive SiC papers and thoroughly cleaned with acetone. The coating parameters that investigated for coating quality in the present study were particle size, the number of deposition pass, and gas pre-heat temperature.

Preliminary investigation of thermal spray deposition was made with a commercial company Thermal Spray Technologies (Sun Prairie, WI). The facility used Ar/He mixed gas plasma with 35 kW to melt $ZrSi_2$ powders, and the powders spayed to Zirc-4 flats by the carrier gas of 0.25 MPa. The thermal spray deposition was performed for 10 passes to achieve tens of micron thickness of coating and transverse speed of the spray gun was 76 cm/s. Substrate temperature right after the spray process was measured to approximately 75 °C, indicating that detrimental phase alterations of Zirc-4 substrate may be minimal. Effects of a distance between a nozzle system and substrate and surface finishing to coating quality were investigated.

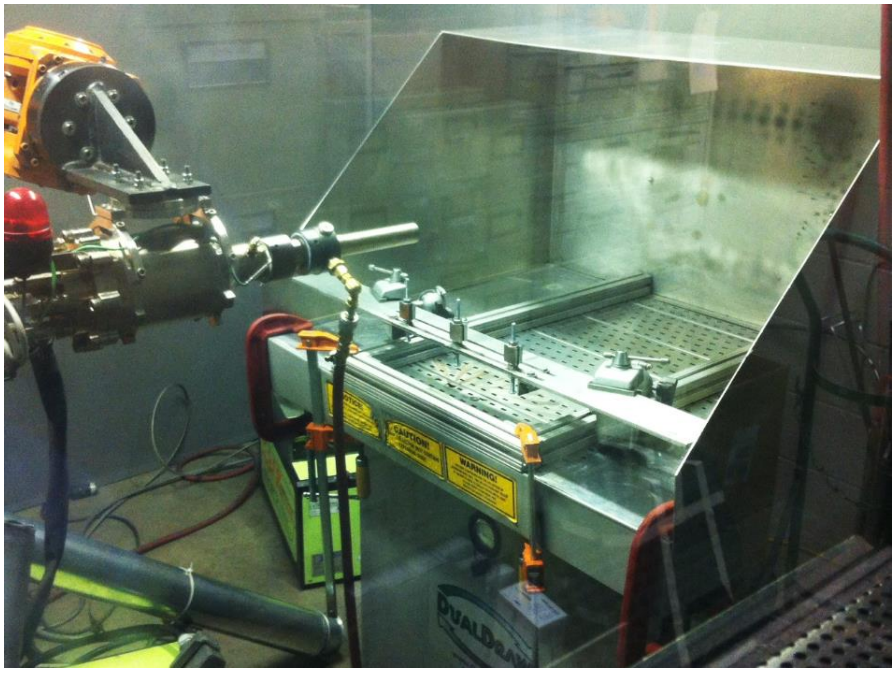

Figure 29: Photograph of the cold spray system in University of Wisconsin-Madison.

Figure 30: Photographs of thermal spray system at Thermal Spray Technologies used for the current study.

3.3. Mechanical Test and Corrosion Test

Scratch testing was carried out for zirconium-silicide coatings on Zirc-4 substrate to evaluate coating adhesion and cohesion. A standard Rockwell indenter (20 ° cone with 0.2 mm radius) was slowly traversed across the coated surface under a force of 2.5 N with velocity of 15 mm/min to make a controlled scratch on the coating surface. Coating damages (e.g., cracks and spallation) and scratch width on surface indicate that mechanical integrity of the coating.

Oxidation tests for the bulk materials and the coatings has been performed at elevated temperatures using commercial furnaces (e.g., Lindberg box furnace, model#51442) at the University of Wisconsin. For the bulk materials, the samples were polished with 320, 600, 800, and 1200 grit SiC papers and then ultrasonically cleaned with acetone and methanol. The coated samples were cleaned with acetone and methanol before the test. For air oxidation tests, samples were exposed at high temperatures (e.g., 700 °C, 1000 °C, 1200 °C) in ambient air. The samples were removed each hour for weight change measurement (as an initial measure of the extent of oxidation) performed with Satorius micro-precision balance (model#CPA26P) with 0.002 mg resolution. Annealing of some coatings was carried out in argon environment to understand high temperature stability. For this, the samples were encapsulated in argon back-filled quartz tube along with pure zirconium granules to reduce residual oxygen gas during annealing.

Isothermal corrosion tests in pressurized steam simulating accelerated corrosion in LWR environment was performed for bulk and coating samples. A high-temperature water/steam autoclave had a dimension of 4 cm in diameter and 50.8 cm in length. Figure 31 show the autoclave system for the steam corrosion test. The test section was made of nickel alloy 625 and it is capable of operating at maximum temperature and pressure of 650 °C and 35 MPa, respectively. The minimum measurable dissolved oxygen is 3 ppb. The variation of the temperature and pressure in the sample test section are ±1 °C and ±0.2 MPa, respectively. The samples were mounted onto a holder, also made of Alloy 625, with electrical isolation being achieved by using alumina washers between the samples and sample holder. The purpose of the test is to evaluate oxidation resistance of the material in prototypical water conditions.

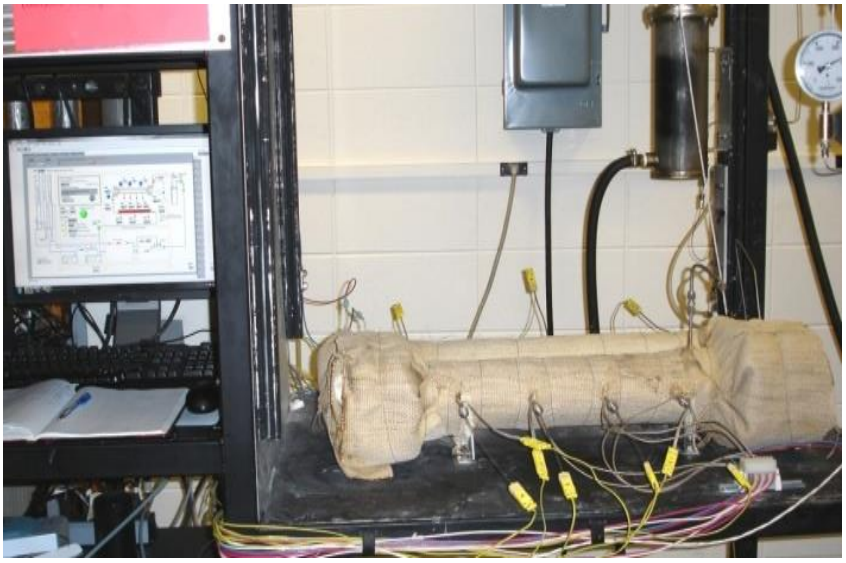

Figure 31: A photograph of the high pressure/high temperature autoclave (NS4653, Parr Instrument Company)

3.4. Material Characterization

Observation of surface morphology and cross-section of bulk zirconium-silicide and zirconium-silicide coatings were performed by a Zeiss LEO Scanning Electron Microscope (SEM) integrated with Energy Dispersive Analysis system (EDS). X-ray diffraction (XRD) with Cu Kα radiation was conducted to identify phases on surface of the samples. Diffraction peaks were acquired from 30° to 90° with coupled 2θ mode and from 30° to 50° in 2θ with a 2° grazing incident beam. The very near-surface chemical compositions and binding energies are evaluated by Thermo-Scientific Kα X-ray Photoemission Spectroscopy (XPS). Prior to the binding energy acquisition, surface cleaning was performed by 3keV Ar ion source for 30 seconds under high vacuum to remove any residual surface contamination. To identify microstructures of coatings and oxide scales at high resolutions, thin foils of the samples were lifted out by a Zeiss Auriga Focus Ion Beam (FIB) milling and imaged with a Tecnai 12 Transmission Electron Microscope (TEM) and Titan Scanning Transmission Electron Microscope in conjunction with EDS (STEM-EDS). In addition, the surface factors influencing boiling heat transfer were characterized in terms of surface roughness as measured with a Zygo optical profilometer and cross-sectional imaging and

wettability by measuring water droplet contact angle on the sample surfaces using Dataphysics OCA 15 Optical Contact Angle Measurement System.

3.5. Quenching Test

3.5.1. Facility Description

A schematic diagram and photograph of the quenching test facility are shown in Figure 32 and Figure 33, respectively. The facility essentially consists of the following components: an air actuator, a Teflon seal assembly, a heating zone, a cylindrical test section, a water quenching chamber, and electronics. The air actuator (51 cm-bore diameter and a 30 cm-stroke length) was installed above the water chamber and aligned concentrically with the top flange of the water chamber. As shown in Figure *34*, the air actuator was connected to 6 mm-diameter 316 stainless steel supporting rod via the aluminum connector. It was operated by compressed air (~ 0.7 MPa) supplied from the laboratory wall and the linear motion was controlled by a mechanical toggle switch. The downward linear speed was approximately 100 mm/s.

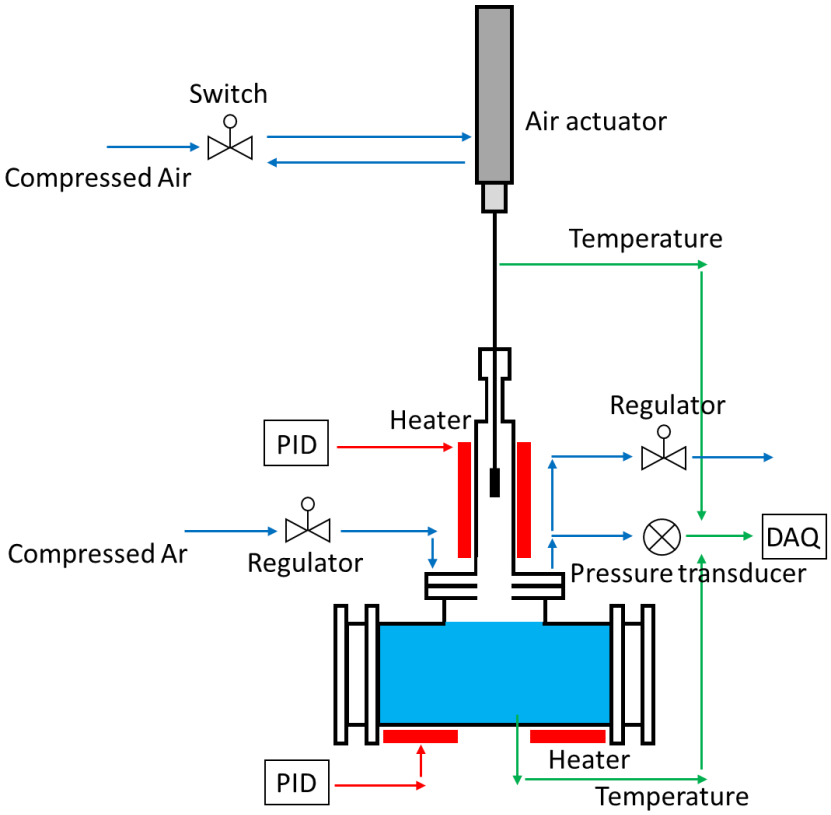

Figure 32: Schematic illustration of the quenching test facility designed and built for this research.

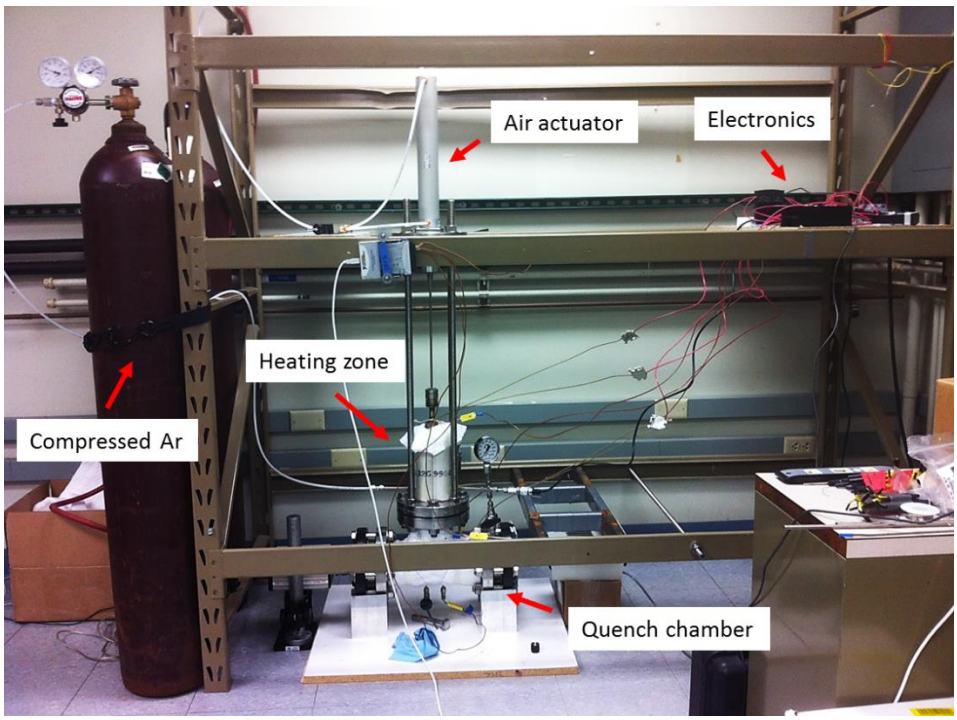

Figure 33: A photograph of the quenching test facility.

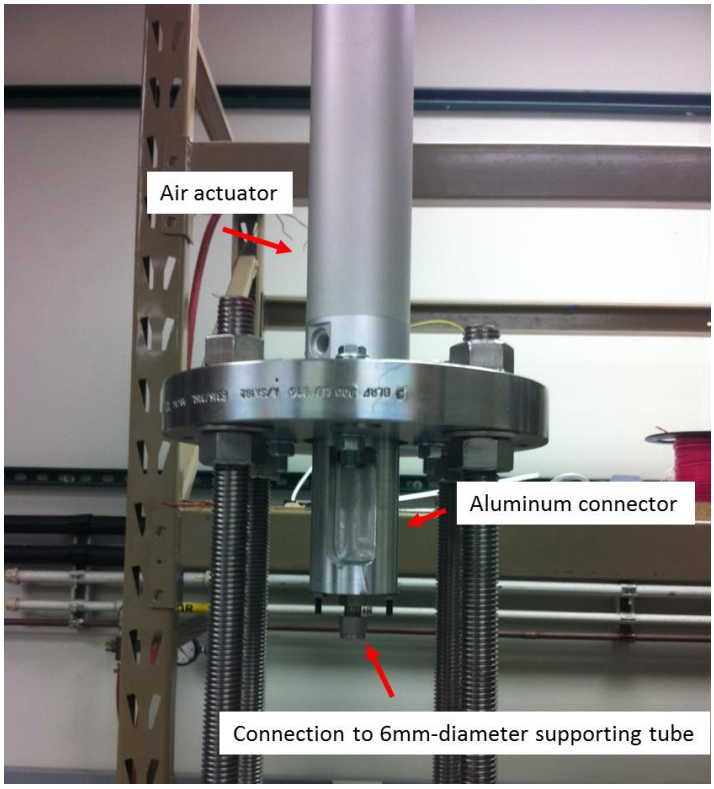

Figure 34: Photograph of the air actuator and the aluminum connector.

The Teflon seal assembly is one of key parts in the experimental facility. Its function is to maintain high pressures in the quenching chamber during experiments while allowing the support tube to slip through in a linear motion. As a dynamic seal, a Teflon O-ring (2-202 size) was selected because its maximum operating temperature is relatively high (230 °C) and friction coefficient is low (0.1~0.2). Based on the properties, it was expected that leakage under elevated pressures of the chamber would be minimal and buckling of the support tube would not occur. The seal holder was made of 316 stainless steel and consisted of a top cap and a bottom seal housing, as shown in Figure 35. By tightening the bolts, the bore on the top cap compresses the O-ring, being able to adjust contact force between the support tube and the Teflon seal. The bottom of the seal housing was machined to have fine grooves (2.5 mm-width) on the surface, increasing surface area and therefore heat dissipation by convection from the heating zone. Based on heat transfer calculation, the design would reduce the temperature of the Teflon seal by about 50 °C compared to that without the grooves.

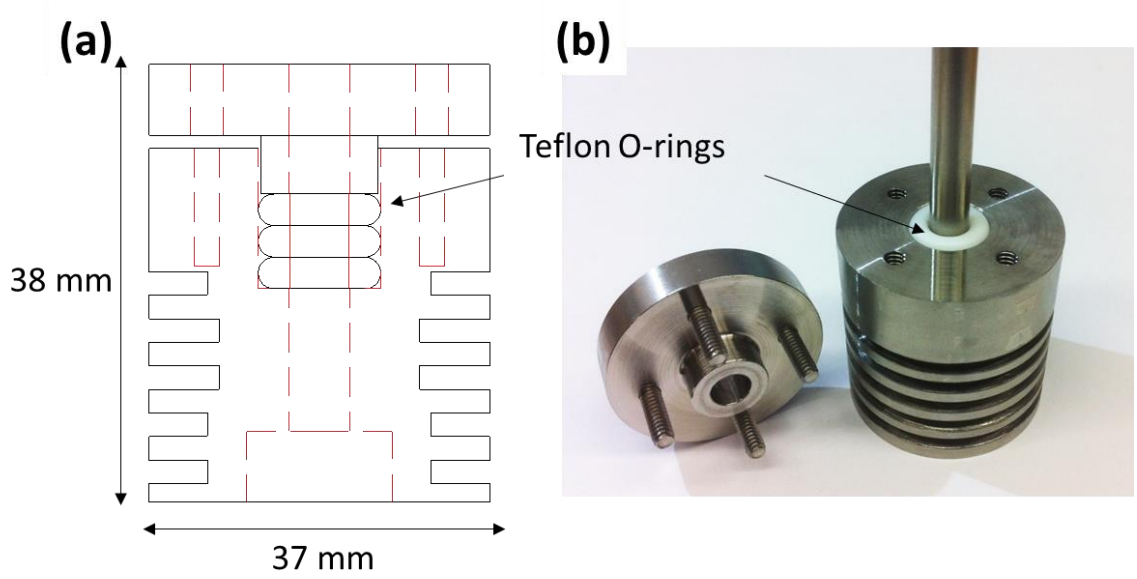

Figure 35: (a) Schematic illustration of the Teflon seal assembly and (b) a picture of the assembly.

The sample can be heated up to 700 °C in the heating zone. The upper limit of temperature was determined by the maximum operating temperature of the heater and the mechanical properties of the 316-stainless steel tube at elevated temperatures. A 312 W heating tape (13 mm in width and 1.2 m in length) wrapped the entire surface of the 316-stainless steel tube (25 mm in diameter) and was insulated by a Kawool blanket and microtherm molding, minimizing heat loss to the atmosphere (see Figure 36). The insulation layers were tightened by a Ni-Cr wire, and a K-type sheathed thermocouple was installed on the heater surface to control the heater temperature.

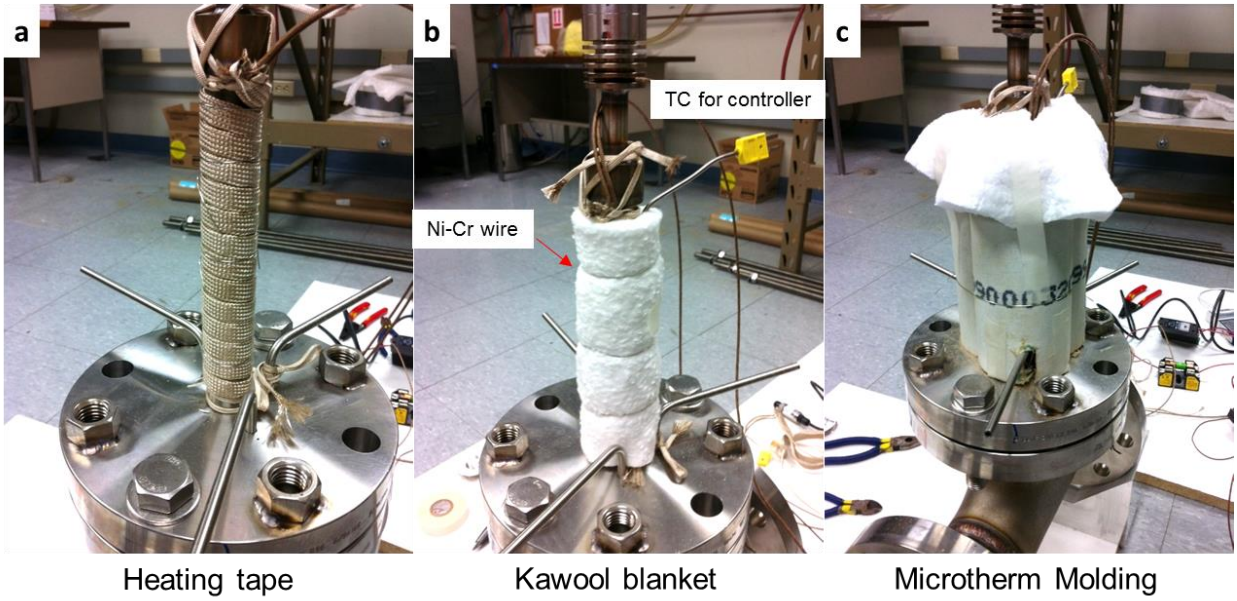

Figure 36: Photographs of the heating zone, consisting of (a) a heating tape, (b) kawool insulation, and (c) microtherm insulation molding.

Dimensions of the cylindrical Zircaloy-4 test section are shown in Figure *37*. The diameter of the vertical rod is 10 mm and the height is 51 mm. A hole, stepped from 3.2 mm to 1.6 mm in diameter, was drilled on the top surface of the sample. To measure the temperature history of the sample during a quenching process, a K type, ungrounded thermocouple (1.6 mm in diameter) with an Inconel sheath (Omega, model KMQIN-062U-22) tightly inserted via interference fitting into the center of the sample. A reinforcing 316 stainless steel tube of 3.2 mm in diameter was inserted between the thermocouple and 3.2 mm-diameter hole, where staking fitting (deforming the top Zirc-4 surface to fix the tube) was used to connect the reinforcing tube and the test section. The reinforced tube was connected to the 316 stainless steel supporting tube of 6.3 mm in diameter using Swagelok tube fittings. The experimental uncertainty during quenching is assumed to be ±1.1 °C, as provided by the thermocouple manufacturer.

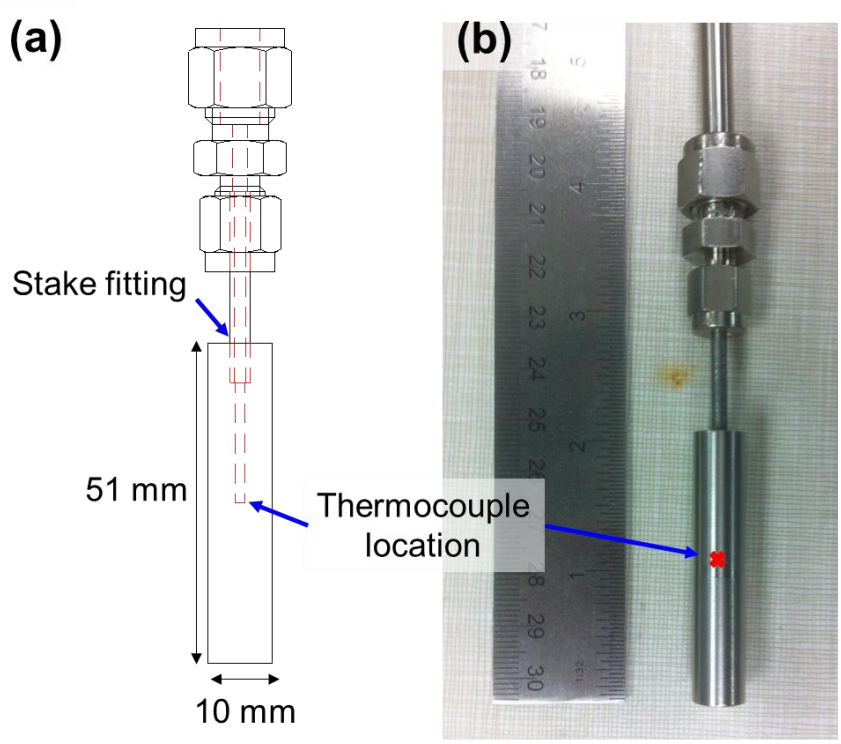

Figure 37: (a) Schematic illustration and (b) a photo of the test section.

Figure 38 is a photograph of the quenching chamber, for which a 316-stainless steel butt-welded tee pipe of three inch-nominal pipe size (schedule 80) was welded to a weld-neck flange on each opening. Two borosilicate windows having 70 mm in diameter and 20 mm in thickness (John C. Ernst Co., Inc, model 501BO-3-300ss ASSY) rated for 2 MPa were placed between black window cover and each welded neck flange to visualize bubble evolution on a hot specimen during quenching experiments. The quenching chamber can contain approximately 1.7 L of deionized water (18 MΩ), and its temperature was controlled by a 624 W heating tape (13 mm in width and 2.4 m in length) installed on the outer surface of the tee pipe. To measure the water temperature, a K-type, sheathed thermocouple of 3.2 mm in diameter was mounted at the bottom of the water pool. The chamber pressure was regulated by compressed argon gas, an inlet pressure regulator, and a back-pressure regulator. The desired pressure was set by the inlet pressure regulator and overpressure during the test was decreased by a back-pressure regulator. A pressure transducer (Omega, model PX309-300GI) and mechanical pressure gauge mounted on the top flange

monitored the system's pressure. Error of the pressure transducer is known as ±1.0 % by the manufacturer. Finally, the whole facility was supported by aluminum V-shaped blocks on the floor.

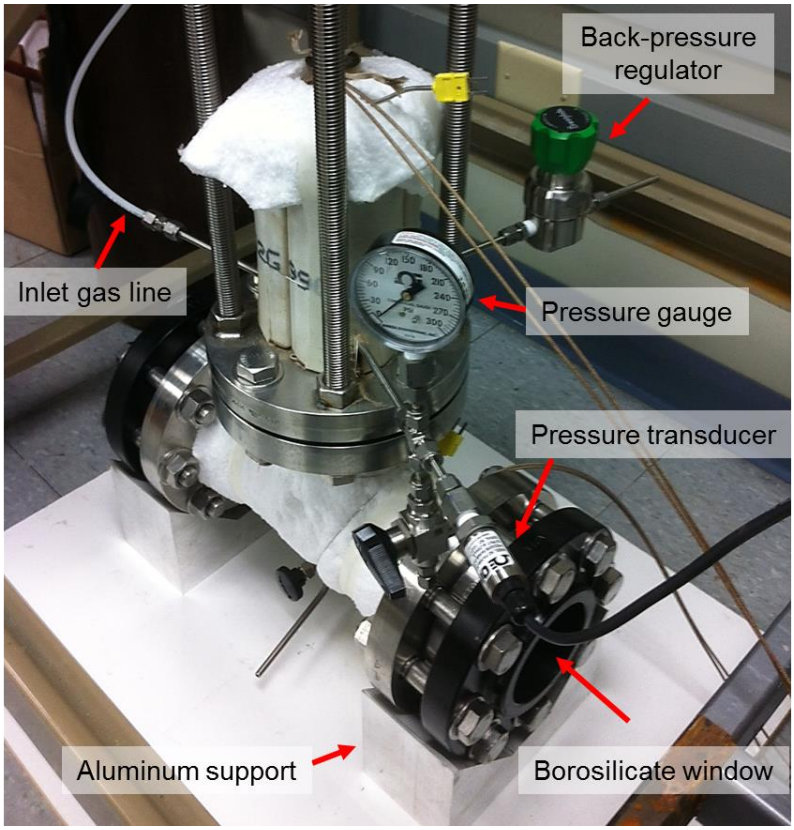

Figure 38: Photograph of the quenching chamber.

The electrical control system was designed to supply power to the heaters so that temperature of the test section and the quenchant pool was controlled as shown in Figure 39. The duty cycle of the heaters is controlled by a solid-state relay operated by a 24 VDC power supplier (Omega, model LP-PS-6024) and a PID (proportional-integral-derivative) temperature controller (Omega, model CN7533) sending on/off signals to the solid-state relay. A data acquisition system (National Instruments) with a sampling rate of 10Hz was used to record sample temperature, quenchant temperature, and chamber pressure during quenching experiments. In addition, a high-speed camera (Motion Pro HS-3, 100 to 300 frame per seconds) was installed, together with Xenon light (Streamlight, model 45621) to visualize bubble dynamics in the quenchant pool.

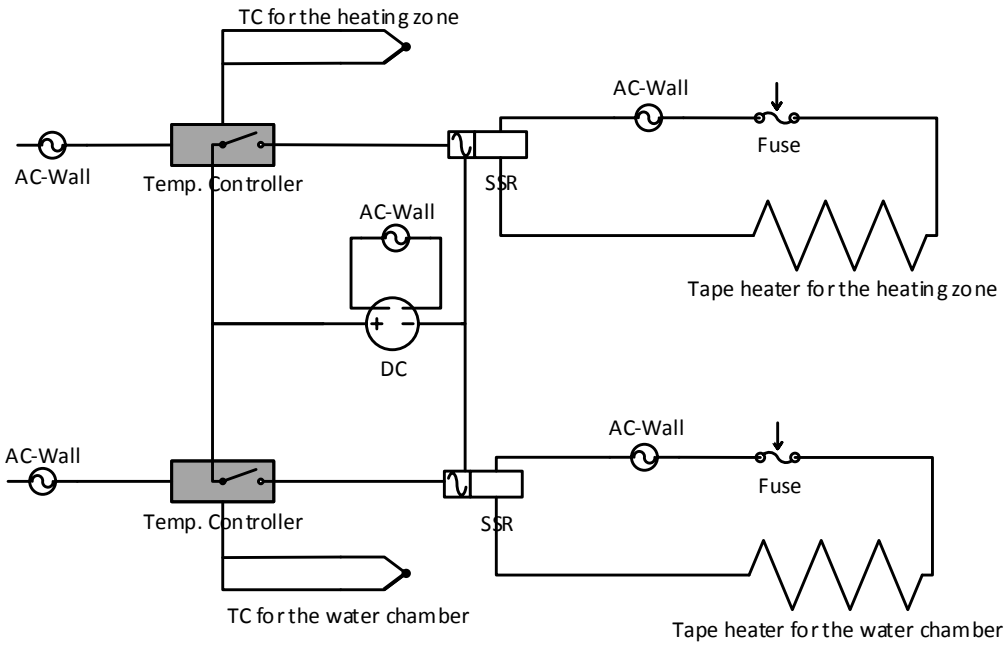

Figure 39: A schematic diagram of the electric circuit of the quenching facility.

3.5.2. Quench Experimental Procedures

The experimental procedure for quenching experiments is as follows:

- Before the test, an inlet pressure regulator and a back pressure regulator are set to a target pressure.
- The water chamber filled with deionized water (1.4 L) is heated up to saturation temperature at atmospheric pressure and the temperature is maintained for 20 minutes while a vent valve is open to remove any dissolved gasses in the water.
- After the degassing, the vent valve is closed and an inlet valve for the Ar gas is opened to pressurize the chamber to a target pressure in a case for pressurized quenching experiments.
- In subcooled tests, temperature is set to be desired temperature (e.g., 85 °C) in the controller for the quenchant pool.
- When the water temperature is reached desired temperature, power is supplied to the heater tape in the heating zone in order to increase temperature of the test section.
- The test sample is plunged into the quenching pool using an air actuator when the center temperature of the test specimen reaches the desired value (i.e., 700 °C).

- The temperature variation at the center of the test sample and bubble evolution on the surface are recorded using a data acquisition system and a high-speed camera.
- The test is completed when thermal equilibrium is identified between the test section and water pool.
- Depending on the purpose of the test, post-characterization of the test sample is performed such as visual observation and electron microscopy.

3.5.3. Post-processing of Measured Data

Surface Temperature and Surface Heat Flux

The temperature history was measured by a thermocouple installed at the center of the cylindrical specimen during the quenching experiments. If the spatial temperature distribution in the specimen cannot be neglected during the cooling process ($Bi<<0.1$), the surface temperature is a better indicator of the thermal phenomena on the solid surface instead of the center temperature. Moreover, it is unknown whether the modified surfaces induce a higher Biot number so the assumption for uniform temperature distribution in the solid is not reasonable. In addition, determination of the surface heat flux is necessary to plot boiling curves, surface heat flux vs. surface superheat (T_{sup}), which would be used to evaluate the minimum film boiling temperature (T_{min}). To obtain the surface temperature and surface heat flux, the inverse heat transfer problem was solved by using INTEMP, a commercial inverse heat transfer software.

The forward heat conduction problem is to determine temperature distribution in terms of location and time in a solid if both the initial and boundary conditions are given such as surface temperature, surface heat flux, and convective conditions. For example, a forward problem for a two-dimensional plane wall with convective boundary conditions is shown in Figure 40.

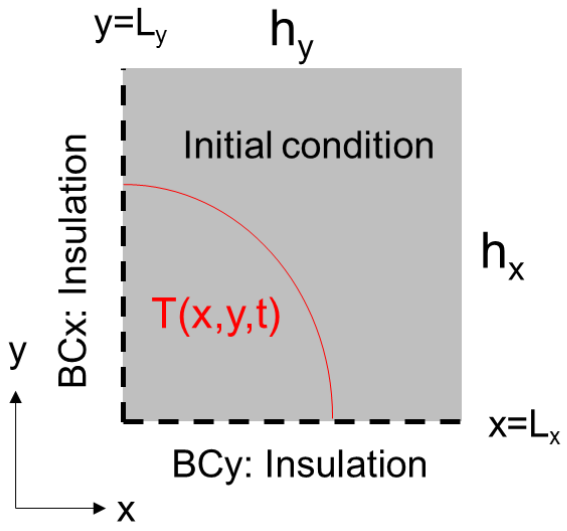

X- direction BCs:

$$\frac{\partial T}{\partial x} = 0 \; at \; x = 0$$

$$k\frac{\partial T}{\partial x} = -h_x(T - T_\infty) \; at \; x = L_x$$

$$T(x, 0) = T_i$$

Y- direction BCs:

$$\frac{\partial T}{\partial y} = 0 \; at \; y = 0$$

$$k\frac{\partial T}{\partial y} = -h_x(T - T_\infty) \; at \; y = L_y$$

$$T(y, 0) = T_i$$

Figure 40: Two-dimensional transient heat conduction problem for plane wall [88]

A solution for the problem may be obtained by the separation of variable technique so that it consists of a product of one-dimensional solutions as follows:

$$\frac{T(x,y,t)-T_\infty}{T_i-T_\infty} = \frac{T(x,t)-T_\infty}{T_i-T_\infty}_{Plane\ wall} \cdot \frac{T(y,t)-T_\infty}{T_i-T_\infty}_{Plane\ wall} \tag{18}$$

Exact solution in x-direction:

$$\frac{T(x,t)-T_\infty}{T_i-T_\infty} = \sum_{n=1}^{\infty} C_n \exp(-\zeta_n^2 Fo)\cos(\zeta_n x^*) \tag{19}$$

where $Fo = \frac{\alpha t}{{L_x}^2}$, $\alpha = \frac{k}{\rho C_p}$, $C_n = \frac{4sin\zeta_n}{2\zeta_n+\sin(2\zeta_n)}$, $\frac{h_x L_x}{k_x} = Bi = \zeta_n tan\zeta_n$, $x^* = \frac{x}{L_x}$

where ζ (discrete eigenvalues) is determined by Bi= $\zeta_n$tan(ζ_n).

On the other hand, the inverse heat conduction problem is an estimation of unknown boundary conditions using known temperature history in the interior solid. Due to the complexity of the ill-posed problem (a solution is not unique), INTEMP, a commercial software package (Version 5.1, Nov.2009)

based on dynamic programming and finite element method was utilized to perform the inverse heat conduction problem. The input data for the software are geometry data (nodes and elements), measured temperature-time histories at certain locations, known boundary conditions, and thermal properties for the solids. The output data are the surface heat flux and surface temperature at the unknown boundaries. The basic principle of the software is to perform iterations, which compare both the measured and estimated temperature from assumed boundary conditions until their difference is below a criterion. The finite element model for a quadrant of the cylindrical test section in the current experiment is illustrated in Figure 41, consisting of 561 nodes and 500 axisymmetric elements with temperature-dependent properties (i.e., density, thermal conductivity, and heat capacity) of Zircaloy-2 (see Table 3).

Table 3: Thermal conductivity, density, and heat capacity of Zircaloy-2 [89].

Thermal conductivity (W/m·K)	$k=12.767-5.4348\cdot10^{-4}\cdot T+8.9818\cdot10^{-6}\cdot T^2$ (300K<T<1800K)
Density (kg/m^3)	$\rho=6595.2-0.1477\cdot T$ (<1083K)
Heat capacity (J/kg·K)	$C_p=255.66+0.1024\cdot T$ (273K<T<1100K)

The measured temperature-time history, which is indicated at the left bottom corner in Figure 41 was used in the INTEMP model. Since temperature-time data was available at a single location, the boundary condition for the top surface was assumed to be a constant heat transfer coefficient with a constant external temperature. In other words, accurate estimation of boundary conditions for both the top surface and the open boundary is only allowable if temperature-time data in multiple locations are available. The inner boundaries were symmetry conditions, and heat conduction in the angular direction was neglected. Lastly, using the calculated heat fluxes and surface temperatures on the open boundary, heat transfer coefficients were calculated by Newton's law of cooling.

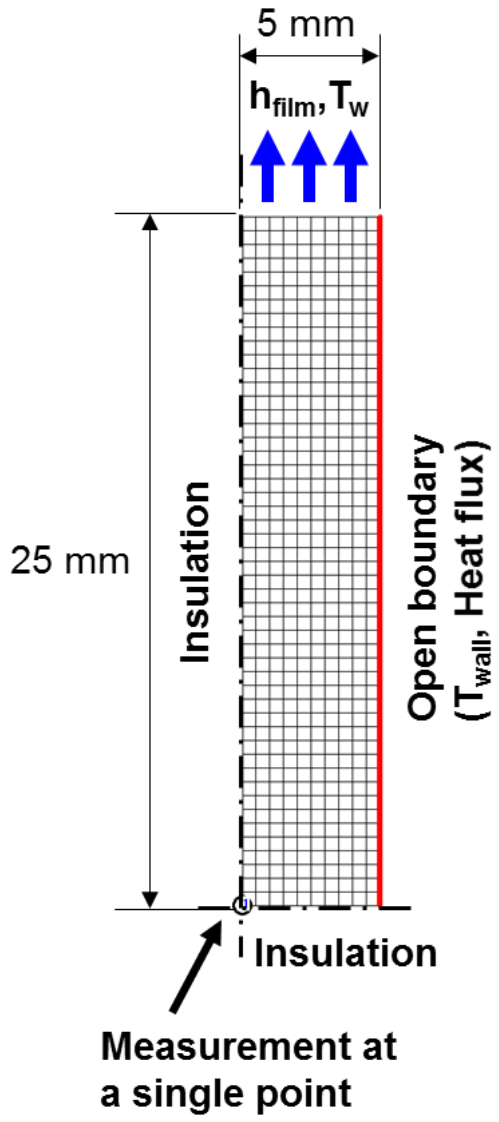

Figure 41: Problem definition for INTEMP model in the current study.

Due to the nature of the ill-posed problem, the estimated boiling curve exhibits jagged behavior and is very sensitive to spurious input data. Thus, INTEMP offers a smoothing process to eliminate the noise in the output data. Trujillo and Busby introduced a dynamic programming filter which optimally smoothing the output data using a third-order filter [90,91]. The basic concept is building a cubic spline function passing near output data points with maintaining a certain degree of smoothness and minimizing a deviation from the output data. The degree of smoothness is controlled by a smoothing factor (SF) in INTEMP model. Detailed explanation for the smoothing process are specified in the literatures. Boiling curves for a bare

Zirc-4 specimen at ambient conditions, which were calculated with the three different smoothing factors, are shown in Figure 42. The effect of smoothing factor on the boiling curve is evident. The small SF causes oscillations even if the result curve closely matches the raw data. On the other hand, the large SF leads to a smoother curve but a loss of heat flux data due to oversmoothing is identified in the nucleate boiling regime. Finally, the intermediate smoothing factor (10^{-2}) has been used as an optimal value for all inverse heat conduction calculations.

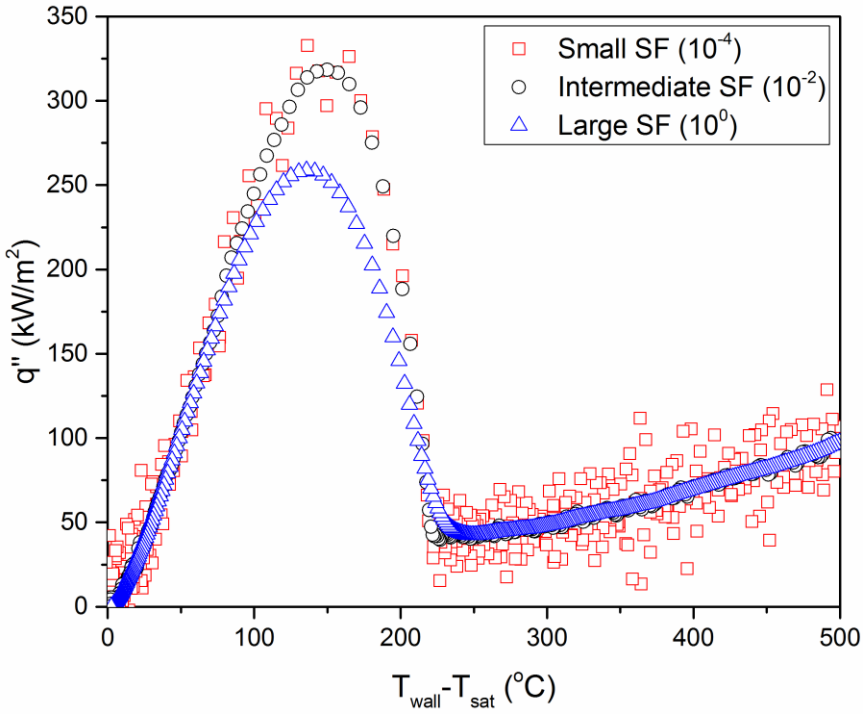

Figure 42: Boiling curves calculated with three different smoothing factors.

Validation of the INTEMP results was performed by comparing it with the lumped capacitance method. Surface heat flux using the lumped thermal capacitance method is determined by equation (20) below:

$$q" = -\frac{\rho \cdot C_p \cdot V}{A_s} \cdot \frac{d\Delta T}{dt} \qquad (20)$$

where V is volume, A_s is surface area, and $d\Delta T/dt$ is a rate of temperature change at the center of the specimen. Figure 43 shows three boiling curves for a bare Zirc-4 quenching test at atmospheric condition evaluated by one-dimensional INTEMP, two-dimensional INTEMP, and the lumped capacitance method,

respectively. Surface heat flux in the one-dimensional INTEMP appears to be overestimated because the axial conduction and the geometric term (solid volume and surface area) were neglected in the estimation. Figure 43 displays good agreement between the two-dimensional INTEMP method and the lumped capacitance method, when in the film boiling regime. This is likely because the regime has a low Biot number. Therefore, it can be concluded that the two-dimensional INTEMP calculation is useful to estimate surface heat flux and surface temperature while eventually being utilized to evaluate T_{min}.

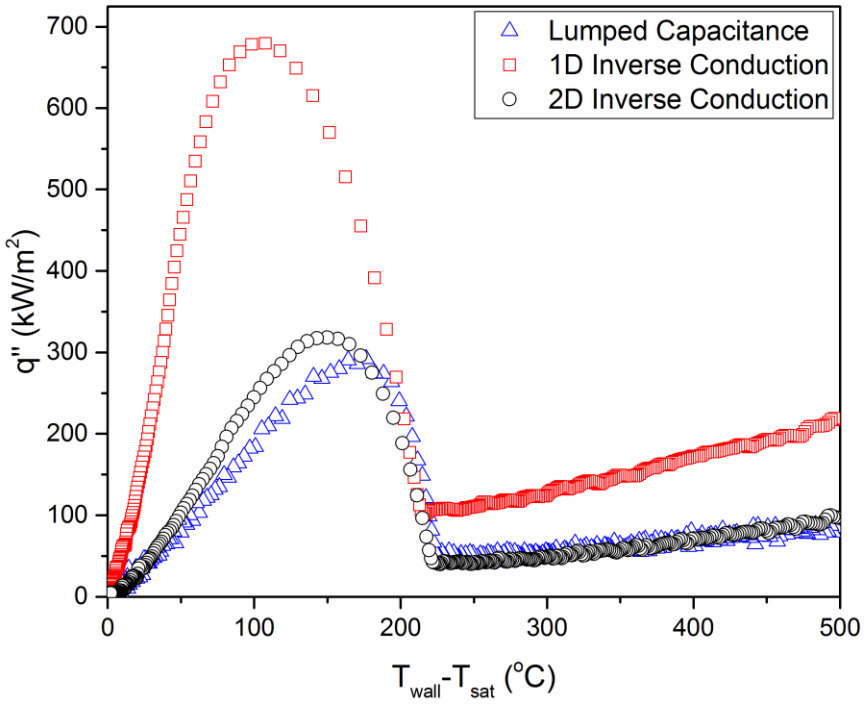

Figure 43: Boiling curves of bare Zirc-4 plotted by lumped capacitance method, one-dimensional INTEMP, and two-dimensional INTEMP analysis.

As mentioned before, the heat transfer coefficient on the top surface was predefined in the INTEMP model because two unknown boundary conditions cannot be estimated by using temperature-time data at a single location. Thus, it is worthwhile to check the sensitivity of the heat transfer coefficient to the output on the open boundary. Figure 44 shows the boiling curves evaluated with different heat transfer coefficients. Lower h_{film} in the model leads to a higher heat flux on the open boundary but the estimated curve is not significantly sensitive to h_{film}, indicating that dominant heat transfer occurs in the radial direction. Therefore,

the film boiling heat transfer coefficient (200W/m^{2}K reported in Dhir) [92] on the top surface has been assumed in INTEMP analysis.

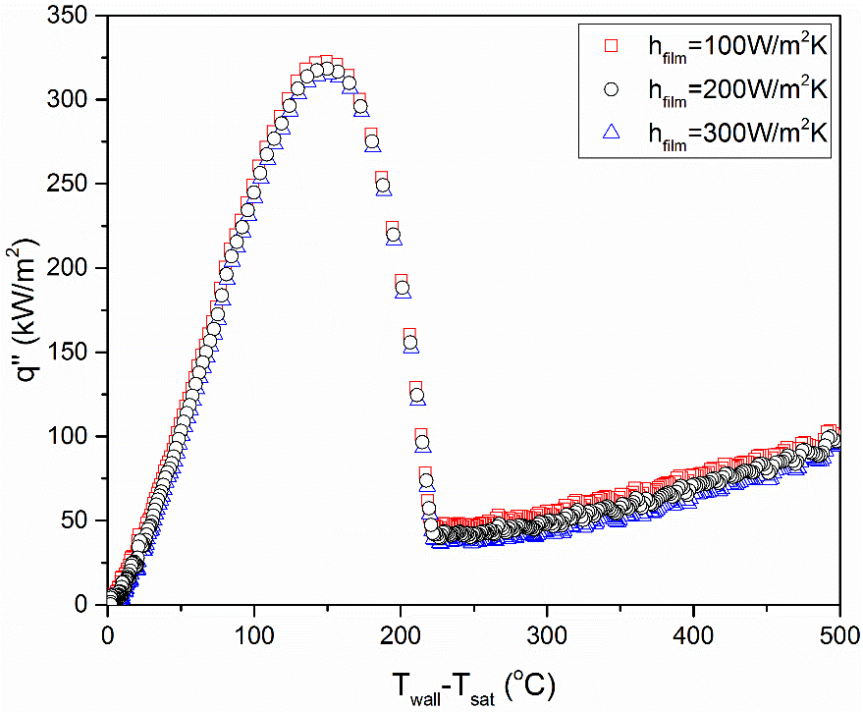

Figure 44: Boiling curves with different heat transfer coefficients on the top surface in INTEMP model.

Finally, effect of mesh size in INTEMP model on the calculated boiling curves is shown in Figure 45. The boiling curves were plotted with the three size of the square mesh. The finite element model for the large, the medium, the small mesh condition was consisted of 125, 500, and 2000 elements, respectively. It

appears that effect of mesh size in results of INTEMP model is negligible. Consequently, the medium size mesh (a length of the square mesh is 0.5 mm) was used in the current analysis.

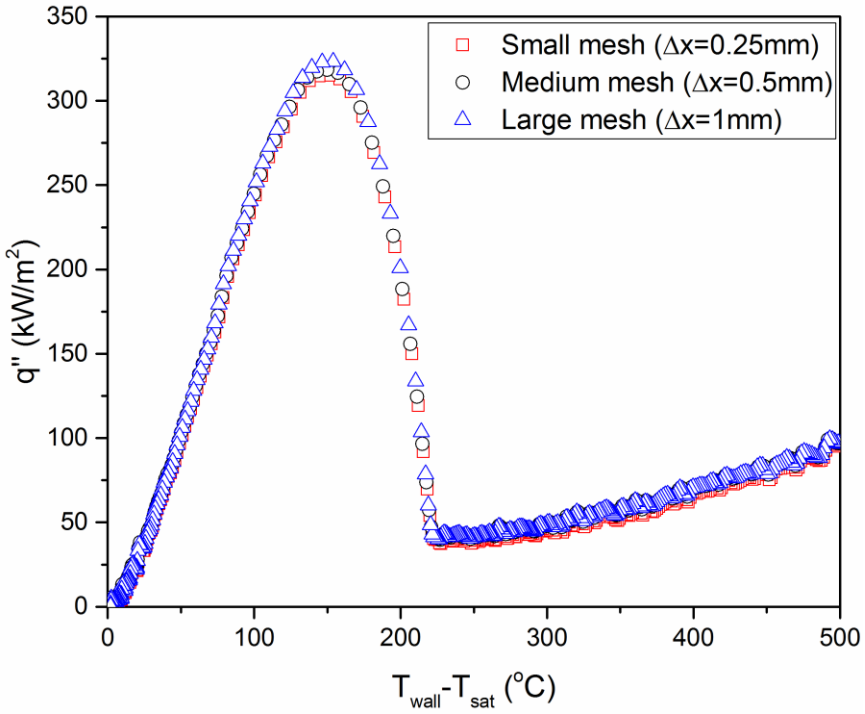

Figure 45: Boiling curves of a bare Zirc-4 quenching experiment calculated with three different square mesh sizes in the two-dimensional INTEMP model.

Determination of Minimum Film Boiling Temperature (T_{min})

Suppose that the temperature of hot material covered by a stable vapor film decreases in the quenching process. At a certain point, the wall superheat temperature is too low to sustain the stable vapor film, resulting in a breakdown of the continuous vapor layer followed by frequent liquid-solid contacts with vigorous boiling. Again, the boundary point between the transition boiling regime and the stable film boiling regime is referred to as the minimum heat flux or the minimum film boiling temperature. Carey [93] defined the minimum heat flux as the lowest heat flux that can maintain stable film boiling. Based on experimental technique to capture the phenomenon, several ways to determine T_{min} have been reported in literature. First, Yamada et el. [94] determined T_{min} as a point where the slope of the cooling curve (center temperature vs. time) is at a minimum, corresponding the lower limit of film boiling. Kim et al. [70] assumed that T_{min} is the temperature at which sudden change in slope of the boiling curve plotted by inverse

heat transfer method was clearly observed. Peterson [84] used commercial inverse heat transfer software to plot the boiling curve, and found the surface temperature showing minimum heat flux values in the film boiling regime.

In current study, T_{min} is defined by the criterion as follows:

$$T_{min} = T_{wall} \quad if \ \frac{dq''_{film}}{dt} = 0 \tag{21}$$

As a stable film blanket covers the hot surface, surface superheat temperature decreases gradually by heat conduction through the vapor layer, resulting in that the surface heat flux decreases because the thickness of the vapor layer gets thinner. Once the stable boiling regime is terminated, the heat flux value starts to increase due to augmentation of heat transfer by frequent liquid-solid contacts. Therefore, a sign of surface heat flux rate changes at the boundary between two distinct boiling regimes. Surface temperature at that point was assumed to be T_{min}. This criterion is identical to the Carey's definition. Figure 46 shows one example of determination of T_{min} using surface heat flux and surface temperature. Temporal change of surface heat flux and corresponding surface heat flux with respect to time are plotted in Figure 46a. Beginning in the stable film boiling regime (around zero to five seconds in Figure 46a), the heat flux rate has a negative sign because heat flux decreases. At the point of minimum film boiling, the heat flux starts to increase and the rate of change would be zero. The surface heat flux corresponds to the minimum heat flux, and the surface temperature at the point in the boiling curve (see Figure 46b) is assumed to be T_{min}.

Lastly, it may be argued that radiation heat transfer would affect the determination of T_{min}. The radiation heat transfer with an assumption of gray surface was calculated by $q''_{rad} = \varepsilon \cdot \sigma \cdot (T_{wall}^4 - T_{water}^4)$ with the emissivity for the oxidized surface (ε=0.6) [95] and the Stefan-Boltzmann constant (σ=5.67·10^{-8} W/m^{2}K). The calculated heat flux via radiation (1.8 kW/m^2) was too small to contribute to the total heat flux; it was about 1.4 % of the total heat flux at T_{min}. Therefore, radiation heat transfer was ignored in the process of determining T_{min}.

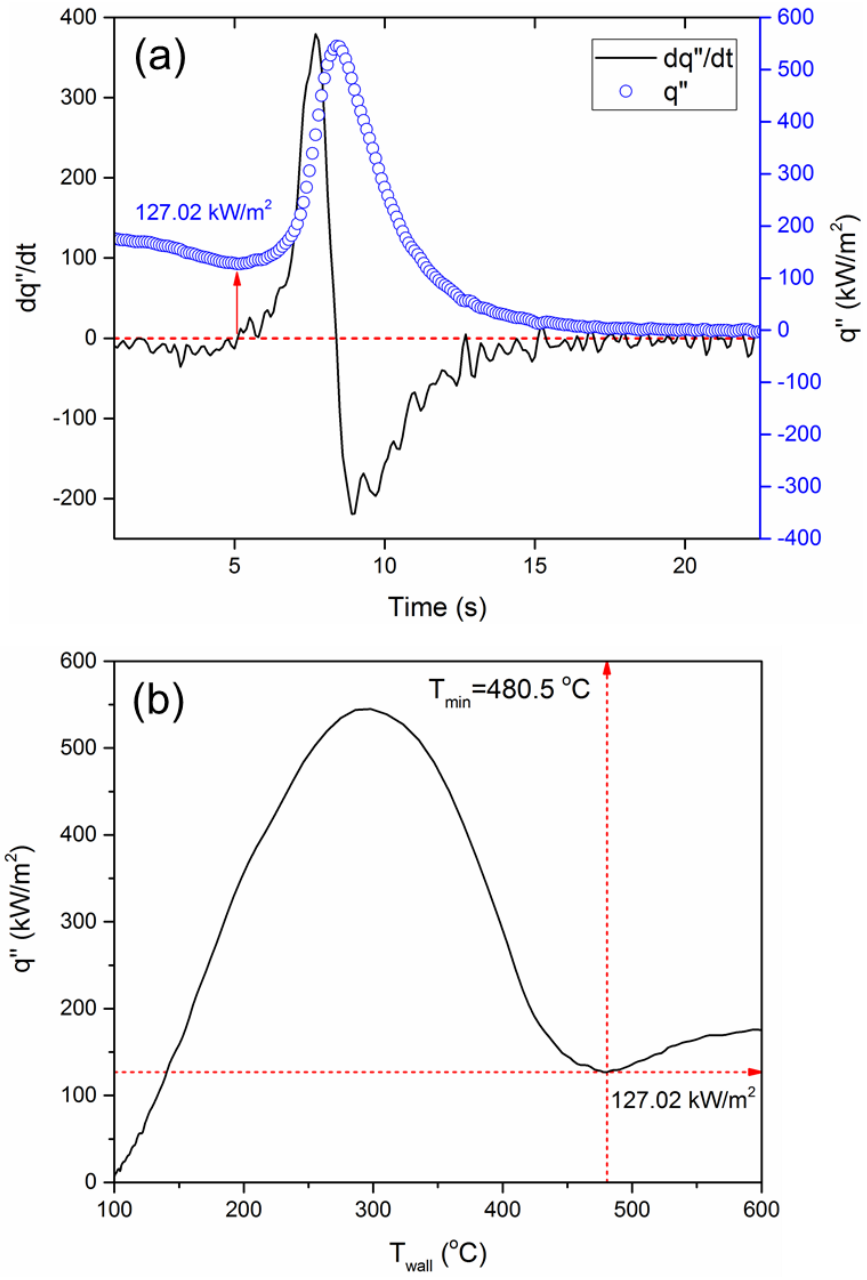

Figure 46: (a) Surface heat flux and rate of the surface heat flux are plotted in quenching time. The red dots indicate dq"/dt equals to zero. (b) the minimum film boiling temperature and minimum heat flux are defined by the criterion shown in the boiling curve.

Evaluation of Vapor Film Thickness

With the aid of the high-speed imaging during the quenching process, dynamic vapor film and bubble evolution on the hot surface was investigated. The thickness of the vapor film on a hot surface is strongly correlated to the boiling regime so, Matlab code was utilized to perform image processing for individual

high-speed images. The reference image (Figure 47a), which does not have any bubbles or vapor layer, was processed first. The image was converted to binary black and white image, and any defects in the image were eliminated. At the center of the test section where the thermocouple tip was located, the number of pixels was counted. With known diameter of the sample, a ratio of actual scale to pixels was determined. Image sequences taken during quenching tests were retrieved and processed. Then, the number of pixels containing both the vapor layer and the specimen at a certain axial location was counted (see Figure 47b). Finally, the number of pixels subtracted by the reference pixels representing only the vapor film converted to the actual scale.

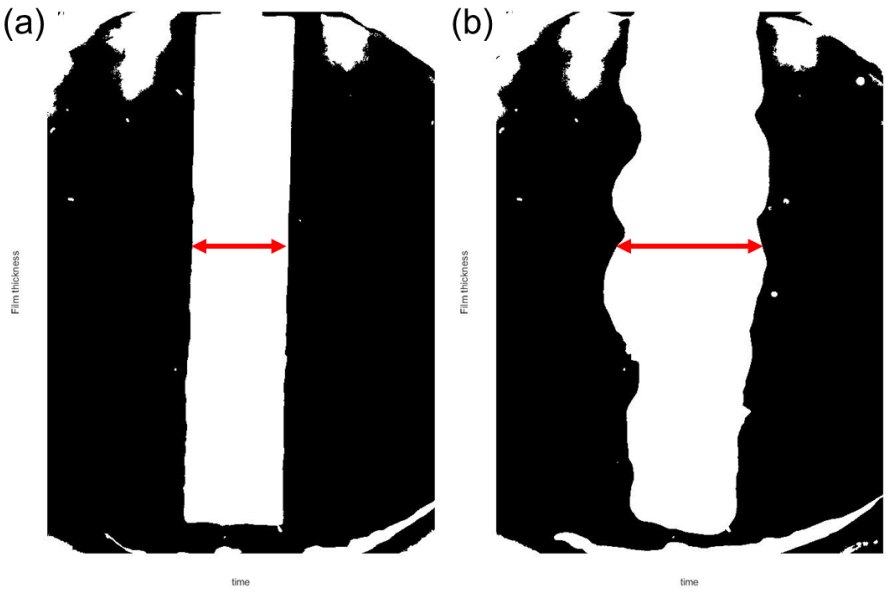

Figure 47: Binary images of (a) a reference image without vapor film and (b) an image with vapor film in Matlab code. The red arrows indicate boundary at the center of the test section to count the number of pixels.

4. Results and Discussions

4.1. Oxidation/Corrosion behavior of bulk Zr-silicide material

Understanding oxidation and corrosion behavior of bulk zirconium silicide materials (e.g., $ZrSi_2$, Zr_2Si) is must precede the evaluation feasibility of zirconium silicide coatings as a protective barrier for Zr-alloy. To this end, air oxidation of bulk $ZrSi_2$ and Zr_2Si in ambient air and steam corrosion tests of bulk $ZrSi_2$ were performed and characterized in detail.

4.1.1. High temperature air oxidation

The oxidation behavior of dense bulk forms of $ZrSi_2$ in high temperature air (700 °C, 1000 °C, 1200 °C, and 1400 °C) was investigated. A temperature of 700 °C was chosen to determine if the material degrades at low temperature, while higher temperature tests (1000 °C, 1200 °C, and 1400 °C) were performed to simulate a postulated loss of coolant accident (LOCA) scenario in light water reactors. To demonstrate compositional effects on oxidation behavior, bulk Zr_2Si was oxidized at 1200 °C in ambient air. In addition, Zircaloy-4 (Zirc-4) was also oxidized under similar conditions as a base-line for comparison with $ZrSi_2$. All oxidized samples were rigorously characterized with the goal of understanding compositional and morphological evolution of micro- and nano- oxide structures at the materials' surface.

Oxidation Kinetics and Oxidation Products of $ZrSi_2$

The kinetics of oxidation of the dense bulk $ZrSi_2$ was determined by weight change measurements at each hour during oxidation. The weight gain values (per unit area of the sample) of Zirc-4 and dense $ZrSi_2$ at 700 °C, 1000 °C, and 1200 °C are shown in Figure 48. As may be noted, the weight gain of the dense $ZrSi_2$ is negligible compared to that of the Zirc-4 at the high temperatures. Zirc-4 showed the formation of a thick oxide scale and its spallation led to weight reduction at 1000 °C (4 hours) and 1200 °C (3 hours) as shown in Figure 48a. On the other hand, the bulk $ZrSi_2$ appeared to be stable without significant degradation at the high temperatures. It is worth noting that no pest oxidation was observed on the surface of the $ZrSi_2$ samples, as has been observed for example in oxidation of $MoSi_2$ for other applications [60]. Minor chipping

on the edge of the bulk $ZrSi_2$ samples was observed at 1200 °C after 3-hour oxidation. Therefore, the weight gain values at 5 hours have not been reported in Figure 48b. The general oxidation kinetics followed a power law, with oxidation kinetics at 700 °C and 1000 °C following approximately a parabolic rate kinetics while at 1200 °C the oxide layer growth obeyed more closely the cubic growth rate law. More protective nature with increasing temperatures have been reported in $MoSi_2$ and $TiSi_2$ as well, resulting from denser SiO_2 formation [60,61,64]. The weight gain relationships are empirical and were plotted with the limited data points so that it is difficult to elucidate physical and chemical processes of the oxide growth. Nevertheless, the weight gain trends imply the kinetics of oxidation of $ZrSi_2$ as a material is controlled by the diffusion of charged species (e.g., Si^{4+}, O^{2-}) through the growing oxide layer.

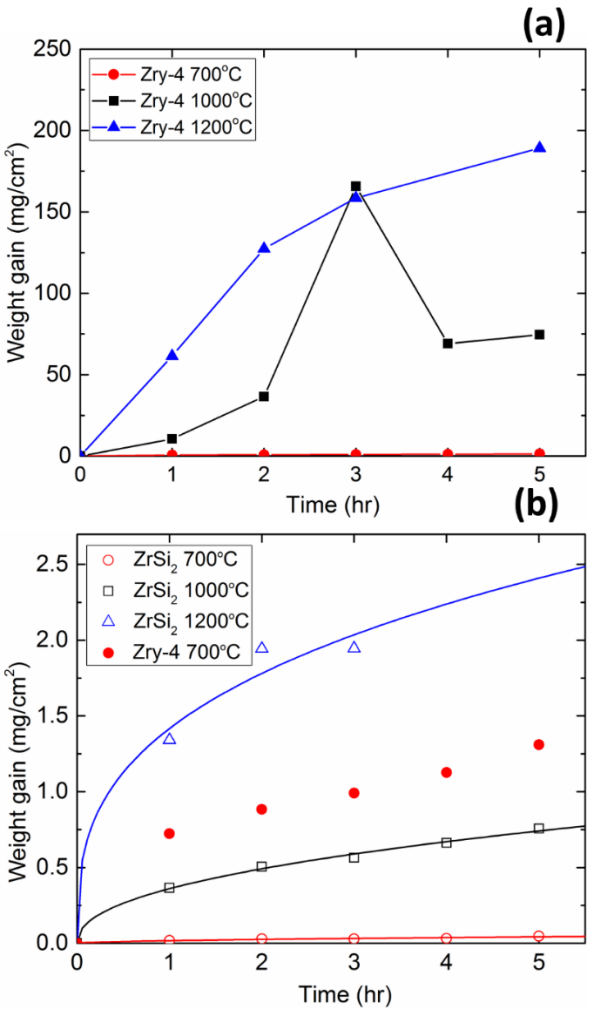

Figure 48: Weight gain vs. exposure time for (a) Zirc-4 and (b) bulk $ZrSi_2$ samples constructed with least square fits at 700 °C, 1000 °C, and 1200 °C in ambient air.

The oxide layer thickness was measured in SEM cross-sectional images and shown in the Figure 49. The average oxide layer thickness of the dense $ZrSi_2$ at 700 °C, 1000 °C, 1200 °C, 1400 °C for 5-hour oxidation was determined to 470 nm, 6.7 µm, 37 µm, and 31 µm, respectively. In addition, the oxide layer thickness at 1000 °C for 15-hour oxidation was 12 µm, which considered together with other exposure times at this temperature is indicative of parabolic oxidation kinetics at 1000 °C. An important observation was that the average thickness of oxide layer at 1400 °C was thinner than that at 1200 °C even though both oxidation tests were performed for 5 hours in ambient air environment. In general, oxidation process is strongly accelerated at higher temperature conditions. The thinner oxide scale in 1400 °C has been attributed to the formation of a highly corrosion resistant zircon layer ($ZrSiO_4$) at this high temperature. Furthermore, no spallation and delamination of the oxide layer were observed and only minor cracks were identified in unreacted $ZrSi_2$ matrix underneath the oxide scale at 1200 °C possibly due to thermal cycling due to periodic removal of samples from the furnace.

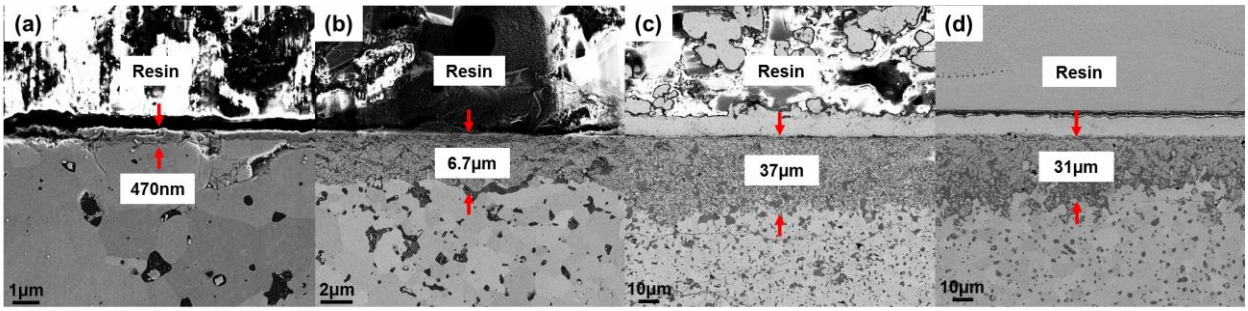

Figure 49: Cross-sectional SEM images of the dense $ZrSi_2$ at (a) 700 °C, (b) 1000 °C, (c) 1200 °C, and (d) 1400 °C for 5-hour exposure in air. The red arrows indicate the oxide layer between a mounting resin and unreacted $ZrSi_2$.

Although thickness of the $ZrSi_2$ oxide layer formed at high temperatures is significantly lower than that formed on Zirc-4, the oxide scale is much thicker than for $TaSi_2$, $MoSi_2$, and WSi_2 in the similar oxidation tests (1000 °C air) reported in literature [54]. One of possible reason for this is the thermodynamically favored ZrO_2 formation in $ZrSi_2$ oxidation. Figure 50 shows Gibbs free energy of formation of oxide per a mole of O_2 of Si as compared to those of Ta, Ti, Mo, W, and Zr, which was calculated by HSC Chemistry thermodynamics software. In these other metal-silicides except for Ti, selective oxidation of Si leads to

formation of a continuous oxidation resistant SiO_2 layer while the absence of continuous SiO_2 layer in $ZrSi_2$ may result in relatively faster oxide growth [57]. Likewise, $TiSi_2$ has at least five times higher oxidation rate compared to $MoSi_2$ [64].

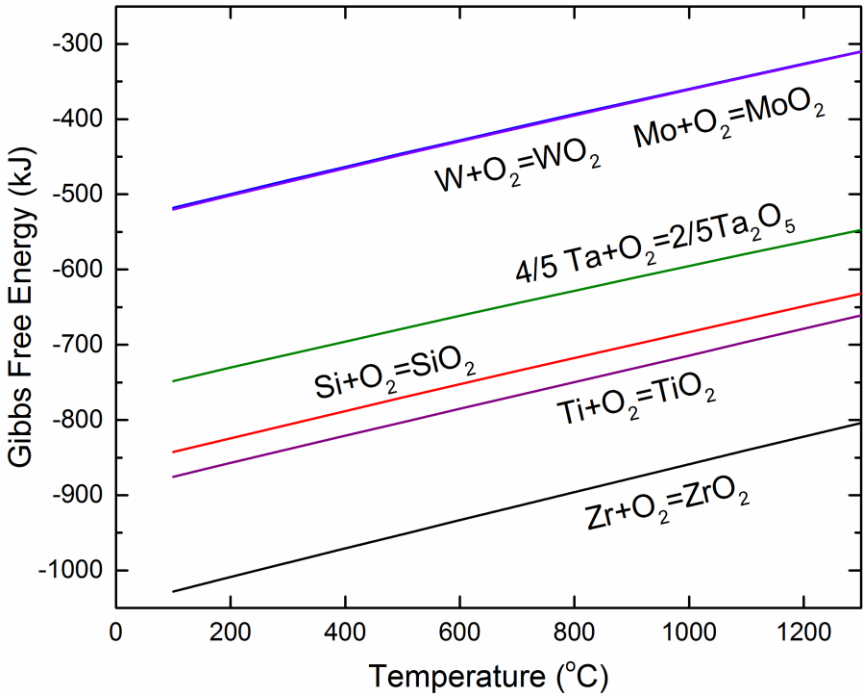

Figure 50: Gibbs free energies of oxide formation for Zr, Ti, Si, Ta, W, and Mo per 1 mole O_2, calculated by HSC Chemistry thermodynamics software.

The phases present in the oxide layer formed at different temperatures for 5-hour exposure were identified by full-theta x-ray diffraction analysis and the results are shown in Figure 51. At 700 °C oxidation (Figure 51a), pronounced diffracted peaks stemming from unreacted $ZrSi_2$ and weak Si and monoclinic ZrO_2 (m-ZrO_2) peaks were also identified. At 1000 °C (Figure 51b) and 1200 °C (Figure 51c) oxidation, intensity of m-ZrO_2 remarkably increased and weak Si peaks were also seen. Grazing incidence XRD scan (2 ° incident beam angle) showed the same results. For higher temperatures, the intensity of the strongest m-ZrO_2 peak at 28 ° (111) gets sharper but the strongest peak of $ZrSi_2$ at 39 ° (131) gets weaker and broader, which corresponds to thicker ZrO_2 oxide layer at higher temperature. In addition, absence of peaks of thermodynamically favored SiO_2 and zircon ($ZrSiO_4$) phases observed in Zr-Si-O system does not preclude their presence, since they may be present as amorphous phases. During the selective oxidation of Zr in

$ZrSi_2$, some Si may be newly formed as an intermediate product which represents the weak silicon peak at 47º (220). Geβwein et al. postulated selective oxidation producing SiO_2 and Si at low temperature (as shown in equation 22) from thermogravimetric experiments of $ZrSi_2$ powders oxidation in air [68].

$$ZrSi_2 + O_2 \rightarrow ZrO_2 + (2-y)SiO_x + ySi \ (500°C < T < 800°C) \quad (22)$$

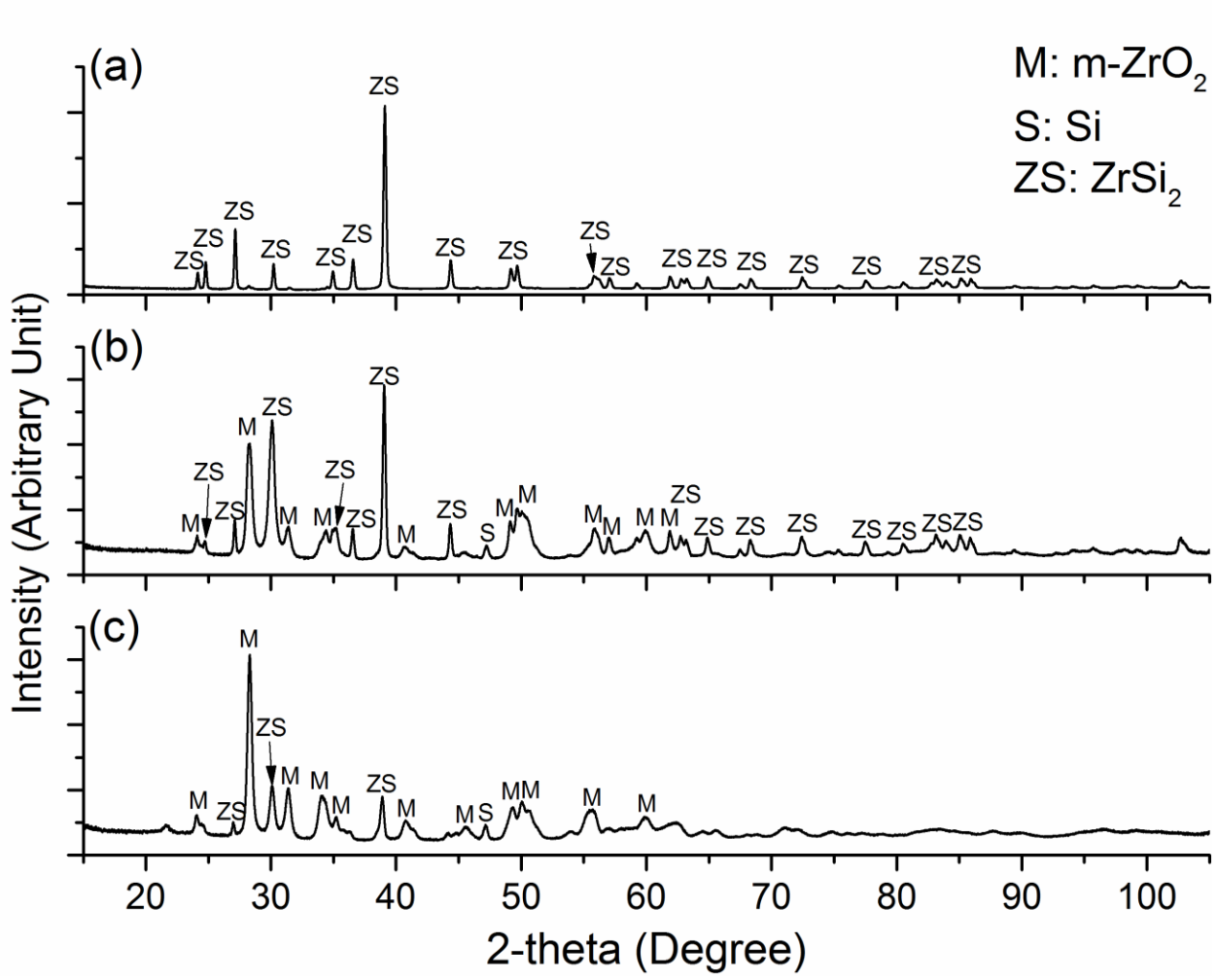

Figure 51: XRD patterns of the $ZrSi_2$ oxidized at (a) 700 °C, (b) 1000 °C, and (c) 1200 °C for 5 hours showing monoclinic zirconia, silicon, and $ZrSi_2$ peaks.

To test the hypothesis that formation of zircon is a kinetically limited process even if formation is thermodynamically favored, long-term oxidation tests of $ZrSi_2$ at 1200 °C for 50-hours was performed. The oxidized $ZrSi_2$ showed spallation of the oxide layer during the cooled down period. X-ray diffraction analysis of the oxidized $ZrSi_2$ sample (Figure 52) revealed strong peaks of zircon and weak peaks for ZrO_2 and SiO_2. This result supports the hypothesis that the formation of zircon is kinetically limited.

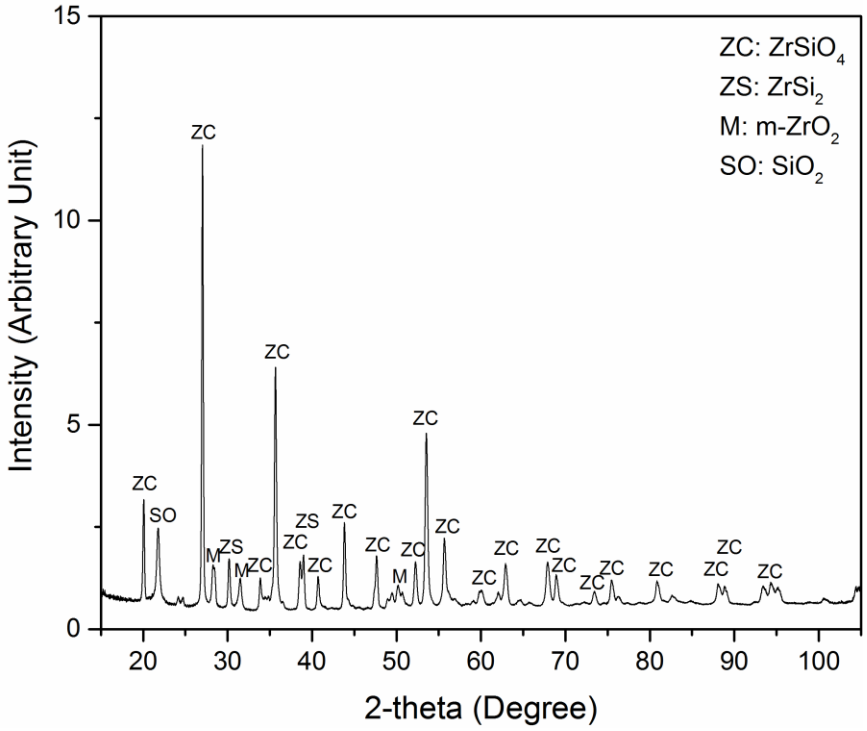

Figure 52: XRD pattern of oxidized $ZrSi_2$ at 1200 °C for 50 hours in ambient air, revealing crystalline $ZrSiO_4$ (zircon) phase.

Evolution of Oxide Surface Morphology in $ZrSi_2$

To investigate the compositional and morphological evolution of the oxide layer at high temperatures, plan-view SEM-EDS examinations were first performed for samples exposed to each of the temperatures. Figure 53a shows SEM image of the surface of the as-received $ZrSi_2$ and Figure 53b shows surface of $ZrSi_2$ sample that was subject to oxidation at 700 °C for 5 hours. Figure 53c and Figure 53d show results of EDS analysis of the oxide layer. Micron-sized spherical phases were observed to evolve on the oxidized surface (Figure 53b). Semi-quantitative EDS point scan confirmed that there were local variations in the concentration of Si, Zr, and O on the surface and the spherical phases were enriched in Si (i.e., point 1 and 2 in Figure 53c). This represents a significantly higher Si concentration than in the as-received $ZrSi_2$ for which the Zr-to-Si ratio was 1:2.4 as determined by our XPS, to be discussed later. Therefore, the micron-scale spherical phases appear to be Si-rich oxides formed by Si diffusion from the surrounding area.

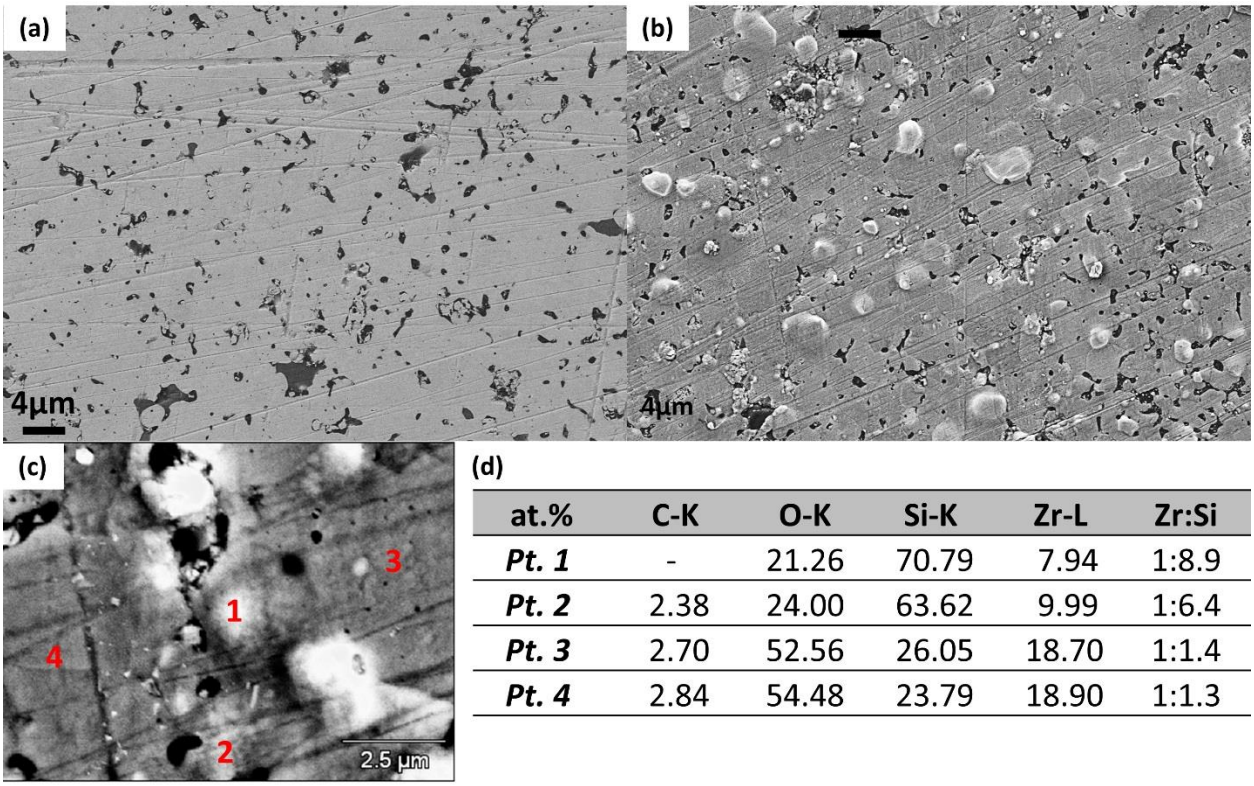

(d)

at.%	C-K	O-K	Si-K	Zr-L	Zr:Si
Pt. 1	-	21.26	70.79	7.94	1:8.9
Pt. 2	2.38	24.00	63.62	9.99	1:6.4
Pt. 3	2.70	52.56	26.05	18.70	1:1.4
Pt. 4	2.84	54.48	23.79	18.90	1:1.3

Figure 53: Plan-view of SEM images of (a) as-received $ZrSi_2$, (b) $ZrSi_2$ oxidized at 700 °C for 5 hours, (c) high voltage SEM (12 kV) image of the oxidized sample, and (d) EDS compositions in regions indicated in (c). Points 1 and 2 indicate the regions of spherical phases shown in the image (b).

On surfaces of samples oxidized at higher temperatures, the surface morphology was different as shown in Figure 54 for samples oxidized at 1000 °C, 1200 °C, and 1400 °C. The Si rich humps were not clearly observed but new surface features started revealing. At 1000 °C, fine oxide phase particles also emerged on the surface but the size of structure was too small to be quantified by SEM imaging. The nano-scale precipitation of oxide phase particulates (40nm to 100nm in size) appeared particularly on the surface of samples oxidized at 1200 °C for 5 hours (Figure 54b). The imaging contrast between the background matrix and oxide particulates suggests differences in their compositions and TEM-EDS analysis determined that these nano-sized particulates were ZrO_2 as will be discussed later. The surface morphology of the long-term oxidized $ZrSi_2$ (Figure 54c) showed distinct features 100-200 nm in size of zircon phase in SiO2 matrix. It is speculated that the nano-scale spherical ZrO_2 phases was formed in SiO_2 matrix in the early stages of $ZrSi_2$ oxidation and then reacted with each other to form zircon phase and coalesce as oxidation progressed. Finally, fully developed zircon phases were observed at the oxidized surface at 1400 °C for 5 hours (Figure

54d) with grains which were 10 to 20 times larger than those formed on the surface on oxidized $ZrSi_2$ at 1200 °C for 50 hours. The result indicates that oxidation temperature is a more dominant factor than duration of oxidation process.

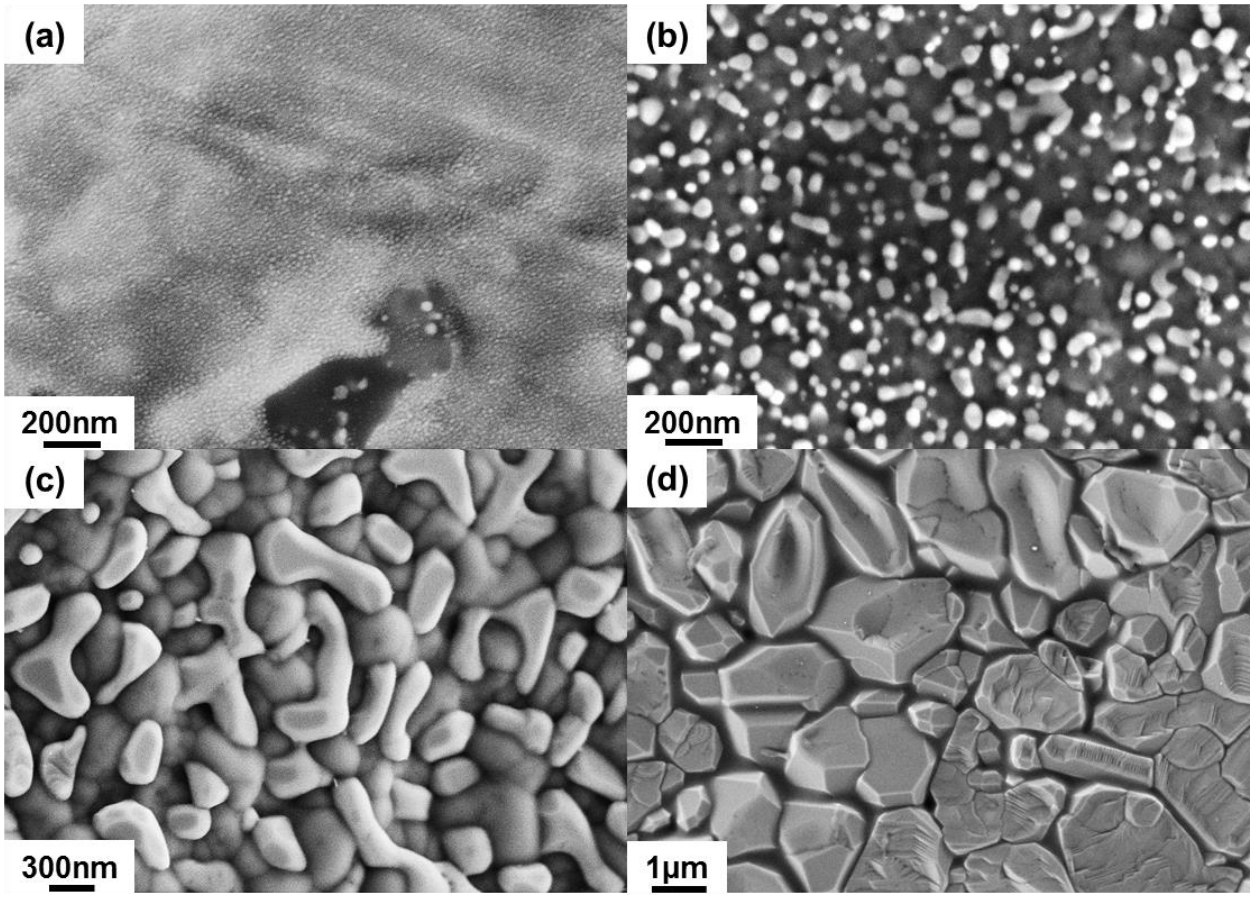

Figure 54: SEM plan-view images of oxidized $ZrSi_2$ at (a) 1000 °C for 5-hours, (b) 1200 °C for 5-hours, (c) 1200 °C for 50-hours and (d) 1400 °C for 5-hours in ambient air.

To understand evolution of oxide layer's surface morphology at high temperatures, XPS analysis was performed. The chemical states of Si, Zr, and O were acquired over a 400 µm diameter circular region on the surface of samples oxidized at each of the temperatures for 5 hours and the results are shown in Figure 55. The intensity of Si 2p binding energy peak increases with increasing oxidation temperature - the peak binding energy shifted +1 eV (102.8 eV→103.8 eV) between samples oxidized at 700 °C and those oxidized at higher temperatures (1000 °C and 1200 °C). On the other hand, signal intensity of the Zr $3d_{3/2}$ and Zr $3d_{5/2}$ binding energies decreased with increasing oxidation temperature. Here, the peak values shifted -

0.7eV at 1000 °C compared to 700°C (183.6eV→182.9eV). The O1s binding energy associated with the elements showed the same trends with respect to temperature. The intensity of O1s binding energy associated with Zr atom decreased but that of Si atom increased with the binding energy shifts, indicating fundamental differences compositional shifts between 700 °C to 1000 °C/1200 °C exposures. Based on the reported XPS binding energies [96], the binding energy of Si 2p and Zr 3d at 1000 °C and 1200 °C corresponded to SiO_2 and ZrO_2 but those at 700°C did not clearly match with simple oxides. The shifts in x-ray photoelectron peaks are likely associated with a transition in binding states. Such shifts have been reported in a complex mixed oxide (i.e., $ZrSiO_4$) in comparison to simple oxides (i.e., ZrO_2 and SiO_2) due to different covalency of cations. The Si 2p bonding is more covalent but the Zr 3d is more ionic in $ZrSiO_4$ [97]. Therefore, it is speculated that at 700 °C a Zr-Si-O phase forms however at 1000 °C and 1200 °C this phase is not stable but rather decomposes to distinct SiO_2 and ZrO_2 simple oxide phases. This is also in good agreement with phase conversion from amorphous $ZrSiO_4$ film to simple oxides at 900 °C annealing (i.e., Si-O-Zr → O-Si-O + O-Zr-O) reported in a previous study [98,99]. Interestingly, oxidation product of $TiSi_2$ at 600 °C in oxygen is glassy Ti-Si-O phase as well [100]. The near-surface chemical composition of oxidized surfaces as determined by the XPS technique is summarized in Table 4. The variation of the concentration ratio of Zr to Si indicates that there was not only lateral diffusion of species shown in Figure 55 but also depth-wise diffusion of species. The compositional ratio of Si to Zr was slightly reduced (less Si) at 700 °C but it increased again (more Si) at 1000 °C and gets doubled at 1200 °C compared to the as-received $ZrSi_2$. Based on the published high diffusion rate of Si compared to Zr [101,102], it appears that a part of newly formed Si during oxidation diffused inward in the thin oxide layer so that the Si concentration on the surface is diminished during oxidation at 700 °C. However, a net outward flux of Si atoms at the higher temperatures increases the Si concentration on the outer-most surface.

Table 4: XPS near-surface chemical compositional analysis of as-received and $ZrSi_2$ oxidized at high temperatures.

Atomic %	Si2p	Zr3d	C1s	O1s	Zr:Si
As-polished	32.23	13.59	8.35	45.84	1.0:2.4
700°C for 5hr	21.16	11.40	1.79	65.64	1.0:1.8
1000°C for 5hr	23.38	8.60	3.37	64.65	1.0:2.7

1200°C for 5hr	27.86	6.74	1.69	63.72	1.0:4.1

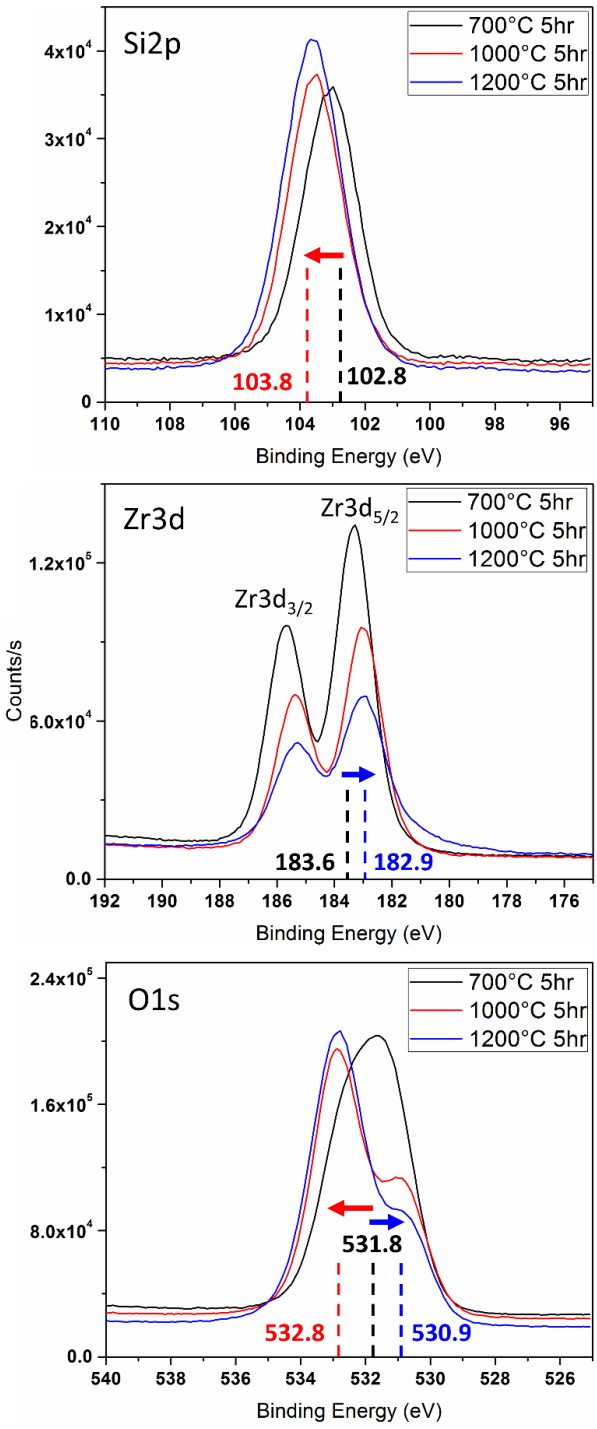

Figure 55: XPS spectrum (Si2p, Zr3d, O1s binding energy) of $ZrSi_2$ oxidized at 700 °C, 1000 °C, and 1200 °C after 5-hour oxidation. Position of the peak maximum (eV) is specified and the arrows indicate the trend in binding energy shift with increasing temperature (from 700 °C to 1000 °C/1200 °C). The red arrows and blue arrows are associated with silicon and zirconium, respectively.

Depth-wise structural evolution of $ZrSi_2$

In order to correlate the observed surface chemical and morphological evolution with depth-wise species diffusion, cross-sectional analysis using high magnification SEM imaging and STEM imaging was performed (Figure 56). A 700 °C, 10-hour oxidation was carried out to get thicker oxide layer and subsequent STEM analysis showed dark wavy structures (Figure 56a) in the ~630 nm thick oxide layer that formed. EDS line scan analysis showed the structures to be Si-rich oxide phase (Figure 56b) and consequently a reduction of Si concentration was identified in the adjacent regions. Based on STEM observations, phase identification by XRD, and the binding energy shift in XPS, the major phases in the oxide layer at 700 °C are likely amorphous and nanocrystalline Zr-Si-O and Si-rich oxide. The cross-sectional images of samples oxidized at 1000 °C and 1200 °C showed complex nano/micron structures. Four types of structures were identified in the 7 μm thick oxide layer formed at 1000 °C (please see Figure 56c, d): (i) submicron layer with fine structural features, (ii) underlying wavy dark structures, (iii) a thick region consisting of irregular structures, and (iv) unreacted $ZrSi_2$ region. It is speculated that the wavy structures developed by the inward diffusion of Si in the early stages of oxidation and the non-directional irregular structures were formed by spinodal decomposition in the Zr-Si-O matrix, which will be discussed in detail.

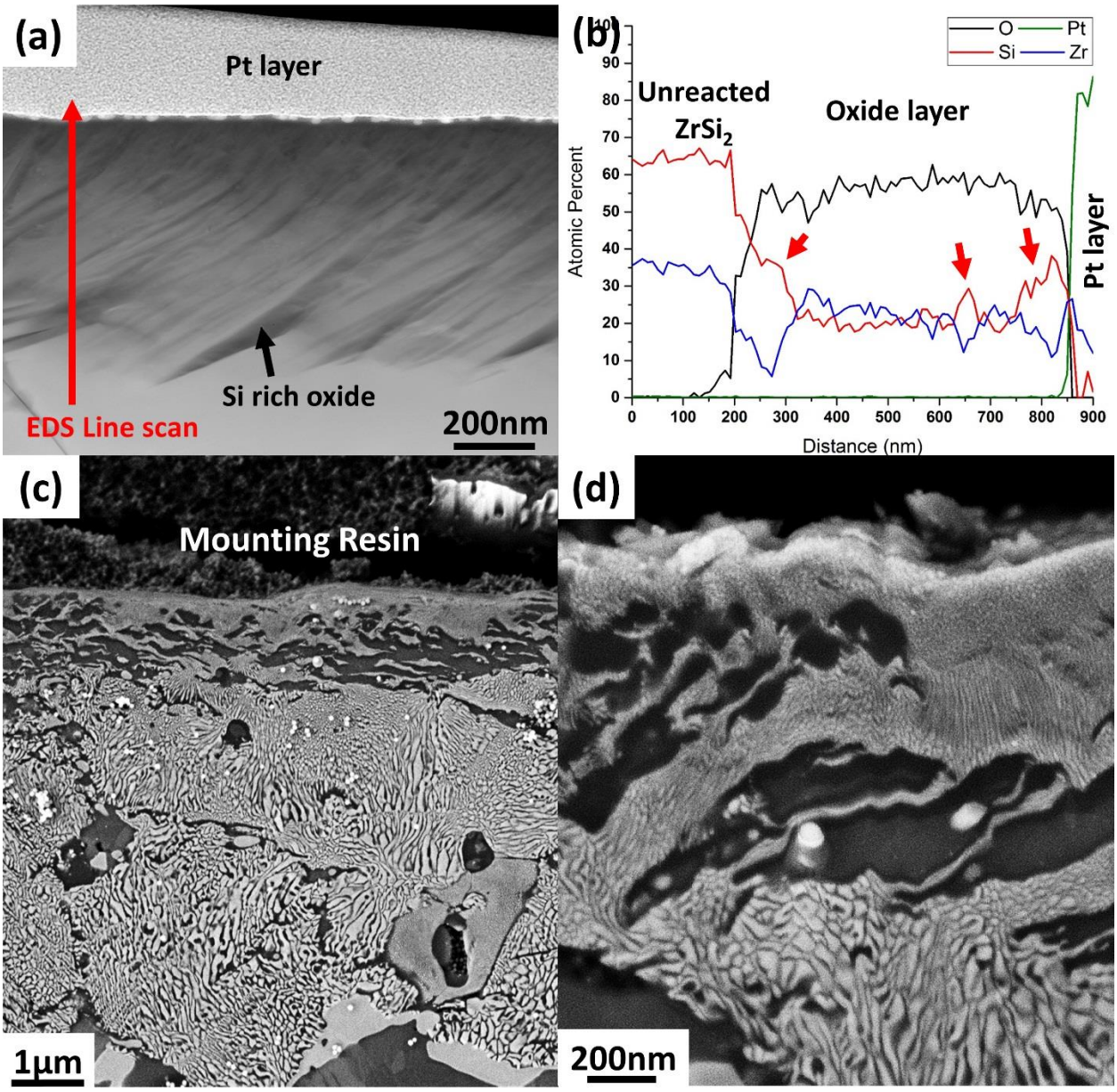

Figure 56: (a) HAADF STEM cross sectional image of $ZrSi_2$ oxidized at 700 °C for 10 hours and (b) corresponding EDS line-scan showing composition fluctuation even in the thin (~630 nm) oxide layer. The red arrows indicate Si-rich oxide. (c) cross sectional SEM image with low voltage (3 kV) of the oxide layer on $ZrSi_2$ formed at 1000 °C for 5 hours at low magnification and (d) and at high magnification near the top layer.

Similar evolution of oxide structures was observed for samples oxidized at 1200 °C for 5 hours. A large numbers of Si islands indicated by the red arrow in Figure 57a were identified at the interface between the oxide layer and unreacted $ZrSi_2$. In addition, charging effects were observed in Figure 57a, indicating a fully oxidized structure (bright regions) which has dielectric properties. However, some regions appeared

not to be oxidized significantly and manifested as dark and grey areas shown in Figure 57b. The nanoscale spherical particulates, which was seen on the plan view image (Figure 54b), were dispersed only in regions adjacent to air interface (Figure 57c). The uniform irregular nanoscale structures were again observed in Figure 57d. EDS analysis (Figure 58a) showed that the less oxidized regions were composed of Si-rich oxide and unreacted $ZrSi_2$. The origin of the Si-rich oxide is the slow reaction kinetics of SiO_2 growth during oxidation of the newly formed Si and some $ZrSi_2$ was not completely consumed while the oxide layer was developing. The irregular structures seem to consist of ZrO_2 and SiO_2 based on the EDS point scan (point 1 in Figure 58b), corresponding to the Si-depleted regions in the EDS mapping. In addition, the existence of Si islands in the interface between the oxide scale and $ZrSi_2$ suggests that selective oxidation occurs at the high temperatures. Due to relatively large SEM-EDS spot size (~1 μm), TEM-EDS analysis was performed to understand mechanism of evolution of this compositionally alternating oxide structure.

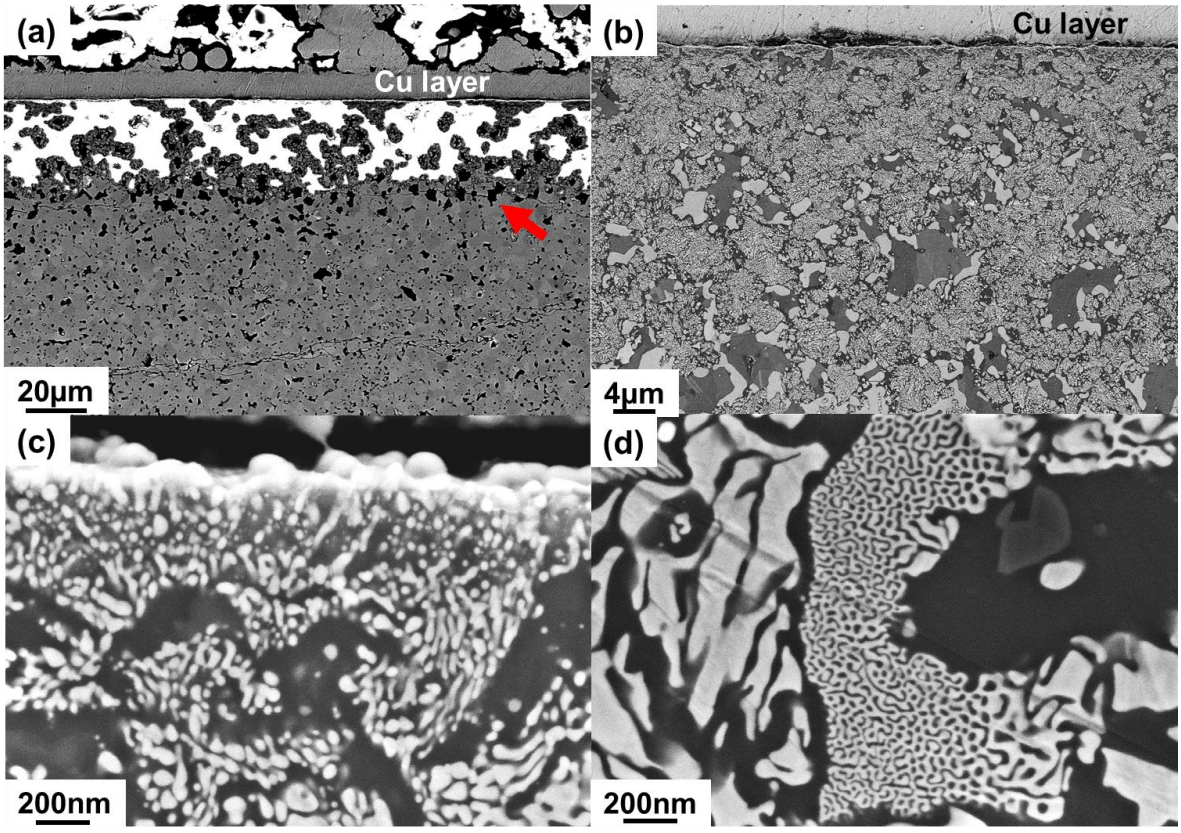

Figure 57: SEM images of $ZrSi_2$ oxidized at 1200 °C for 5 hours, taken at (a) 12kV and (b) 3kV at low magnifications. High magnification 3kV SEM images (c) at interface between air and oxide layer and (d) in the middle of oxide scale showing different shapes of nanoscale structures.

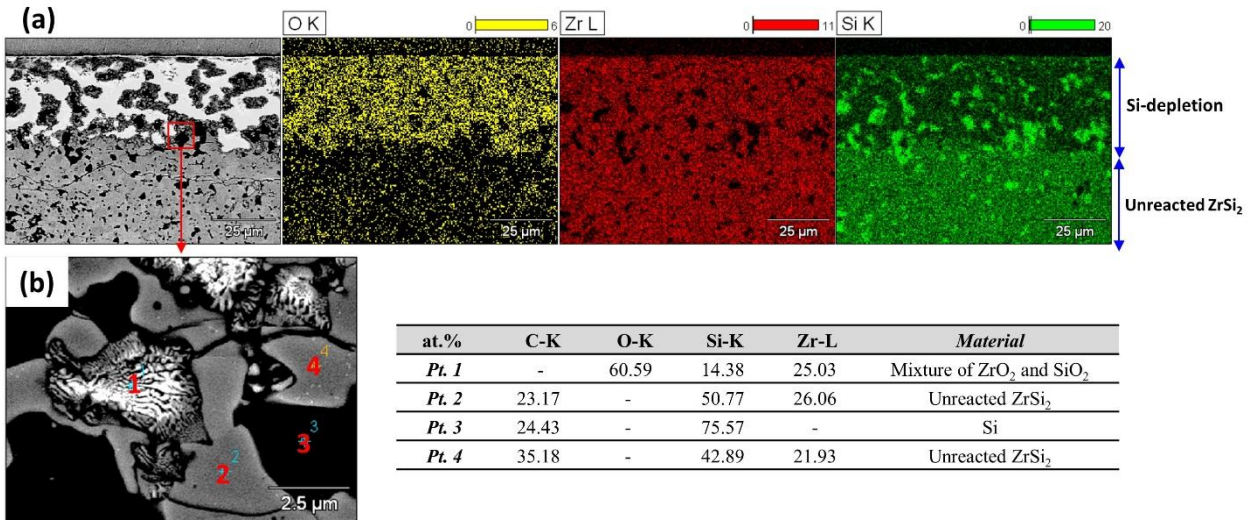

at.%	C-K	O-K	Si-K	Zr-L	*Material*
Pt. 1	-	60.59	14.38	25.03	Mixture of ZrO_2 and SiO_2
Pt. 2	23.17	-	50.77	26.06	Unreacted $ZrSi_2$
Pt. 3	24.43	-	75.57	-	Si
Pt. 4	35.18	-	42.89	21.93	Unreacted $ZrSi_2$

Figure 58: EDS spectra mapping (a) of oxidized $ZrSi_2$ at 1200 °C for 5 hours showing Si depleted region, and point EDS analysis (b) at the interface between oxide layer and unreacted $ZrSi_2$. The carbon signal is an artifact from the mounting resin.

The irregular nanoscale structures and spherical phases observed in Figure 57c and Figure 57d were analyzed using STEM-EDS (Figure 59). The high angle annular dark field (HAADF) STEM images of the $ZrSi_2$ oxidized at 1200 °C for 5 hours revealed nanoscale particulate phases (Figure 59a) adjacent to the air interface and the irregular structures (Figure 59b) uniformly dispersed in the entire oxide scale. Since brightness in HAADF images is proportional to atomic number of material, it is speculated that the structures were composed of higher atomic number elements compared to the background matrix material. STEM-EDS analysis confirmed the chemical composition of the structures as shown in Figure 59c. The spherical particulates and irregular structures were crystalline ZrO_2 in SiO_2 background matrix. The fuzzy ring diffraction pattern (inset, Figure 59b) of the background matrix suggests that the SiO_2 phase is amorphous, in agreement with the XRD result where no crystalline SiO_2 peaks were identified.

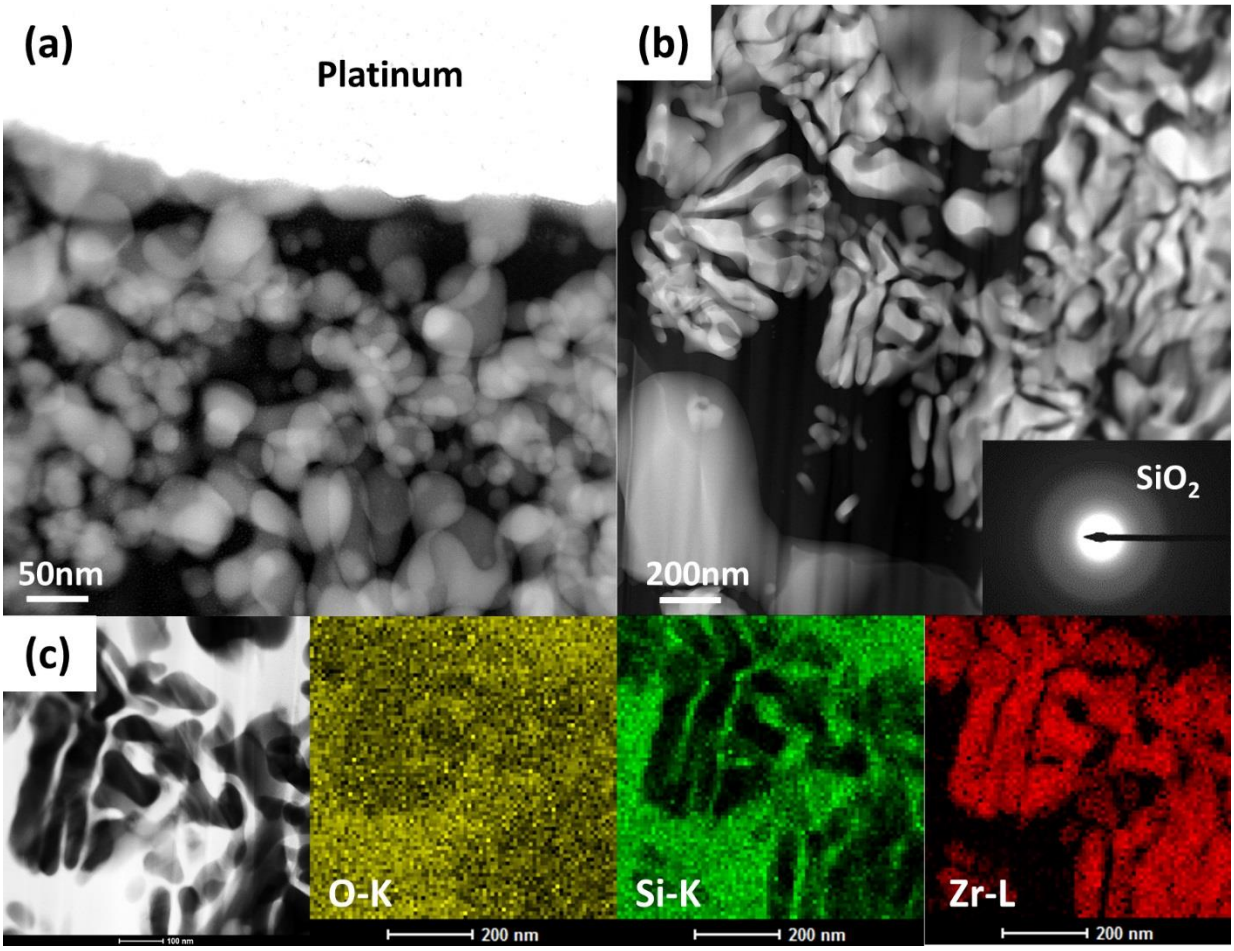

Figure 59: HAADF STEM cross sectional images of $ZrSi_2$ oxidized at 1200 °C for 5 hours. (a) nanoscale spherical phases at the interface with air (i.e., top surface) and (b) irregular structures uniformly dispersed in oxide scale. The inset shows SiO_2 diffraction pattern indicating an amorphous structure. The platinum layer was deposited on the top of the sample during sample preparation by FIB. Higher atomic number material exhibits brighter contrast in these images. (c) Bright field STEM image and STEM-EDS elemental mapping images of the irregular structures. These images clearly indicate the irregular structures consist of ZrO_2 and amorphous SiO_2.

High magnification SEM image of the near-surface oxidized $ZrSi_2$ at 1400 °C shown in Figure 60a, indicates distinct layers $ZrSiO_4$ and SiO_2. The layers were continuous, suggesting that they are resistant to oxygen diffusion. Underneath the SiO_2 layer, the mixture of zircon, ZrO_2, and SiO_2 was identified. It is believed that the solid-state reaction to form zircon was not completed. The morphology of the mixture is in good agreement with the literature modeling zircon formation by solid state reaction of tetragonal ZrO_2 and amorphous SiO_2 (Figure 60b) [103].

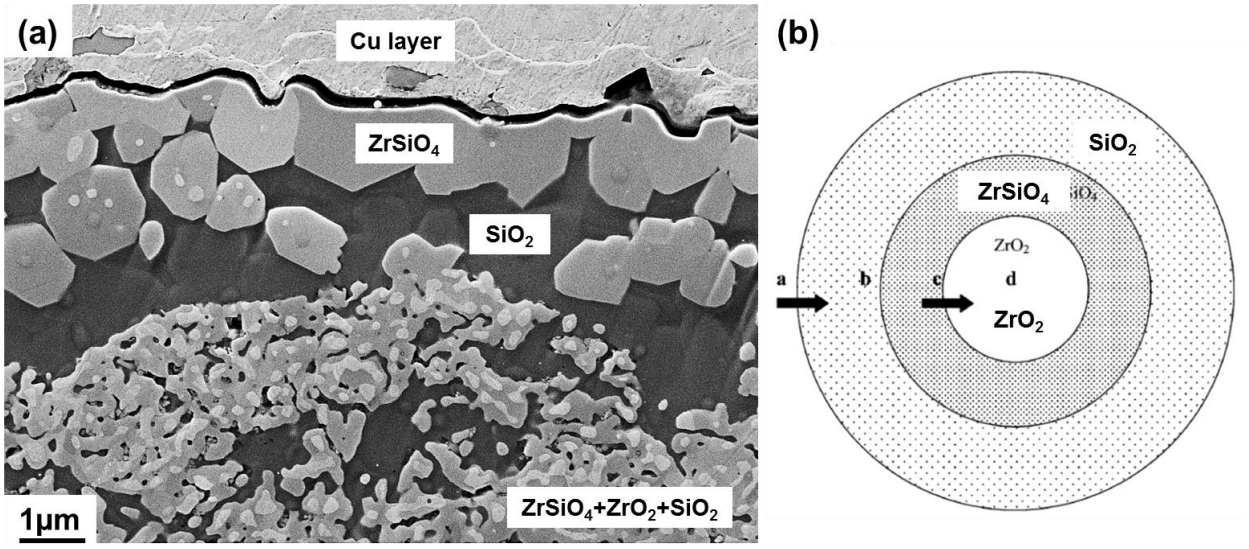

Figure 60: (a) SEM cross sectional images of oxidized $ZrSi_2$ at 1400 °C for 5 hours and (b) schematic diagram of a reaction model for the formation of $ZrSiO_4$ by a reaction of ZrO_2 and SiO_2 solid phases by Veytizou et al. [103].

Spinodal Decomposition of $ZrSi_2$ at 1000 °C and 1200 °C

As mentioned earlier, a plausible explanation to the formation of an alternating nano-layered structure of ZrO_2 and SiO_2 is phase separation of Zr-Si-O phase by spinodal decomposition, a diffusion driven process that occurs in unstable undercooled or supersaturated phases, resulting in homogenous two-phase fine scale mixture. Lucovsky et al. first reported that annealing of ~400 nm amorphous $ZrSiO_4$ thin film at 900 °C for 60 seconds led to chemical phase separation consisting of crystalline ZrO_2 and amorphous SiO_2 based on infrared absorption spectroscopy [98,99]. A thermodynamic driving force exists if the solid mixture is within unstable spinodal boundary. Kim et al. estimated the excess Gibbs free energy of mixing in supercooled liquid of ZrO_2 and SiO_2 using a subregular model utilizing the invariant points in pseudo-binary ZrO_2-SiO_2 phase diagram [104]. In addition, Stemmer et al. predicted extension of the liquid miscibility gap and spinodals to lower temperature using commercially available thermodynamic software and published oxide data [105]. Based on their estimations, the composition of spinodal boundary between 1000 °C and 1200 °C in ZrO_2 and SiO_2 mixture is in the range of 0.4~0.9 SiO_2 mole fraction and its corresponding decomposed equilibrium phases are ZrO_2 rich phase (0.2~0.4 SiO_2 mole fraction) and SiO_2

rich phase (0.9~0.98 SiO_2 mole fraction). Therefore, it is suggested that there is a thermodynamic driving force that induces spinodal decomposition in $ZrSi_2$ oxidation at high temperatures.

At 1000 °C, the spinodal structures near the top surface were finer than those at the center of the oxide layer, which may be attributed to ZrO_2/SiO_2 composition effect on Gibbs free energy of mixing. The minimum wavelength of phase modulation decreases with increasing negative values of second derivative of Gibbs free energy of mixing [106]. The absolute value of the negative free energy is maximized at 73% mole fraction of SiO_2 at 1000 °C calculated by the subregular model proposed by Stemmer et al., which is consistent with Si concentration of the 1000 °C surface, resulting in formation of the finer spinodal structures.

Additionally, nucleation of the ZrO_2 particulates at 1200 °C on the top surface would also be explained by the extension of the liquid miscibility gap. Due to the highest concentration of SiO_2 on the top surface by outward Si diffusion in oxide layer (see Table 4) at 1200 °C, the composition may not be within the spinodal boundary but within miscibility gap. Therefore, nucleation and growth of ZrO_2 in SiO_2 matrix will likely lower its free energy *in lieu* of spinodal decomposition.

Kinetic Suppression of Crystalline $ZrSiO_4$ Formation

It is worth noting that crystalline $ZrSiO_4$ was not identified in the $ZrSi_2$ oxidation at 1000 °C for 10 hours and 1200 °C for 5 hours even though its formation is preferred as indicated in binary ZrO_2-SiO_2 phase diagram at either temperature with any composition. However, the phase identification of $ZrSiO_4$ at longer oxidation (1200 °C for 50 hours) and higher temperature oxidation (1400 °C for 5 hours) of $ZrSi_2$ agree with published results that $ZrSiO_4$ formation from a reaction of ZrO_2 and SiO_2 requires at least 1300°C annealing temperature [103,107–109]. Formation of crystalline $ZrSiO_4$ is a solid state reaction – it is hypothesized that Si^{4+}cations from amorphous SiO_2 diffuse through the highly refractory $ZrSiO_4$ layer and reacts with t-ZrO_2 in order to produce new phase and there are no mobile liquid or gas species [103].

Therefore, the growth rate of crystalline $ZrSiO_4$ is kinetically limited although it is thermodynamically favored.

Summary of $ZrSi_2$ Oxidation

Based on the analysis in this study, a physical model for microstructural evolution during the isothermal oxidation at each test temperature has been developed and is schematically shown in Figure 61 to understand microstructural evolution in the oxide layer. At 700 °C, a thin oxide layer consisting of Zr-Si-O phase matrix with Si-rich oxide wavy structures forms. Additionally, small amount of Si and ZrO_2 was identified in XRD analysis. The role of the newly formed Si by the selective oxidation in $ZrSi_2$ is important. The Si diffuses around the oxide layer and leads to the formation of Si-rich spherical phases on the surface and its inward diffusion induced reduction of Si concentration in the top surface while promoting the formation of Si-rich wavy oxide. Although the composition of the oxide is within the estimated spinodal boundary, mobility of species at this temperature is not enough to show distinct phase separation.

At 1000 °C, in the initial stages of oxidation, the Si diffused inward first when it reacted with oxygen in the thin oxide layer and agglomerated resulting in wavy Si rich oxide structures. The wavy structures seen in 700 °C oxidation tests were likely precursors of those observed at 1000 °C. While oxidation continues, outward diffusion of the newly formed Si dominates as confirmed by the increment of Si concentration at the surface. In the oxide/$ZrSi_2$ interface, the amorphous Zr-Si-O mixture decomposed quickly so that the isotropic irregular structures consisting of ZrO_2 and SiO_2 were generated. At the same time, the Si produced Si-rich oxide islands near the spinodal structures.

At 1200 °C, the oxidation behavior was similar to that at 1000 °C except for the nucleation of the nanoscale ZrO_2 particulates near the air interface. Due to remarkable outward diffusion of Si ions, the Zr-Si-O mixture was metastable and reduced its free energy by ZrO_2 nucleation. During short time oxidation, an intermediate unstable Zr-Si-O mixture exists which undergoes phase separation to ZrO_2 and SiO_2.

At 1400 °C, crystalline $ZrSiO_4$ phase develops through solid-state reactions between ZrO_2 phases and SiO_2 phases, resulting in the formation of continuous $ZrSiO_2$ layer on the top of the oxide scale. Surplus SiO_2 phases in the reaction for $ZrSiO_4$ remain as a thin layer underneath the $ZrSiO_4$ layer. Due to the excellent oxidation resistance of the two layers, oxidation process becomes so slow that thickness of the whole oxide scale is thinner than that formed at 1200 °C. The solid-state reaction continues in the middle of the oxide layer so that a mixture of ZrO_2, SiO_2, and $ZrSiO_4$ phases and islands of SiO_2 coexist.

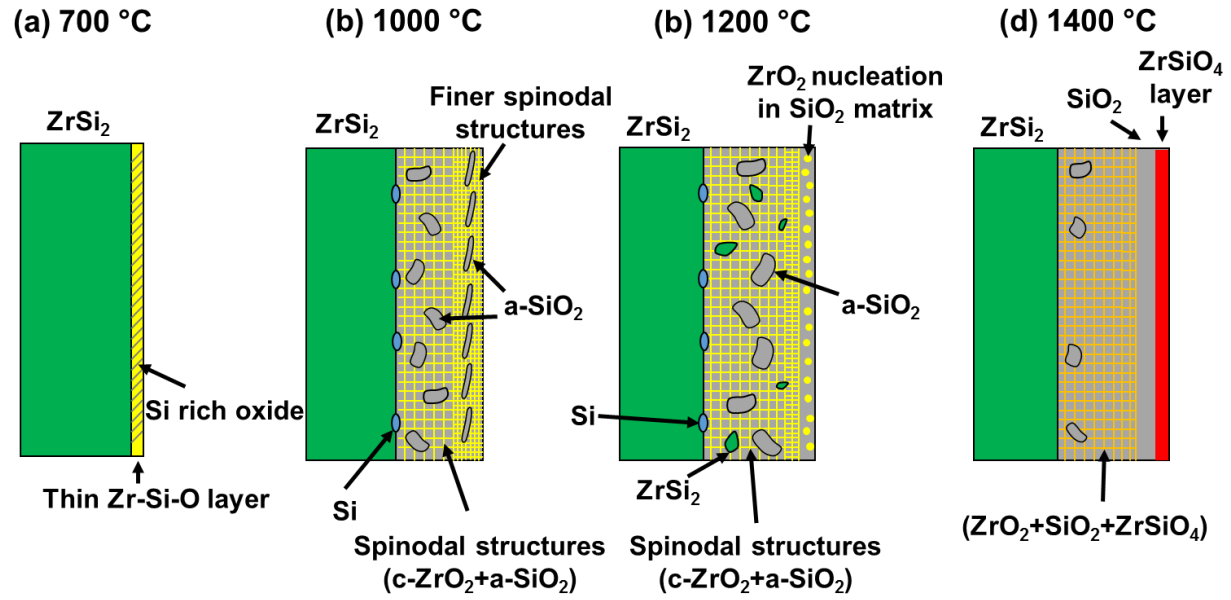

Figure 61: Schematic illustration of the microstructural evolution during isothermal oxidation of $ZrSi_2$ oxidation at (a) 700 °C, (b) 1000 °C, (c) 1200 °C, (d) 1400 °C. c=crystalline and a=amorphous. The features in the figures are disproportionately scaled for clarity.

Oxidation of Zr_2Si at 1200 °C

Oxidation behavior of one of Zr-rich silicides, Zr_2Si, was investigated by characterization after oxidation at 1200 °C for 1 hour. The behavior may be different from Si-rich silicide ($ZrSi_2$). As shown in the photograph in Figure 62, the Zr_2Si samples got completely crumpled during the oxidation while the $ZrSi_2$ samples maintained their rectangular shape. This confirms in a very practical sense, the expected result that $ZrSi_2$ is superior to Zr_2Si in terms of oxidation resistance and mechanical integrity in high temperatures.

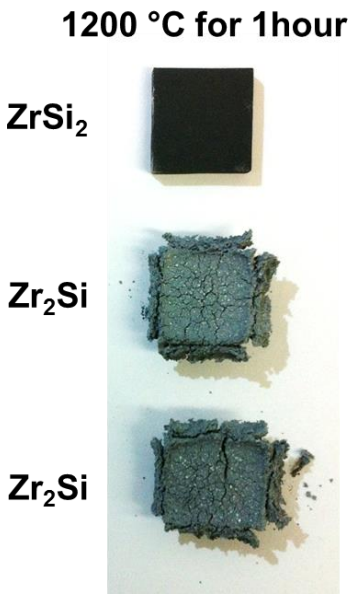

Figure 62: Photograph showing the oxidized $ZrSi_2$ and Zr_2Si after oxidation at 1200 °C for 1 hour in air.

The cross-sectional SEM images of a small particle of the oxidized Zr_2Si are shown in Figure 63. Most regions of the Zr_2Si particle were oxidized heavily and a large amount of ZrO_2 had formed as manifested in the charged area of the image (bright area) in Figure 63a. The less oxidized regions at the center were identified as newly formed $ZrSi_2$ by the compositional analysis. Moreover, only monoclinic-ZrO_2 and $ZrSi_2$ phases were identified in XRD analysis as shown in Figure 64. The origin of material disintegration appeared to be crack propagation in ZrO_2 regions (see Figure 63b). The tetragonal-ZrO_2 formed during Zr_2Si oxidation at 1200 °C underwent phase transformation to monoclinic-ZrO_2 upon cooling, resulting in significant compressive stresses due to volume increase. A similar failure morphology was also observed in Zirc-4 oxidized at 1200 °C. In addition, the spinodal structures were also confirmed as shown in Figure 63c but only limited area near $ZrSi_2$ regions, differing from the $ZrSi_2$ oxidation. Based on the experimental data, the postulated oxidation reaction of Zr_2Si at 1200 °C is as follows:

$$2Zr_2Si + 3O_2 \rightarrow 3ZrO_2 + ZrSi_2, \Delta G_f = -2200kJ \quad (23)$$

Subsequently, the newly formed $ZrSi_2$ decomposed into crystalline ZrO_2 and amorphous SiO_2 so that the spinodal structures were only observed near $ZrSi_2$ regions as discussed in detail in the previous section.

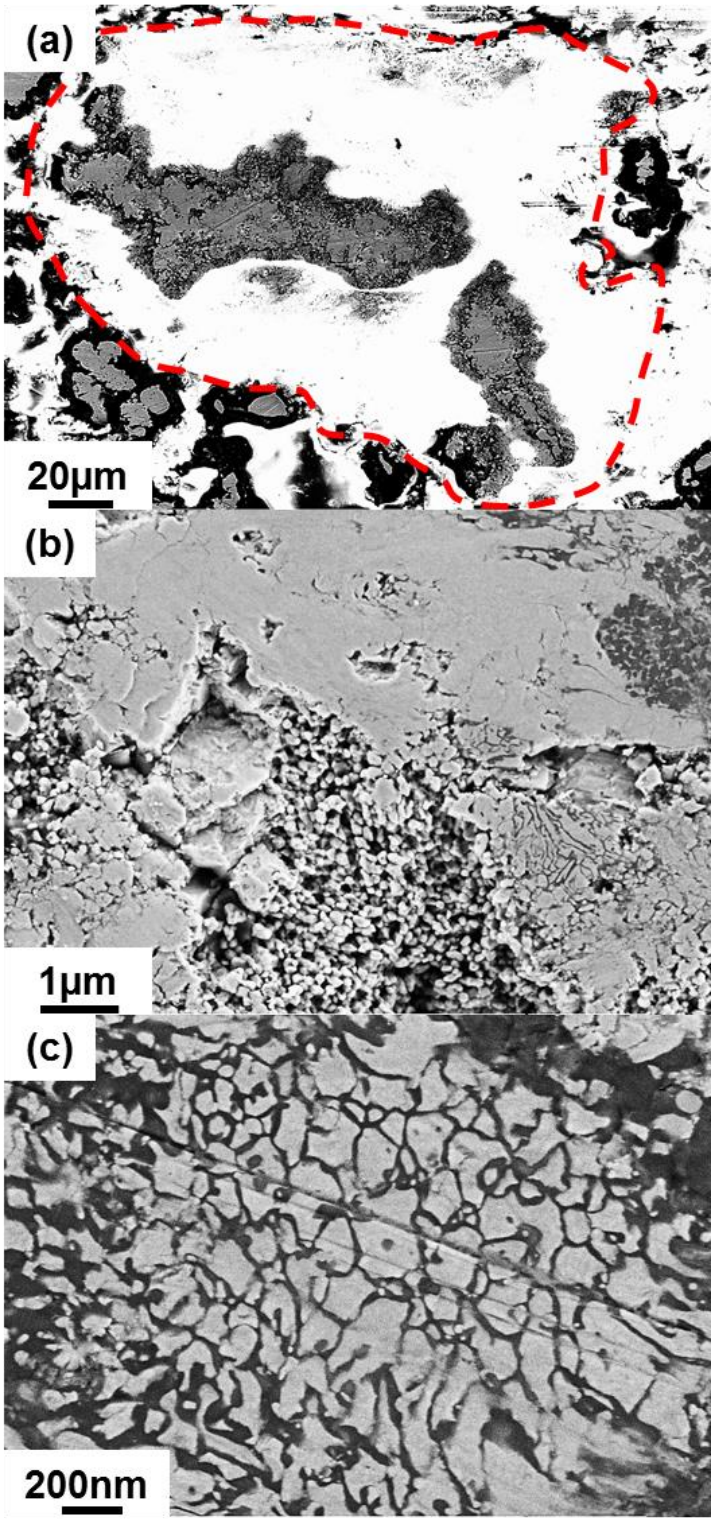

Figure 63: Cross-sectional SEM images of a Zr_2Si samples oxidized at 1200 °C for 1 hour. (a) Red dots in the high voltage (12kV) SEM image indicate the particle boundary, (b) cracks leading to structural disintegration were identified in ZrO_2 region, and (c) spinodal structures are seen locally near $ZrSi_2$ phase.

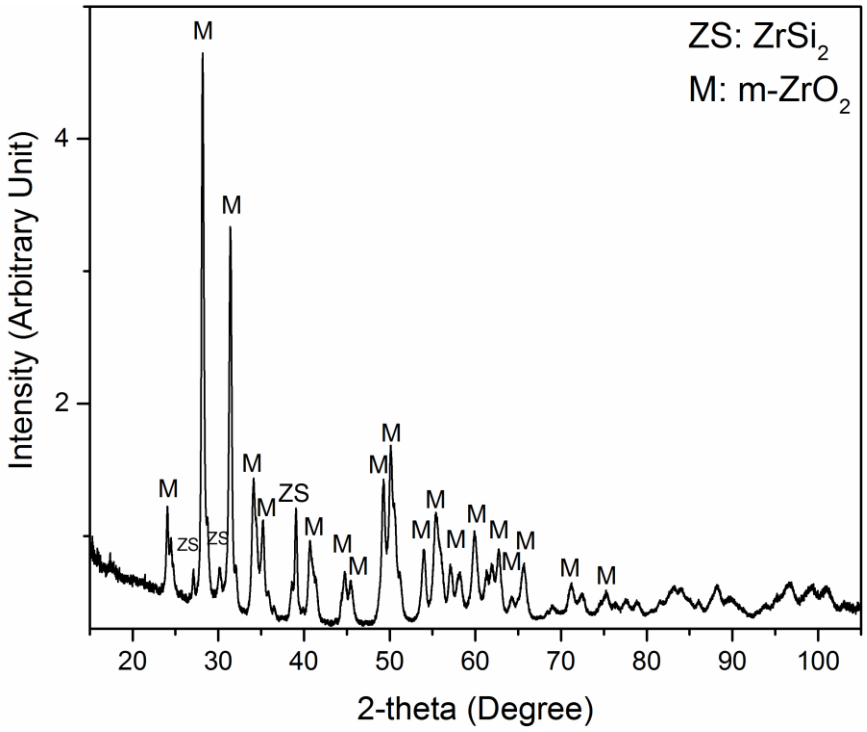

Figure 64: Full-theta X-ray diffraction (XRD) peaks of the Zr_2Si oxidized at 1200 °C for 1 hour in air.

4.1.2. High pressure steam corrosion

Oxidation of bulk $ZrSi_2$ at high temperatures was investigated as reported in the last section, but potential materials for protective coating on Zr-alloy cladding should maintain or improve corrosion resistance under normal reactor operation conditions as well. The improved corrosion resistance by protective surface coatings at normal operating temperatures such as 300 to 320 °C for PWRs and 250 to 300 °C for BWRs would reduce overall oxidation and hydriding of the Zr-alloy cladding, resulting in extension of allowable fuel burn-up and improved economics [110]. Therefore, material behavior of bulk $ZrSi_2$ in high pressure water/steam conditions prototypic of corrosion in normal LWR operating conditions were characterized by SEM-EDS and is discussed in this section.

Water Autoclave Test by Westinghouse Electric Company

Polished bulk $ZrSi_2$ samples were shipped to Westinghouse Electric Company (WEC, Pittsburgh PA) for water autoclave corrosion tests. For these tests, the samples were exposed in pure water at 330 C in 18.6

MPa for 72 hours. The metallic surfaces of the samples before the corrosion (Figure 65a) changed to white color (Figure 65b) and degraded during the test.

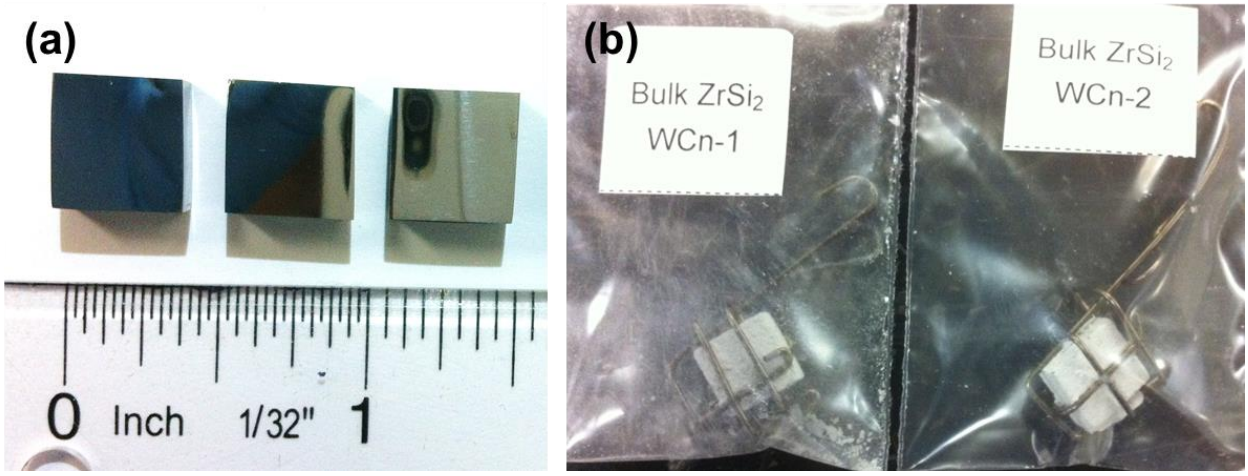

Figure 65: Photographs of (a) as-polished bulk $ZrSi_2$ before corrosion test at 330 °C and 18.6 MPa in pure water for 72 hours and (b) the samples after the autoclave test.

Plan-view SEM images of the bulk $ZrSi_2$ samples before and after the autoclave test are shown in Figure 66. After the test, surface morphology became rough and cracked. The near-surface region of the material was disintegrated and pores and debris were observed on the surface. It is speculated that formation of the pores is related to the preexisting free silicon impurites in the $ZrSi_2$ matrix shown in Figure 66a which subsequently got leached out during the corrosion tests.

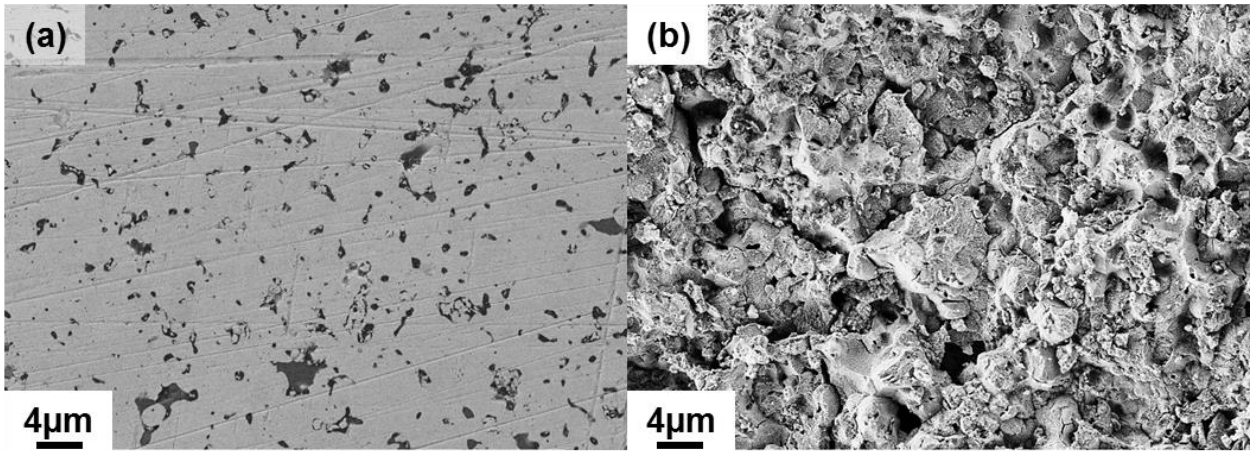

Figure 66: SEM plan-view images of (a) as-polished $ZrSi_2$ and (b) $ZrSi_2$ after 330 °C, 18.6 MPa water corrosion test.

SEM cross-sectional images of the corroded $ZrSi_2$ samples is shown in Figure 67. Thickness of the oxide layer formed during the corrosion test was approximately 40 μm and displayed as very bright region as shown in Figure 67a due to dielectric properties of ZrO_2. In the local cross-sectional area underneath the oxide layer, micron-size pores in the $ZrSi_2$ matrix were identified (Figure 67b), which is consistent with the pores observed in the plan-view images. Again, it appears that the pores were originally free silicon grains present as impurities. In addition, thin darker boundaries were observed at the interfaces between the corroded regions and the unreacted regions, and the corroded area revealed nano-scaled porous structures. The darker boundaries may be a silicon-rich layer, related to corrosion process of $ZrSi_2$ in high temperature, pressurized water. Thin silicon-dioxide layer has been reported in high temperature corrosion of CVD-SiC in moisture containing air at 1200 °C and 1 MPa after testing for 500 hours [111]. The layer was identified between porous silica scale and unreacted SiC matrix. It is believed that the porous structure forms due to loss of silicon in the $ZrSi_2$ matrix because the EDS elemental mapping for cross-section of the sample shows a small concentration of silicon (Figure 68a). Only 7 to 8 at. % of silicon was detected in the corroded region (point 1, 2, and 3 in Figure 68b)., and the major phase present in the corroded region is ZrO_2.

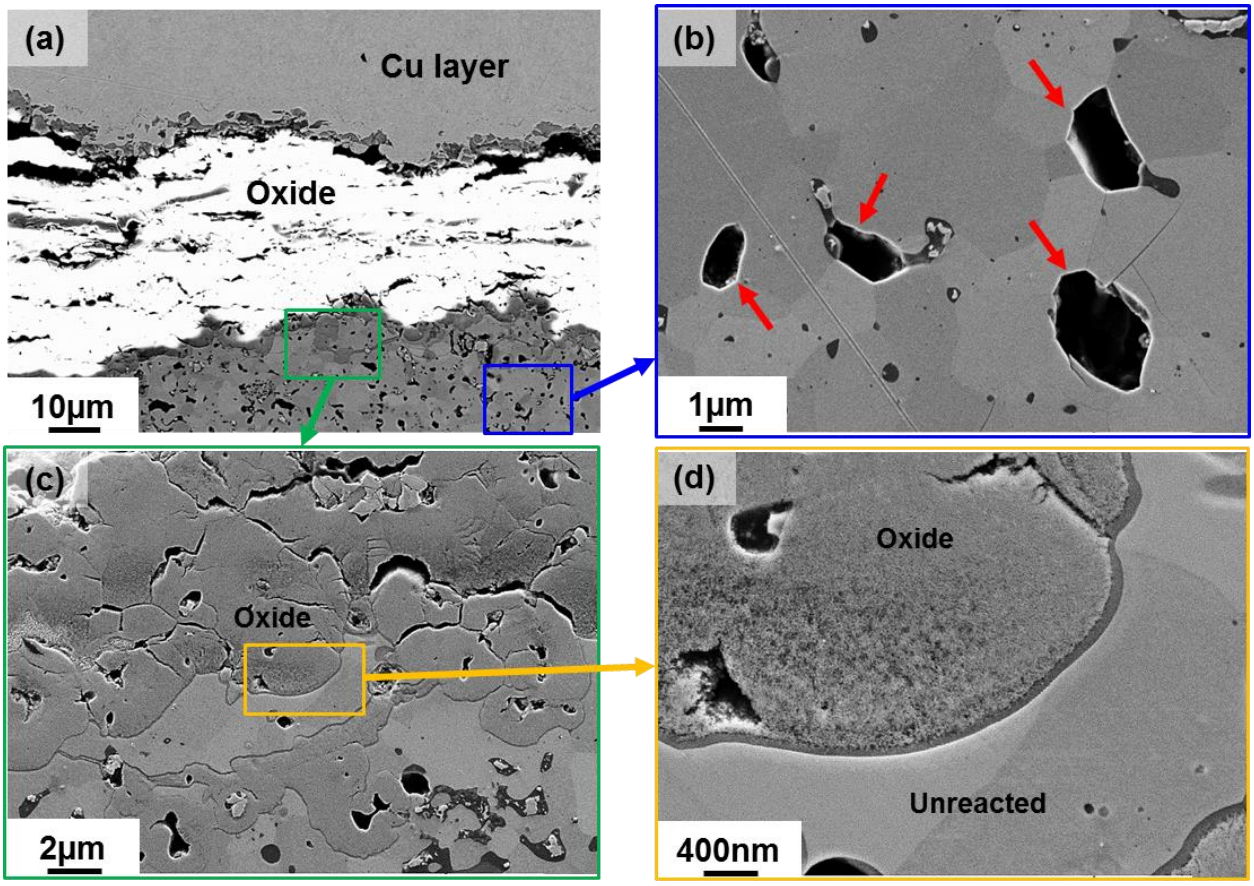

Figure 67: Cross-sectional SEM images of bulk $ZrSi_2$ after the water corrosion tests at 330 °C and 18.6 MPa for 72 hours: (a) low magnification, and (b-d) local areas with high magnifications. The red arrows indicate pores in $ZrSi_2$ matrix.

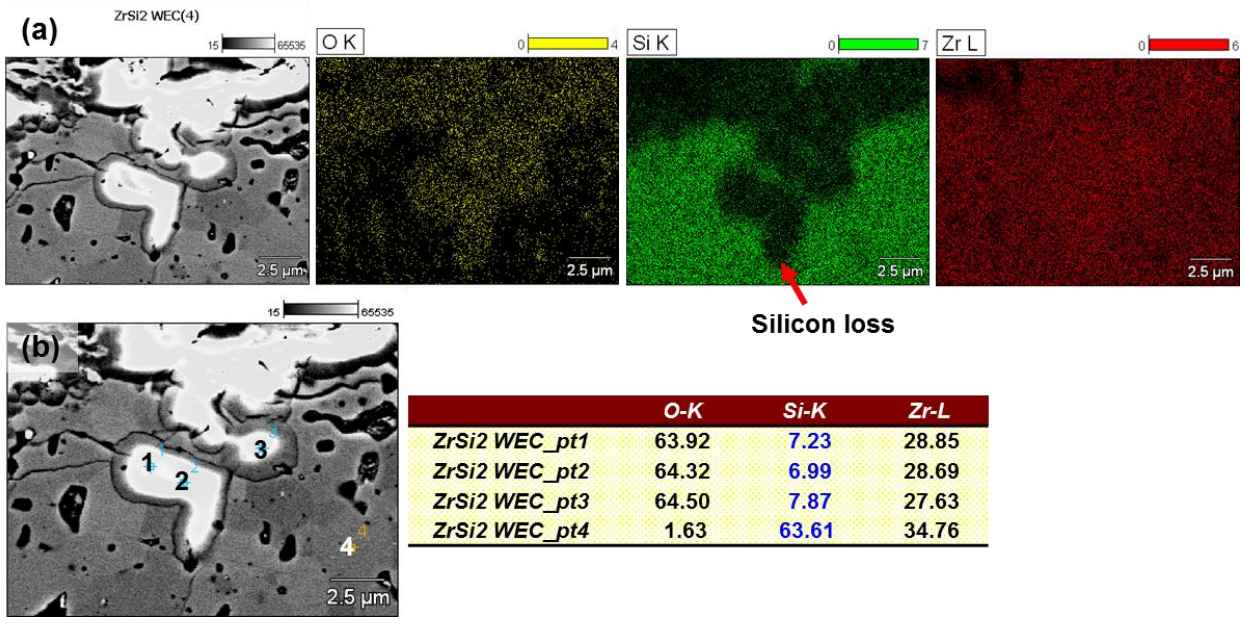

	O-K	Si-K	Zr-L
ZrSi2 WEC_pt1	63.92	7.23	28.85
ZrSi2 WEC_pt2	64.32	6.99	28.69
ZrSi2 WEC_pt3	64.50	7.87	27.63
ZrSi2 WEC_pt4	1.63	63.61	34.76

Figure 68: EDS analysis of cross-section of bulk $ZrSi_2$ after the water corrosion test at 330 C and 18.6 MPa for 72 hours: (a) elemental mapping and (b) elemental point scan.

Steam Autoclave Test at UW-Madison

Steam corrosion tests for bulk $ZrSi_2$ were conducted at UW-Madison to investigate how this environment compares with the water corrosion test performed at WEC. Single crystal silicon flats and Zirc-4 flats were polished using 320, 400, and 600 SiC abrasive papers and introduced in the autoclave as reference samples. Bulk $ZrSi_2$ and bulk Si samples were pre-oxidized in ambient air at high temperatures to demonstrate effect of surface oxidation on silicon loss. The oxidation conditions were 700 °C for 100 hours and 1400 °C for 5 hours for both sample materials. The oxidation processes resulted in thin oxide layers on the silicon samples as shown in Figure 69. Based on XRD patterns, phase of the oxide scale produced at 700 °C and 1400 °C air was quartz SiO_2 and cristobalite SiO_2, respectively. As presented in the last section, bulk $ZrSi_2$ formed a thin oxide layer consisting of Zr-Si-O and SiO_2 at 700 °C and thin oxide layer containing $ZrSiO_4$ and 1400 °C in ambient air.

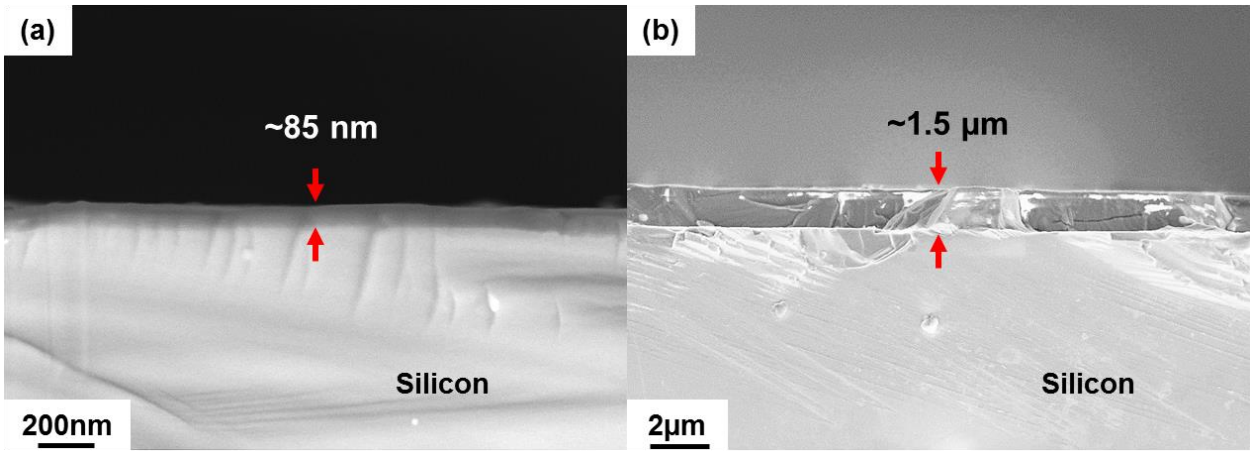

Figure 69: Formation of thin oxide layers on bare silicon surface after high temperature oxidation at (a) 700 °C for 100 hours and (b) 1400 °C for 5 hours. The images are SEM cross-sectional fracture surface images.

All samples were exposed in high temperature steam (400 °C) at 10.3 MPa for 72 hours, and deionized pure water (18 MΩ) was flowed into the test chamber with a slow flow rate (~ 5 ml/min). The weight changes for the samples after the steam test are summarized in Figure 70. All samples showed weight loss after corrosion test except for bare Zirc-4. The weight of the bare and oxidized silicon samples decreased significantly after the test indicating that silicon loss in $ZrSi_2$ matrix is a primary factor for the weight

reduction. While the corrosion of silicon species in $ZrSi_2$ occurs by removal of silicon atoms on the surface under pressurized steam, zirconium species in $ZrSi_2$ would be oxidized and remains as ZrO_2. Spallation of thin oxide layer was identified on the oxidized samples at 1400 °C for 5 hours by visual inspection, resulting in the largest weight reduction in Figure 70. It appears that the weight loss decreased after pre-oxidation at 700 °C in $ZrSi_2$ (58%) and Si (20%) samples compared to the as-polished samples but an explanation to this observation is not clear.

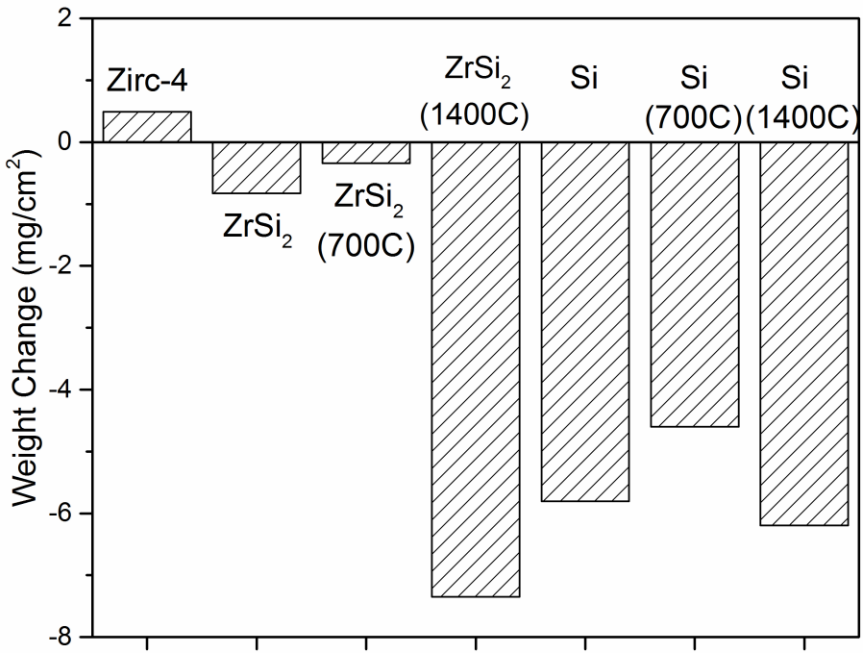

Figure 70: Weight change for bare Zirc-4, $ZrSi_2$, Si, and pre-oxidized samples (700 °C for 100 hours and 1400 C for 5 hours) after the steam test at 400 °C and 10.3 MPa for 72 hours.

The plan-view SEM images for the bare $ZrSi_2$ and the pre-oxidized $ZrSi_2$ at 700 °C after the steam autoclave test are shown in Figure 71. As presented in the water corrosion test in Westinghouse Electric Company, the bare $ZrSi_2$ surface after the steam test revealed surface cracks and pores. Again, the silicon impurities in the $ZrSi_2$ matrix may be leached out during the steam corrosion and leave pores on the surface. Mechanical integration of the top surface was so weak that a significant number of debris particulates were detected on the surface. On the other hand, the pre-oxidized surface was smoother and cleaner than the bare $ZrSi_2$ surface. Surface pores were observed in the images but severe cracks and local spallation of oxide layer were not observed. The observation is consistent with results of the weight gain plot (Figure 70) that

the pre-oxidation mitigated the weight loss. Therefore, the pre-oxidized surface was relatively stable under the high temperature steam environment compared to the bare $ZrSi_2$. Nevertheless, the top surface of the pre-oxidized $ZrSi_2$ after the steam test showed the nano-scaled pores as shown in Figure 72a. Significant reduction of silicon concentration on the surface in the EDS result (Figure 72b) supports a hypothesis that material degradation of $ZrSi_2$ (cracks and porous structures) is caused by a loss of silicon species by an interaction of $ZrSi_2$ and water.

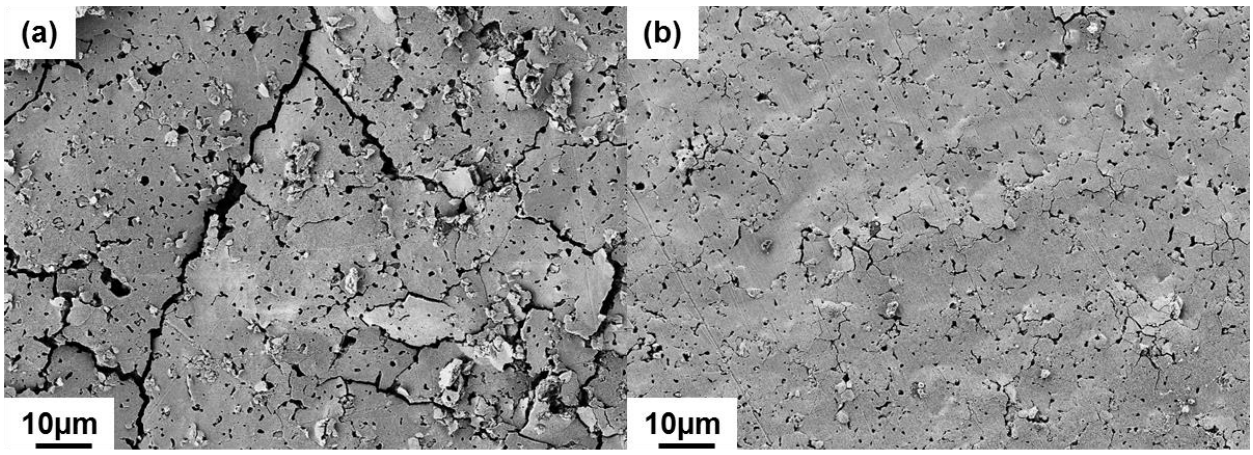

Figure 71: SEM plan view images for (a) bare $ZrSi_2$ and (b) pre-oxidized $ZrSi_2$ (700 °C for 100 hours in ambient air) after steam corrosion test at 400 C and 10.3 MPa for 72 hours.

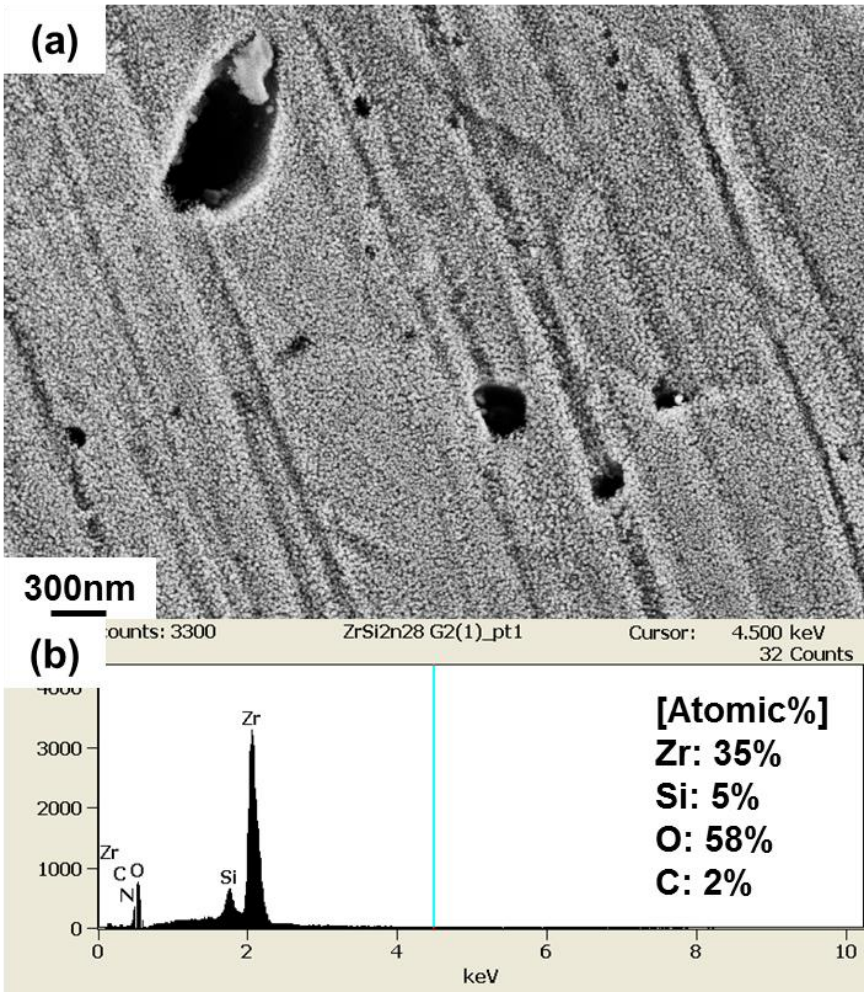

Figure 72: (a) High magnification SEM plan-view image of pre-oxidized $ZrSi_2$ (700 °C for 100hrs) after the steam autoclave tests (400C, 10.3 MPa for 72 hrs) and (b) results of corresponding EDS average scan.

The weight loss for the silicon samples is confirmed by SEM imaging of the samples after the steam corrosion test as shown in Figure 73. The high temperature steam reacted with the samples so that distinct surface morphologies were displayed. Before the steam corrosion test, all the silicon samples were smooth and the only surface features were identified were polishing marks. The oxygen concentration increased with increasing temperature of the pre-oxidation in ambient air. On the contrary, the surfaces become rough and noticeable surface features were identified after the corrosion test. For example, the high temperature steam attacked preferential area on the pre-oxidized surface (700 °C for 100 hours in air), resulting in the micron-scaled triangular surface features (Figure 73d). In addition, the network of micron cracks on local area of pre-oxidized silicon (1400 °C for 5 hours in air) was identified as shown in Figure 73f. The oxide

scale was not fully consumed, but rather grain boundaries of cristobalite SiO_2 scale would be attacked under the steam environment. It appears that the grain boundary attack weakened mechanical integrity of the oxide layer, resulting in local spallation of the top layer associated with the large weight loss. Moreover, oxygen concentration on the bare Si surface and the oxidized Si surface at 700 °C decreased after the corrosion. This indicates that surface recession on the Si samples with removal of the thin oxide layer occurred under the high temperature steam environment.

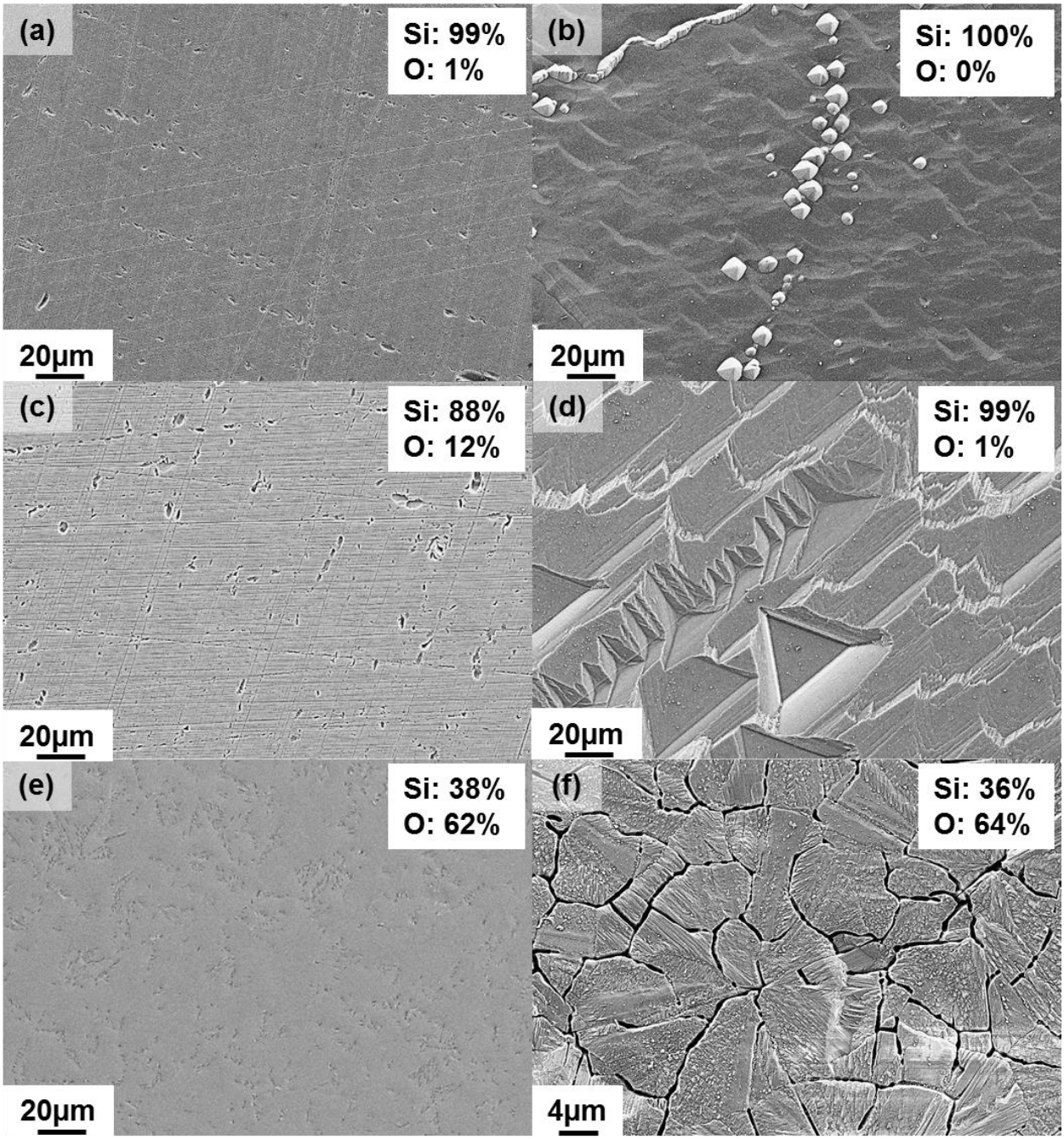

Figure 73: SEM plan-view images of (a) bare Si, (b) bare Si after steam test, (c) pre-oxidized Si at 700 °C for 100 hours, (d) pre-oxidized Si (700 °C) after the steam test, (e) pre-oxidized Si at 1400 °C for 5 hours, and (f) pre-oxidized Si (1400 °C) after the steam test. The steam test was performed at 400 °C and 10.3 MPa for 72 hours in pure water. The silicon and oxygen atomic percent on each surface are specified.

The loss Si from bulk $ZrSi_2$ and Si samples in the water/steam environment was not observed in high temperature air. Another example for water vapor effects on oxidation of transition metal silicides is presented by Wood et al. [112] The authors reported that $MoSi_2$ displayed different oxidation behavior in water vapor environment than in dry air. The tests were performed under atmospheric pressure. Mass gain of $MoSi_2$ in 75% water vapor at 600 °C was approximately 100 times higher than that in dry air condition. Moreover, the oxidized samples in water vapor displayed swelling and warping. It was believed that the water vapor inhibited formation of a uniform SiO_2 layer for passivation. It is speculated that increased solubility of SiO_2 in water, formation of gaseous silicon hydroxide and gaseous SiO phase at elevated pressures and temperatures in water environment are responsible for the weight loss and the surface recession of the $ZrSi_2$ and Si materials. First, the postulated reaction between $ZrSi_2$ and H_2O at 400 °C is as follows:

$$ZrSi_2 + 6H_2O \rightarrow ZrO_2 + 2SiO_2 + 6H_2(g), \Delta G_f = -1298.9\ kJ \quad (24)$$

The reaction products (zirconia and silica) should have a dense microstructure and good adhesion to base material to act as a passive layer. However, SiO_2 is dissolved by water to some extent. Fournier and Rowe measured concentration of dissolved SiO_2 species in water during high pressure autoclave test using a colorimetric method and reported that solubility of amorphous SiO_2 in pure water increased exponentially with increasing water temperature at the vapor pressure of the solution [113]. A linear relationship between the solubility and system pressure at constant temperature (i.e., 200 °C) was observed. In addition, volatility of SiO_2 would contribute to degradation of surface oxide layer in $ZrSi_2$ in water environments. Opilia et al. concluded that volatilization of SiO_2 below 1300 °C was dominated by equation 25 with linear kinetics [114].

$$SiO_2(s) + 2H_2O(g) \rightarrow Si(OH)_4(g) \quad (25)$$

Silica-forming structural materials like SiC show the weight loss material recession as well. As presented by Terrani et al., [113] SiO_2 layer formed on CVD SiC surfaces contained significant porosity under high

pressure and high temperature steam environment (1200 °C and 0.34 to 2.07 MPa) so that material recession rate was an order of magnitude higher than atmospheric pressure conditions. Finally, non-protective SiO is formed if the oxygen partial pressure is very low even in the presence of water, leading to rapid material recession.

Immobilization of Silicon in Water Corrosion

The zircon ($ZrSiO_4$) formed $ZrSi_2$ surface was the only condition in which the silicon concentration remained constant after steam corrosion test. As shown in Figure 74a, the surface maintained the original surface morphology of dense and micron sized $ZrSiO_4$ grains except for many etch pits around the grain boundaries. Moreover, spallation of the zircon layer on the local surface was revealed, being related to the weight loss shown in Figure 70. Even though zircon is one of the most corrosion resistant materials under water conditions [115], it seems that corrosion started at grain boundaries with elimination of silicon species and weakened mechanical integrity of the zircon layer. Ueno et al. also reported the same phenomenon during static water corrosion test (1300 °C for 100 hours) for bulk zircon samples [116]. The authors observed that amorphous SiO_2 rich phases present in the grain boundaries from silicate compounds, and the grain boundaries were easily corroded by water vapor. EDS results (Figure 74b) showed that silicon loss on the oxidized surface was prevented. Thus, our studies demonstrate that forming a zircon layer is highly effective in immobilizing Si in normal LWR water environments, however for this to be a practical solution the compactness of the zircon grains must be improved (minimizing surface area of grain boundaries).

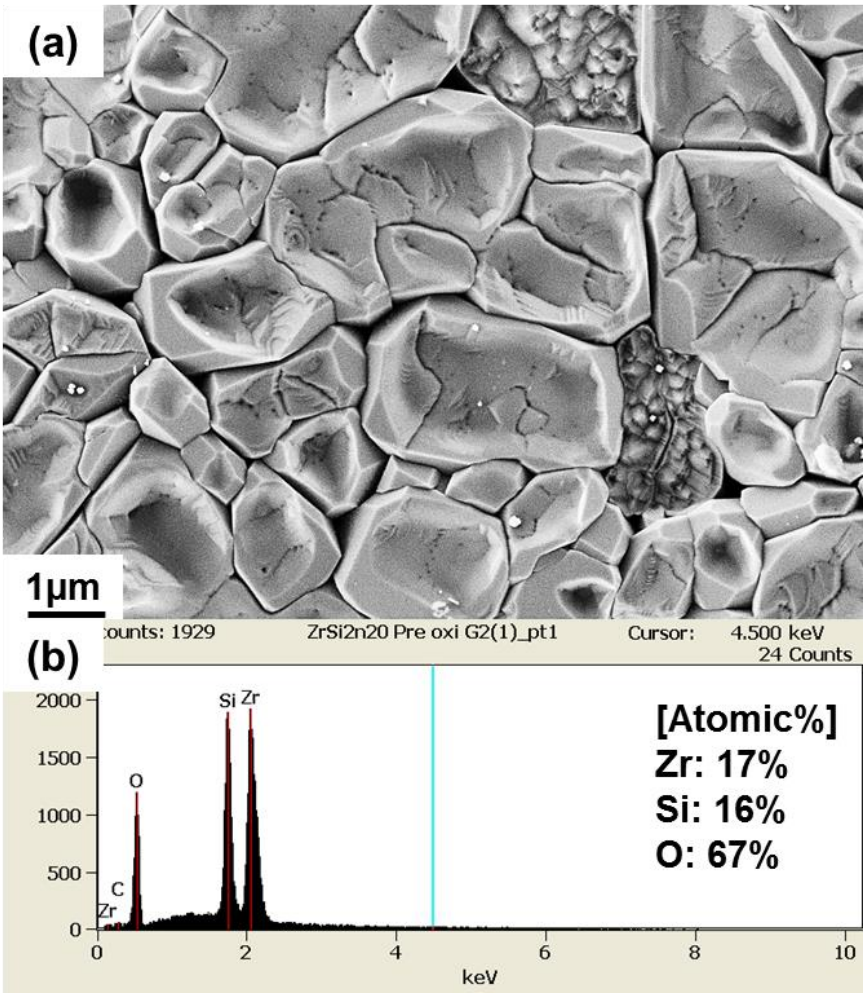

Figure 74: (a) SEM plan-view image of pre-oxidized $ZrSi_2$ (1400 °C for 5 hours in air) after the steam corrosion test at 400 °C at 400 °C and 10.3 MPa for 72 hours in pure water, and (b) results of EDS chemical analysis for the corresponding area.

4.2. Optimization of magnetron sputter coating on Zr-alloy for oxidation resistance

4.2.1. Parametric investigation for coating quality

Investigation of magnetron sputter deposition process to fabricate zirconium-silicide coating as a protective barrier under extreme conditions was performed. Process parameters such as deposition power, sputtering gas pressure, and samples surface preparation determine coating quality and efficiency of deposition process. To the best of author's knowledge, experimental data for magnetron sputter process for

zirconium-silicide coatings has not been reported so optimization of deposition parameters was conducted, and the results are presented and discussed in this section.

Deposition Parameters

The dc sputter power was determined to be linearly proportional to a sputter yield rate (the number of ejected atoms per incident ion), as shown in Table 5, indicating that higher sputter power is beneficial to deposit desired thickness more rapidly. However, sputter targets experience significant thermal stress as increasing sputter power can cause target failure, particularly for ceramic targets. For example, a $ZrSi_2$ sputter target was damaged at 160 W. To eliminate this problem, sputter power was lowered to 135W and a copper plate was bonded on the backside of the target to accommodate the thermal shock.

In addition, it was found that the deposition rate for $ZrSi_2$ sputter coating at a constant sputter power was inversely proportional to pressure of sputtering gas (i.e., argon gas) as shown in Table 6. The deposition rate was measured by a crystal monitor in the vacuum chamber and is a relative value.

Table 5: Deposition rate of $ZrSi_2$ coating at 10 mtorr Ar pressure as a function of sputter power.

Sputter power (W)	Deposition rate (Å/s)
90	0.63
135	0.89
160	1.1

Table 6: Deposition rate of $ZrSi_2$ coating at 135 W sputter power as a function of Ar pressure.

Argon pressure (mtorr)	Deposition rate (Å/s)
4	1.07
6	1.02
8	0.97
10	0.89
12	0.83

As shown in Figure 75a, local areas of the as-deposited sputter coating of $ZrSi_2$ displayed coating delamination. This may be attributed to residual compressive stress and a weak adhesion to the Zirc-4 substrate due to native oxide layer on the surface and surface contamination. To enhance coating adhesion to the substrate, the bare Zirc-4 flats were subjected to in-situ plasma cleaning (dc 500W for 5 minutes

under 1.6 Pa argon pressure) prior to initiating the coating deposition process in the sputter chamber. Figure 75b shows that yellowish surface color of the bare Zirc-4 flat changed to the metallic surface color after the plasma cleaning. After the effective removal of surface contamination, defects on surface of coatings were not identified. This cleaning process was performed for all Zirc-4 substrates before deposition of zirconium-silicide coatings.

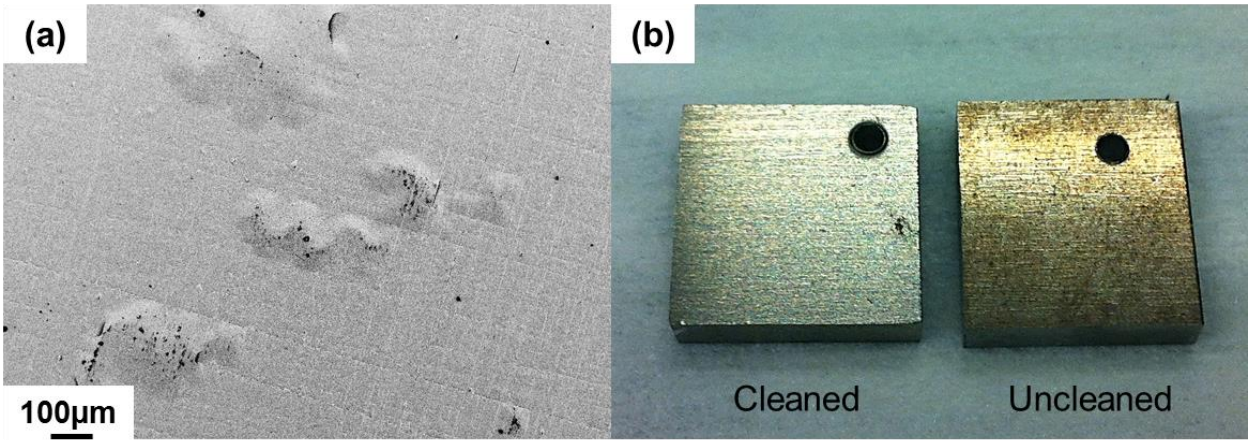

Figure 75: (a) SEM image of $ZrSi_2$ coating without the plasma surface cleaning of Zirc-4 substrate and (b) photograph of Zirc-4 flats after plasma surface cleaning.

Surface morphology and cross sectional microstructure of the coatings were examined and investigated using SEM. The coatings showed uniform and smooth surface with no indication of spallation. Argon gas pressure influenced microstructure significantly as shown for example for $ZrSi_2$ in Figure 76. The $ZrSi_2$ coating deposited at higher argon pressure (i.e., 1.33 Pa) exhibited relatively rougher surface and showed nanometer scale gaps in the microstructure (Figure 76a). Cross-sectional fracture surfaces of these coatings deposited on Si substrate showed tapered columnar microstructures which are revealed more clearly in Figure 76c. In contrast, at the lower argon pressure (i.e., 0.53 Pa) the $ZrSi_2$ coating exhibited short and dense columnar structures with smoother surface, which are shown in Figure 76b and Figure 76d. The observation is in good agreement with Thornton's model suggesting that the columnar tapered morphology of the films is a result of atomic shadowing and a low mobility of sputtered atoms on the growing surface at low temperatures [49]. In addition, this morphology would be promoted by increased scattering between argon atoms and target atoms at higher argon pressures. It is expected that the nanoscale gaps between the

long columnar structures at the higher argon pressure may act as paths for the transport of oxygen to the underlying Zirc-4 substrate during the oxidation tests. Therefore, all coatings for oxidation tests were prepared at the low argon pressure (0.53 Pa).

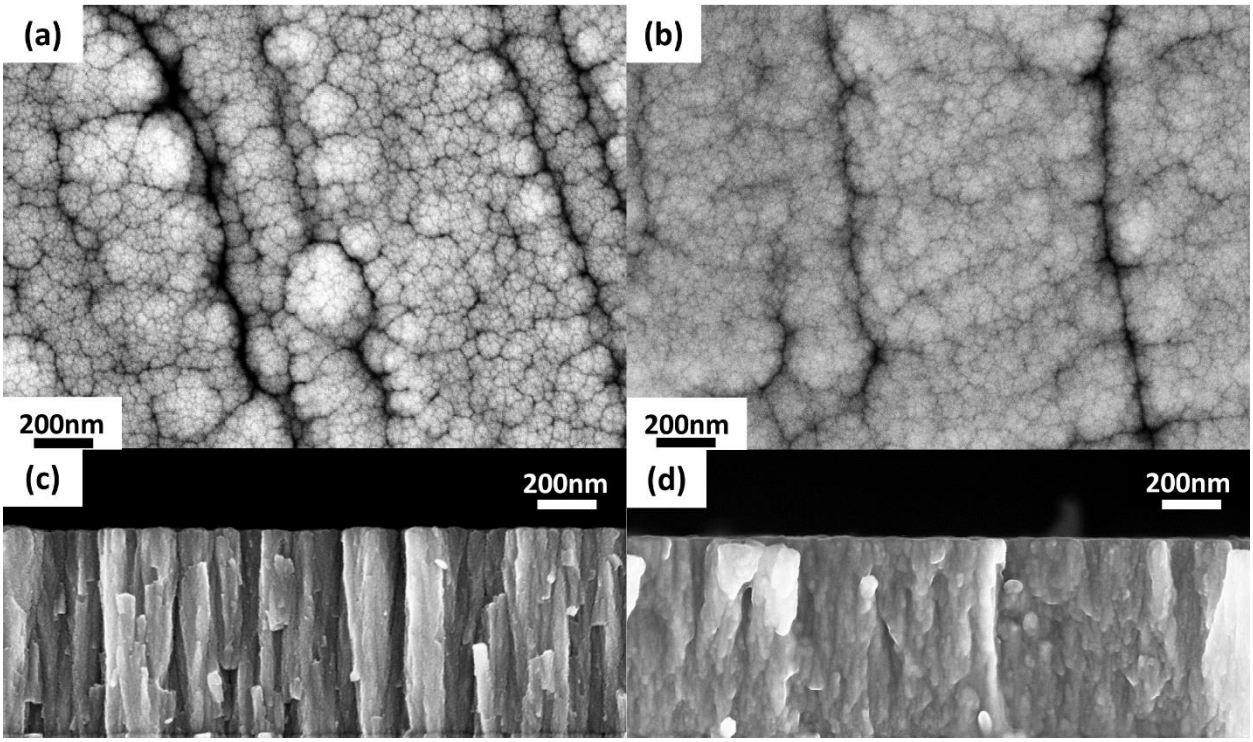

Figure 76: SEM plan-view images of coatings of (a) $ZrSi_2$ deposited at 1.33 Pa Ar gas pressure and (b) $ZrSi_2$ deposited at 0.53 Pa Ar gas pressure on Zirc-4 substrate. SEM cross-sectional fracture surface images of (c) $ZrSi_2$ deposited at 1.33 Pa Ar gas pressure and (d) $ZrSi_2$ deposited at 0.53 Pa Ar gas pressure on a silicon wafer. The dimensional difference for the microstructure in Figure 76a and Figure 76c is attributed to nature and roughness of the substrates. The image in Figure 76a was from the coating deposited on 600 grit surface finish Zirc-4 substrate while Figure 76c is the image of the coating deposited on atomically smooth Si wafers.

Effect of substrate temperature during the sputter deposition on coating quality was briefly investigated. The $ZrSi_2$ coating deposited at 300 °C showed slightly thicker coating than at room temperature but surface morphology was bulbous in nature typical of sputter coating. Due to concern about thermal stress in the coating during the heating profile, deposition process at higher temperature was excluded from this study.

Structural Phase of As-deposited Coatings

Elemental composition of the very near surface of the as-deposited coatings, as analyzed by the XPS, was consistent in trend with the corresponding target chemistry. Argon gas pressure during the deposition

process did not influence the coating composition. Grazing incidence XRD patterns showed only peaks corresponding to zirconium from the underlying substrate and no peaks corresponding to the coatings was observed for any of the coating stoichiometries (Figure 77).

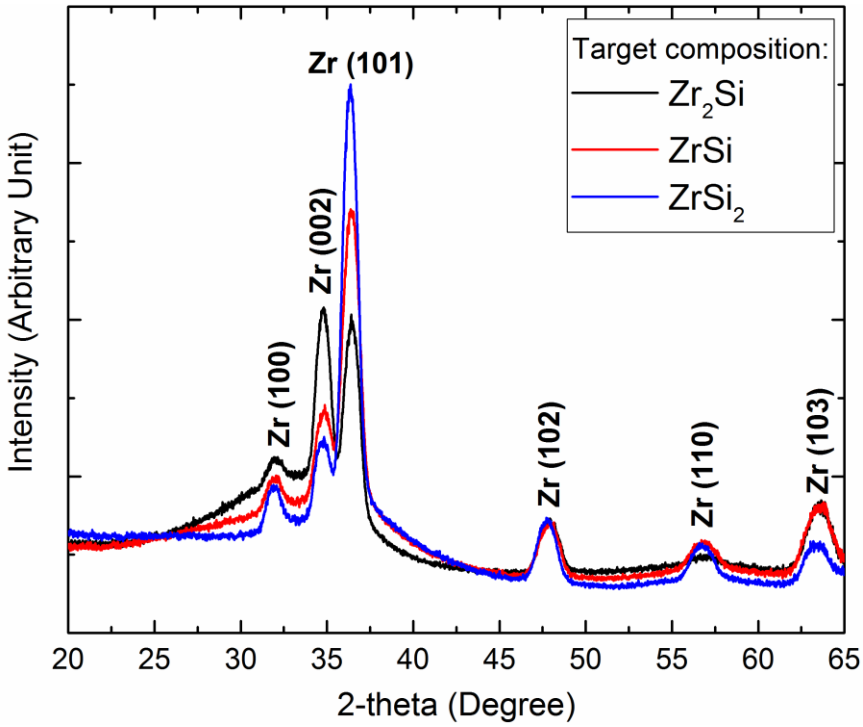

Figure 77: XRD patterns of thin coatings (Zr_2Si, ZrSi, and $ZrSi_2$) deposited at 1.33Pa Ar and 135 W at room temperature for 150 minutes with 2° incident x-ray beam. Only zirconium peaks from the underlying substrate were identified.

The microstructures of the as-deposited coatings were additionally investigated by TEM. The cross-sectional bright field TEM image (Figure 78a) for the as-deposited $ZrSi_2$ (0.53 Pa) coating displayed a columnar structure defined by the voided boundaries aligned with the film growth direction, but no clear contrast was observed between the grains. Selected area diffraction (SAD) pattern (Figure 78b) for the corresponding area exhibited diffused halos with fuzzy rings. No distinct diffraction spots characteristic of crystalline phases was observed. Based on XRD patterns and the TEM-SAD analysis, it is speculated that the as-deposited zirconium-silicide coatings are likely amorphous or consist of small volume fraction of nanocrystalline phases in an amorphous matrix. High resolution TEM (HRTEM) images will be required for further analysis of the structure of the as-deposited coatings.

The coating composition, phase content, microstructure, and thickness are summarized in Table 7.

Table 7: Composition, phase content, microstructure, and thickness of the as-deposited coatings.

Target Composition	Ar pressure (Pa)	Temperature (°C)	Coating composition	Major structural phase	Microstructure	Thickness (nm)
Zr_2Si	1.33	19	$Zr_{2.2}Si_{1.0}$	Amorphous	Long, tapered, columnar	920
ZrSi	1.33	19	$Zr_{1.1}Si_{1.0}$	Amorphous	Long, tapered, columnar	870
$ZrSi_2$	1.33	19	$Zr_{1.0}Si_{1.9}$	Amorphous	Long, tapered, columnar	800
Zr_2Si	0.53	19	$Zr_{2.2}Si_{1.0}$	Amorphous	Short, dense, columnar	800
ZrSi	0.53	19	$Zr_{1.0}Si_{1.0}$	Amorphous	Short, dense, columnar	750
$ZrSi_2$	0.53	19	$Zr_{1.0}Si_{2.2}$	Amorphous	Short, dense, columnar	720

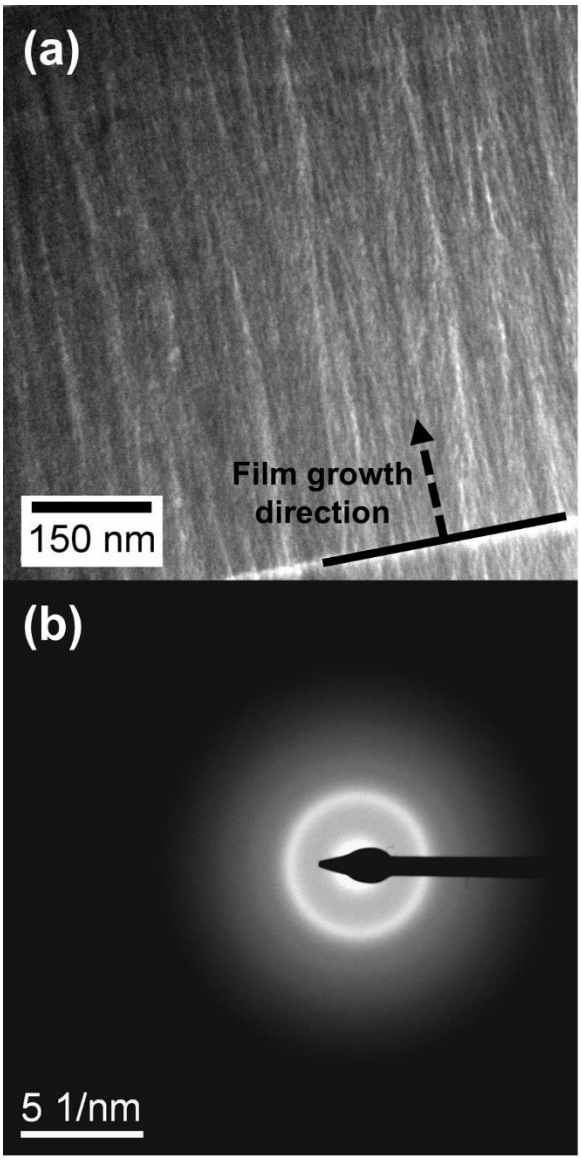

Figure 78: (a) Cross-sectional bright field TEM image and (b) diffraction pattern of $ZrSi_2$ (deposited at 0.53 Pa Ar pressure and room temperature). The coating thickness was 3 μm and was prepared by a four-step deposition for the diffraction pattern observation because an electron beam should illuminate the area of

interested through the SAD aperture (1 μm diameter). Coating growth direction is indicated by the black dot arrow.

Compositional Effects on Oxidation

The thin coatings at the lower pressure with three compositions (Zr_2Si #2, ZrSi#2, and $ZrSi_2$#2) deposited on Zirc-4 coupons were oxidized at 700 °C for 5 hours in ambient air to evaluate their oxidation resistance as a function of coating stoichiometry. Figure 79 shows the weight changes (per unit area of the sample) of the coatings of the three stoichiometries and uncoated Zirc-4 at each hour of oxidation. Rapid uptake of oxygen was identified for all the samples during the first hour of exposure, followed by relatively moderate oxidation rate. The formation of passive oxide layer during the initial exposure results in a self-limiting oxidation behavior. All the coatings revealed lower weight gain compared to the bare Zirc-4. In particular, the coating with highest Si content (i.e., $ZrSi_2$) displayed the lowest weight gain (about 60% compared to the bare Zirc-4). Since only the two major surfaces of the substrates were primarily coated, the weight gain results underestimate the actual improvements in oxidation resistance of the coatings. Therefore, observation of oxide layer thickness by cross-sectional SEM images was deemed to be a more realistic assessment of the improvements in oxidation behavior due to the coatings.

The thickness of oxide layer of the coatings was measured by cross-sectional SEM images (Figure 80), and the trends were in good agreement with the weight gain results. Significant oxide layer (13-15 μm) developed underneath the Zr_2Si coating due to permeation of oxygen through the coating and its diffusion into the underlying Zirc-4 substrate. The ZrSi coating appeared to form a thinner zirconium oxide in the underlying Zirc-4 alloy substrate. However, no oxide layer was observed in the underlying Zirc-4 alloy substrate for the $ZrSi_2$ coating. The high magnification images of the oxide scales (Figure 80d-f) revealed local variation of composition in the thin coatings and substrate. In the upper region of the Zr_2Si and the ZrSi coatings, zirconium-rich oxide was identified by EDS analysis (the brighter regions in Figure 80d-e), which also contained microcracks which would allow for oxygen permeation to the underlying substrate. However, the oxidized $ZrSi_2$ coating did not show the zirconium-rich oxide in the coating but instead revealed a homogenous microstructure. In addition, for the $ZrSi_2$ coating, silicon diffusion from the coating

to the substrate was clearly detected which may promote coating-substrate adhesion. The Si diffusion depth was about 590 nm, and the composition of this region was predominantly ZrSi.

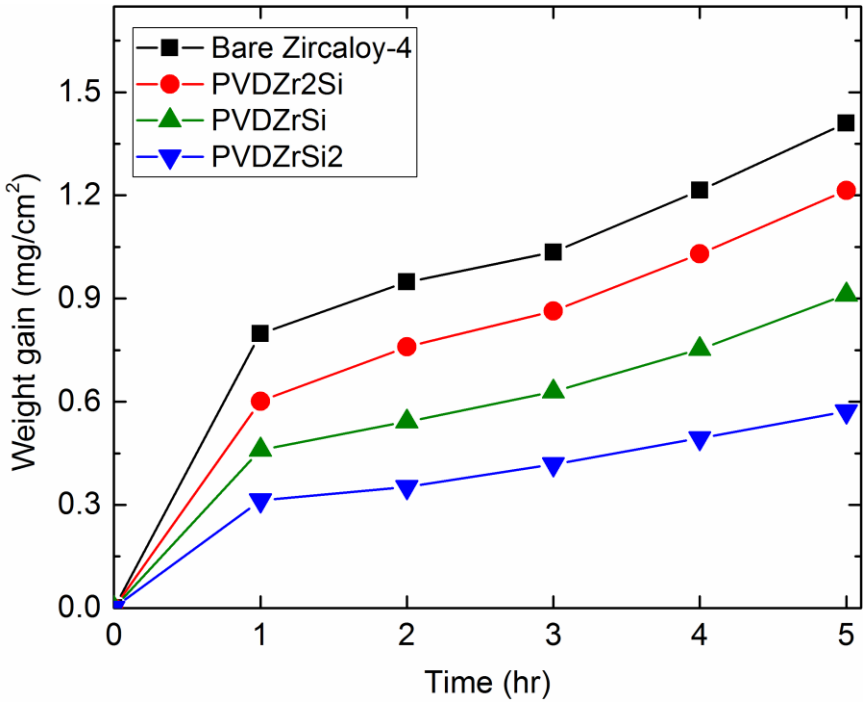

Figure 79: Weight gain of the zirconium-silicide coatings with different compositions (Zr_2Si, ZrSi, and $ZrSi_2$) in 700 °C air oxidation test. The coatings were deposited at 0.53 Pa argon pressure.

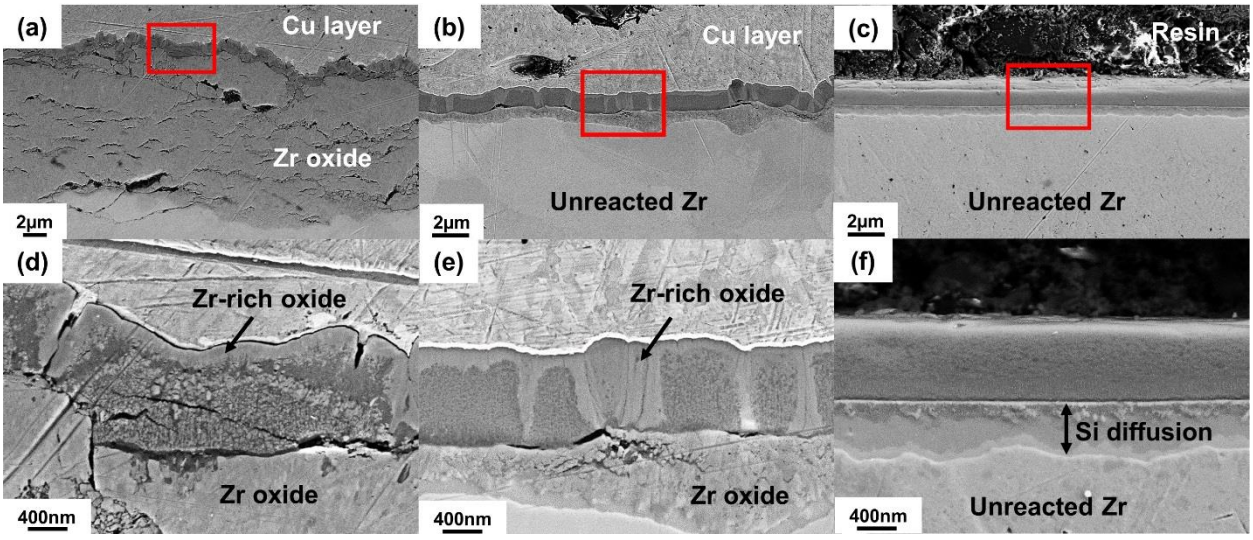

Figure 80: SEM cross sectional images of (a, d) Zr_2Si, (b, e) ZrSi, and (c, f) $ZrSi_2$ coatings at low and high magnifications after 700 °C for 5-hours air oxidation test. The high magnification images were acquired in the areas indicated by the red frames in the low magnification images. Cu layer was deposited on the coating surface by electroplating to minimize coating damage and edge retention during the sample preparation. All the coatings were deposited at 0.53 Pa argon pressure.

Figure 81 shows scratch track (120 ° diamond tip - a standard Rockwell indenter under 250 g applied load) on the coatings after the oxidation test to evaluate adhesion to the substrate and coating cohesion. The cracks and spallation were observed on only the Zr_2Si coatings. It is believed that the damage is attributed to the weak adhesion between the Zr_2Si coating and ZrO_2 scale as shown in Figure 81a. However, it was difficult to identify scratch marks and delamination of layers on the ZrSi and $ZrSi_2$ coating surfaces, indicating a good mechanical robustness of the coatings. It appears that development of ZrO_2 underneath the coatings is related to the mechanical performance, and the results are consistent with the SEM cross-sectional images shown in Figure 80.

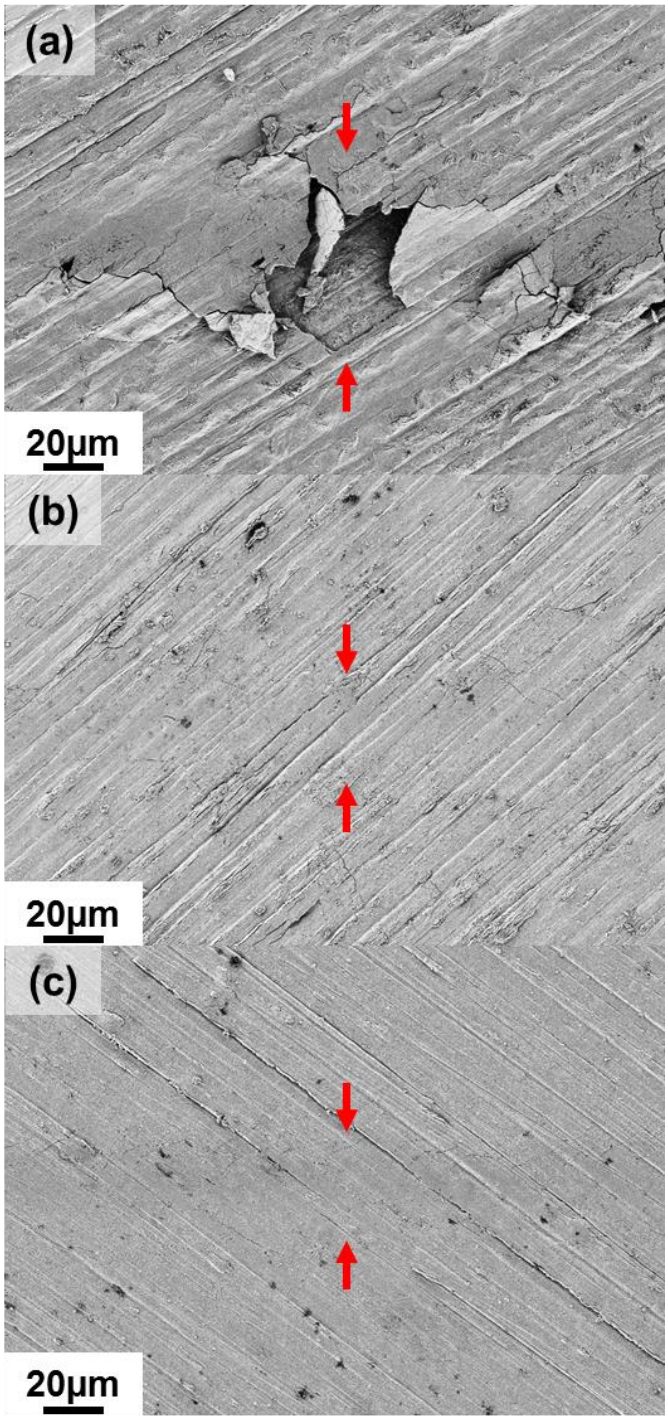

Figure 81: SEM plan-view images of oxidized zirconium-silicide coatings (a) Zr_2Si, (b) ZrSi, and (c) $ZrSi_2$ after the scratch test (250g, applied load). The red arrows indicate scratch tracks.

The near-surface chemical composition and phase evolution of the oxidized coatings was analyzed by XPS (signal acquired over a 400 μm diameter circular region). The binding energy spectrum for O1s in each coating after the oxidation is shown in Figure 82. The peak binding energy increased with increasing

silicon concentration in the coating, which means that characteristics of chemical bonds associated with oxygen were different depending on coating composition. To provide for a better understanding of the binding energy shift, deconvolution of O1s binding energy for the oxidized coatings was performed via commercial software (Origin 2015). First, the possible binding energy spectrum was assumed to be from three types of potential oxides with Gaussian distribution. The peak energies of these oxides were taken from literature to be, 531.8 eV ($ZrSiO_4$) [117], 532.4 eV (SiO_2) [118], and 530.5 eV (ZrO_2) [117,119]. The intensity and FWHM for the components were arbitrarily chosen and iteration using the software was conducted up to the minimum residue between the sum of the estimated oxide spectra and the measured O1s binding energy curve. The deconvolution results indicate the intensity of each oxide component strongly depends on concentration of silicon or zirconium in the coating. The major oxide phase for the zirconium-rich coating (i.e., Zr_2Si) was ZrO_2 with minor $ZrSiO_4$ but that for the silicon-rich coating (i.e., $ZrSi_2$) it was SiO_2 with minor $ZrSiO_4$. The oxidized ZrSi coating showed strong $ZrSiO_4$ peak with weak ZrO_2 and SiO_2 peaks. The XPS data for the coatings are in good agreement with the pseudo-binary ZrO_2-SiO_2 phase diagram [120]. Theoretically, $ZrSiO_4$ is the only single stable phase in ZrSi oxidation but compositional alteration (see Figure 80e) due to the high mobility of silicon may result in ZrO_2 and SiO_2 formation by modulation of activities of zirconium and silicon. In addition, it is speculated that ZrO_2 formation in the coating is one factor that undermines oxidation resistance of the zirconium-silicide coating at elevated temperatures. The weight gain and oxide layer underneath the coatings are proportional to the intensity of ZrO_2 spectrum in the oxidized coating. This is because of relatively higher oxygen transport rate for ZrO_2 through grain boundaries [121] and crack formation in zirconium-rich oxide. However, very low oxygen permeation in SiO_2 and excellent corrosion resistance of $ZrSiO_4$ [7] appeared to be very beneficial in preventing oxygen permeation to underlying Zirc-4 alloy substrate in high temperature air environment.

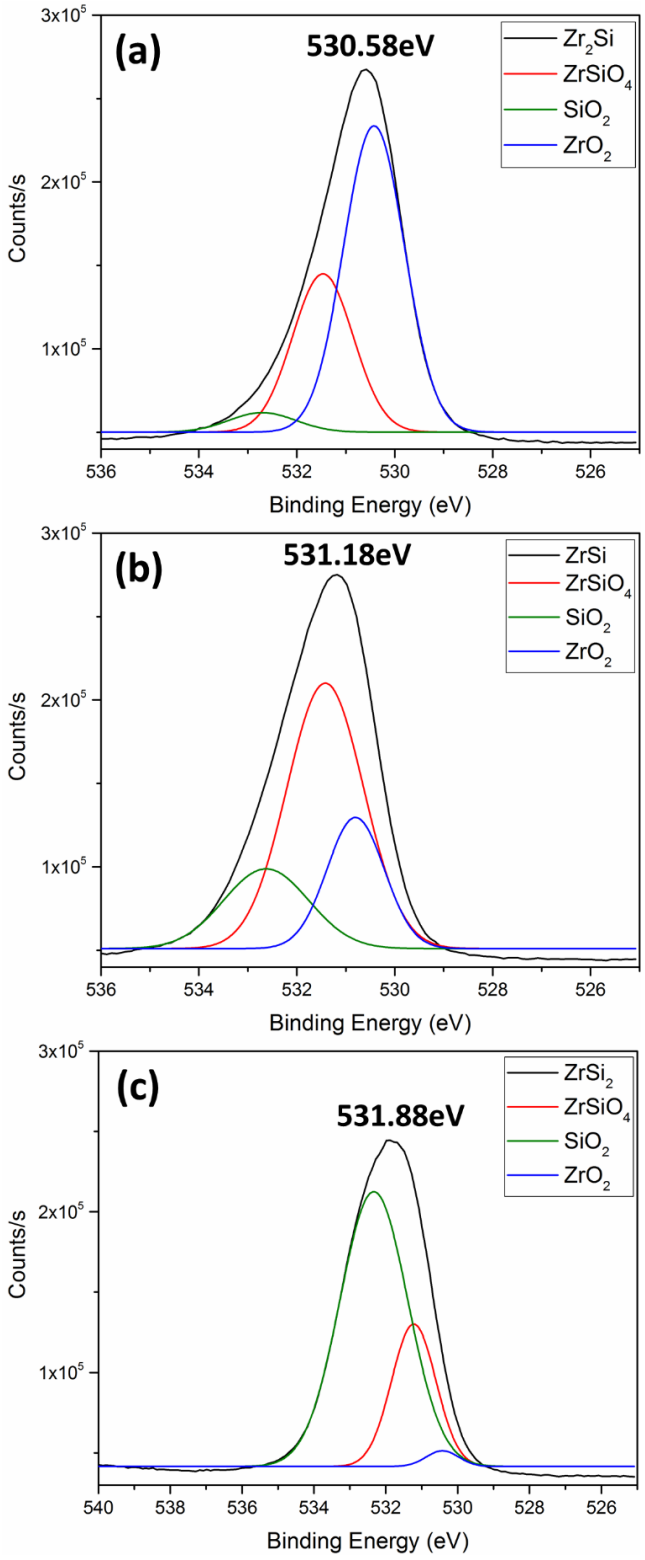

Figure 82: XPS O1s spectra of zirconium-silicide coatings after 700 °C for 5-hours oxidation: (a) Zr_2Si, (b) ZrSi, and (c) $ZrSi_2$. The O1s spectra were resolved into possible oxide components (red curve: $ZrSiO_4$, green curve: SiO_2, and blue curve: ZrO_2). The measured spectrum is indicated by dark curve. The coatings were deposited on Zirc-4 substrate under 0.53 Pa Ar pressure and room temperature.

Multilayered Zirconium-Silicide Coating

Deposition of multilayered PVD coating with all three aforementioned stoichiometries was performed in order to achieve a compositionally and functionally graded coating with the goal of maximizing coating adhesion to substrate and oxidation resistance. The multilayered coating architecture is as follows: The first layer contacting with the Zirc-4 substrate is Zr_2Si, acting as buffer layer to increase adhesion and the middle layer was ZrSi, and the top layer was $ZrSi_2$ to achieve oxidation resistance. The multilayered coating was deposited on silicon wafers for a preliminary investigation. The cross-sectional images (Figure 83a-b) of the coating deposited on the Si wafer shows that the interfaces between coatings were indistinguishable and defect free. In addition, elemental concentration of silicon and zirconium at each layer was consistent with the proposed multilayered coating, as confirmed by EDS line scan analysis (Figure 83c-d).

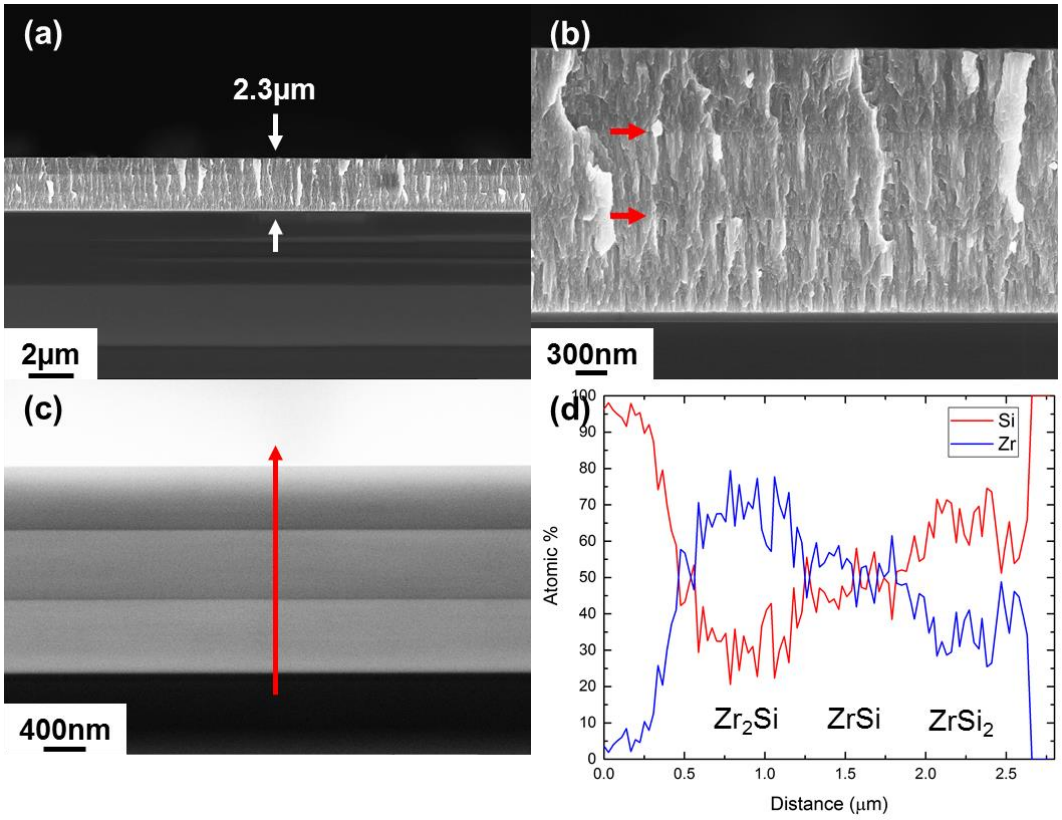

Figure 83: SEM cross-sectional images (5kV) of the multilayered coating on Si wafer at (a) low magnification and (b) high magnification. The red arrows indicate the interface between each compositional layer. (c) SEM image with high voltage (12kV) for EDS line scan and (d) corresponding the EDS line scan result for Si and Zr concentration.

The multilayered coating on Zirc-4 substrate was oxidized at 700 °C for 5 hours in ambient air to demonstrate oxidation resistance of the coatings. The cross-sectional SEM images (Fig. 84a) showed excellent adhesion of the coating to the Zirc-4 substrate. It appeared that the multilayered coating protected the substrate from the high temperature air. However, the substrate oxidation and cracks were identified in local areas (Fig. 84b), which may be attributed to a microstructure of the Zr_2Si layer (i.e., dome shape microstructures) acting as a short circuit for oxygen to be permeated. The tapered microstructure in magnetron sputter coating is generally associated with low processing temperature and surface contamination. The results of EDS line-scan reveals that oxygen could not reach the Zirc-4 substrate but significant oxygen concentration was detected in the $ZrSi_2$ and ZrSi layers. Composition of the coatings in terms of Si and Zr were altered during the oxidation test. Formation of the defect in the coating and thermal stability of the coatings were investigated further by heat treatment in inert gas.

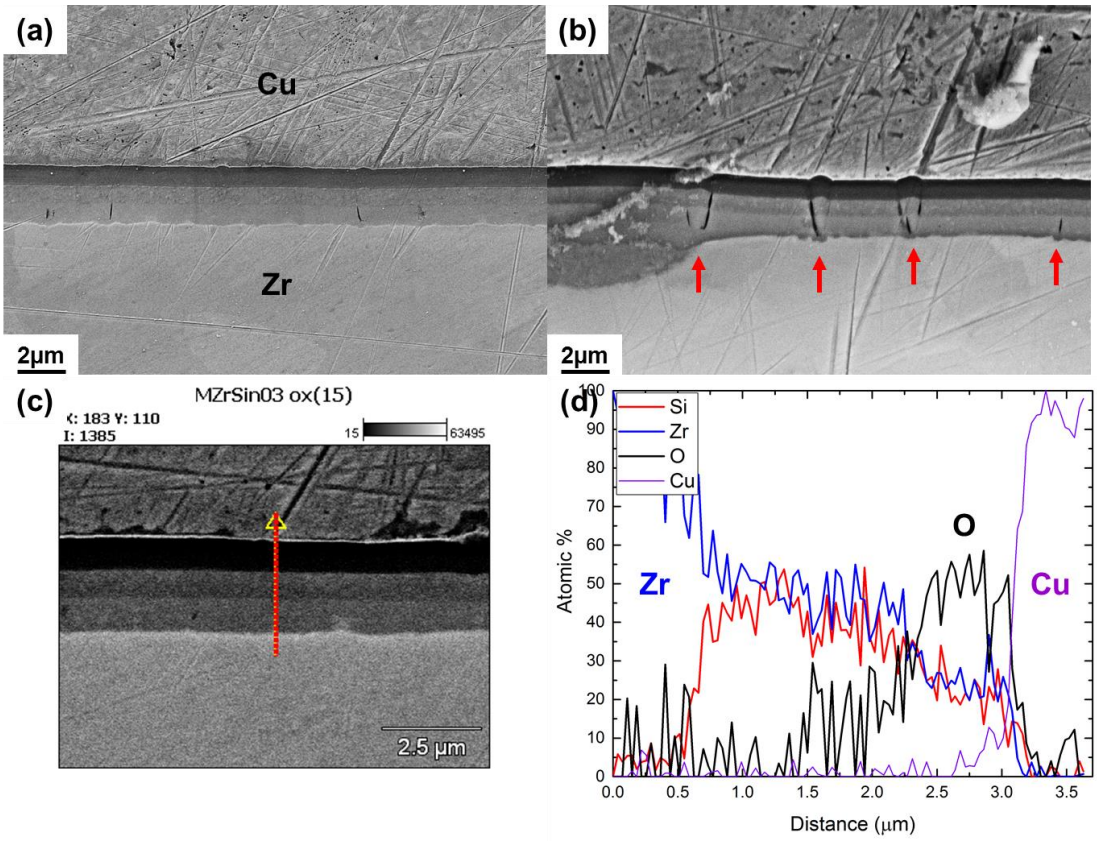

Figure 84: SEM cross-sectional images of the multilayered coating on Zirc-4 substrate after exposure at 700 °C for 5 hours: (a) imaged at 3 kV and (b) imaged at 12 kV. The red arrows indicate tapered structures being initiated in the Zr_2Si layer. (c, d) results of EDS line scan in terms of Zr, Si, O, and Cu.

Phase Stability of Zirconium-Silicide Coating on Zircaloy-4

One of key properties of an oxidation resistant coating is its thermodynamic stability at elevated temperatures [122]. For example, thermal exposure could lead to undesired phase formation in a coating or detrimental chemical interaction between a coating and the substrate. To elucidate the phase stability of zirconium-silicide coatings on Zirc-4 alloy substrate at high temperatures, the thin and single-layer coatings were annealed at 700 °C for 5-hours in an argon environment. High magnification cross-sectional SEM images and zirconium-to-silicon ratio determined by EDS analysis for the coatings (Zr_2Si, ZrSi, and $ZrSi_2$) after the annealing are shown in Figure 85.

The Zr_2Si coating showed a local variation of composition but reactivity with the substrate was not distinctively identified based on the SEM image and EDS analysis (Figure 85a). A decrease in zirconium-to-silicon ratio in the middle of the Zr_2Si coating (indicated by the cross mark in Figure 85a) was observed. It is believed that residual oxygen inside the quartz capsule reacted with the surface of the Zr_2Si coating, followed by the formation of Zr-rich oxide on the surface. Thus, silicon atoms on the surface diffused inward and increased the Si concentration however this diffusion was not far enough to reach the substrate. The SEM image of the annealed ZrSi coating displays a thin silicon-rich dark line arising from oxidation-induced silicon diffusion from the surface and silicon diffusion zone in the substrate (Figure 85b). It is worth noting that a network of micron-scale cracks in the annealed Zr_2Si and ZrSi coatings was observed as shown in Figure 85c. The cracks appeared to initiate from conical-shaped defects which propagated to the substrate. Formation of the defects in Zr_2Si coating was also observed in the multilayered coating at 700 °C. It is expected that oxygen would readily permeate the coating through the open gap around these defects at elevated temperatures, resulting in reduced oxidation resistance. The annealed $ZrSi_2$ coating showed silicon diffusion to the substrate similar to the oxidized $ZrSi_2$ coating discussed earlier but the diffusion depth was smaller (~310 nm) than the air-oxidized samples (~590 nm), indicating that surface oxidation also drives Si inward towards to the coating-substrate interface. One plausible explanation is that oxidation generates additional unbound silicon atoms in oxide scale, which is supported by a previous study

[123] - bulk $ZrSi_2$ oxidation at 700 °C in ambient air produced a solid-state mixture Zr-Si-O and a silicon phase. The newly released free silicon atoms showed a high diffusivity, and were associated with evolution of complex microstructures. In addition, XRD analysis for the annealed coatings showed not only strong zirconium peaks from the substrate but also weak zirconium-silicide peaks, indicating initiation of crystallization of the coatings. In summary, the annealing experiments confirmed compositional alteration of zirconium-silicide coatings (Zr_2Si, ZrSi, and $ZrSi_2$) on Zirc-4 substrate at 700 °C mainly due to the mobility of silicon atoms in the coatings followed by the reaction with the substrate.

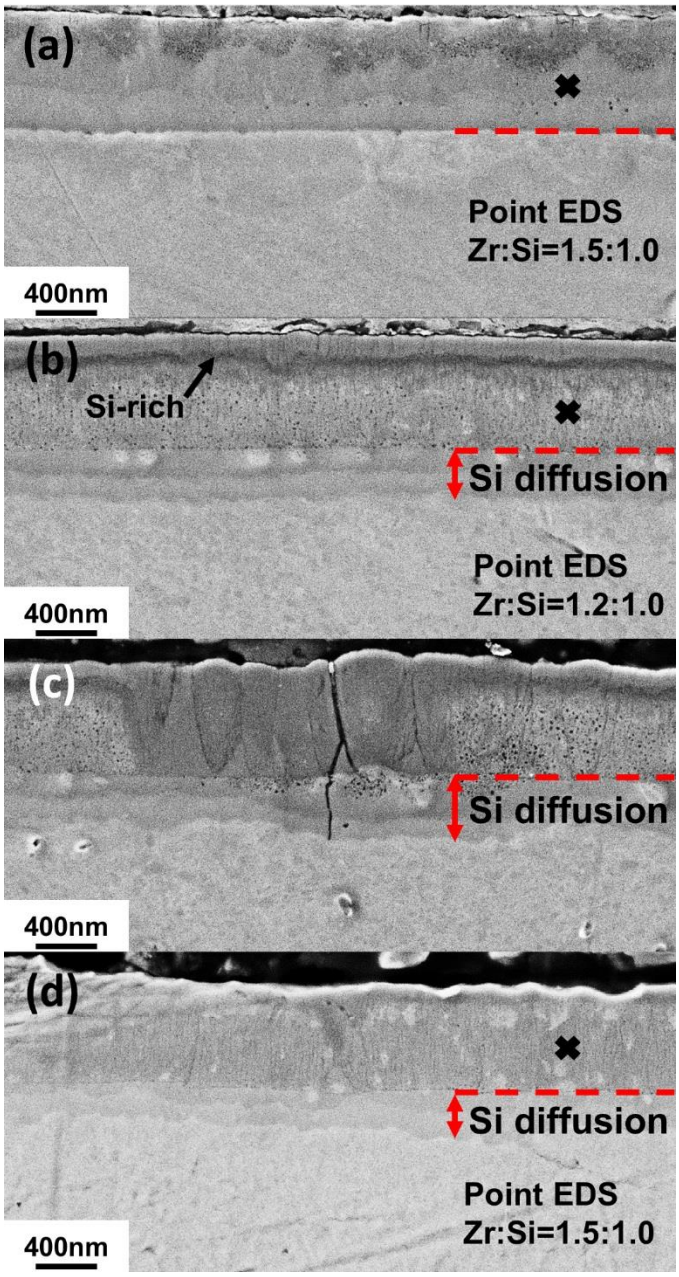

Figure 85: SEM cross-sectional images of (a) Zr_2Si, (b, c) ZrSi, and $ZrSi_2$ annealed at 700 °C for 5 hours in argon gas. Interface between the coating and the substrate and silicon diffused zone are indicated by the red dot line and red arrow, respectively. A ratio of zirconium-to-silicon at the dark cross is stated on each figure as measured by EDS point scan analysis.

4.2.2. High temperature air oxidation

Based on the oxidation and annealing of the zirconium-silicide coatings at 700 °C for 5 hours discussed in Section 4.2.1, silicon-rich zirconium-silicide stoichiometry, $ZrSi_2$, was selected as a potential oxidation resistant coating for Zirc-4. For this next phase of the study, a thicker optimized $ZrSi_2$ coating was prepared

by multiple deposition steps under 0.53 Pa Ar pressure and 19 °C substrate temperature. Plasma cleaning for substrates was performed prior to deposition of the coating.

A cross-sectional SEM in-lens image for the optimized coating is shown in Figure 86. The coating thickness was approximately 3.9 µm. The coating displayed dense and columnar microstructure and the interface between each deposition step is revealed as the faint horizontal lines. No spallation or cracks were identified. To evaluate oxidation resistance of the optimized coating, three oxidation experiments were conducted for the $ZrSi_2$ coating on Zirc-4 flats: 1) 700 °C for 20 hours, 2) 1000 °C for 1 hour, and 3) 1200 °C for 10 minutes. Extremely high temperature oxidation (1400 °C for 5 hours in ambient air) was performed for $ZrSi_2$ coatings only on SiC flats (as a test for future use of SiC-SiC composite cladding) due to severe degradation of Zirc-4 substrate at this high temperature.

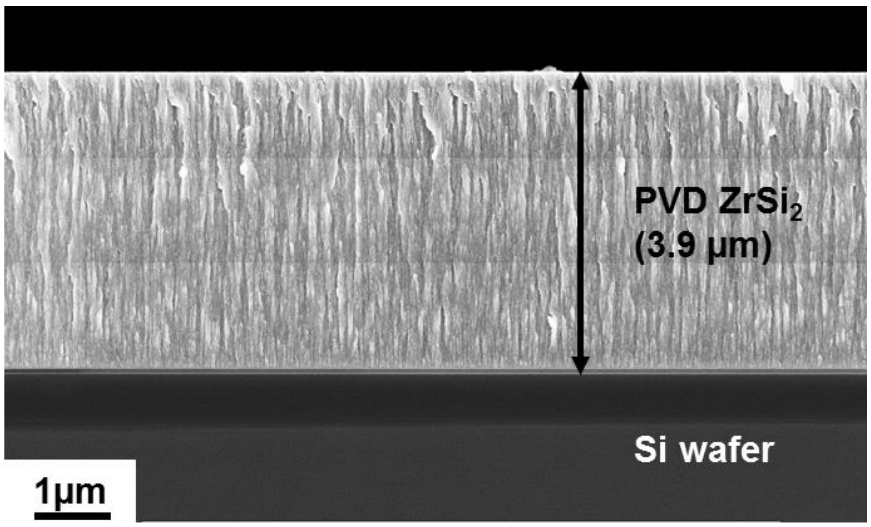

Figure 86: SEM cross-sectional image of as-deposited $ZrSi_2$ coating on silicon water for the 700 °C, 1000 °C, and 1200 °C oxidation tests.

Oxidation of Optimized $ZrSi_2$ Coating at 700 °C

The longer oxidation for the coating at 700 °C enabled us to better understand oxide scale growth on the coating and phase stability in the coating/substrate interface. The samples were heated up to 700 °C with slow ramp rate (5 °C/min) and then held at this temperature for 20 hours, followed by air cooling. As shown in Figure 87a, oxygen permeation through the coating was very low and the thin oxide layer of

thickness of only about 750 nm formed on the top surface of the coating during the 20-hour oxidation. In contrast, the bare Zirc-4 substrate developed about a 65 μm thick oxide layer. This suggests that oxidation resistance factor of improvement of the coating is more than 85 compared to bare Zirc-4 at 700 °C air. The very near-surface atomic percent of the oxide layer was 14%-Zr, 19%-Si, and 66%-O as measured by XPS (Table 8) and corresponding binding energy spectra are identical to those of the thin $ZrSi_2$ layer (see Section V.2.1) after the 700 °C for 5-hours air oxidation. The protective nature of the coating is mainly attributed by the SiO_2 and $ZrSiO_4$ oxide layer.

The XRD pattern (Figure 87b) revealed not only $ZrSi_2$ arising from crystallization of the unreacted coating and zirconium substrate peaks, but also a broad halo in the range of 24° to 30° in 2θ. Possible phases associated with the broad hump are $ZrSi_2$, SiO_2 (quartz), and $ZrSiO_4$ listed as follows: $ZrSi_2$ (040) at 24.05°, $ZrSi_2$ (021) at 24.79°, $ZrSi_2$ (130) at 30.19°, SiO_2 (011) at 25.16°, SiO_2 (220) at 28.41°, SiO_2 (310) at 28.48°, and $ZrSiO_4$ (200) at 26.67°. The XRD pattern could be a superposition of the nanocrystalline phases and amorphous phase, assuming that nanocrystalline phases ($ZrSiO_2$, SiO_2, and $ZrSi_2$) were precipitating in amorphous oxide matrix during the 700 °C oxidation. The phases constituting the thin protective oxide layer is also consistent with an oxide layer formed on bulk $ZrSi_2$ in 700 °C in ambient air. In addition, the silicon diffusion zone into the Zirc-4 alloy of thickness of 630 nm was identified. Interestingly, the silicon atoms were supplied from about 1.4 μm of the $ZrSi_2$ coating contacting with the substrate because the region displayed silicon reduction ($ZrSi_2 \rightarrow ZrSi_{1.5}$) and formation of nano-scale pores due to clustering of vacancies from the substitutional diffusion of Si (dark spots in Figure 87a).

Table 8: XPS compositional analysis of the optimized coatings ($ZrSi_2$) after the oxidation tests. The numbers are in atomic percent of each element on the very near-surface. The last column shows the atomic percent ratio of zirconium and silicon.

Oxidation Test	Si2p	Zr3d	O1s	C1s	Zr : Si
700 °C for 20 hours	18.82	13.63	65.50	2.06	1.0:1.4
1000 °C for 1 hour	15.06	17.88	64.78	1.67	1.2:1.0
700 °C for 5 hours → 1000 °C for 1 hour	17.24	14.40	67.07	1.30	1.0:1.2
700 °C for 5 hours → 1200 °C for 10 minutes	15.99	15.10	67.68	1.23	1.0:1.1

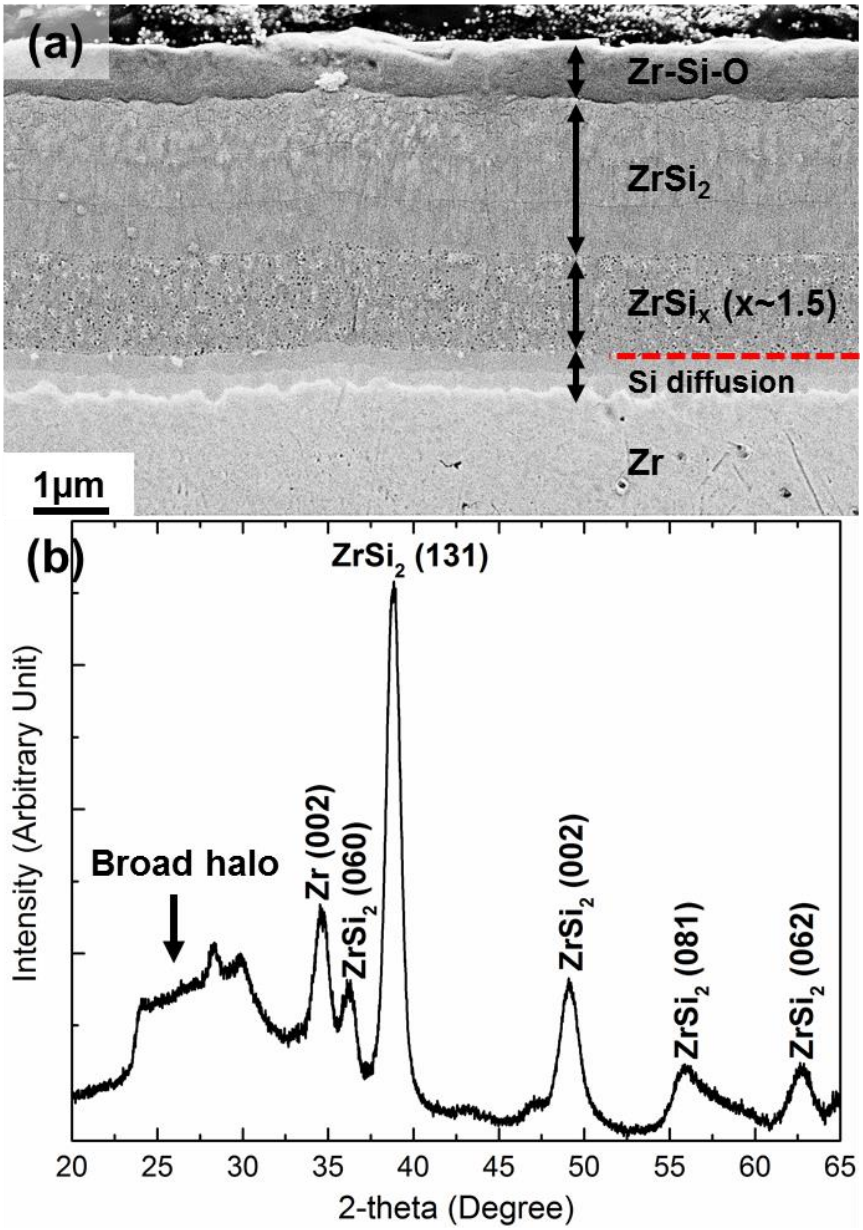

Figure 87: SEM cross-sectional image of (a) oxidized $ZrSi_2$ coating on Zirc-4 at 700 °C for 20 hours. Interface between the coating and the substrate is indicated by the red dots. (b) XRD pattern for the oxidized $ZrSi_2$ on Zirc-4 at 700 °C for 20 hours. The dark arrow in Figure 87b points to broad halo (or hump) associating with the thin oxide layer in Figure 87a.

Oxidation of Optimized $ZrSi_2$ Coating at 1000 °C and 1200 °C

The high temperature oxidation tests for the optimized coatings were conducted at 1000 °C for 1 hour and 1200 °C for 10 minutes. For these tests, the coated samples were inserted directly in a pre-heated furnace resulting in a rapid heating rate. After the exposure, the samples were air-cooled to room temperature. These tests demonstrated material degradation due to oxidation and thermal shock. For these

tests, two types of samples were evaluated, (i) as-deposited coating and (ii) after pre-oxidation at 700 °C air for 5 hours. The pre-oxidation condition was the same as was used for the oxidation tests for thin coatings discussed earlier. Thus, the pre-oxidized samples used for the 1000 °C and 1200 °C would have the same submicron thickness protective oxide layer. As shown in Figure 88a-b, significant differences in surface morphology between the as-deposited coating and the pre-oxidized coating were observed after the 1000 °C oxidation. Micron-scale cracks were observed (Figure 88a) on the entire area of the as-deposited coating, indicating the coating did not provide the necessary oxidation resistance. The degradation of the as-deposited coating might be explained by the absence of the protective oxide layer and loss of thermal stability of the coating. A sudden temperature surge to 1000 °C in air produced ZrO_2 on the surface due to silicon inward diffusion rather than formation of the Zr-Si-O protective oxide layer. As discussed in the previous section, silicon diffusion from the $ZrSi_2$ coating to Zirc-4 substrate was identified at 700 °C in both oxidation and annealing. Increase in Zr-to-Si ratio on the oxidized surface at 1000 °C without the pre-oxidation as confirmed in XPS analysis (Table 8), and the local silicon rich area in the cross-sectional image of the coating (Figure 88c) also support this explanation. According to the diffusion couple experiments between Ti_3SiC_2 and Zirc-4 [101], the effective diffusion coefficient of Si in Zirc-4 at 1300 °C was approximately six times larger than that at 1100 °C. Therefore, remarkably rapid silicon loss in the coating, which accelerated by the surface oxidation at 1000 °C in the absence of the protective layer, generated microstructural defects (i.e., clusters of voids) in the coating, which in turn induced the crack formation and intensified material degradation. On the other hand, not only no noticeable defects such as delamination, cracks, or spallation but also higher silicon concentration compared to zirconium on the very near-surface was observed on the pre-oxidized coating surfaces with the 1000 °C and 1200 °C exposures.

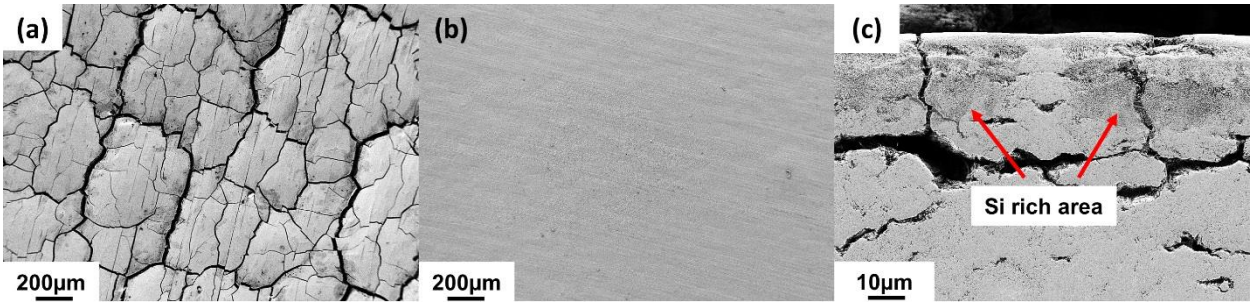

Figure 88: SEM plan-view images of (a) $ZrSi_2$ oxidized at 1000 °C for 1 hour, (b) $ZrSi_2$ with pre-oxidation (700 °C for 5 hours) oxidized at 1000 °C for 1 hour, and (c) cross-sectional image of $ZrSi_2$ with pre-oxidation (700 °C for 5 hours) oxidized at 1000 °C for 1 hour, showing cracks and Si rich area in the thick oxide scale. The samples were rapidly heated up to the high temperature air. After the exposure, the coating was air-cooled to room temperature.

The protective nature of the top oxide layer formed on the pre-oxidized sample was also confirmed in the cross-sectional SEM image of the sample after the 1000 °C and 1200 °C oxidation tests (Figure 89). After oxidation at 700 °C for 5 hours followed by the 1000 °C for 1 hour, total thickness of the oxide scale for the coating was about 7 μm, but that of the bare Zirc-4 oxidized at the same condition was about 89 μm. However, the as-deposited coating (i.e., without pre-oxidation) after the test had thicker oxide scale (approximately 106 μm) than the bare Zirc-4, possibly resulting from oxygen ingress through the cracks as observed in Figure 88a-c. The oxygen penetration depth for the pre-oxidized coating after the 1000 °C test was also measured by EDS line scan analysis as shown in Figure 89b. The pre-conditioning produced about 730 nm thickness oxide layer on the top, ZrO_2 (~6.3 μm), $ZrSi_2$ (~0.9 μm), and ZrSi layer (~3.5 μm) subsequently. In addition, the oxide layer thickness of the pre-oxidized coating after the 1200 °C test was about 20 μm, which was nearly one-tenth of oxide scale thickness of the bare Zirc-4 (about 208 μm) at this test condition. The oxide scale for the coated samples consisted of thin protective layer (750 nm) on the top, thick ZrO_2 layer (~17 μm), $ZrSi_2$ islands, and ZrSi layer (~2.3 μm). Interestingly, the protective oxide layer formed on the pre-oxidation (700 °C) transformed to nanoscale ZrO_2 phase particulates in a SiO_2 matrix at the 1000 °C and 1200 °C exposures as shown in Figure 89c-d. The microstructure was not identified in the oxide scale at 700 °C.

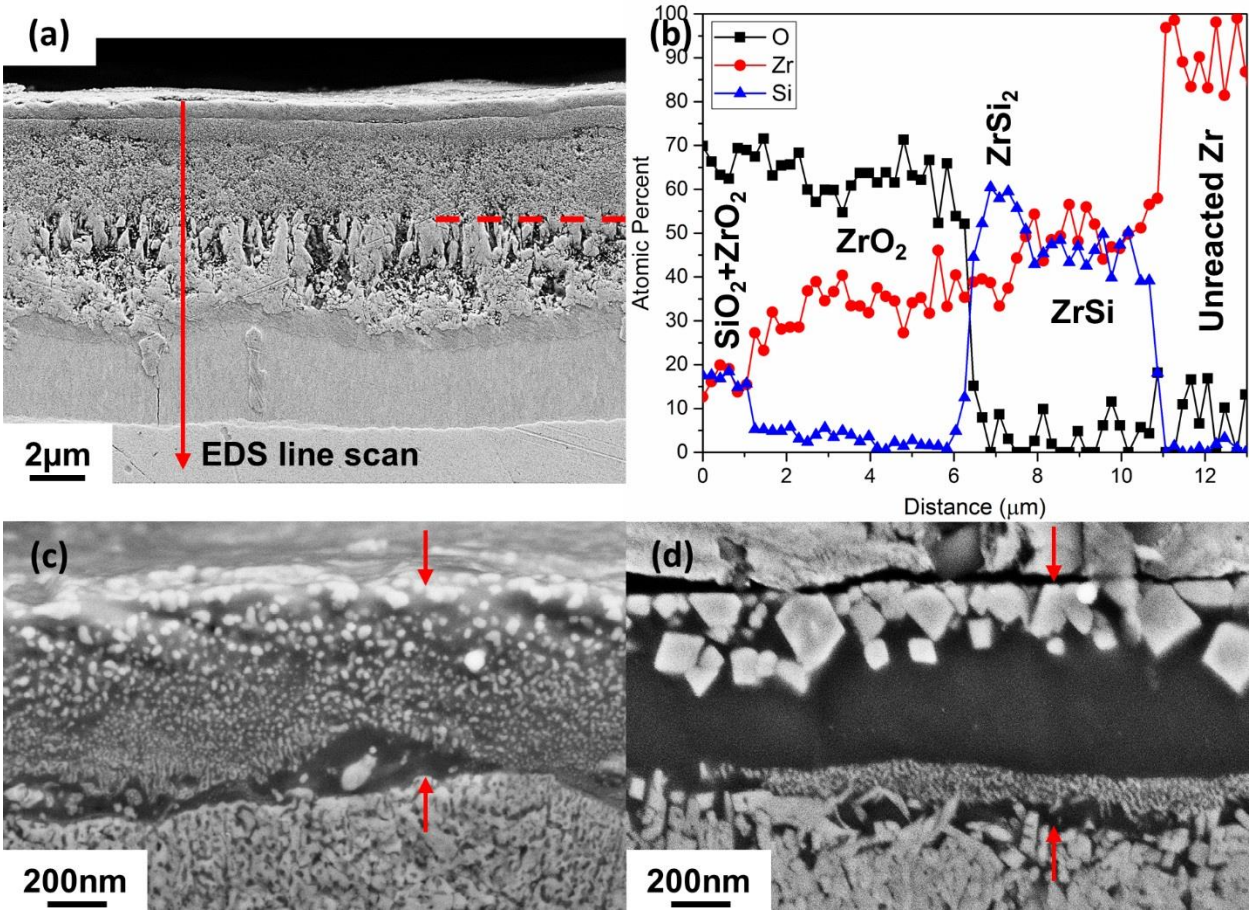

Figure 89: SEM cross-sectional images and EDS line scan of $ZrSi_2$ with the pre-oxidation (700 °C for 5 hours) after the 1000 °C for 1-hour air oxidation: (a) Low magnification and (b) EDS line scan result. The red dots and the solid red arrow in Figure 89a refer to interface between the coating and substrate and the EDS scan direction, respectively. High magnification cross-sectional SEM images of top surface of the pre-oxidized coatings after (c) the 1000 °C for 1 hour and (d) the 1200 °C for 10 minutes. The red solid arrows in Figure 89c-d refer to the thin protective layer consisting of nanoscale ZrO_2 phases in SiO_2 matrix.

The phase transformation from the Zr-Si-O oxide mixture to the ZrO_2 and SiO_2 phase was also reported in annealing of mixture of ZrO_2 and SiO_2 thin film at 900 °C for 60 seconds [99] and oxidation of bulk $ZrSi_2$ at 1000 °C and 1200 °C for 5 hours in ambient air. The authors suggested that a thermodynamic driving force exists in disordered Zr-Si-O mixture, leading to nucleation and growth of ZrO_2 in SiO_2 matrix instead of formation of $ZrSiO_4$. During the pre-conditioning, the oxide layer consisting of a mixture of nanocrystalline phases and amorphous phase forms, which might heal inherent microstructural defects (i.e., conical defects) so that the oxide layer hindered oxygen permeation during the 1000 °C and 1200 °C oxidation. In addition, the multi-layered scale structure at the high temperatures evolves due to slow oxidation kinetics arising from the thin protective layer. The partial pressure for oxygen might be

significantly decreased in the protective layer, resulting in a slower oxidation process of the rest of the $ZrSi_2$ coating. In the meantime, the silicon in the coating migrates inward to the substrate, increasing activity of zirconium in the outer regions. The mobile silicon atoms reacted with the substrate and formed the $ZrSi_2$ and ZrSi layers, which is supported by the zirconium-silicon diffusion couple experiments at 900 °C to 1400 °C in inert environments [124]. Thus as expected, when oxygen diffused through the protective layer and reacted with zirconium atoms, the ZrO_2 scale formed. Lastly, it is expected that oxidation of the $ZrSi_2$ coating by a pre-oxidation step at even higher temperatures (e.g., 1300 °C or 1400 °C) produces micron-grained $ZrSiO_4$ phase in the protective layer by solid state reaction of the ZrO_2 particulates and the SiO_2 matrix, which would provide enhanced oxidation resistance.

Oxidation of Optimized $ZrSi_2$ Coating at 1400 °C

To understand oxidation performance of the $ZrSi_2$ coatings at extremely high temperatures, the coatings deposited on the two major surfaces of Zirc-4 flats were oxidized at 1400 °C for 5 hours in ambient air. The ramp rate for the oxidation process was 5 °C/min. As shown in Figure 90a, the samples were excessively oxidized and crumbled after the oxidation due to oxygen ingress through the uncoated areas (e.g., side areas of the samples). To avoid the substrate effect, commercially available Moissanite 3C (β) – CVD SiC flats were procured and polished progressively with 600 grit SiC abrasive paper followed by cleaning with acetone and methanol. $ZrSi_2$ coatings of 3 μm thickness of were deposited on one side of these SiC flats using the same magnetron sputter technique. The coated SiC flats were oxidized at 1400 °C for 5 hours in ambient air, and Figure 90b shows the oxidized $ZrSi_2$ coating on SiC samples with the light grey color. No noticeable spallation of the coatings was not observed by the visual inspection.

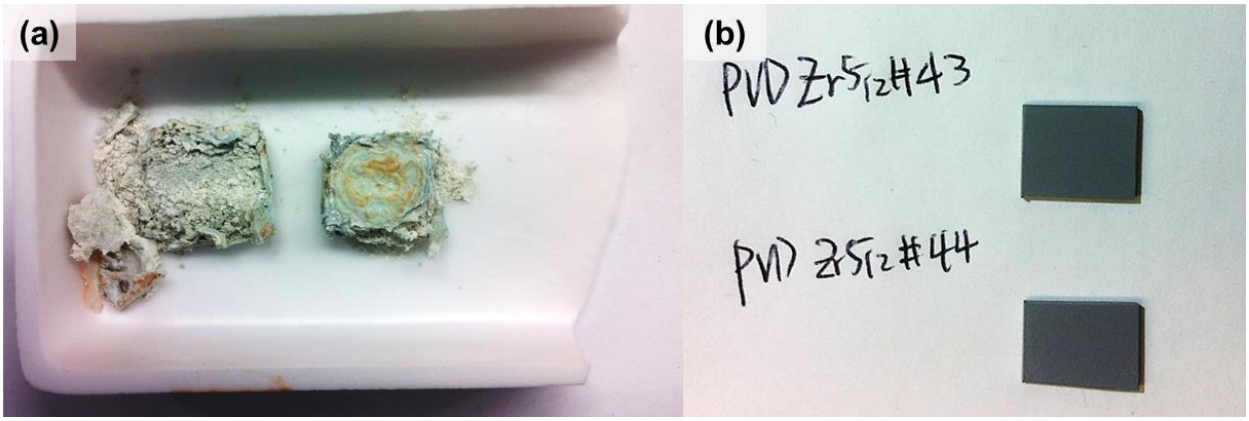

Figure 90: Photograph of (a) oxidized $ZrSi_2$ coatings on Zirc-4 flats and (b) oxidized $ZrSi_2$ coatings on SiC flats at 1400 C for 5 hours in ambient air.

Figure 91 shows SEM plan-view images for bare SiC, as-deposited $ZrSi_2$ and oxidized $ZrSi_2$ at 1400 °C. Elemental compositions for the surfaces were also specified on the images. Due to the high hardness of SiC, it was difficult to make the surface smooth and the bare SiC appears to be rough as shown in Figure 91a. Nevertheless, the surface $ZrSi_2$ coating fully covered and filled the pockets on the surface, smoothening the surface as confirmed in Figure 91b. The coating surface did not reveal any cracks and delamination after the 1400 °C oxidation test but nano-scale surface structures were identified in the high magnification image (Figure 91d), and similar concentration of Zr and Si on the surface is an indicative of formation of $ZrSiO_4$ phase.

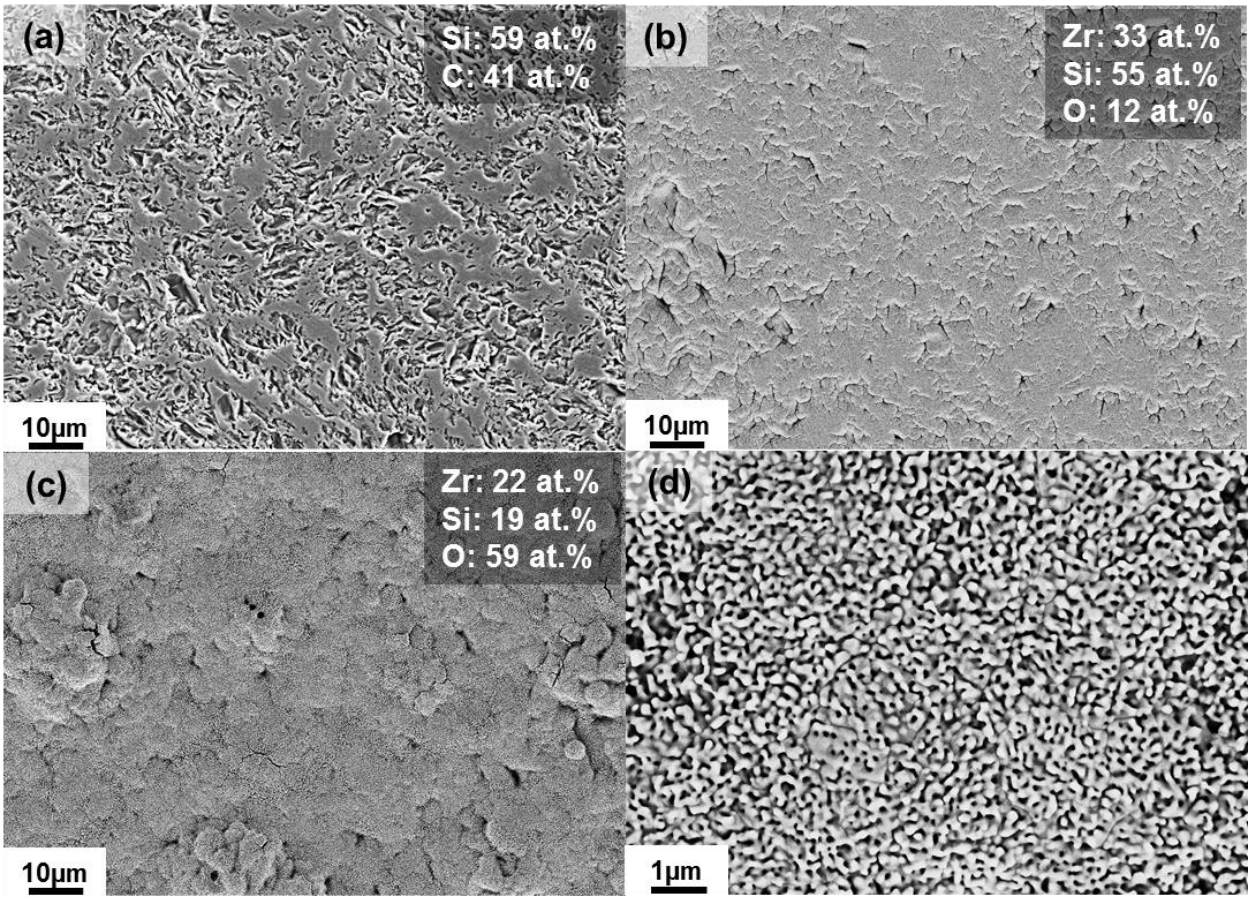

Figure 91: SEM plan-view images of (a) bare SiC sample, (b) as-deposited $ZrSi_2$ coating on SiC and (c) and (d) as-deposited $ZrSi_2$ coating on SiC after oxidation at low magnification and high magnification, respectively. The insets show area-average EDS results on each surface. The oxidation test was performed at 1400 °C for 5 hours in ambient air.

XRD patterns for the oxidized $ZrSi_2$ coating are shown in Figure 92. The strong zircon peaks, SiC peaks, weak $ZrSi_2$ peaks, and SiO_2 peaks were identified. It is worth noting that $ZrSi_2$ coating could produce zircon phase during high temperature oxidation and has the potential to drastically mitigate oxidation given that just underneath the zircon layer unreacted $ZrSi_2$ phase is still detected after the high temperature oxidation. The SiC of course peaks come from the substrate.

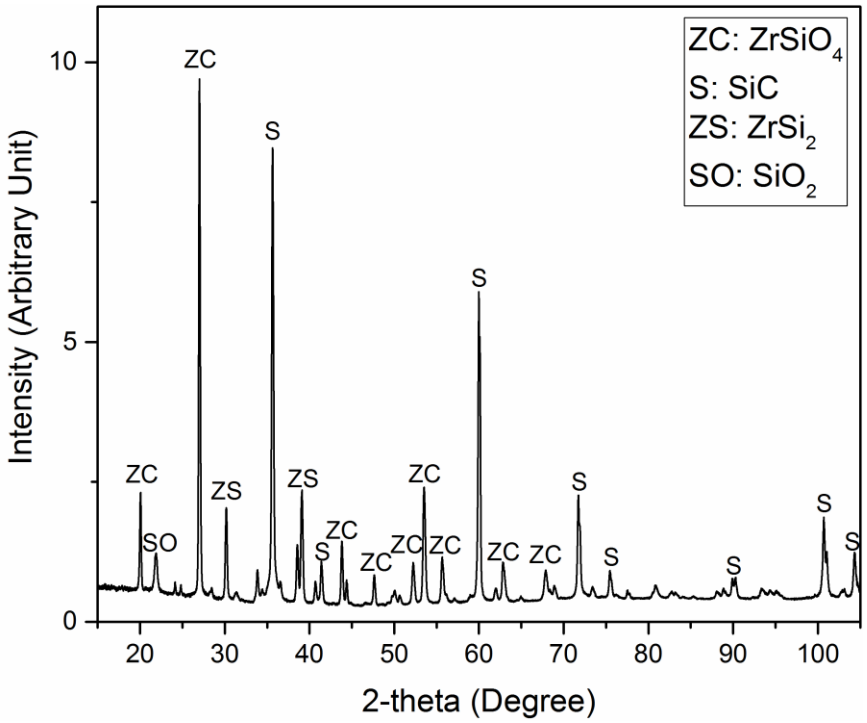

Figure 92: XRD pattern for oxidized $ZrSi_2$ coating on SiC after exposure at 1400 °C for 5 hours in ambient air.

Microstructure of the oxidized $ZrSi_2$ coating was characterized by SEM cross-sectional imaging as shown in Figure 93. The oxide scale for the coating consisted of continuous zircon layer with thickness of approximately 1.9 µm, SiO_2 layer, and islands of unreacted $ZrSi_2$. The thickness of the oxide scale was doubled (~5.4 µm) compared to the as-deposited coating (~3 µm). This is because the volume of the coating increased during the oxidation process which produces $ZrSiO_4$ and SiO_2. Additionally, silicon diffusion to SiC substrate was not identified, a difference from the oxidation for similar coatings on Zirc-4 substrate discussed earlier. It is speculated that top region of the coating reacted with oxygen followed by formation of ZrO_2, SiO_2, corresponding to the microstructure of oxide scale for the 1000 °C and 1200 °C oxidation. And then, solid state reaction of the ZrO_2 phases and the SiO_2 produced $ZrSiO_4$ layer. The inwardly diffusing free Si then oxidizes, resulting in the SiO_2 layer. Due to the excellent oxidation resistance of $ZrSiO_4$ and SiO_2 layers, unreacted $ZrSi_2$ islands were observed in the oxide scale. It appears that the SiC substrate remains unreacted because of very low partial pressure of oxygen at the interface. The zircon phases had columnar structures with nano-sized ZrO_2 and SiO_2 phases based on the contrast difference in Figure 93b. It is assumed that the dark spots and the bright circles in the zircon layer were SiO_2 and ZrO_2

phases, respectively. The EDS line scan of the cross-sectional image of the oxide scale (Figure 94a) was performed and the results are plotted in Figure 94b. The compositional plot shows that diffusion of oxygen was effectively mitigated by the $ZrSiO_4$ and SiO_2 layers.

It is well-known that fabrication of zircon coating is a very difficult process. For example, thermal spray for this material is limited due to phase decomposition of zircon during melting the feed powders above 1670 °C [125,126], and formation of micron-scale thickness of zircon layer takes very long time via atomic layer deposition because of a low yield rate. Moreover, crystalline zircon layer would not be achieved via plasma enhanced chemical vapor deposition at relatively low temperature due to spinodal phase decomposition [98,99]. In the previous sections, performance of the zircon layer at the oxidation/corrosion environments was demonstrated. For instance, the oxide scale of bulk $ZrSi_2$ at 1400 °C air was thinner that that at 1200 °C air due to formation of zircon surface layer. Under the high temperature steam environment, the immobilization of Si by zircon phase imparted corrosion stability to the material. It is anticipated that the thin and continuous zircon layer on the SiC substrate, produced by the high temperature oxidation of $ZrSi_2$ coating, might mitigate potential degradation of SiC in higher temperature and water/steam conditions.

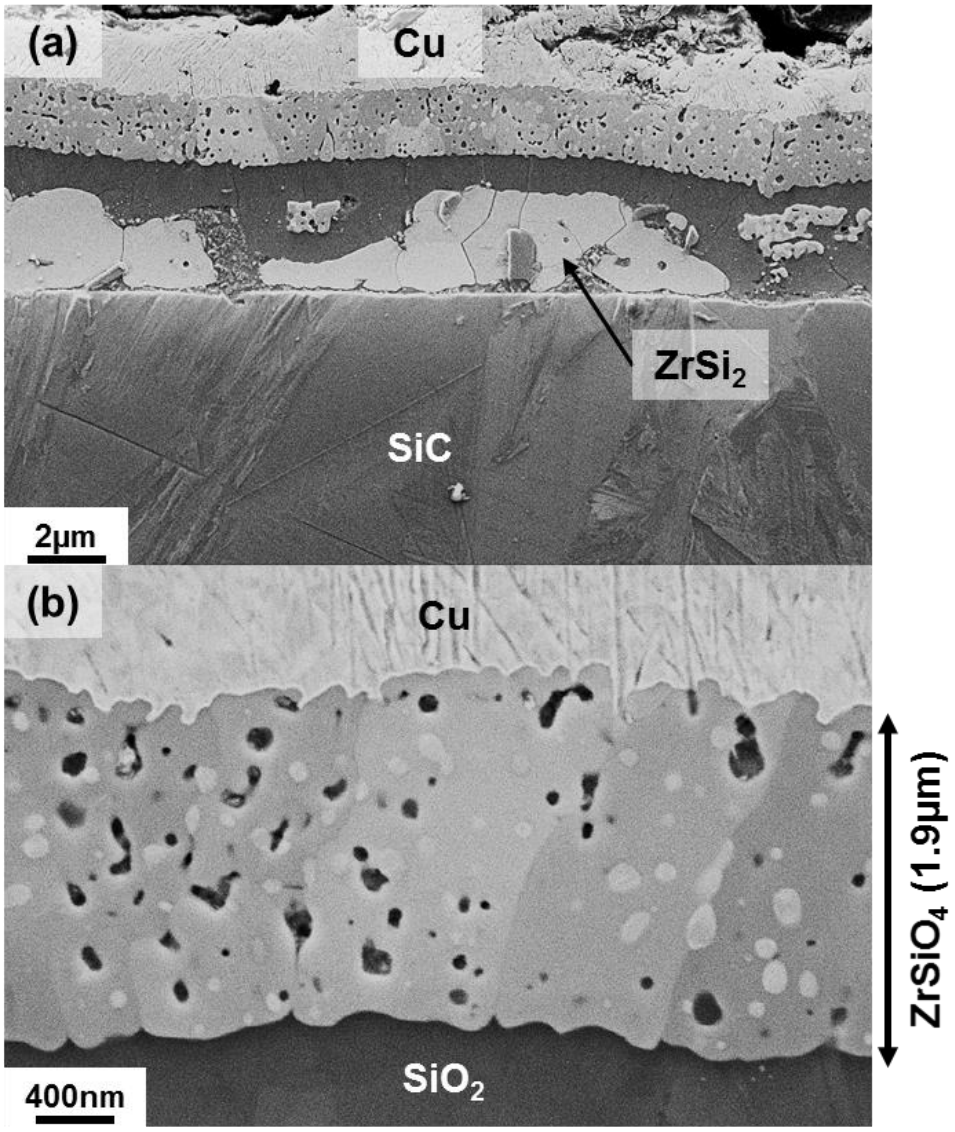

Figure 93: SEM cross-sectional images of oxidized $ZrSi_2$ coating on SiC substrate at 1400 °C for 5 hours in ambient air with (a) low and (b) high magnification.

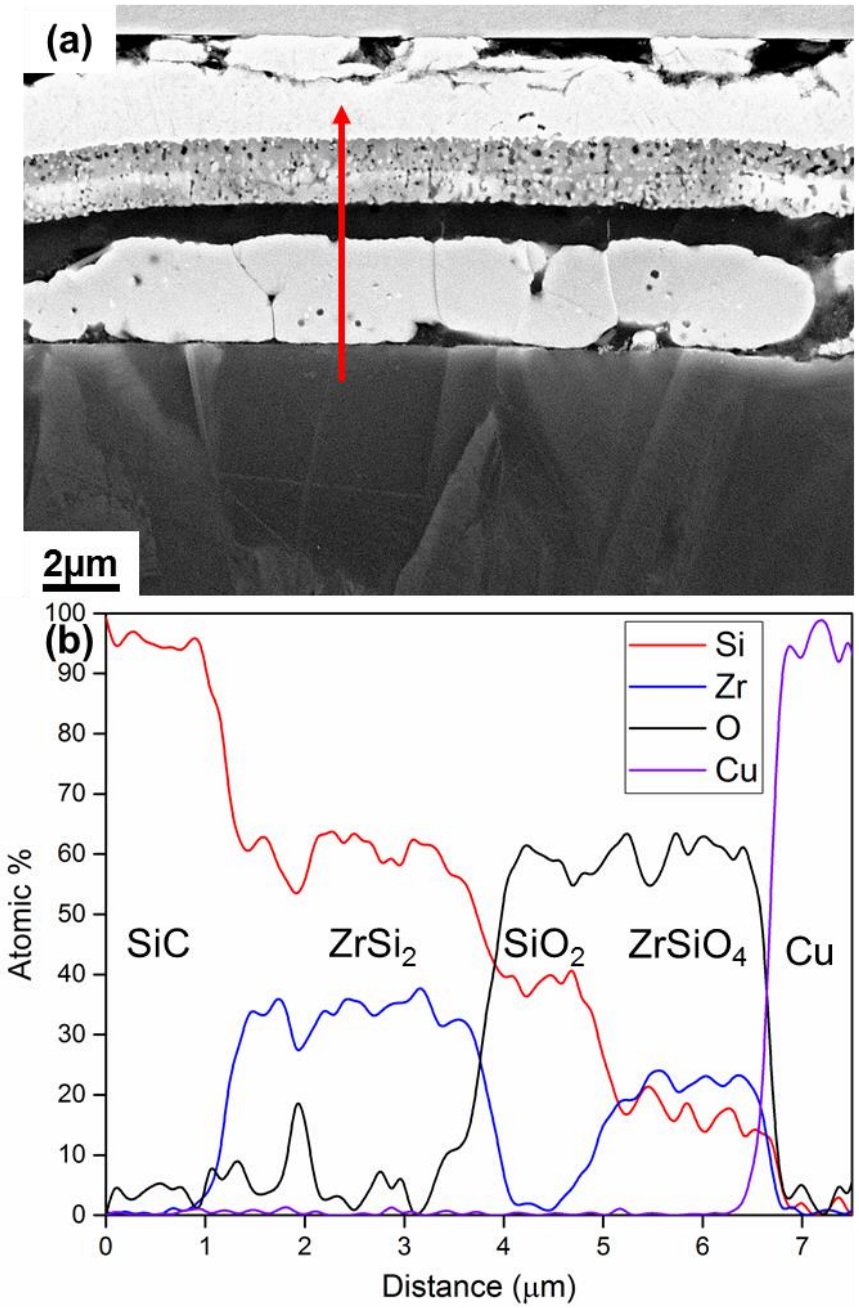

Figure 94: (a) Cross-sectional image of oxidized $ZrSi_2$ coating on SiC for EDS line scan analysis. The red arrow indicates a path of data collections and (b) the results for Si, Zr, O, and Cu are plotted. The Cu signal was detected from Cu plated layer prepared during a sample preparation.

4.2.3. High pressure steam corrosion

In the last section (Section 4.2.2), parametric investigations for optimized $ZrSi_2$ coating were performed, and the oxidation tests examined protective-nature of the optimized coating at elevated temperatures in ambient air. In addition, it was found that zircon ($ZrSiO_4$) phase was generated during air oxidation of $ZrSi_2$

coating in 1400 °C air environment. Given the outstanding corrosion resistance of zircon, it was anticipated that it provides corrosion resistance for SiC substrate, which is known to experience silicon depletion in high temperature water/steam environment. In this section, initial evaluation of corrosion resistance of the zirconium-silicide coatings under high temperature water conditions were conducted. $ZrSi_2$ was first deposited on one surface of Zirc-4 and CVD SiC test flats. After the steam corrosion test, the coatings were characterized by SEM-EDS analysis to quantify any alterations in surface morphology and composition, and thickness of oxide scale. The steam test conditions were identical to the experiments for bulk materials as discussed in section 4.1.2. The coated samples were exposed to 400 °C, pure steam (18 MΩ), and 10.3 MPa for 72 hours.

Zirconium-silicide Coatings for Steam Corrosion Test

Based on the results of optimization process for zirconium-silicide coatings to maximize oxidation resistance under high temperature air, silicon-rich silicide ($ZrSi_2$) coatings with thickness of 3.9 μm were deposited for the steam corrosion test. Pre-oxidation of the $ZrSi_2$ coating was performed at 700 °C air for 5 hours prior to the steam test in order to attain the thin oxide layer that showed excellent oxidation resistance in high temperature air environment. To mitigate silicon loss in $ZrSi_2$ in steam environment several coating system designs were investigated. First, a double-layered Zr-Si coating was investigated – here the inner layer was $ZrSi_2$ coating for oxidation resistance at high temperatures and outer layer was Zr_2Si coating as a potential water corrosion resistance barrier at high temperature steam environment. In the second approach, some of the double-layered coatings were oxidized at 400 °C air for 10 hours to facilitate formation of Zr-rich oxide on the top surface. Finally, the zircon formed $ZrSi_2$ coatings, prepared by the 1400 °C air oxidation, were exposed to the steam conditions and surface corrosion of the coatings was observed. The coating designs for steam corrosion test is summarized in Table 9.

Table 9: Composition, coating thickness, coating substrate, and heat treatment conditions of zirconium-silicide coatings for steam corrosion experiment (400 °C pure steam and 10.3 MPa for 72 hours).

Coating ID	Composition [thickness]	Substrate	Heat Treatment in Air
Zirc-4	Zirconium alloy	Zircaloy-4	None
ZrSi#1	$ZrSi_2$ [3.9 μm]	Zircaloy-4	None
ZrSi#2	$ZrSi_2$ [3.9 μm]	Zircaloy-4	700 °C for 5 hours
ZrSi#3	Outer Zr_2Si [3 μm] + Inner $ZrSi_2$ [3 μm]	Zircaloy-4	None
ZrSi#4	Outer Zr_2Si [3 μm] + Inner $ZrSi_2$ [3 μm]	Zircaloy-4	400 °C for 10 hours
ZrSi#5	$ZrSi_2$ [3 μm]	SiC	1400 °C for 5 hours

The double-layered Zr-Si coatings (ZrSi#3) was fabricated by four deposition steps on Zirc-4 flats and Si wafer. The contrast between the two zirconium-silicide layers of different stoichiometries is revealed clearly in SEM cross-sectional image (Figure 95a) of the double layered coating system. The brighter area contains more zirconium and less silicon, which is Zr_2Si layer. The columnar microstructures were continuous across the compositional boundary so that excellent adhesion between each layer is expected. The EDS line scan data (Figure 95b) confirms again that the double-layered coating consists of Zr_2Si (3 μm in thickness) and $ZrSi_2$ (3 μm).

Pre-oxidation of the double-layered coatings at 400 °C air for 10 hours facilitated ZrO_2 formation on the surface. Visual inspection showed that the surface color of the coating changed from the original metallic grey to blue. EDS elemental analysis on top of the coating showed an increase in oxygen concentration to 40 at. % but there was no emergence of peaks associated with the formation of crystalline phases (the only peaks were from Zr from the substrate).

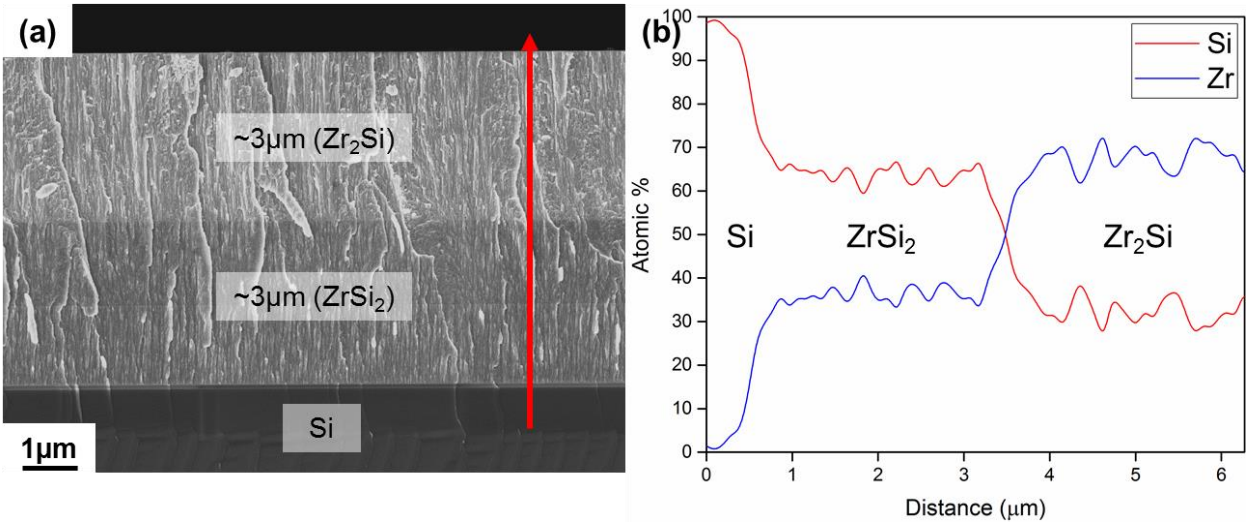

Figure 95: (a) SEM cross-sectional image of the double-layered Zr-Si coating on Si wafer and (b) EDS line scan result corresponding to the red arrow.

Steam Corrosion of Optimized $ZrSi_2$ and Multilayered Coatings

Figure 96 shows the surface morphology and elemental composition for the as-deposited $ZrSi_2$ (ZrSi#1), the pre-oxidized $ZrSi_2$ (ZrSi#2), and the pre-oxidized double-layered coating (ZrSi#4) after the steam corrosion test. The surface of all the steam autoclave tested Zr-Si coatings showed an increase in oxygen concentration and depletion of silicon atomic percent, and surface cracking. The lesser surface cracks on the ZrSi#1 (Figure 96a) compared to the bulk $ZrSi_2$ (section 4.1.2) indicates that the micron sized silicon particulates embedded in the $ZrSi_2$ matrix weakened mechanical integrity of oxide scale during the steam corrosion. The high magnification SEM images (Figure 96b, d, and f) reveal alterations in surface morphology. Due to the reaction with steam, the typical bulbous surface structure of the as-deposited coating changed to the sponge-like surface as shown in Figure 96b. The major phase of the porous structure was zirconium-rich oxide. The pre-oxidized $ZrSi_2$ (ZrSi#2) and the double-layered coatings (ZrSi#3 and ZrSi#4) show coarser and denser porous structure than the as-deposited coating (ZrSi#1), associated with higher activity of zirconium on the surface than silicon while the steam reacted with the coating surface. Nevertheless, existence of the porosity of the surface layer contributed to local cracking, resulting in steam permeation and corrosion.

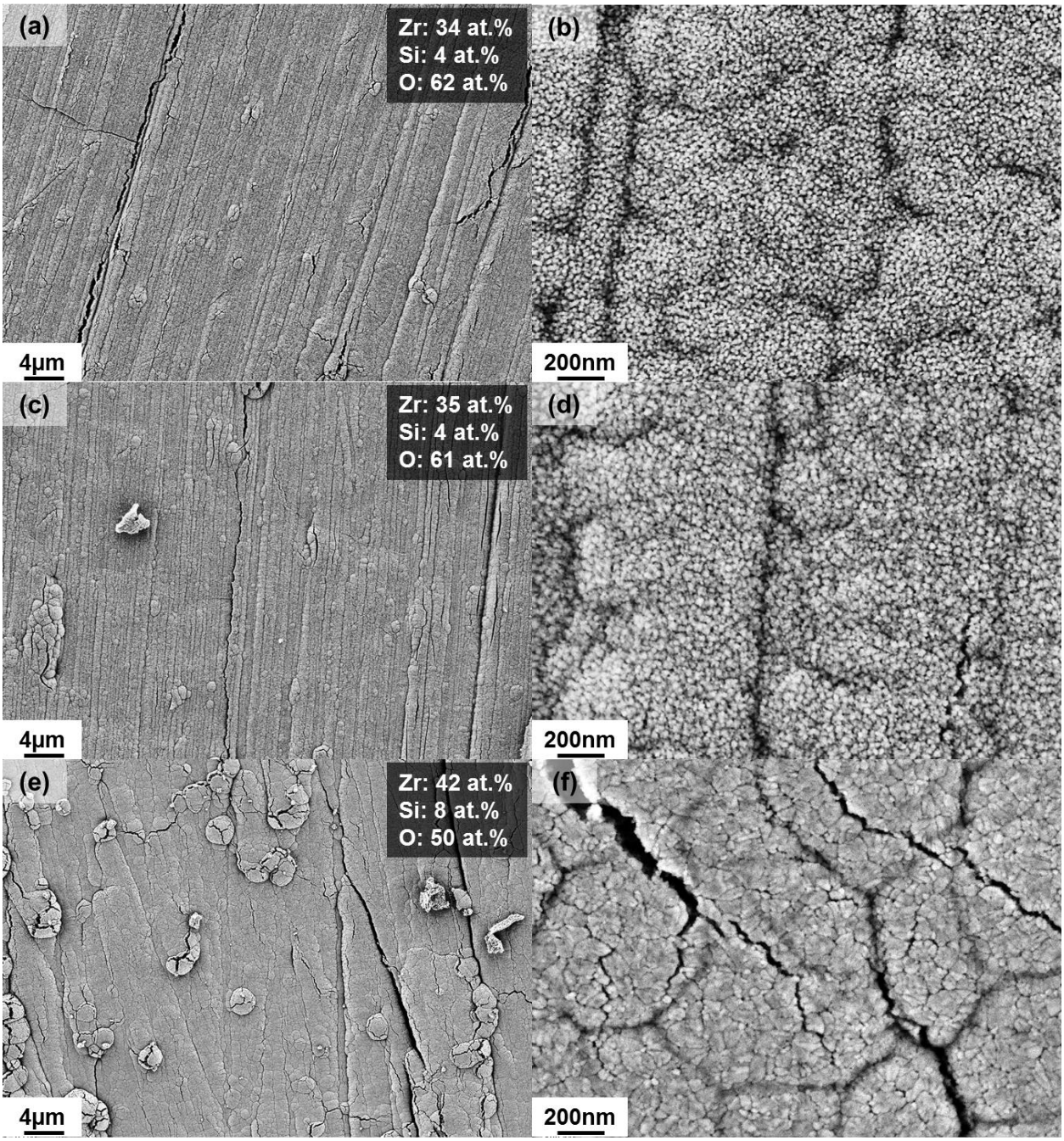

Figure 96: SEM plan view images of zirconium-silicide coatings on Zirc-4 and results of EDS analysis after the steam autoclave test: (a, b) as-deposited $ZrSi_2$ coating (ZrSi#1) at low and high magnifications, (c, d) pre-oxidized $ZrSi_2$ coating (ZrSi#2) at low and high magnifications, and (e, f) pre-oxidized double-layered coating (ZrSi#4) with magnification.

Cross-sectional SEM images of bare Zirc-4 and zirconium-silicide coatings corroded for 72 hours in autoclave are shown in Figure 97. Oxide layer developed on bare Zirc-4 has a thickness of approximately 1.6 μm, and this is consistent with other experimental data for zirconium-alloys after steam corrosion test

at 415 °C and 10.5 MPa for 3 days [127,128]. All zirconium-silicide coatings reacted with steam and produced the thick Zr-rich oxide layer with depletion of silicon species. The oxide scale for the pre-oxidized $ZrSi_2$ coatings (ZrSi#2) was so weak that the Si-depletion layer was damaged and removed during sample preparation for the SEM imaging. Therefore, it is not shown in Figure 97c. The images reveal that the $ZrSi_2$ coatings (ZrSi#1 and ZrSi#2) prevented oxide formation at the Zirc-4 interface. After the autoclave test, thickness of the uncorroded coating for ZrSi#2 is thicker than that of ZrSi#1. It is speculated that the thin oxide layer formed at 700 °C air is beneficial to mitigating the kinetics of the reaction between $ZrSi_2$ and steam. The amorphous-nanocrystalline phase of the oxide scale might act as a diffusion barrier even if the oxide layer containing SiO_2 is removed by dissolution or volatilization in the steam environment. Moreover, the remaining $ZrSi_2$ coating in ZrSi#2 after the test is confirmed in EDS elemental mapping as shown in Figure 98. Small portion of the coating (approximately 0.6 μm) disappeared during the steam corrosion (and a lesser degree during sample preparation) but the rest of the coating was intact, as indicated by a pronounced silicon signal in absence of oxygen in the EDS map. However, the double-layered coatings (ZrSi#3 and ZiSi#4) were fully oxidized and even a thin oxide scale on Zirc-4 substrate was identified. It appears that there was no positive contribution of the Zr_2Si coating to corrosion resistance. Furthermore, the Zr_2Si coating might accelerate corrosion of the underneath $ZrSi_2$ layer because of evolution of micro-cracks, resulting in oxidation of Zirc-4 substrate. The detrimental effect could be associated with the conical microstructures in Zr_2Si and thermal expansion mismatch in the compositional interface.

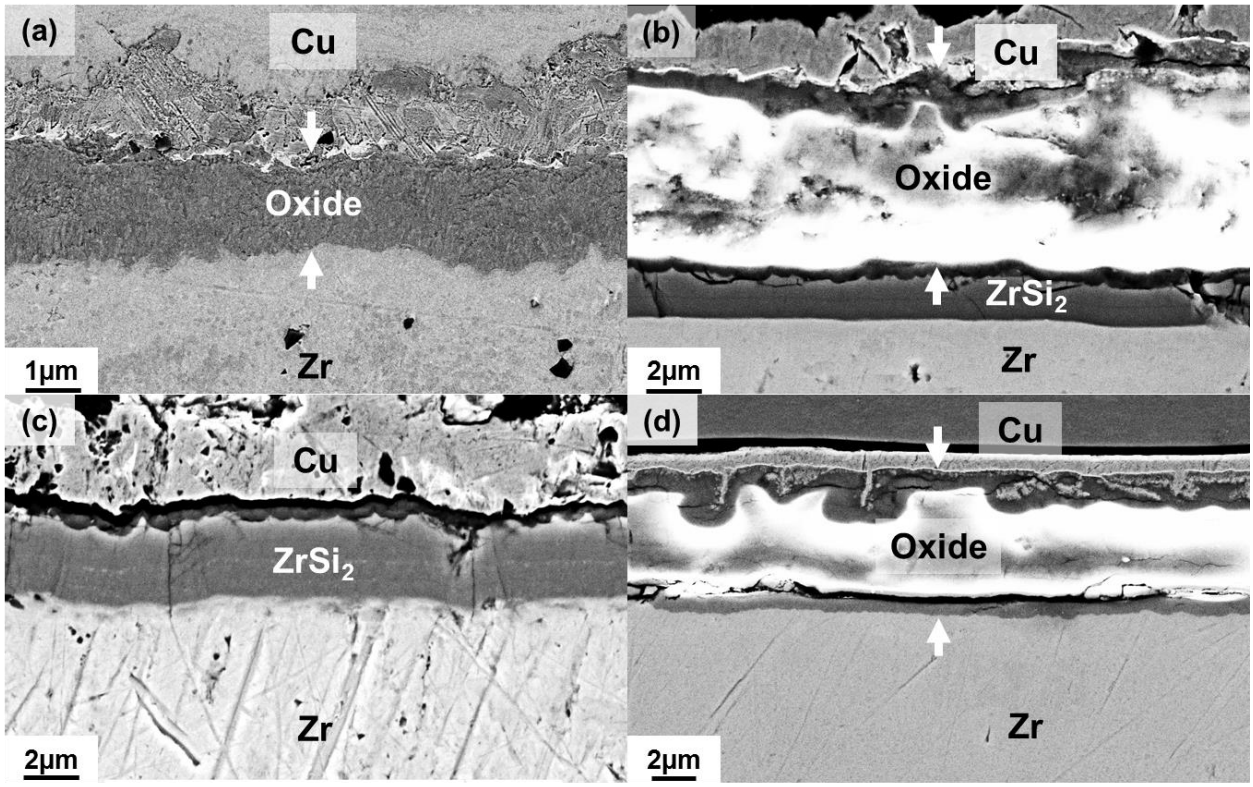

Figure 97: SEM cross-sectional images of (a) bare Zirc-4, (b) as-deposited $ZrSi_2$ (ZrSi#1), (c) pre-oxidized $ZrSi_2$ at 700 °C (ZrSi#2), and (d) pre-oxidized double-layered coating (ZrSi#4) after the steam corrosion test. Cu plating was performed on the corroded surfaces as a surface protection. The white arrows indicate the oxide scales.

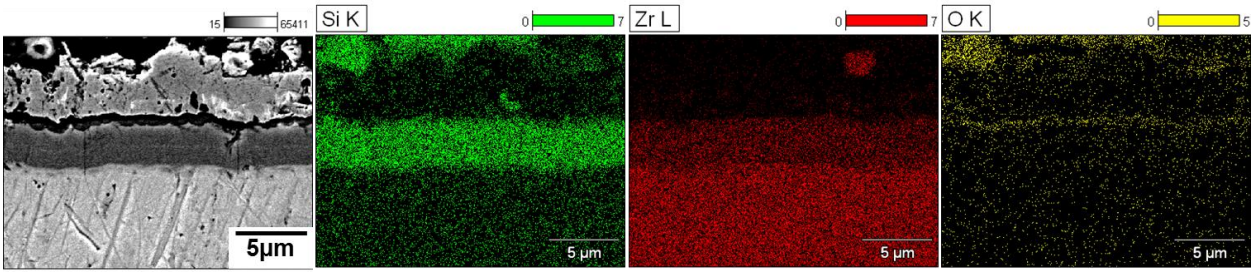

Figure 98: EDS spectra mapping of the pre-oxidized $ZrSi_2$ at 700 °C (ZrSi#2) after the steam corrosion test, showing unreacted $ZrSi_2$ coating on Zirc-4 substrate.

Table 10 provides a summary of performance of the zirconium-silicide coatings under the high temperature steam conditions. It is evident that $ZrSi_2$ coating with the pre-oxidation (700 °C air for 5 hours) provides the best corrosion resistance for Zirc-4 substrate among the Zr-Si coatings.

Table 10: Summary of corrosion of the zirconium-silicide coatings under 400 °C and 10.3 MPa steam for 72 hours.

Coating ID	Composition [thickness]	Remained Coating (µm)	Substrate Oxidation (µm)
Zirc-4	Zirconium alloy	N/A	1.6 – 2.2
ZrSi#1	$ZrSi_2$ [3.9 µm]	1.4 – 1.6	None
ZrSi#2	$ZrSi_2$ [3.9 µm]	2.9 – 3.3	None
ZrSi#3	Zr_2Si - $ZrSi_2$ [6 µm]	Fully reacted	0.5 – 0.7
ZrSi#4	Zr_2Si - $ZrSi_2$ [6 µm]	Fully reacted	0.3 – 0.8

Steam Corrosion of $ZrSiO_4$ Coating

Surface morphology of zircon formed $ZrSi_2$ coating (ZrSi#5) after the steam corrosion test is presented in Figure 99. The low magnification image (Figure 99c) show cracks and partial delamination of the surface scale. However, very importantly the EDS result shows that chemical composition of the surface was not altered by the steam corrosion tests. This indicates that the Si in zircon is greatly immobilized during the corrosion process. The high magnification images display that the grain boundaries of zircon phases (Figure 99b) was mainly attacked by water vapor so that the surface etching was localized around the grain boundaries (Figure 99d). The preferential attack is consistent with the SEM image of corroded bulk $ZrSi_2$ discussed in section 4.1.2. The corrosion process led to steam infiltration through the boundaries and corrosion of SiO_2 underneath, leading to delamination of zircon grains, however the zircon grains themselves remained resistant to corrosion. It is known that grain boundaries are prone to be attacked due to less stable atomic bonding or accumulation and segregation of impurities [129]. To mitigate the degradation of the zircon layer under steam corrosion, formation of denser and continuous zircon layer is desirable. In future study, optimization of the zircon formation on SiC will be performed by adjusting heat treatment parameters (heating profile and oxygen partial pressure) and composition of zirconium-silicide coatings. For example, Gao et al. reported that better quality and thicker of zircon layer by oxidation of ZrB_2 and SiC composite at 1400 °C under a low oxygen partial pressure (PO_2 = 200 Pa) than ambient air condition [130].

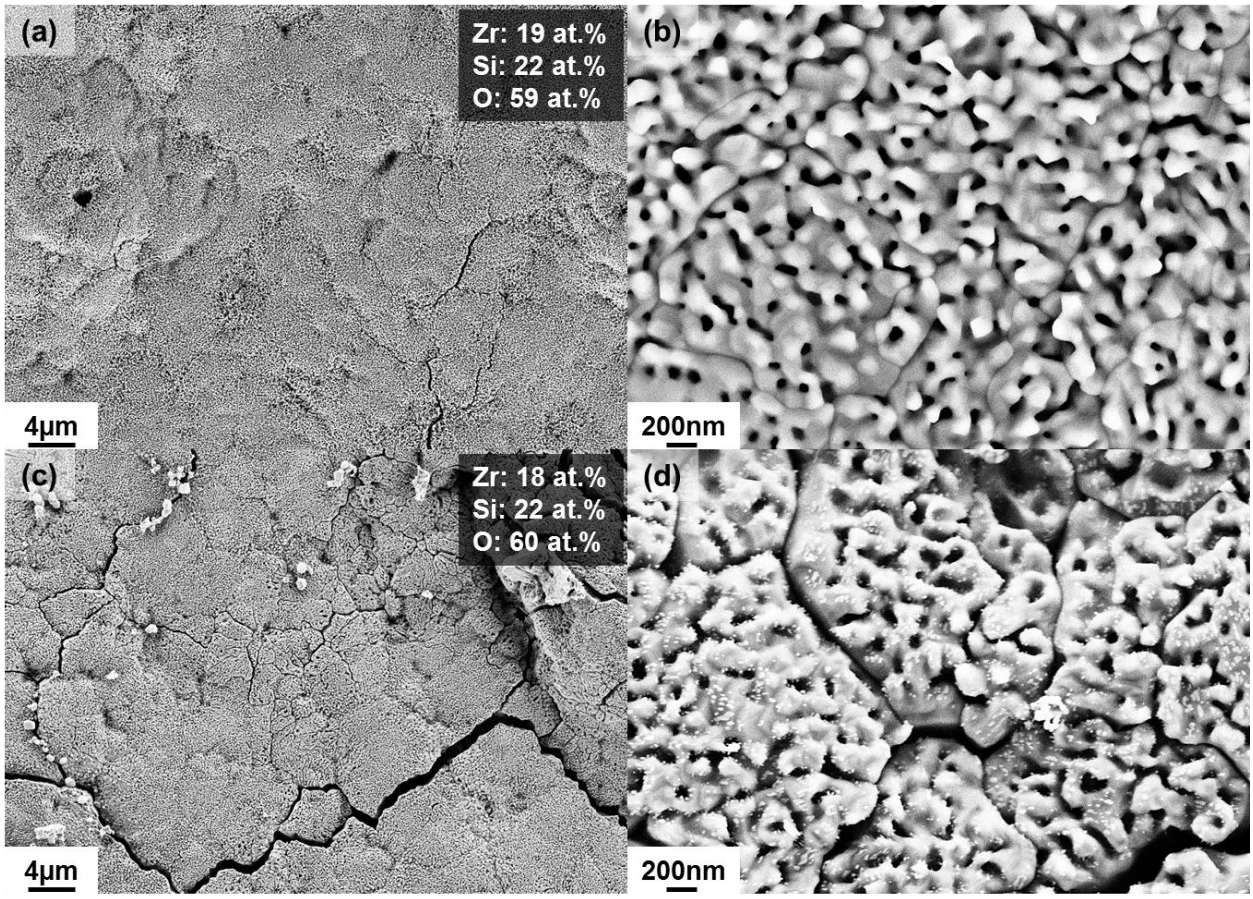

Figure 99: Plan-view SEM images of (a-b) as-prepared zircon surface (ZrSi#5) on SiC with magnification, and (c-d) the zircon surface (ZrSi#5) after the steam corrosion test.

4.3. Investigation of spray deposition coating

In addition to the magnetron sputter deposition technique, spraying coating technologies (cold spray and thermal spray) were investigated to make the coating thicker and to increase deposition efficiency. The spray depositions propel powders of coating material at high velocity to target substrate to form a coating. In general, the spray deposition processes are performed in ambient environments and high deposition rates and efficiencies making them and conducive to industrial scale-up for various applications. In this section, preliminary results of $ZrSi_2$ coating on Zirc-4 substrate using cold spray and thermal spray techniques were demonstrated, and the feasibility of these technologies is discussed.

4.3.1. Cold spray

In the cold spray process, solid powder particles of the coating material are accelerated at supersonic velocity (i.e., 2 to 3 Mach) on to the surface of the substrate using pressurized inert gas and a nozzle system. The solid particles experience severe plastic deformation during impact and deposit on the surface. Flat Zirc-4 substrate samples were polished with 320 grit SiC abrasive paper and cleaned prior to the cold spray of $ZrSi_2$ powder. Pressurized nitrogen at 3.5 MPa was utilized as a carrier gas. Parameters of cold spray process were investigated to optimize coating quality, which were gas pre-heat temperature (e.g., 600 °C, 700 °C, and 800 °C), powder size, and the number of spray passes.

The commercial $ZrSi_2$ powders produced by oxide reduction and mechanical milling were procured from SCI Engineering Materials. As shown in Figure 100a, the as-received powders have irregular shape and a wide size distribution with average size at 20 μm in diameter. EDS analysis and XRD pattern of the powders showed that the major composition of the powder was $ZrSi_2$ while Si existed as an impurity. Figure 100b shows $ZrSi_2$ particles on Zirc-4 after a preliminary cold spray run. As a ceramic, the powder has a higher hardness (850 HV) compared to Zirc-4 substrate (190 HV). Therefore, deformation and compaction effect were not observed due to a lack of significant plastic deformation of the particles. Figure 101 shows the X-ray diffraction patterns for the as-received powder and the cold sprayed coating. The diffraction peaks for the powder and the coating were identical except for the zirconium peaks from the Zirc-4 substrate in the coating. Since the cold spray process was performed in ambient air, any oxidation and phase transformation of the feedstock powder during the deposition process did not occur.

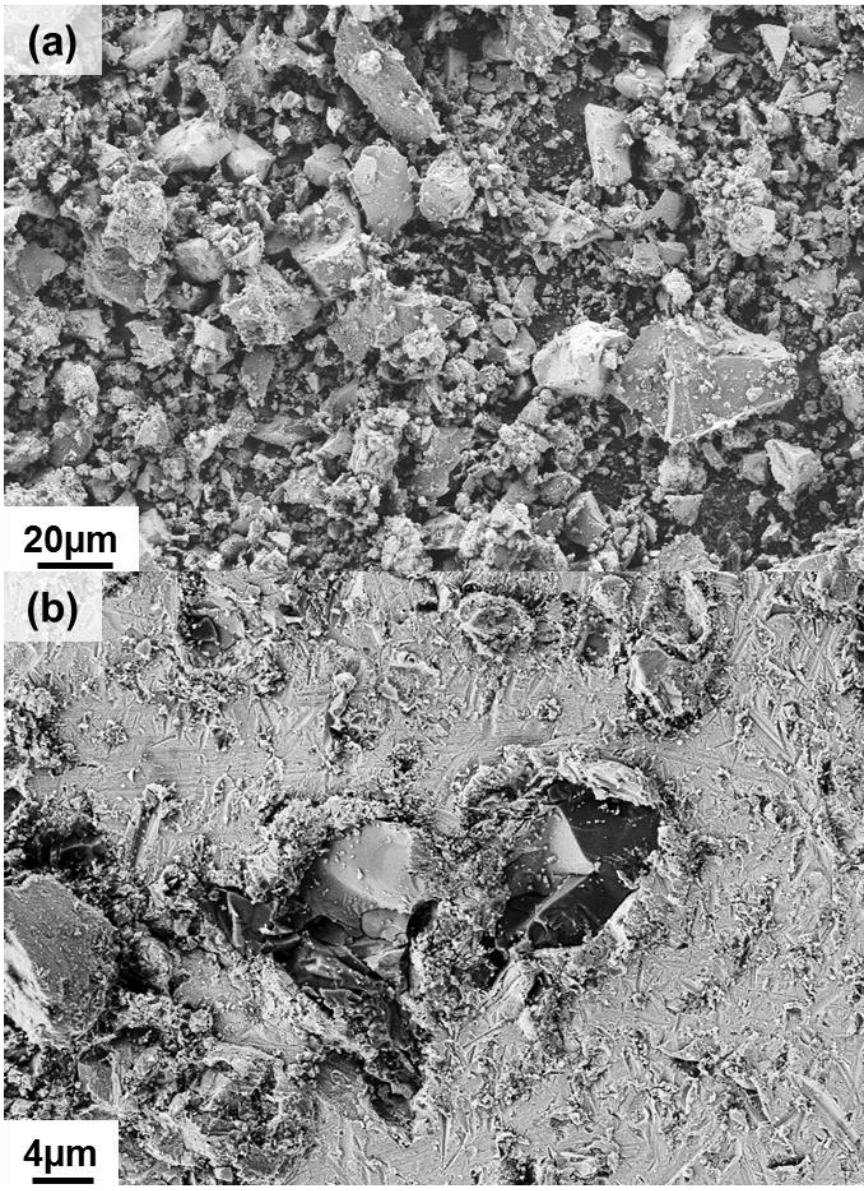

Figure 100: SEM plan-view images of (a) as-received $ZrSi_2$ powder and (b) a local area of $ZrSi_2$ cold-sprayed coating on Zirc-4 surface.

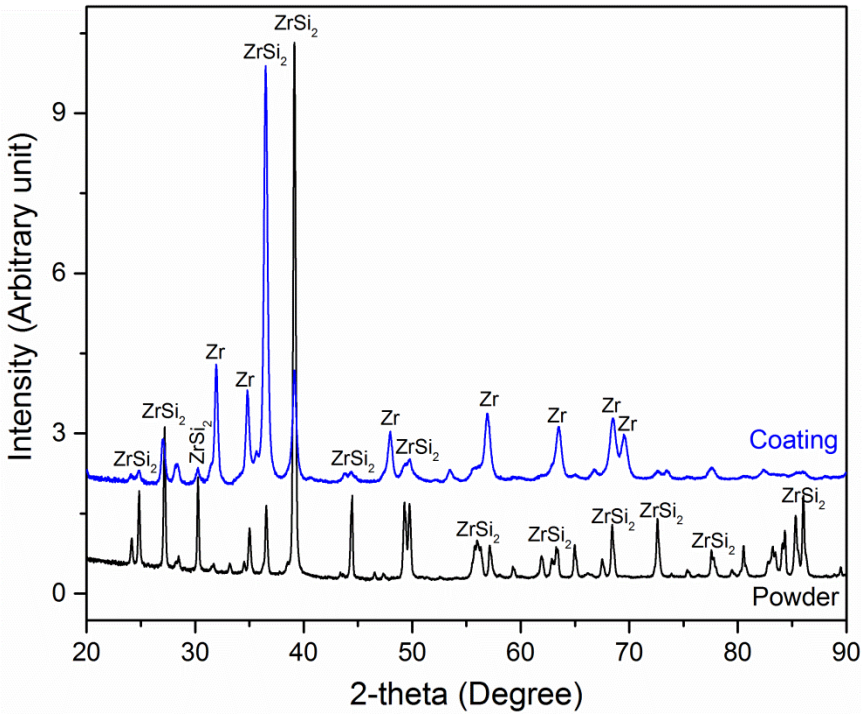

Figure 101: X-ray diffraction patterns for as-received $ZrSi_2$ powders and (b) $ZrSi_2$ coating deposited by cold spray process.

Effect of Gas Preheat Temperature

The $ZrSi_2$ powders were sprayed using N_2 gas at 3.5 MPa with gas pre-heat temperatures of 600 °C, 700 °C, and 800 °C. Generally, higher gas pre-heat temperature provides increase in carrier gas velocity, resulting in dense coating. However, the cross-sectional images for the three coating parameters (Figure 102) revealed similar thickness of coatings in the range of 5 to 10 μm. The significant roughness in the interface between the substrate and the coating suggests that erosion of the substrate occurred during the spraying process. The lowest gas pre-heat of 600°C had the least erosion, but overall none of the conditions produced a good quality coating.

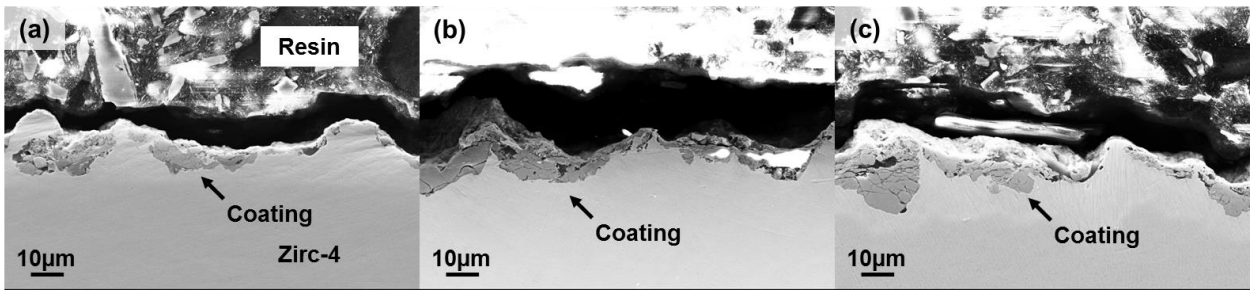

Figure 102: Cross-sectional SEM images of cold spray coatings of $ZrSi_2$ deposited at (a) 600 °C, (b) 700 °C, and (c) 800 °C gas preheat temperatures. Single-pass deposition was used in the spraying process.

Effect of Powder Size

To minimize the substrate erosion, the as-received $ZrSi_2$ powder was ball-milled using a silicon-nitride vial ball miller for 1 hour and sieved to narrow down the particle size below 25 μm in diameter. As compared to the as-received powder, size of the ball milled powder was distinctively decreased. The effect of the powder size on surface morphology of the coatings and deposition efficiency are shown in the plan-view and cross-sectional SEM images as shown in Figure 103 and Figure 104. Surface roughness was decreased by spraying the smaller particles so that less substrate erosion was expected. However, the cold spray coatings of the ball-milled powders with various the carrier gas velocities showed substrate erosion and only a thin coating on local areas. Thus while smaller particle sizes led to less roughness, high enough deposition efficiencies was not achieved by using the smaller powders.

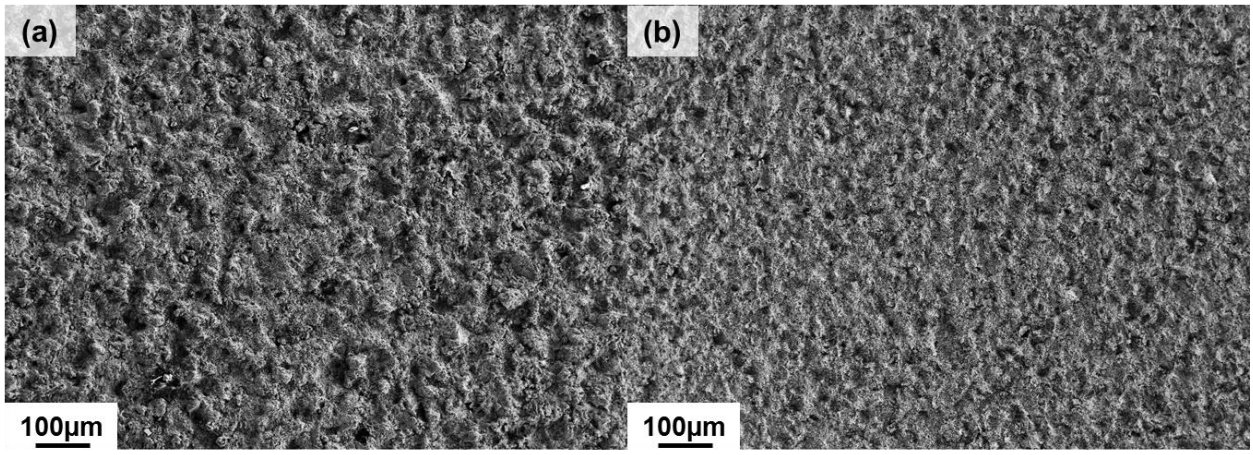

Figure 103: SEM plan-view images of (a) $ZrSi_2$ cold sprayed surface using the as-received powder and (b) the sprayed surface using the ball-milled powder. Two-pass deposition was performed in the both cases.

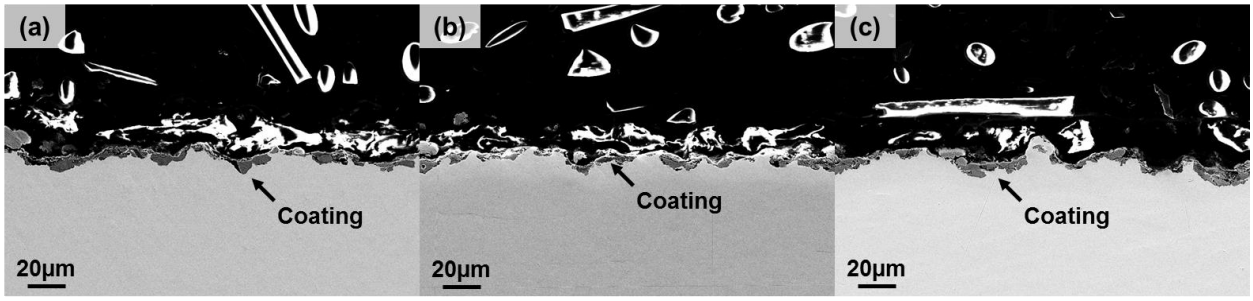

Figure 104: SEM cross-sectional images of $ZrSi_2$ cold sprayed coating with the ball-milled power at (a) 600 °C, (b) 700 °C, and (c) 800 °C gas pre-heat temperatures. Single-pass deposition was used in the spraying process.

Effect of the Number of Spray Passes

It was postulated that a high flow rate of the $ZrSi_2$ particles was beneficial to efficiency of the cold spray deposition. Multiple spraying passes (up to four passes) on the substrate were performed at 700 °C gas preheat to increase coating coverage and thickness. However, substrate erosion was still dominant as shown in Figure 105. Again, the mechanical properties of $ZrSi_2$ limit deposition of the powders on Zirc-4 substrate via cold spray technology, at least with the parameters investigated in this study. Therefore, thermal spray deposition which involves melting of the powder particles before spraying was investigated a method to achieve higher deposition rates and with less substrate erosion. The next section summarizes results of preliminary investigation of thermal spray coating of $ZrSi_2$ on Zirc-4 substrate.

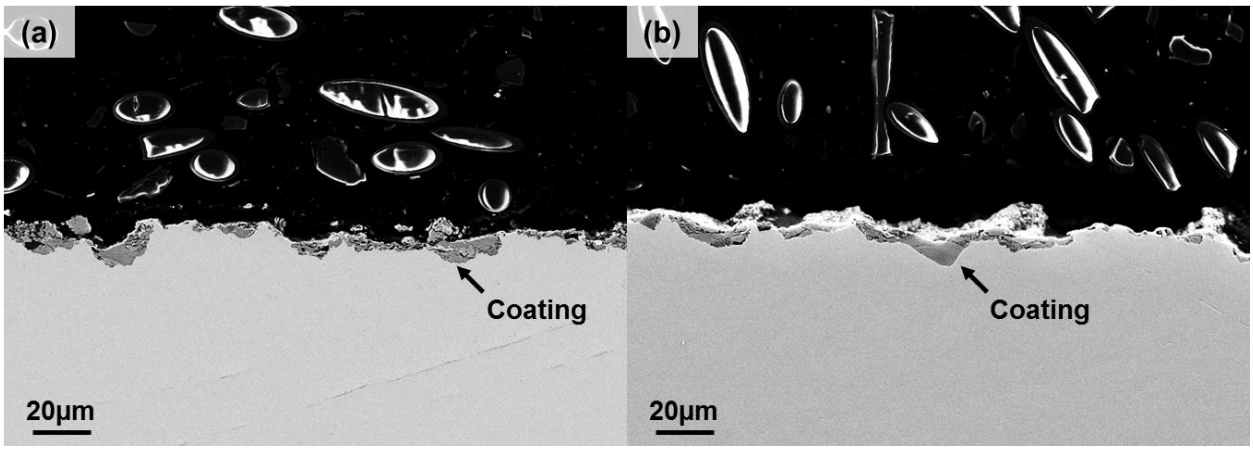

Figure 105: SEM cross-sectional images of $ZrSi_2$ cold spray coating on Zirc-4 substrate at (a) a single pass (b) four passes. The preheat gas temperature was 700 °C.

4.3.2. Thermal spray coating deposition process

In thermal spray process, the feed powders are melted using concentrated heat sources such as plasma and high temperature gas and then the molten particles are propelled on to the substrate surface. After the molten particles impact the substrate, they were cooled rapidly via heat transfer to the substrate to form a coating. The $ZrSi_2$ powders (< 44 μm in diameter) were heated up by Ar/He mixed gas plasma at atmospheric condition. The thermal spray deposition was performed for 10 passes for each sample to obtain tens of micron thickness. The particles were sprayed by changing a distance between the spraying nozzle

and the substrate. Also, the effect of surface finish of Zirc-4 substrate (i.e., grit blast) before the spraying was investigated. Figure 106 shows a micron-sized $ZrSi_2$ splat, a flat disk-shaped morphology, on the coating after the thermal spraying. Even if the original powders had irregular shapes, the high temperature plasma melted and atomized the powders so that they have the spherical shapes before the impact.

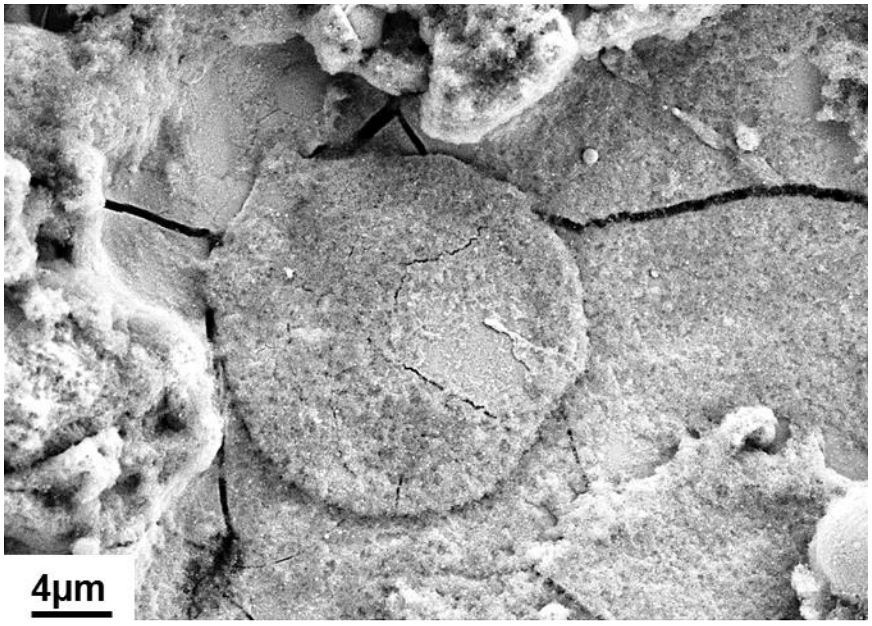

Figure 106: SEM plan-view image of a $ZrSi_2$ splat on thermal sprayed Zirc-4 substrate.

Surface morphology of as-sprayed $ZrSi_2$ coatings at different spraying distances are shown in Figure 107. The coatings were successively formed on the Zirc-4 surface and the top surfaces were significantly rougher than the bare surface. Microcracks and pores can also be seen in these images. However, delamination or spallation of the coatings were not observed. The coating surface with the largest spray distance (i.e., 12.7 cm) appears smoother and flatter than that of the shortest distance (i.e., 7.6 cm). Moreover, the spherical particles were frequently observed on the surface with the shortest distance. The short interaction time of the $ZiSi_2$ particles and the high temperature plasma (the time for spray powders stay in the plasma flume) could not fully melt the particle. Therefore, some particles may have rebounded or just remained on the top surface in the form of the spherical shapes instead of deposition, leading to a decrease in deposition efficiency.

The cross-sectional SEM images display the microstructures of the thermal sprayed coatings as shown in Figure 108. The coating deposited at longer spraying distance were thicker. The 12.7 cm distance parameters produced coating in the range of 50 to 63 µm in thickness but the 7.6 cm spray distance resulted in coating thickness of 40 to 47 µm. It is believed that the powder melting ratio increases with increasing the spray distance to some extent, leading to spreading out of the molten particles when they impact on the surface. Coating defects such as microcracks and pores were identified, which would be detrimental to the oxidation resistance of the coatings. Moreover, the cross-sectional images reveal the contrast difference in the coatings, indicating that the melting and solidification let to thermodynamically dictated segregation of phases in the coatings. It appears that the darker phase represents Si-rich zirconium-silicide and the light phase is made up of Zr-rich zirconium-silicide as would be predicted by the Zr-Si phase diagram.

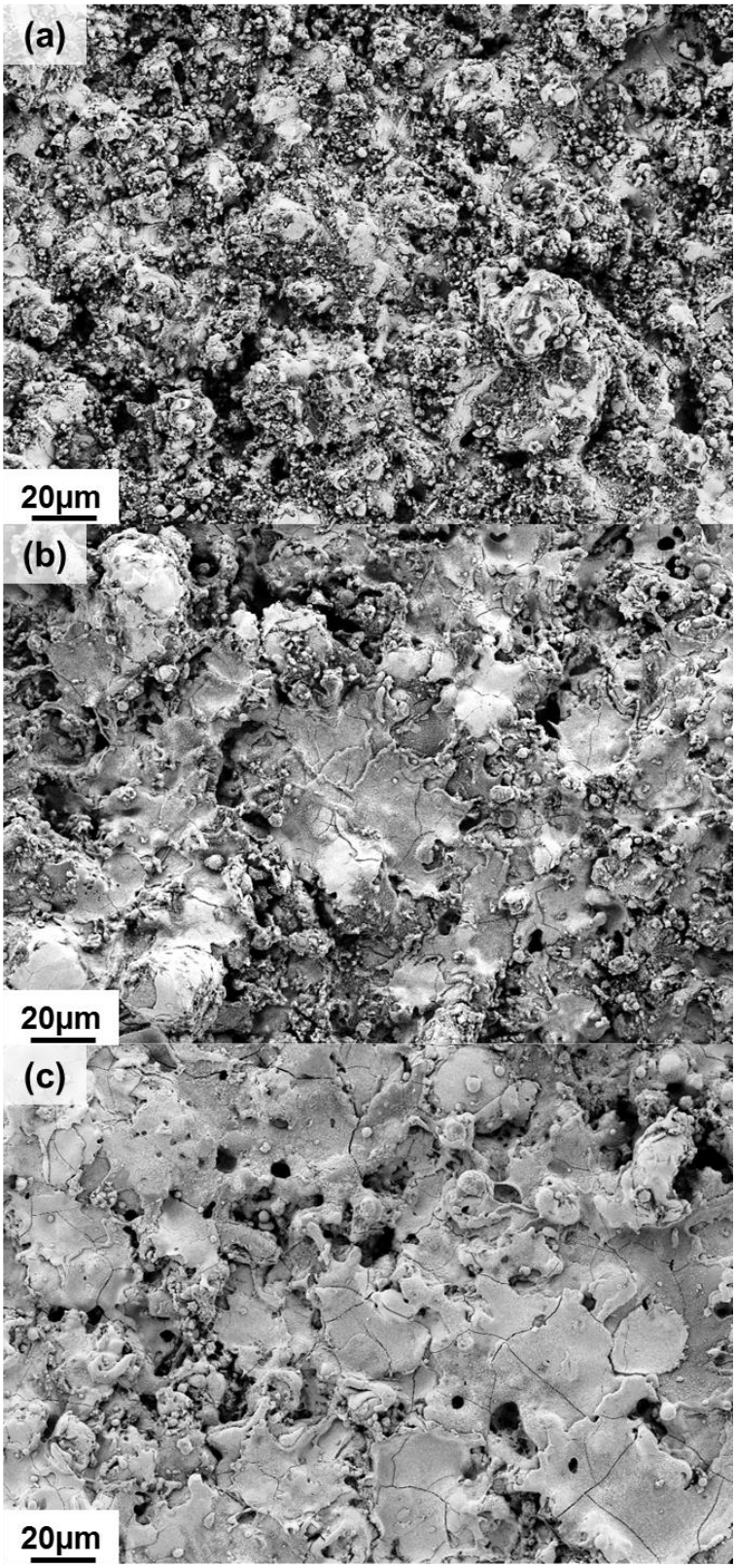

Figure 107: Surface morphologies of the $ZrSi_2$ coatings at different spray distance. (a) 7.6 cm, (b) 10.2 cm, and (c) 12.7 cm.

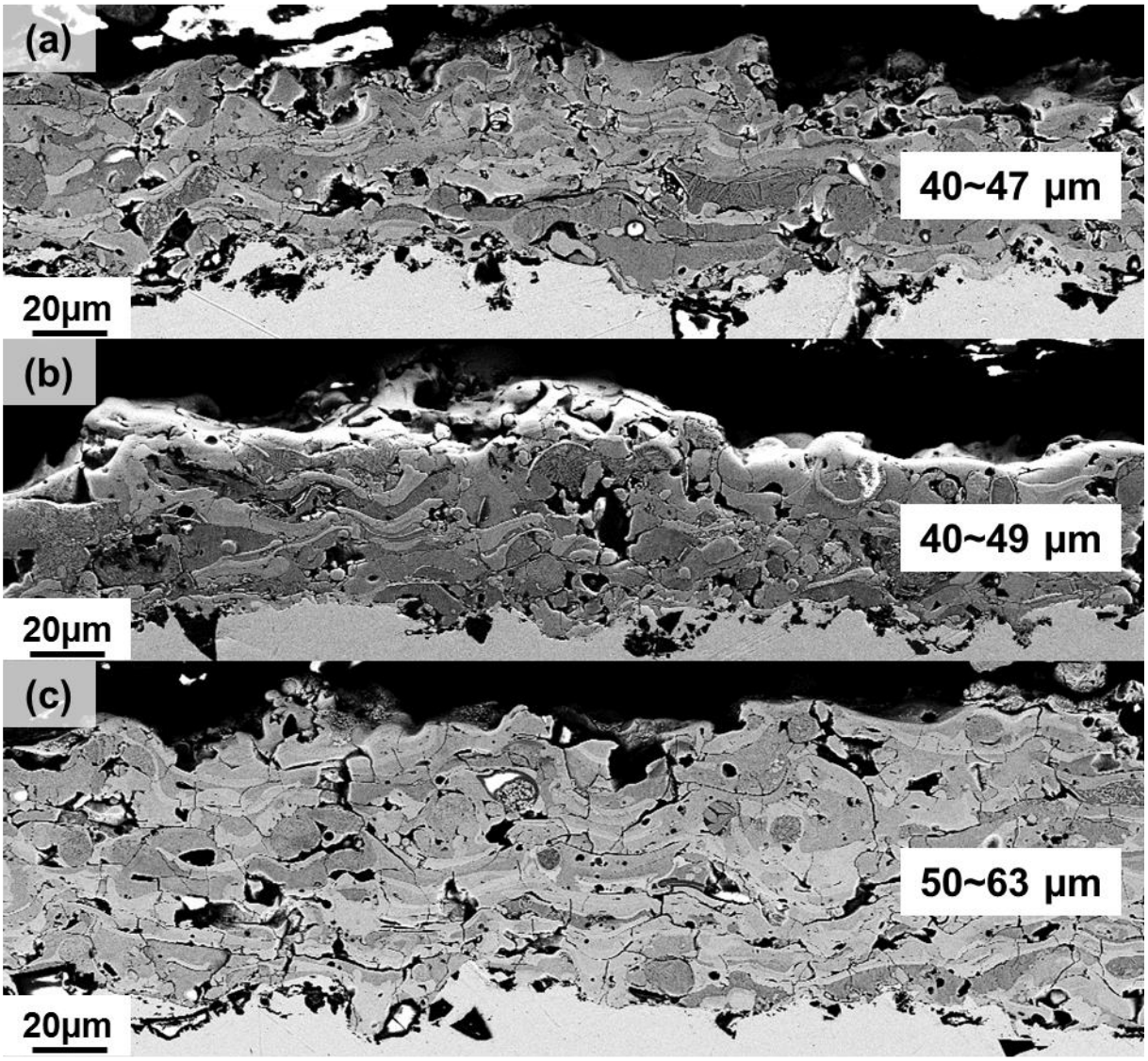

Figure 108: SEM image of cross-section of the $ZrSi_2$ coatings at different spraying distance. (a) 7.6 cm, (b) 10.2 cm, and (c) 12.7 cm.

Figure 109 shows surface X-ray diffraction patterns of the thermal sprayed coatings for different spray distances and confirms the phase separation in $ZrSi_2$ powders during the spraying process. The major phases in the coatings were intermetallic compounds of zirconium-silicides ($ZrSi_2$, ZrSi, Zr_5Si_3) and ZrO_2. The feedstock $ZrSi_2$ powder undergoes phase changes during the spraying. There was no significant effect of spraying distance on the phases of the thermal sprayed coatings. High magnification of SEM image for the thermal sprayed coating (Figure 110a) displays complex microstructures consisting of $ZrSi_2$, ZrSi, and Si based on results of EDS analysis, which are in good agreement with the XRD peaks. To investigate

formation of the multiple phases in the thermal sprayed coating, bulk $ZrSi_2$ was melted using Ar arc melter and cooled quickly in ambient air. The cross-sectional image (Figure 110b) of the solidified bulk $ZrSi_2$ displays the complex phases as well, which supports the observations made for the thermal sprayed zirconium-silicide coatings. Therefore, it was concluded that even the high cooling rate of the deposited molten $ZrSi_2$ particles is not sufficient to prevent phase decomposition. As shown in the Zr-Si phase diagram (Figure 110c), ZrSi phase first precipitates from the melt and then $ZrSi_2$ and Si solidified due to the different melting points (e.g., 1626 °C for $ZrSi_2$ and 2203 °C for ZrSi).

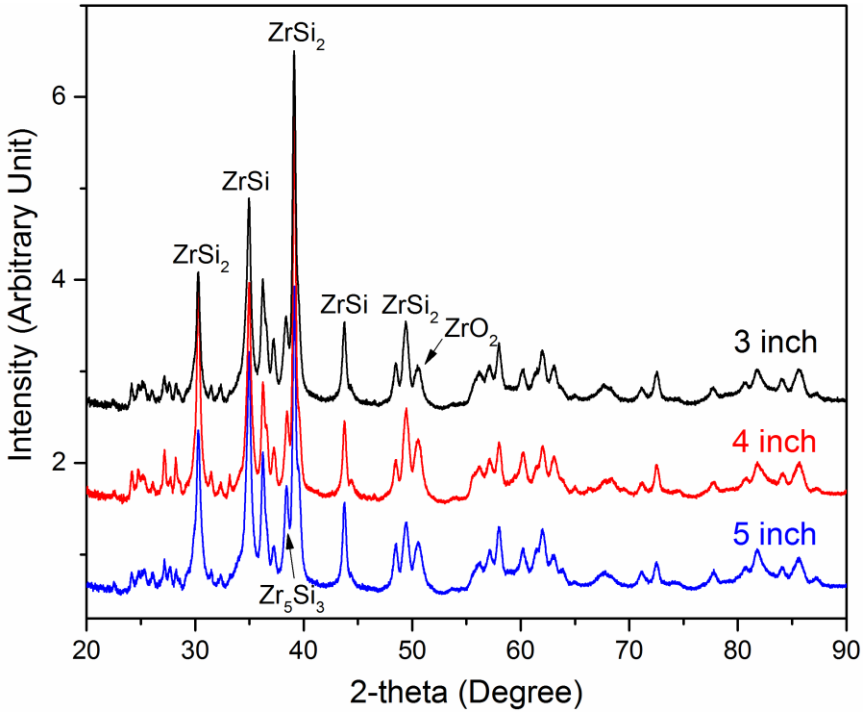

Figure 109: XRD patterns of the $ZrSi_2$ thermal spray coatings prepared using various spraying distances.

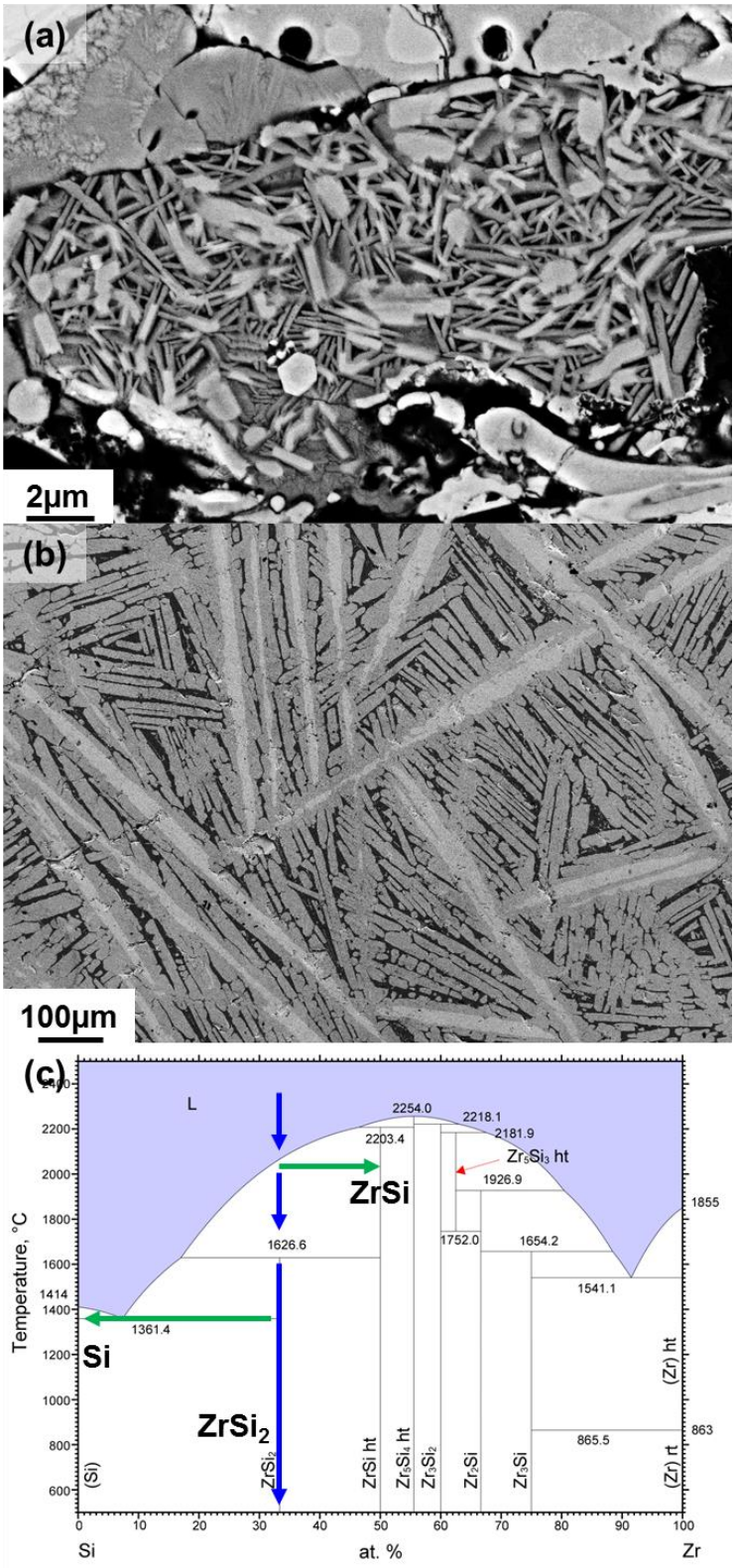

Figure 110: SEM cross-sectional image of (a) local area of the thermal sprayed $ZrSi_2$ coating, (b) arc-melted bulk $ZrSi_2$, and (c) Zr-Si binary phase diagram [120] indicating cooling path and possible phase formation.

Effect of Substrate Surface Grit Blasting on Thermal Spray Coating

Effects of the grit blast process were demonstrated by performing thermal spray for Zirc-4 surface without grit blast process. While the previous thermal spray runs were performed after grit blasting, thermal spray coatings were also investigated after finishing the surface with only320 grit SiC abrasive paper. The cross-sectional image of the coating (Figure 111) displayed spallation of coating due to the weaker adhesion between the coating and the substrate. Mechanical interlocking of the coating appeared to be improved by the roughened surface, resulting in strong adhesion.

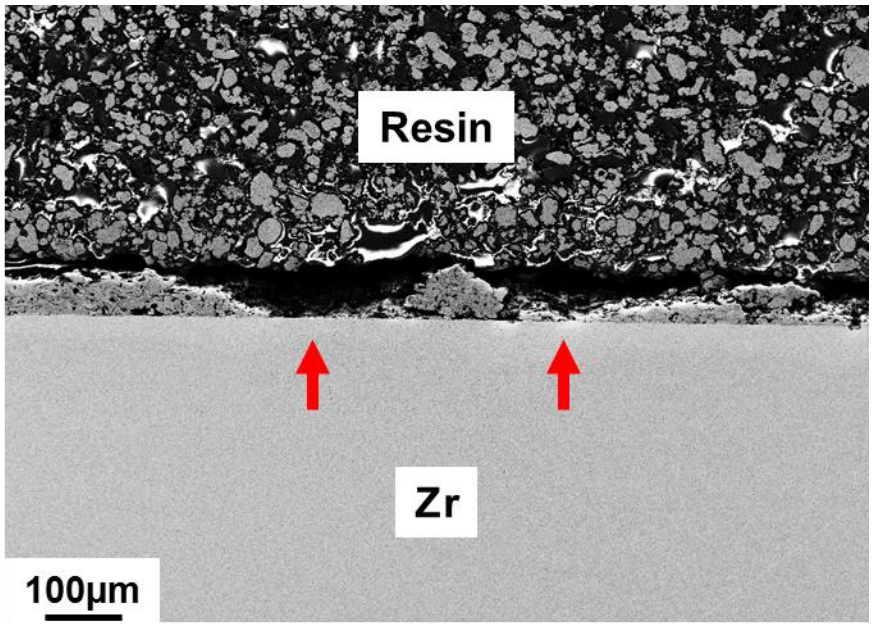

Figure 111: Cross-sectional image of thermal spray coating of $ZrSi_2$ without grit blast of Zirc-4 substrate. The red arrows indicate the local area showing coating damages during sample preparations. Only 320 grit SiC grinding was used.

The thermal sprayed $ZrSi_2$ coating (deposited at 7.6 cm distance and 10 passes) was exposed at 700 °C air for 10 hours to evaluate its oxidation behavior. After the oxidation, the coating was delaminated and surface oxidation of Zirc-4 substrate was observed as shown in Figure 112. It is speculated that oxygen infiltrated through the cracks and pores in the as-deposited coating and reacted with the substrate. The substrate oxidation resulted in the delamination of the coating. Thermal spray technique is efficient method to deposit $ZrSi_2$ but further optimization process is required to make the coatings thicker and more homogeneous and dense to realize the full benefits of the coating.

Figure 112: Photograph of oxidized thermal spraying ($ZrSi_2$ coating) at 700 °C air for 10 hours. Coating delamination was clearly identified.

4.4. Quenching experiment for bare Zircaloy-4

The quench test facility was designed and built successfully. The heating zone has the capability of increasing the temperature of the test sample up to 720 °C, and the limiting factor is the maximum allowable temperature of the heating tape wrapped around the 316-stainless-steel pipe. The pressure rating for the quench chamber is 2 MPa, limited by the borosilicate windows for visualization and the wall thickness of the tee-pipe. However, to allow for a safety margin, test sections were not heated above 700 °C prior to insertion into the water pool and the system pressure in the actual experiment was limited to 1 MPa. During scoping tests to check performance of the facility, the heating zone was maintained at 700 °C for 30 minutes at 1 MPa via the compressed Ar gas. No significant Teflon seal degradation was observed after the scoping test. This is because the 316-stainless steel seal housing was designed to be much cooler (~150 °C) than the heating zone. Moreover, the system pressure could be controlled by the inlet regulator and the backpressure regulator without gas leakage.

4.4.1. Reference condition (saturated water in atmospheric pressure)

Reliability Tests

An initial set of tests used bare zircaloy-4 rodlet test sections, quenched in saturated water at atmospheric conditions, all at nearly identical conditions. Repeatability of the tests was confirmed with three consecutive quenching tests using the same sample. Results revealed excellent repeatable temperature-time curves (quenching or cooling curve) as shown in Figure 113a. In addition, quenching tests for three different individual samples displayed reproducibility of the cooling curves as well (Figure 113b). Based on the results of nine quenching tests and INTEMP calculations, experimental uncertainty for the minimum film boiling temperature and the minimum film boiling heat flux under saturated water was approximately 2% and 8% of an average value, respectively. The uncertainties in the quenching experiments were attributed to slight variation of water temperature and surface conditions of the samples, and a dimensional error in sample machining.

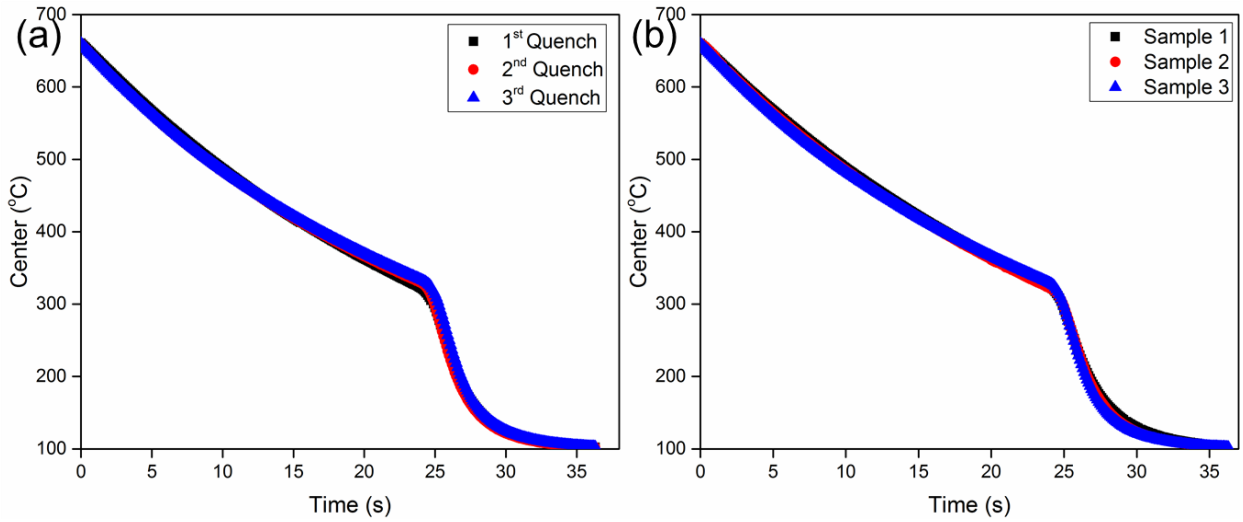

Figure 113: Quenching curves of (a) three consecutive tests for the same Zirc-4 sample and (b) three individual tests for different Zirc-4 samples. The tests were performed under saturated water in ambient pressure.

Surface Oxidation

Boiling heat transfer phenomena are strongly affected by surface/heater conditions so that characterizations of surface oxidation produced during the quenching experiments was needed. Since Zirc-4 tends to be oxidized easily in oxygen-containing environments at high temperatures, the surface color was changed from gray metallic to black after the quenching test. Experimentally, it was confirmed that the

oxidation occurred when the sample was heated up to 700 °C in the heating zone. Once the oxide layer formed during the first quenching test, the thickness did not change significantly in the following consecutive quench tests due to the protective nature of zirconium oxide; the first quenching test produced a ~3 μm thick oxide layer but the third test for the identical sample showed a ~3.6 μm thick oxide layer on the bare Zirc-4 surface. The quenching curves like Figure 113 were converted to boiling curves by solving the inverse heat conduction problem, and the thin oxide layer on the surface might affect the results. Using the measured temperature-time data at the center of the sample, estimated surface temperatures with a thick ZrO_2 layer (50 μm) on the surface were compared to those without an oxide layer. Thermal properties for ZrO_2 was assumed in the calculation as shown in Table 11:

Table 11: Thermal conductivity, density, and heat capacity of ZrO_2.

Thermal property	Value
Thermal conductivity (W/m·K)	k=2.00 [131]
Density (kg/m^3)	ρ=5680 (273 K) [132]
Heat capacity (J/kg·K)	C_p=455 (273 K) [133]

As shown in Figure 114, the difference of surface temperature, determined using the same temperature-time data, between the non-oxidized and heavily oxidized conditions appear to be negligible. Therefore, INTEMP calculations for any Zirc-4 specimen were performed under the non-oxidation assumption for simplicity of the calculation. The detailed analysis for surface properties of bare Zirc-4 and modified surfaces such as oxide layer thickness, surface morphology, roughness, and wettability will be discussed in later chapters.

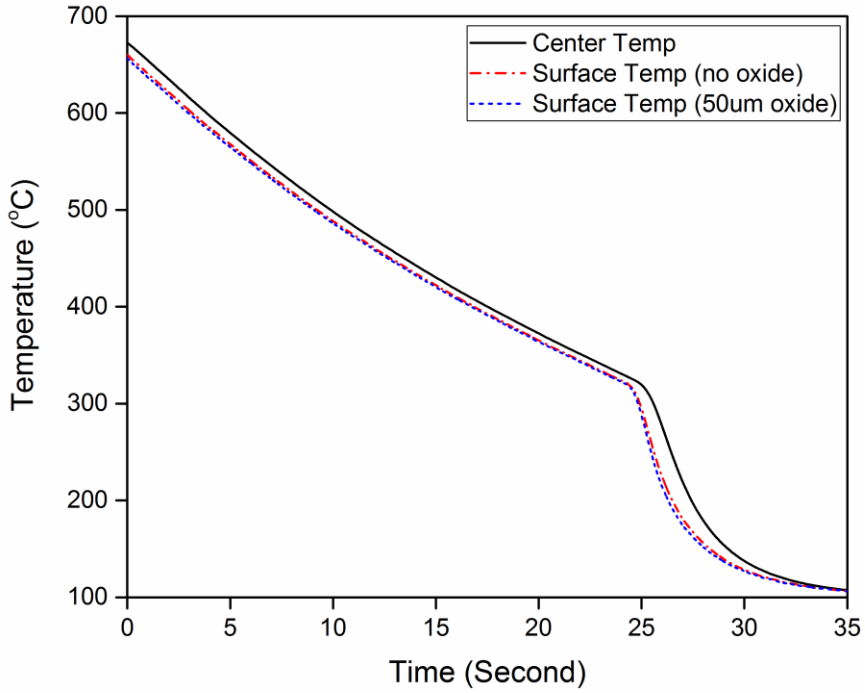

Figure 114: Measured temperature at the center of bare Zirc-4 sample and estimated surface temperatures by INTEMP with two assumptions (non-oxidized and 50 µm oxide on the surface).

Boiling Regime

As shown in Figure 113, the typical quenching curve introduces the general changes in pool boiling heat transfer regimes over time: stable film boiling, transition boiling, nucleation boiling, and natural convection. The corresponding boiling curve, estimated using INTEMP software, was shown in Figure 115. The temperature gradually decreases over time in the initial stage of quenching because the surface heat flux monotonically decreases as the surface superheat decreases, where the stable film layer covers the entire hot surface. The high-speed images in Figure 116 displays the hot specimen in saturated water insulated by a thin vapor layer. As surface temperature decreases, the vapor film gets thinner, and the vapor layer becomes unstable. The point at which the transition from stable film boiling to transition boiling occurs is referred to as a lower limit to film boiling or minimum film boiling point, showing a sudden temperature drop (an inflection point) in a quenching curve. The surface heat flux in the boiling curve starts to increase rapidly due to enhanced heat transfer coefficient. For instance, as shown in Figure 115, surface heat flux at the end of stable film boiling (at 221 °C superheat) was 48 kW/m^2 but was 319 kW/m^{2}at

transition boiling (at 150 °C superheat). This transition at local areas takes place in a short time (e.g., the transition needs only 1.3 seconds from lowest heat flux to the highest heat flux in Figure 115) with rapid and frequent liquid contacts on dry regions. The vapor film destabilizes at the bottom of the cylindrical specimen and a wetting front propagates toward the top of the specimen as shown in Figure 116b and Figure 116c. Vigorous bubble nucleation and growth occurs on the surface in which the stable vapor disappears, which is called nucleate boiling regime (Figure 116d). Finally, the natural convection regime is reached at the end of the quenching process. In short, the quenching experiment for bare Zirc-4 samples in saturated water at atmospheric pressure revealed the general boiling heat transfer phenomena.

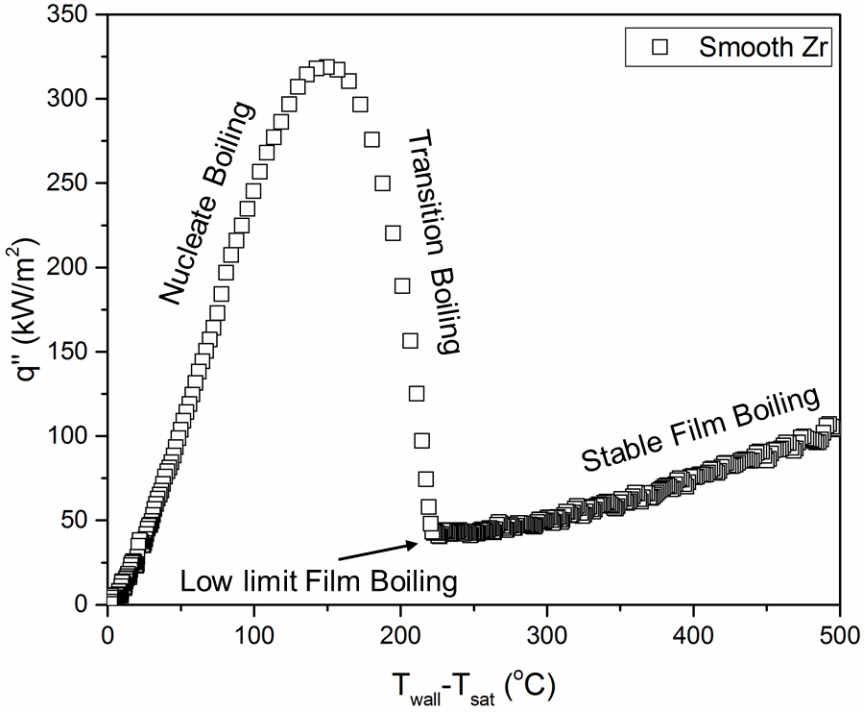

Figure 115: Typical boiling curve of bare Zirc-4 specimen during quenching at saturated water in ambient pressure, estimated by using INTEMP.

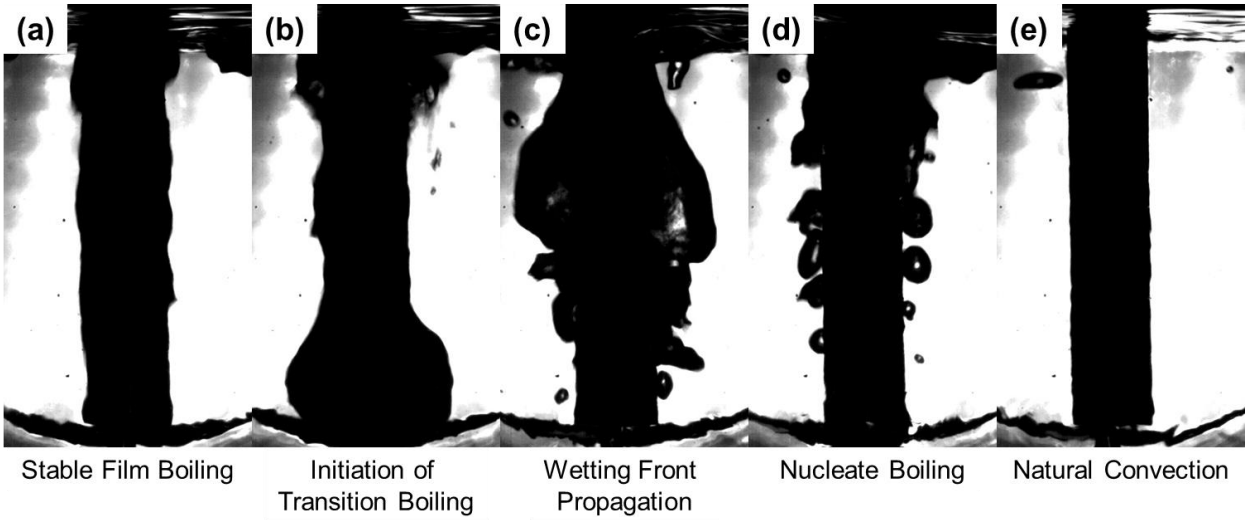

Figure 116: High speed images (100 fps) of bare Zirc-4 specimen during quenching at saturated water in ambient pressure, showing transition of boiling regime over time.

Vapor Layer Thickness

As mentioned in the previous chapter, the thickness of the vapor layer in the high-speed images recorded during the quenching tests was estimated via image processing and associated data analysis with the Matlab code. Figure 117 shows the vapor film thickness on a bare Zirc-4 surface, the polynomial fit as a function of quenching time, and the surface temperature. Just after submerging, a thick vapor film covering the cylindrical sample was identified. A strong wavy motion of the vapor-liquid interface indicates the fluctuation of the vapor film thickness. Intermittent and a large amplitude vapor film in the stable film region correspond to violent vapor formation. The polynomial fit describes the average vapor film thickness in the stable film boiling region. As the surface superheat decreases, the wave of the vapor-liquid interface reduces and the average vapor thickness also decreases. The minimum vapor thickness was identified in the vicinity of the minimum film boiling temperature. Then, a sudden increase of the vapor film thickness arises as rapid boiling occurs. During the transition boiling, the maximum film thickness was identified. The termination point of a stable film boiling is consistent with the inflection point in surface temperature-time curves as shown in Figure 117. In the nucleation boiling regime, smaller bubbles were observed as the surface superheat decreased, and finally the hot surface was fully covered by saturated liquid water at the end of the quench process.

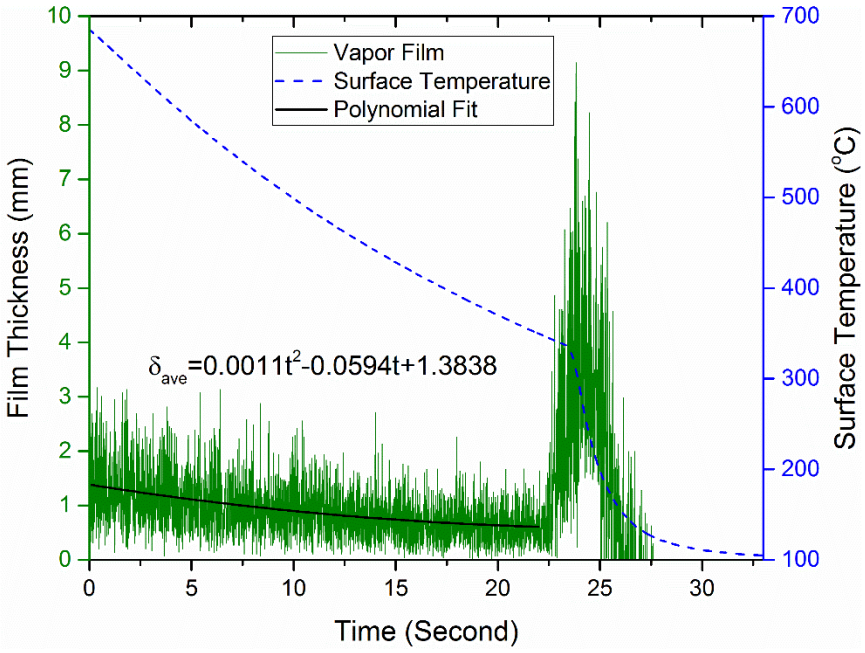

Figure 117: Film thickness (green) with polynomial fit (thick dark line) and surface temperature (blue dash) during quenching test.

Minimum Film Boiling Temperature (T_{min})

The temperature and heat flux at the lower limit of stable film boiling were determined by the boiling curve and the criterion as discussed in the previous chapter (section 3.5.3). Table 12 displays T_{min} and q''_{min} values for saturated water, which have been reported in the literature. The measured minimum film boiling temperature and minimum film boiling heat flux were 325 ± 6 °C and 45 ± 4 kW/m^2, respectively. The values were averaged by results of nine quenching experiments in saturated water at atmospheric pressure. Three individual bare Zirc-4 samples were used and each sample was quenched for three times. Berenson [79] predicted the minimum film boiling temperature with the hydrodynamic considerations with a consideration of required surface temperature to generate minimum vapor production supporting stable film layer. His model is independent of the thermal properties of surface and water subcooling. Henry [80] incorporated surface and liquid thermal properties in the Berenson's model and proposed that the collapse of stable film boiling is strongly correlated to the transient liquid-solid contacts followed by evaporation of the microlayer on the contact area. These formulations will be introduced in the next section (section 4.4.2). It is worthwhile noting that their predictions are smaller than the experimental values. One of reasons is a

difference of geometry of heating surface. These models are based on infinite horizontal surfaces but cylindrical test sections were used in the experimental investigation. The sample dimensions were specified in Table 12. Generally, the experimental values in the literatures are in good agreement with those in present study. Peterson's data have slightly higher T_{min} and $q"_{min}$ values, and it might be due to oxidation of the Zirc-4 specimen during heating up the quenching samples even if he reported that nitrogen was filled in the test facility. However, a degree of oxidation for the samples was not described in his report so the sample might have an oxide layer of unknown extent, leading to the higher measured T_{min} values.

Table 12: Summary of minimum film boiling temperature and heat flux for cylindrical samples for saturated water in ambient pressure as reported in the literature.

Material	Geometry	T_{min} (°C)	$q"_{min}$ (kW/m^2K)	Reference
-	Empirical model, infinite horizontal surface	166	17	Berenson (1961) [79]
Zircaloy-4	Empirical model, infinite horizontal surface	244	-	Henry (1974) [80]
Zircaloy-4	Cylinder (D:9.5mm, L:60mm)	371-397	62-69	Peterson (2001) [84]
Brass	Cylinder (D:20mm, L:75mm)	321	39	Bolukbasi et al. (2011) [134]
Zirconium	Cylinder (D:10mm, L:60mm)	324	56	Kang et al. (2016) [75]
Zircaloy-4	Cylinder (D:9.9mm, L:51mm)	319-331	41-49	Present study

4.4.2. Pressurized conditions

Quenching behaviors of bare Zirc-4 in saturated water were investigated in the range of 0.1 MPa to 0.7MPa system pressure using Argon cover gas. The highest pressure was determined based on the heating time required for the quenchant water to reach a saturated point at a high pressure. For example, it took more than seven hours to heat up 1.4 L water from room temperature to 163.2 °C (saturated temperature at 0.67 MPa). Even if the Kawool thermal blanket insulated the outer surface of the quenchant chamber, it was difficult to minimize the heat loss as the water temperature increased because there was heat loss through exposed parts (e.g., borosilicate windows). Similar to the quenching tests at the reference condition (i.e., saturated water at atmospheric pressure), degassing was performed for 30 minutes prior to increasing system pressure. As the saturated condition at the desired pressure was reached, it was observed that the temperature reading for the water revealed a saturated temperature and tiny bubbles began to evolve on the

inner surface of the water chamber. Finally, the test sample was heated up to 700 °C at which point the sample was inserted into the saturated water.

Quenching Curves and Boiling Curves

The quenching curves and the corresponding boiling curves with elevated pressures are shown in Figure 118. The cooling period from the initial temperature to the saturation temperatures decreased with increasing pressure, indicating that quenching performance was enhanced at high pressures. However, the effect of pressure on the cooling performance decreased as pressure increased. For instance, cooling time to reach 200 °C from the initial temperature at 0.10 MPa and at 0.17 MPa was 26.6 seconds and 17.4 seconds, respectively (ΔP= +0.07 MPa → Δt= -9.2 seconds). In contrast, the time at 0.30 MPa and at 0.39 MPa was 12.6 seconds and 10.0 seconds, respectively (ΔP= +0.09 MPa → Δt = -2.6 seconds). The corresponding quenching curves, estimated by INTEMP, confirm the trends. As system pressure increases, the stable film boiling regime shows a higher heat flux and an earlier transition (i.e., at higher surface temperature) of the boiling regime. The heat transfer enhancement in film boiling regime at high pressures may be due to bubble dynamics and thermal properties of the vapor and liquid. The measured minimum film boiling temperature will be discussed.

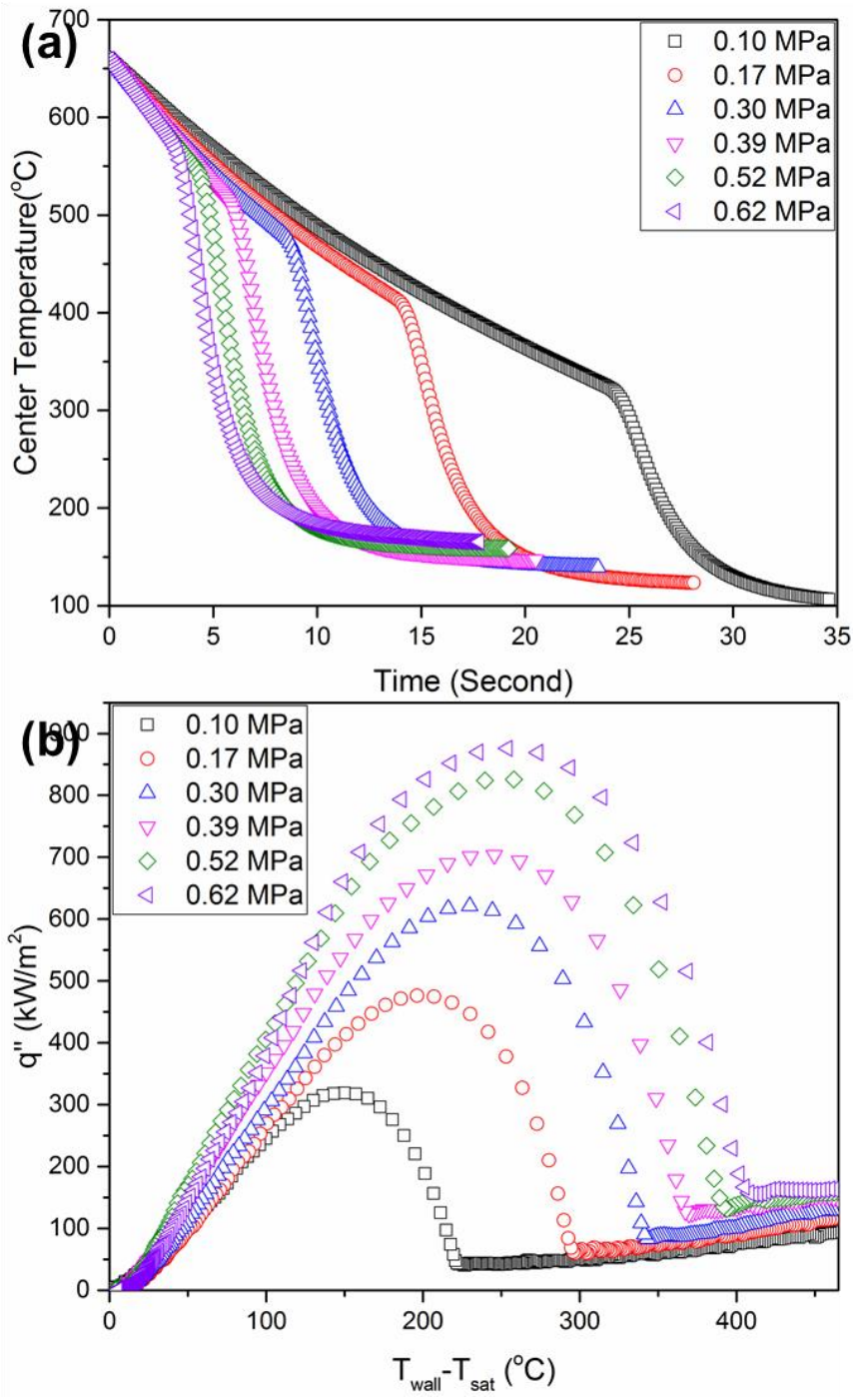

Figure 118: (a) Quenching curves (temperature-time history at the center of the sample) and corresponding boiling curves estimated by INTEMP software at elevated pressures.

Bubble Dynamics at High Pressure

High-speed images recorded bubble evolution on the sample surface at 0.33 MPa as shown in Figure 119. The typical bubble dynamics was observed as displayed in the reference condition. Starting from the

stable film boiling regime at high superheat, the stable film started to collapse at the lower end of the cylindrical test section. The quench front propagated toward the top of the sample. Once the quenching front passed the hot surface, small bubbles nucleated and departed from the surface. Finally, the boiling heat transfer was completed when it reached the natural convection regime. Noticeable observations of bubble dynamics at higher pressures are a thinner vapor film in the stable film boiling regime, a lower magnitude of vigorous vapor generation in the transition boiling regime, a smaller bubble size, and crowded bubble nucleation sites in the nucleation boiling regime compared to those under atmospheric conditions. Based on Mikic and Rohsenow's correlations [135], bubble departure diameter is smaller and the number of active nucleation sites increase to a certain extent at elevated pressures due to the thermal properties of vapor.

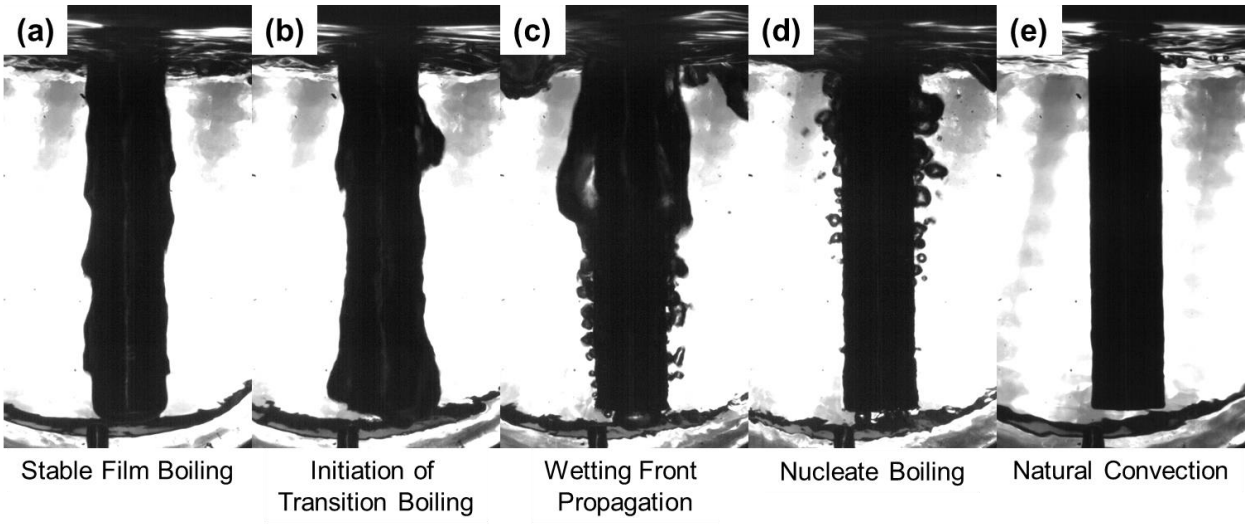

Figure 119: High-speed images (100 fps) of bare Zirc-4 specimen during quenching in saturated water at 0.33 MPa.

Figure 120 shows three plots: thickness of vapor layer, polynomial fit using commercial software (Origin 2015) at stable film boiling regime, and surface temperature during the quenching test at 0.55 MPa. The oscillation of the vapor layer at stable film boiling in the figure was due to the wavy motion of the vapor film induced by shear stress between upward vapor (buoyancy) and stagnant liquid (drag force). Once the sample temperature reached near the minimum film boiling temperature, enhanced heat transfer on the

surface generated a large amount of vapor. It shows the large amplitudes of the vapor film thickness, which correlates to the deflection point in the cooling curve.

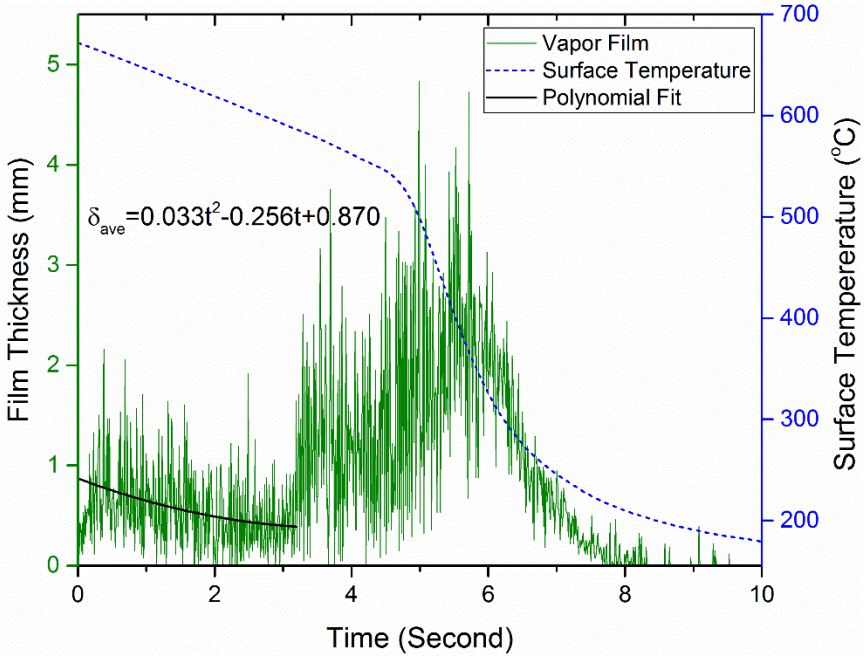

Figure 120: Vapor layer thickness (green) with a quadratic polynomial fit (thick dark line) and estimated surface temperature (blue dash) during a quenching test at 0.55 MPa.

The average film thicknesses at elevated pressures, determined by the quadratic polynomial fit in stable film boiling regime, are plotted in Figure 121. In general, the vapor layer tends to be thinner as the system pressure increases and as the quenching process progresses (as surface superheat decreases) in the stable film boiling regime. Interestingly, the pressure dependency on the vapor film thickness becomes weak above 0.39 MPa; the averaged vapor thicknesses at 0.39 MPa, 0.55 MPa, and 0.63 MPa are quite similar in the narrow range of 500 µm to 750 µm. The analytical derivation for vapor film thickness on a vertical plate at saturated conditions was proposed by Lubin [136], which is based on two-dimensional momentum and energy conservation. The assumption for the derivation was that the stable film boiling regime has a smooth laminar vapor flow and the major heat transfer mode is heat conduction through the vapor layer. Prediction of the vapor layer thickness is shown in equation (26):

$$\delta_v = \left(\frac{4k_v \cdot \mu_v \cdot (T_{wall} - T_{water}) \cdot x}{g \cdot \rho_v \cdot (\rho_l - \rho_v) \cdot h_{lv}}\right)^{0.25} \quad (26)$$

where k_v, μ_v, ρ_v are thermal conductivity, viscosity, and density for saturated vapor, respectively. ρ_l is liquid density, and h_{lv} is enthalpy for vaporization. x is a distance from a leading edge (x is assumed to be 25 mm in this calculation – a half of the sample length).

The predicted vapor film thickness with high system pressures is plotted in Figure 122. The trends of the vapor film thickness are consistent with experimental data; the thickness decreases with increasing system pressure and with decreasing surface superheat. The pressure effects tend to diminish as pressure gets higher. Therefore, one could say that the vapor layer thickness under pressurized conditions is strongly correlated to the thermal properties of liquid and vapor, particularly density of vapor (please see Table 13). It is worth noting that the predicted film thickness is about two to four times smaller than the measured film thickness. The Lubin correlation does not take the dynamic wavy motion of vapor-liquid interface into consideration, so the theoretical estimation would be smaller than measured vapor film thickness. Moreover, the theoretical model neglects the formation of large, local vapor bulges on a vertical surface. They would be generated if vapor velocity becomes so high that the interface becomes unstable. Bui and Dhir [137] proposed the distribution of the vapor bulges on a vertical surface are related to the most dangerous wavelength (Kelvin-Helmholtz instability).

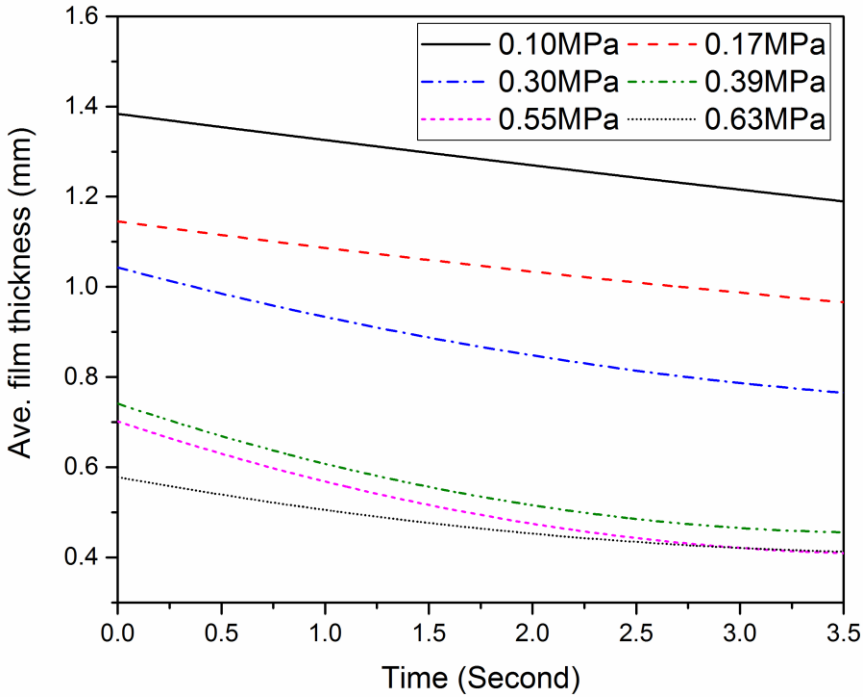

Figure 121: Averaged vapor film thickness using a quadratic polynomial fit using the high-speed images in stable film boiling regime at different pressures.

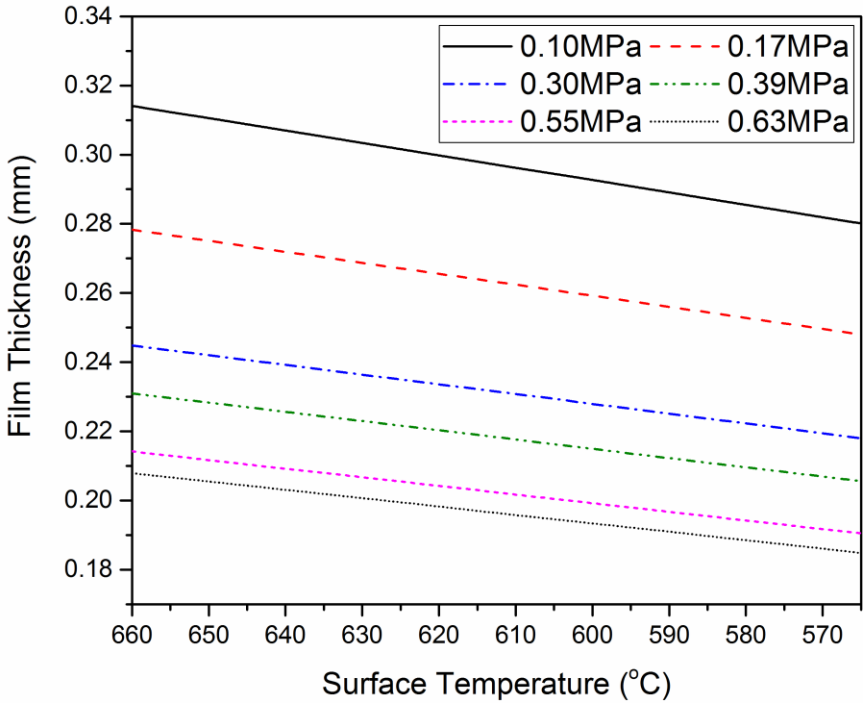

Figure 122: Prediction of vapor layer thickness based on Lubin's analytical derivation [136]. Vapor properties were determined by the film temperature, $(T_{wall}+T_{water})/2$.

Table 13: Viscosity of vapor, thermal conductivity of vapor, density of vapor and liquid, and enthalpy of vaporization at saturation condition with different pressures. Temperature of the hot surface is assumed to be 600 °C.

Pressure (MPa)	μ_v [kg/(s·m)]	k_v [W/m·K]	h_{lv} [kJ/kg]	ρ_l [kg/m^3]	ρ_v [kg/m^3]
0.1	$2.237 \cdot 10^{-5}$	0.04895	2257	958.5	0.3518
0.2	$2.279 \cdot 10^{-5}$	0.05022	2201	942.9	0.6893
0.3	$2.306 \cdot 10^{-5}$	0.05108	2163	931.8	1.023
0.4	$2.326 \cdot 10^{-5}$	0.05175	2133	922.9	1.353
0.5	$2.343 \cdot 10^{-5}$	0.05231	2108	915.3	1.682
0.6	$2.357 \cdot 10^{-5}$	0.05281	2086	908.6	2.010

Figure 123 shows the wavy motion of the vapor-liquid interface in the stable film boiling regime at both ambient pressure and 0.63 MPa. Apparently, the average vapor film thickness and amplitude of the oscillations at 0.63 MPa are smaller than those at 0.10 MPa. In addition, it appears that frequency of the oscillation does not have a strong dependency on the system pressure; 35 oscillation per second was observed at 0.1 MPa and 32 oscillation per second was identified at 0.63 MPa based on Figure 123.

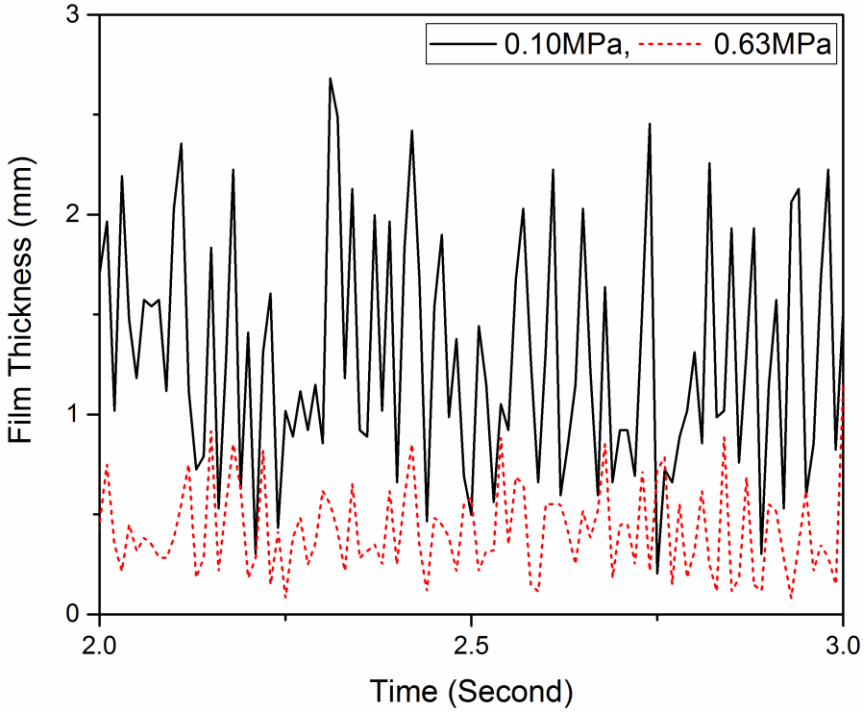

Figure 123: Wavy motion of vapor film in the stable film boiling regime at 0.1 MPa (black solid line) and 0.63 MPa (red dots). The vapor film thickness was converted from high-speed images (100 fps).

Comparison of Experimental Results with Literatures

Finally, Figure 124 compares the minimum film boiling point of the current experimental results for water on bare Zirc-4 with semi-empirical predictions of Berenson [79] and Henry [80] and experimental correlation of Shumway [138] and Sakurai [139], and experimental data of Peterson [84]. Again, Berenson determined minimum film boiling temperature by combining minimum heat flux prediction by Zuber's Taylor instability model [140] and heat transfer coefficient based on hydrodynamic considerations (such as bubble spacing and growth rate) with an assumption of isothermal surface temperature, being given by equation (27).

$$T_{min,Berenson} = T_{sat} + 0.127 \cdot \frac{\rho_v h_{lv}}{k_v} \cdot \left(\frac{g(\rho_l-\rho_v)}{\rho_l+\rho_v}\right)^{2/3} \cdot \left(\frac{\sigma}{g(\rho_l-\rho_v)}\right)^{1/2} \cdot \left(\frac{\mu_v}{g(\rho_l-\rho_v)}\right)^{1/3} \quad (27)$$

Henry's prediction proposed that the minimum film boiling temperature was assumed to be local surface temperature if liquid-solid interfacial temperature reached the Berenson's prediction. The liquid-solid interface is cooled by transient liquid contacting and wetting on the surface followed by evaporation of the thin liquid film. In other words, local surface temperature would be the minimum film boiling point predicted by Berenson's model even if average surface temperature is higher than it. The experimental data was used to formulate a correlation for the model. The prediction is given in equation (28):

$$\frac{T_{min,Henry}-T_{min,Berenson}}{T_{min,Berenson}-T_l} = 0.42 \cdot \left(\sqrt{\frac{k_l \rho_l c_{pl}}{k_{wall}\rho_{wall}c_{pwall}}} \cdot \frac{h_{lv}}{c_{pwall}(T_{min,Berenson}-T_{sat})}\right)^{0.6} \quad (28)$$

where k_{wall}, ρ_{wall}, c_{pwall} are thermal conductivity, density, and heat capacity of solid wall, respectively.

Shumway correlation as a function flow rate, pressure, void faction, and fluid and wall properties was formulated using available data in the literature. It is known that the correlation has been incorporated in computer codes for estimation of the minimum film boiling temperature under accident scenarios. The correlation is shown in equation (29).

$$T_{min,Shumway} = T_{sat} + 3.7\left(\frac{\rho_l+\rho_v}{\rho_l-\rho_v}\right) \cdot \frac{hlv}{c_{pl} \cdot Pr_l} \cdot [1 + (1-\alpha)^2] \cdot (1 + 1.5 \cdot 10^{-5} \cdot Re_l)^{0.15} \cdot \left(1 - \frac{P}{P_{crit}}\right)^{0.1} \cdot \beta \quad (29)$$

where β is the non-dimensional term including wall and liquid properties; $\beta = \sqrt{\frac{(k\cdot\rho\cdot c_p)_l}{(k\cdot\rho\cdot c_p)_{wall}}}$. The void term $(1+(1-\alpha)^2)$ and Reynold number (Re) were neglected in Figure 124.

Sakurai derived the empirical correlation for the minimum film boiling point based on experimental results for various liquids tested. Thermal properties of liquid and surface were considered in the correlation as well. It was postulated that minimum film boiling occurred at the lower limit of the heterogenous spontaneous nucleation temperature.

$$\frac{T_{min,Sakurai}+\beta\cdot T_{sat}}{1+\beta} = 0.92\cdot T_{crit}\cdot\left(1-0.26\cdot\exp\left(\frac{-20\left(\frac{P}{P_{crit}}\right)}{1+1700/P_{crit}}\right)\right) \quad (30)$$

where T_{crit} is critical temperature and P_{crit} is critical pressure in kilopascals.

The current experimental results do not agree with any of the theoretical predictions and experimental correlations except for the experimental data reported by Peterson. The discrepancy between the hydrodynamic models and the experimental results indicates that the Tayler instability vapor removal limitation is not the major mechanism to determine the minimum film boiling temperature at elevated pressures. In addition, Sakurai's experimental correlation is only in good agreement with the data in ambient pressure. Shumway's correlation shows a very similar trend with the quadratic polynomial fit for the experimental results, but it has approximately 150 °C offset.

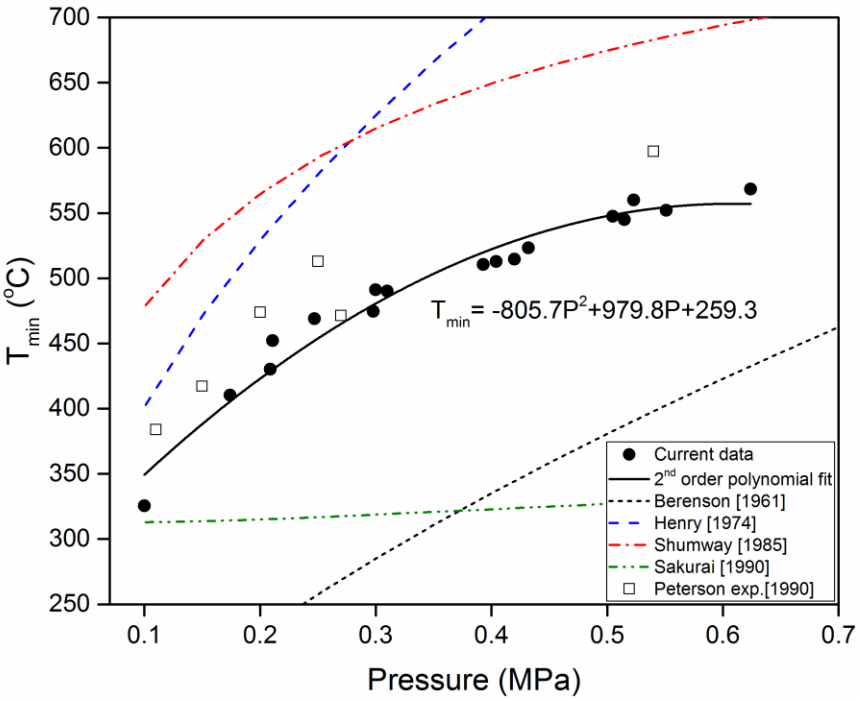

Figure 124: Minimum film boiling wall temperatures for water at elevated system pressures.

4.4.3. Subcooling conditions

Quenching tests in subcooled water were performed at atmospheric pressure. After the degassing step, the temperature controller was set to a desired subcooled water temperature. The temperature of the water quenchant was adjusted by a heat balance between the external heat input from the heating tape and the heat loss from the test chamber. Finally, the heated rodlet test specimen was plunged into the subcooled water and the output data were recorded. The range of the water temperature for the experiments was from saturation temperature to 60 °C water ($\Delta T_{sub} = T_{sat} - T_{water}$ = 40 K) with approximately 5 K steps.

Quenching Curves and Boiling Curves

Both quenching and boiling curves under subcooled water are summarized in Figure 125. As the quenchant temperature decreases, the total cooling time is reduced. As expected increased water subcooling has a beneficial effect on boiling performance. For example, the cooling time at 40 K subcooling took about six seconds from the initial temperature to 100 °C. In contrast, it took about 35 seconds in no subcooling conditions (i.e., saturated water) for the cooling process. The boiling curves show that heat flux at stable film boiling and temperature of the low limit of stable film boiling increases with increasing water

subcooling. It reveals that minimum film boiling temperature is higher than 600 °C, which is beyond measurable limit, if the degree of subcooling of the water quenchant is higher than 30 K. It is interesting to note that the surface heat flux around the minimum film boiling point increases with a slower rate as the surface temperature decreases in Figure 125b, instead of the sudden jump shown in saturated water conditions. It would be attributed to a slower wetting front propagation on the surface at the subcooled water compared to that at saturated water. In other words, at high subcooling showed the longer transition boiling regimes.

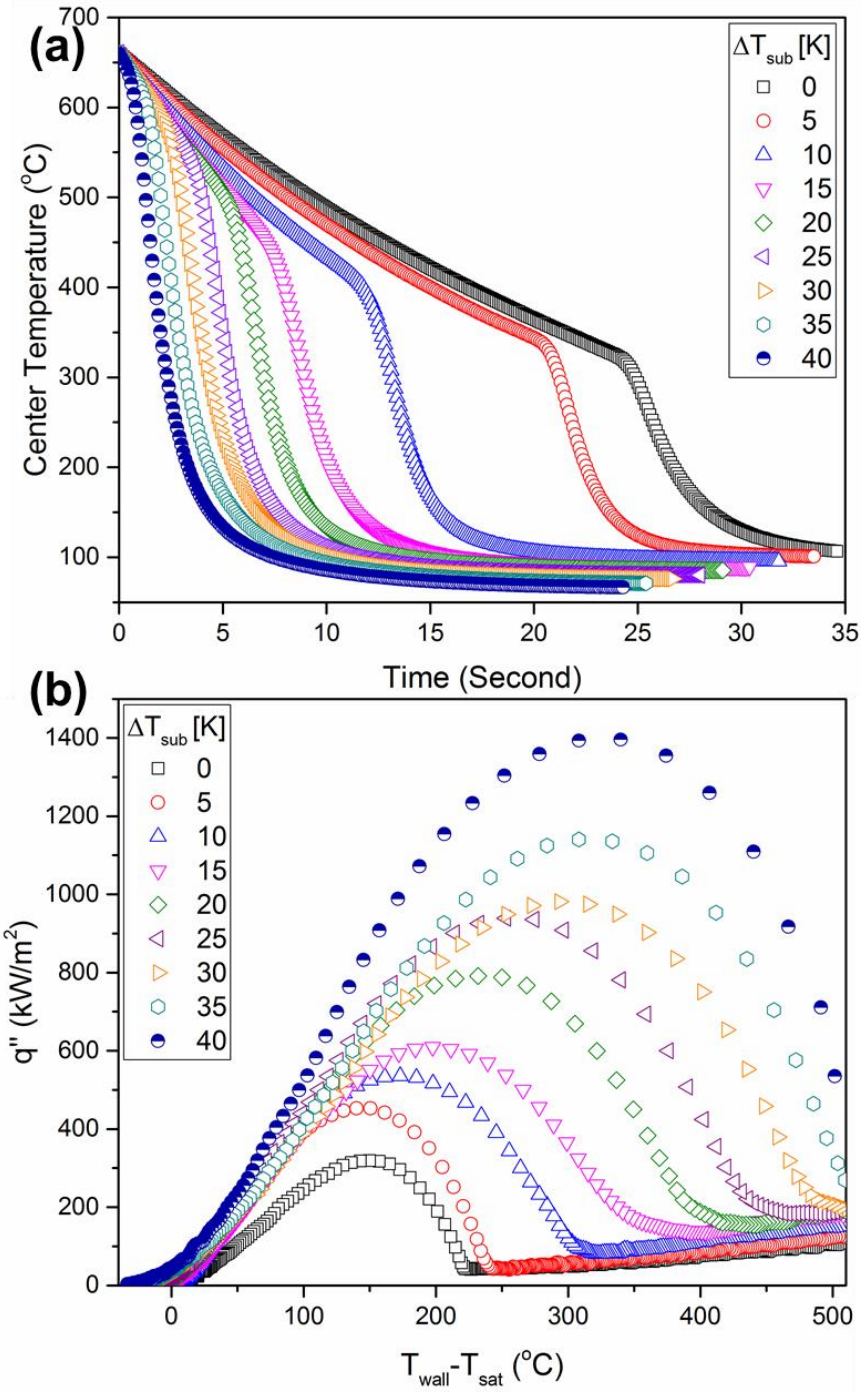

Figure 125: Quenching curves (temperature-time history at the center of the sample) and corresponding boiling curves for bare Zirc-4 estimated by INTEMP software in subcooled water.

Bubble Dynamics at Subcooled Water

Figure 126 shows bubble evolution on the hot surface during the quenching experiment in subcooled water (ΔT_{sub} = 25 K). The vapor film, just after submerging appeared to be thinner and the vapor-liquid

interface, smoother than that in saturated conditions. Many waves in liquid, due to deflection of light around the hot surface, indicate that the liquid boundary layer was developed on the thin vapor layer. Figure 126b reveals the moment of initiation of transition boiling around the edge of the lower end of the cylindrical test sample. The wetting front moved up along the rod with a slower speed (~ 6 mm/s) than the saturated water condition (~ 17 mm/s), measured by high-speed imaging. Since the wetting front propagation in the subcooled condition was initiated at a higher temperature than that in the saturation condition, it is speculated that hot average surface is still hot enough to sustain the generation of a vapor layer even if liquid contacts on local surfaces is promoting destabilization of the vapor layer. In other words, the stable vapor film boiling with partial liquid contacts is maintained for a longer time prior to starting nucleate boiling compared to the saturation conditions. In subcooled conditions, the vapor leaving the hot surface was condensed. Thus, vigorous boiling as shown in the saturation conditions (Section 4.4.1.) was not displayed during transition boiling regime. Small bubbles grew on the surface if the wetting front passed (Figure 126d), and eventually the boiling heat transfer was completed in the natural convection regime (Figure 126e).

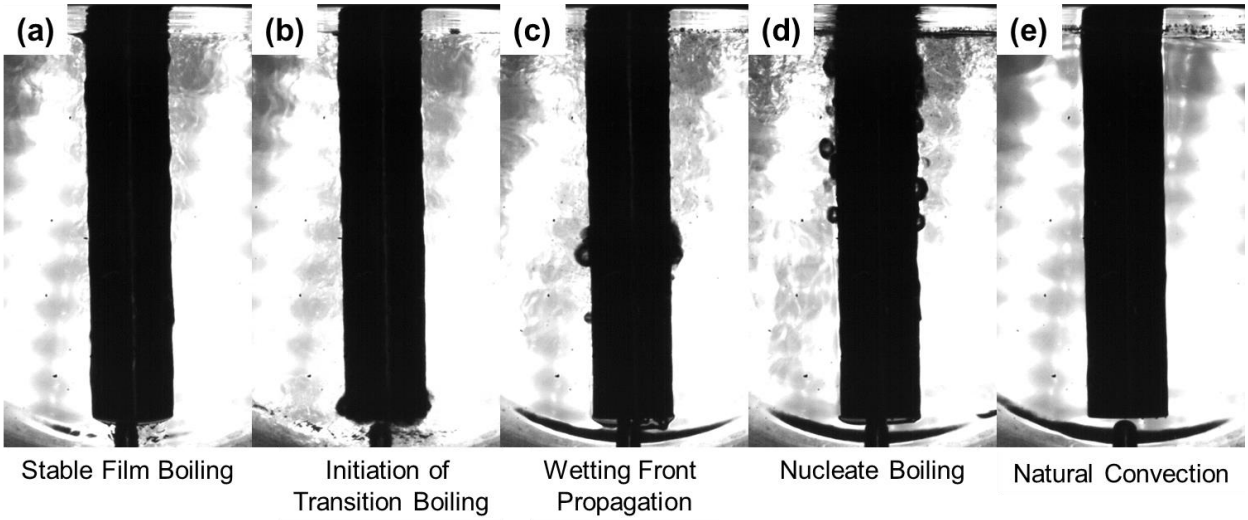

Figure 126: High-speed images (100fps) of bare Zirc-4 sample during quenching at ΔT_{sub} = 25 K water (75 °C water).

Figure 127 includes the thickness of the vapor layer, its quadratic polynomial fit using Origin 2015 at stable film boiling regime, and the surface temperature during the quenching test in subcooled water (ΔT_{sub} = 25 K). As observed in the saturated conditions, the film boiling regime shows oscillation of the liquid-vapor interface, and large amplitudes of vapor are identified near the minimum film boiling point. The point corresponds to the deflection point in the surface temperature-time curve. Plots for thickness of vapor layer at different water subcooling temperatures presented in the Appendix.

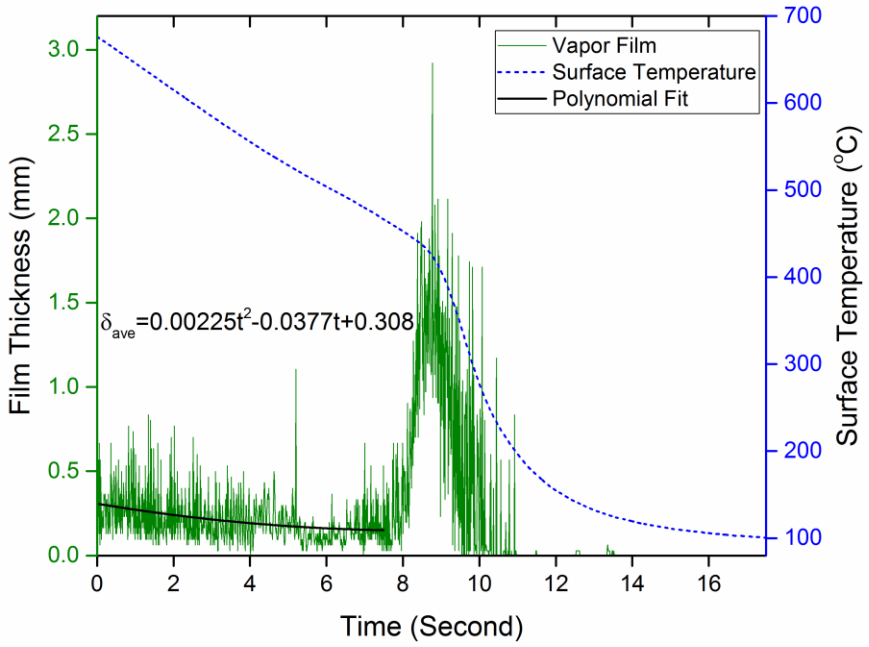

Figure 127: Vapor film thickness (thin green line) with a quadratic polynomial fit (thick black line) and estimated surface temperature (blue dash) during quenching test at 85 °C water.

Vapor film thickness at stable film boiling regime estimated by the high-speed images at various water subcooling and quadratic polynomial fits are plotted in Figure 128. The results at very large subcooling tempertures (ΔT_{sub} > 30 K) were excluded because the stable film boiling regime at the conditions was not observed even at initial sample temperatures. When the hot sample was fully submerged in the subcooled water, transition boiling started upon contact. The average film thickness strongly depends on the degree of water subcooling. As water subcooling increases, the average film thickness decreased. However, the relative effect of subcooling is diminished with increasing the subcooling. There were some uncertainties to calculate the vapor layer thickness due to limitations of vapor layer visualizations such as image

distortions near the hot surface (because of the liquid boundary layer) and resolution of recorded images. Therefore, the vapor layer thickness at 25 K water subcooling is thicker that those at 15 K and 20 K water subcooling conditions.

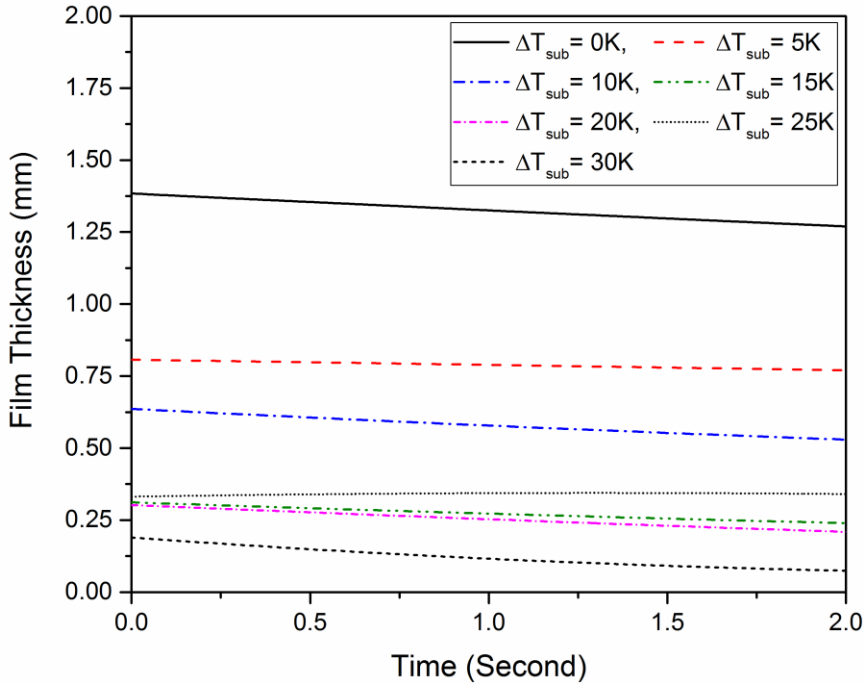

Figure 128: Vapor film thickness using a quadratic polynomial fit of high-speed images in stable film boiling regime at different water subcooling.

The vapor layer thickness with water subcooling is predicted using a derivation of the surface heat flux at stable film boiling by Michiyoshi et al. [141] Michiyoshi et al. assumed that a hot surface submerged in subcooled water is covered by a thin laminar vapor film and the vapor layer is surrounded by a liquid laminar boundary layer with functional profiles of velocity and temperature. The detailed solutions of the integral equations of heat balance in the layers on vertical surface are introduced in the literature. The estimation of vapor film thickness was used in the following relation between the calculated surface heat flux and vapor thermal conductivity:

$$\delta_{film} = \frac{k_v \cdot (T_{wall} - T_{water})}{q"_{film}} \quad (31)$$

Again, the prediction shows that the vapor film thickness decreases with decreasing wall superheat and with increasing water subcooling due to the increase of contribution of sensible heat to surface heat removal, confirming the trend shown in the visual analysis (Figure 129). The predicted vapor thickness is much smaller than the measured one because the wavy motion of vapor-liquid interface was not considered in the prediction.

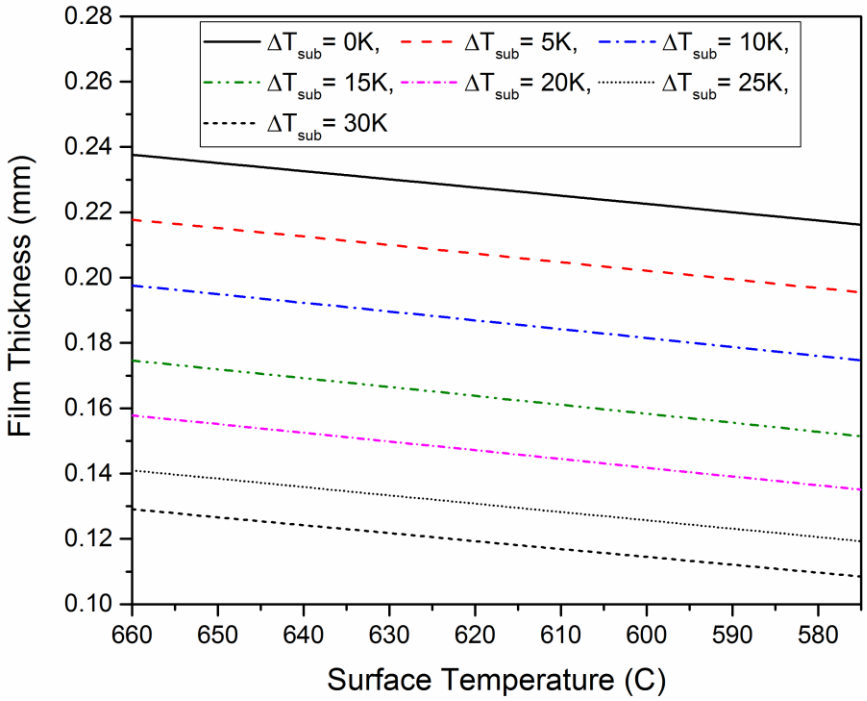

Figure 129: Predicted vapor film thicknesses on a vertical surface based on Michiyoshi et al. [141]. Vapor properties were determined at the film temperature.

At subcooled conditions, the magnitude of the wavy motion of liquid-vapor interface at stable film boiling regime was found to be diminished as shown in Figure 130. The observations are consistent with Toda and Mori's subcooled film boiling experiment on a horizontal wire and sphere [142]. It is postulated that the liquid boundary layer where temperature is lower than the saturation temperature makes the generated vapor layer condense, leading to the thin and smooth vapor layer. In addition, the frequency of the oscillations appears to be the same order of magnitude with that under the saturation conditions.

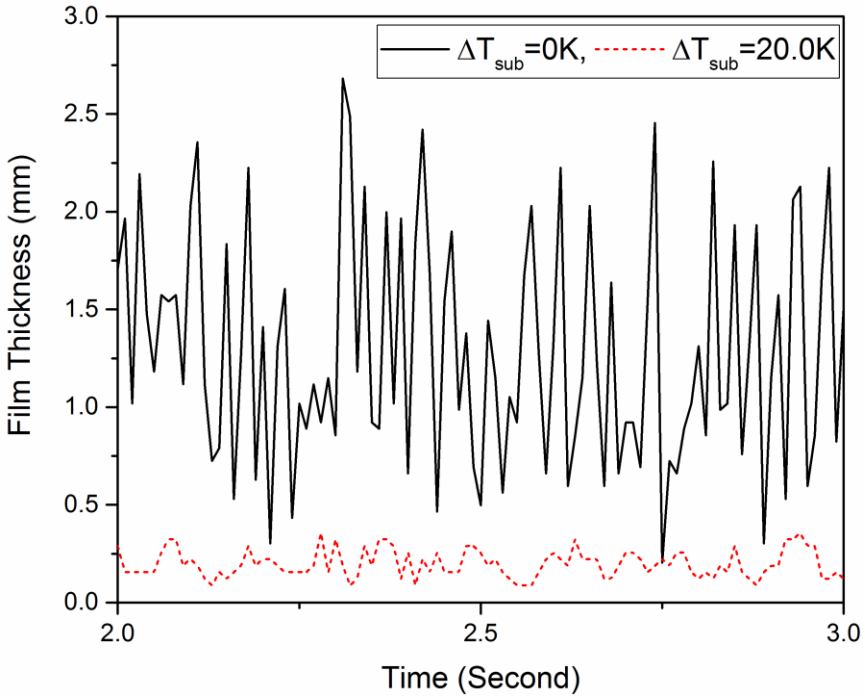

Figure 130: Oscillation of vapor film interface in the stable film boiling regime at the saturation condition (black solid line) and at 20 K subcooled water (red dots). The vapor film thickness was measured using high-speed images (100 fps).

Comparison of T_{min} with Literatures at Subcooled Water

Minimum film boiling temperature vs. liquid subcooling is plotted in Figure 131, and compared with predictions based on Henry [80], Dhir [92], and Yamada [94] and Peterson's data [84]. The present results show the linear relationship between the minimum film boiling temperature and liquid subcooling, which is in good agreement with the predictions. However, the rate of increase of minimum film boiling temperature with liquid subcooling was steeper. Henry's empirical model includes liquid temperature term as introduced in the previous chapter. Dhir and Purohit performed quench tests using 19 and 25.4 mm diameter stainless steel spheres in subcooled water and proposed the correlation as the equation (32):

$$T_{min} = T_{sat} + 101 + 8\Delta T_{sub} \quad (32)$$

Yamada's quenching experiments investigated the relationship between the degree of wall superheating at the low limit of film boiling and liquid subcooling. The quenching samples were cylindrical pure silver samples which were 32 mm in diameter and 48 mm in length. The relationship was approximated as follows:

$$T_{min} = T_{sat} + 133 + 4.65\Delta T_{sub} \quad (33)$$

Peterson's experimental data for the minimum film boiling temperature of Zirc-4 are 80 K-150 K higher than the current experimental results. Moreover, it was reported that the liquid subcooling effect is less pronounced at higher water subcooling temperatures. The results might be due to surface oxidation during the test (initial temperature at Peterson's test was about 760 °C) or uncertainties in his one-dimensional inverse heat conduction calculation.

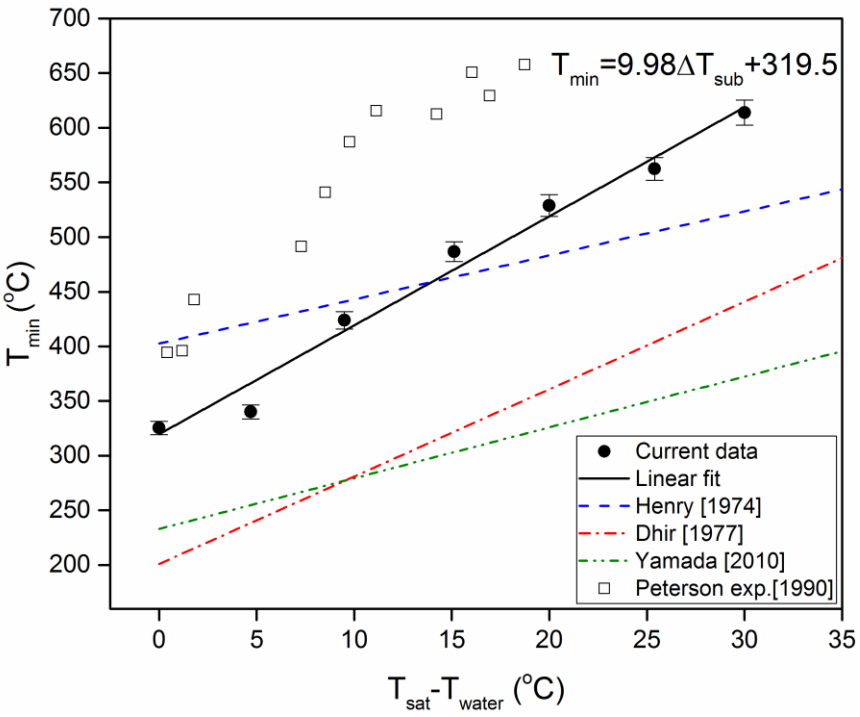

Figure 131: Comparison of present results with predictions by experimental data and correlations for the minimum film boiling wall temperature for water.

Effect of System Pressure and Water Subcooling on Heat Flux in Film Boiling

Estimations of surface heat flux in the film boiling region (q''_{film}) in atmospheric saturated water, saturated water at 0.5 MPa, and subcooled water (ΔT_{sub}=15 K) in atmospheric pressure are summarized in Figure 132. The measured surface heat flux is compared with the predicted surface heat flux by Bromley [143] and Lubin [136] for saturated conditions and by Michiyoshi [141] for subcooled conditions, respectively. In the calculations, radiation heat transfer was considered with an assumption of moderated oxidized surfaces (emissivity=0.6) [144]. The film boiling surface heat fluxes are in good agreement with

Bromley, Lubin, and Michiyoshi's theoretical predictions. However, the measured values are usually slightly higher than the predictions, which could be caused by the effects of vapor film oscillation on the total heat transfer; i.e., an increase in interfacial area due to the wavy motion would enhance the heat conduction and radiative heat transfer from the hot surface to the subcooled water.

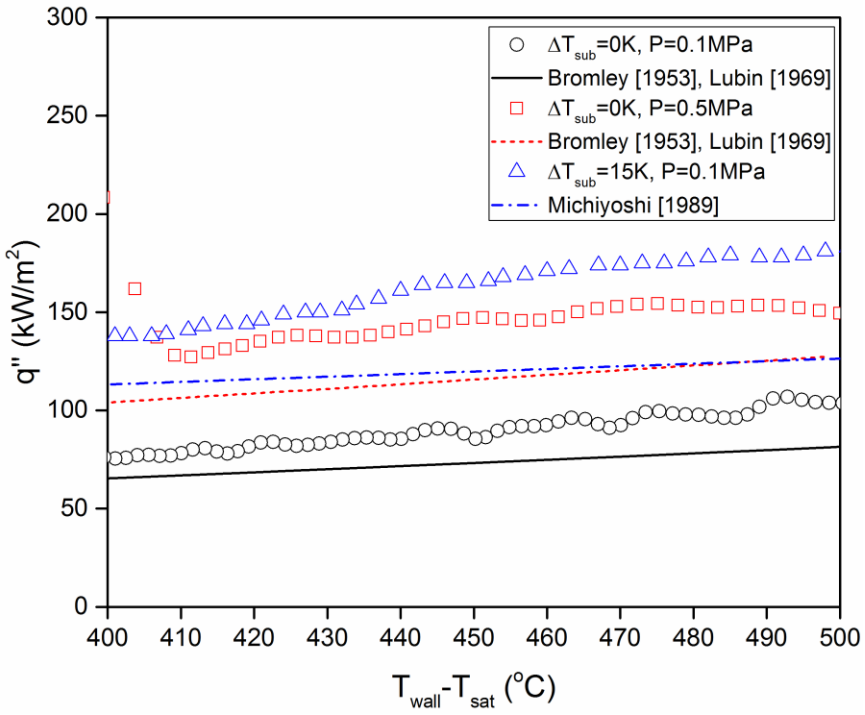

Figure 132: Film boiling heat flux (experimental results and theoretical predictions) at saturation in ambient pressure and 0.5 MPa and 15 K subcooling for bare Zirc-4 samples.

4.5. Quenching experiments for the modified surfaces

As described in the chapter 4.4, it was found that the system conditions (i.e., system pressure and water subcooling) have a significant effect on quenching heat transfer phenomena such as the stable film boiling regime and the minimum film boiling temperature. In the chapter 4.5, effects of surface properties on quenching performance at a certain system condition (saturation water at ambient pressure or saturation condition at 0.5 MPa or 15 K subcooled water at atmospheric condition) were discussed. Surface properties of interest to the current study were surface oxidation, roughness, and a coated surface. The modified surfaces were briefly introduced in the first section and the results of quenching experiments for the modified surfaces at the different system conditions will be discussed in the following sections.

4.5.1. Surface preparation and characterization

To investigate a relationship between surface properties of quenching samples and high temperature boiling heat transfer, five types of surfaces were prepared as follows: bare surface, pre-oxidized smooth surface, rough surface, thin coating on smooth surface (CS-surface), and thin coating on rough surface (CR-surface). Materials for the modified surface were zircaloy-4 flats and zircaloy-4 cylindrical test sections. The flat samples were used for SEM plan-view observations, surface roughness results, and water droplet contact angle measurements. Quenching experiments for the cylindrical samples were performed at least three times to make sure a reliability of temperature-time data at the center of the samples. Some of the quenched samples were cut perpendicular to the longitudinal direction to measure thickness of the oxide layer.

The bare surface was prepared by polishing the as-machined surface with abrasive SiC polishing papers up to 600 grit. The surface with a thick oxide layer was fabricated by performing pre-oxidation of the bare surface samples at 700 °C for five hours with a 5 °C/min ramp up rate in ambient air. A dry sand blast facility (manufactured by Skat Blast Inc.) was utilized to make the bare surface roughened as shown in Figure 133a. The size of the alumina grits being sprayed by compressed air to the surfaces were in the range of 600 μm to 900 μm (Figure 133b). They impacted and eroded the bare Zirc-4 surface due to the alumina grit's high hardness (~1900 HV) compared to the Zirc-4 substrate (~190 HV), leading to a roughened surface.

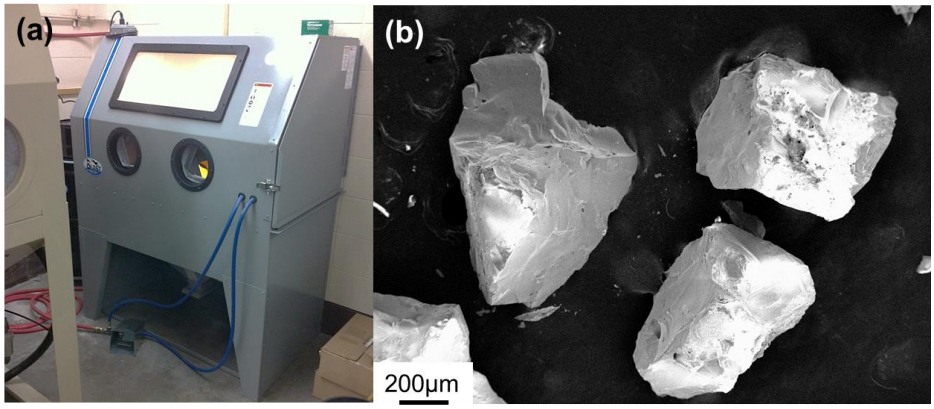

Figure 133: (a) A photograph of the facility for a sand blaster at UW-Madison, and (b) SEM plan-view image for alumina media for the surface roughening process.

The bare surfaces were modified to a thin coating on smooth surface (CS-surface) by using the magnetron sputter of a $ZrSi_2$ target. Batches of five or six flat substrates and four or five cylindrical samples fixed on aluminum plates were placed on the sputter stage. The short plates had a single rectangular channel of 3.2 mm in width and the parts had dimensions of 76 mm x 25 mm x 3.2 mm. Since the sputtering process is a line-of-sight process, the cylindrical samples were flipped over 180° after the first deposition, improving uniformity of the deposition of the coating as shown in Figure 134. The samples showed a slight thickness variation (approximately 0.4 μm) of the $ZrSi_2$ coating between its top region and the side area. Figure 135a shows the cylindrical Zirc-4 sample on the aluminum plate and CS-surfaces with the reinforcing 316 stainless steel tube are displayed in Figure 135b.

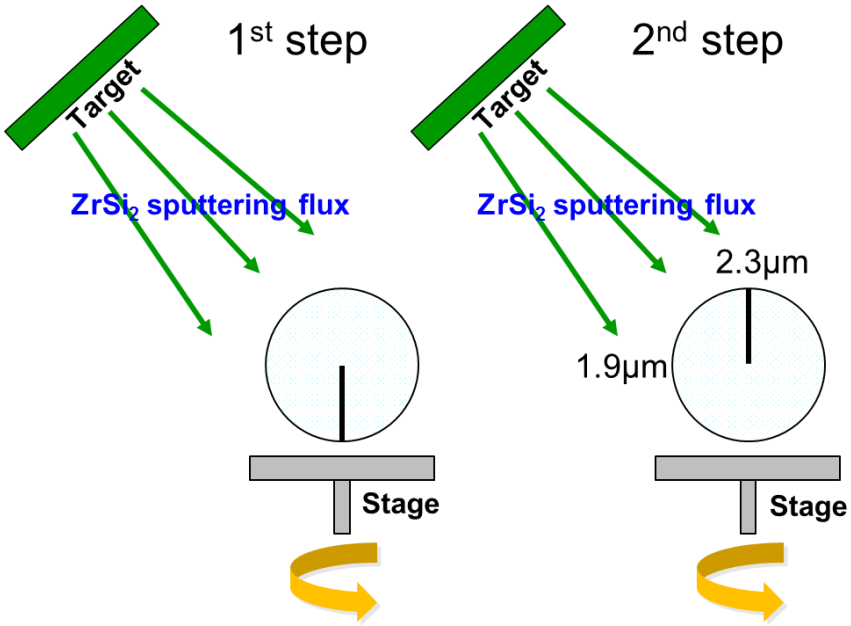

Figure 134: A schematic diagram of magnetron sputter deposition for the cylindrical test sections. Two-step deposition was performed to make coating deposition uniform.

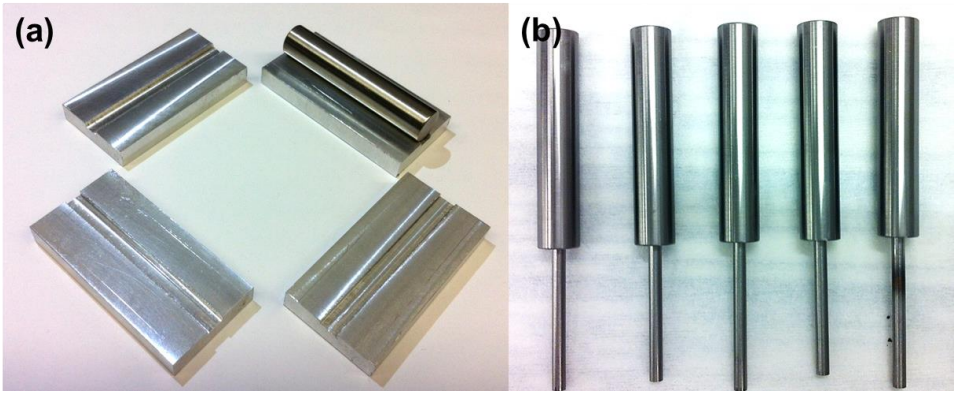

Figure 135: Photograph of (a) a cylindrical Zirc-4 sample on the aluminum supports and (b) a $ZrSi_2$ thin coating on Zirc-4 samples (CS-surface).

The sputter deposition of $ZrSi_2$ on the roughened surface produced the thin coating on rough surfaces (CR-surface). After the bare surface was roughened by the sand blast process, the sample was sonicated for 20 minutes in an acetone bath, removing any contaminants on the surface from the roughening process. Thin $ZrSi_2$ coatings were deposited on the rough surface, which coating process was the identical to the CS-surfaces.

In Figure 136, photographs of the modified surfaces for Zirc-4 flats and Zirc-4 rodlets after three consecutive quenching tests are displayed. Originally, all the surface had shiny and gray surfaces except for the pre-oxidized surface. After the three repeated quenching tests, both the bare surface and rough surface turned black and gray and lost light reflectivity. The CS-surface and CR-surface turned a yellow and orange color. The brown spots on smooth, black surface were developed during the air oxidation. After the three quenching tests, the surface did not appear to be changed considerably. Any type of surface damage during the quenching experiments via visual inspection was not identified.

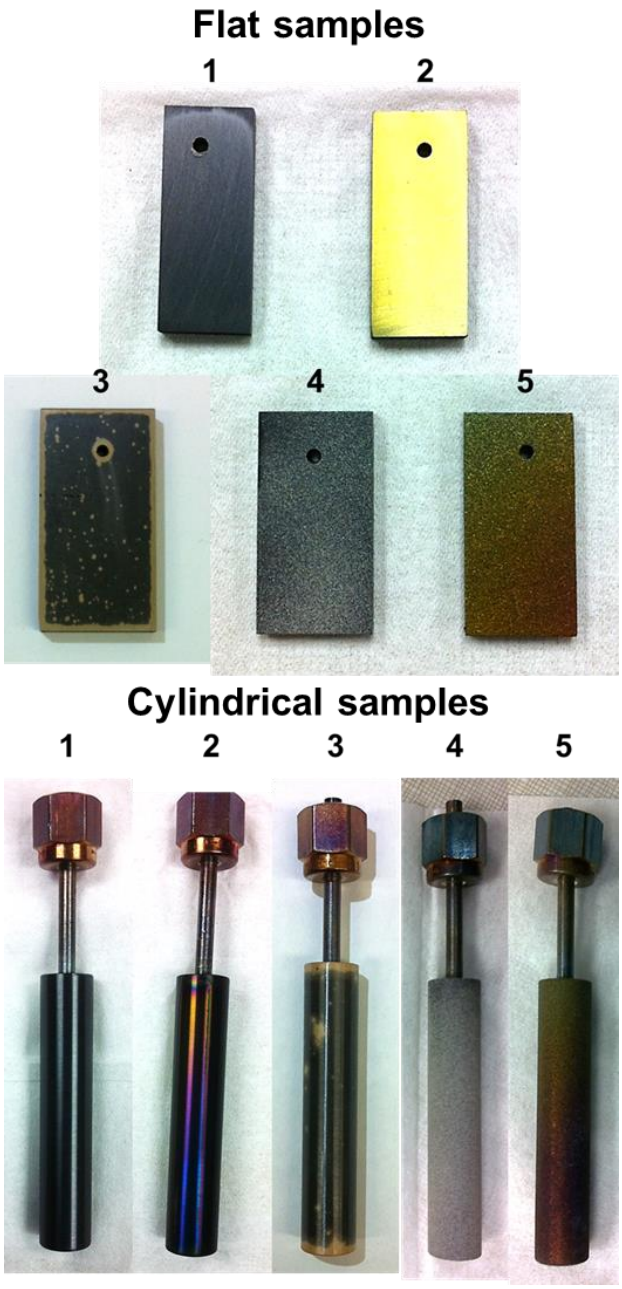

Figure 136: Images of the modified surfaces on Zirc-4 flats and cylindrical Zirc-4 samples after three consecutive quenching tests (1: bare surface, 2: CS-surface, 3: pre-oxidized surface, 4: roughened surface, and 5: CR-surface).

Surface Morphology

The modified surfaces were characterized via SEM after the last quenching run for each case (after three repeated tests) and the SEM plan-view images are presented in Figure 137. All the images were taken at the same magnification. The bare surface (Figure 137a) and the CS-surface (Figure 137b) revealed

smooth surfaces without any irregularities. Only fine scratches on the surface due to the polishing process were identified. The rough surface and CR-surfaces prepared by sandblasting resulted in micro-mechanical roughening of the Zirc-4 surface. A high kinetic energy of the alumina particles caused erosion of the surface. Some of the media was randomly embedded in the surface and the media left micron-scale pores when they were removed by the ultrasonic cleaning. The thin $ZrSi_2$ coating prevented the base substrate from oxidation during the quenching tests so the CR-surface did not display cracks as a result of oxidation. On the contrary, localized oxidation at ridges and tips on the rough surface led to formation of cracks.

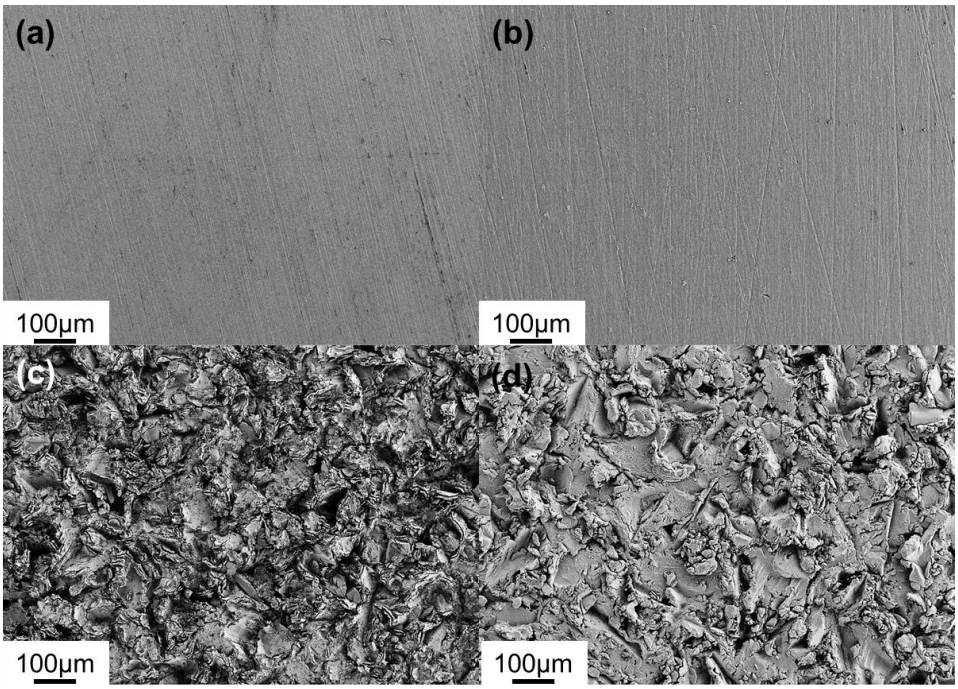

Figure 137: Microscopic surface morphology characterized by SEM on (a) bare surface, (b) thin $ZrSi_2$ coating on smooth surface (CS-surface), (c) rough surface, and (d) thin $ZrSi_2$ coating on rough surface (CR-surface) flats.

In addition, surface roughness (R_a), an arithmetic mean of the absolute values of the evaluation profile deviations from the mean line, was measured for the smooth surfaces via a scanning white light interferometry microscope (Zygo) and for the rough surfaces using cross-sectional SEM images. As shown in Figure 138, the R_a for both the bare surface and the CS-surface after the three quenching tests was found to be about 0.25 µm and 0.28 µm, respectively. The characterization confirms the smoothness of the surfaces, and only polishing scratches induced the surface roughness. Due to limited light reflection on the

rough surfaces, surface roughness for the rough surfaces and CR-surfaces was directly measured by cross-sectional observation. As displayed in Figure 139, the surface roughness was increased significantly as the result of the sandblasting process. The roughness surface and CR-surface had 22 μm and 20 μm in averaged roughness, respectively. The roughness values are two orders of magnitude greater than that of the smooth surfaces. The local maximum height (distance from a peak to a valley) of structures on the CR-surface was about 40 μm. In addition, a thin oxide layer and a thin coating were found on the rough surface and CR-surface, respectively.

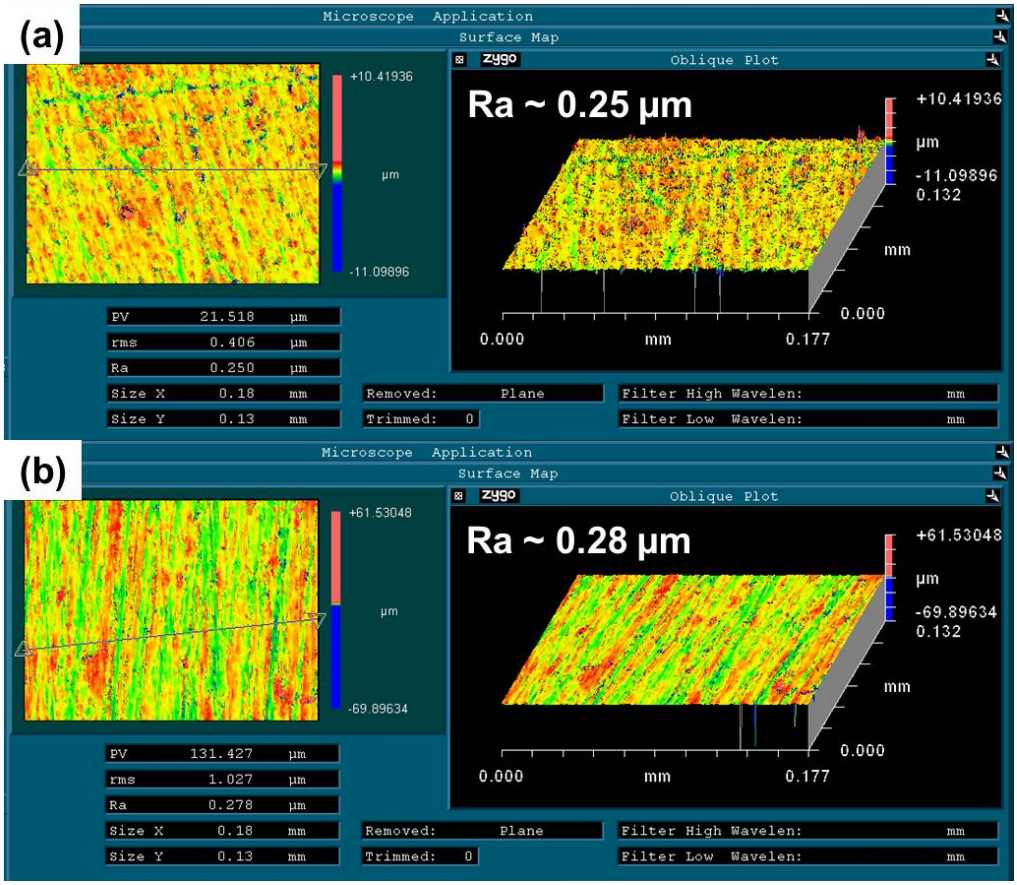

Figure 138: Roughness profile of a bare surface and a CS-surface (acquisition area: 177 μm × 177 μm) flats after three quenching tests, measured by a white light interferometer at UW-Madison.

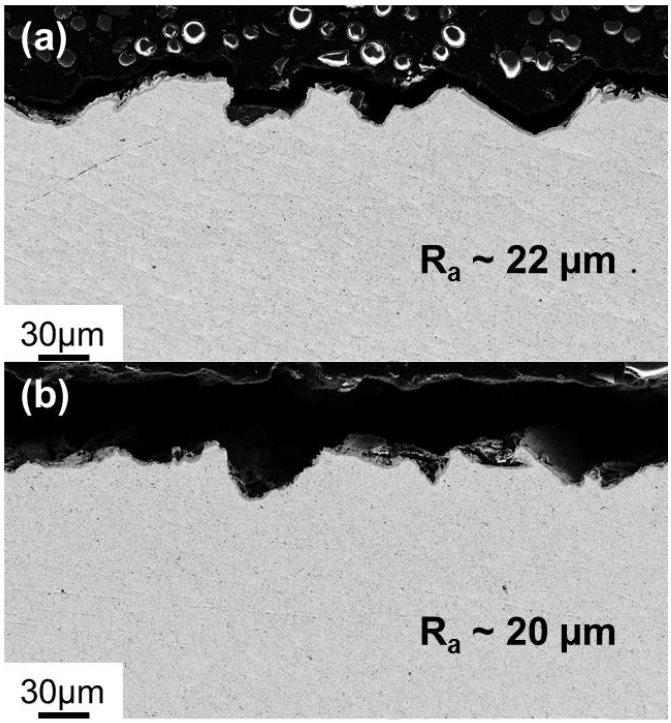

Figure 139: Cross-sectional SEM images of (a) rough surface and (b) CR-surface flats after three quenching tests. The R_a values were averaged from images on five different locations of the sample.

Thickness of Oxide Layer

Cross-sectional SEM images were used for measuring the oxide layer thickness and the thin coating thickness of the smooth surfaces as shown in Figure 140. The curvature in the images are results from that cylindrical samples were used for the characterization. During three repeated quenching tests, a thin zirconium oxide layer was grown on the bare Zirc-4, and its thickness was found to be approximately 3.6 µm. On the other hand, the pre-oxidation of the bare surface produced a thick oxide layer, resulting in a 55.6 µm thick oxide layer as identified in the image. The thick oxide layer contained circumferential cracks, indicating compressive stress might be built up while zirconium reacts with oxygen during the pre-oxidation step. It was revealed that thin $ZrSi_2$ coating (2.2 µm in thickness) was successfully deposited on the smooth surface without any spallation or cracking. Moreover, substrate oxidation was not identified even if the sample experienced three quenching tests. This lack of oxidation of the substrate is associated with the protective nature of the $ZrSi_2$ coating at high temperature environment.

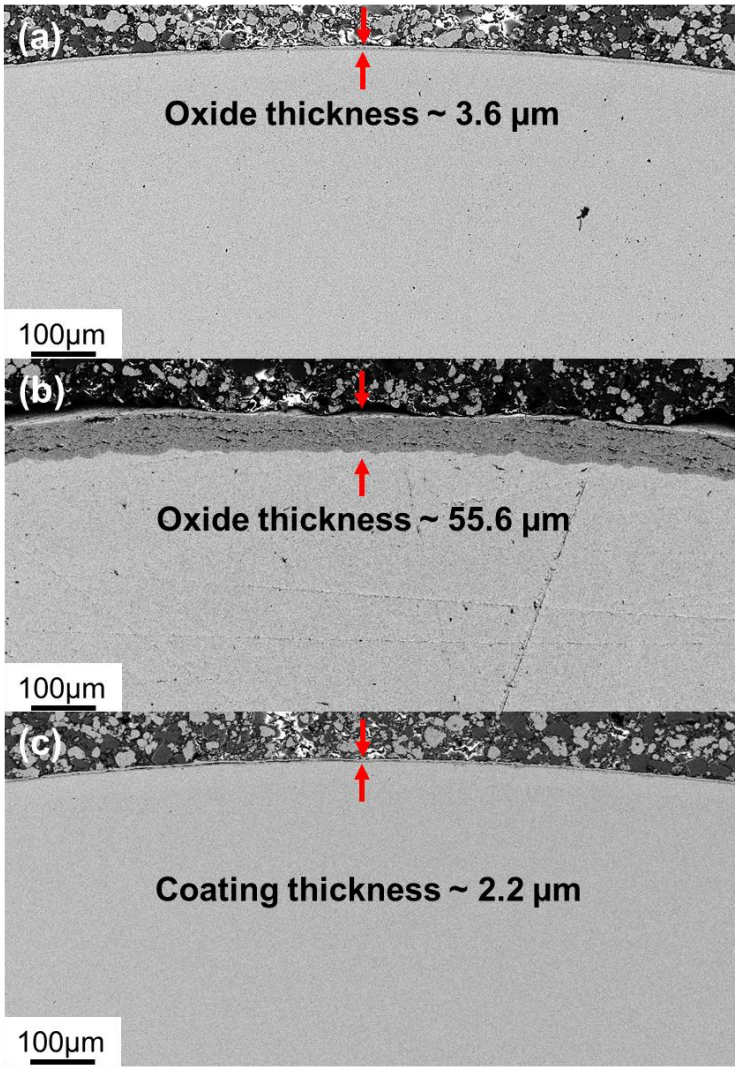

Figure 140: SEM cross-sectional images of (a) bare surface, (b) pre-oxidized surface, and (c) CS-surface after three repeated quenching tests. All the images were acquired at the same magnification. The oxide layer and coating on the surfaces were indicated by the red arrows.

Static Contact Angle of a Water Droplet

Results of the water static contact angle measurements are presented in Figure 141. The measurements were carried out more than five times at different locations on the quenched surfaces. In general, all the quenched surfaces showed hydrophilicity (contact angle < 90 °). Compared to the smooth surface, the CS-surface and the pre-oxidized surface revealed smaller water contact angles. Detail investigation for a relationship between the degree of oxidation and the water contact angle was not performed. Moreover,

hydrophilicity was enhanced more by the combination of the increase in surface roughness and the thin oxide layer or the thin coating, showing the smallest contact angles in Figure 141d-e.

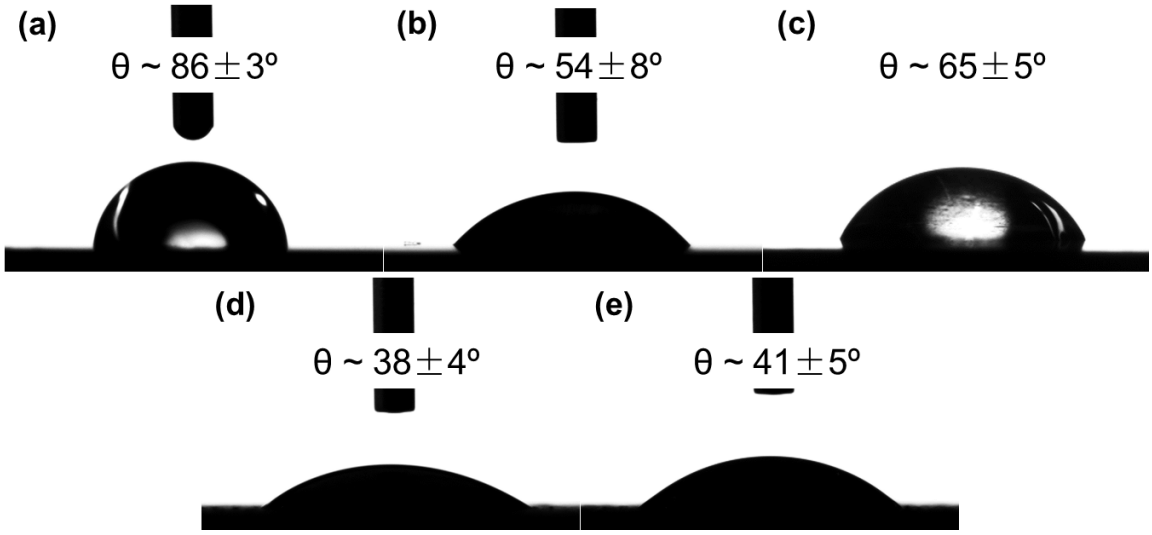

Figure 141: Water static contact angle measurements of the quenched surfaces: (a) smooth surface, (b) thin coating on smooth surface (CS-surface), (c) pre-oxidized surface, (d) rough surface, and (e) thin coating on rough surface (CR-surface).

4.5.2. Reference condition

Quenching experiments for the cylindrical Zirc-4 samples with the modified surfaces were carried out in saturated water at atmospheric conditions. The experiments for each condition were performed multiple times to ensure repeatability for experimental results. It was expected that the surface conditions (oxide layer, roughness, thin coating of $ZrSi_2$) may have a significant influence on boiling heat transfer during the quenching process. Quenching curves for the modified surfaces were plotted using the measurement of temperature-time data at the center of the sample during the rapid cooling step. This data was then used to calculate the surface temperature of the sample during the quench process. The high-speed images captured vapor film and bubble evolutions during the quenching test and were used for visual illustration of the surface effects on boiling regimes. Finally, minimum film boiling points depending on surface conditions were determined.

Quenching Curves and Boiling Curves

In Figure 142, both quenching and boiling curves for the five types of surfaces in saturated water at ambient pressure are plotted. The bare Zirc-4 cooled from the initial temperature to equilibrium conditions the longest while the roughened surfaces (i.e., rough surface and coating rough surface) took the shortest to cool. During initial cooling, the roughened surfaces showed larger cooling rates compared to the smooth surfaces, corresponding to the large surface heat flux at high superheat in the boiling curves. For example, the heat flux for the bare surface in the stable film boiling (T_{wall} - T_{sat} = 400 K) was 76 kW/m^2 but that of the rough surface was 181 kW/m^2. It is interesting to note that surface heat flux for the roughened surfaces increased with decreasing surface superheat until the point showing the sudden increase of surface heat flux. This observation contradicts the general trend of a boiling curve in the stable film boiling regime; surface heat flux decreases with decreasing surface superheat due to thinning of the vapor layer. The phenomenon shown in the roughened surfaces is called a "climbing effect" in the present study. This climbing effect will be discussed more at the end of this section. Inflection points were identified in the all conditions and the points were indicative of a change of boiling regimes. Near the inflection point, a wetting front passed by the center of the sample where the thermocouple was installed, being accompanied by development of individual bubbles.

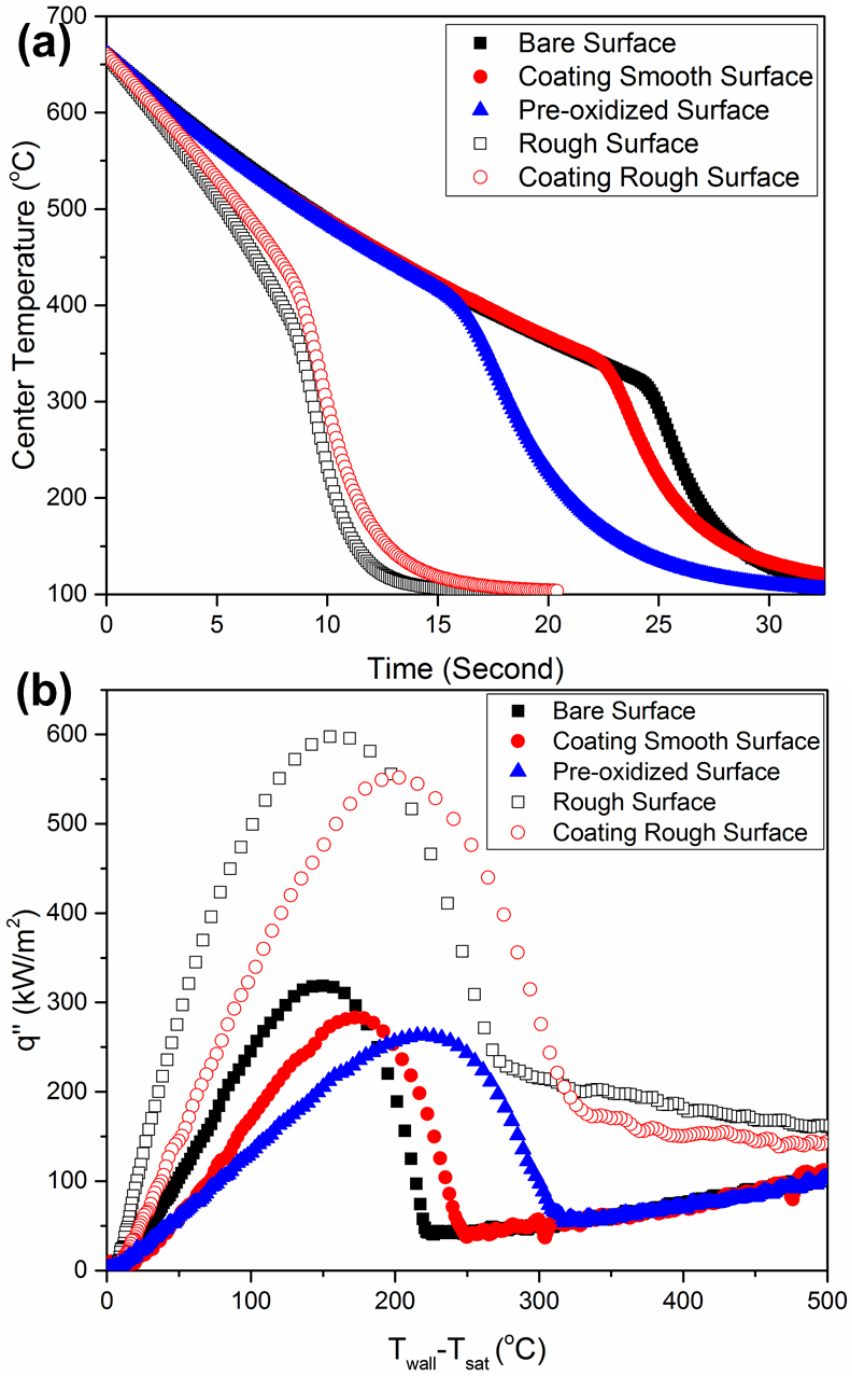

Figure 142: (a) Quenching curves and (b) boiling curves of modified surfaces in saturation water at atmospheric pressure. The experimental reliability of the tests was discussed in section 4.4.1.

Bubble Dynamics

Bubble dynamics, observed by the high-speed imaging, is helpful to elucidate the mechanisms underlying the distinct boiling curves that depend on the surface conditions. As presented in Figure 143,

snapshots of the hot sample submerged in the saturated water are displayed as the quenching process progressed. The classical bubble dynamics that shown in the bare Zirc-4 sample were also revealed in the smooth surface conditions (CR-surface and pre-oxidized surface). At the initial temperature, the stable vapor layer with oscillatory motions completely covered the hot specimen, and its thickness decreased with decreasing surface superheat. When the surface temperature reached the transition temperature, a large vapor bulge grew at the bottom of the sample, indicating an initiation of transition boiling. The quenching front (i.e., wetting front) propagated toward the top of the sample followed by a nucleation of individual bubbles on the surface. Even if the timing or surface superheat were different, the trends were identical among the smooth surfaces. On the contrary, the rough surface conditions (rough surface and CR-surface) revealed a remarkable discrepancy from the classical bubble dynamics. Even at the highest surface superheat, fluctuation of the vapor layer was so strong that small bubbles escaped from the thick vapor layer. The stable film boiling regime was not identifiable, but the vigorous vapor generation being displayed for the smooth surface conditions in the transition boiling regime was maintained until the nucleation boiling regime started at the bottom of the sample. In short, there was no distinct transition from the stable film boiling regime to the nucleation boiling regime in the rough surface conditions. As a wetting front propagated upward, small bubbles were nucleated and departed from the sample surface. A large number of bubbles grew on the roughened surfaces compared to those on the smooth surface conditions. This is because there were many cavities, which acted as bubble nucleation sites on the roughened surfaces.

Dynamic changes of the vapor layer thickness were measured in the middle of the sample. Surface temperatures as a function of quenching time are shown in Figure 144. As observed in the bare Zirc-4 in the previous chapter (4.4), the three types of smooth surface conditions (Figure 144a-c) showed the classical vapor generation. In the range of the minimum film boiling temperature (around the inflection point in the cooling curve), a wavy motion of vapor layer was amplified significantly, leading to the destabilization of the stable vapor film. The termination point appears to be affected by both the thin coating and the surface oxidation. Earlier collapse of the stable vapor layer was identified in the pre-oxidized surface and the CS-

surface. It is postulated that the smaller heat diffusivity of the zirconium oxide layer or $ZrSi_2$ thin film on the surface led to the earlier destabilization of the stable vapor film. Vapor layer dynamics for the roughened conditions (Figure 144d-e) were dissimilar to those for the smooth conditions. The wavy motion of vapor film was so strong even in the high superheat that it was difficult to define the point of destabilization of the stable vapor film. The large magnitude of the vapor fluctuation ended if the nucleation boiling regime developed. Additionally, an effect of a thin surface coating on the roughened surfaces was not clearly identified. Detailed discussion in regards to the effects of modified surfaces on bubble dynamics will be followed in later chapter (Chapter 4.6).

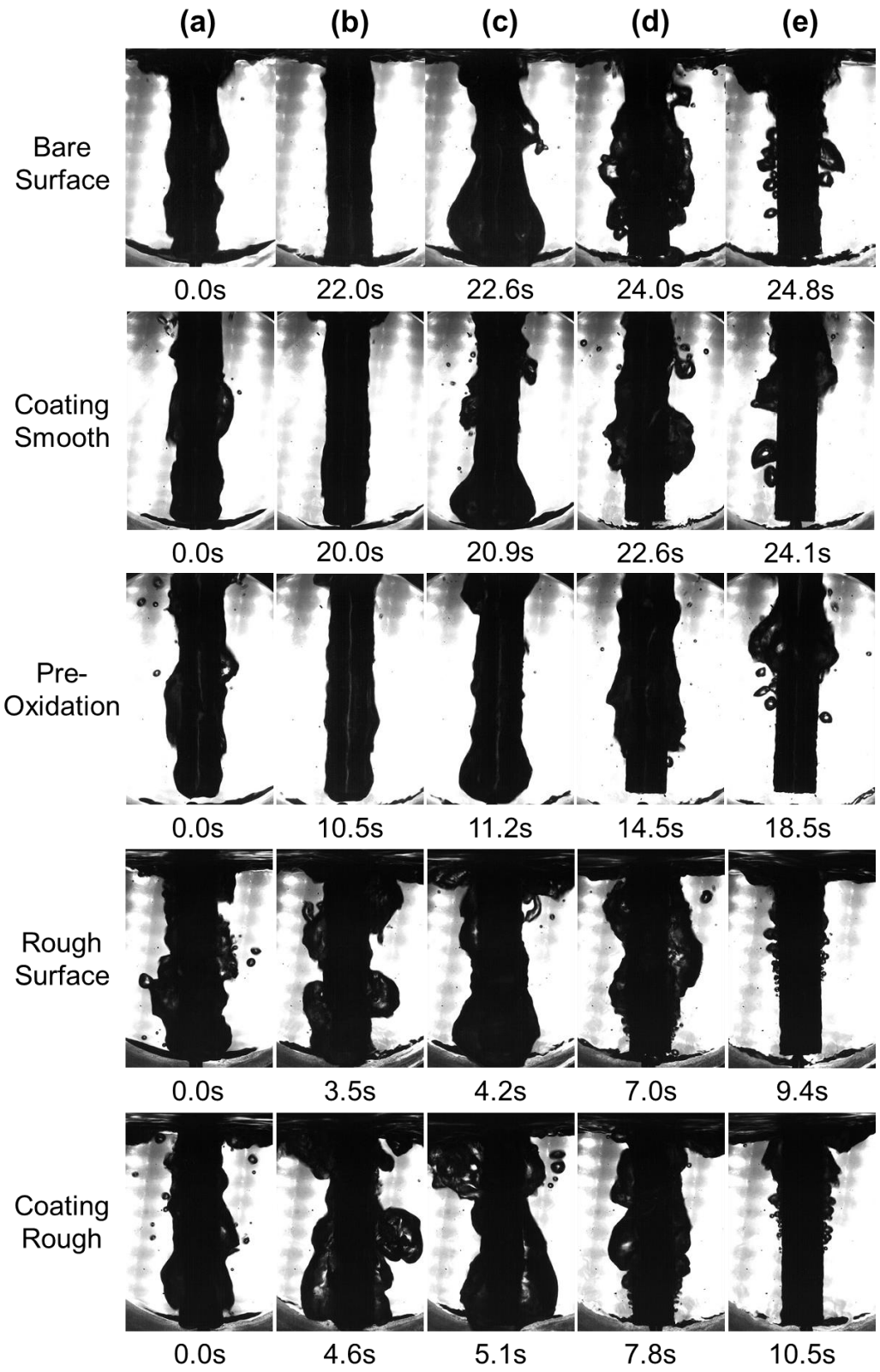

Figure 143: High-speed images (100fps) of bubble evolution on the modified surfaces during quenching tests in saturated water at atmospheric pressure.

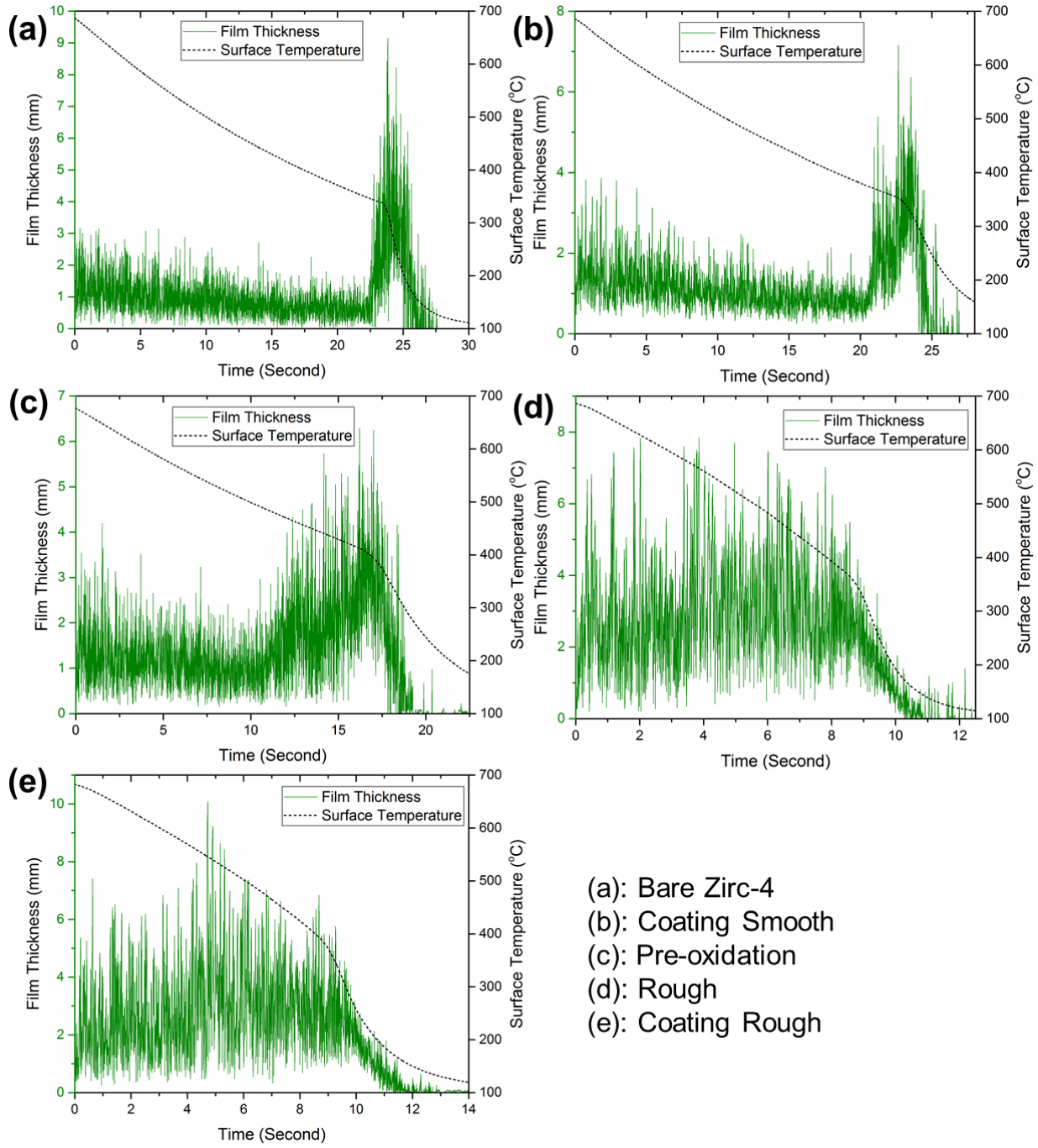

Figure 144: Vapor layer thickness (green) and estimated surface temperature (black dash) for the modified surfaces during a quenching test in saturated water at ambient pressure.

Average film thickness for the modified surfaces at high wall superheat based on the high-speed images and a quadratic polynomial fit is presented in Figure 145. Average thickness of the vapor film for the bare surface, the CS-surface, and pre-oxidized surface decrease gradually as quenching time increases. It is consistent with the typical observation of the stable film boiling regime. However, the averaged vapor

thickness for the roughened surfaces (rough surface and CR-surface) increases with cooling time. It is believed that a boiling regime for the roughened surfaces is quite different from that for the smooth surfaces at the high wall superheat. Surface superheat in the range of 400 – 500 K, the stable film boiling was observed in the smooth surface conditions but the transition boiling accompanied by the vigorous vapor generation due to partial liquid-solid contact was appeared in the roughened surface conditions.

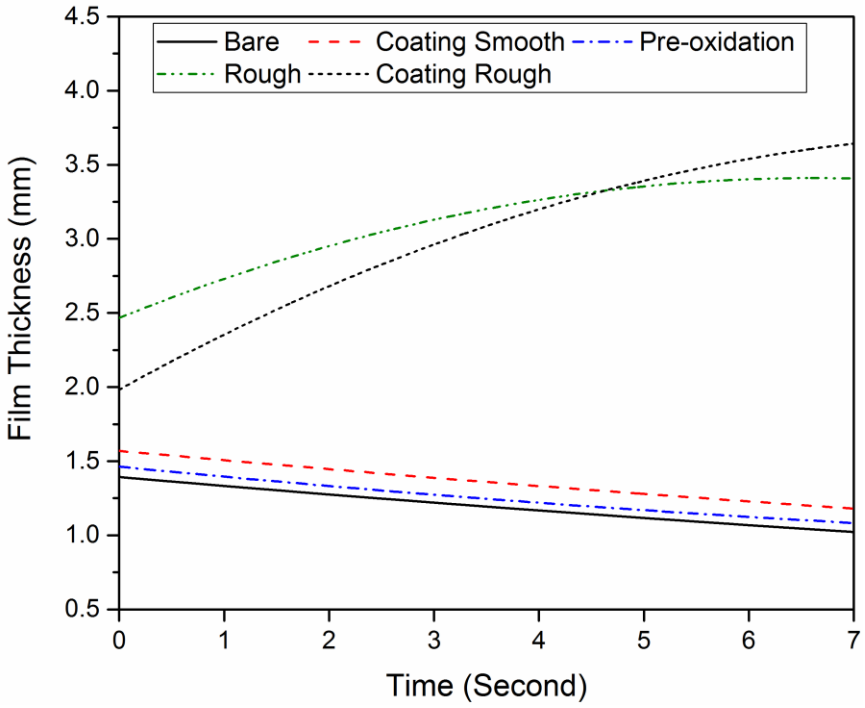

Figure 145: Averaged vapor film thickness for the modified surfaces using a quadratic polynomial fit suing the high-speed images at initial quenching process.

Figure 146 shows oscillations of the liquid-vapor interface during the initial quenching process for the bare surface and for the rough surface in saturated water at atmospheric pressure. The amplitude of the wavy motion is strongly enhanced by the increase in surface roughness, and we consider that the phenomenon is a result of amplified partial liquid-solid contacts. However, noticeable dependency of frequency of the oscillatory motion on the degree of surface roughness was not clearly identified. For instance, the frequency for the bare surface was 34 ± 2 oscillations per second but that for the rough surface was 36 ± 4 oscillations per second. Moreover, interfacial oscillations for the oxidized surfaces, the CS-

surfaces, and the CR-surfaces were 34 ± 2, 34 ± 2, and 36 ± 5 during the quenching period, respectively. The three quenching tests for the conditions were performed to obtain the experimental uncertainties.

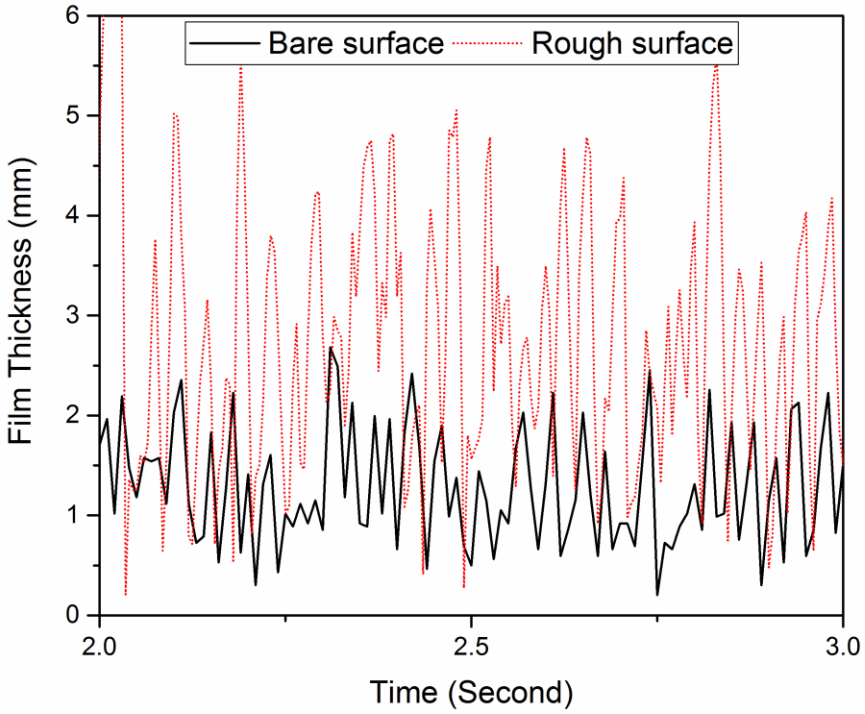

Figure 146: Fluctuation of vapor film at high wall superheat for the bare surface (black line) and the rough surface (red dots). The vapor film thickness was measured by high-speed images (100 fps).

Minimum Film Boiling Temperature

Minimum film boiling temperature in the saturated water at atmospheric pressure for the bare Zirc-4, the coating smooth surface (CS-surface), and the pre-oxidized surface was determined and shown in Figure 147. The characteristic temperature for each condition was averaged from more than three experimental data points. The pre-oxidized surface with about 56 μm oxide layer had the highest minimum film boiling point (at 432 °C) in the saturation water, which is 33 % higher than the bare conditions. The CS-surfaces with 2.2 μm $ZrSi_2$ surface coating improved the minimum film boiling temperature slightly so that it was approximately 20 K higher than that of the bare surface. In accordance with the T_{min} criterion described in Section 3.5.3, the roughened surfaces did not show the lower limit of the stable film boiling regime during the quenching experiments. Therefore, the roughened surfaces values were excluded in Figure 147. The boiling curves for the rough surface and the CR-surface in Figure 142b do not display a sign change of

surface heat flux rate in the temperature range that the smooth surfaces show the stable film boiling regime. Therefore, one may conclude that the roughened surfaces appear to have minimum film boiling temperatures above the initial temperature (~700 °C).

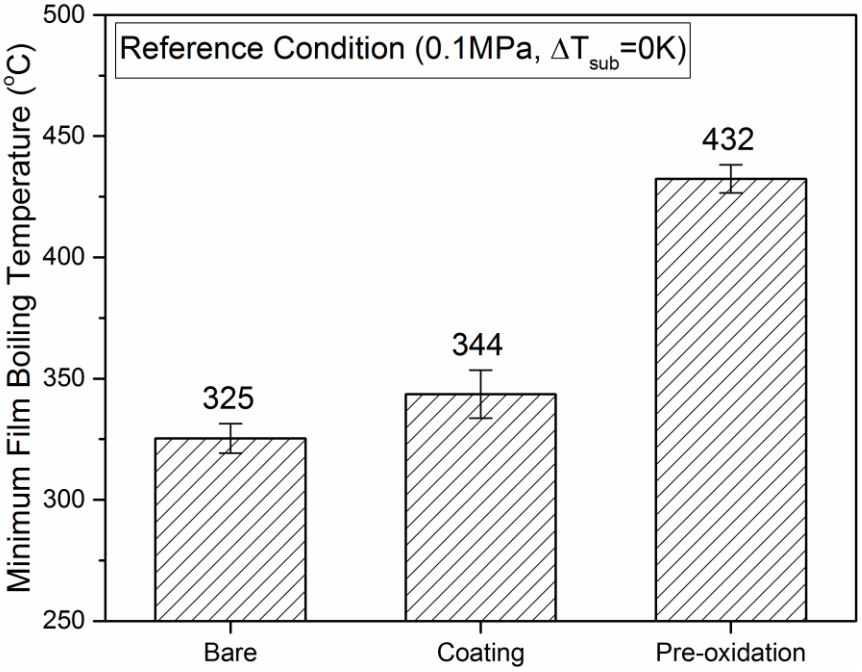

Figure 147: Surface temperature of minimum film boiling point for bare surface, CS-surface, and pre-oxidized surface at saturated conditions.

The climbing effect that was revealed in boiling curves for the roughened surfaces has been reported in the previous literature. They performed quenching experiments for different types of modified surfaces in the saturated water as shown in Figure 148. Fan et al., [77] fabricated a superhydrophilic surface (water contact angle ~ 0°) on a 304 stainless steel sphere using a silica nanoparticle deposition. The boiling curve for the modified surface (Figure 148a) showed the climbing effect instead of a decreasing heat flux as the wall superheat decreased. It is believed that the nanoparticle deposited surface might have the minimum film boiling point higher than the initial surface superheat (200 K). Micro-porous CuO structures (100 μm in height) on a brass sphere were prepared by Kang et al., [145] and the boiling curves for the modified surface was plotted as shown in Figure 148b. The climbing effect is also presented in the boiling curve for the micro-structured surface. The authors assumed that the modified surface had the T_{min} point higher than the highest surface temperature (600 °C). Again, boiling curves for the rough surface and the bare surface

in the present study are shown in Figure 148c. It is reasonable that the enhanced surface roughness caused the increase of the lower limit of the stable film boiling above the initial sample temperature (700 °C). Based on the current criterion for the minimum film boiling temperature and the extended lines in the boiling curves, the T_{min} point for the rough surface might be around 710 °C.

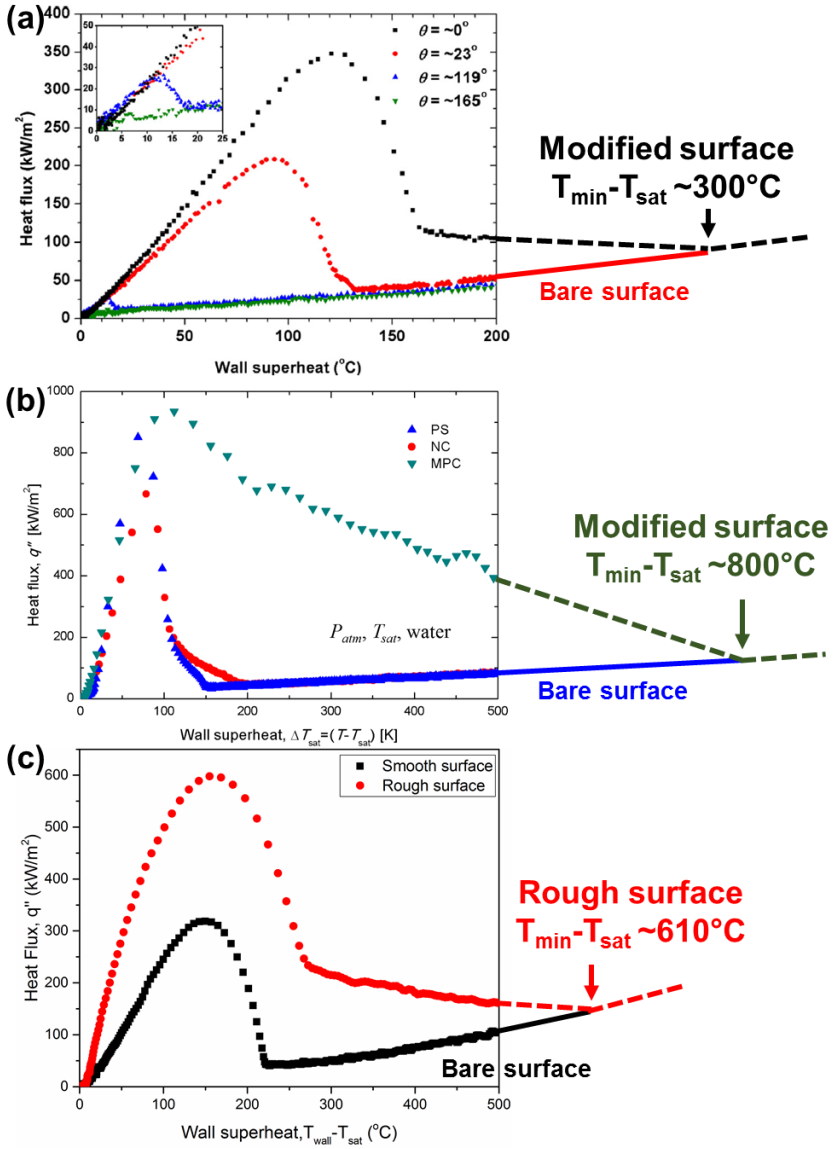

Figure 148: Comparison of the boiling curves for modified surfaces in saturated water reported in literatures and the present study. (a) Silica nanoparticle coating on a 304 stainless steel sphere (diameter of 10 mm) and the bare sphere [77], (b) CuO microparticle coating on a brass sphere (diameter of 15 mm) and the bare sphere [145], and (c) the cylindrical Zirc-4 sample with the rough surface and the bare sample. The extended lines indicate possible boiling curves above the temperature range.

4.5.3. Pressurized condition (0.5 MPa)

Quenching experiments for the five types of the modified Zirc-4 surfaces (bare surface, thin $ZrSi_2$ coating on smooth surface, pre-oxidized surface, rough surface, and thin coating on the rough surface) were performed in saturated water at a pressure of approximately 0.5 MPa. In the previous section (4.5.2), the modified surfaces had significant effects on quenching behaviors under saturated water. The surface effects were also investigated with measurements of temperature-time data using a thermocouple installed in samples in the pressurized condition (0.5 MPa). High-speed images that record the dynamics of vapor generation on the modified surfaces provided information about transitions of boiling regimes. Due to a limited access to the high-speed camera, bubble dynamics for the pre-oxidized surface were not recorded. Finally, minimum film boiling points for the modified surfaces were discussed.

Quenching Curves and Boiling Curves

Quenching curves for the modified surface in saturated water at the high pressure (0.5 MPa) is shown in Figure 149a. The cooling time for the surfaces under high system pressure were shorter than those under atmospheric pressure. The bare surface had the longest cooling time from the initial temperature to the surrounding water temperature, but the thin coating on the rough surface (CR-surface) showed the shortest cooling time. Enhanced cooling performance was provided by not only surface roughness but the thin coating and the surface oxidation. The effects of modified surfaces can be seen in the results of the boiling curves (surface superheat vs. surface heat flux) shown in Figure 149b. Because of the high system pressure, stable film boiling regimes for the smooth surfaces (bare surface, CS-surface, and pre-oxidized surface) were observed only at high wall superheat temperatures ($T_{sup} > 400K$). The thin coating and the surface oxidation had the minimum film boiling point temperature higher than the bare surfaces. Similar to the boiling curves for the roughened surfaces at atmospheric pressure, a climbing effect was identified in the rough surfaces and CR-surfaces. It indicates that the stable film boiling regime for the roughened surfaces did not fully develop even at the high wall superheat. It is speculated that micro-features on the surfaces enable the liquid-vapor interface to instantaneously make contact to the hot surface at high wall superheat,

resulting in a large heat transfer in the stable film boiling. For instance, surface heat flux for the bare surface in the stable film boiling (at T_{wall} - T_{sat} = 411 K) was 127 kW/m^2 but that of the rough surface was 503 kW/m^2. The factor of improvement of surface heat flux was approximately four via the surface roughening, which is larger than that at atmospheric pressure. Therefore, roughness effects on the boiling heat transfer during quenching appear to be amplified under elevated system pressures.

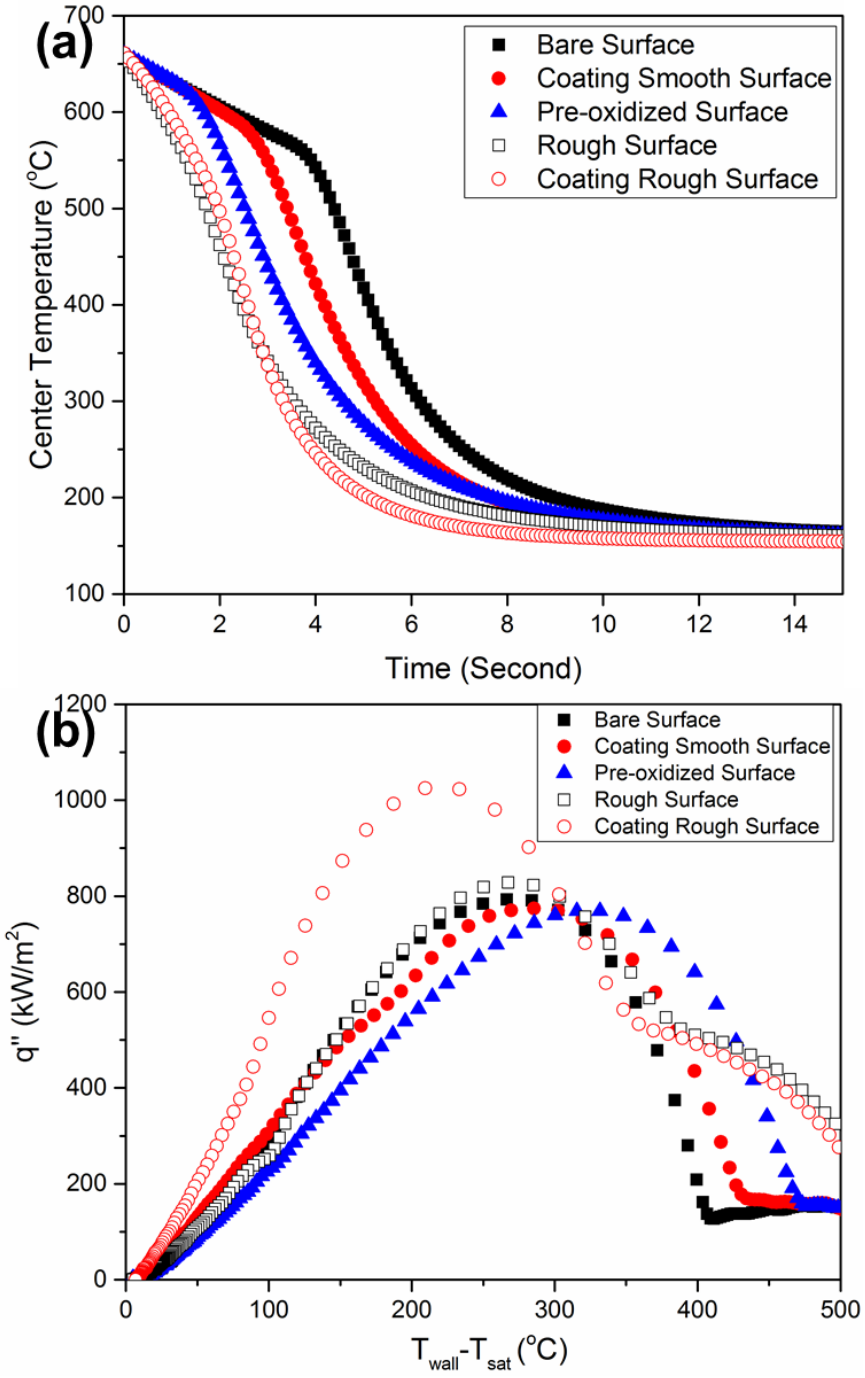

Figure 149: (a) Quenching curves and (b) boiling curves for the modified surfaces in saturation water at 0.5 MPa condition.

Bubble Dynamics

Snapshots of vapor generation on the modified surfaces (bare Zirc-4, CS-surface, rough, and CR-surface) during the quenching tests at 0.5 MPa are shown in Figure 150. The bubble dynamics on the CS-

surfaces were in a good agreement with the typical boiling regimes. However, the stable film boiling regime for the CS surfaces was destabilized earlier than that of bare surface. For example, the CS-surface had a formation of a large vapor bulge on the bottom of the sample at 1.9 seconds after the sample insertion, but the bare surface showed the same phenomenon at 3.2 seconds. The boiling process was slightly accelerated by the thin surface coating. The roughness effect on bubble dynamics is evident. During the initial insertion, violent expansion of a vapor film on the entire surface of the cylindrical sample was observed and the stable wavy motion were not displayed. Onset of termination of the strong vapor generation occurred at the bottom of the sample followed by the nucleation of tiny bubbles. Finally, boiling heat transfer was completed earlier than the smooth surfaces. The observations are quite similar to the bubble dynamics for the roughened surfaces in the saturated water at atmospheric pressure. Additionally, many bubble nucleation sites were identified regardless of the surface conditions under the increased system pressure.

Figure 151 shows vapor film thickness and surface temperature as a function of increasing quenching time for the bare surface, the CS-surface, the rough surface, and the CR-surface at 0.5 MPa. As presented in section 4.4.2, the bare surface revealed the classical dynamics of the vapor thickness. Gentle oscillations of a vapor film were observed in the early quenching, and the fluctuations were enhanced near the minimum film boiling point, associated with the inflection point in the surface temperature-time curve. As shown in Figure 151b, the thin surface coating accelerated boiling heat transfer modes to some extent. A stable film boiling regime was observed for a shorter period (~ one second) than that of the bare surface (~ three seconds). Moreover, the inflection point in the surface temperature-time curve is identified a few seconds earlier than the bare surface. However, the modest wavy motion of a vapor film at the early cooling process was not shown in the roughened surface conditions (Figure 151c-d). Instead, large amplitudes of vapor oscillations maintained until onset of nucleation boiling regime. The amplitudes of a vapor film are comparable to the vapor fluctuation for the smooth surfaces around the wall superheat of inflection points. In addition, it is difficult to distinguish the inflection point in the surface temperature-time curves for the roughened surfaces, meaning that a minimum film boiling point does not exist in the quenching experiments.

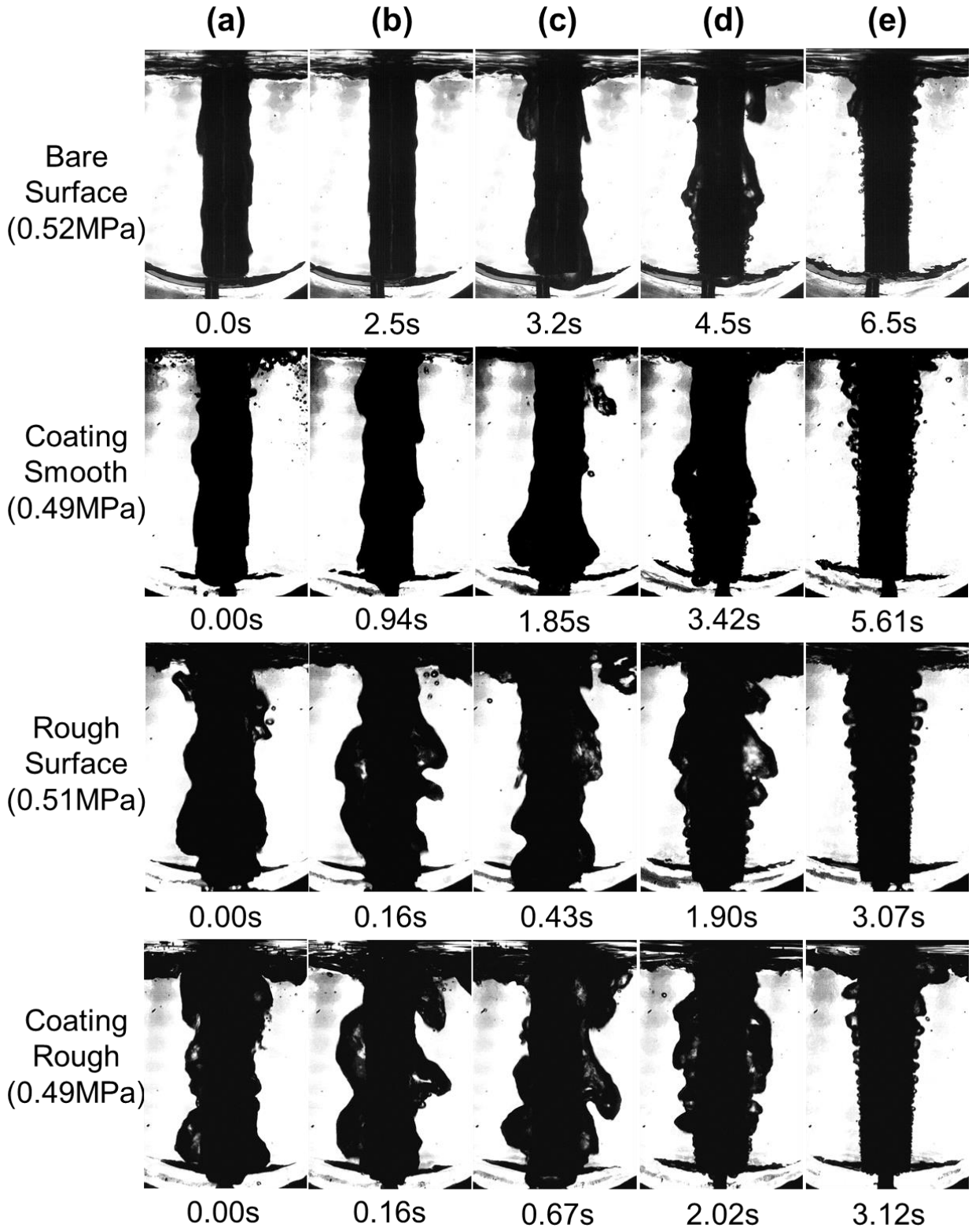

Figure 150: High-speed images (125 fps) of bubble dynamics on the modified surfaces during quenching experiments in the saturated water around 0.5 MPa.

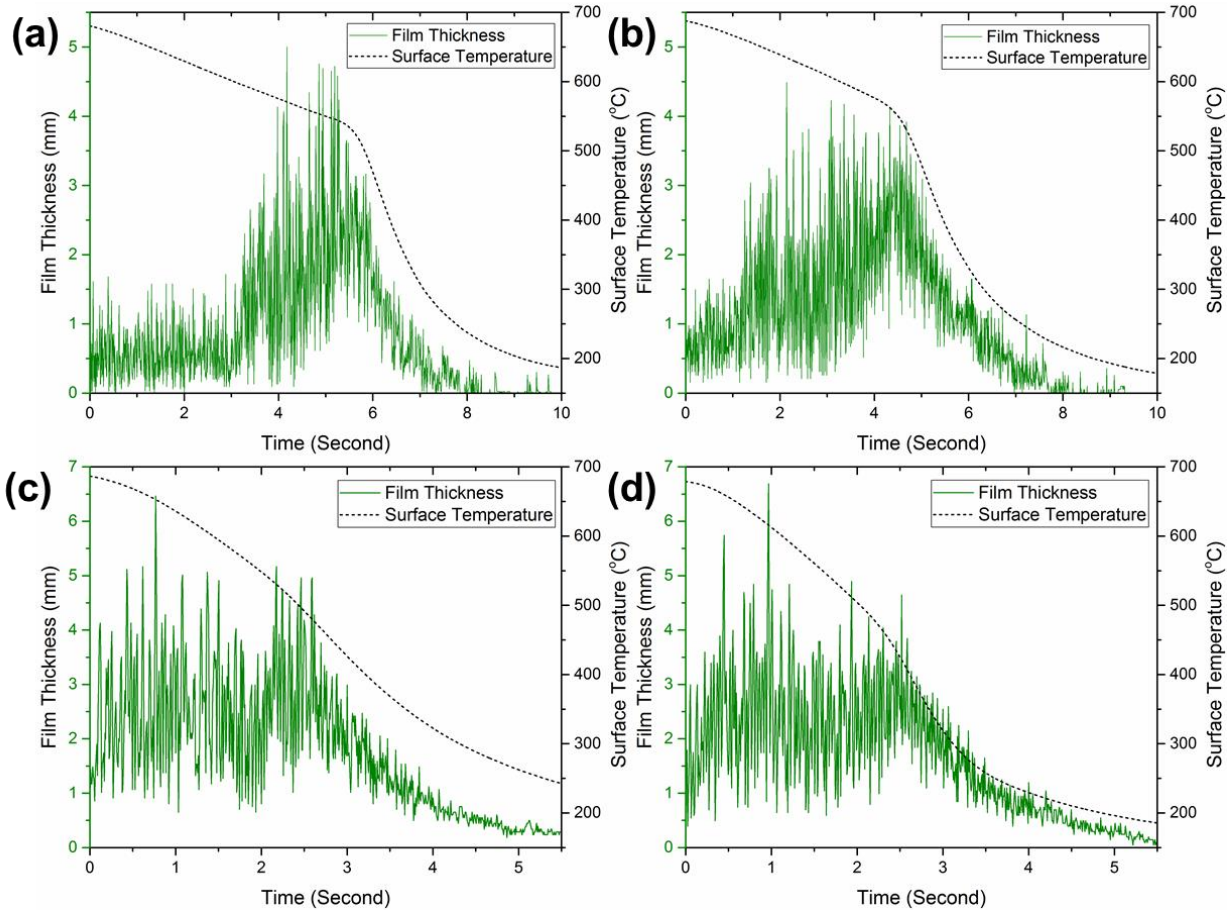

Figure 151: Vapor film thickness (green) and estimated surface temperature (black dash) for the modified surfaces during quenching tests in saturated water at 0.5 MPa.

Average film thickness for the modified surfaces during the initial quenching are presented in Figure 152. At the high wall superheat, the two roughened surfaces had a vapor layer four times thicker than the smooth surfaces. Again, the roughness effect on bubble dynamics was confirmed at the high pressure. It is interesting to note that the film thickness for the smooth surfaces is approximately one third of the vapor thickness at atmospheric pressure (section 4.5.2) due to the pressure effect. On the contrary, the film thickness for the roughened surfaces is not significantly affected by the increased system pressure. In addition, the trend shown in atmospheric conditions that the CS-surface had a slightly thicker vapor layer than the bare surfaces is also observed in the high pressure.

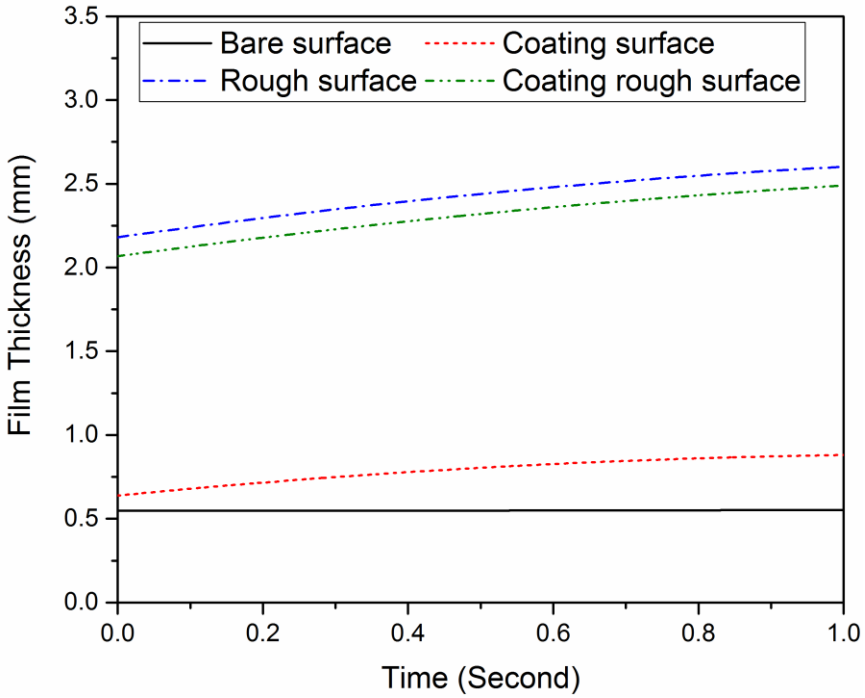

Figure 152: Average vapor film thickness for the modified surfaces at 0.5 MPa using a quadratic polynomial fitting of the high-speed images at initial quenching process.

Detailed plots showing an oscillatory motion of the vapor film for the bare Zirc-4 and the rough Zirc-4 during the initial cooling under 0.5 MPa are shown in Figure 153. Large fluctuations of the vapor-liquid interface are observed in the rough surface condition. In addition, frequency of the oscillations for the rough surface and the bare surface was determined to be 33 ± 2 oscillations per second and 37 ± 3 oscillations per second, respectively. Furthermore, the coated rough surfaces and the coated smooth surfaces had 31 ± 1 oscillations per second and 42 ± 2 oscillations per second, respectively. The figure is shown in the Appendix. A frequency of the wavy motion was slightly decreased by the surface roughness, which was not shown under atmospheric pressure.

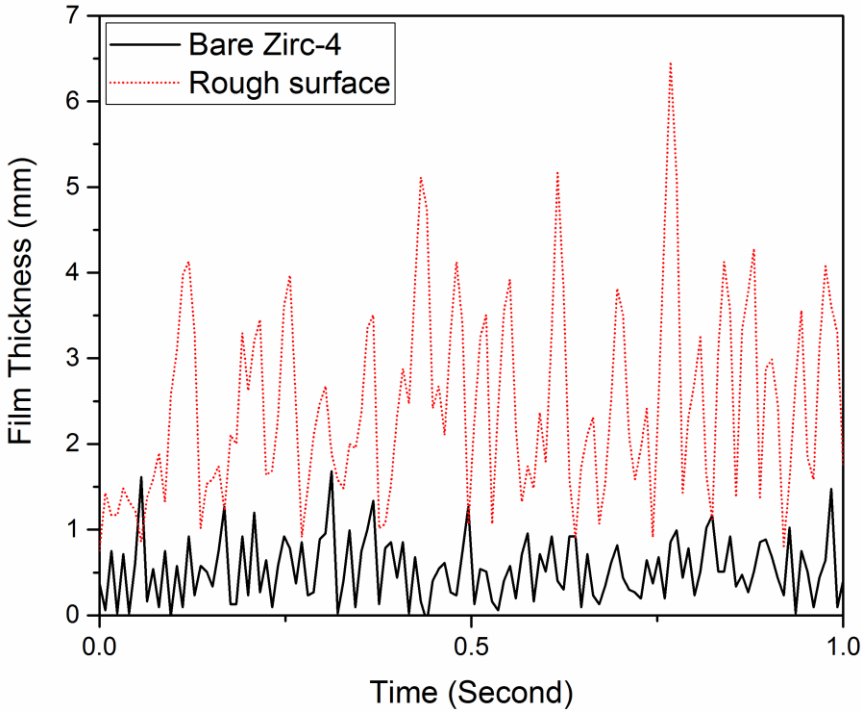

Figure 153: Wavy motion of vapor film of the bare Zirc-4 (black line) and the roughened Zirc-4 (red dots) at the initial quenching under the pressurized condition (0.5 MPa). The vapor layer thickness was measured by the high-speed images (125 fps).

Minimum Film Boiling Temperature

In accordance with the criterion for a minimum film boiling temperature, an average lower limit temperature of stable film boiling regime for the bare Zirc-4, the coating smooth surfaces, and the pre-oxidized surfaces is presented in Figure 154. Since the climbing effect was observed in the roughened surfaces, the characteristic temperatures are assumed to exist above the initial sample temperature (700 °C). The trend confirmed in the saturated water (section 4.5.2) is also revealed in the pressurized condition (0.5 MPa); the modified surfaces with the thin coating or the oxide layer had a higher T_{min} point than the bare surfaces had. Because the surfaces have similar surface smoothness and wettability, changes of thermal properties due to the thin surface coating or the air oxidation might be a major reason to induce the acceleration of the boiling performance.

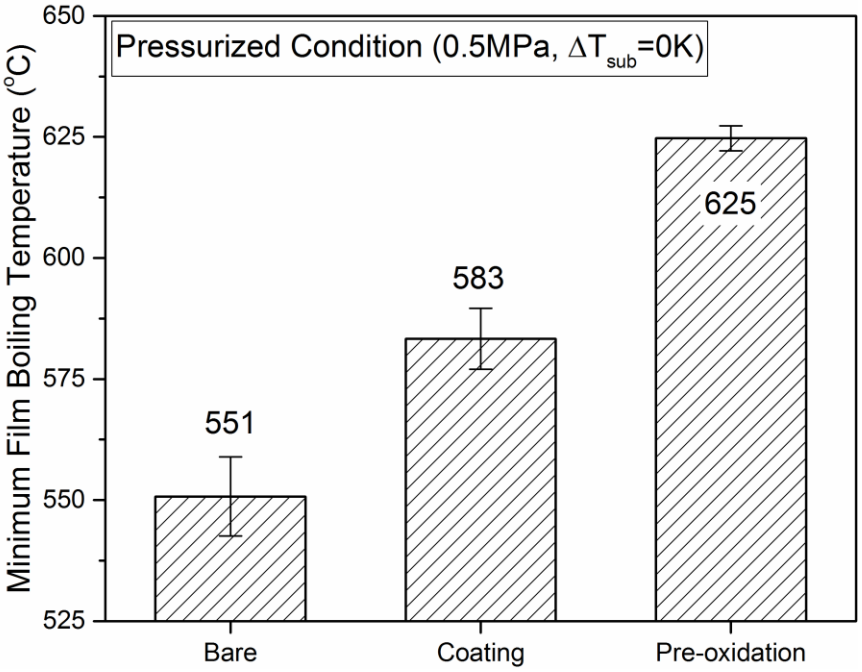

Figure 154: Average minimum film boiling temperature for bare surfaces, CS-surfaces, and pre-oxidized surfaces in saturation water at 0.5 MPa.

4.5.4. Subcooling condition (ΔT_{sub} = 15K)

Quenching performance of the modified surfaces in subcooled conditions at ambient pressure was investigated in this section. The degree of water subcooling was approximately 15 K (i.e., 85 °C water) in the experiments. Temperature-time data at the center of the samples were acquired to plot boiling curves and to determine a minimum film boiling temperature. High-speed images were analyzed by the post-imaging process to demonstrate the effect of surface properties on bubble dynamics. Due to a limit access to the high-speed camera, images for the pre-oxidized surfaces were not recorded.

Quenching Curves and Boiling Curves

Figure 155 shows the cooling and boiling curves of the samples with the surface modifications at 15K subcooled condition in atmospheric pressure. Due to the subcooled effects, all the curves were shifted to the left compared to those of the saturated water. The roughened surfaces (rough surface and coat-rough surface, CR-surface) revealed the shortest cooling time and the bare surface showed the longest cooling time. Total cooling time for the pre-oxidized surface was shortest in the smooth surface conditions. The

CR-surface had a slightly longer cooling time than that of the rough surface. The inflection points for the roughened surfaces were less distinct than those of the smooth surfaces. All the observations are consistent with the observations in both the atmospheric pressure (section 4.5.2) and the pressurized conditions (section 4.5.3). The shift of the quenching curves for the roughened surfaces indicates the presence of roughness effects on boiling performance in the subcooled water. In addition, the boiling curves for the modified surfaces in the subcooled water are presented in Figure 155b. Considerable effects of the surface modifications are clearly identified. The climbing effect is again shown in the roughened surfaces at high wall superheat temperatures. On the other hand, the smooth surfaces (bare, CS-surface, pre-oxidation) showed the nearly flat heat flux region which corresponds to a stable film boiling regime. Surface heat flux was enhanced significantly by the surface features on the roughened surfaces. The surface heat flux on the rough surface at 400 K wall superheat was 397 kW/m^2, which is 2.9 times larger than that on the bare surface (138 kW/m^2 at 400 K superheat). The factor of improvement (2.9) is close to the value (2.4) in saturated water at atmospheric pressure, but the improvement factor is smaller than the enhancement (4.0) in the pressurized condition (0.5 MPa).

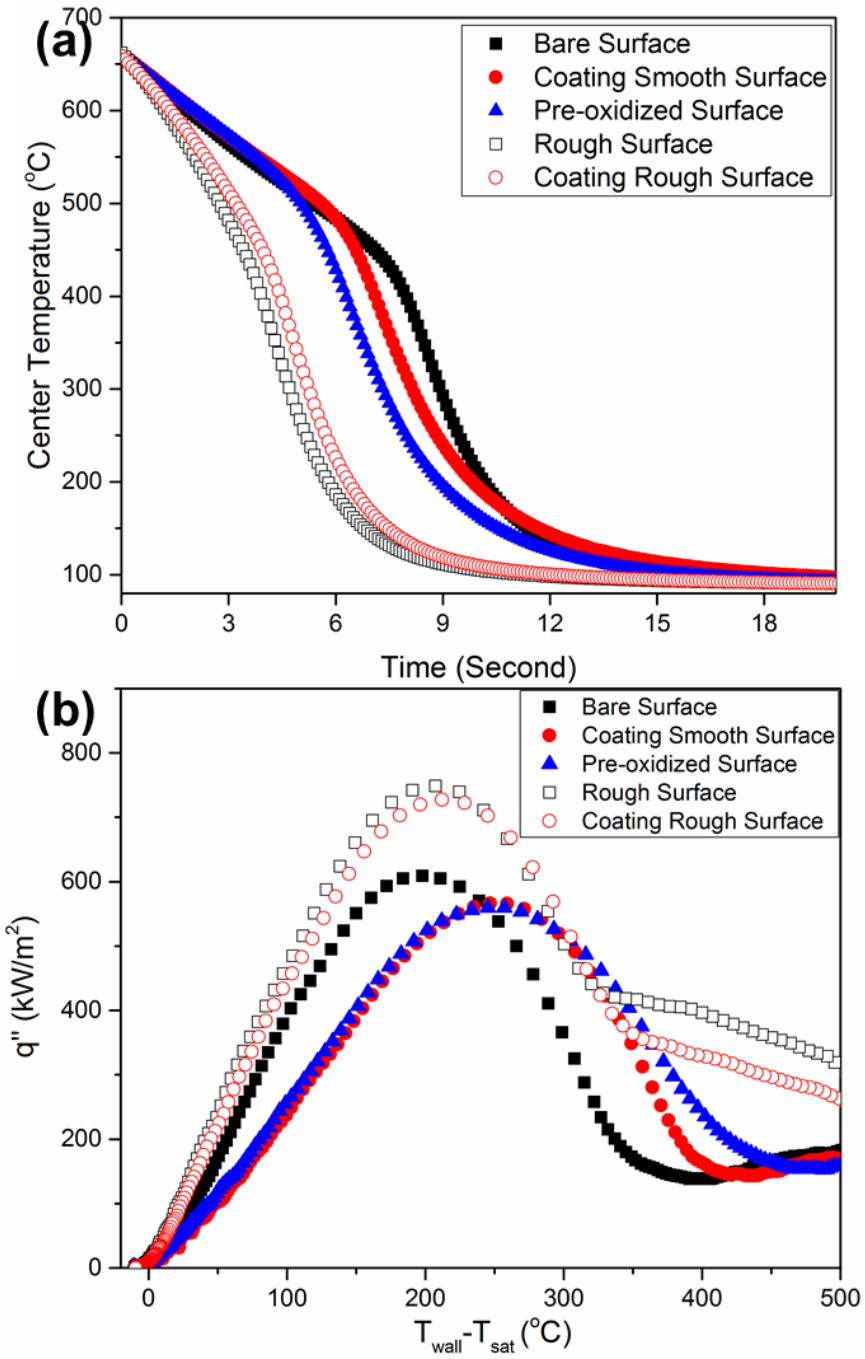

Figure 155: (a) Quenching curves and (b) boiling curves for the modified surfaces in subcooled water (ΔT_{sub}=15K) at atmospheric condition.

Bubble Dynamics

The visualization results of the modified surfaces in the subcooled water are summarized in Figure 156. During the initial stage of quenching, the subcooling effect led to the formation of a thin vapor layer

covering the bare surface and the CS-surface samples. The wavy motion of the vapor layers was less evident compared to the smooth surfaces in saturated water discussed in the previous section (4.5.2). As cooling time increases, the vapor film started to destabilize at the bottom of the test sections, and a wetting front moved toward the top of the test sections. The individual bubble size of the CS-surface in the nucleate boiling regime was generally larger than that of the bare surface, which was attributed to the improved hydrophilicity (water-attraction) by the thin surface coating (please see section 4.5.1). Eventually, the boiling process on the surfaces was terminated and eventually reached a natural convection regime. On the contrary, boiling visualization for the roughened surfaces showed distinctive features. Once the hot samples were immersed in the subcooled water, the vapor film covering the hot surface displayed large-scale perturbations and the vapor-liquid interface had many wiggles. The strong interfacial movement was disrupted by formation of a large vapor bulge at the bottom of the sample followed by the propagation of the wetting front toward the top of the sample. The boiling process for the roughened surfaces was completed faster than the smooth surfaces.

The dynamic change of the vapor film thickness at the center of the cylindrical samples and surface temperature as a function of the cooling time are presented in Figure 157. In smooth surfaces conditions (Figure 157a and Figure 157b), a thin vapor layer with the oscillations and a gradual decrease of surface temperature were shown during the initial quenching, corresponding to the stable film boiling regime. Once the surface superheat cooled down to a minimum film boiling temperature, a large amplitude of the vapor and an inflection point in the surface temperature-time curve were identified. As reported in the last two sections, the dynamics of vapor layer thickness were affected by high surface roughness. As shown in Figure 157c and Figure 157d, large scaled perturbation of the vapor-liquid interface was displayed even in the early stage of quenching, and the behavior was continued until the initiation of the nucleation boiling regime. In addition, the inflection point in the surface temperature-time curve was less evident. It appears that a local wetting (i.e., liquid-solid contacts) at high wall superheats is more effective on the roughened surfaces, leading to generation of a large amount of vapor and enhanced oscillatory motions of the vapor-

liquid interface. The roughness effects in the subcooled water are in good agreement with those in the saturated water at atmospheric pressure.

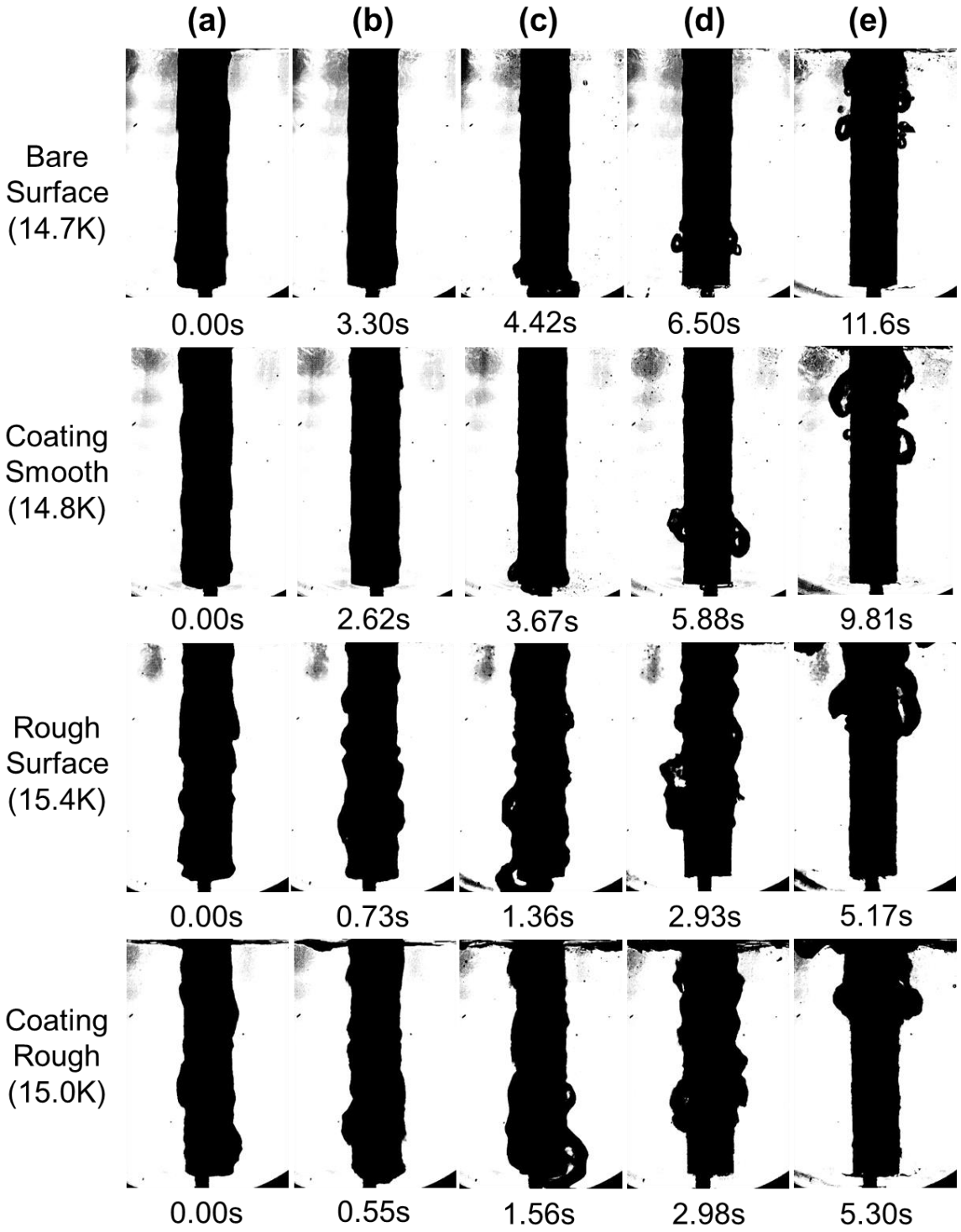

Figure 156: High-speed images (125 fps) of bubble dynamics on the modified surfaces during quenching experiments in the subcooled water (ΔT_{sub} = 15 K) at atmospheric pressure.

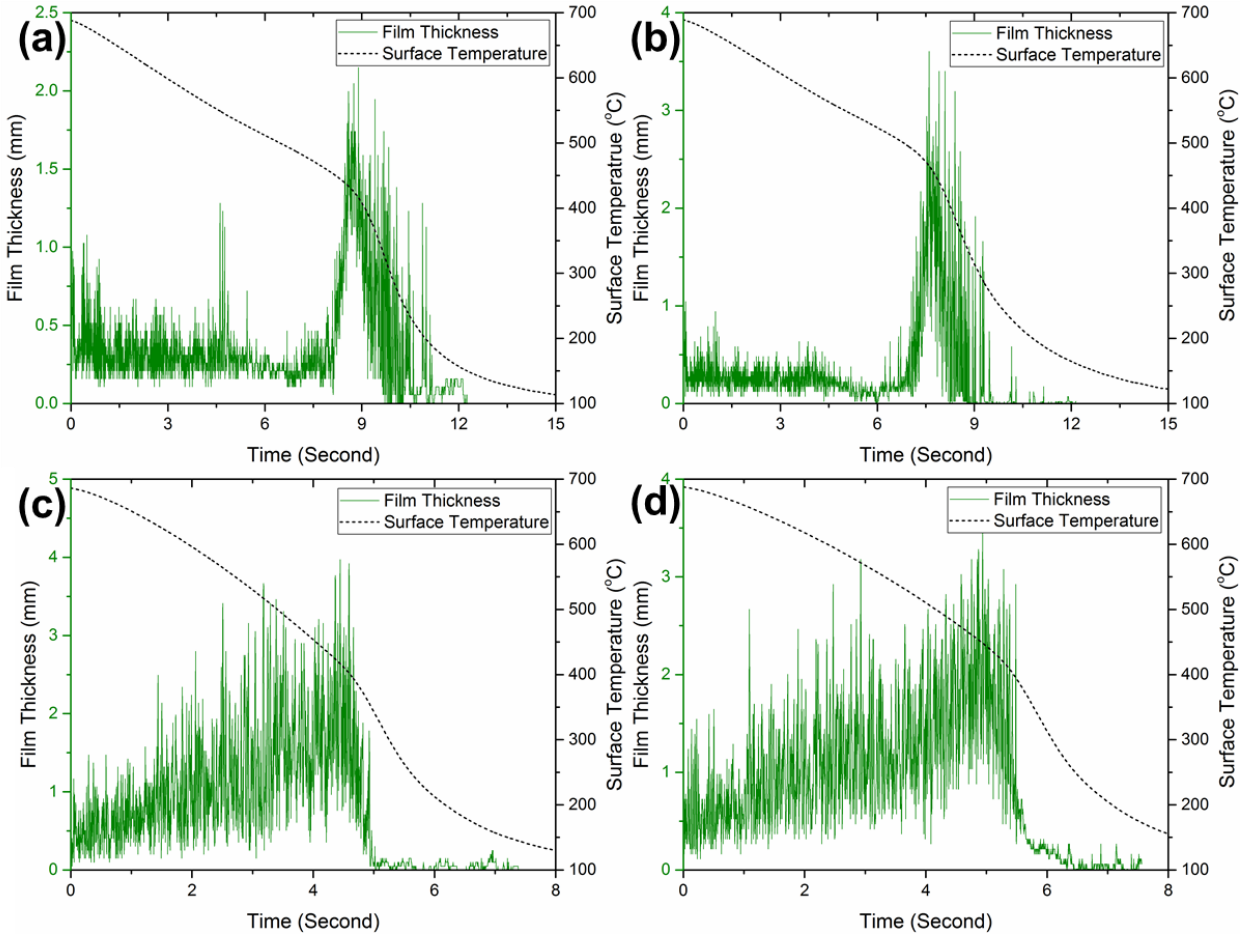

Figure 157: Vapor film thickness (green) and surface temperature (black dash) for the modified surfaces during quenching tests in subcooled water (ΔT_{sub} = 15 K) at atmospheric pressure.

Figure 158 shows the average vapor film thickness for the modified surfaces obtained by a quadratic polynomial fitting during the early quenching step under the subcooled conditions (ΔT_{sub} = 15 K). First, all the modified surfaces were substantially affected by the water subcooling so the vapor film thickness was much smaller than those under atmospheric saturated water. The vapor layer thickness for the smooth surfaces decreases monotonically as the cooling time progresses, being consistent with the general trend of the stable film boiling regime. The bare surface has a slightly thicker vapor layer than the CS-surface. However, measurement of the micro-scale vapor film under the subcooled water will have some uncertainties arising from the distortion of images (because of a convective motion of the liquid boundary layer) and the limited resolution of the high-speed images (approximately 50μm). The roughened surfaces had a different trend of vapor layer thickness; the average vapor thickness increased with increasing

quenching time in the range of high wall superheats. The results, both qualitative and quantitative, support that the stable film boiling regime does not develop on the roughened surfaces at the high surface temperatures.

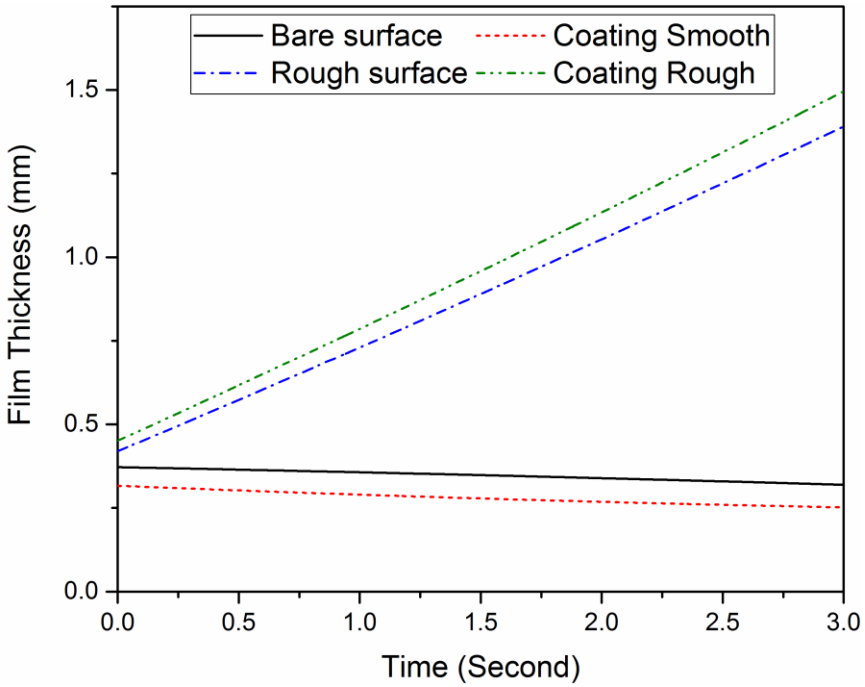

Figure 158: Average vapor film thickness for the modified surfaces in subcooled water (ΔT_{sub} = 15 K) using a quadratic polynomial fit of the high-speed images at early quenching process.

The fluctuation of the vapor-liquid interface on the bare surface and the rough surface during early quenching is presented in Figure 159. The amplitude of the oscillatory motion of the interface for the rough surface was significant when compared with the more mild and calm oscillations observed in the bare surface. Analysis of the CS-surfaces and the CR-surfaces revealed the same results, and the plots are shown in the Appendix. It appears that the frequency of the fluctuation is not a function of the surface conditions. For example, the bare surface and the rough surface had 42 ± 2 oscillations per second and 43 ± 5 oscillations per second in the range of high surface superheats, respectively. Furthermore, oscillations for the CS-surface and the CR-surface were 41 ± 2 and 40 ± 4 per second, respectively.

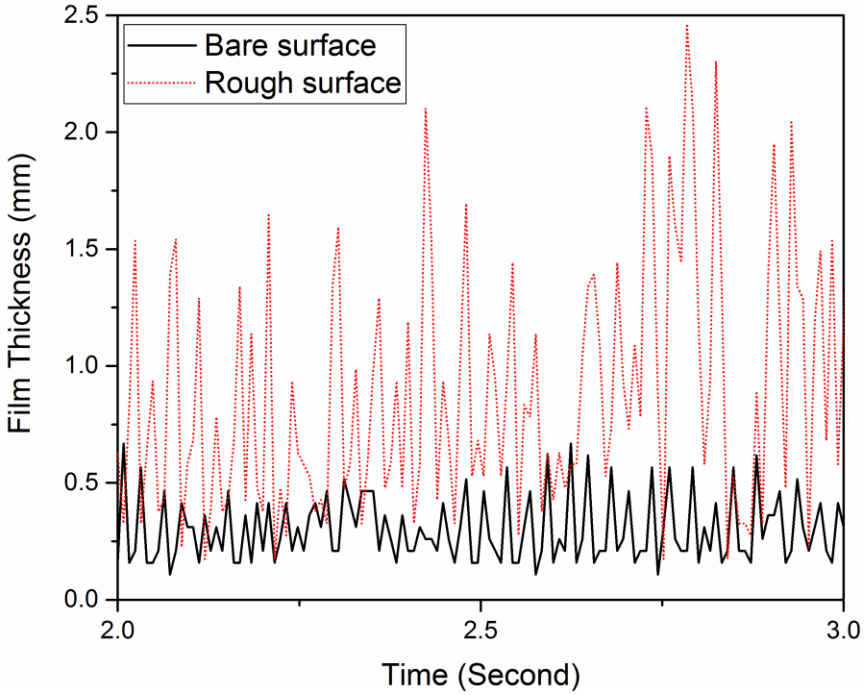

Figure 159: Wavy motion of vapor film of bare Zirc-4 (black line) and the roughened Zirc-4 (red dots) at the early quenching under subcooled water (ΔT_{sub}= 15 K) measured by the high speed-images (125 fps).

Minimum Film Boiling Temperature

Figure 160 shows an average minimum film boiling temperature of the bare surfaces, the CS-surfaces, and the pre-oxidized surfaces. The roughened surfaces were excluded in the analysis because a lower limit temperature of stable film boiling for the surfaces was assumed to be higher than the heated rodlet initial temperature. In general, the boiling process for all the smooth surfaces was accelerated by the water subcooling. Moreover, the minimum film boiling temperature was increased as a result of both the thin surface coating and the surface oxidation under the subcooled water conditions. This was also confirmed in the previous quenching experiments in saturated water. The increased temperature of termination of stable film boiling regime for the CS-surface and the pre-oxidized surface was 38 K and 102 K compared to the bare Zirc-4 surface, respectively. The extent of the improvement of the minimum film boiling temperature by the thin coating and the pre-oxidation is comparable with that in saturated water at atmospheric pressure. In conclusion, the surface modifications (i.e., a thin coating, surface oxidation, and increased surface roughness) are responsible for the enhancement of the boiling heat transfer in quenching under the subcooled water at atmospheric pressure and is qualitatively consistent with other test results.

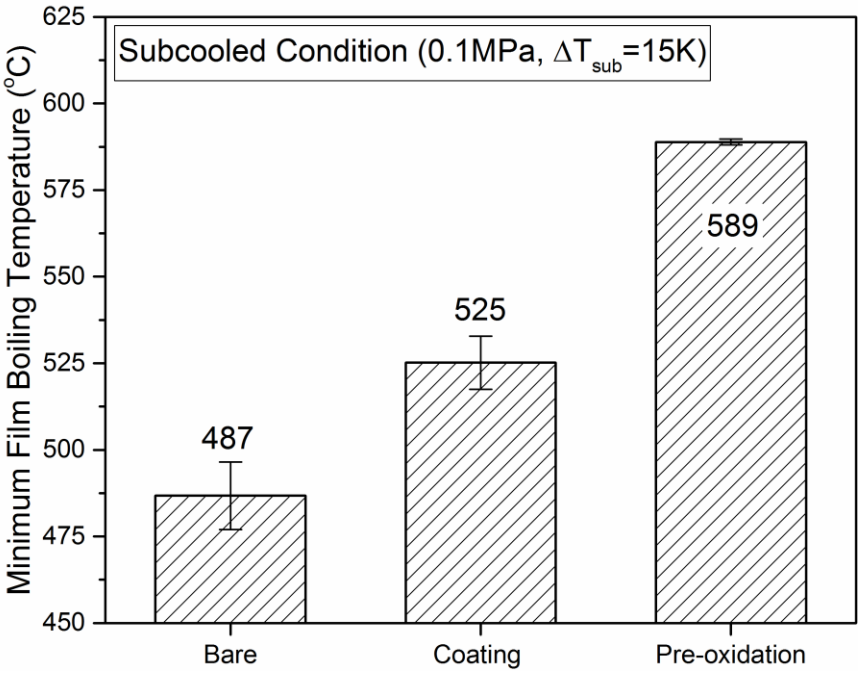

Figure 160: Average minimum film boiling temperature for bare surfaces, CS-surfaces, and pre-oxidized surfaces in subcooled water (ΔT_{sub}= 15 K) at atmospheric pressure.

4.6. Hypothesis of minimum film boiling temperature for the modified surfaces

In the last chapter (4.5), the effects of the modified Zirc-4 surfaces (a thin coating of $ZrSi_2$, an oxidized surface, and the roughened surfaces) on boiling heat transfer during quenching in water with different system conditions (i.e., atmospheric pressure, 0.5 MPa, and 15K subcooled water) had been investigated. Based on the quenching and boiling curves, all the modified surfaces enhanced cooling performance such as shortening the cooling time and increasing the minimum film boiling temperature regardless of the system conditions. Particularly, vapor film and bubble dynamics were strongly affected by surface roughness, resulting in the large surface heat flux during the early quenching process.

Potential mechanisms underlying the enhancement of boiling heat transfer by surface modifications reported in the literature are introduced in this chapter. Based on these past investigations, a plausible hypothesis with assumptions proposed to explain the augmented boiling heat transfer and the bubble dynamics on the modified surfaces. The prediction of minimum film boiling temperature based on the hypothesis was compared to experimental results. Finally, sensitivity analysis of this theoretical model for the prediction is discussed.

4.6.1. Hypothesis and Assumptions

Potential Mechanisms reported in the Literature

Past research proposed that surface roughness would promote a breakup of stable film boiling. The surface roughness features may penetrate a vapor layer covering the hot surface and contact with liquid, leading to disruption of the stable film boiling. Bradfield [146] observed water droplets behaviors on heated chrome plates and quenching behaviors of chrome-copper spheres with different surface roughness in subcooled water. He postulated that liquid-solid contacts existed in the stable film boiling regime, and the contacts are periodic on smooth surfaces, and it was quasi-continuous if sufficient surface roughness existed. Onset of liquid-solid contact may occur if maximum roughness element is equal to the thickness of the vapor layer in the stable film boiling. Ahn et al., [147] prepared multiwalled carbon nanotube (MWCNT) aligned vertically on flat silicon wafers used as a heater surface in subcooled or saturated test fluid (PF-5060). In the pool boiling experiments, the larger height of MWCNT structures (25 μm) enhanced surface heat flux in the film boiling regime and increased the Leidenfrost point compared to shorter MWCNT structured surface with 9 μm in height and bare silicon surfaces. The authors speculated that surface roughness that was greater than the minimum vapor film thickness in the stable film boiling regime could disrupt the vapor film, leading to termination of the film boiling. Lee et al., [73] performed quenching experiments of cylindrical copper test samples oxidized at 500 °C air for two hours under saturated water. The pre-oxidation produced a rough and black colored surface with millimeter-scaled feather-like structures. The rough copper surfaces with the two-hour oxidation enhanced the boiling heat transfer during the quenching compared to the bare copper surface. Based on visualization results of bubble evolution, the authors hypothesized that the vapor film was disrupted by the feather-like structures being sufficiently taller than the vapor film thickness. However, in the present study, the roughened surfaces have surface features with the maximum peak-to-valley distance of 44 μm and the predicted vapor film thickness at high wall superheats was in the range of 250 μm to 320 μm in saturated water at atmospheric pressure (see section

4.4.2). Therefore, the hypothesis that disruption of the vapor film by the significant height of the surface features does not explain the effects of roughness on the current quenching results.

Kang et al., [145] proposed that continuous liquid-solid contact is thermodynamically available on heated surfaces with porous microstructures due to fin effects even at high wall superheats, leading to acceleration of the boiling process. The microstructured surface consisting of porous CuO cones (100 μm in height and 20 μm in diameter) on brass spheres was quenched in atmospheric saturated water. The authors reported that the minimum film boiling temperature for the modified surface was at least 350 K higher than that of the bare brass surface. They performed a quasi-steady state and one-dimensional fin analysis and concluded that temperature of the conical porous oxide structures can be lower than the homogeneous nucleation temperature of water even if the base temperature (i.e., the brass sphere) is quite high (i.e., 600 °C), leading to termination of the stable film boiling with continuous liquid-solid contacts. To check the fin effect for the roughened surfaces in the present study, material and surface features were assumed to be a conical shape or a cylindrical rod being made of ZrO_2. The base temperature, water temperature, and the ambient film temperature was assumed to be 600 °C, 100 °C, and 350 °C, respectively. Heat transfer coefficient from the solid surface was predefined as 200 $W/m^2 \cdot K$ that was already used in the INTEMP model. The postulated surface features had 45 μm of height and 20 μm of diameter. Formulation of the one-dimensional and steady-state thermal analysis to determine temperature at a tip of the features were derived in the literatures. [88,145] As a result, the minimum temperature for the ZrO_2 triangular fin and for the ZrO_2 pin fin was 595 °C and 593.9 °C if the base surface temperature is 600 °C, respectively. The temperature drop is too small to cause collapse of the stable film boiling. Therefore, the fin effect is not a major reason for the enhancement of boiling heat transfer in the present quenching experiments.

Kim et al., [76] investigated effects of surface wettability on the minimum film boiling temperature and bubble dynamics by conducting quenching experiments of Al_2O_3 nanoparticles deposited stainless steel spheres and rodlets under subcooled water conditions. The enhanced hydrophilicity (water contact angle ~ 15 °) increased the minimum film boiling temperature approximately 400 K compared to the bare surface

(water contact angle ~ 80 °) under 20 K subcooled water. They postulated that surface wettability had a significant effect on liquid contact duration and extension of liquid spreading. It is true that the modified surfaces in the present study were more wettable surfaces than the bare Zirc-4 so the increased wettability might contribute to the enhanced boiling heat transfer during quenching. However, the oxidized surface had a higher minimum film boiling temperature than the coating smooth surface even if the $ZrSi_2$ coating surface was more hydrophilic. This indicates that the wettability effect would not be a single factor to influence quenching performances.

Hypothesis

It is hypothesized that the effects of surface characteristics on boiling heat transfer during quenching in water correlates with direct liquid-solid contacts on local portions of solid surface. Modified surfaces may play a role in the transient heat transfer during the liquid-solid contacts. Suppose the intermittent liquid-solid contacts exist at stable film boiling regime, a large amount of heat transfer is anticipated due to a large temperature gradient between liquid and heated solid surface for a short period. It may trigger destabilization of the stable vapor film if the surface temperature during the contacts is lower than a certain temperature. The characteristic temperature is assumed to be the homogenous nucleation temperature of water (T_{hm} ~ 305 °C at atmospheric pressure) [148]. The assumption that an intermittent liquid-solid contact occurs at stable film boiling regime would be counter-intuitive if surface temperature is higher than the critical temperature of water (374 °C) [149]. It is based on the fact that liquid phase of water is thermodynamically unstable above the critical temperature. Nevertheless, experimental data showing liquid contacts on a high superheated solid surface in the film boiling were reported by Dhuga and Winterton [150], and Kikuchi et al. [151]

The physical picture of this hypothesis is presented in Figure 161 to explain a lower limit of stable film boiling depending on postulated surface conditions. There are intermittent liquid-solid contacts in stable film boiling regime so that vapor-liquid interface approaches to a local solid surface. When the cold liquid rushes toward the surface, a heat removal of the local area occurs primarily by heat conduction from the

solid to the liquid. If the surface temperature is higher than the critical temperature water, the liquid cannot wet the solid surface completely due to a micro-vapor layer between the liquid and solid surface. It is assumed that heat transfer contribution of the micro-vapor layer is negligible. During the momentary heat conduction, a great amount of heat was removed from the local area of heated surface. The temperature drop of the local solid surface during the intermittent contact depends on thermal properties of the liquid and the solid. The similar concept that thermal transient of solid surface by the intermittent liquid-solid contact near a minimum film boiling point was introduced by Henry [80]. If the local surface temperature drop is not severe (e.g., $T_{local} > T_{hm}$), the liquid front was quickly dried out and the continuous vapor film was maintained. This case is illustrated in Figure 161aa-ac. Otherwise, the local surface temperature falls below the characteristic temperature (T_{hm}) even if the average surface temperature is quite high, the liquid wets the local portion of the solid surface and is evaporated rapidly. Finally, a rate of vapor generation increases on the local area, resulting in improvement of total heat transfer. The discontinuity of the vapor layer due to the rapid surface temperature drop indicates destabilization of the stable film boiling. The average surface temperature at which the local surface temperature fall in T_{hm} is defined as the minimum film boiling temperature. This scenario is shown in Figure 161bb-bc and Figure 161ca-cc. It is believed that a thick oxide layer or surface features on heated surface amplifies the temperature fluctuation during the direct liquid-solid contacts. Thus, the surfaces might have higher minimum film boiling temperature compared to bare surfaces. For instance, Kikuchi et al., [152] proposed theoretical prediction of a minimum film boiling temperature for Teflon coated copper surfaces under a liquid nitrogen. The model was based on local surface temperature drop during the transient contacting and subsequent evaporation of liquid layer. The authors investigated an effect of thickness of the Teflon coating on the minimum film boiling point, and they mentioned that the experimental results were in good agreement of theoretical predictions based on one-dimensional transient heat conduction equations.

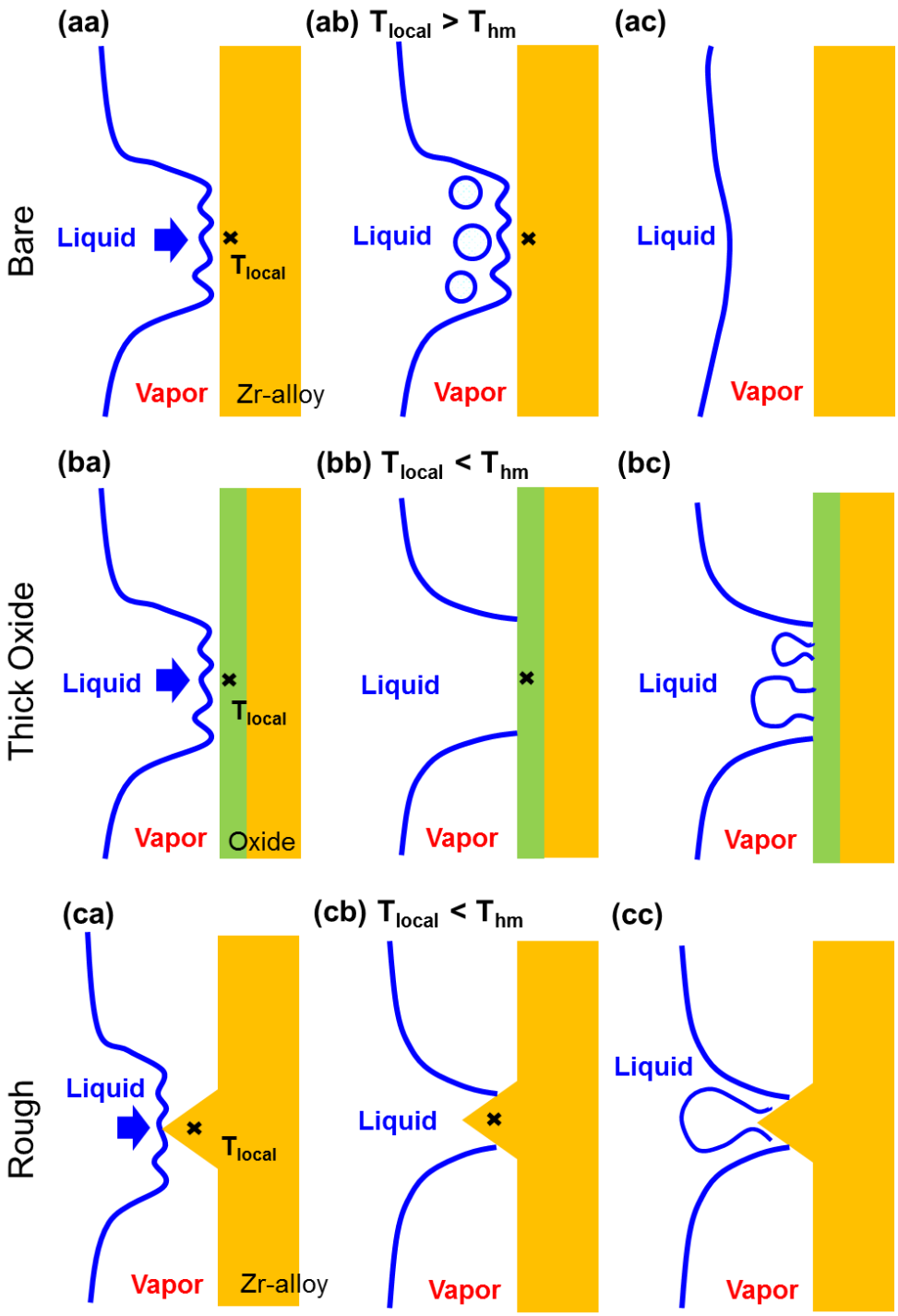

Figure 161: Schematic illustration of bubble dynamics during liquid-solid contact at high wall superheat depending on different surface properties: (a) bare surface, (b) surface with thick oxide layer, and (c) surface feature on roughened surface.

Assumptions

It is necessary that assumptions for a frequency of the liquid-solid contact, heat flux values during the contact, a liquid contact area, and a duration of liquid contact are reasonable in order to estimate thermal response of solid surface during the simulated liquid-solid contacts. The contact conditions would be used in a transient heat conduction model.

Frequency of liquid-solid contacts in stable film boiling regime was measured by Kikuchi et al. [151] A silver sphere of 20 mm in diameter coated by electrical insulation paint was quenched under saturated water. Measured impedance across a vapor layer and the insulating layer to water environment was converted to a frequency of liquid-solid contacts. The authors concluded that a range of frequency of the contacts was one to three contacts per second at high wall superheats (350 K to 500 K). Moreover, Lee and Chen[153] reported that frequency of liquid-solid contacts on a horizontal copper surface was approximately 3 contacts/s at high wall superheat (200 K) in saturated water. The number of contacts increased to 50 contacts/s as the surface superheat reached 100 K at which a breakdown stable vapor film was observed. In summary, the liquid-solid contact exists in stable film boiling regime but its frequency is extremely low.

Since liquid-solid contacts appear to occur randomly over heated surface for a short period in stable film boiling regime, it is difficult to acquire surface heat flux data during a liquid-solid contact by quenching experiments. Instead, experiments of a water droplet impingement on heated surfaces have been used to estimate the surface heat flux values because of an analogy of heat transfer mode with quenching experiments. Makino and Michiyoshi [154] measured changes of local surface temperature on mirror polished metal surfaces when a water droplet of 2.54 - 4.50 mm in diameter impacted on the superheated surfaces (T_{sup} = 50 K to 250 K). The authors reported that the highest surface heat flux was an order of 10^7 W/m^2 during a liquid-solid contact. Chen and Hsu [155] estimated average heat flux during a liquid droplet contact by measuring transient thermal response on preheated Inconel plates using a high sensitive microthermocouple probe. Instantaneous surface heat flux estimated by a two-dimensional transient heat

conduction model and the transient temperature response, which is replotted in Figure 162. It was found that the average heat flux during a liquid contact with the 20 K subcooled water droplet was in the range of 10^6 to 10^7 W/m^2 at the given wall superheats. The Chen's surface heat flux data were used in the present study.

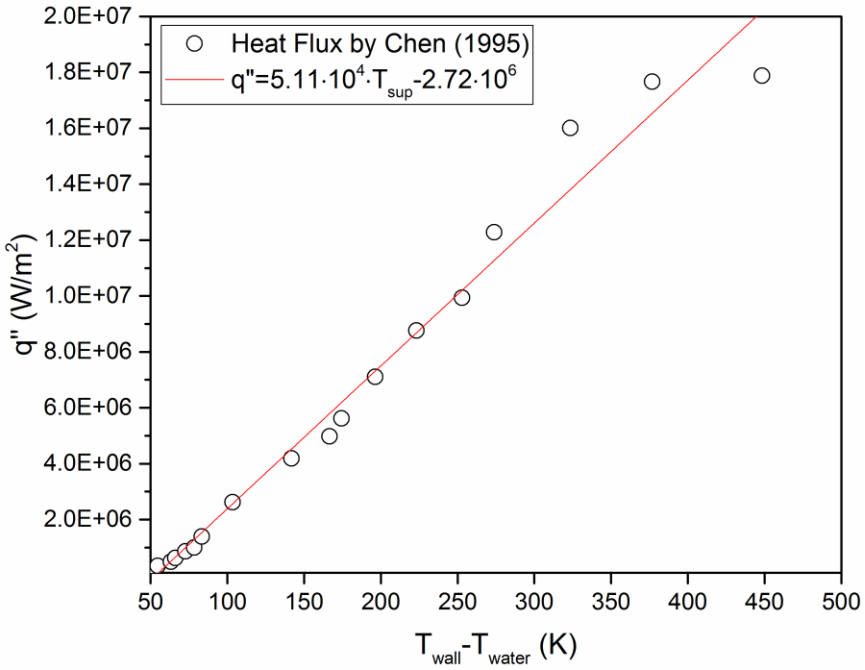

Figure 162: A linear fit and experimental results of average heat flux during droplet impingement experiments by Chen (1995) [155].

Measured liquid contact areas on a horizontal gold plated surface during a film boiling in saturated water at atmospheric pressure were reported by Yao and Henry [148]. The instantaneous liquid contact area was estimated by measurements of electrical conductance between the boiling liquid globule and the solid heater. Rigorous calibration and visual examination was performed to minimize uncertainty of the measurement. The authors concluded that the measured liquid contact area was between $1.1 \cdot 10^{-5}$ cm^2 to $1.5 \cdot 10^{-5}$ cm^2 in the range of 200 K to 300 K wall superheats. A diameter of the area is approximately 40 µm if the area has a circular shape. In addition, the authors mentioned that the contact area decreased rapidly as the surface temperature approached the homogenous nucleation temperature of water. The contact diameter (D = 40 µm) was used in the theoretical model in the following section (4.6.2).

Duration of liquid-solid contacts was measured by Lee and Chen during the atmospheric pool boiling in water [153]. Average contact duration decreases monotonically with increasing surface superheat. The authors reported that the average liquid-solid contact durations hovered around one millisecond with high wall superheats (T_{sup} = 80 to 200 K), and increased to 15 milliseconds rapidly before complete contacts with the heated surface. At an average surface superheat of 115 K, 97% of the liquid contacts were less than four milliseconds in the experiments. Therefore, the contact duration of three milliseconds was used as a condition in a thermal analysis for modified surfaces in the next section.

4.6.2. Estimation of localized temperature drop

In the last section, a hypothesis was proposed as an attempt to explain the surface effects on quenching heat transfer in water. To examine the hypothesis, thermal response of solid surfaces during liquid-solid contacts was investigated in this section. A transient heat conduction model was prepared, and temperature drop on a local point during direct liquid-solid contacts was calculated using analytical models and commercial heat conduction software, COMSOL (version 4.4). Temperature changes on the postulated surfaces (e.g., thin ZrO_2 layer on Zirc-4 surface) after a single liquid contact were also simulated and the results discussed.

Transient Heat Conduction Problem

The problem of transient heat conduction in a semi-infinite medium with a thin surface layer of thickness δ is illustrated in Figure 163. It is assumed that a liquid contact occurs on a circular area of diameter D for a short time (t_w) with a large constant surface heat flux (q''_{surf}) and the other area is applied by a lower vapor heat flux (q''_{vapor}). Thermal properties (density, heat capacity, thermal conductivity) for the base material (i.e., Zircaloy-4) and the surface layer (ZrO_2 or $ZrSi_2$) were assumed to be temperature independent in this analysis. In addition, thermal radiation is neglected, and a perfect thermal contact between the thin surface layer and the base material is assumed. For the specified model, the temperature of the layer and the base material should follow the heat conduction equations in the cylindrical coordinates as follows:

$$\frac{\partial T_s}{\partial t} = \frac{k_s}{\rho_s c p_s}\left(\frac{\partial^2}{\partial r^2} + \frac{1}{r}\cdot\frac{\partial}{\partial r} + \frac{\partial^2}{\partial x^2}\right)\mathrm{T}_s = \alpha_s \nabla^2 T_s, (0 < x < \delta, t > 0) \quad (34)$$

$$\frac{\partial T_z}{\partial t} = \alpha_z \nabla^2 T_z, (x > \delta, t > 0) \quad (35)$$

Initial condition (t=0) is:

$$T_s(r, x, 0) = 0, (0 < x < \delta) \quad (36)$$

$$T_z(r, x, 0) = 0, (x > \delta) \quad (37)$$

The condition at the interface x=δ is in:

$$T_s(r, \delta, t) = T_z(r, \delta, t) \quad (38)$$

$$k_s \frac{\partial}{\partial x} T_s(r, \delta, t) = k_z \frac{\partial}{\partial x} T_z(r, \delta, t) \quad (39)$$

The condition at the boundary at x=0 is:

$$k_s \frac{\partial T_s}{\partial x}(r, 0, t) = -q''_{surf}, (|r| < R = \frac{D}{2}) \quad (40)$$

$$k_s \frac{\partial T_s}{\partial x}(r, 0, t) = -q''_{vapor}, (|r| > R) \quad (41)$$

And finally,

$$T_s(r \to \infty, x, t) = 0 \quad (42)$$

$$T_z(r \to \infty, x \to \infty, t) = 0 \quad (43)$$

Unfortunately, it is difficult to find an exact solution for the transient and two-dimensional heat conduction problem with a layered system associated with the boundary conditions using the conventional methods such as a separation of variables and green function technique. Only steady-state solution for the problem was reported by Dryden et al. [156], and Hui and Tan [157]. They used double transformation (an inverse Laplace transformation and an inverse Hankel transformation) to solve the steady-state problem. However, a transient one-dimensional heat conduction problem for the coated solid surface neglecting a

two or three-dimensional thermal spreading phenomenon was solved analytically using an inverse Laplace integral transformation method [158,159]. Additionally, an exact solution of temperature distribution for a transient and two-dimensional semi-infinite body insulated except for the disk 0 < r < R without the coating (i.e., bare surface) is reported by Carslaw and Jaeger [160], and Beck et al. [161] Integral form of the solution is:

$$T(r,x,t) = T_{ini} + \frac{q"}{2Rk_z}\int_0^\infty \frac{J_0(\lambda r)J_1(\lambda R)}{\lambda}\{e^{-\lambda x}erfc\left[\frac{x}{2\sqrt{\alpha_z t}} - \lambda\sqrt{\alpha_z t}\right] - e^{\lambda x}erfc[\frac{x}{2\sqrt{\alpha_z t}} + \lambda\sqrt{\alpha_z t}]\}d\lambda \quad (44)$$

where J_0 and J_1 are the Bessel function of the first kind of order zero and first. The complimentary error function, erfc(x), is defined as:

$$erfc(x) = 1 - \text{erf}(x) = \frac{2}{\sqrt{\pi}}\int_x^\infty e^{-\eta^2}d\eta \quad (45)$$

The temperature at the center point (0, 0, t) in eqn. (46) is simplified as follows:

$$T(0,0,t) = T_{ini} + \frac{2q"\sqrt{\alpha_z t}}{k_z}\left\{\frac{1}{\sqrt{\pi}} - ierfc\left(\frac{R}{2\sqrt{\alpha_z t}}\right)\right\} \quad (46)$$

where $ierfc(x) = \frac{1}{\sqrt{\pi}}e^{-x^2} - x[1 - \text{erf}(x)]$ and this term in eqn. (46) corresponds to the effect of lateral heat diffusion. Therefore, an analytical solution for a one-dimensional problem in a semi-infinite solid for constant surface heat flux can be expressed as eqn. 47:

$$T(0,t) = \frac{2q"}{k_z}\sqrt{\frac{\alpha_z t}{\pi}} \quad (47)$$

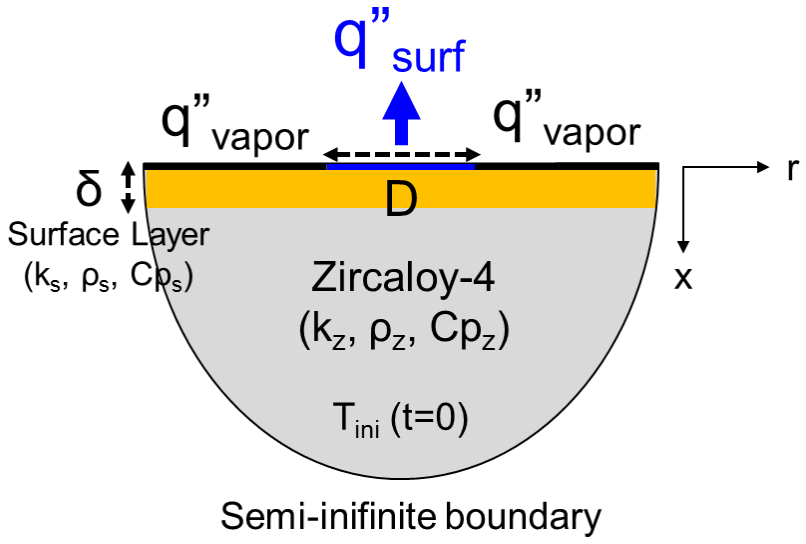

Figure 163: Schematic illustration of half space with a thin surface layer with axisymmetric surface heat flux, simulating instantaneous liquid contact on heated surface.

Significance of a thermal spreading effect on the instantaneous heat conduction during a simulated liquid-solid contact was demonstrated by plotting temperature changes at the center point (0, 0, t) of bulk Zirc-4 and bulk ZrO_2 using the two-dimensional solution (eq. 46) and the one-dimension solution (eq. 47) with the constant heat flux (using Chen's test data) and the constant contact area (D = 40 μm). Figure 164 shows that surface temperature in the one-dimensional model of bulk Zirc-4 decreases approximately 300 K for the short time (5 ms). Due to the smaller thermal diffusivity of ZrO_2, the surface temperature in the one-dimensional model for five milliseconds falls rapidly. On the other hand, the thermal response of Zirc-4 and ZrO_2 in the two-dimensional model appears to be more realistic. The surface temperature in bulk Zirc-4 falls in 522 °C from the initial temperature (550 °C) during the simulated liquid-solid contact. Temperature drop in the bulk ZrO_2 was approximately 185 K. Therefore, it can be concluded that lateral conduction from the localized high heat flux region into low heat flux region (e.g., the insulated region in the 2D model) is so significant that it is not reasonable to use the one-dimensional model to simulate the liquid-solid contact in stable film boiling.

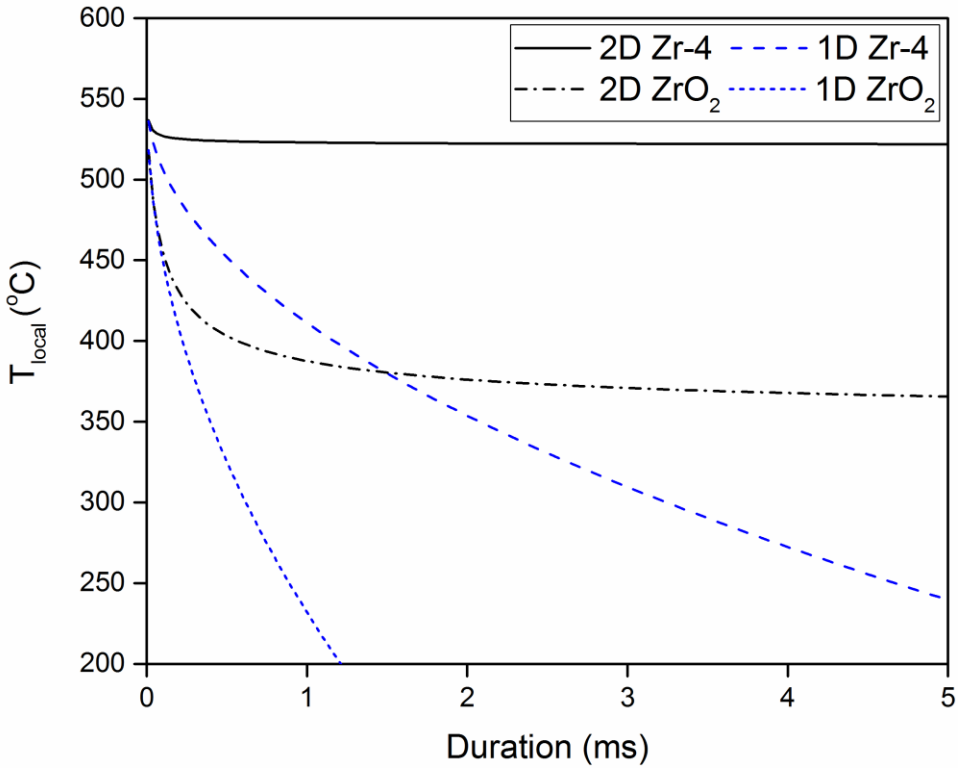

Figure 164: Temperature change of bulk Zirc-4 and bulk ZrO_2 at the simulated liquid-solid contact under constant heat flux (Chen's data [155]) and constant contact area (D = 40 μm) using the one-dimensional model and the two-dimensional model.

Based on the analysis, the thermal spreading effect should be considered to predict dynamic temperature change during postulated liquid-solid contacts, but analytical solutions for complex multi-dimensional geometries with thin $ZrSi_2$ coating, an oxidized surface, and solid surfaces with micro-features are limited. Therefore, transient temperature response for the modified surfaces was calculated numerically using commercial software, COMSOL Multiphysics (version 4.4). Figure 165 illustrates the model geometries and snapshot of temperature distribution of the flat surface (Figure 165a) and the surface with a triangular cone (Figure 165b). The heat conduction model is a cube of 600 μm in each length, which is large enough that semi-infinite media assumption is valid. The oxide layer (ZrO_2) or the thin $ZrSi_2$ coating was embedded in the model. The surface heat source is applied at the local area of the top surface and has a circular shape of 40 μm in diameter, which is a constant value based on Chen's data. The vapor covered surface in stable film boiling is simulated by applying a constant surface heat flux (85 kW/m^2) on the top surface except for the liquid contact area. The surface heat flux is the value measured for bare Zirc-4 sample

with 550 °C surface temperature in saturated water at atmospheric pressure where the entire surface is covered by continuous vapor layer. The bottom surface in the model maintains the initial temperature and four of the side surfaces are thermally insulated. Radiation heat transfer for the surfaces is not directly considered and is estimated to be a small fraction of the assumed film boiling heat flux. Initial temperature of the model is varied from 550 °C to 200 °C. The surface feature on the postulated surface condition for the roughened surfaces has 40 μm of height and 40 μm of diameter as shown in Figure 165b. In addition, a thin ZrO_2 layer (3 μm in thickness) is covered on the top surface of the model. The surface heat flux is applied on the outer surface of the conical structure if a liquid contact occurs.

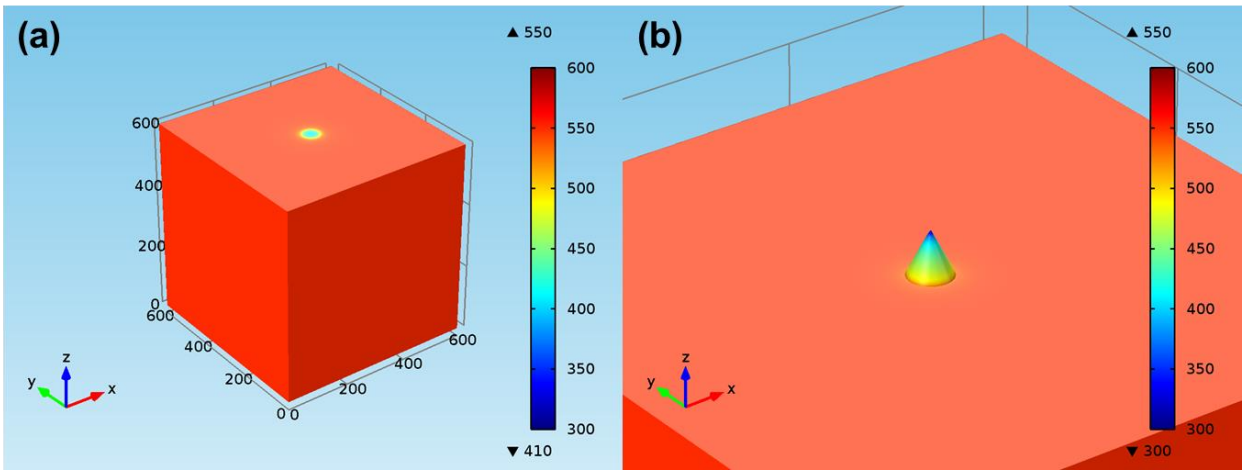

Figure 165: Illustrations of the numerical simulation of the liquid-solid contact using COMSOL: (a) flat surface and (b) the surface with a triangular surface feature. The variation of surface color in the model represents the localized cooling due to the liquid contact.

An example of a periodic liquid-solid contact at high wall superheat is presented in Figure 166. The oscillations of surface temperature at the center of liquid contact area with the five types of surfaces are shown. When the cold liquid (i.e., saturated water) suddenly comes into contact with the local area for one millisecond, the interface temperature falls rapidly. The temperature drop strongly depends on the thermal properties of surface and the surface structure. The local temperature increases again to a point close to the initial temperature while a vapor layer covers the contact area for two milliseconds; a dry condition is recovered. Even if bulk solid maintains the initial temperature (550 °C), the local area experiences the fluctuation of surface temperature. Due to the highly-localized heat removal in the triangular structure, local

temperature drop on the roughened surface is much larger compared to the flat surface cases. Additionally, increasing thickness of the ZrO_2 layer leads to larger local surface temperature drop. The $ZrSi_2$ coated surface behaves like the bare Zirc-4 surface, which is not exactly consistent with the experimental results, where a small effect is noted. This is because theoretical thermal properties of bulk $ZrSi_2$ implanted in the numerical model are comparable to that of Zircaloy-4. Thermal conductivity and density of bulk $ZrSi_2$ are known as 15.6 W/m·K (at 40 °C) and 4890 kg/m^3, respectively [162,163]. Due to limited data for heat capacity of $ZrSi_2$, the value for Zr_3Si_2, 366.6 J/kg·K (at 40 °C), was used in the calculation. However, it has been reported that thin coatings prepared by physical vapor deposition techniques such as magnetron deposition and electron beam evaporation have lower thermal conductivity than a bulk material. Cahill and Allen found out that thermal conductivity of a sputtered SiO_2 film deposited at 100 °C had 77% of the bulk material even though the film had density the same as the bulk [164]. Moreover, thermal conductivity of sputtered TiO_2 thin coatings showed a dramatic dependence on substrate temperature during the deposition process. The sputtered film at 250 °C had the thermal conductivity approximately 66% of that of the bulk material, but the conductivity of a film deposited at 400 °C approached bulk crystalline TiO_2. It was concluded that the thermal conductivity of sputtered coating is related to film density, grain size, and concentration of atomic-scale defects (interstitials or vacancies) [165]. Since the $ZrSi_2$ coating was deposited at room temperature, thermal conductivity of the coating might be much less than the reported value for bulk $ZrSi_2$. Moreover, there is no guarantee that heat capacity of a sputtered coating is the same as the bulk material. Because the $ZrSi_2$ coating was deposited by the four steps process to get the desired thickness, there might be a significant thermal resistance between each thin layer. In short, the temperature variations for the $ZrSi_2$ coating in Figure 166 cannot represent the actual thermal behavior of the coated surface during liquid-solid contacts.

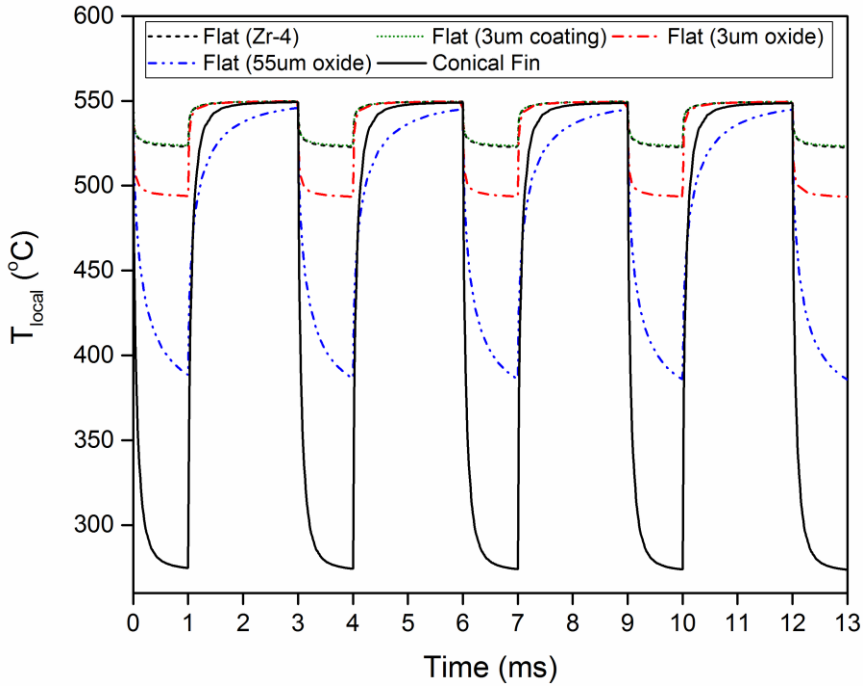

Figure 166: Temperature transients for various surface conditions postulating the modified surfaces under period liquid-solid contact (t_w = 1 ms, t_v = 2 ms).

Estimation of Minimum Temperature during a Single Contact

As shown in Figure 166, local surface temperature drops significantly at a single liquid-solid contact. According to the previous experimental data, frequency of the contacts was lower than four contacts per second. Therefore, it is speculated that the minimum surface temperature during a single liquid contact in stable film boiling regime would be a dominant factor to determine transition of the boiling regimes. Figure 167 shows the minimum local temperature in the postulated modified surfaces during a single contact as a function of initial temperature. Temperature drop for the bare Zirc-4 surface is the smallest in the conditions because the heat removal during the contact was readily recovered by lateral heat conduction. The results for a thin coating calculated by thermal properties of bulk $ZrSi_2$ are the same as the bare Zirc-4 surface. The analytical model and the COMSOL model for the bare Zirc-4 surface produces the identical results, proving a reliability of the COMSOL model. As increasing of thickness of ZrO_2 layer on Zirc-4, the minimum surface temperature during the contact decreases. Thickness of ZrO_2 layer on the pre-oxidized surface is so thick (55 μm in thickness) that the results are almost identical to bulk ZrO_2. The minimum surface temperature of the triangular fin is smallest in all surface conditions in the entire range of initial temperature,

which is attributed to the increased surface area that the heat flux applied. The result may explain that the bubble dynamics of the roughened surfaces at high wall superheats during the quenching experiments. The surface temperature of the microstructures on the roughened surfaces would be much lower than the average temperature measured by the thermocouple at the center of the sample. Therefore, it was possible that the local surface area was wetted by cold water, leading to the generation of vigorous vapor. As seen in the schematic illustration of bubble dynamics model in Section 4.6.1, only the extruded area on the roughened surface would be wetted and produce vapor with high rate even if the flat area is still covered by vapor layer. It leads to the large surface heat flux even in high wall superheats. It is worth it to note that the initial temperatures for the surfaces with 3 μm and 55 μm ZrO_2 layer if the local temperatures after the liquid contact equal to the homogeneous nucleation temperature of water are very close to the experimental results of minimum film boiling temperature for the bare Zirc-4 and the pre-oxidized surfaces. The predicted T_{min} for Zirc-4 with an oxide layer thickness of 3 μm and 55 μm is 330 °C and 431 °C, respectively. The average T_{min} for the bare Zirc-4 surfaces and the pre-oxidized surfaces measured in saturated water at atmospheric conditions was 325 °C and 432 °C, respectively. The results support the hypothesis that the lower limit of stable film boiling regime is strongly correlated with the local temperature of the solid surface during a single liquid-solid contact. For additional examination of the hypothesis, pre-oxidized Zirc-4 samples with different thickness of ZrO_2 layer were prepared and tested in saturated water at atmospheric pressure. The experimental results are presented in the next section.

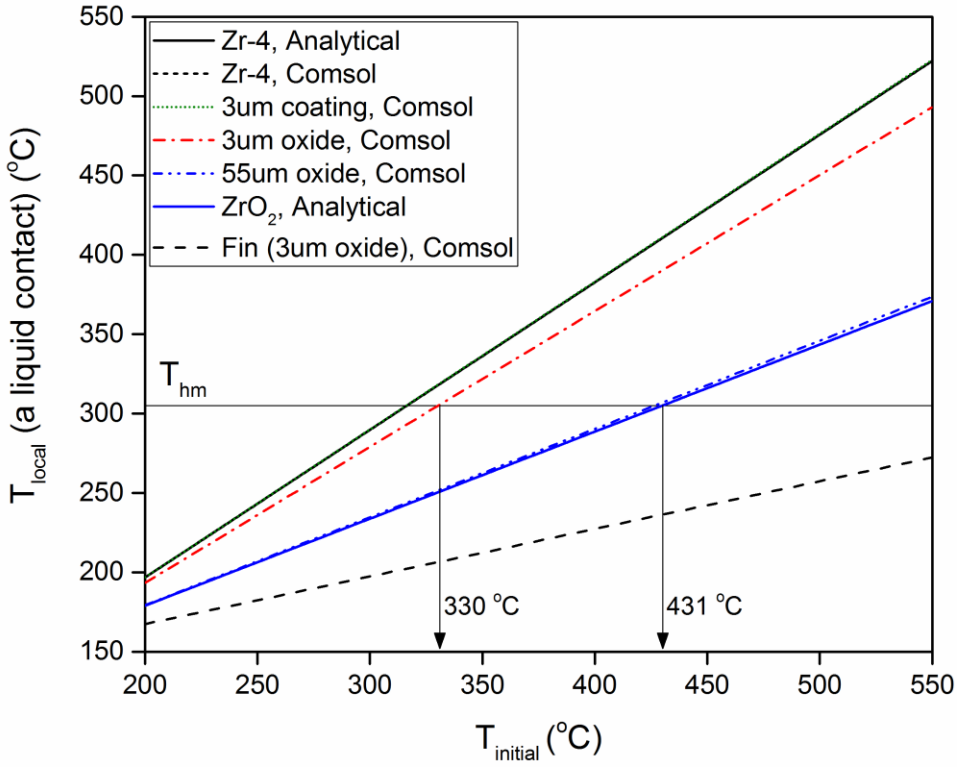

Figure 167: Minimum contact surface temperature for various surfaces during a liquid-solid contact as a function of the initial temperature of the model, calculated by the analytical model and COMSOL. Duration of the contact is 3 ms, and contact diameter is 40 µm. The black arrows indicate the initial temperature when the local temperature for the contact area equals to the homogenous nucleation temperature of water at atmospheric pressure.

4.6.3. Prediction of minimum film boiling temperature for oxidized surfaces

The transient heat conduction analysis for the modified surfaces using the analytical model and the COMSOL model demonstrated that a degree of surface temperature drop on a local area of heated surface during an instantaneous liquid-solid contact may correlate with a lower limit of stable film boiling regime; i.e., the homogeneous nucleation temperature. The predictions of minimum film boiling temperature for modified surfaces are consistent with the measured transition temperatures in saturated water at atmospheric pressure. Because of local fin cooling with an oxide surface, the predicted T_{min} for a surface with the conical fin is higher than the initial temperature in the quenching experiments, and the predicted temperatures for ZrO_2 layered surfaces in thickness of 3 µm and 55 µm were close to the experimental results. For further validation of the hypothesis, quenching experiments of oxidized surfaces with a varying thickness of ZrO_2 layer were performed and the experimental results were compared with the predicted results.

Preparation of Oxidized Surfaces with ZrO_2 layer

The oxidized Zirc-4 samples with different thickness of ZrO_2 layer were prepared by pre-oxidation at 700 °C in ambient air by changing oxidation time. The sample conditions were as follows: bare Zirc-4, pre-oxidation for 30 minutes, pre-oxidation for 120 minutes, and pre-oxidation for 300 minutes under 700 °C ambient air (with 5 °C/min ramp up rate). Thickness of the oxide layer for each condition was measured by cross-sectional SEM imaging as shown in Figure 168. Since the oxide layer thickness of the samples after three repeated quenching tests were characterized, the bare Zirc-4 samples had 3.6 μm oxide layer. The thickness of oxide layer was averaged by more than 10 measurements in randomly selected locations at the cross-sectional images, which was almost linearly proportional to the pre-oxidation time as presented in Figure 169. Additionally, micron-scale circumferential cracks were identified in the SEM image for 120-minutes and 300-minutes oxidation conditions. It may affect thermal properties of the oxide layers but was not considered in the theoretical model.

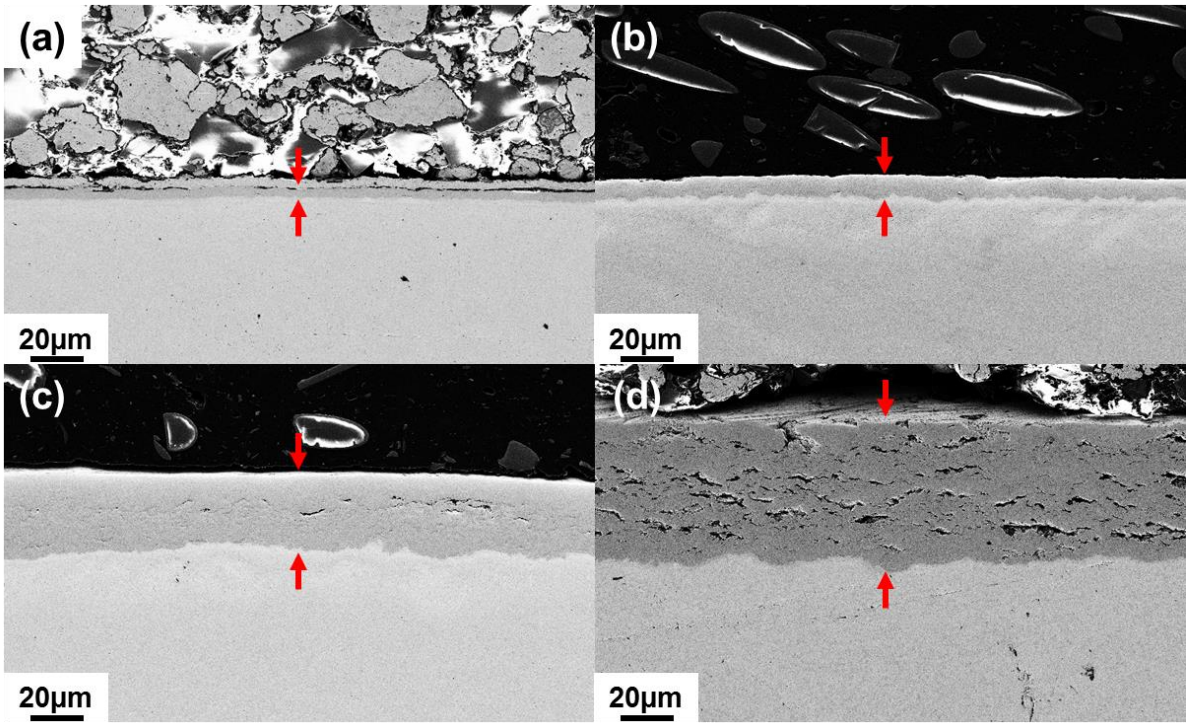

Figure 168: Cross-sectional SEM images of oxidized Zirc-4 samples after three repeated quenching tests in saturated water at atmospheric pressure: (a) bare Zirc-4, (b) pre-oxidized at 700 °C for 30 minutes, (c) pre-oxidized at 700 °C for 120 minutes, and (d) pre-oxidized at 700 °C for 300 minutes.

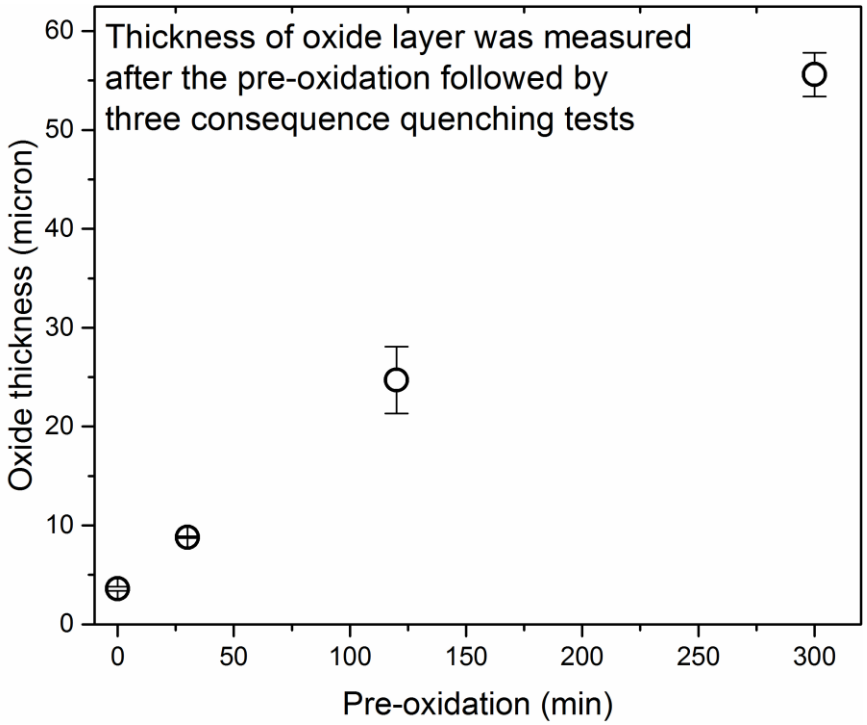

Figure 169: Oxide layer thickness in Zirc-4 samples vs. pre-test oxidation time in 700 °C ambient air.

Quenching and Boiling Curves

Quenching and boiling curves of the oxidized Zirc-4 surfaces in saturated water at atmospheric condition are shown in Figure 170. The quenching experiments for each condition performed more than three times and a repeatability of the tests was confirmed. The cooling performance was improved with increasing thickness of the oxide layer on the surface. The surface with the 55.6 μm oxide layer cooled from the initial temperature to equilibrium temperature the fastest while the surface with the 3.6 μm oxide layer took the longest to be cooled. The inflection point in the quenching curves is displayed at higher temperature as thickness of the oxide layer increases, indicating minimum film boiling temperature increases with increasing the oxide layer thickness. It is reasonable that enhancement of surface heat flux at stable film boiling was not observed because roughness effects was not associated in the boiling heat transfer; all the oxidized surfaces were smooth and flat. The results support the hypothesis that thermal properties of heated surface are important factors to determine the transition at the minimum film boiling point.

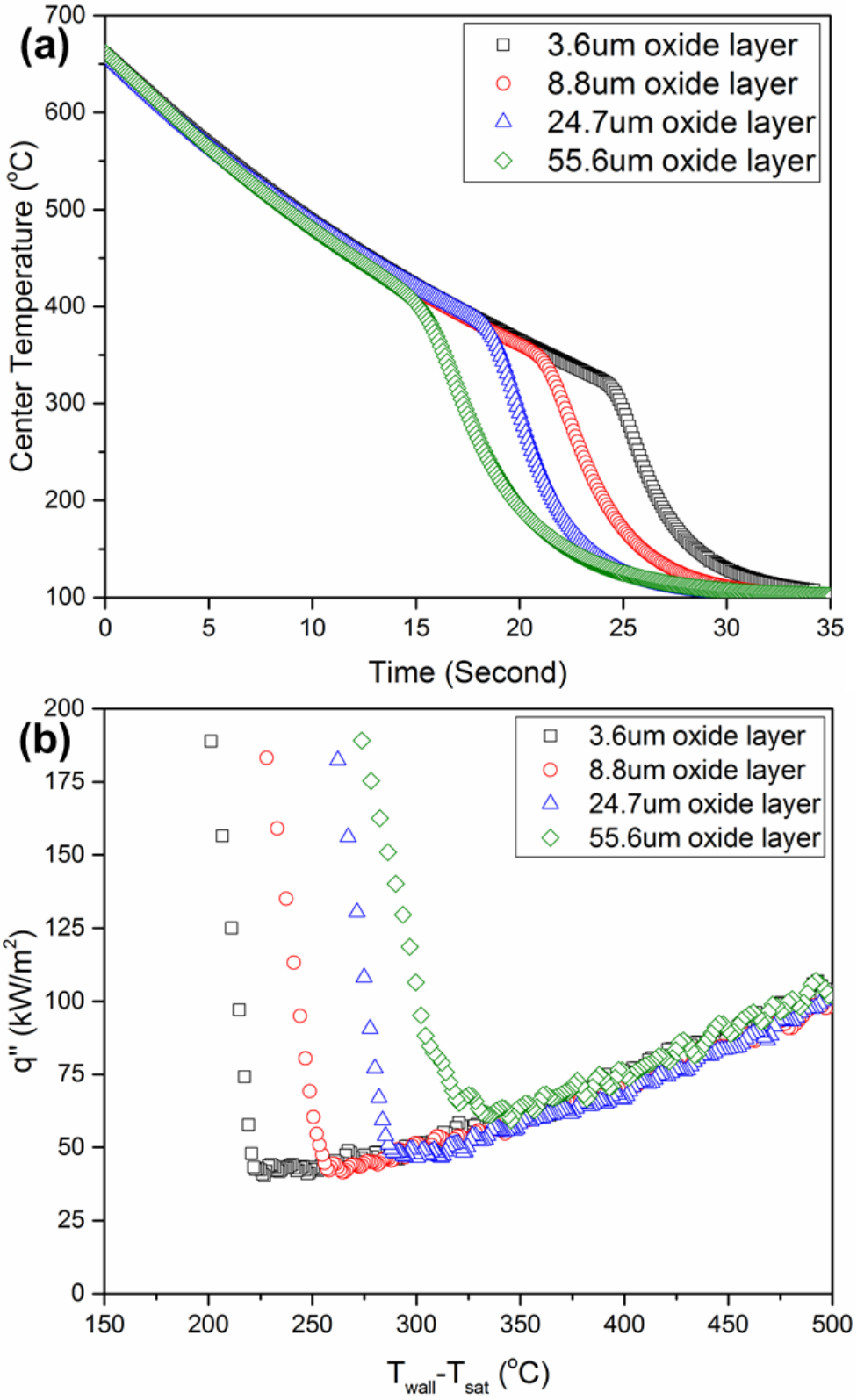

Figure 170: (a) Quenching curves and (b) boiling curves of oxidized surfaces with different thickness of oxide layer in saturated water at atmospheric pressure.

Prediction of Minimum Film Boiling Temperature for the Oxidized Surfaces

With the assumption that the homogenous nucleation temperature of water is the minimum film boiling temperature, the effect of liquid-solid contact and thickness of surface oxide layer on the point given frequency, duration, and size of the contact was solved using transient heat conduction models. Figure 171 shows the calculated minimum film boiling temperatures and experimental temperatures determined by the quenching experiments as a function of thickness of ZrO_2 scale on Zirc-4 solid. The experimental results agree well with the theoretical predictions under the given assumptions of a liquid-solid contact. The predicted curve displays that minimum film boiling temperature increases sharply with the initial development of oxide layer on the bare surface, and finally has the asymptotic behavior of T_{min} as further increase in thickness of the oxide scale. It infers that the minimum film boiling point of oxidized surfaces approaches to that of bulk ZrO_2 if the oxide scale continues to grow on the surface. The deviation between the predicted curve and experimental data would be attributed to the assumptions in the theoretical models such as a theoretical density of the oxide layer, no thermal resistance in the interface between the oxide layer and the Zirc-4 solid, and the conditions of the liquid contact. It is worth it to note that the strong dependency of T_{min} on thickness of the oxide layer cannot be explained by Henry's model [80]. Henry proposed that T_{min} would be correlated with the interfacial temperature between cold liquid and hot solid surface during a liquid contact, but the temperature is determined without the consideration of thickness of the oxide layer. It is believed that the interfacial temperature in Henry's model may represent the average value of the present data for the various thickness of the oxide. The effect of thickness of surface layer on quenching behaviors is also investigated by Kikuchi et al. [152] The authors reported that earlier onset of transition boiling in liquid nitrogen occurred on a thick insulation coating (i.e., Teflon layer), resulting from a rapid drop of the local surface temperature during intermittent liquid-solid contacts.

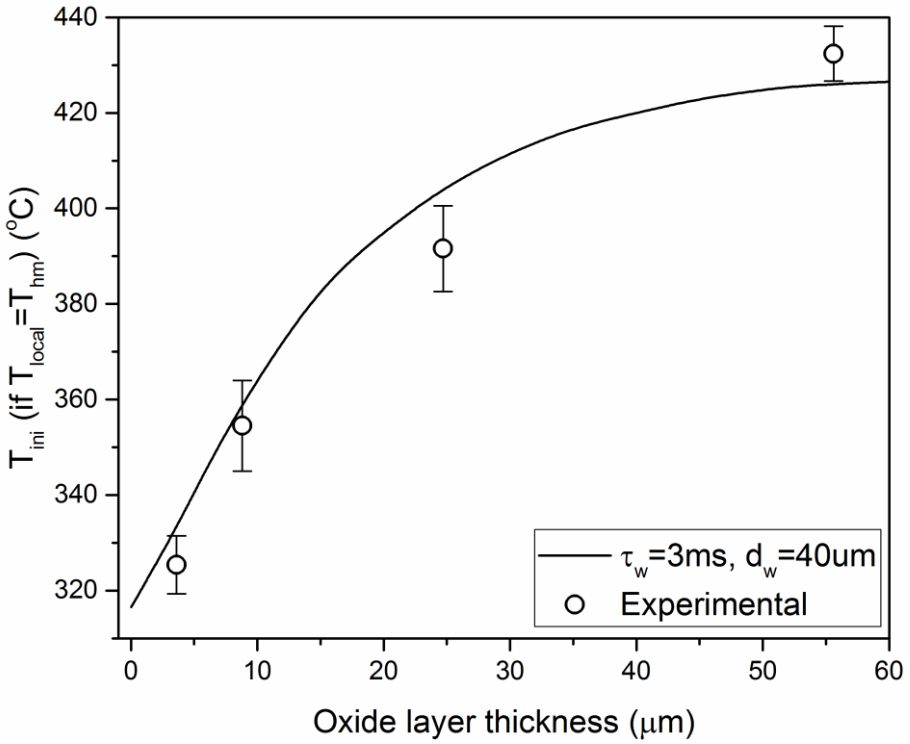

Figure 171: Predicted minimum film boiling temperature on various thickness of ZrO_2 layer on Zirc-4 solid and experimental data for saturated water in atmospheric pressure.

Sensitivity Analysis of Contact Duration and Contact Area

Figure 172 shows the effect of the liquid contact duration (τ_w) and the liquid contact diameter (d_w) on the prediction of lower limit of stable film boiling temperature on the oxidized surfaces. An exact integral solution for temperature distribution in a solid at the steady-state liquid contact ($\tau_w \rightarrow \infty$) was derived by Hui and Tan [157] and shown in Figure 172a. The predicted minimum film boiling temperature increases with longer duration and larger area of the direct contact, particularly in the thick oxide layer region due to a large contribution of the oxide layer with the small thermal diffusivity to the entire heat transfer calculation. In the thin-layer region, there are a weak dependency of the contact duration and the contact area on the prediction of minimum film boiling temperature. Moreover, the instantaneous liquid contact area has a stronger sensitivity to the prediction than the liquid contact duration. Therefore, precise measurement of the liquid contact area is essential for accurate prediction of the minimum film boiling temperature compared to frequency and duration.

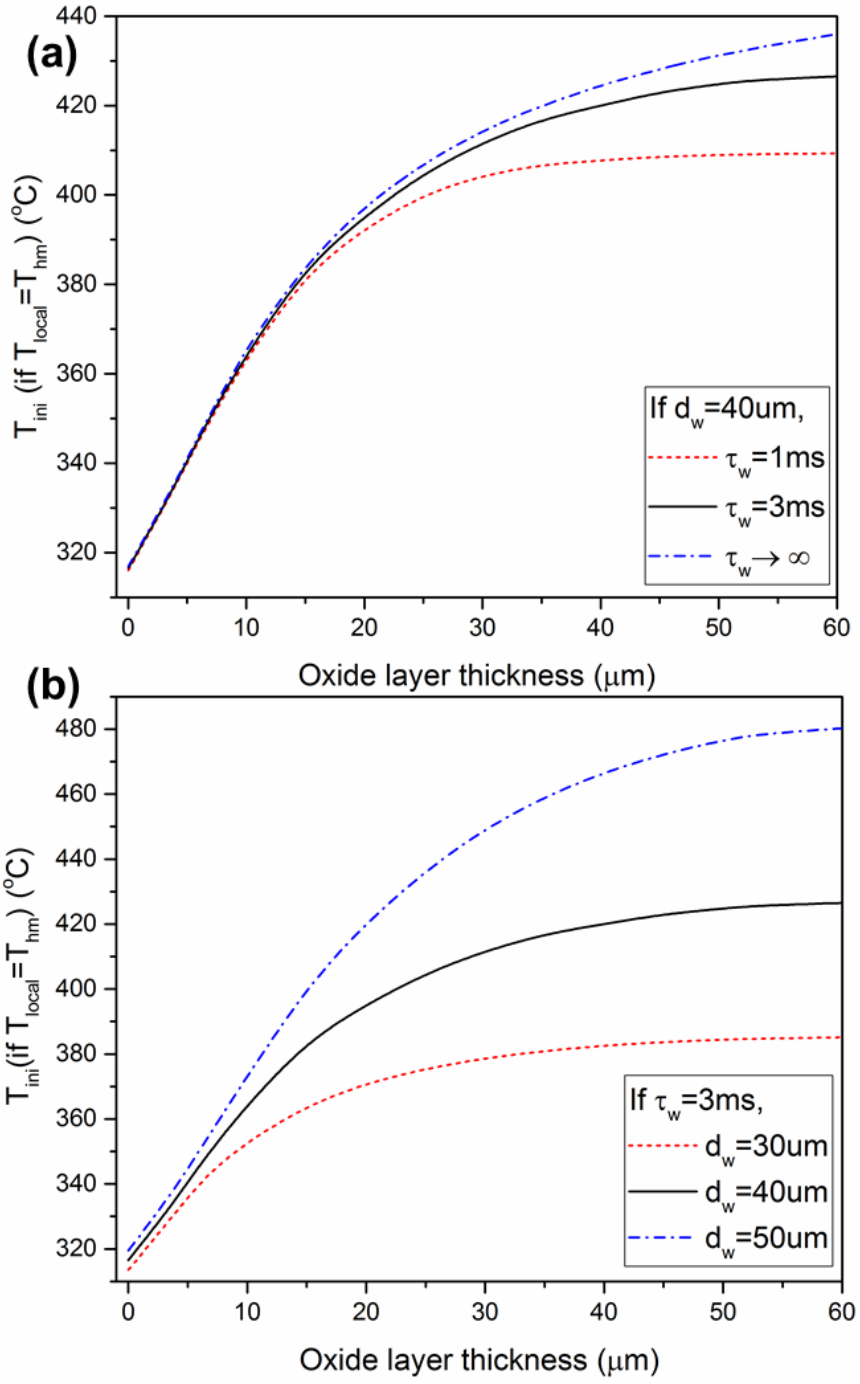

Figure 172: Effect of (a) liquid contact duration and (b) liquid contact area on prediction of minimum film boiling temperature depending on oxide layer thickness.

The hypothesis has been proposed to explain the enhancement of quenching performance by the modified surfaces showing earlier transition from stable film boiling at higher wall superheats. With assumption that intermittent liquid-solid contacts exist in stable film boiling regime, surface temperature drop on local heated surface during a single liquid-solid contact depending on surface conditions was

calculated by the analytical model and the COMSOL model. The models simulated that instantaneous conductive heat removal due to the local contact decreased the surface temperature rapidly, and predicted minimum film boiling temperatures for the heavily oxidized surfaces and roughened surfaces are higher than the bare surface. The calculated results show good agreement with the experimental results except for the thin $ZrSi_2$ coating surface due to limited information about thermal properties of the sputtered coating. The assumptions and formulations of the present transient heat conduction model appears to be valid to demonstrate the effects of modified surfaces on the lower limit of stable film boiling in saturated water at atmospheric pressure. Accurate measurement of liquid-solid contact parameters such as contact duration, contact heat flux, and contact area at different system conditions will be useful for prediction of the minimum film boiling temperature under subcooled water or pressurized conditions.

5. Summary & Future Work

Experimental results investigating the feasibility of zirconium-silicide coating for enhanced accident tolerance of LWR fuel cladding coating has been presented. High temperature oxidation behavior of bulk $ZrSi_2$ and Zr_2Si was investigated. It was shown that complex micro- and nano-oxide structures consisting of alternating SiO_2 and ZrO_2 layers evolved during transient oxidation of $ZrSi_2$, which was explained by spinodal phase decomposition of Zr-Si-O oxide. The oxidation resistance of $ZrSi_2$ appeared to be significantly superior to bare Zircaloy-4 and Zr_2Si in high temperature air. Coating optimization in regards to oxidation resistance was performed mainly using magnetron sputter deposition method. Cold spray and thermal spray methods were successfully demonstrated to deposit $ZrSi_2$ coatings, however further process optimization is required to make the coatings thicker and denser. $ZrSi_2$ coating (~3.9 μm) was synthesized using the optimized parameters in magnetron sputter deposition. The coatings showed improvement of almost two orders of magnitude when compared to bare Zircaloy-4 after air-oxidation at 700 °C for 20-hours. Pre-oxidation of $ZrSi_2$ coating at 700 °C for 5 h significantly mitigated oxygen diffusion in air-oxidation tests at 1000 °C for 1-hour and 1200 °C for 10-minutes. No spallation or cracks were observed in the $ZrSi_2$ coating due to air cooling to room temperature after high temperature oxidation tests. The zirconium-silicide coating with pre-oxidation at 700 °C air for 5 hours was found to be the best condition to prevent oxide formation in Zircaloy-4 substrate without spallation and cracking of the coating in the steam condition even if the top surface of the coating was degraded by formation of zirconium-rich oxide layer. Only the zircon phase ($ZrSiO_4$), formed by exposing the $ZrSi_2$ coating on SiC substrates at 1400 °C in air, allowed for immobilization of silicon species in the oxide scale in the aqueous environments. A quench test facility was designed and built to study transient boiling heat transfer of modified Zircaloy-4 surfaces (e.g., roughened surfaces, oxidized surfaces, $ZrSi_2$ coated surfaces) at various system conditions (e.g., elevated pressures and water subcooling). The minimum film boiling temperature for bare Zircaloy-4 increased with increasing system pressure and water subcooling, consistent with past literature. Quenching behavior was notably affected by the types of surface modification regardless of the

environmental conditions. Quenching heat transfer was improved by the $ZrSi_2$ coating, a degree of surface oxidation (δ_{ox} = 3 to 50 μm), and surface roughening (R_a ~ 20 μm). A plausible hypothesis based on transient heat conduction models during intermittent liquid-solid contact in quenching process was proposed to explain the enhanced boiling heat transfer behavior. The theoretical model incorporated localized temperature behavior on the modified surfaces and elucidated bubble dynamics qualitatively, and predicts minimum film boiling temperature of oxidized Zirc-4 surfaces, which are reasonably in good agreement with experimental data.

These research results have also led to recommendations for proposed future research work as follows:

- Optimization of zirconium-silicide coating process to steam corrosion resistance
    - Improvement of quality of thin $ZrSiO_4$ layer produced by high temperature oxidation of $ZrSi_2$ coating on SiC by adjusting parameters of the heat treatment process
- Investigation of ion irradiation behavior of multi-structural oxide scale in bulk $ZrSi_2$ and $ZrSi_2$ coatings
- Investigation of a relationship between minimum film boiling temperature and a degree of surface roughness, including a theoretical prediction
- Improvement of the quenching experimental facility
    - Direct measurement of surface temperature of test specimen
    - Improved visual images to increase the resolution of bubble dynamics
    - Direct measurement of parameters of direct liquid-solid contacts for a range of conditions (elevated pressures and liquid subcooling)

6. Publications

6.1. Journal Articles:

1) G.Stange, **H.Yeom**, B.Semerau, K.Sridharan, and M.Corradini, A Study of Nanoparticle Surface Modification Effects on Pool Boiling Critical Heat Flux, *Nuclear Technology*, Vol.182, n.3, pp.286-301, 2013.
2) **H.Yeom**, K. Sridharan, and M. Corradini, Bubble Dynamics in Pool Boiling on Electrophoretic Nanoparticle coated Surfaces, *Heat Transfer Engineering*, Vol. 36, n.12, pp.1013-1027, 2015.
3) H.Jo, J. Kim, **H.Yeom**, G. Lee, K. Sridharan, M. Corradini, M. Kim, H. Park, Boiling Performance and Material Robustness of Modified Surfaces with Multi-Scale Structure for Fuel Cladding Development, *Nuclear Engineering Design*, Vol. 291, pp.204-211,2015
4) **H.Yeom**, B.Hauch, G.Cao, B.Garcia-Diaz, M.Martinez-Rodriquez, H.Colon-Mercado, L.Olson, K.Srihanran, Laser Surface Annealing and Characterization of Ti2AlC PVD Coating on Zirconium-alloy Substrate, *Thin Solid Films*, Vol. 615, pp.202-209, 2016
5) **H.Yeom**, B.Maier, R.Mariani, D.Bai, K.Sridharan, Evolution of Multi-Layered Scale Structures during High Temperature Oxidation of $ZrSi_2$, *Journal of Materials Research*, Vol. 31, n. 21, pp. 3409-3419, 2016
6) **H.Yeom**, B.Maier, R.Mariani, D.Bai, S.Fronek, Peng Xu, K.Sridharan, Magnetron Sputter Deposition of Zirconium-Silicide Coating for Mitigating High Temperature Oxidation of Zirconium-Alloy, *Surface and Coatings Technology*, Vol. 316, pp. 30-38, 2017
7) H.Jo, **H.Yeom**, D.Yoon, M.Corradini, Minimum Heat Flux (MHF) on Structured Surfaces with Different Surface Energies, *International Journal of Multiphase Flow*, under review, 2017
8) **H.Yeom**, H.Jo, G.Johnson, K.Sridharan, M.Corradini, Transient Pool Boiling Heat Transfer of Oxidized and Roughened Zircaloy-4 Surfaces during Water Quenching, *Nuclear Engieering Design*, submitted, 2017

9) **H.Yeom,** C.Lockhart, R.Mariani, X.Bai, P.Xu, M.Corradini, K.Sridharan, Evaluation of steam corrosion and water quenching behavior of zirconium-silicide coating for LWR fuel claddings, *Journal of Nuclear Materials*, in preparation, 2017

6.2. Conference Proceedings

1) H.J. Jo, J.M. Kim, M.H. Kim, H.S. Park, **H. Yeom**, K. Sridharan, and M.L. Corradini, Enhancement of Boiling Performance on a Surface Modified by Micro-Millimeter Posts and Nanoparticles, Proc. Trans. American Nuclear Society Conf., Reno, NV, 2014
2) **H. Yeom**, B. Maier, R. Mariani, D. Bai, P. Xu, and K. Sridharan, "Development of Zirconium-Silicide Coatings for Accident Tolerant Zirconium-Alloy Fuel Cladding", Proc. International Congress on Advances in Nuclear Power Plants, San Francisco, CA, 2016
3) **H. Yeom**, B. Maier, S. Fronek, G. Johnson, E. Strand, R. Mairani, X. Bai, P. Xu, E Lahoda, K. Sridharan, Development of Zirconium-Silicide Coatings for Improved Performance Zirconium-Alloy Fuel Cladding, Proc. 2016 ANS Winter Meeting and Nuclear Technology Expo, Las Vegas, NV, 2016
4) **H. Yeom**, H. Jo, B. Maier, M. Corradini, K. Sridharan, G.C. Lee, H.W. Lee, T.K. Kim, M.H. Kim, H.S. Park, "Multi-Functional Zirconium-Silicide Coatings on Zirconium-alloy for Improved Accident Tolerance", ANS Annual Meeting, San Francisco, CA, 2017
5) M. Kim, J.Y. Kang, J.M. Kim, H. Noh, G.C. Lee, H.J. Kwak, T.K. Kim, **H. Yeom**, H. Jo, M. Corradini, K. Sridharan, H.S. Park, "Evaluation of accident tolerant cladding thermally enhanced by anodic oxidation and electrophoretic deposition", submitted, 2017 Water Reactor Fuel Performance Meeting, Jeju Island, Republic of Korea, 2017
6) H. Shah, J. Romero, P. Xu, B. Maier, G. Johnson, J. Walters, T. Dabney, **H. Yeom**, and K. Sridharan, "Development of Surface Coatings for Enhanced Accident Tolerant Fuel (ATF)", submitted, 2017 Water Reactor Fuel Performance Meeting, Jeju Island, Republic of Korea, 2017

6.3. Conference Presentations/Abstracts.

1) International Congress on Advanced Nuclear Power Plants (ICAPP) 2016: Development of Zirconium-Silicide Coatings for Accident Tolerant Zirconium-Alloy Fuel Cladding, San Francisco, CA, April 20th, 2016
2) 4th Annual Collaboration for Advanced Research for Accident Tolerance (CARAT) Cladding Meeting 2016: Development of Zirconium-silicide Coatings on Zr-alloy Cladding for Enhanced Accident Tolerance, Boise State University, Boise, ID, September 9th,2016
3) Materials Science & Technology (MS&T) 2016: Development of Zirconium-silicide Coating for Enhancement of Accident Tolerance of Zirconium-alloy LWR Cladding Material, Salt Lake City, UT, October 24th, 2016
4) Materials Science & Technology (MS&T) 2016: Ti-Al-C MAX Phase Coating for Accident Tolerant Fuels, Salt Lake City, UT, October 25th, 2016
5) American Nuclear Society Winter Meeting & Expo 2016: Development of Zirconium-Silicide Coatings for Improved Performance Zirconium-Alloy Fuel Cladding, Las Vegas, NV, November 9th, 2016
6) American Nuclear Society Annual Meeting 2017: Multi-fuctional zirconium-silicide coatings on zirconium-alloy for improved accident tolerance, San Francisco, CA, June 13th, 2017

References Cited

[1] G.. Sabol, R.J. Comstock, R. Weiner, P. Larouere, R.. Stanutz, In-reactor corrosion performance of ZIRLO and Zircaloy-4, Zircon. Nucl. Ind. Tenth Int. Symp. (1994) 724–744.

[2] S. Bragg-Sitton, Development of advanced accident-tolerant fuels for commercial LWRs, Nucl. News. (2014) 83–91.

[3] M. Steinbruck, N. Ver, M. Grobe, Oxidation of advanced zirconium cladding alloys in steam at temperatures in the range of 600-1200C, Oxid. Met. 76 (2011) 215–232. doi:10.1007/s11085-011-9249-3.

[4] S.J. Zinkle, K.A. Terrani, J.C. Gehin, L.J. Ott, L.L. Snead, Accident tolerant fuels for LWRs: A perspective, J. Nucl. Mater. 448 (2014) 374–379. doi:10.1016/j.jnucmat.2013.12.005.

[5] M. Steinbrück, Prototypical experiments relating to air oxidation of Zircaloy-4 at high temperatures, J. Nucl. Mater. 392 (2009) 531–544. doi:10.1016/j.jnucmat.2009.04.018.

[6] M. Steinbrück, M. Böttcher, Air oxidation of Zircaloy-4, M5® and ZIRLO™ cladding alloys at high temperatures, J. Nucl. Mater. 414 (2011) 276–285. doi:10.1016/j.jnucmat.2011.04.012.

[7] B.A. Pint, K.A. Terrani, Y. Yamamoto, L.L. Snead, Material Selection for Accident Tolerant Fuel Cladding, Metall. Mater. Trans. E. 2 (2014) 190–196. doi:10.1007/s40553-015-0056-7.

[8] Development of Light Water Reactor Fuels with Enhanced Accident Tolerance, (2015).

[9] Y. Yamamoto, B. Pint, K.A. Terrani, K. Field, S. Maloy, J. Gan, Progress Towards the Development of Nuclear Grade FeCrAl Fuel Cladding, TopFuel2015. 467 (2015) 703–716. doi:10.1016/j.jnucmat.2015.10.019.

[10] T. Cheng, J.R. Keiser, M.P. Brady, K.A. Terrani, B.A. Pint, Oxidation of fuel cladding candidate materials in steam environments at high temperature and pressure, J. Nucl. Mater. 427 (2012) 396–400. doi:10.1016/j.jnucmat.2012.05.007.

[11] M. Ben-Belgacem, V. Richet, K.A. Terrani, Y. Katoh, L.L. Snead, Thermo-mechanical analysis of LWR SiC/SiC composite cladding, J. Nucl. Mater. 447 (2014) 125–142. doi:10.1016/j.jnucmat.2014.01.006.

[12] B. Cheng, Y.-J. Kim, P. Chou, Improving Accident Tolerance of Nuclear Fuel with Coated Mo-alloy Cladding, Nucl. Eng. Technol. 48 (2015) 16–25. doi:10.1016/j.net.2015.12.003.

[13] I. IDARRAGA-TRUJILLO, M. LE FLEM, J.-C. BRACHET, M. LE SAUX, D. HAMON, S. MULLER, et al., Assessment At Cea of Coated Nuclear Fuel Cladding for Lwrs With Increased Margins in Loca and Beyond Loca Conditions, Proc. TopFuel 2013. (2013) 860–867.

[14] H.-G. Kim, I.-H. Kim, Y.-I. Jung, D.-J. Park, J.-Y. Park, Y.-H. Koo, Adhesion property and high-temperature oxidation behavior of Cr-coated Zircaloy-4 cladding tube prepared by 3D laser coating, J. Nucl. Mater. 465 (2015) 531–539. doi:10.1016/j.jnucmat.2015.06.030.

[15] B.R. Maier, B.L. Garcia-Diaz, B. Hauch, L.C. Olson, R.L. Sindelar, K. Sridharan, Cold spray deposition of Ti2AlC coatings for improved nuclear fuel cladding, J. Nucl. Mater. 466 (2015) 712–717. doi:10.1016/j.jnucmat.2015.06.028.

[16] J.H. Sung, T.H. Kim, S.S. Kim, Fretting damage of TiN coated zircaloy-4 tube, Wear. 250 (2001) 658–664. doi:10.1016/S0043-1648(01)00674-3.

[17] K.A. Terrani, L.L. Snead, J.C. Gehin, Microencapsulated fuel technology for commercial light water and advanced reactor application, J. Nucl. Mater. 427 (2012) 209–224. doi:10.1016/j.jnucmat.2012.05.021.

[18] J.P. Mardon, A. LESBROS, C. Bernaudat, N. Waeckel, Recent data on M5 alloy under RIA and LOCA conditions, Proc. 2004 Int. Meet. LWR Fuel Perform. (2004) 507–515.

[19] V.F. Urbanic, T.R. Heidrick, HIGH-TEMPERATURE OXIDATION OF ZIRCALOY-2 AND ZIRCALOY-4, J. Nucl. Mater. 5 (1978) 251–261.

[20] C. Duriez, T. Dupont, B. Schmet, F. Enoch, Zircaloy-4 and M5 high temperature oxidation and nitriding in air, J. Nucl. Mater. 380 (2008) 30–45. doi:10.1016/j.jnucmat.2008.07.002.

[21] D.. Powers, L.. Kmetyk, R.. Schmidt, A review of technical issues of air ingression during severe reactor accidents, NUREG/CR-6218. (1994).

[22] A.S. Khanna, Introduction to high temperature oxidation and corrosion, 1st ed., ASM International, 2002.

[23] F.J.E.J.S. Leistikow, Zircaloy Fuel Cladding Behavior in a LOCA -A Review, in: Zircon. Nucl. Ind. Seventh Int. Symp., 1985: pp. 24–27.

[24] S. Leistikow, Exposed To High Temperature Steam and Hydrogen-Steam Mixtures, (1987).

[25] F. Fichot, B. Adroguer, A. Volchek, Y. Zvonarev, Advanced treatment of zircaloy cladding high-temperature oxidation in severe accident code calculations Part III. Verification against representative transient tests, Nucl. Eng. Des. 232 (2004) 97–109. doi:10.1016/j.nucengdes.2004.02.010.

[26] E.T. Hayes, A.H. Roberson, Some effects of heating zirconium in air, oxygen, and nitrogen, J. Electrochem. Soc. 96 (1949) 142–151.

[27] L. Bakeer, L. Just, Studies of metal-water reactions at high temperatures III. Experimental and theoretical studies of the zirconium-water reaction, 1962.

[28] J.H. Baek, Y.H. Jeong, Breakaway phenomenon of Zr-based alloys during a high-temperature oxidation, J. Nucl. Mater. 372 (2008) 152–159. doi:10.1016/j.jnucmat.2007.02.011.

[29] A. Zieliński, S. Sobieszczyk, Hydrogen-enhanced degradation and oxide effects in zirconium alloys for nuclear applications, Int. J. Hydrogen Energy. 36 (2011) 8619–8629. doi:10.1016/j.ijhydene.2011.04.002.

[30] M. Hansen, R. Elliot, F. Shunk, Constitution of binary alloys. First supplement, McGraw-Hill, 1965.

[31] R. Chen, M.C. Lu, V. Srinivasan, Z. Wang, H.H. Cho, A. Majumdar, Nanowires for enhanced boiling heat transfer, Nano Lett. 9 (2009) 548–553. doi:10.1021/n18026857.

[32] S. Roy, A. Paul, Growth of hafnium and zirconium silicides by reactive diffusion, Mater. Chem. Phys. 143 (2014) 1309–1314. doi:10.1016/j.matchemphys.2013.11.039.

[33] R. Rosenkranz, Frommeyer Georg, Microstructures and properties of the refractory compounds TiSi2 and ZrSi2, Zeitschrft Fur Met. 83 (1992) 685–689.

[34] T. Nakano, Y. Omomoto, K. Hagihara, Y. Umakoshi, Plastic deformation behavior and operative slip systems of ZrSi2 single crystals with C49 type of structure, Scr. Mater. 48 (2003) 1307–1312. doi:10.1016/S1359-6462(03)00022-8.

[35] S.P. Ju, T.Y. Wu, S.H. Liu, Mechanical and dynamical behaviors of ZrSi and ZrSi2 bulk metallic glasses: A molecular dynamics study, J. Appl. Phys. 117 (2015). doi:10.1063/1.4913707.

[36] R. Hao, X. Zhang, J. Qin, S. Zhang, J. Ning, N. Sun, Theoretical prediction of structural stability, electronic and elastic properties of ZrSi2 under pressure, RSC Adv. 5 (2015) 36779–36786. doi:10.1039/C5RA01964H.

[37] I.J. Cho, K.T. Park, S.K. Lee, H.H. Nersisyan, Y.S. Kim, J.H. Lee, Rapid and cost-effective method for synthesizing zirconium silicides, Chem. Eng. J. 165 (2010) 728–734. doi:10.1016/j.cej.2010.09.038.

[38] M. Wang, B.O. Sundman, Thermodynamic Assessment of the Si-Zr System, Capphad. 18 (2000) 319–327. doi:http://dx.doi.org/10.1111/j.1551-2916.2004.00683.x.

[39] Y. Fei, ASM Ready Reference: Thermal Properties of Metals, ASM International, 1995. doi:10.1029/RF002p0029.

[40] Surface Coating Methods, Tribol. Ser. 28 (1994) 7–32.

[41] F. Khatkhatay, J. Jian, L. Jiao, Q. Su, J. Gan, J.I. Cole, et al., Diffusion barrier properties of nitride-based coatings on fuel cladding, J. Alloys Compd. 580 (2013) 442–448. doi:10.1016/j.jallcom.2013.06.108.

[42] G. Reisel, B. Wielage, S. Steinhauser, I. Morgenthal, R. Scholl, High temperature oxidation behavior of HVOF-sprayed unreinforced and reinforced molybdenum disilicide powders, Surf. Coatings Technol. 147 (2001) 19–26. doi:10.1016/S0257-8972(01)01364-0.

[43] X. Pang, K. Gao, F. Luo, H. Yang, L. Qiao, Y. Wang, et al., Annealing effects on microstructure and mechanical properties of chromium oxide coatings, Thin Solid Films. 516 (2008) 4685–4689. doi:10.1016/j.tsf.2007.08.083.

[44] Y. Al-Olayyan, G.E. Fuchs, R. Baney, J. Tulenko, The effect of Zircaloy-4 substrate surface condition on the adhesion strength and corrosion of SiC coatings, J. Nucl. Mater. 346 (2005) 109–119. doi:10.1016/j.jnucmat.2005.05.016.

[45] V. Firouzdor, J. Brechtl, L. Wilson, B. Semerau, K. Sridharan, T.R. Allen, Development of Yttrium Stabilized Zirconia (YSZ) diffusion barrier coatings for mitigation of Fuel-Cladding Chemical Interactions, J. Nucl. Mater. 438 (2013) 268–277. doi:10.1016/j.jnucmat.2013.02.032.

[46] Jong Sung Yoo, In Sup Kim, Effect of ($\alpha + \beta$) heat treatment on the mechanical properties of Zircaloy-4, J. Nucl. Mater. 185 (1991) 87–95. doi:10.1016/0022-3115(91)90368-H.

[47] C.R.F. Azevedo, Selection of fuel cladding material for nuclear fission reactors, Eng. Fail. Anal. 18 (2011) 1943–1962. doi:10.1016/j.engfailanal.2011.06.010.

[48] P.. Kelly, R.. Arnell, Magnetron sputtering: a review of recent developments and applications, Vacuum. 56 (2000) 159–172. doi:10.1016/S0042-207X(99)00189-X.

[49] J.A. Thornton, High Rate Thick Film Growth, Annu. Rev. Mater. Res. 7 (1977) 239–260.

[50] B. Maier, Cold Spray Materials Deposition of Coatings for applications in corrosive environments, University of Wisconsin-Madison, 2015.

[51] a. Moridi, S.M. Hassani-Gangaraj, M. Guagliano, M. Dao, Cold spray coating: review of material systems and future perspectives, Surf. Eng. 30 (2014) 369–395. doi:10.1179/1743294414Y.0000000270.

[52] University of Wisconsin Cold Spray Program, (2014). http://coldspray.ep.wisc.edu/program.html.

[53] L. Pawlowski, The Science and Engineering of Thermal Spray Coatings, John Wiley & Sons, Inc, 2008.

[54] L.N. Lie, W.A. Tiller, K.C. Saraswat, Thermal oxidation of silicides, J. Appl. Phys. 56 (1984) 2127. doi:10.1063/1.334212.

[55] B.E. Deal, A.S. Grove, General relationship for the thermal oxidation of silicon, J. Appl. Phys. 36 (1965) 3770–3778. doi:10.1063/1.1713945.

[56] K. Kurokawa, A. Yamauchi, Classification of Oxidation Behavior of Disilicides, Solid State Phenom. 127 (2007) 227–232.

[57] D.A. Berztiss, R.R. Cerchiara, E.A. Gulbransen, F.S. Pettit, G.H. Meier, Oxidation of MoSi2 and comparison with other silicide materials, Mater. Sci. Eng. A. 155 (1992) 165–181. doi:10.1016/0921-5093(92)90324-T.

[58] A.D. Chirkin, V.O. Lavrenko, V.M. Talash, High-temperature and electrochemical oxidation of transition metal silicides, Powder Metall. Met. Ceram. 48 (2009) 330–345. doi:10.1007/s11106-009-9124-9.

[59] E. Fitzer, Molybdandisilizid als Hochtemperaturwerkstoffeo, in: Warmfest Und Korrosionbestandige Sinterwerkstoffe, 2nd Plansee Semin., 1956: p. 56.

[60] Y. Liu, G. Shao, P. Tsakiropoulos, On the oxidation behaviour of MoSi 2, Intermetallics. 9 (2001) 125–136. doi:10.1016/S0966-9795(00)00114-X.

[61] A.A. Sharif, High-temperature oxidation of MoSi2, J. Mater. Sci. 45 (2010) 865–870. doi:10.1007/s10853-009-4012-8.

[62] F. Schwettmann, R. Graff, M. Kolodney, Mechanism of the oxidation of titanium disilicide, J. Electrochem. Soc. (1971) 654–663.

[63] S. Melsheimer, M. Fietzek, V. Kolarik, A. Rahmel, M. Schiitze, Oxidation of the Intermetallics MoSi2 and TiSi2 - A Comparison, Oxid. Met. 47 (1997) 139–203. doi:10.1007/BF01682375.

[64] S. Becker, A. Rahmel, M. Schutze, Oxidation of TiSi2 and MoSi2, Solid State Ionics. 53–56 (1992) 280–289. doi:10.1016/0167-2738(92)90391-2.

[65] P. Pérez, M.. López, J.. Jiménez, P. Adeva, Oxidation behaviour of Al-alloyed ZrSi2 at 700°C, Intermetallics. 8 (2000) 1393–1398. doi:10.1016/S0966-9795(00)00087-X.

[66] W.J. Strydom, J.C. Lombaard, R. Pretorius, Thermal oxidation of the silicides CoSi2, CrSi2, NiSi2, PtSi, TiSi2 and ZrSi2, Thin Solid Films. 131 (1985) 215–231. doi:10.1016/0040-6090(85)90142-7.

[67] P. Pérez, Oxidation behavior of Al-alloyed ZrSi2, Oxid. Met. 56 (2001) 163–176. http://www.scopus.com/inward/record.url?eid=2-s2.0-0043205868&partnerID=tZOtx3y1.

[68] H. Geßwein, A. Pfrengle, J.R. Binder, J. Haußelt, Kinetic model of the oxidation of ZrSi2 powders, J. Therm. Anal. Calorim. 91 (2007) 517–523. doi:10.1007/s10973-007-8461-5.

[69] A. Dasgupta, P.P. Kulkarni, G.J. Gorade, D.K. Chandraker, A.K. Nayak, S.P. Walker, Quenching of a Heated Rod : Physical Phenomena and Heat Transfer, (2015) 7348–7358.

[70] H. Kim, G. DeWitt, T. McKrell, J. Buongiorno, L. w. Hu, On the quenching of steel and zircaloy

spheres in water-based nanofluids with alumina, silica and diamond nanoparticles, Int. J. Multiph. Flow. 35 (2009) 427–438. doi:10.1016/j.ijmultiphaseflow.2009.02.004.

[71] S.K. Roy Chowdhury, R.H.S. Winterton, Surface effects in pool boiling, Int. J. Heat Mass Transf. 28 (1985) 1881–1889. doi:10.1016/0017-9310(85)90210-8.

[72] D.M. Freebairn, The influence of surface conditions on runoff and soil loss, Natl. Soils Conf. (1980) 280–290.

[73] C.Y. Lee, T.H. Chun, W.K. In, Effect of change in surface condition induced by oxidation on transient pool boiling heat transfer of vertical stainless steel and copper rodlets, Int. J. Heat Mass Transf. 79 (2014) 397–407. doi:10.1016/j.ijheatmasstransfer.2014.08.030.

[74] I.U. Vakarelski, N. a Patankar, J.O. Marston, D.Y.C. Chan, S.T. Thoroddsen, Stabilization of Leidenfrost vapour layer by textured superhydrophobic surfaces., Nature. 489 (2012) 274–7. doi:10.1038/nature11418.

[75] J.Y. Kang, S.H. Kim, H. Jo, G. Park, H.S. Ahn, K. Moriyama, et al., Film boiling heat transfer on a completely wettable surface with atmospheric saturated distilled water quenching, Int. J. Heat Mass Transf. 93 (2016) 67–74. doi:10.1016/j.ijheatmasstransfer.2015.09.049.

[76] H. Kim, J. Buongiorno, L.W. Hu, T. McKrell, Nanoparticle deposition effects on the minimum heat flux point and quench front speed during quenching in water-based alumina nanofluids, Int. J. Heat Mass Transf. 53 (2010) 1542–1553. doi:10.1016/j.ijheatmasstransfer.2009.11.029.

[77] L.W. Fan, J.Q. Li, D.Y. Li, L. Zhang, Z.T. Yu, Regulated transient pool boiling of water during quenching on nanostructured surfaces with modified wettability from superhydrophilic to superhydrophobic, Int. J. Heat Mass Transf. 76 (2014) 81–89. doi:10.1016/j.ijheatmasstransfer.2014.04.025.

[78] N. Zuber, Hydrodynamic Aspects of Boiling Heat, University of California-Los Angeles, 1959. doi:10.2172/4175511.

[79] P.J. Berenson, Film-Boiling Heat Transfer From a Horizontal Surface, J. Heat Transfer. 83 (1961) 351. doi:10.1115/1.3682280.

[80] R. Henry, A correlation for the minimum film boiling temperature, AlchE Symp. Ser. 70 (1974) 81–90.

[81] S. Ya, R.E.H. Henry, An Investigation of the Minimum Film Boiling Temperature on Horizontal Surfaces, Trans. ASME. 100 (1978) 260–267.

[82] A. Sakurai, M. Shiotsu, K. Hata, Effect of System Pressure on Film-Boiling Heat Transfer , Minimum Heat Flux , and Minimum Temperature, 330 (1984) 321–330.

[83] Nishiom Shigefumi, Prediction technique for minimum-heat-flux (MHF) -point condition of saturated pool boiling, Int. J. Heat Mass Transf. 30 (1987) 2045–2057.

[84] L. Peterson, An experimental study of the minimum film boiling temperature for vertical cylinders at elevated pressure, Kansas State University, 2000.

[85] S.P. Murarka, Silicides for VLSI Applications, 1st ed., Academic Press, 2012.

[86] P. Zeman, J. Musil, Difference in high-temperature oxidation resistance of amorphous Zr-Si-N and W-Si-N films with a high Si content, Appl. Surf. Sci. 252 (2006) 8319–8325. doi:10.1016/j.apsusc.2005.11.038.

[87] C.K. Chung, T.S. Chen, N.W. Chang, S.C. Chang, M.W. Liao, Oxidation resistance and mechanical property of cosputtered quasi-amorphous Ta-Si-N films under vacuum rapid thermal annealing, Surf. Coatings Technol. 205 (2010) 1268–1272. doi:10.1016/j.surfcoat.2010.08.080.

[88] F. Incropera, D. Dewitt, T. Bergman, A. Lavine, Fundamentals of Heat and Mass Transfer, 6th ed., John Wiley & Sons, Inc, 2007.

[89] Y. Kim, J. Park, J. Cleveland, Thermophysical Properties Database of Materials for Light Water Reactors and Heavy Water Reactors, 2006. http://scholar.google.com/scholar?hl=en&btnG=Search&q=intitle:Thermophysical+properties+database+of+materials+for+light+water+reactors+and+heavy+water+reactors#2.

[90] H.R. Busby, D.M. Trujillo, Numerical Experiments with A New Differentiating Filter, J. Biomech. 107 (1985) 293–299.

[91] C.R. Dohrmann, H.R. Busby, D.M. Trujillo, Smoothing noisy data using dynamic programming and generalized cross-validation, J. Biomech. Eng. 110 (1988) 37–41.

[92] V.K. Dhir, G.P. Purohit, Subcooled film-boiling heat transfer from spheres, Nucl. Eng. Des. 47 (1978) 49–66. doi:10.1016/0029-5493(78)90004-3.

[93] V. Carey, Liquid-Vapor Phase Change Phenomena, Hemisphere Publishing Corporation, 1992.

[94] T. Yamada, K. Toyoda, T. Shigechi, S. Momoki, K. Kanemaru, T. Yamaguchi, Film boiling heat transfer around a vertical finite-length cylinder with a convex hemispherical bottom, Heat Transf. - Asian Res. 39 (2010) 166–177. doi:10.1002/htj.20289.

[95] C. Liu, Film boiling on spheres in single- and two-phase flows, University of California, Santa Barbara, CA, 1995.

[96] A. Naumkin, A. Kraut-Vass, S. Gaarenstroom, NIST X-ray photoelectron spectroscopy database, 2012. (n.d.). http://srdata.nist.gov/xps/Default.aspx.

[97] M.J. Guittet, J.P. Crocombette, M. Gautier-Soyer, Bonding and XPS chemical shifts in ZrSiO4 versus SiO2 and ZrO2: Charge transfer and electrostatic effects, Phys. Rev. B. 63 (2001) 125117. doi:10.1103/PhysRevB.63.125117.

[98] G. Rayner, R. Therrien, G. Lucovsky, The Structure of Plasma-Deposited and Annealed Pseudo-Binary ZrO2-SiO2 Alloys, MRS Proc. 611 (2000) C1.3.1-C1.3.9. doi:10.1557/PROC-611-C1.3.1.

[99] G. Lucovsky, G.B. Rayner, Microscopic model for enhanced dielectric constants in low concentration SiO2-rich noncrystalline Zr and Hf silicate alloys, Appl. Phys. Lett. 77 (2000) 2912. doi:10.1063/1.1320860.

[100] F. Schwettmann, R. Graff, M. Kolodney, Mechanism of the oxidation of titanium disilicide, J. Electrochem. Soc. 118 (1971) 1973–1977.

[101] D.J. Tallman, J. Yang, L. Pan, B. Anasori, M.W. Barsoum, Reactivity of Zircaloy-4 with Ti3SiC2 and Ti2AlC in the 1100–1300°C temperature range, J. Nucl. Mater. 460 (2015) 122–129. doi:10.1016/j.jnucmat.2015.02.006.

[102] S. Roy, A. Paul, Growth of hafnium and zirconium silicides by reactive diffusion, Mater. Chem. Phys. 143 (2014) 1309–1314. doi:10.1016/j.matchemphys.2013.11.039.

[103] C. Veytizou, J.F. Quinson, O. Valfort, G. Thomas, Zircon formation from amorphous silica and tetragonal zirconia: Kinetic study and modelling, Solid State Ionics. 139 (2001) 315–323. doi:10.1016/S0167-2738(01)00676-2.

[104] H. Kim, P.C. McIntyre, Spinodal decomposition in amorphous metal-silicate thin films: Phase diagram analysis and interface effects on kinetics, J. Appl. Phys. 92 (2002) 5094–5102. doi:10.1063/1.1510590.

[105] S. Stemmer, Z. Chen, C.G. Levi, P.S. Lysaght, B. Foran, J. a. Gisby, et al., Application of metastable phase diagrams to silicate thin films for alternative gate dielectrics, Japanese J. Appl. Physics, Part 1 Regul. Pap. Short Notes Rev. Pap. 42 (2003) 3593–3597. doi:10.1143/JJAP.42.3593.

[106] D. Porter, K. Easterling, Phase transformations in metals and alloys, 1st ed., Van Nostrand Reinhold, 1981.

[107] A. Kaiser, M. Lobert, R. Telle, Thermal stability of zircon (ZrSiO4), J. Eur. Ceram. Soc. 28 (2008) 2199–2211. doi:10.1016/j.jeurceramsoc.2007.12.040.

[108] T. Itoh, Formation of polycrystalline zircon (ZrSiO4) from amorphous silica and amorphous zirconia, J. Cryst. Growth. 125 (1992) 223–228. doi:10.1016/0022-0248(92)90336-H.

[109] S. Ramani, E. Subbarao, K. Gokhale, Kinetics of Zircon ynthesis, J. Am. Ceram. Soc. 52 (1969) 619–623.

[110] B. Pint, K. Terrani, Y. Yamamoto, L. Ott, L. Snead, Practical & Scientific Aspects of FeCrAl Oxidation, 2013.

[111] K. More, P. Tortorelli, M. Ferber, J. Keiser, Observations of Accelerated Silicon Carbide Recession by Oxidation at High Water-Vapor Pressures, J. Am. Ceram. Soc. 83 (2000) 211–213. doi:10.1111/j.1151-2916.2000.tb01172.x.

[112] E. Sooby Wood, S.S. Parker, A.T. Nelson, S.A. Maloy, MoSi2 Oxidation in 670-1498 K Water Vapor, J. Am. Ceram. Soc. 99 (2016) 1412–1419. doi:10.1111/jace.14120.

[113] R. Fournier, J. Rowe, The solubility of amorphous silica in water at high temperatures and high pressures, Am. Mineral. 62 (1977) 1052–1056.

[114] E.J. Opila, N.S. Jacobson, D.L. Myers, E.H. Copland, M. Total, Predicting Oxide Stability in High-Temperature Water Vapor, J. Met. (2006) 22–28.

[115] S.N. Rashkeev, M. V. Glazoff, A. Tokuhiro, Ultra-high temperature steam corrosion of complex silicates for nuclear applications: A computational study, J. Nucl. Mater. 444 (2014) 56–64. doi:10.1016/j.jnucmat.2013.09.021.

[116] S. Ueno, T. Ohji, H.T. Lin, Corrosion and recession behavior of zircon in water vapor environment at high temperature, Corros. Sci. 49 (2007) 1162–1171. doi:10.1016/j.corsci.2006.08.013.

[117] A.P. Dementjev, O.P. Ivanova, L.A. Vasilyev, A. V. Naumkin, D.M. Nemirovsky, D.Y. Shalaev, Altered layer as sensitive initial chemical state indicator∗, J. Vac. Sci. Technol. A Vacuum, Surfaces, Film. 12 (1994) 423–427. doi:10.1116/1.579258.

[118] R.B. Shalvoy, P.J. Reucroft, Characterization of coprecipitated nickel on silica methanation catalysts by X-ray photoelectron spectroscopy, J. Catal. 56 (1979) 336–348. doi:10.1016/0021-9517(79)90126-X.

[119] T. Romotowski, J. Komorek, J. Stoch, V.M. Mastikhin, ZSM-5 zeolite modified with zirconyl ions, Pol. J. Chem. 69 (1995) 621–626.

[120] W.C. Butterman, Zircon Stability and ZrO2-SiO2 Phase Diagram, Am. Mineral. 52 (1967) 880.

[121] B.W. Busch, W.H. Schulte, E. Garfunkel, T. Gustafsson, Oxygen exchange and transport in thin zirconia films on Si (100), Phys. Rev. B. 62 (2000) 290–293.

[122] K.N. Lee, Current status of environmental barrier coatings for Si-based ceramics, Surf. Coatings Technol. 133–134 (2000) 1–7. doi:10.1016/S0257-8972(00)00889-6.

[123] H. Yeom, B. Maier, Evolution of Multi-Layered Scale Structures during High Temperature Oxidation of ZrSi2, J. Mater. Res. 31 (2016) 3409–3419.

[124] N. Bertolino, U. Anselmi-Tamburini, F. Maglia, G. Spinolo, Z.A. Munir, Combustion synthesis of Zr-Si intermetallic compounds, J. Alloys Compd. 288 (1999) 238–248. doi:10.1016/S0925-8388(99)00077-8.

[125] P. Chraska, K. Neufuss, H. Herman, Plasma spraying of zircon, J. Therm. Spray Technol. 6 (1997) 445–448. doi:10.1007/s11666-997-0029-1.

[126] S. Schelz, F. Enguehard, N. Caron, D. Plessis, B. Minot, F. Guillet, et al., Recombination of silica and zirconia into zircon by means of laser treatment of plasma-sprayed coatings, J. Mater. Sci. 43 (2008) 1948–1957. doi:10.1007/s10853-007-2406-z.

[127] B. Srivivas, Experimental evaluation of oxide growth in binary zirconium alloys along with pure zirconium and zircoly-2 by steam corrosion testing, Royal Institute of Technology, 2012.

[128] C. Proff, Microstructural aspects of the oxidation of zirconium alloys, University of Grenoble, 2011.

[129] M. Fritsch, H. Klemm, M. Herrmann, B. Schenk, Corrosion of selected ceramic materials in hot gas environment, J. Eur. Ceram. Soc. 26 (2006) 3557–3565. doi:10.1016/j.jeurceramsoc.2006.01.015.

[130] D. Gao, Y. Zhang, J. Fu, C. Xu, Y. Song, X. Shi, Oxidation of zirconium diboride-silicon carbide ceramics under an oxygen partial pressure of 200Pa: Formation of zircon, Corros. Sci. 52 (2010) 3297–3303. doi:10.1016/j.corsci.2010.06.004.

[131] B. Nait-Ali, K. Haberko, H. Vesteghem, J. Absi, D.S. Smith, Thermal conductivity of highly porous zirconia, J. Eur. Ceram. Soc. 26 (2006) 3567–3574. doi:10.1016/j.jeurceramsoc.2005.11.011.

[132] D. Askeland, W. Wright, The Science and Engineering of Materials, 7th ed., Cengage Learning, 2016.

[133] Y. Moriya, A. Navrotsky, High-temperature calorimetry of zirconia: Heat capacity and thermodynamics of the monoclinic-tetragonal phase transition, J. Chem. Thermodyn. 38 (2006) 211–223. doi:10.1016/j.jct.2005.05.002.

[134] A. Bolukbasi, D. Ciloglu, Pool boiling heat transfer characteristics of vertical cylinder quenched by SiO2–water nanofluids, Int. J. Therm. Sci. 50 (2011) 1013–1021. doi:10.1016/j.ijthermalsci.2011.01.011.

[135] B.B. Mikic, W.M. Rohsenow, A New Correlation of Pool-Boiling Data Including the Effect of Heating Surface Characteristics, J. Heat Transfer. 91 (1969) 245. doi:10.1115/1.3580136.

[136] B. Lubin, Analytical Derivation for Total Heat Transfer Coefficient in Stable Film Boiling From Vertical Plate, Trans. ASME. (1969) 452–452.

[137] T.D. Bui, V.K. Dhir, Film Boiling Heat Transfer on an Isothermal Vertical Surface, Trans. ASME. 107 (1985) 764–771.

[138] R.. Shumway, Use of the Shumway Tmin Correlation with Zircaloy for TRACG Analysis, Wilmington, 2013.

[139] A. Sakurai, M. Shiotsu, K. Hata, Effects of system pressure on minimum film boiling temperature for various liquids, Exp. Therm. Fluid Sci. 3 (1990) 450–457. doi:10.1016/0894-1777(90)90043-7.

[140] N. Zuber, Hydrodynamic aspect of boiling heat transfer, University of California, Los Angeles, 1959. doi:10.2172/4175511.

[141] I. Michiyoshi, O. Takahashi, Y. Kikuchi, Heat transfer and the low limit of film boiling, Exp. Therm. Fluid Sci. 2 (1989) 268–279. doi:10.1016/0894-1777(89)90016-2.

[142] S. Toda, M. Mori, Subcooled film boiling and the behavior of vapor film on a horiontal wire and a sphere, Heat Transf. 4 (1982) 173–178.

[143] L.A. Bromley, N.R. LeRoy, J.A. Robbers, Heat transfer in forced convection film boiling, Ind. Eng. Chem. 45 (1953) 2639–2646.

[144] C. Liu, T.G. Theofanous, Film boiling on spheres in single-and two-phase flows, University of California, Santa Barbara, 1994. http://www.osti.gov/scitech/servlets/purl/10115439.

[145] J. Kang, G.C. Lee, M. Kaviany, H.S. Park, K. Moriyama, M.H. Kim, Minimum film-boiling quench temperature increase by CuO porous-microstructure coating, Appl. Phys. Lett. 110 (2017) 43903. doi:10.1063/1.4974923.

[146] W. Bradfield, Liquid-solid contact in stable film boiling, Ind. Eng. Chem. Fundam. 5 (1966) 200–204. doi:10.1021/i160018a008.

[147] H.S. Ahn, V. Sathyamurthi, D. Banerjee, Pool Boiling Experiments on a Nano-Structured Surface, IEEE Trans. Components Packag. Technol. 32 (2009) 156–165.

[148] S. Yao, R.E. Henry, An Investigation of the Minimum Film Boiling Temperature on Horizontal Surfaces, J. Heat Transfer. 100 (1978) 260–266.

[149] M. Moran, H. Shapiro, D. Boettner, M. Bailey, Fundamentals of Engineering Thermodynamics, 8th ed., John Wiley & Sons, Inc, 2014.

[150] D. Dhuga, R. Winterton, Measurement of surface contact in transition boiling, Int. J. Heat Mass Transf. 28 (1985) 1869–1880. doi:10.1016/0017-9310(85)90209-1.

[151] Y. Kikuchi, T. Ebisu, I. Michiyoshi, Measurement of liquid-solid contact in film boiling, Int. J. Heat Mass Transf. 35 (1992) 1589–1594.

[152] Y. Kikuchi, T. Hori, I. Michiyoshi, Minimum film boiling temperature for cooldown of insulated metals in saturated liquid, Int. J. Heat Mass Transf. 28 (1985) 1105–1114. doi:10.1016/0017-9310(85)90119-X.

[153] L. Lee, J. Chen, Liquid-solid contact measurements using a surface thermodouple temperature probe in atmospheric pool boiling water *, Int. J. Heat Mass Transf. 28 (1985) 1415–1423.

[154] K. Makino, I. Michiyoshi, The behavior of a water droplet on heated surfaces, Int. J. Heat Mass Transf. 27 (1984) 781–791. doi:10.1016/0017-9310(84)90147-9.

[155] J. Chen, K. Hsu, Heat Transfer During Liquid Contact on Superheated Surfaces, J. Heat Transf. 117 (1995) 693–697.

[156] J. Dryden, M. Yovanovich, A. Deakin, The Effect of Coatings on the Steady-State and Short Time

Constriction Resistance for an Arbitrary Axisymmetric Flux, J. Heat Transfer. 107 (1985) 33–38.

[157] P. Hui, H.S. Tan, Temperature distributions in a heat dissipation system using a cylindrical diamond heat spreader on a copper heat sink, J. Appl. Phys. 75 (1994) 748–757. doi:10.1063/1.356480.

[158] M.K. El-Adawi, M.A. Abdel-Naby, S.A. Shalaby, Laser heating of a two-layer system with constant surface absorption: an exact solution, Int. J. Heat Mass Transf. 38 (1995) 947–952. doi:10.1016/0017-9310(94)00162-O.

[159] Z. Shijun, L. Zhanqiang, Analytical and numerical solutions of transient heat conduction in monolayer-coated tools, J. Mater. Process. Technol. 209 (2009) 2369–2376. doi:10.1016/j.jmatprotec.2008.05.028.

[160] H. Carslaw, J. Jaeger, Conduction of Heat in Solids, 2nd ed., Oxford University Press, London, 1959.

[161] J. Beck, K. Cole, A. Haji-Sheikh, B. Litkouhi, Heat Conduction using Green's Functions, Hemisphere Publishing Corporation, London, 1992.

[162] M. Flem, J. Canel, S. Urvoy, Processing and characterization of Zr3Si2 for nuclear applications, J. Alloys Compd. 465 (2008) 269–273. doi:10.1016/j.jallcom.2007.10.047.

[163] S. Murarka, Silicides for VLSI Applications, Academic Press, New York, 1983.

[164] D.G. Cahill, T.H. Allen, Thermal conductivity of sputtered and evaporated SiO2 and TiO2 optical coatings, Appl. Phys. Lett. 65 (1994) 309–311. doi:10.1063/1.112355.

[165] S.M. Lee, D.G. Cahill, T.H. Allen, Thermal conductivity of sputtered oxide films, Phys. Rev. B. 52 (1995) 253–257. doi:10.1103/PhysRevB.52.253.

Appendix

Appendix A: Matlab code for T_{min} calculation

```
clear all;
filename = 'BS24-2.xlsx'; %Input data - Surface Temp vs. Heat flux
raw = xlsread(filename);
n_temp=length(raw(:,1));
temp=raw(:,1);
HF=raw(:,2);
refine=5; % constant for reduction of data (unstable data)
maxVal=590; % set upper limit of surface temp
minVal=460; % set lower limit of surface temp
d_t=0.1; % time step
totaltime=d_t*n_temp;
t(:,1)=linspace(0,totaltime,n_temp+1); % elpase time

for i=1:n_temp-1 % slope of surface heat flux
    dq_dt(i,2)=(HF(i+1)-HF(i))/(d_t);
    dq_dt(i,1)=raw(i,1);
    dq_dt(i,3)=t(i,1);
end

for i=1:n_temp-1 % slope of surface temp.
    dT_dt(i,2)=(temp(i+1)-temp(i))/d_t;
    dq_dt(i,4)=dT_dt(i,2);
    dT_dt(i,1)=t(i,1);
end

for i=1:n_temp-1 % time vs. surface heat flux
    data_2(i,1)=t(i,1);
    data_2(i,2)=raw(i,2);
end

for i=1:refine % refine data
    dq_dt(i,2)=0;
    data_2(i,2)=0;
end

for i=1:n_temp-1 % a range of data for Tmin determination
    if (dq_dt(i,1)>=minVal) && (dq_dt(i,1)<=maxVal) && (dq_dt(i,1)>0)
        crop(i,1)=dq_dt(i,2);
    end
end
standard=abs(max(crop));

for i=1:n_temp-1 % Tmin and qmin criterion
  if (dq_dt(i,1)<minVal)&&(dq_dt(i,2)>standard)
    Tmin=dq_dt(i+1,1)
    dq_dt_min=dq_dt(i+1,2)
    Qmin=HF(i+1)
    break
  end
end
```

```
scatter (temp,HF)
xlabel('Tw')
ylabel('HF')

figure
plot(dq_dt(:,3),dq_dt(:,2),'b');
hold on
plot(data_2(:,1),data_2(:,2),'k');
hold on
plot(dT_dt(:,1),dT_dt(:,2),'r');
xlabel('Time(s)')
legend('dq"/dt','q"','dT/dt')
```

Appendix B: Matlab code for vapor film thickness

```
clc
clear all

% "Setting up of reference length scale"
r=1373; % reference image number
framerate=125; % camera frame rate
jpgFilename = sprintf('%04d.jpg',r);
fullFileName = fullfile('C:\Users\902ERB-o7020\Desktop\Surface effect
images\15K\RC23-1_85.0',jpgFilename); % location of refernece image

loadimage=imread(fullFileName);
gray_image=loadimage;

thresholdValue = 100; % critical value for binary image conversion
binaryImage = gray_image < thresholdValue; % black objects are chosen for
this study

binaryImage = imfill(binaryImage, 'holes'); % get rid of any background
pixels or "holes" inside the object
imshow(binaryImage)
hold on
rows=512;% # of pixels of reference image
columns=351; % # of columns of reference image
k= round(rows/2);% center of picture row
kstart=round(rows/2); % integar of center of pixel row
k1=k-10; % starting point in row
k2=k+10; % ending point in row
l1=50; % starting point in column
l2=columns-50; % ending point in column

for k = k1:k2
    count=0;
for l=l1:l2
    if binaryImage(k,l)==1
        count=count+1;
    end
cou(1,k-(kstart-11))=count; % counting pixel of object
end

end
length=mean(cou); % average pixel of object

% The count indicates 0.39 inches diamter -> 9.9 mm
lp = 9.9/length; % mm/pixel

% "Imaging process for actual images"
dirData = dir('C:\Users\902ERB-o7020\Desktop\Surface effect images\15K\RC23-
1_85.0\*.jpg'); % location for actual images
total=numel(dirData); % the number of data images

z=0; % z is starting number for image analysis
```

```
n=total-1; % total number of images

for s = z:n
    jpgFilename = sprintf('%04d.jpg',s);
    fullFileName = fullfile('C:\Users\902ERB-o7020\Desktop\Surface effect
images\15K\RC23-1_85.0',jpgFilename);

    loadimage=imread(fullFileName);
    gray_image=loadimage;

    thresholdValue = 100;
    binaryImage = gray_image < thresholdValue;
    binaryImage = imfill(binaryImage, 'holes');

    u=k;
    count=0;
        for l = l1:l2 % define conting window in column
            if binaryImage(u,l)==1
                count=count+1;
            end
        end
        c(1,s-z+1)=count;
        if count ==0
            count=length;
        end
        a(1,s-z+1)=(count-length)*0.5*lp;

end
totalstep=n-z;
totaltime=totalstep/framerate;
t(:,1)=linspace(0,totaltime,totalstep+1);
Result(:,1)=t(:,1);
Result(:,2)=a(1,:);
%Average film thickness
AvFilm=mean(a)
%Max film thickness
MxFilm=max(a)
%Min film thickness
MnFilm=min(a)

plot (t,a,'k')
xlabel('time')
ylabel('Film thickness')
```

Appendix C: Labview code for data acquisition in quenching experiment

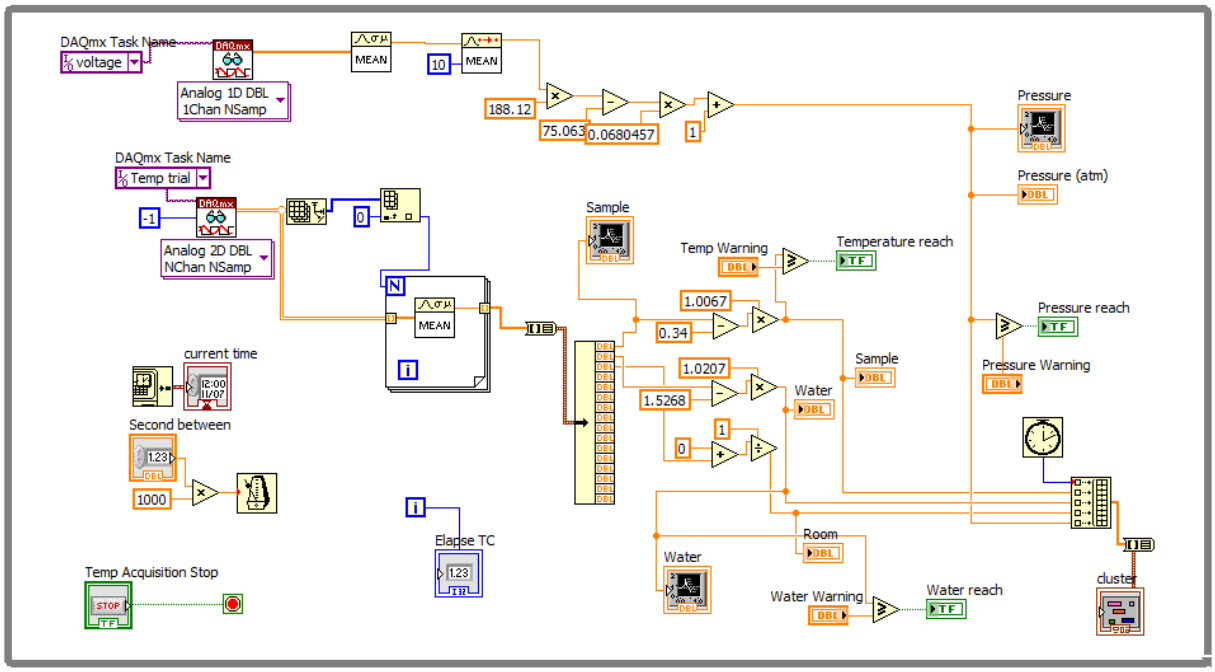

Figure 173: Labview code for data acquisition and data processing (sample temperature, water temperature, room temperature, and system pressure).

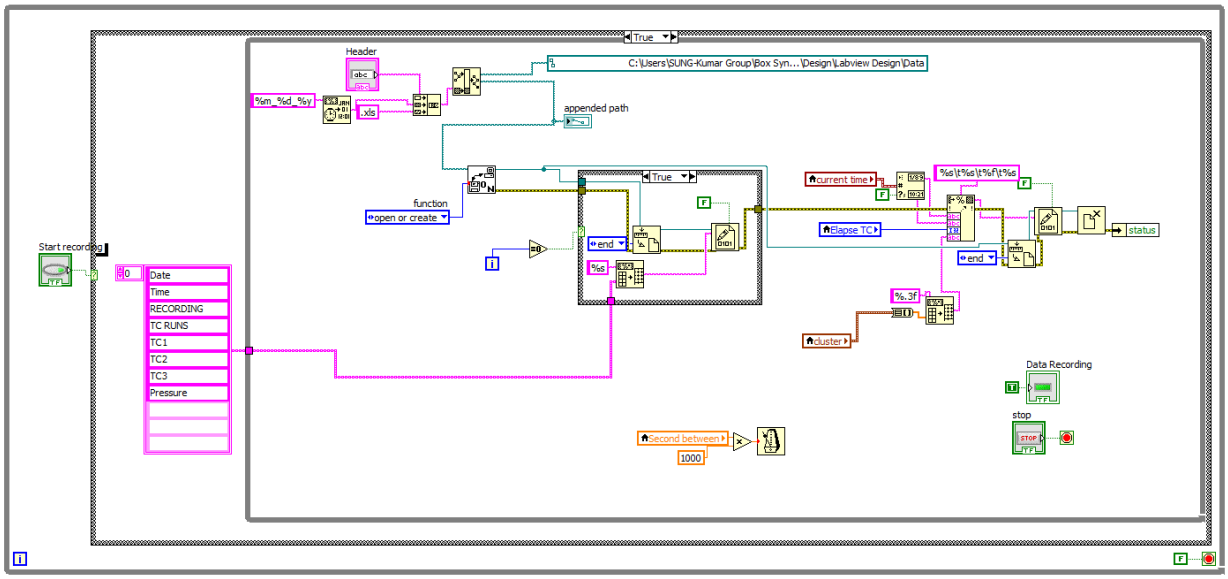

Figure 174: Labview code for data record (sample temperature, water temperature, room temperature, and system pressure).

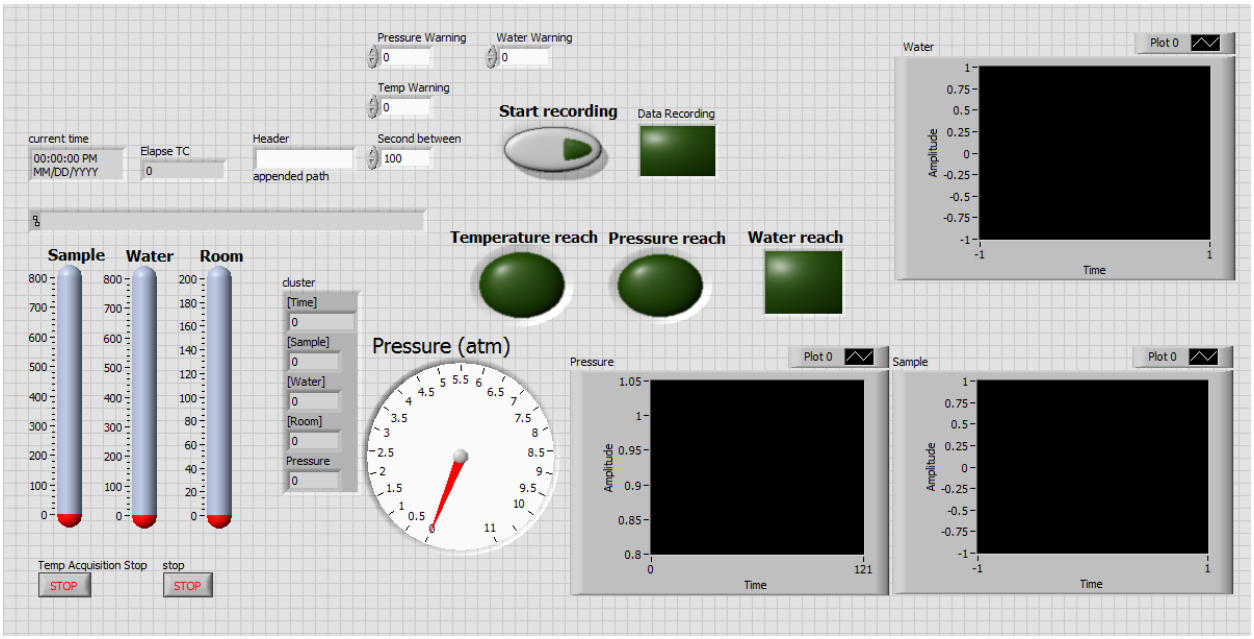

Figure 175: Display of data acquisition in Labview system.

Appendix D: CAD design for quenching facility

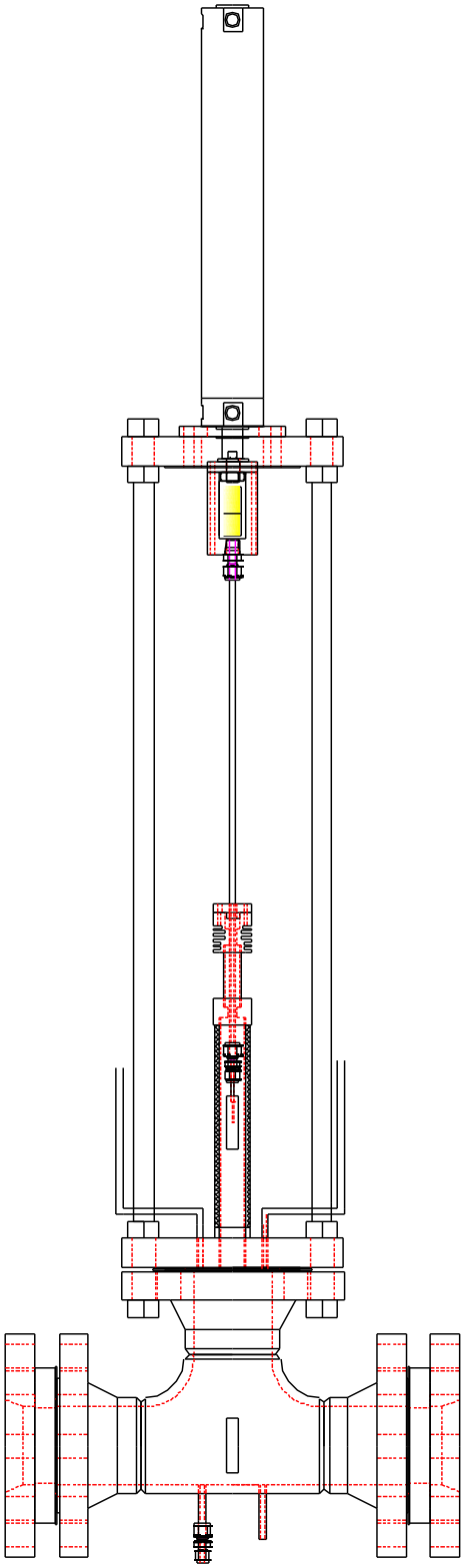

Figure 176: Full Drawing of quenching experiment facility.

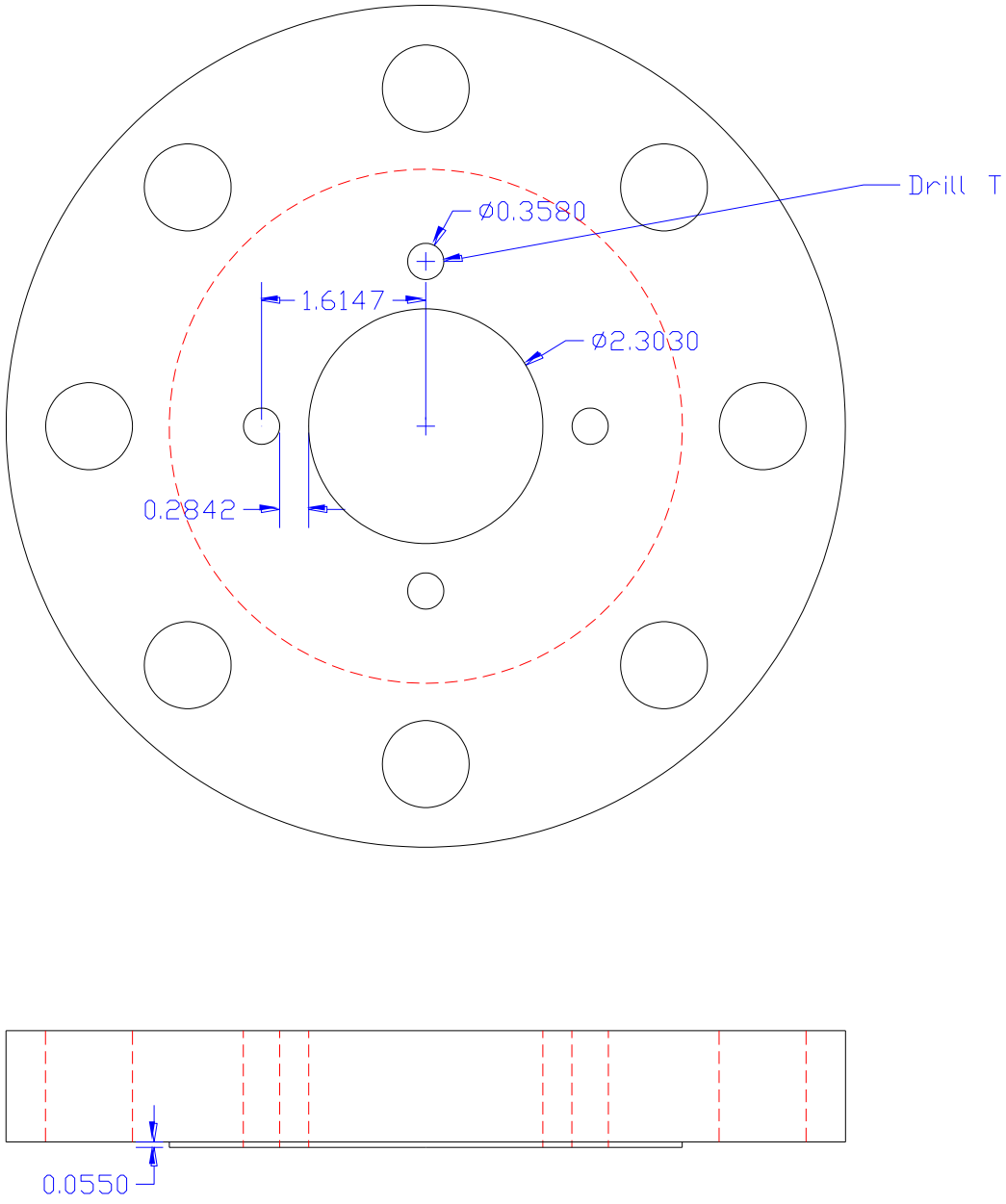

Figure 177: Top and front view of the top flange for the air actuator (dimensional scale is inch).

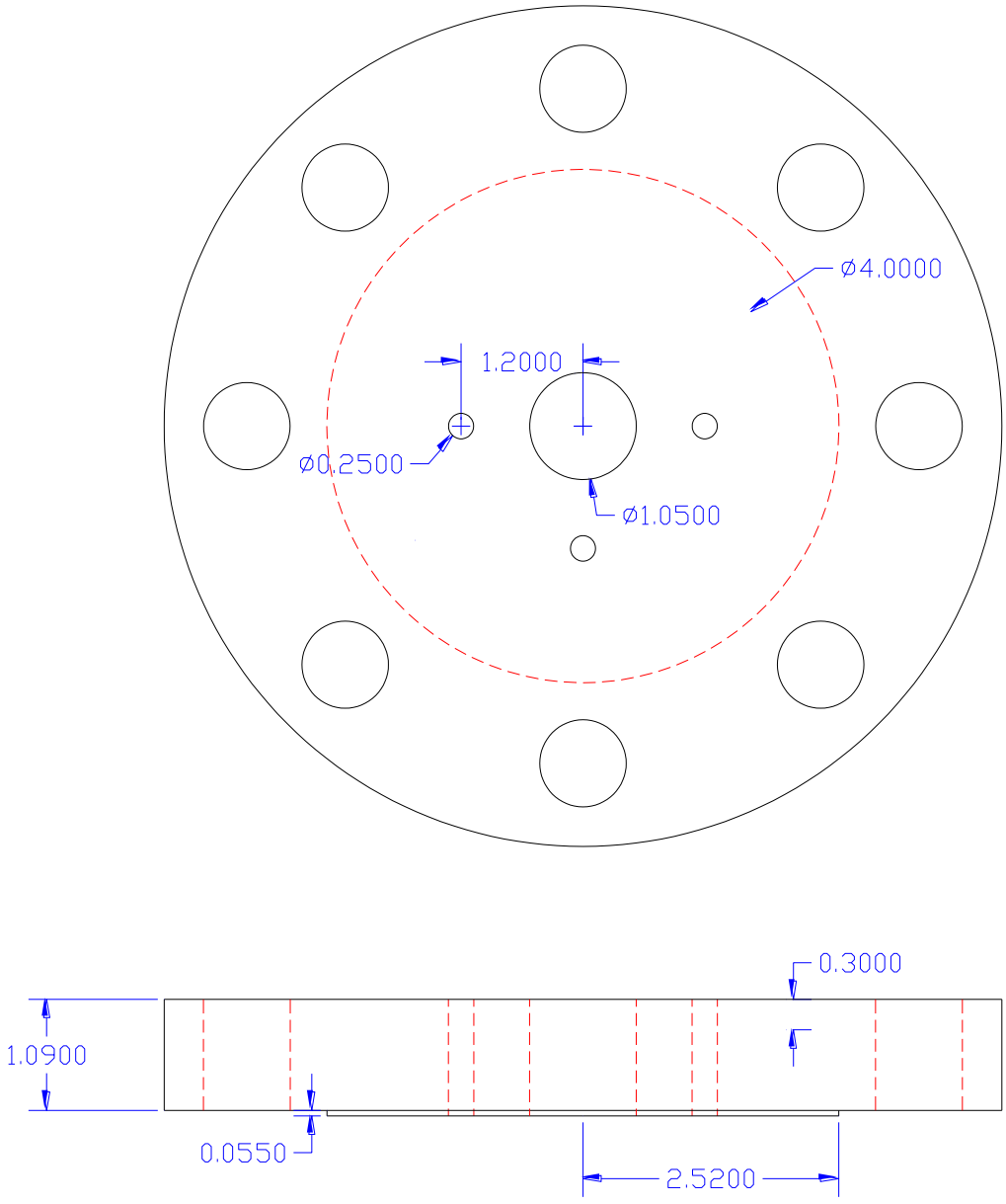

Figure 178: Top and front view of the top flange welded with the heating pipe.

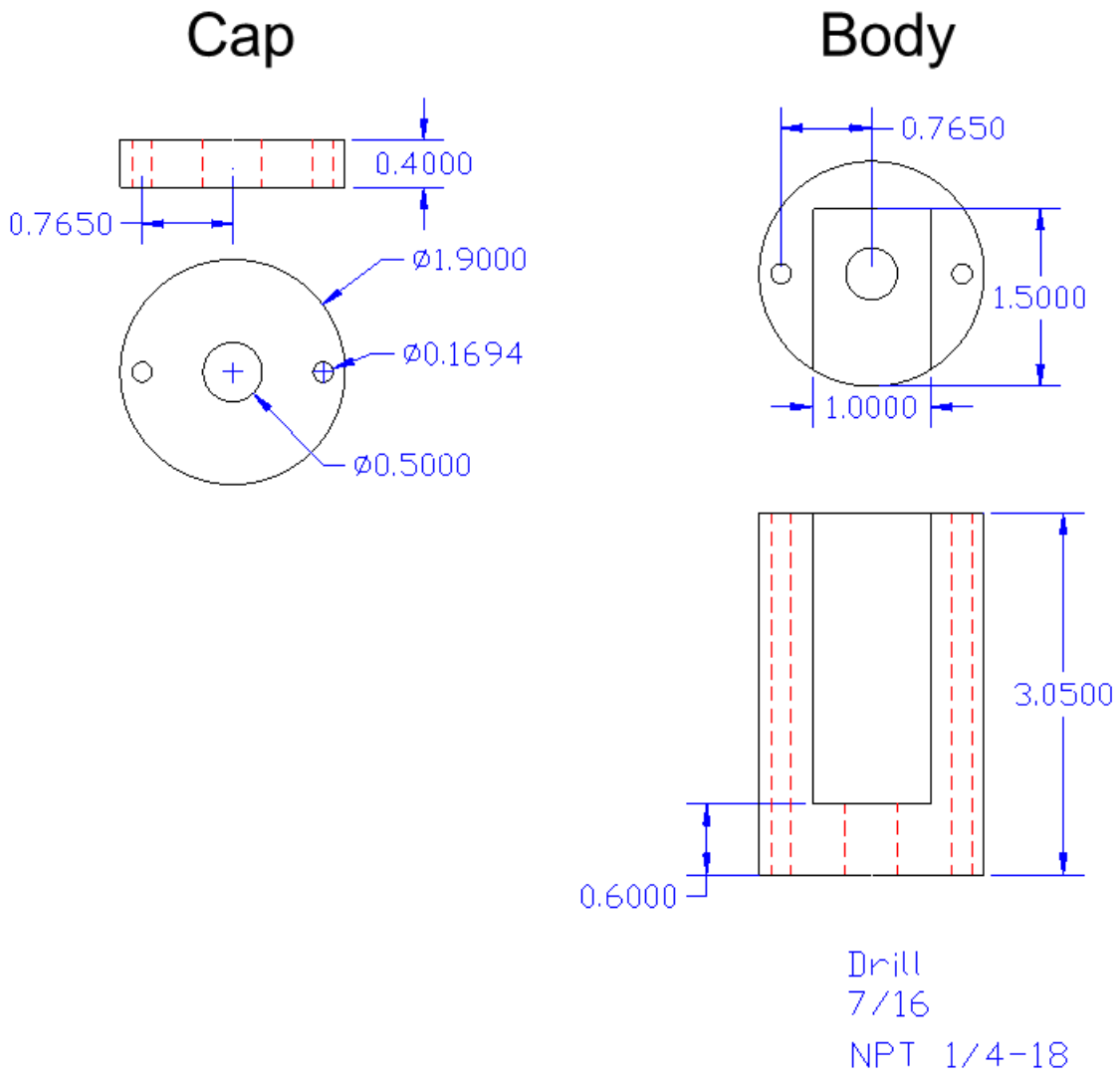

Figure 179: Top and front view of the aluminum connector.

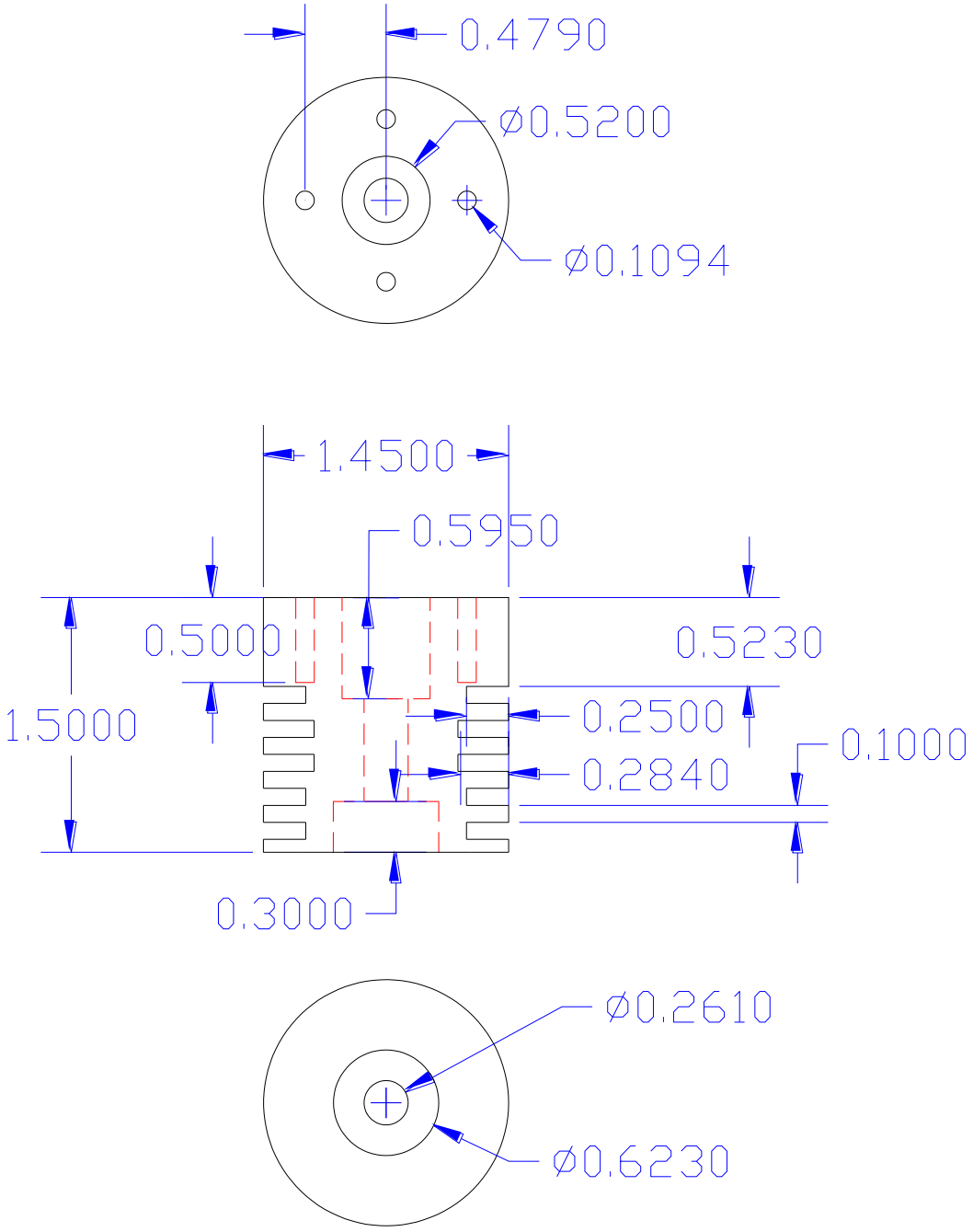

Figure 180: Top, front, and bottom view of the Teflon seal assembly.

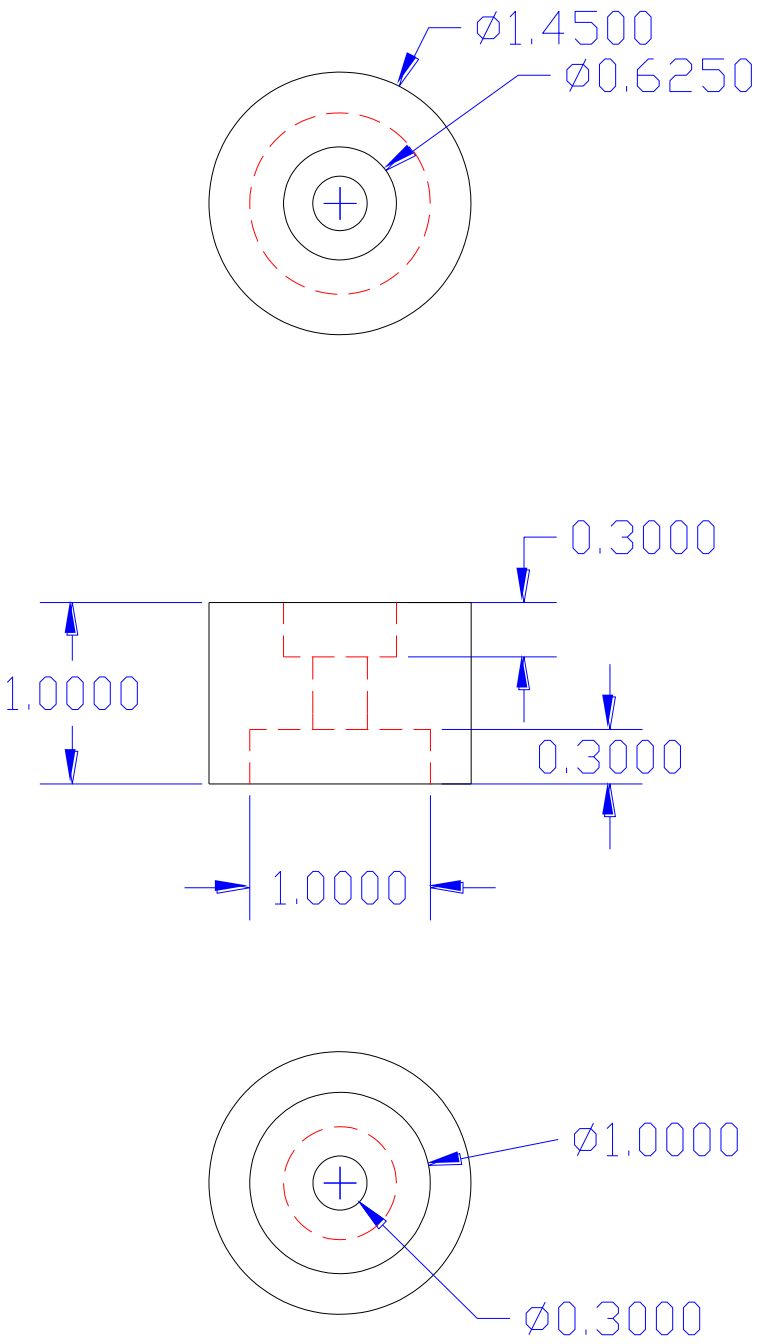

Figure 181: Top, front, and bottom view of the stainless steel connector for the heating pipe and the connecting pipe.

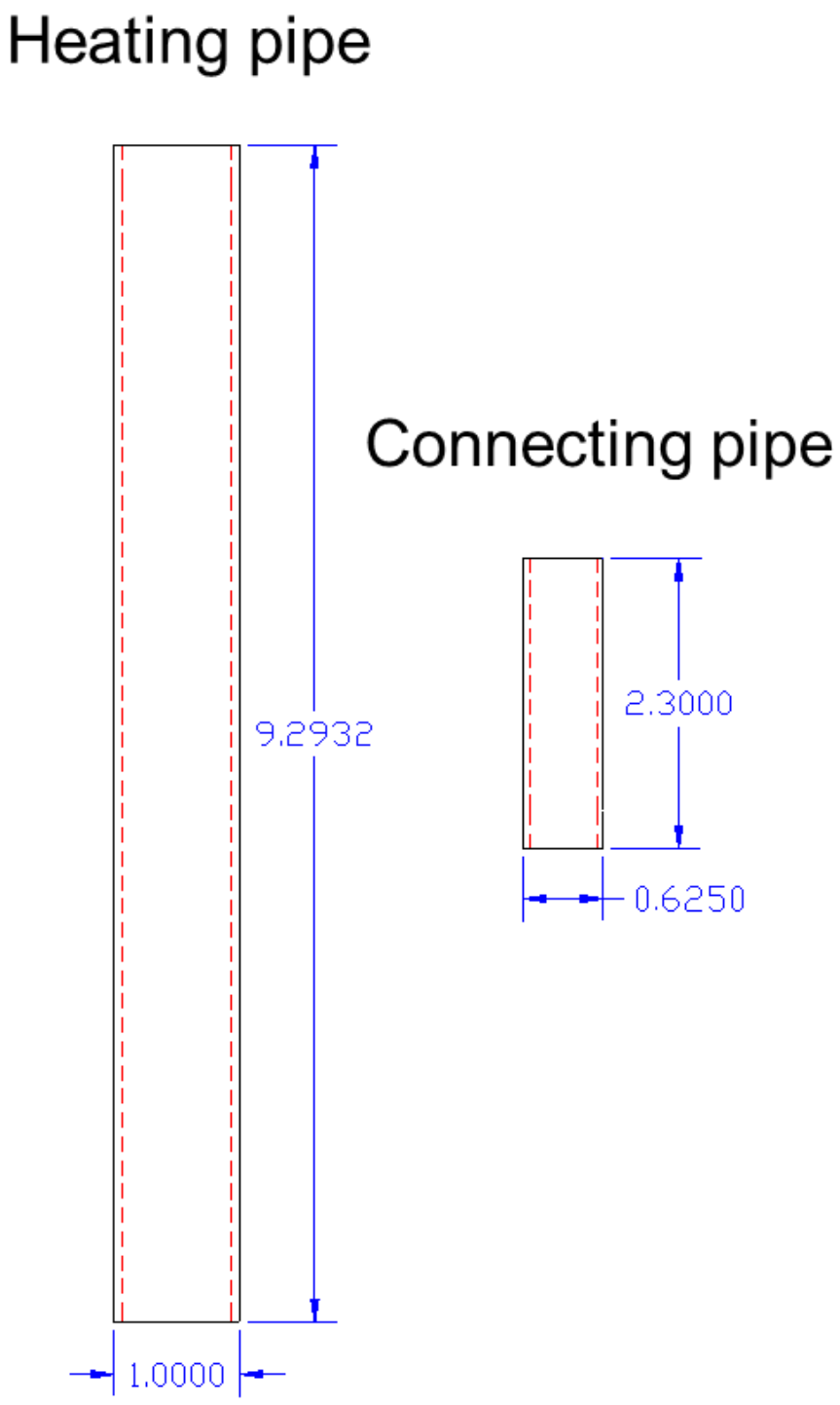

Figure 182: Front view of the heating pipe and the connecting pipe.

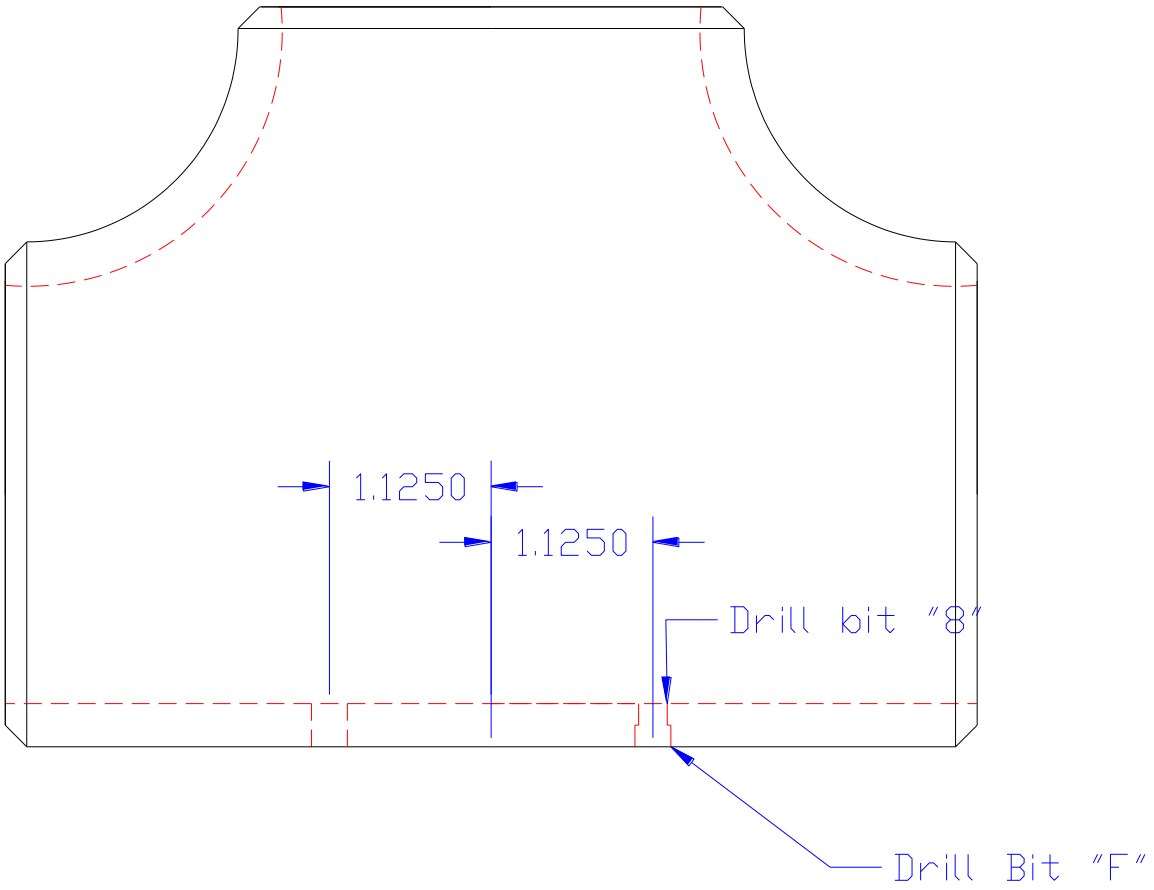

Figure 183: Front view of the tee pipe.

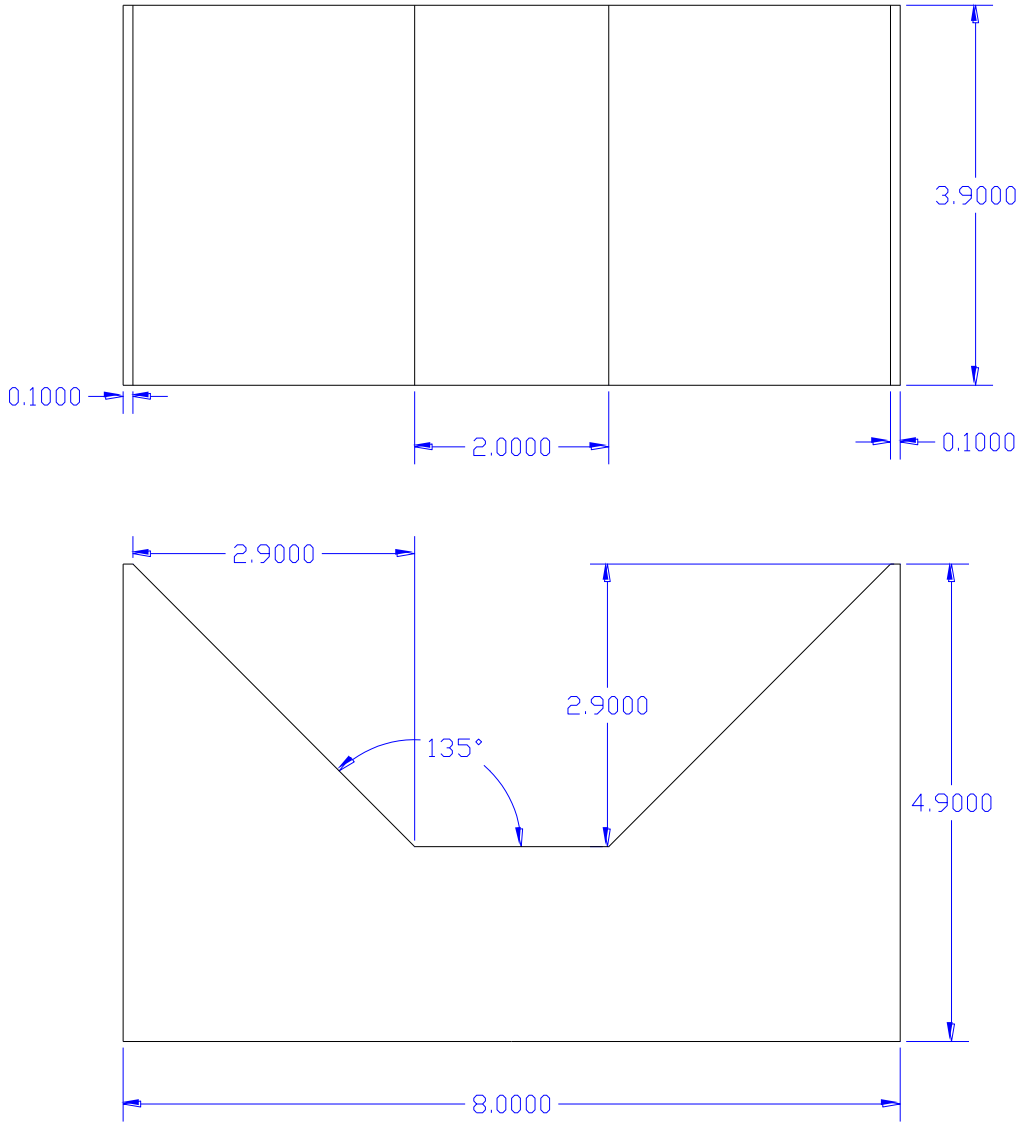

Figure 184: Top and front view of aluminum V-shaped block.

Appendix E: Quenching/Boiling curves of three repeated tests

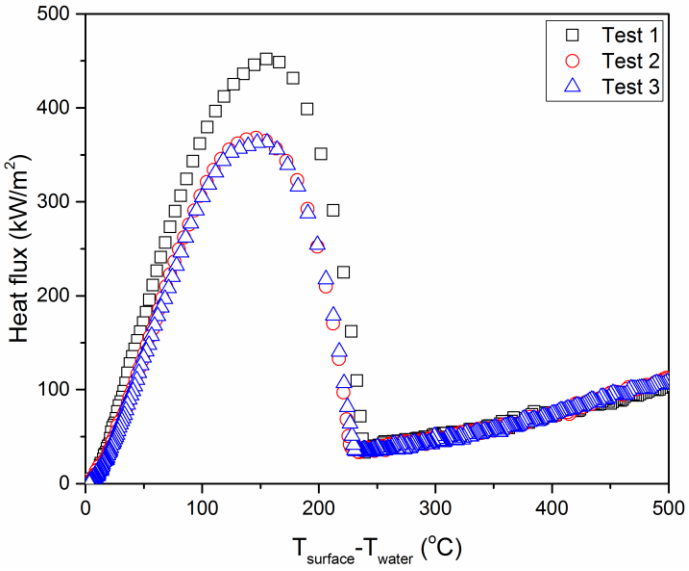

Figure 185: Boiling curves of bare Zirc-4 in saturated water at atmospheric pressure.

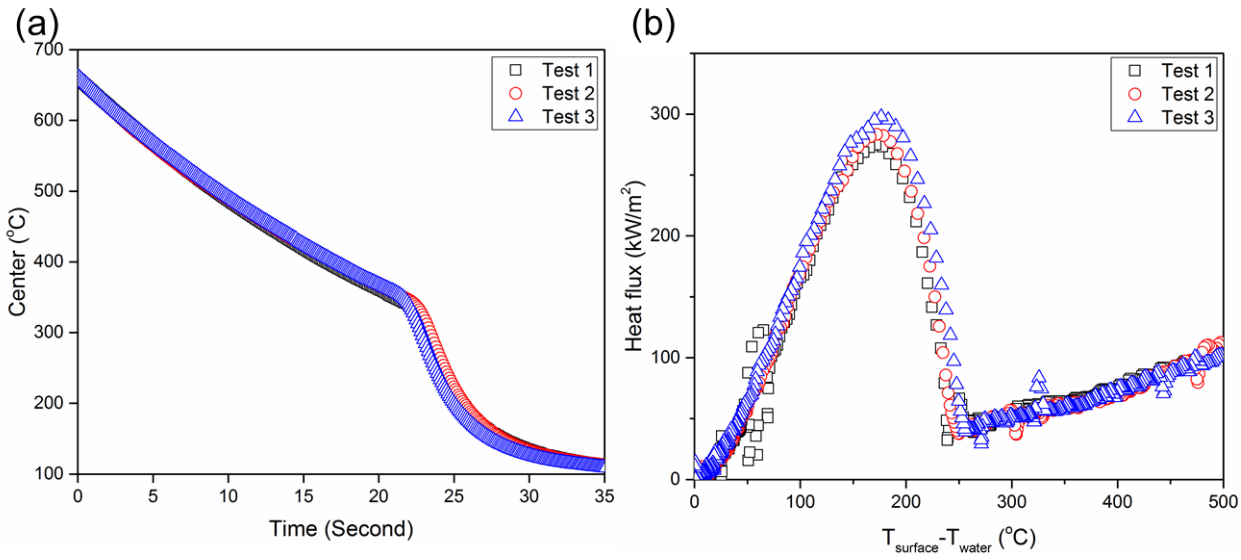

Figure 186: Quenching and Boiling curves of $ZrSi_2$ coatings in saturated water at atmospheric pressure.

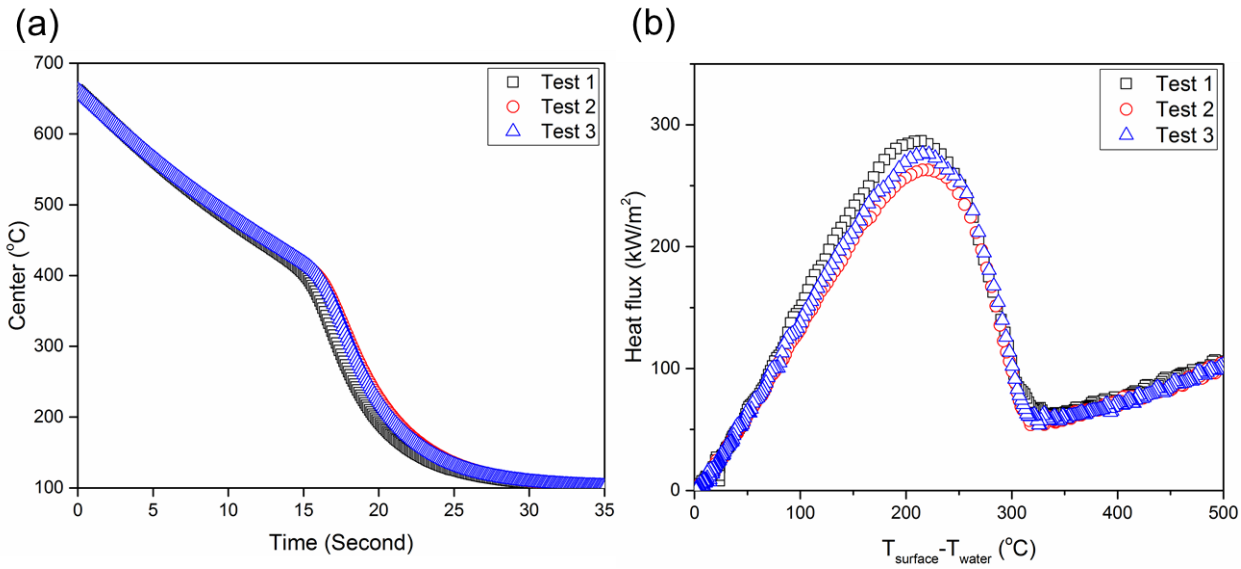

Figure 187: Quenching and Boiling curves of oxidized Zirc-4 (700 °C for 5 hours) in saturated water at atmospheric pressure.

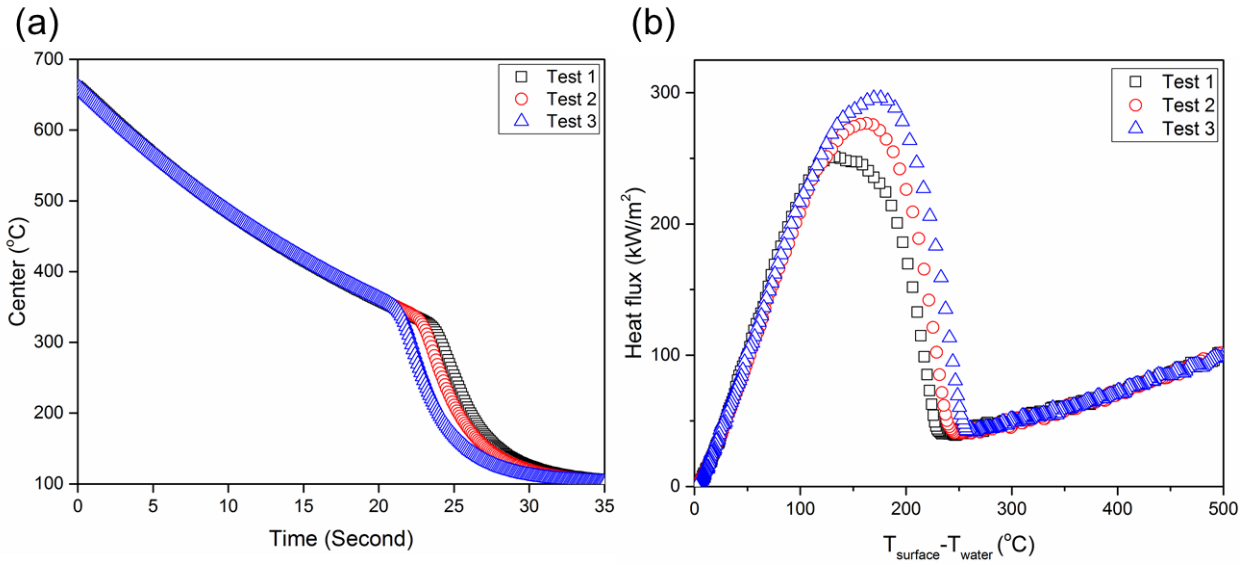

Figure 188: Quenching and Boiling curves of oxidized Zirc-4 (700 °C for 30 minutes) in saturated water at atmospheric pressure.

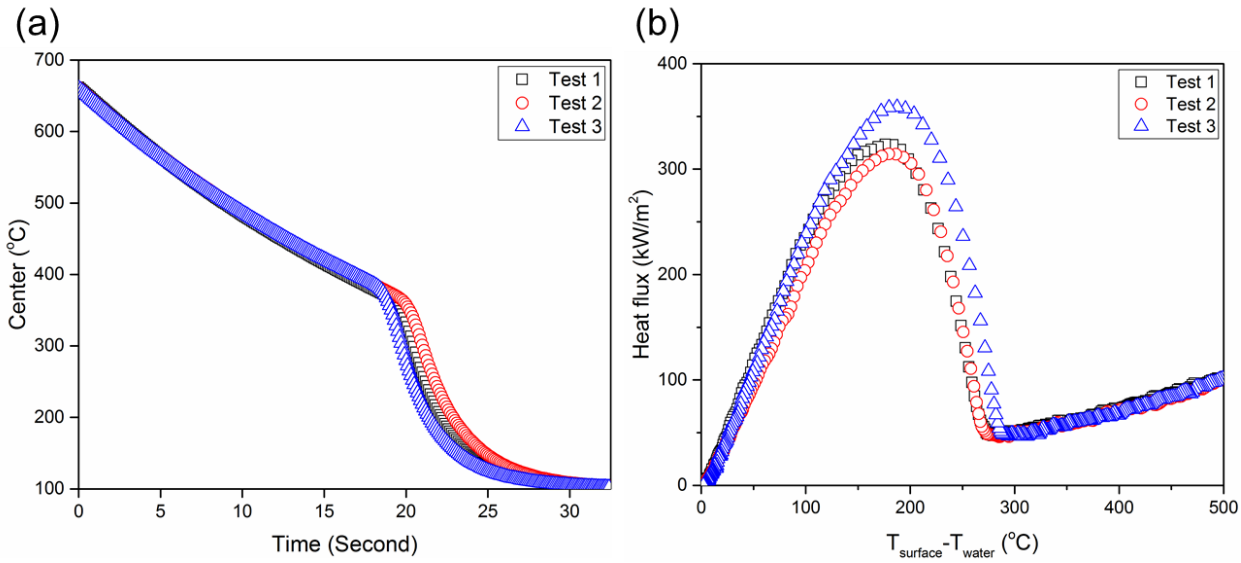

Figure 189: Quenching and Boiling curves of oxidized Zirc-4 (700 °C for 120 minutes) in saturated water at atmospheric pressure.

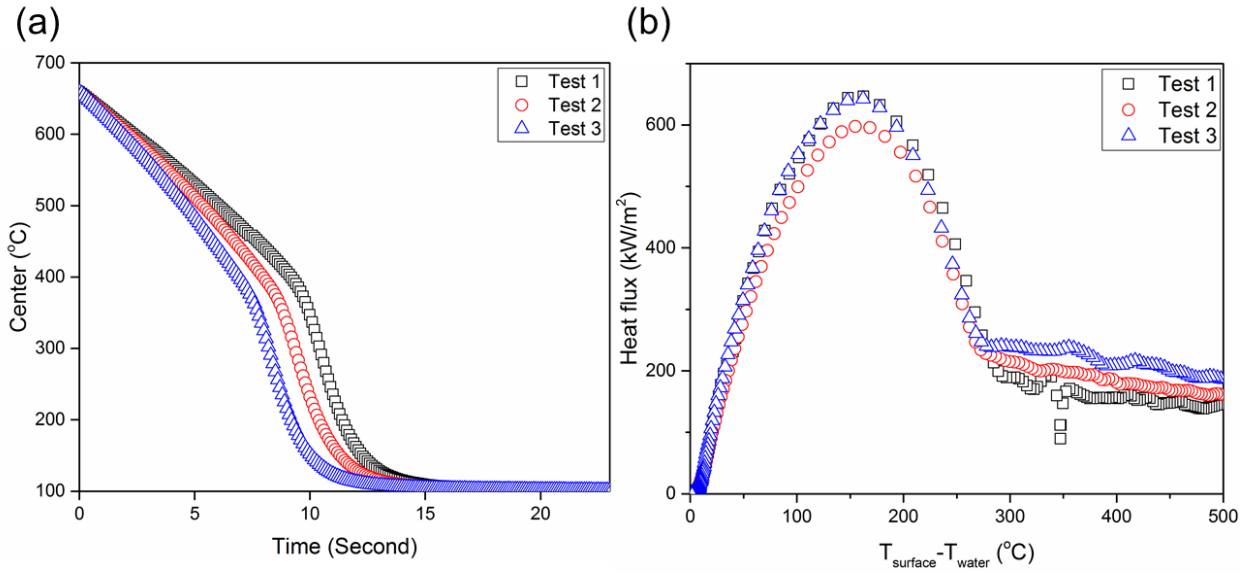

Figure 190: Quenching and Boiling curves of roughened Zirc-4 in saturated water at atmospheric pressure.

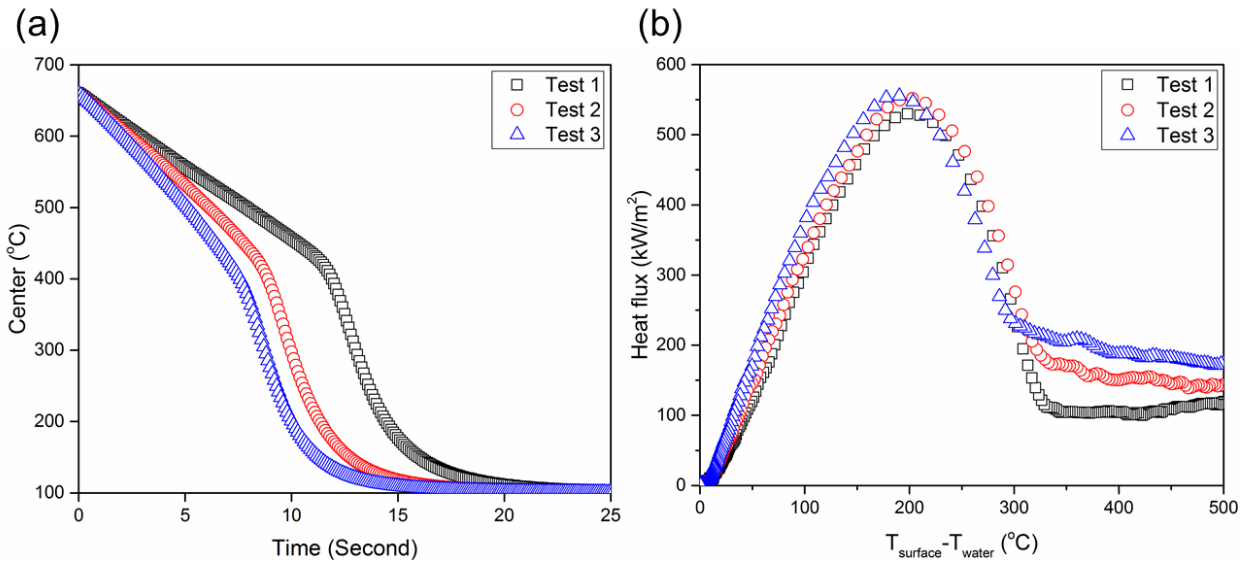

Figure 191: Quenching and Boiling curves of $ZrSi_2$ coating on roughened Zirc-4 in saturated water at atmospheric pressure.

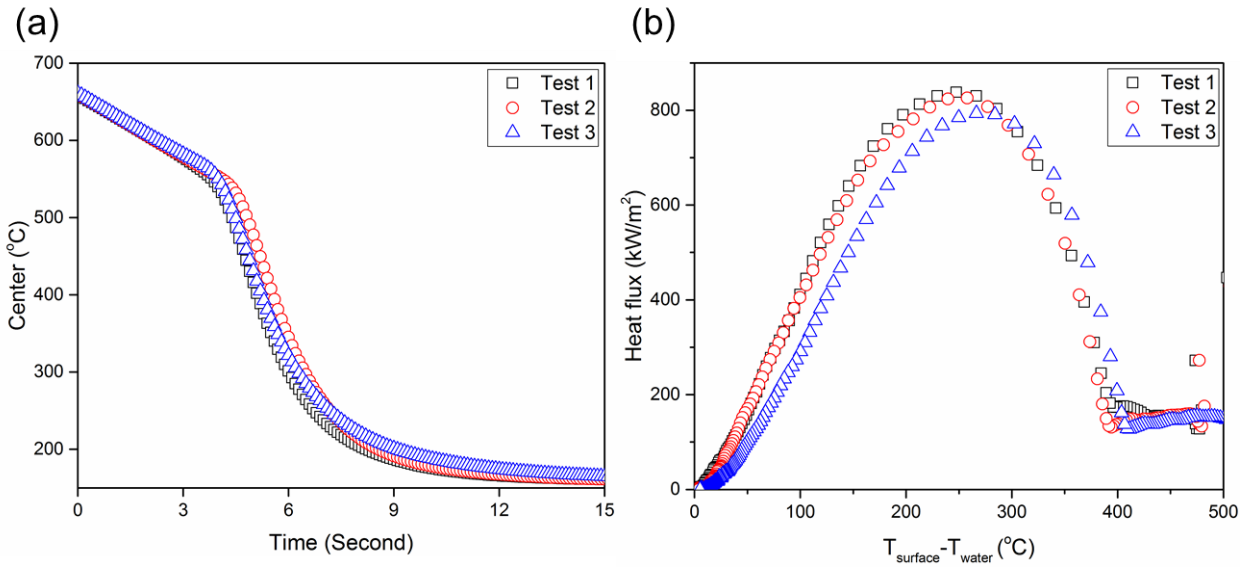

Figure 192: Quenching and Boiling curves of bare Zirc-4 in saturated water at 0.5 MPa.

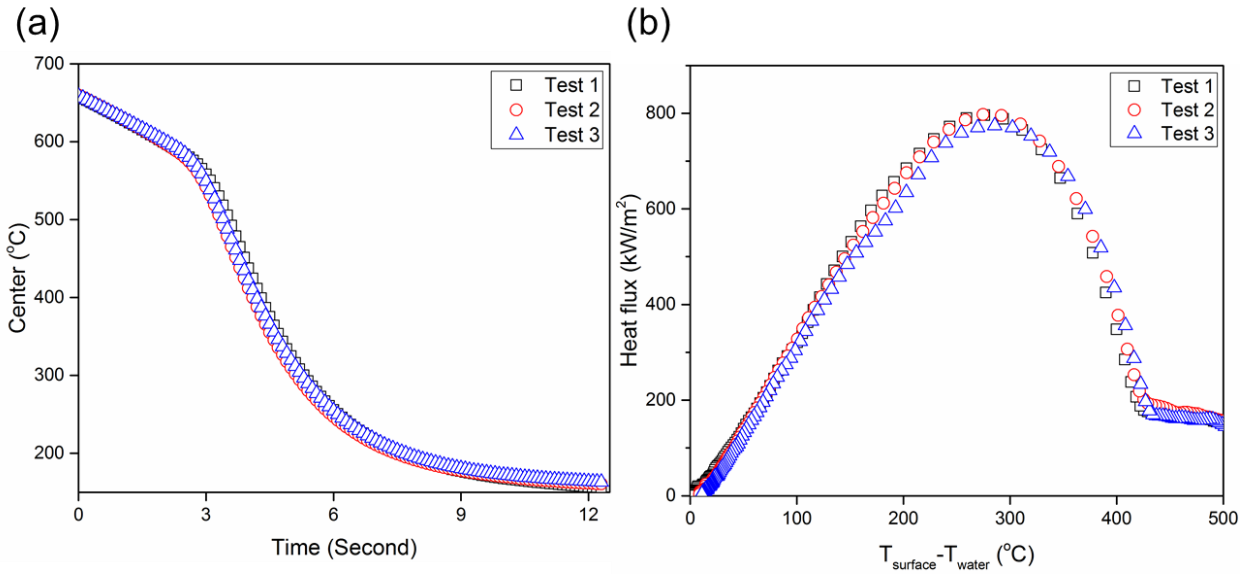

Figure 193: Quenching and Boiling curves of $ZrSi_2$ coating in saturated water at 0.5 MPa.

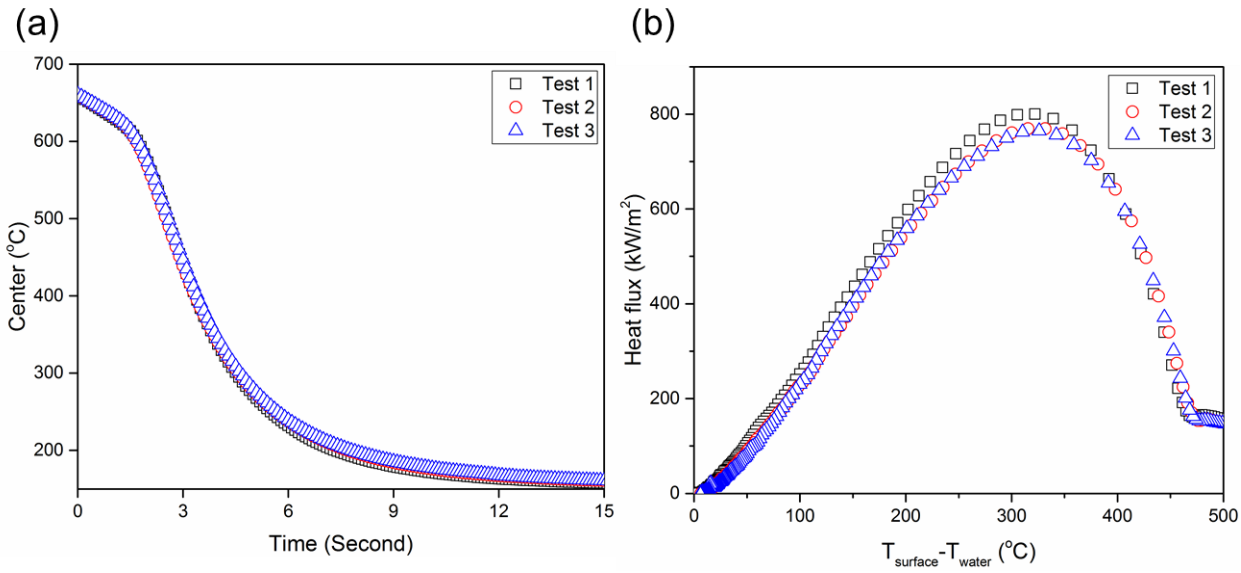

Figure 194: Quenching and Boiling curves of oxidized Zirc-4 (700 °C for 5 hours) in saturated water at 0.5 MPa.

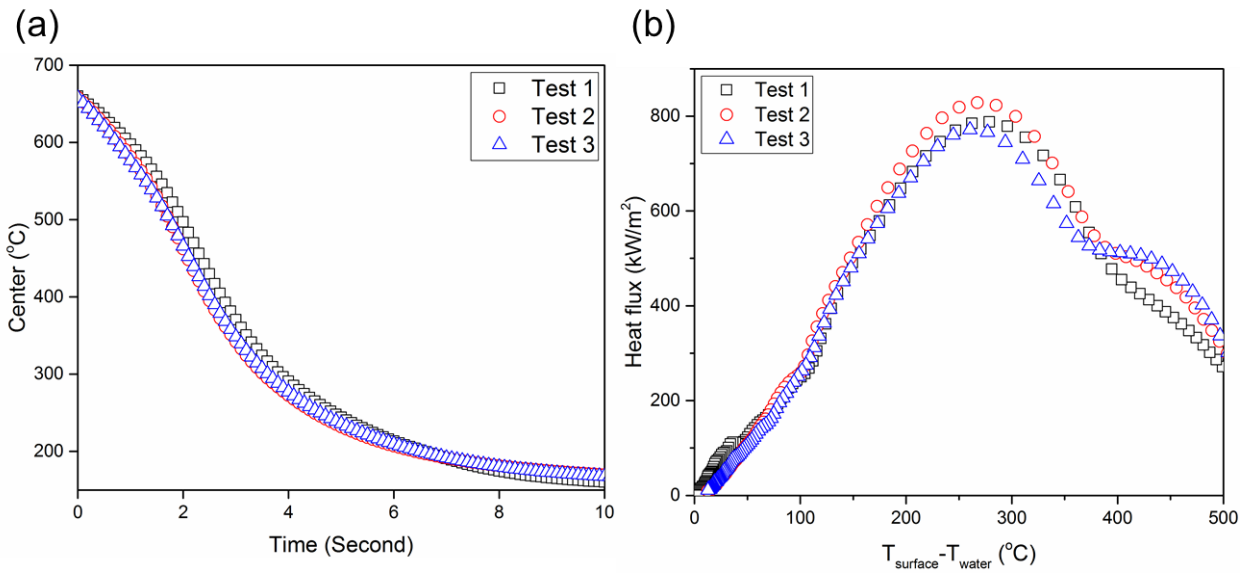

Figure 195: Quenching and Boiling curves of roughened Zirc-4 in saturated water at 0.5 MPa.

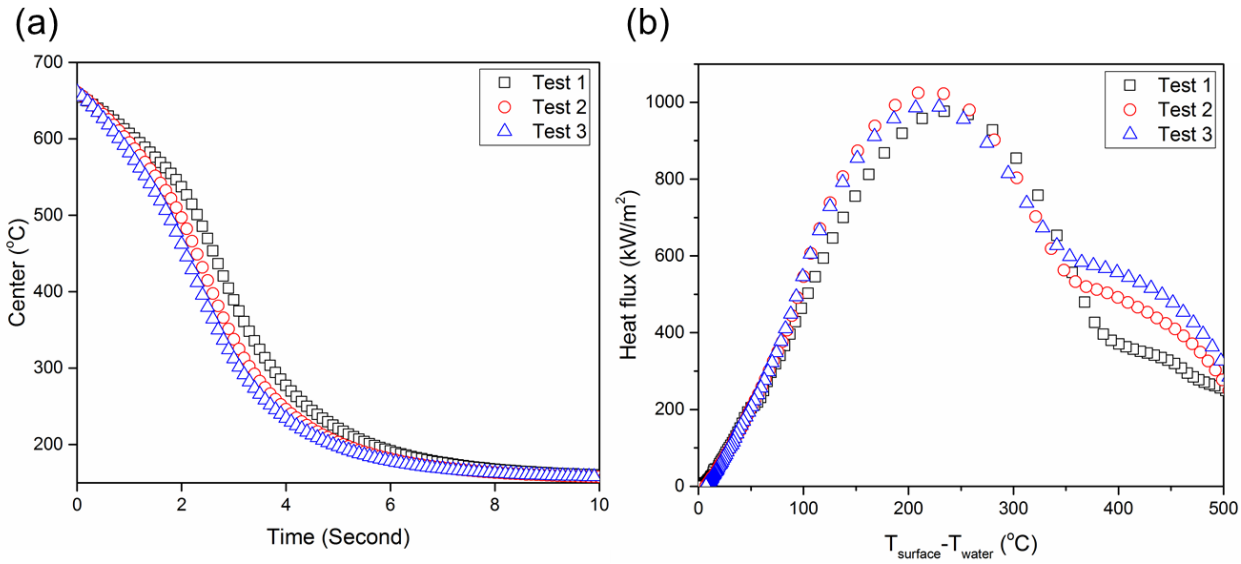

Figure 196: Quenching and Boiling curves of $ZrSi_2$ coating on roughened Zirc-4 in saturated water at 0.5 MPa.

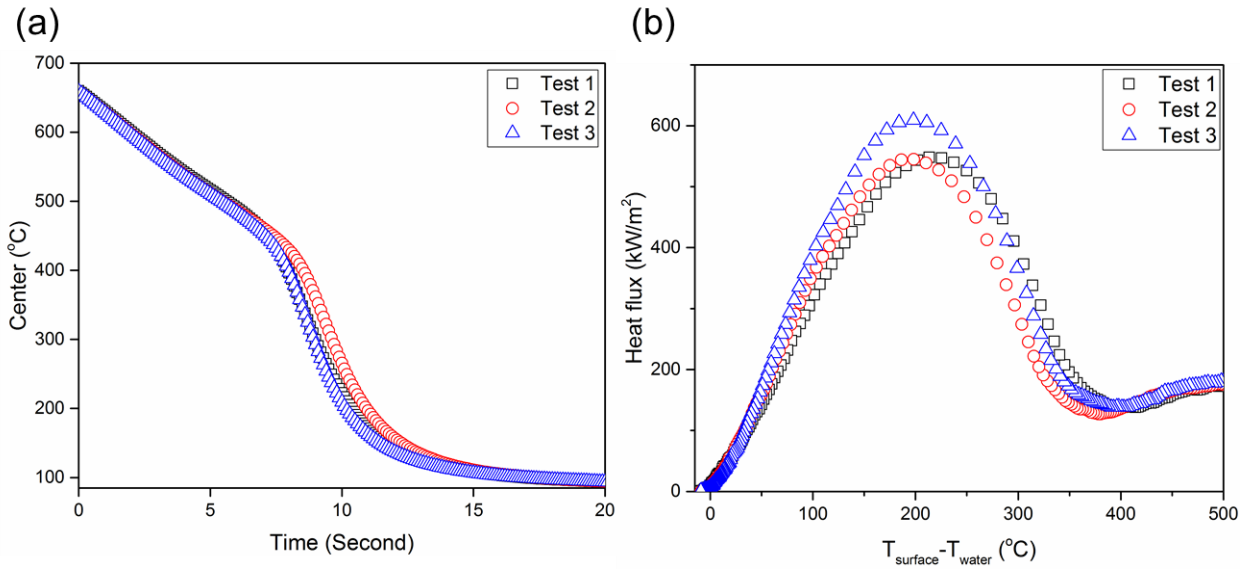

Figure 197: Quenching and Boiling curves of bare Zirc-4 in 15 K subcooled water at atmospheric pressure.

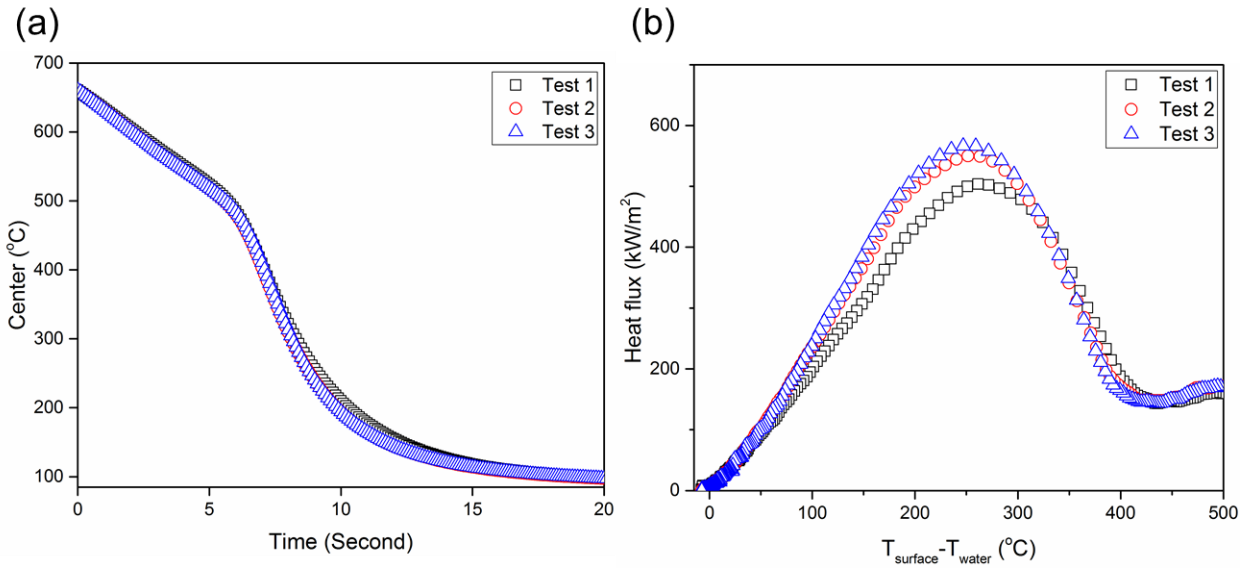

Figure 198: Quenching and Boiling curves of $ZrSi_2$ coating in 15 K subcooled water at atmospheric pressure.

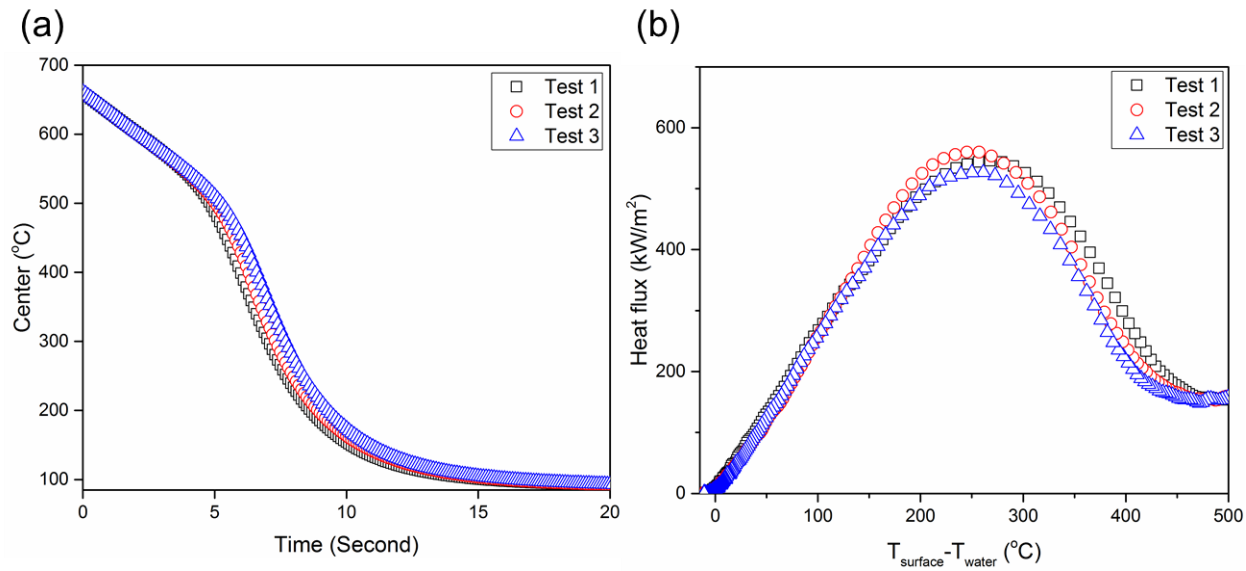

Figure 199: Quenching and Boiling curves of oxidized Zirc-4 (700 °C for 5 hours) in 15 K subcooled water at atmospheric pressure.

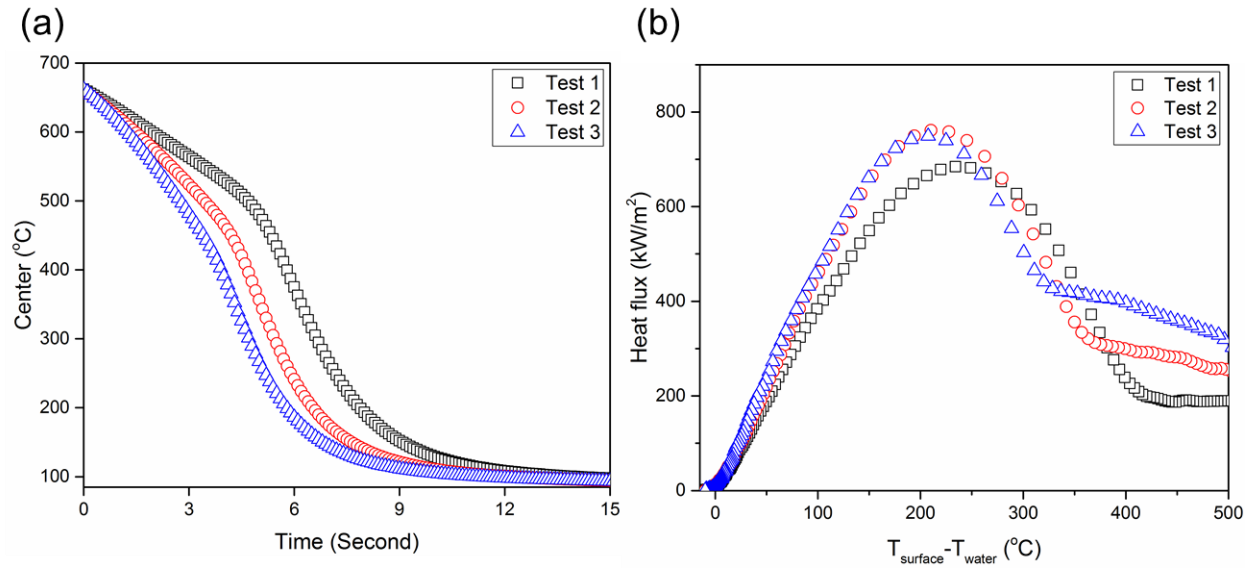

Figure 200: Quenching and Boiling curves of roughened Zirc-4 in 15 K subcooled water at atmospheric pressure.

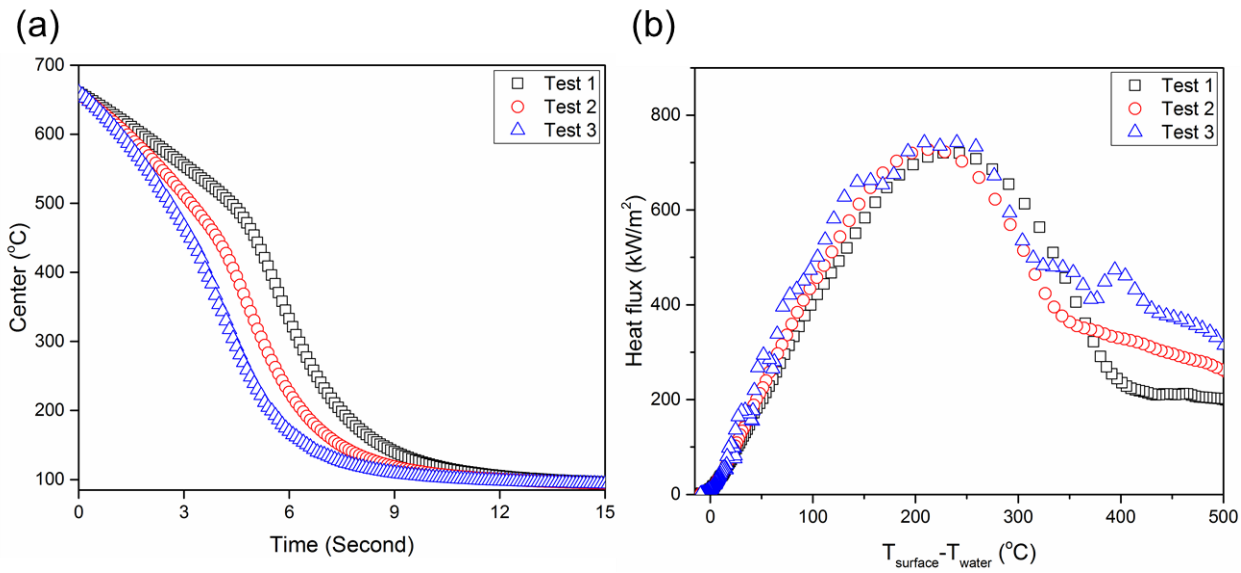

Figure 201: Quenching and Boiling curves of $ZrSi_2$ coating on roughened Zirc-4 in 15 K subcooled water at atmospheric pressure.

Appendix F: Thickness of vapor layer on bare Zirc-4 samples with pressures and degrees of subcooling

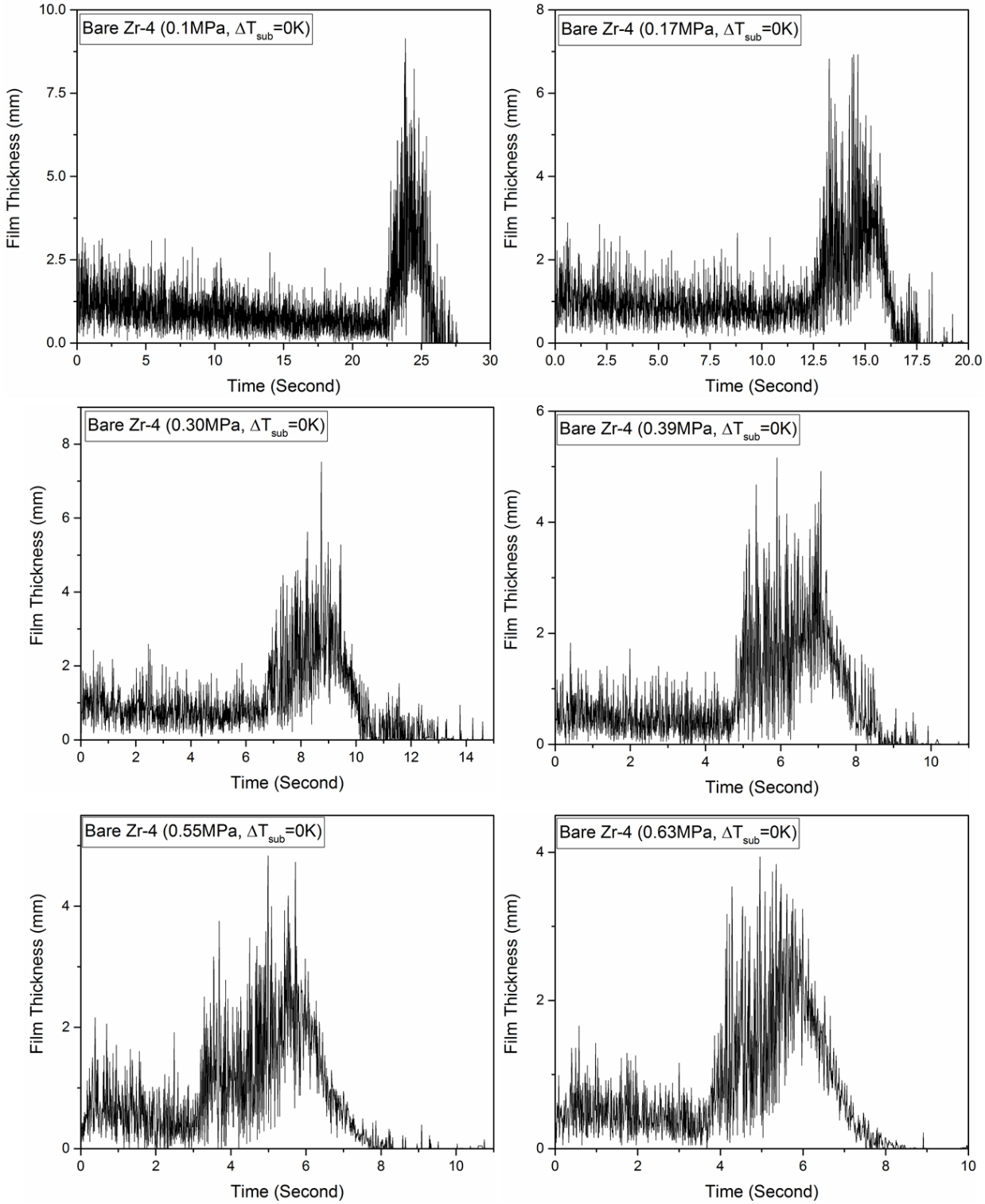

Figure 202: Vapor film vs. quenching time of bare Zirc-4 in saturated water at elevated system pressures.

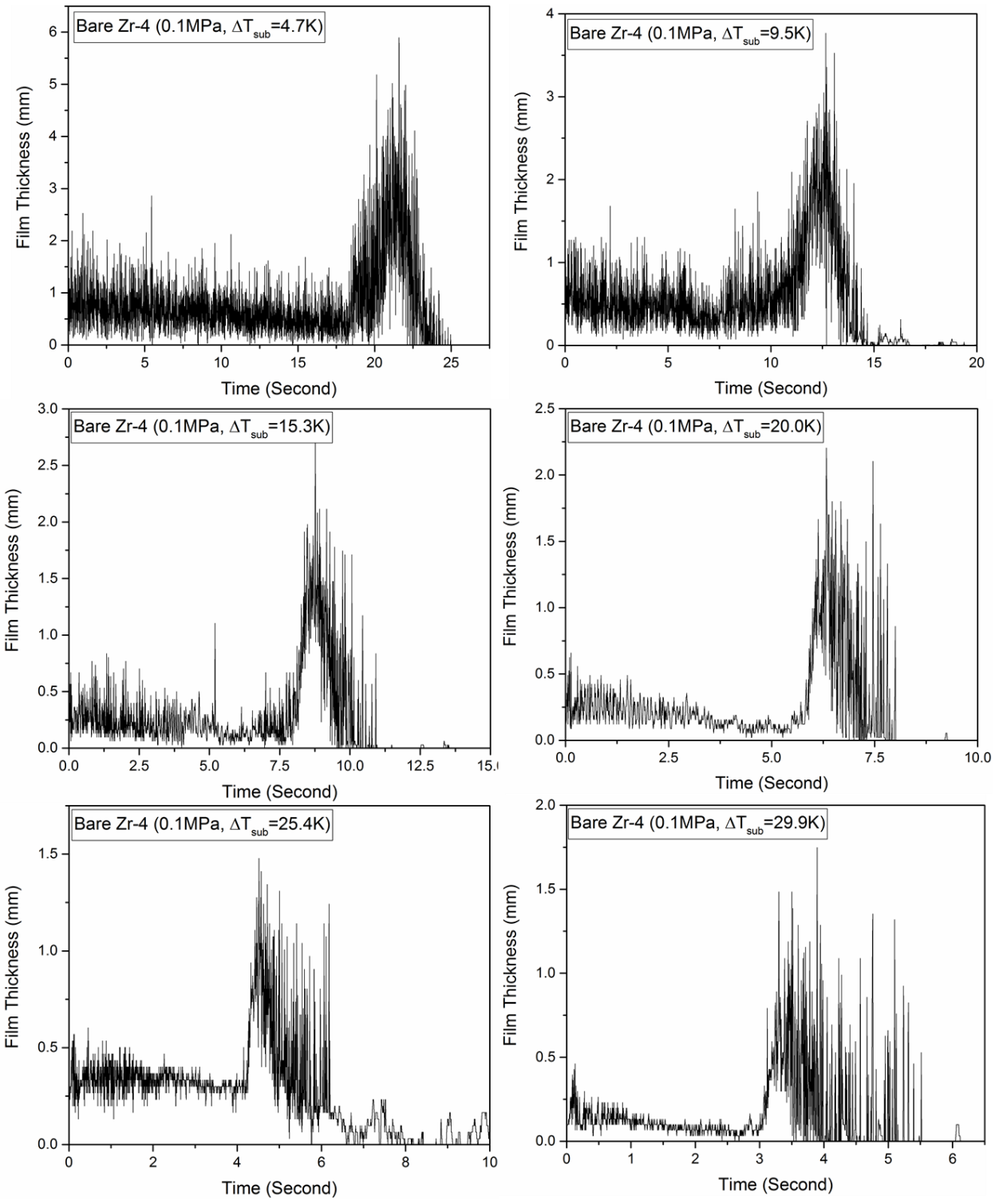

Figure 203: Vapor film vs. quenching time of bare Zirc-4 at different water subcooling at atmospheric pressure.

Appendix G: Oscillations of vapor layer for $ZrSi_2$ coating surfaces and $ZrSi_2$ coating on rough surfaces

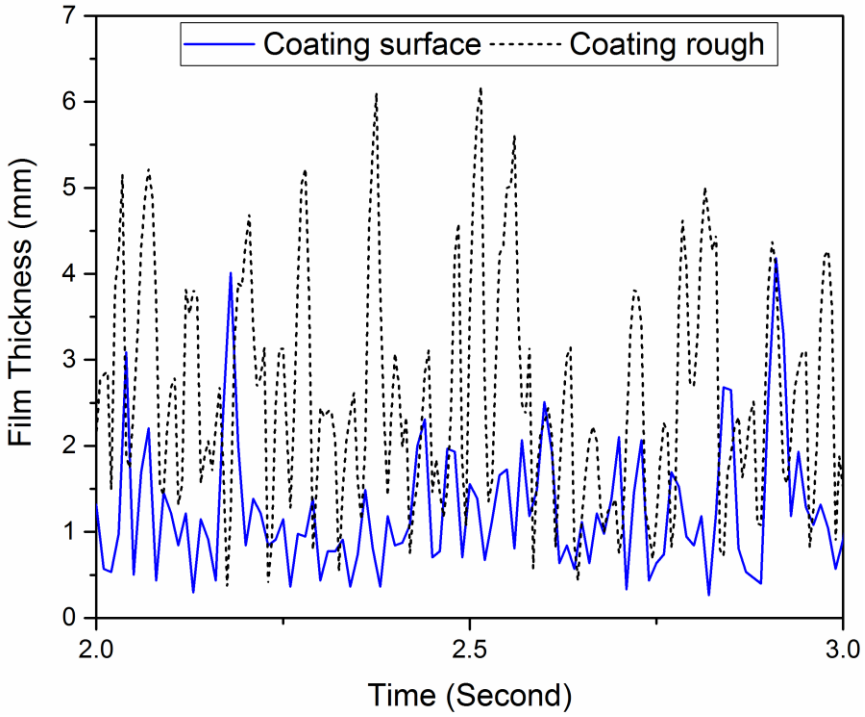

Figure 204: Fluctuation of vapor film at high wall superheat for $ZrSi_2$ coating (blue line) and $ZrSi_2$ coating on rough surface (black dots). The vapor film thickness was measured by high-speed images (100 fps).

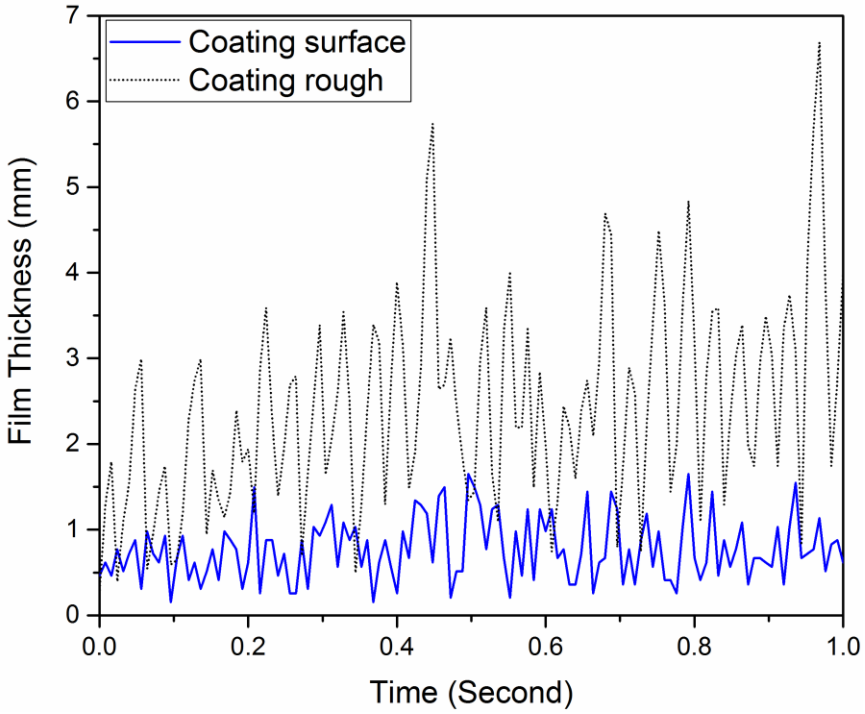

Figure 205: Fluctuation of vapor film at high wall superheat for $ZrSi_2$ coating (blue line) and $ZrSi_2$ coating on rough surface (black dots). The vapor film thickness was measured by high-speed images (100 fps).

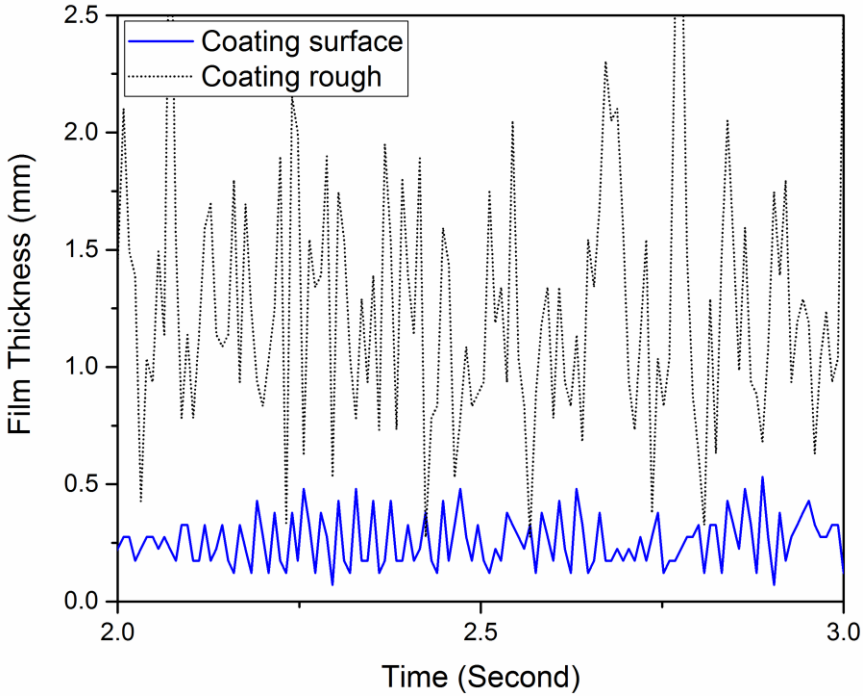

Figure 206: Fluctuation of vapor film at high wall superheat for $ZrSi_2$ coating (blue line) and $ZrSi_2$ coating on rough surface (black dots). The vapor film thickness was measured by high-speed images (125 fps).

Appendix H: Summary of quenching time and minimum film boiling temperatures for all test conditions (environmental effect and surface effect)

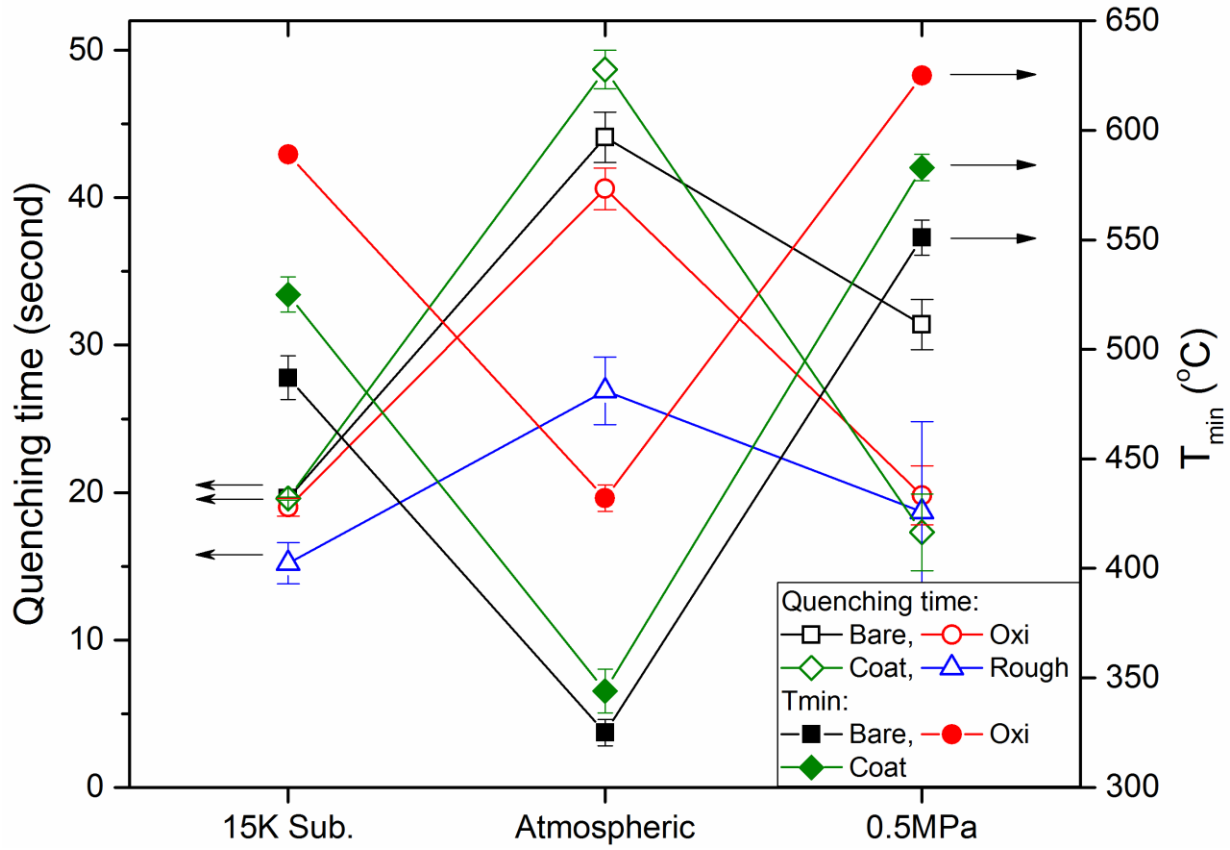

Figure 207: Quenching time and minimum film boiling temperature for the bare surfaces, $ZrSi_2$ coating surfaces, the pre-oxidized surfaces (~55 µm oxide layer), and the rough surfaces in the three experimental conditions - atmospheric water, saturated water at 0.5 MPa, and atmospheric subcooled water (ΔT_{sub} = 15 K).